vehicles

Special Issue Reprint

Intelligent Mobility and Sustainable Automotive Technologies

Edited by
Nicolae Vlad Burnete, Florin Mariasiu and Calin Iclodean

mdpi.com/journal/vehicles

MDPI

Intelligent Mobility and Sustainable Automotive Technologies

Intelligent Mobility and Sustainable Automotive Technologies

Guest Editors

Nicolae Vlad Burnete
Florin Mariasiu
Calin Iclodean

MDPI

Basel • Beijing • Wuhan • Barcelona • Belgrade • Novi Sad • Cluj • Manchester

Guest Editors

Nicolae Vlad Burnete
Department of Automotive Engineering and Transports
Technical University of Cluj-Napoca
Cluj-Napoca
Romania

Florin Mariasiu
Department of Automotive Engineering and Transports
Technical University of Cluj-Napoca
Cluj-Napoca
Romania

Calin Iclodean
Department of Automotive Engineering and Transports
Technical University of Cluj-Napoca
Cluj-Napoca
Romania

Editorial Office

MDPI AG
Grosspeteranlage 5
4052 Basel, Switzerland

This is a reprint of the Special Issue, published open access by the journal *Vehicles* (ISSN 2624-8921), freely accessible at: https://www.mdpi.com/journal/vehicles/special_issues/BWL25MIOU0.

For citation purposes, cite each article independently as indicated on the article page online and as indicated below:

Lastname, A.A.; Lastname, B.B. Article Title. *Journal Name* **Year**, *Volume Number*, Page Range.

ISBN 978-3-7258-8543-5 (Hbk)
ISBN 978-3-7258-8544-2 (PDF)
https://doi.org/10.3390/books978-3-7258-8544-2

© 2026 by the authors. Articles in this reprint are Open Access and distributed under the Creative Commons Attribution (CC BY) license. The reprint as a whole is distributed by MDPI under the terms and conditions of the Creative Commons Attribution-NonCommercial-NoDerivs (CC BY-NC-ND) license (https://creativecommons.org/licenses/by-nc-nd/4.0/).

Contents

About the Editors . . . . . **vii**

Preface . . . . . **ix**

Nicolae Vlad Burnete, Florin Mariașiu and Călin Iclodean
Intelligent Mobility and Sustainable Automotive Technologies
Reprinted from: *Vehicles* **2026**, *8*, 156, https://doi.org/10.3390/vehicles8070156 . . . . . **1**

Aron Csato, Florin Mariasiu and Gergely Csiki
Analysis of the Influence of Image Resolution in Traffic Lane Detection Using the CARLA Simulation Environment
Reprinted from: *Vehicles* **2025**, *7*, 60, https://doi.org/10.3390/vehicles7020060 . . . . . **7**

Zoltán Pusztai, Tamás Luspay and Ferenc Friedler
LTV-LQG Control for an Energy Efficient Electric Vehicle
Reprinted from: *Vehicles* **2025**, *7*, 113, https://doi.org/10.3390/vehicles7040113 . . . . . **20**

Csaba Antonya, Radu Tarulescu, Stelian Tarulescu and Silviu Butnariu
Defining the Optimal Characteristics of Autonomous Vehicles for Public Passenger Transport in European Cities with Constrained Urban Spaces
Reprinted from: *Vehicles* **2025**, *7*, 125, https://doi.org/10.3390/vehicles7040125 . . . . . **40**

Ramona-Monica Stoica, Daniela Voicu and Radu Vilău
Investigation of Bearing Condition by Means of Robust Linear Regression and Informative Predictors
Reprinted from: *Vehicles* **2025**, *7*, 127, https://doi.org/10.3390/vehicles7040127 . . . . . **77**

Mihai Stirosu, Stefan Tabacu and Gabriel Cimpeanu
Investigation on the Manufacturing, Testing, and Simulation Processes of the Hood Hinge Assembly
Reprinted from: *Vehicles* **2025**, *7*, 157, https://doi.org/10.3390/vehicles7040157 . . . . . **93**

Ionut Daniel Geonea, Ilie Dumitru, Laurentiu Racila and Cristian Copilusi
Dynamic Finite Element and Experimental Strain Analysis of a Passenger-Car Rear Axle for Durable and Sustainable Suspension Design
Reprinted from: *Vehicles* **2026**, *8*, 9, https://doi.org/10.3390/vehicles8010009 . . . . . **118**

Radu Tarulescu, Stelian Tarulescu, Razvan Gabriel Boboc and Mircea Nastasoiu
Filtration System for Reducing CO_2 Concentration from Combustion Gases of Used Spark Ignition Engines
Reprinted from: *Vehicles* **2026**, *8*, 19, https://doi.org/10.3390/vehicles8010019 . . . . . **157**

Bauyrzhan Sarsembekov, Madi Issabayev, Nursultan Zharkenov, Altynbek Kaukarov, Isatai Utebayev, Akhmet Murzagaliyev and Baurzhan Zhamanbayev
Ultrasonic–Laser Hybrid Treatment for Cleaning Gasoline Engine Exhaust: An Experimental Study
Reprinted from: *Vehicles* **2026**, *8*, 22, https://doi.org/10.3390/vehicles8010022 . . . . . **177**

Eugen Valentin Butilă, Gheorghe-Daniel Voinea, Răzvan Gabriel Boboc and Grigore Ambrosi
Autonomous Vehicles in the Traffic Ecosystem: A Comprehensive Review of Integration, Impacts, and Policy Implications
Reprinted from: *Vehicles* **2026**, *8*, 41, https://doi.org/10.3390/vehicles8020041 . . . . . **194**

Nicolae Filip, Calin Iclodean and Marius Deac
Probabilistic Modeling of Urban Vehicle Traffic Under COVID-19 Mobility Restrictions Using AI-Based Video Data: A Case Study in Cluj-Napoca
Reprinted from: *Vehicles* **2026**, *8*, 59, https://doi.org/10.3390/vehicles8030059 . . . . . **231**

Elena-Daniela Lupu and Ștefan Lucian Tabacu
System-Level Comparative Assessment of PMSM Rotor Topologies in Battery Electric Vehicles Under the WLTP Driving Cycle
Reprinted from: *Vehicles* **2026**, *8*, 66, https://doi.org/10.3390/vehicles8030066 . . . . . **264**

Iulius Alexandru Tudor and Florin Gîrbacia
Mapping Research Trends in Road Safety: A Topic Modeling Perspective
Reprinted from: *Vehicles* **2026**, *8*, 69, https://doi.org/10.3390/vehicles8040069 . . . . . **298**

Oana-Victoria Stanciuc-Otat, Burkhard Scholz, Ilie Dumitru and Cosmin Berceanu
Assessment of the Risk of Injury in Frontal Collision: Comparison Between Real Crash Tests and Simulation, with Analysis of the Worst-Case Scenarios
Reprinted from: *Vehicles* **2026**, *8*, 77, https://doi.org/10.3390/vehicles8040077 . . . . . **324**

Mihaela Racila, Theodor Oprica, Lucian Matei, Ilie Dumitru, Nicoleta Gencarau and Laurentiu Racila
Algorithmic Classification of Constrained Extrema in Low-Dimensional Problems with Applications to Transport Location Problems
Reprinted from: *Vehicles* **2026**, *8*, 131, https://doi.org/10.3390/vehicles8060131 . . . . . **351**

About the Editors

Nicolae Vlad Burnete

Nicolae Vlad BURNETE is a Professor in the Department of Automotive Engineering and Transports at the Technical University of Cluj-Napoca (UTCN), Romania, and Vice-Rector for International Relations, Communications, and Identity. He holds a Ph.D. in Mechanical Engineering from UTCN, with research focused on the influence of fuel injection on pollutant emissions in compression ignition engines, and completed his postdoctoral research on increasing internal combustion engine efficiency through waste heat recovery using thermoelectric generators. His research interests include internal combustion engines, pollutant emissions, alternative fuels, energy efficiency, thermoelectric conversion, vehicle simulation, intelligent and sustainable mobility, and advanced automotive systems. His scientific activity includes ISI-indexed journal articles, ISI Proceedings papers, BDI-indexed publications, books, book chapters, application guides, and patents, including German and United States patents related to internal combustion engine operation. Professor Burnete has received several research distinctions, including the Romanian Academy "Traian Vuia" Award, and is affiliated with the Romanian Automotive Society, as well as international organizations.

Florin Mariasiu

Florin MARIASIU is a Full Professor at the Technical University of Cluj-Napoca (UTCN), specializing in Automotive and Transport Engineering. He obtained his PhD in Mechanical Engineering from UTCN (2003), as well as his Habilitation diploma in Mechanical Engineering (2015) from UTCN. His areas of research and interest are sustainable energy solutions for mechanical and thermal systems, along with recent concerns related to the application of artificial intelligence tools in engineering and hybrid education in the automotive field. Professor Florin Mariasiu's research activity can be summarized as 4 patents, 16 books/chapters, over 100 published scientific articles, over 1,500 citations, and more than 20 national and international awards and distinctions for research and innovation in the fields of Mechanical and Automotive Engineering.

Calin Iclodean

Calin Iclodean is an Associate Professor (Habil.) in the Department of Automotive Engineering and Transport at the Technical University of Cluj-Napoca, Romania. He holds both a Ph.D. and a Habilitation in Mechanical Engineering. He graduated from the Faculty of Electronics and Telecommunications, Department of Applied Electronics, at the Technical University of Cluj-Napoca in 1994, and has more than 25 years of professional experience in the IT&C sector. His research interests focus on electric and autonomous vehicles, fuel cell vehicles, advanced powertrain systems, electronic control units, in-vehicle communication networks, energy efficiency, computer modeling, and automotive simulation.

Preface

This Reprint presents a collection of high-quality, peer-reviewed articles published in the Special Issue Intelligent Mobility and Sustainable Automotive Technologies. It highlights recent advances in electric and hybrid vehicles, autonomous mobility, advanced powertrain systems, energy management, simulation, manufacturing technologies, and sustainable automotive engineering. Intended for researchers, engineers, and graduate students, this Reprint provides an overview of current trends and emerging technologies while promoting scientific collaboration and innovation toward safer, cleaner, and more efficient mobility.

Nicolae Vlad Burnete, Florin Mariasiu, and Calin Iclodean
Guest Editors

vehicles

MDPI

Editorial

Intelligent Mobility and Sustainable Automotive Technologies

Nicolae Vlad Burnete, Florin Mariașiu and Călin Iclodean *

Department of Automotive Engineering and Transports, Technical University of Cluj-Napoca, 400641 Cluj-Napoca, Romania; vlad.burnete@campus.utcluj.ro (N.V.B.); florin.mariasiu@auto.utcluj.ro (F.M.)
* Correspondence: calin.iclodean@auto.utcluj.ro

1. Introduction

The automotive industry is undergoing a profound transformation driven by decarbonization objectives, digitalization, automation, connectivity, and the demand for safe and sustainable transportation systems. Modern transportation is evolving into a complex ecosystem in which vehicles, infrastructure, users, energy systems, and digital services interact in real time [1–5]. In this context, electrification, automation, artificial intelligence, advanced manufacturing technologies, and alternative propulsion systems are no longer independent research directions, but interdependent elements of modern mobility systems [6–10].

The Special Issue "*Intelligent Mobility and Sustainable Automotive Technologies*" was launched with the objective of gathering recent research contributions addressing the scientific and engineering challenges associated with modern mobility.

Associated with the AMMA 2025 Congress (*Automotive Mobility, Management and Automation*), this Special Issue brings together contributions from researchers, engineers, and specialists from academia, industry, and research institutions. The result is a collection of papers reflecting the diversity and complexity of contemporary automotive research, covering intelligent vehicle systems, advanced control strategies, alternative propulsion technologies, digital engineering methodologies, and emerging transportation concepts.

The published articles address several aspects of the transition toward a future characterized by low- and zero-emission mobility, data-driven decision-making processes, and automated driving functions. Furthermore, they demonstrate that achieving such ambitious goals depends on the integration of expertise from multiple disciplines, including mechanical engineering, electrical and electronic systems, computer science, artificial intelligence, materials engineering, energy systems, and transportation sciences. This interdisciplinary collaboration is essential for addressing the technological, environmental, economic, and societal challenges associated with the mobility of the future.

The findings presented in the included contributions also point to several important trends in automotive research and development: the accelerated adoption of electrified propulsion systems, the growing importance of the Software-Defined Vehicle (SDV) paradigm, the expansion of connected and cooperative mobility ecosystems, the increasing importance of cybersecurity and functional safety, and the need for sustainable manufacturing and lifecycle-oriented design approaches [11–14].

2. Overview of Contributions

The papers featured in this Special Issue address complementary aspects of intelligent mobility and sustainable automotive engineering. This section presents an overview of the fourteen published contributions, focusing on their objectives, methodological approaches,

main findings, contributions, and relevance to the scope of the present issue. Collectively, the papers address various topics of intelligent mobility and sustainable automotive technologies, such as vehicle perception and control, electrified propulsion, emissions reduction, digital engineering, reliability, road safety, traffic systems, and transport optimization.

Csato et al. [15] investigated the influence of image resolution on traffic lane detection performance for Advanced Driver Assistance Systems (ADASs) based on a combination of synthetic data generated in the CARLA simulation environment and real-world data from the TuSimple dataset. Using a U-Net convolutional neural network for image segmentation, the authors evaluated the trade-off between detection accuracy and computational efficiency across different image resolutions. Their results indicated that a resolution of 512×256 offers an effective balance between segmentation performance and real-time processing capability. The study also supports the use of combined synthetic and real datasets for training robust lane detection models in autonomous driving applications.

Pusztai et al. [16] proposed and evaluated a Linear Time-Varying Linear Quadratic Gaussian (LTV-LQG) control strategy for energy-efficient electric vehicles operating under realistic driving conditions. Based on a nonlinear vehicle model and a predefined near-optimal driving trajectory, the authors developed a time-varying controller incorporating a Kalman filter to estimate external disturbances such as wind. The simulation results showed that the proposed approach satisfied travel-time constraints and reduced energy consumption compared with a conventional rule-based driving strategy, particularly under favorable wind conditions.

Antonya et al. [17] addressed the integration of sustainable public transportation into historic urban centers characterized by narrow streets, heritage preservation constraints, and limited infrastructure adaptability. The authors proposed the use of autonomous electric buses and developed a vehicle dynamics and optimization framework that incorporates mobility demand, road network geometry, and vehicle energy consumption. For a set of operational scenarios, the study identified vehicle characteristics that balance energy efficiency with passenger service quality. The proposed methodology provides a decision-support framework for planning autonomous transit solutions in urban environments with multiple constraints.

Stoica et al. [18] studied the condition monitoring of rolling bearings using robust linear regression techniques applied to vibration-based statistical indicators, including RMS, skewness, kurtosis, and crest factor. Experimental data collected under different alignment and rotational speed conditions were analyzed to assess the relationship between operating parameters and vibration behavior. Although bearing misalignment was associated with a slight increase in vibration levels, the statistical analysis indicated no significant influence of either rotational speed or alignment on the measured acceleration signals. The study indicates that robust data analysis methods and appropriate feature selection can improve the reliability of condition monitoring systems in rotating machinery, which makes it relevant to predictive maintenance and reliability assessment in automotive systems.

Stirosu et al. [19] investigated the role of digital transformation in the manufacturing and validation of stamped automotive components. The study combined material testing, LS-DYNA simulations, non-contact dimensional analysis, and digital workflow modeling to evaluate the accuracy and reliability of modern manufacturing processes. The strong agreement between experimental and simulation data confirmed the usefulness of the digital twin method for improving product quality and reducing development time in automotive component design and manufacturing.

Geonea et al. [20] presented an integrated numerical–experimental methodology for assessing and optimizing the durability of a passenger-car rear axle. The authors combined a dedicated suspension test bench with multibody dynamics and a finite element model

https://doi.org/10.3390/vehicles8070156

to evaluate structural behavior under realistic operating conditions. Experimental strain measurements were used to validate the numerical models, allowing the identification of critical stress regions and supporting the optimization of safety-critical suspension components, thereby contributing to durability-oriented vehicle design.

Tarulescu et al. [21] proposed and experimentally evaluated a filtration system designed to reduce CO_2 emissions from spark-ignition engine exhaust gases. The system, based on a reactive aqueous solution containing water, CaO, and MgO, was tested under different operating configurations on a gasoline-powered vehicle. The results showed a measurable reduction in CO_2 emissions without increasing other major pollutants, indicating the potential relevance of the proposed approach for internal combustion engines used in both vehicles and stationary applications. The contribution is aligned with ongoing efforts to mitigate the environmental impact of existing vehicle fleets.

Sarsembekov et al. [22] investigated a hybrid exhaust gas treatment system combining ultrasonic waves and infrared laser irradiation to reduce gasoline engine emissions. Through experimental testing under different operating conditions, the authors assessed the individual and combined effects of ultrasound and laser exposure on exhaust gas composition. The results demonstrated significant reductions in CO and unburned hydrocarbon emissions, with the combined treatment leading to the lowest emission values. The results suggest that physical exhaust treatment technologies could complement existing emission-control solutions to reduce the environmental impact of internal combustion engines.

Butilă et al. [23] presented a comprehensive review of the integration of connected and autonomous vehicles in mixed traffic environments. The review considered implications for road safety, traffic efficiency, infrastructure requirements, urban mobility, and policy development. The authors concluded that the benefits of automation depend strongly on market penetration rates, control strategies, and human behavioral adaptation, noting that early deployment stages may generate new operational challenges. The paper underscores the importance of appropriate regulatory frameworks and integrated mobility policies to ensure that autonomous vehicles contribute to safe, efficient, and sustainable transportation systems.

Filip et al. [24] investigated the impact of COVID-19 mobility restrictions on urban traffic patterns using a combination of radar-based traffic monitoring and AI-assisted video analysis at a signalized intersection in Cluj-Napoca, Romania. By comparing traffic conditions before and during the lockdown period, the authors developed a probabilistic traffic flow model based on the Poisson distribution to characterize vehicle arrival patterns. The results showed a notable reduction in traffic demand and confirmed the predominance of free-flow conditions under low-density scenarios. The study provides insights into urban traffic behavior during extreme mobility disruptions and offers a framework that may support data-driven traffic management and resilient urban mobility planning.

Lupu et al. [25] performed a system-level assessment of permanent magnet synchronous motor rotor topologies for battery electric vehicles operating under the WLTP driving cycle. Using detailed energy-based models of the traction motor, inverter, and battery, the authors evaluated the influence of rotor design and regenerative braking on overall vehicle efficiency and driving range. The results showed that rotor topology has a significant impact on energy consumption, with the dual-layer interior permanent magnet configuration providing improved efficiency and extended driving range compared with a conventional design. The authors emphasize the importance of considering realistic operating conditions when optimizing electric powertrain components for next-generation battery electric vehicles.

Tudor et al. [26] conducted a large-scale bibliometric and topic-modeling analysis of road safety research published between 2016 and 2025 to identify emerging trends in

https://doi.org/10.3390/vehicles8070156

the field. Using a transformer-based BERTopic framework, the authors analyzed more than 15,000 scientific publications and identified key research themes related to crash severity, human factors, vulnerable road users, artificial intelligence applications, and spatial safety analysis. The results indicate a growing emphasis on predictive and AI-supported approaches to road safety within intelligent transportation systems, reflecting a shift from traditional post-crash investigations toward proactive and data-driven risk assessment. The study also provides an overview of the evolving road safety landscape as well as the opportunities and challenges associated with the adoption of advanced analytical technologies in intelligent transportation systems.

Stanciuc-Otat et al. [27] investigated occupant injury risk in full-overlap frontal collisions through a combined experimental and numerical analysis. Using FMVSS 208 crash tests with Hybrid III anthropomorphic test devices and complementary LS-DYNA simulations, the authors evaluated the influence of impact speed, seat belt use, and occupant anthropometry on injury outcomes. The results identified the parameters with the greatest effect on occupant safety and highlighted the importance of physical crash testing for validating injury assessment methodologies. The study also provides insights relevant to the development of safer vehicle restraint systems and broader road safety objectives.

Racila et al. [28] presented an algorithmic framework for the classification of constrained extrema in low-dimensional optimization problems, with applications in transport and logistics location planning. The proposed method replaces the explicit manipulation of constraint differentials with algebraic test coefficients derived from the Lagrangian formulation. Its application to a transport depot location problem demonstrates its potential as a transparent and computationally efficient decision-support tool for transport and logistics infrastructure planning.

3. Future Directions

The contributions presented in this Special Issue address several challenges central to the development of intelligent and sustainable mobility. Collectively, the published papers highlight the growing importance of data-driven methodologies, advanced simulation environments, intelligent control systems, and sustainable propulsion technologies in the development of next-generation vehicles.

Future research is likely to focus increasingly on software-defined vehicles, artificial intelligence and machine learning applications, cybersecurity and functional safety, digital twins and virtual validation platforms, connected and cooperative mobility, and advanced electrified and hydrogen-based propulsion systems.

Equally important will be the development and adoption of holistic approaches that integrate technological innovation with sustainability, economic viability, regulatory compliance, and societal acceptance.

The articles gathered in this Special Issue provide a useful basis for further research and collaboration aimed at developing safer, smarter, and more sustainable mobility solutions.

The launch of "*Intelligent Mobility and Sustainable Automotive Technologies, 2nd Edition*" continues this thematic focus and provides a further venue for research in intelligent and sustainable mobility.

Acknowledgments: The authors sincerely thank the editorial team of *Vehicles* for their support in organizing this Special Issue. The authors also wish to thank all the contributing authors for their valuable work and the reviewers for their thoughtful comments and suggestions.

Conflicts of Interest: The authors declare no conflicts of interest.

https://doi.org/10.3390/vehicles8070156

References

1. Kashem, M.A.; Shamsuddoha, M.; Nasir, T. Sustainable Transportation Solutions for Intelligent Mobility: A Focus on Renewable Energy and Technological Advancements for Electric Vehicles (EVs) and Flying Cars. *Future Transp.* **2024**, *4*, 874–890. [CrossRef]
2. Elassy, M.; Al-Hattab, M.; Takruri, M.; Badawi, S. Intelligent transportation systems for sustainable smart cities. *Transp. Eng.* **2024**, *16*, 100252. [CrossRef]
3. Satpathy, P.R.; Ramachandaramurthy, V.K.; Radha Krishnan, T.R.; Padmanaban, S. Technological innovations and sustainable strategies for advancing electric vehicle performance and market integration. *Energy Strategy Rev.* **2025**, *60*, 101790. [CrossRef]
4. Dakić, P.; Stupavský, I.; Todorović, V. The Effects of Global Market Changes on Automotive Manufacturing and Embedded Software. *Sustainability* **2024**, *16*, 4926. [CrossRef]
5. Kussl, S.; Wald, A. Smart Mobility and its Implications for Road Infrastructure Provision: A Systematic Literature Review. *Sustainability* **2023**, *15*, 210. [CrossRef]
6. Verde, A.; Meléndez-Useros, M.; Viadero-Monasterio, F. A Literature Review on Challenges and Solutions for Smart and Sustainable Urban Mobility. *Urban. Sci.* **2026**, *10*, 326. [CrossRef]
7. Di Gerlando, A.; Gobbi, M.; Magnanini, M.C. Circularity potential of electric motors in e-mobility: Methods, technologies, challenges. *J. Remanufactur.* **2024**, *14*, 315–357. [CrossRef]
8. Santos, C.; Neto, M.K.; Kanieski, J.M.; Rufino Júnior, C.A.; Schweiger, H.-G.; Zanin, H. A multidimensional assessment of electrification in automotive powertrains: Technical, operational, and strategic perspectives. *Results Eng.* **2025**, *28*, 107377. [CrossRef]
9. Kovačić, M.; Mutavdžija, M.; Buntak, K. New Paradigm of Sustainable Urban Mobility: Electric and Autonomous Vehicles—A Review and Bibliometric Analysis. *Sustainability* **2022**, *14*, 9525. [CrossRef]
10. Rojek, I.; Dostatni, E.; Kopowski, J.; Lewandowski, J.; Mikołajewski, D. Automation and Sustainability—The Impact of AI on Energy Consumption and Other Key Features of Industry 4.0/5.0 Technologies. *Appl. Sci.* **2026**, *16*, 2550. [CrossRef]
11. Gao, J.; Qiu, Y.; Chen, Z. Systemic Integration of EV and Autonomous Driving Technologies: A Study of China's Intelligent Mobility Transition. *World Electr. Veh. J.* **2025**, *16*, 574. [CrossRef]
12. Hey, F.; Zombek, M. Digital Control and Market Power in the Automotive Sector: OEMs, Gatekeeping, and the Future of Aftermarket Regulation. *J. Ind. Compet. Trade* **2026**, *26*, 8. [CrossRef]
13. Braidy, A.; Pokharel, S.; ElMekkawy, T.Y. Research Perspectives on Innovation in the Automotive Sector. *Sustainability* **2025**, *17*, 2795. [CrossRef]
14. Khamis, A.; Goswami, P. Rethinking Vehicle Architecture Through Softwarization and Servitization. *IEEE Access* **2025**, *13*, 126213. [CrossRef]
15. Csato, A.; Mariasiu, F.; Csiki, G. Analysis of the Influence of Image Resolution in Traffic Lane Detection Using the CARLA Simulation Environment. *Vehicles* **2025**, *7*, 60. [CrossRef]
16. Pusztai, Z.; Luspay, T.; Friedler, F. LTV-LQG Control for an Energy Efficient Electric Vehicle. *Vehicles* **2025**, *7*, 113. [CrossRef]
17. Antonya, C.; Tarulescu, R.; Tarulescu, S.; Butnariu, S. Defining the Optimal Characteristics of Autonomous Vehicles for Public Passenger Transport in European Cities with Constrained Urban Spaces. *Vehicles* **2025**, *7*, 125. [CrossRef]
18. Stoica, R.; Voicu, D.; Vilău, R. Investigation of Bearing Condition by Means of Robust Linear Regression and Informative Predictors. *Vehicles* **2025**, *7*, 127. [CrossRef]
19. Stirosu, M.; Tabacu, S.; Cimpeanu, G. Investigation on the Manufacturing, Testing, and Simulation Processes of the Hood Hinge Assembly. *Vehicles* **2025**, *7*, 157. [CrossRef]
20. Geonea, I.; Dumitru, I.; Racila, L.; Copilusi, C. Dynamic Finite Element and Experimental Strain Analysis of a Passenger-Car Rear Axle for Durable and Sustainable Suspension Design. *Vehicles* **2026**, *8*, 9. [CrossRef]
21. Tarulescu, R.; Tarulescu, S.; Boboc, R.; Nastasoiu, M. Filtration System for Reducing CO2 Concentration from Combustion Gases of Used Spark Ignition Engines. *Vehicles* **2026**, *8*, 19. [CrossRef]
22. Sarsembekov, B.; Issabayev, M.; Zharkenov, N.; Kaukarov, A.; Utebayev, I.; Murzagaliyev, A.; Zhamanbayev, B. Ultrasonic–Laser Hybrid Treatment for Cleaning Gasoline Engine Exhaust: An Experimental Study. *Vehicles* **2026**, *8*, 22. [CrossRef]
23. Butilă, E.; Voinea, G.; Boboc, R.; Ambrosi, G. Autonomous Vehicles in the Traffic Ecosystem: A Comprehensive Review of Integration, Impacts, and Policy Implications. *Vehicles* **2026**, *8*, 41. [CrossRef]
24. Filip, N.; Iclodean, C.; Deac, M. Probabilistic Modeling of Urban Vehicle Traffic Under COVID-19 Mobility Restrictions Using AI-Based Video Data: A Case Study in Cluj-Napoca. *Vehicles* **2026**, *8*, 59. [CrossRef]
25. Lupu, E.; Tabacu, Ș. System-Level Comparative Assessment of PMSM Rotor Topologies in Battery Electric Vehicles Under the WLTP Driving Cycle. *Vehicles* **2026**, *8*, 66. [CrossRef]
26. Tudor, I.; Gîrbacia, F. Mapping Research Trends in Road Safety: A Topic Modeling Perspective. *Vehicles* **2026**, *8*, 69. [CrossRef]

27. Stanciuc-Otat, O.; Scholz, B.; Dumitru, I.; Berceanu, C. Assessment of the Risk of Injury in Frontal Collision: Comparison Between Real Crash Tests and Simulation, with Analysis of the Worst-Case Scenarios. *Vehicles* **2026**, *8*, 77. [CrossRef]
28. Racila, M.; Oprica, T.; Matei, L.; Dumitru, I.; Gencarau, N.; Racila, L. Algorithmic Classification of Constrained Extrema in Low-Dimensional Problems with Applications to Transport Location Problems. *Vehicles* **2026**, *8*, 131. [CrossRef]

Disclaimer/Publisher's Note: The statements, opinions and data contained in all publications are solely those of the individual author(s) and contributor(s) and not of MDPI and/or the editor(s). MDPI and/or the editor(s) disclaim responsibility for any injury to people or property resulting from any ideas, methods, instructions or products referred to in the content.

vehicles

MDPI

Article

Analysis of the Influence of Image Resolution in Traffic Lane Detection Using the CARLA Simulation Environment

Aron Csato [1], Florin Mariasiu [1,2,*] and Gergely Csiki [1]

[1] Automotive Engineering and Transport Department, Technical University of Cluj-Napoca, Bdul. Muncii 103-105, 400114 Cluj-Napoca, Romania; csato.jo.aron@campus.utcluj.ro (A.C.); gergely.csiki@campus.utcluj.ro (G.C.)
[2] EMARC Research Centre, Technical University of Cluj-Napoca, Bdul. Muncii 103-105, 400114 Cluj-Napoca, Romania
* Correspondence: florin.mariasiu@auto.utcluj.ro

Abstract: Computer vision is one of the key technologies of advanced driver assistance systems (ADAS), but the incorporation of a vision-based driver assistance system (still) poses a great challenge due to the special characteristics of the algorithms, the neural network architecture, the constraints, and the strict hardware/software requirements that need to be met. The aim of this study is to show the influence of image resolution in traffic lane detection using a virtual dataset from virtual simulation environment (CARLA) combined with a real dataset (TuSimple), considering four performance parameters: Mean Intersection over Union (mIoU), F1 precision score, Inference time, and processed frames per second (FPS). By using a convolutional neural network (U-Net) specifically designed for image segmentation tasks, the impact of different input image resolutions (512 × 256, 640 × 320, and 1024 × 512) on the efficiency of traffic line detection and on computational efficiency was analyzed and presented. Results indicate that a resolution of 512 × 256 yields the best trade-off, offering high mIoU and F1 scores while maintaining real-time processing speeds on a standard CPU. A key contribution of this work is the demonstration that combining synthetic and real datasets enhances model performance, especially when real data is limited. The novelty of this study lies in its dual analysis of simulation-based data and image resolution as key factors in training effective lane detection systems. These findings support the use of synthetic environments in training neural networks for autonomous driving applications.

Keywords: ADAS; traffic line detection; CARLA; simulation; U-Net; deep learning

1. Introduction

According to the World Health Organization, nearly one-third of the global population will reside in cities by 2030, resulting in many new challenges in urban areas, especially in transportation. Recognizing this challenge, the European Commission released the Transport White Paper in 2011 [1], highlighting the need for innovative mobility solutions to ensure sustainability and safety in transportation. In terms of safety, the paper set a goal to reduce the number of fatalities caused by road accidents in the EU by half between 2010 and 2020. Despite this, over 25,700 people lost their lives on EU roads in 2014 alone, with many of these accidents attributed to improper driver behavior. Furthermore, the National Highway Traffic Safety Administration (NHTSA), reported [2] that human factors contribute to 94% of road accidents. These factors include inappropriate speed, driver

distraction, and age-related issues such as impaired vision, slower reflexes, and reduced joint mobility.

Considering the above facts, new technologies such as autonomous driving (AD) and advanced driver assistance systems (ADAS) have been at the center of research and development in recent decades. Advanced driver assistance systems (ADAS) are essential through direct contributions related to improving safety by significantly reducing human error, improving the driving experience through systems that relieve the driver of monitoring the journey, and reducing road accidents by automating responses to dangerous traffic situations. Through the primary results obtained and with the development of hardware and software components and systems, AD technology has made significant progress in its applicability in the automotive and transportation industries, being considered one of the emerging technologies of the fourth industrial revolution. The initial challenging and unresolved issues regarding safety and implementation in vehicle construction and operation were resolved once modern Artificial Intelligence (AI) methods emerged through Deep Learning (DL) processes, supported by:

- Advances in computer vision;
- Data and knowledge accumulated in vehicle dynamics;
- Development and availability of new sensors;
- Datasets for different operating situations;
- Hyper-realistic simulators.

Thus, more and more advanced driver assistance systems are being implemented, which either alert the driver to dangerous situations that may arise in traffic or take measures or assist the driver in difficult situations. However, it should be remembered that, currently, the successful development and implementation of a reliable and fully functional autonomous driving system represents one of the most difficult challenges and tasks in automotive engineering.

The main challenge in the development of ADAS systems is the perception problem [3] or, in other words, how vehicles based on sensors interpret the world around them (other vehicles, pedestrians, obstacles, roads, lanes, etc.—all components of traffic environments). Semi- and fully autonomous vehicles are expected to share the road with human drivers, so the main perceptual cues for an AD or ADAS system remain the same as for humans. The main cues that human drivers use to indicate the route they intend to follow are, for example, road markings and road boundaries; autonomous driving systems must fulfill this task while ensuring traffic safety. Therefore, the most promising path for autonomous driving systems remains the perception of the road, lane, and markings using traditional cues [4].

Determining road boundaries and the number and location of traffic lanes in diverse contexts, including urban, rural, and highway contexts, are essential components of road and lane perception. Despite significant advances in recent years, current perceptual systems still struggle with this type of understanding, and several types of sensors have been tested and researched for road and lane understanding: monocular vision (a single video camera), stereo vision, LIDAR, vehicle dynamics information obtained from the vehicle computer or an inertial measurement unit (IMU), and global positioning information obtained using the global positioning system (GPS) [5,6]. Since markings are designed for human vision, the most advanced area of research in lane detection is the ability to accurately obtain road and lane data through the visual process. Other complementary systems, such as GPS and LIDAR, provide additional information (which can validate the data obtained through vision).

These road and lane detection processes provide a lot of data necessary for interpretation and thus lend themselves to the use of DL methods. Vision-based deep learning

DL systems for various functions in AD and ADAS have made and continue to make significant progress in recent years [7,8]. State-of-the-art neural networks now achieve remarkable results on public, real-world benchmarks, but for training neural networks, it must be remembered that they require large, large-scale, labeled datasets (structured data). Obtaining these datasets is a difficult, time-consuming, and relatively expensive process. In this regard, current research is focused on the possibility of acquiring labeled training data using simulation environments (e.g., CARLA [9]). While numerous works have demonstrated the effectiveness of deep learning-based lane detection using either real or synthetic datasets, relatively few have explored the integration of synthetic and real-world data to enhance model robustness. Additionally, limited research exists on understanding how image resolution affects the trade-off between lane detection accuracy and computational efficiency. This study addresses both gaps by evaluating a U-Net segmentation model trained on real, synthetic, and mixed datasets across multiple image resolutions to identify an optimal configuration for effective and efficient lane detection.

2. Related Work

Lane detection is a fundamental capability that enables fully functional autonomous driving systems. Over the past decade, numerous approaches have been proposed for lane detection, which can generally be categorized along two key dimensions: Model-based vs. Learning-based methods and Real-world vs. Synthetic datasets.

2.1. Model-Based vs. Learning-Based Methods

Model-based techniques rely on geometric models and traditional image processing algorithms—such as edge detection and Hough transforms—to identify lane features. These methods are usually lightweight but often struggle under complex environmental conditions. For example, Shashidhar et al. [10] used a model-based approach combining Gaussian filtering, Canny edge detection, and the Hough transformation to achieve a 92% accuracy in band detection. Learning-based methods, on the other hand, employ deep learning techniques and convolutional neural networks (CNNs) to learn features directly from image data. These approaches have demonstrated superior accuracy and adaptability to changing environments, such as poor lighting or adverse weather conditions. Swain and Tripathy [11] developed a YOLOV5-based lane detection model using extensive preprocessing and achieved 89% accuracy at 48 FPS. Song et al. [12] proposed IAED, a CNN with attention modules, improving robustness in complex environments. Liu et al. [13] introduced a top-down lane detection architecture with conditional convolution and a recurrent instance module, while Baek et al. [14] and Chng et al. [15] focused on real-time performance improvements with CNN-based models.

2.2. Real-World vs. Synthetic Datasets

Many traditional and learning-based methods have relied solely on real-world datasets like TuSimple and CULane. On the other hand, synthetic datasets generated using simulation platforms have gained popularity, and the open-source virtual simulation environment CARLA offers several benefits related to the number of sensors that can be synthesized, ground annotations, and the diversity of adverse weather conditions (compared to other virtual simulation environments) [16–18]. They allow for scenario customization and large-scale data generation, and furthermore, the datasets offer the possibility of investigating valuable real-world traffic scenarios involving rare or boundary conditions. Examples of the use of this advantage in research are those published by Swain and Tripathy [10], Song et al. [12], and Liu et al. [13] who conducted experiments using the TuSimple and CULane databases to validate their learning-based methods. Furthermore, to benefit from

the advantages offered by virtual simulation environments, Jeon et al. [19] used CARLA to evaluate the performance of sensors in heavy rain and found that the detection accuracy, especially for curved lanes, decreased with increasing precipitation (something difficult to achieve in real traffic conditions).

2.3. Our Contribution

Unlike most prior studies, this work investigates the trade-off between image resolution and performance, and it combines both real and synthetic data for training. The use of CARLA as a simulation environment allows for efficient generation of high-quality labeled data and the modeling of rare scenarios. By comparing three different input resolutions (512×256, 640×320, and 1024×512), this study identifies an optimal setting that balances accuracy (mIoU and F1 score) and real-time performance (inference time and FPS). Training was conducted using three dataset configurations: images solely from CARLA (3890 labeled), solely from TuSimple (3626 labeled), and a balanced mix (1750 from each). The model's performance was evaluated using four key metrics: Mean Intersection over Union (mIoU), F1 precision score, inference time, and processed frames per second (FPS).

3. Materials and Methods

3.1. CARLA (CAR Learning to Act) Simulation Environment

The CARLA (Car Learning to Act) simulation environment is an open-source simulator for urban environment simulation, focusing on creating a publicly available virtual environment applicable to specific requirements in the automotive industry. Many individual contributors are constantly working to improve it, and as a result, the current version of the CARLA simulation environment (version 0.9.12) is a powerful and suitable tool for simulating real-world scenarios. CARLA was developed from the ground up to support training, prototyping, and validation of autonomous driving models, both on the perception and control side. CARLA was developed from scratch based on the Unreal Engine to use the Open DRIVE standard for defining roads and possible urban environments in which traffic flows. Uniquely, the urban environment content provided with CARLA is also free of charge and the game engine offers state-of-the-art rendering quality (realistic physics, basic logic for NPCs or Non-Player Characters, etc.). Various urban planning scenarios include a multitude of vehicle models, buildings, pedestrians, road signs, etc. The simulation supports flexible sensor configuration and provides signals that can be used to train autonomous driving software, such as GPS coordinates, speed, acceleration, detected objects, and detailed data on collisions with objects or other road users. A wide range of environmental conditions can be specified, including weather and time of day, and several such environmental conditions are illustrated in Figure 1.

CARLA offers the possibility to obtain images in every simulation step from the sensors via python.api, and CARLA maps are based on open drive maps. Open DRIVE files contain detailed information about the road layout, including lane markings, road geometry, and junctions. The simulated vehicle is called "ego vehicle", a vehicle to which the camera sensor is attached. Both the autopilot (initially implemented) and manual control are used for data collection. The autopilot only allows navigation through urban areas (cities) via reference points, which leads to limitations related to no multiple lane changes, no approaches to the vehicle in front, no exit from a parking space without giving priority, no speed limits are exceeded, and so on. So, to cover these ideal situations and simulate the real situation as faithfully as possible, manual control is used.

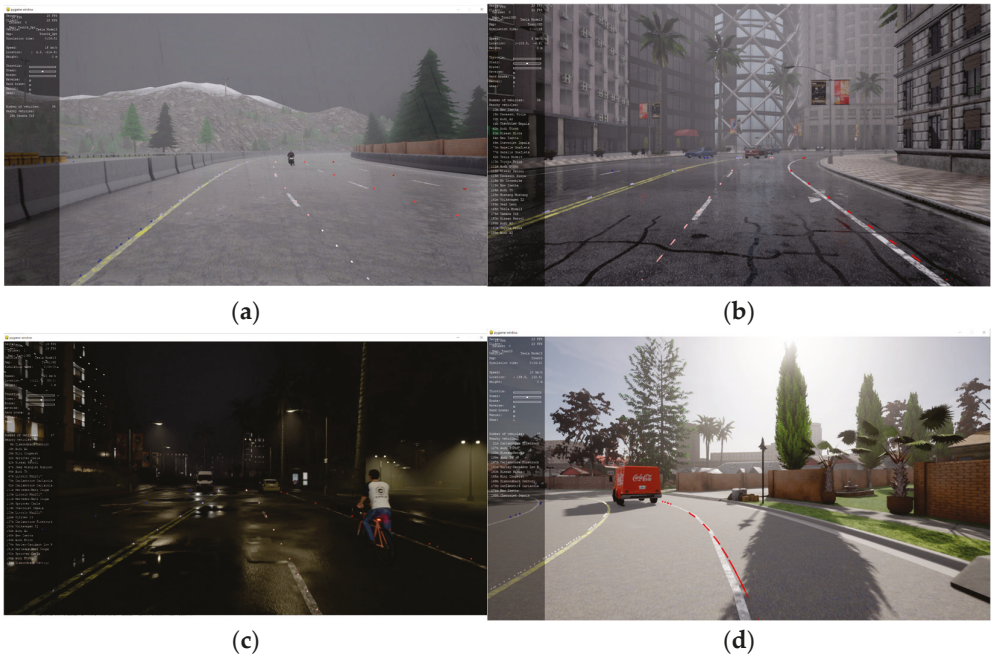

Figure 1. Examples of environmental scenarios in CARLA: (**a**) Daytime and cloudy, highway; (**b**) rain, urban; (**c**) night, urban; (**d**) daytime, clear sky, suburbia.

3.2. Testing the Virtual Dataset Quality

The ego vehicle operates within the speed limits defined by traffic signs. To enhance the diversity of collected images, weather conditions are changed after every 100 saved frames, and other vehicles and pedestrians appear randomly in the urban simulation environment (Figure 1). Lane information is saved in JSON format, storing the coordinates of the lane markings. These coordinates are then transformed from the map reference system to the optical camera coordinate system. Using this data, binary lane masks are created by drawing the lanes on the image based on the transformed coordinates (Figure 2).

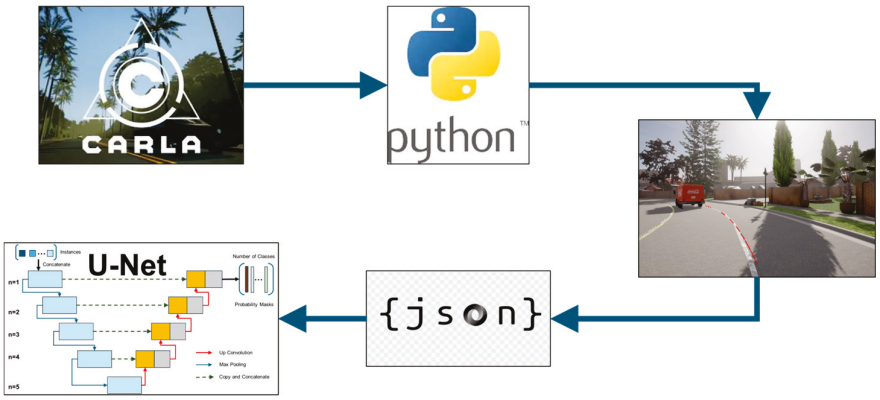

Figure 2. Virtual dataset generation process using CARLA.

To evaluate the quality of the virtual dataset, the following method was used: a neural network was trained on the newly generated CARLA dataset, and the same network was trained separately on the TuSimple dataset [20]. The U-Net architecture was selected for this purpose due to its proven effectiveness in segmentation tasks and its ability to yield high accuracy even when trained on relatively small datasets. Unlike specialized lane detection models such as SCNN, ENet, or PolyLaneNet++, U-Net offers a flexible encoder-decoder structure with skip connections that preserve spatial details. This structure is particularly suitable for the lane detection task, where precise localization is important.

The general structure of the U-Net used is illustrated in Figure 3. The notation h_n refers to the height of the convolutional layers at block level n, and d_{ni} denotes the number of channels in the ith convolutional layer at level n. The width of each convolutional layer follows a consistent pattern, and the depth of the convolutional layers at level n is twice that of the corresponding layer at the previous level $(n-1)$.

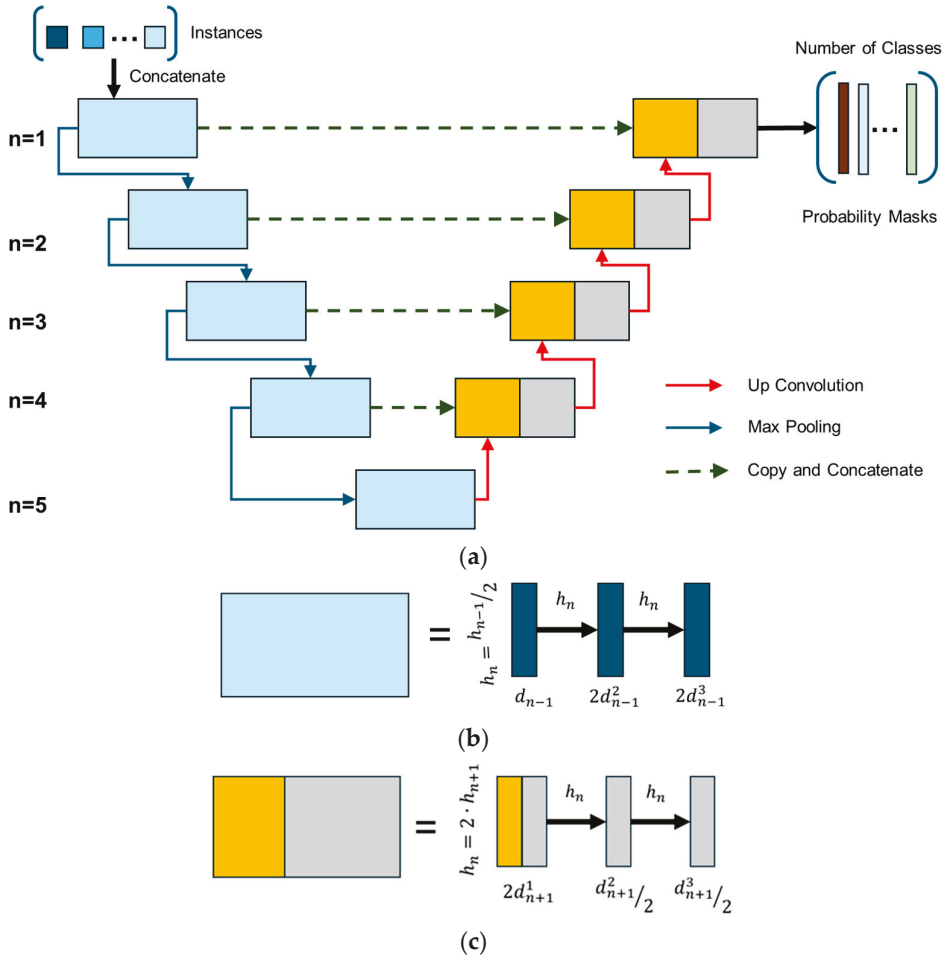

Figure 3. U-net architecture: (**a**) general architecture and information transfer paths; (**b**) structure of pooling blocks; (**c**) structure of convolution blocks (adapted from source [18]).

U-Net is a type of convolutional neural network (CNN) designed specifically for image segmentation tasks. It was originally developed for biomedical image segmentation [21–23]. The architecture features a symmetric encoder–decoder structure, with skip connections between corresponding down-sampling and up-sampling blocks. This design helps preserve fine-grained spatial information that might otherwise be lost due to max pooling.

In this implementation, each down-sampling block consists of two convolutional layers with 3×3 filters and a padding of size 1, followed by a 2×2 max pooling operation with a stride of 2. Batch normalization is applied after each convolutional layer to improve training stability and convergence speed. The up-sampling part mirrors the down-sampling blocks, and concatenation is used to merge high-resolution features from the encoder with the corresponding decoder layers. The number of filters begins at 16 and doubles at each block level, reaching 256 at the bottleneck. Dropout layers are also incorporated to reduce overfitting.

The model was trained using a batch size of 16 and optimized with the Adam optimizer using a learning rate of 1×10^{-4} and a linear decay schedule over 80 epochs. These

hyperparameters were chosen based on commonly effective defaults for segmentation tasks and were not further tuned, as the primary goal of the study was to analyze resolution and dataset effects.

The model takes an RGB image as an input and returns a binary segmentation map indicating the presence of lane lines (Figure 4). The TuSimple dataset, which was used for evaluation, contains labeled road scenes tailored for autonomous driving applications.

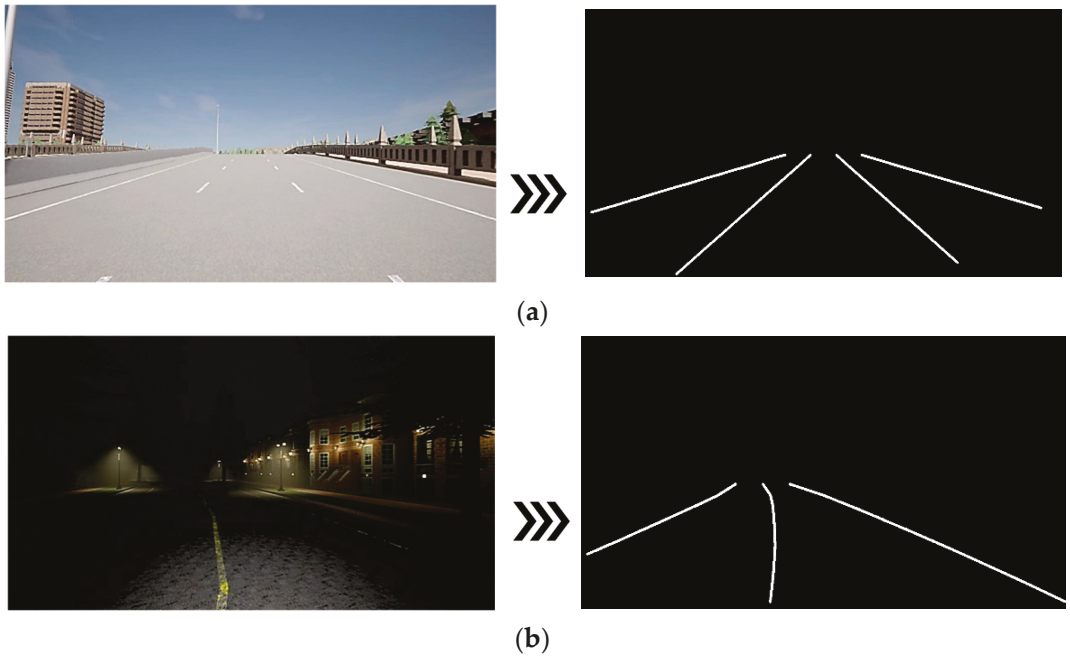

Figure 4. Identification of traffic lanes in different situations and environments: (**a**) Multilane Road, extra urban, sunny environment; (**b**) Single Lane Road, urban, dark environment.

After training on both datasets, the neural network was evaluated using a test image set from the TuSimple dataset. The evaluation focused on two primary aspects: segmentation accuracy, represented by the Mean Intersection over Union (mIoU) and F1 Score, and runtime efficiency, measured by inference time and frames per second (FPS). The mIoU metric quantifies the overlap between the predicted segmentation and the ground truth. It is calculated as the ratio of the area of intersection (correctly predicted lane pixels) to the area of union (all pixels predicted as lanes or labeled as lanes in the ground truth). This provides a single metric that summarizes the overall segmentation performance of the model (Equation (1)).

$$\text{mIoU} = \frac{\text{Intersection}}{\text{Union}} \tag{1}$$

Another important parameter is the F1 score, parameter that combines two factors "precision" and "recall" (Equation (2)). The factor "precision" is defined as the fraction of detected lane pixels that are correct, and the factor "recall" represents the fraction of ground truth lane pixels that are detected.

$$\text{F1} - \text{Score} = 2 * \frac{\text{Precision} * \text{Recall}}{\text{Precision} + \text{Recall}} \tag{2}$$

Inference time (speed) is a critical performance parameter for real-time applications because the implementation and architecture of a neural network on mobile devices has many strict requirements regarding latency and computing resources [24]. The parameter considered in the FPS study measures how many frames can be processed per second and is an important factor in the development of ADAS systems. This is because another major

challenge of incorporating an ADAS vision algorithm is to run it in real time on the target embedded hardware platform, and the frame rate of the general driver assistance system is limited by the camera frame rate and the processing time of the application [25].

4. Results

The results obtained from the simulation and training processes are summarized in Table 1. This table illustrates the impact of varying input image resolutions (512 × 256, 640 × 320, and 1024 × 512) on both lane detection performance and computational efficiency. The neural network was trained using three different datasets:

- TuSimple dataset with 3626 labeled images;
- CARLA dataset with 3890 labeled images;
- Mixed dataset with 3500 images mixed evenly as 1750 from the TuSimple and 1750 CARLA dataset.

Table 1. Results from U-Net trained on considered datasets (different image resolution).

Performance Parameters	Dataset 512 × 256			Dataset 640 × 320			Dataset 1024 × 512		
	TuSimple	CARLA	TuSimple + CARLA	TuSimple	CARLA	TuSimple + CARLA	TuSimple	CARLA	TuSimple + CARLA
mIoU	0.52	0.36	0.56	0.47	0.32	0.49	0.48	0.33	0.49
F1 Score	0.67	0.52	0.69	0.63	0.48	0.67	0.64	0.46	0.67
Inference Time [s]	0.016	0.017	0.016	0.027	0.027	0.027	0.065	0.07	0.065
FPS	60	59	60	36.88	37.08	37.03	15.4	15.3	15.37

Each dataset was split into training and testing sets, with 80% of the data used for training and the remaining 20% used for testing. Training was conducted over 50 epochs using the Adam optimizer (Adaptive Moment Estimation) with a learning rate of 1×10^{-4} [26]. To isolate the influence of dataset composition and image resolution, data augmentation was intentionally excluded from this study. The original size of the images used for training was 1280 × 720 pixels.

The variation in performance across the evaluated parameters and the relative differences between results are illustrated in Figures 5–8.

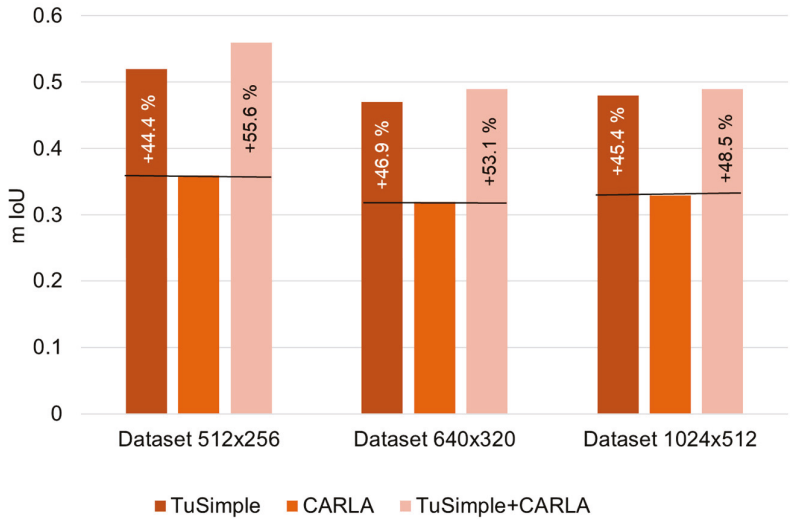

Figure 5. Comparative analysis of mIoU performance.

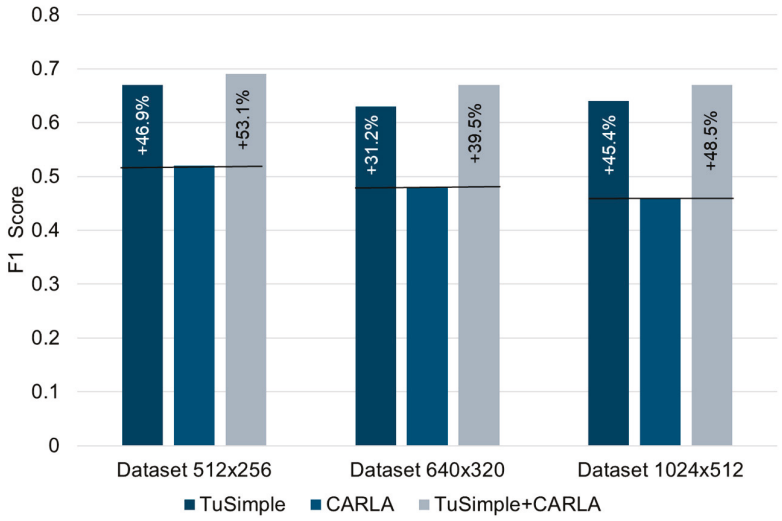

Figure 6. Comparative analysis of F1 score performance.

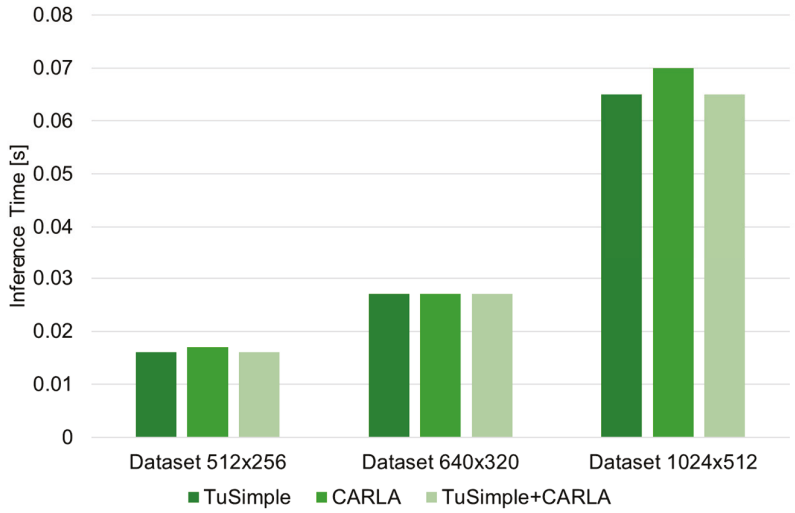

Figure 7. Comparative analysis of inference time performance.

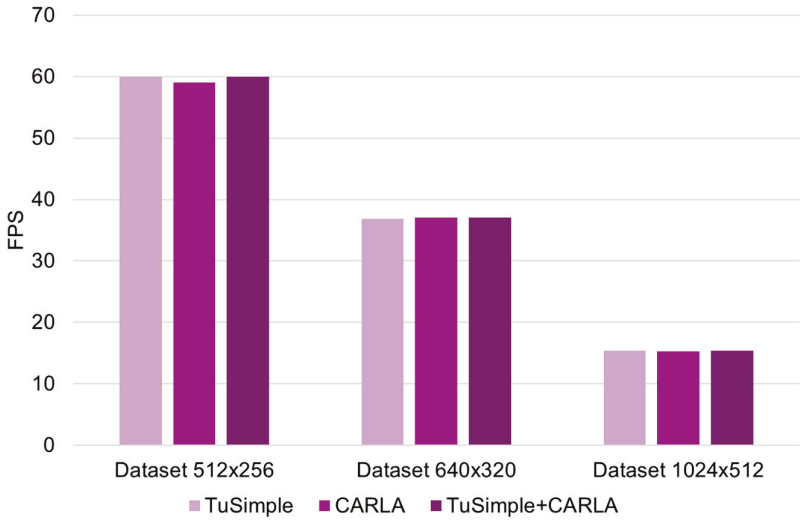

Figure 8. Comparative analysis of FPS parameter performance.

Based on the analysis of the results obtained, it is observed that their variation can be captured through a parametric equation (which defines the variation surface—Figure 9).

Thus, for the calculation of the mIoU parameter, the relationship is presented in Equation 3 (R^2 = 0.9953), and for the F1 Score parameter, it is in Equation 4 (R^2 = 0.9927), with the specification that R represents the image normalized resolution in pixels and p is the normalized percentage of images taken from the TuSimple database vs. virtual images from CARLA (p = 0 for 100% TuSimple dataset and 0% CARLA dataset and p = 1 for 0% TuSimple dataset and 100% CARLA dataset).

$$mIoU(R, P) = 0.12R^2 - 0.40P^2 + 0.01RP - 0.1717R + 0.2417P + 0.5258 \quad (3)$$

$$F1\ Score(R, P) = 0.06R^2 - 0.40P^2 - 0.03RP - 0.081R + 0.295P + 0.6625 \quad (4)$$

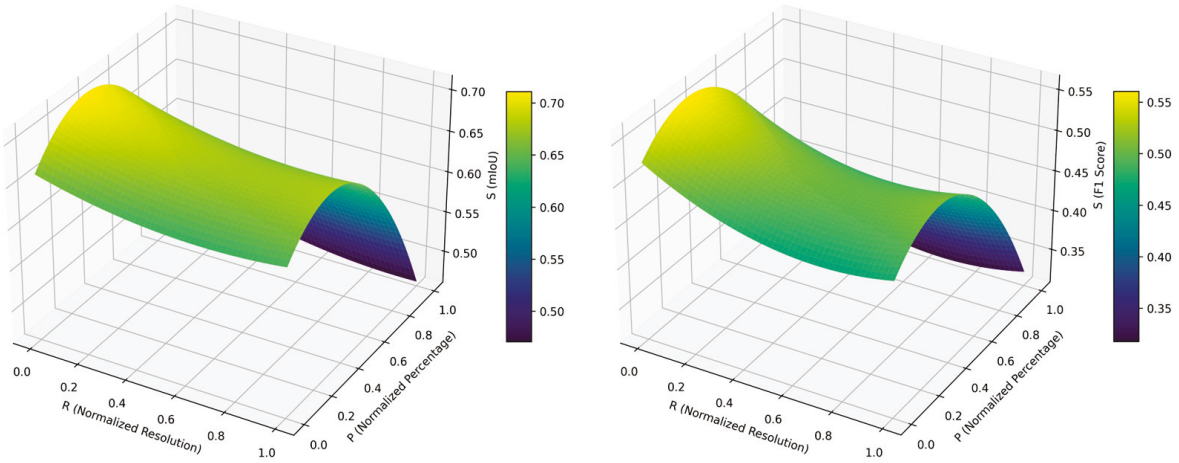

(**a**) (**b**)

Figure 9. Variations of mIoU (**a**) and FPS (**b**) parameter performance.

In the case of the variation of the mIoU parameter, the minimum value was 0.313 (for R = 0.67 and p = 1.0), and the maximum was 0.562 (for R = 0.00 and p = 0.31). In the case of the variation of the FPS parameter, the minimum value was 0.466 (for R = 0.94 and p = 1.0), and the maximum was 0.712 (for R = 0.00 and p = 0.33). It should be noted that these results and variation curves were obtained for the particular case treated in the article, and future research will be carried out using other real and virtual databases to validate these hypotheses.

5. Discussion

While the CARLA dataset alone yields competitive results (Table 1), the best performance in both the mIoU and F1 scores was achieved by the combined TuSimple + CARLA dataset, highlighting the benefits of combining real and synthetic data. The minimum value obtained for the mIoU parameter was 0.32 (CARLA, data set 640 × 320), and the maximum was 0.56 (TuSimple + CARLA, data set 512 × 256), with an average difference of 75%. The F1 score parameter also shows better results when using the CARLA dataset for all cases of image resolution considered. The highest score obtained was 0.69 (TuSimple + CARLA, data set 512 × 256), and the lowest was 0.46 (CARLA, data set 1024 × 512).

It can also be stated from the results obtained that the Inference time (average variation of approx. 5.8%) and FPS score (average variation of approx. 1.6%) values for each case of image resolution considered have a minimal sensitivity relative to the dataset used (specific to each resolution considered). This suggests that the U-Net architecture maintains constant band detection performance in all tested datasets. Such stability can be attributed to the prominent and structured nature of the band markings, which remain solid even at lower resolutions. In the case of band line detection, the fine details that can be captured

by the increased size of the input images (image resolution) are not significant in their tracing/identification.

By analyzing the functional (applicative) efficiency of the proposed method, it is observed that there is a significant inverse relationship between the resolution of the input image and the computational efficiency. Specifically, in terms of frame rate (FPS), when using the TuSimple database, increasing the resolution from 512 × 256 to 640 × 320 results in a 38.53% reduction, and when increasing the 640 × 320 resolution to 1024 × 512, a 58.24% reduction. When using the CARLA Simulation Environment, increasing the resolution from 512 × 256 to 640 × 320 results in a 37.15% reduction, and when increasing the 640 × 320 resolution to 1024 × 512, a 58.73% reduction. However, it is observed that using 1024 × 512 resolution reduces FPS by over 50% compared to 512 × 256, with a negligible gain in mIoU. The values and trends of these indicators indicate a substantial increase in the computational load required with increasing image resolution, once again emphasizing the need to find a compromise, in applications specific to solving such problems, between image resolution and processing speed.

All experiments in this study were conducted using a 12th generation i7 2.3 GHz CPU, without GPU acceleration. Despite this, the U-Net model achieved reasonable inference times and frame rates, indicating its potential viability for real-time applications on modest hardware.

However, several limitations must be acknowledged:

- Only the U-Net architecture was tested. Other models such as SCNN, ENet, or PolyLaneNet++ may exhibit different performance trends, particularly regarding resolution sensitivity and generalization.
- Real-world generalization to unseen roads was not assessed. Testing the trained models on independent datasets or previously unseen road segments would provide a more comprehensive evaluation of robustness.

Given the performance and computational trade-offs, we recommend using a 512 × 256 input resolution combined with a mixed dataset (real + synthetic data) for lightweight ADAS systems.

For actual deployment in embedded systems, further optimization would be necessary. Future work will explore hardware-specific improvements, such as quantization, model pruning, or transitioning to more lightweight architectures (e.g., ENet or MobileNet-based U-Nets) for improved performance on embedded systems.

6. Conclusions

A key advantage of using simulation environments for training lane detection neural networks is the ability to generate rare or uncommon traffic scenarios—such as sharp street corners or unusual lane configurations—that are often missing or underrepresented in real-world datasets. Incorporating such edge cases into the training process is essential for ensuring the safety and robustness of autonomous driving systems.

Additionally, simulation environments like CARLA enable the rapid generation of large volumes of accurately labeled data. This significantly reduces the time and cost typically associated with manual annotation, while also offering flexibility to model diverse environmental conditions.

Future enhancements in simulation-based training may focus on increasing the photo-realism of generated images using game engine technologies. While this may demand more powerful hardware resources, improved visual fidelity can lead to better generalization of trained models in real-world scenarios, as also noted in related research.

Author Contributions: Conceptualization, A.C., G.C. and F.M.; methodology, A.C. and F.M.; software, A.C.; validation, A.C.; investigation, A.C., G.C. and F.M.; writing—original draft preparation, F.M.; writing—review and editing, A.C., G.C. and F.M.; supervision, F.M. All authors have read and agreed to the published version of the manuscript.

Funding: The APC was funded by Technical University of Cluj Napoca.

Data Availability Statement: Data is unavailable due to privacy.

Conflicts of Interest: The authors declare no conflicts of interest.

Abbreviations

The following abbreviations are used in this manuscript:

AD	Autonomous driving
ADAS	Advanced driver assistance systems
AI	Artificial Intelligence
CARLA	CAR Learning to Act
CNN	Convolutional neural network
DL	Deep learning
F1	Precision factor
FPS	Frames per second
GPS	Global positioning system
LIDAR	Light detection and ranging
IMU	Inertial measurement unit
mIoU	Mean Intersection over Union
NPC	Non-player character
RIM	Recurrent instance module

References

1. European Commission. Roadmap to a Single European Transport Area: Towards a Competitive and Resource Efficient Transport System. 2011. ISBN 978-92-79-18270-9. Available online: https://op.europa.eu/en/publication-detail/-/publication/bfaa7afd-7d56-4a8d-b44d-2d1630448855/language-en#:~:text=The%20European%20Commission%20adopted%20a%20roadmap%20of%2040,in%20key%20areas%20and%20fuel%20growth%20and%20employment (accessed on 12 March 2025). [CrossRef]
2. National Highways Traffic Safety Administration, Critical Reasons for Crashes Investigated in the National Motor Vehicle Crash Causation Survey, 2015, DOT HS 812 115. Available online: https://crashstats.nhtsa.dot.gov/Api/Public/ViewPublication/812115 (accessed on 12 March 2025).
3. Gruyer, D.; Magnier, V.; Hamdi, K.; Claussmann, L.; Orfila, O.; Racotonirainy, A. Perception, information processing and modeling: Critical stages for autonomous driving applications. *Annu. Rev. Control* **2017**, *44*, 323–341. [CrossRef]
4. Cai, J.; Jiang, H.; Wang, J.; Li, A. Multi-head attention-based intelligent vehicle lane change decision and trajectory prediction model in highways. *J. Intell. Transp. Syst.* **2024**, 1–18. [CrossRef]
5. Xia, X.; Meng, Z.; Han, X.; Li, H.; Tsukiji, T.; Xu, R.; Zheng, Z.; Ma, J. An automated driving systems data acquisition and analytics platform. *Transp. Res. Part C Emerg. Technol.* **2023**, *151*, 104120. [CrossRef]
6. Chen, G.; Zhao, X.; Gao, Z.; Hua, M. Dynamic drifting control for general path tracking of autonomous vehicles. *IEEE Trans. Intell. Veh.* **2023**, *8*, 2527–2537. [CrossRef]
7. Masmoudi, M.; Friji, H.; Ghazzai, H.; Massoud, Y. A reinforcement learning framework for video frame-based autonomous car-following. *IEEE Open J. Intell. Transp. Syst.* **2021**, *2*, 111–127. [CrossRef]
8. Malligere Shivanna, V.; Guo, J.-I. Object Detection, Recognition, and Tracking Algorithms for ADASs—A Study on Recent Trends. *Sensors* **2024**, *24*, 249. [CrossRef]
9. Malik, S.; Khan, M.A.; El-Sayed, H. CARLA: Car Learning to Act—An Inside Out. *Procedia Comput. Sci.* **2022**, *198*, 742–749. [CrossRef]
10. Shashidhar, R.; Arunakumari, B.N.; Manjunath, A.S.; Ahuja, N.J.; Hoang, V.T.; Tran-Trung, K.; Belay, A. Computer Vision and the IoT-Based Intelligent Road Lane Detection System. *Math. Probl. Eng.* **2022**, 4755113. [CrossRef]
11. Swain, S.; Tripathy, A.K. Real-time Lane detection for autonomous vehicles using YOLOV5 Segmentation Model. *Int. J. Sustain. Eng.* **2024**, *17*, 718–728. [CrossRef]

12. Song, Y.; Wang, L.Y.; Wang, H.D.; Li, M.L. Lane detection based on IBN deep neural network and attention. *Connect. Sci.* **2022**, *34*, 2671–2688. [CrossRef]
13. Silva, I.; Silva, H.; Botelho, F.; Pendão, C. Realistic 3D Simulators for Automotive: A Review of Main Applications and Features. *Sensors* **2024**, *24*, 5880. [CrossRef]
14. Li, Y.; Yuan, W.; Zhang, S.; Yan, W.; Shen, Q.; Wang, C.; Yang, M. Choose your simulator wisely: A review on open-source simulators for autonomous driving. *IEEE Trans. Intell. Veh.* **2024**, *9*, 4861–4876. [CrossRef]
15. Koroglu, Y.; Wotawa, F. Towards a Review on Simulated ADAS/AD Testing. In Proceedings of the 2023 IEEE/ACM International Conference on Automation of Software Test (AST), Melbourne, Australia, 15–16 May 2023; pp. 112–122. [CrossRef]
16. Liu, L.; Chen, X.; Zhu, S.; Tan, P. Condlanenet: A top-to-Down Lane Detection Framework Based on Conditional Convolution. In Proceedings of the 18th IEEE/CVF International Conference on Computer Vision, ICCV 2021, Montreal, QC, Canada, 10–17 October 2021; pp. 3753–3762.
17. Baek, S.W.; Kim, M.J.; Suddamalla, U.; Wong, A.; Lee, B.H.; Kim, J.H. Real-time Lane detection based on deep learning. *J. Electr. Eng. Technol.* **2022**, *17*, 655–664. [CrossRef]
18. Chng, Z.M.; Lew, J.M.H.; Lee, J.A. RONELD: Robust Neural Network Output Enhancement for Active Lane Detection. In Proceedings of the 25th International Conference on Pattern Recognition (ICPR), Milan, Italy, 10–15 January 2021; pp. 6842–6849. [CrossRef]
19. Jeon, H.; Kim, Y.; Choi, M.; Park, D.; Son, S.; Lee, J.; Choi, G.; Lim, Y. CARLA Simulator-Based Evaluation Framework Development of Lane Detection Accuracy Performance Under Sensor Blockage Caused by Heavy Rain for Autonomous Vehicle. *IEEE Robot. Autom. Lett.* **2022**, *7*, 9977–9984. [CrossRef]
20. Yang, C.; Tian, Z.; You, X.; Jia, K.; Liu, T.; Pan, Z.; John, V. Polylanenet++: Enhancing the polynomial regression lane detection based on spatio-temporal fusion. *Signal Image Video Process.* **2024**, *18*, 3021–3030. [CrossRef]
21. Modiboyina, C.; Chakrabarti, I.; Ghosh, S.K. Lightweight Low-Power U-Net Architecture for Semantic Segmentation. *Circuits Syst. Signal Process.* **2024**, *44*, 2527–2561. [CrossRef]
22. Kugelman, J.; Allman, J.; Read, S.A.; Vincent, S.J.; Tong, J.; Kalloniatis, M.; Chen, F.K.; Collins, M.J.; Alonso-Caneiro, D. A comparison of deep learning U-Net architectures for posterior segment OCT retinal layer segmentation. *Sci. Rep.* **2022**, *12*, 14888. [CrossRef] [PubMed]
23. Falk, T.; Mai, D.; Bensch, R.; Çiçek, Ö.; Abdulkadir, A.; Marrakchi, Y.; Böhm, A.; Deubner, J.; Jäckel, Z.; Seiwald, K.; et al. U-Net: Deep learning for cell counting, detection, and morphometry. *Nat. Methods* **2019**, *16*, 67–70. [CrossRef] [PubMed]
24. Tran, L.-A.; Do, T.-D.; Park, D.-C.; Le, M.-H. Enhancement of Robustness in Object Detection Module for Advanced Driver Assistance Systems. In Proceedings of the International Conference on System Science and Engineering (ICSSE), Ho Chi Minh City, Vietnam, 26–28 August 2021; pp. 158–163. [CrossRef]
25. Velez, G.; Otaegui, O. Embedding vision-based advanced driver assistance systems: A survey. *IET Intell. Transp. Syst.* **2017**, *11*, 103–112. [CrossRef]
26. Kingma, D.P.; Ba, L.J. A Method for Stochastic Optimization. In Proceedings of the International Conference on Learning Representations, San Diego, CA, USA, 7–9 May 2015; Available online: https://arxiv.org/abs/1412.6980 (accessed on 19 February 2025).

Disclaimer/Publisher's Note: The statements, opinions and data contained in all publications are solely those of the individual author(s) and contributor(s) and not of MDPI and/or the editor(s). MDPI and/or the editor(s) disclaim responsibility for any injury to people or property resulting from any ideas, methods, instructions or products referred to in the content.

vehicles

MDPI

Article

LTV-LQG Control for an Energy Efficient Electric Vehicle

Zoltán Pusztai [1], Tamás Gábor Luspay [2] and Ferenc Friedler [1,*]

[1] Vehicle Industry Research Center, Széchenyi István University, H-9026 Győr, Hungary; pusztai.zoltan@ga.sze.hu
[2] Systems and Control Laboratory—HUN-REN, Computer and Automation Research Institute, H-1111 Budapest, Hungary; tluspay@sztaki.hu
* Correspondence: f.friedler@ga.sze.hu

Abstract

This paper presents the design and evaluation of a Linear Time-Varying Linear Quadratic Gaussian (LTV-LQG) controller for an energy efficient electric vehicle, using a predetermined driving strategy as the reference trajectory. The proposed approach begins with the development of a structured nonlinear vehicle model based on relevant subsystems, enabling accurate energy consumption estimation with a deviation of less than 2% from experimental measurements. This model serves as the basis for computing a near-optimal driving trajectory. The nonlinear model is linearized along the predefined trajectory to support control design. A time-varying control structure is then developed, integrating a Kalman filter that estimates unmeasured external disturbances, such as wind, and enhances feedback performance. The proposed control strategy is evaluated through simulations and compared to a rule-based switching controller that replicates human-like driving behavior. The simulation results demonstrate that the LTV-LQG controller consistently satisfies the time constraints in both headwind- and tailwind-dominant scenarios, where the switching controller tends to exceed the time limit. Moreover, in tailwind-dominant cases, the LTV-LQG controller achieves lower energy consumption (up to 15.4%). The proposed framework represents a computationally efficient and practically feasible control solution for electric vehicles operating under realistic disturbance conditions.

Keywords: LTV; LQG; LTV-LQG; control; electric vehicle; GA; optimization; energy efficiency; driving strategy; SEM

1. Introduction

Energy and its economical, effective utilization have become major concerns in the modern world. This is a problem that has long been on the industrial processes agenda [1] and is currently becoming more and more significant in the transportation sector. Electrification of road vehicles is one major step toward sustainable transportation, nevertheless, the operation of these vehicles is still essential. Various studies have examined and characterized the technological developments and primary sources of energy loss in road vehicles from different perspectives [2]. Improving vehicle energy efficiency requires minimizing drivetrain losses and addressing the major contributing factors, including vehicle mass, rolling resistance, and aerodynamic drag.

In recent years, significant advancements have been made in the development of electric vehicles, substantially contributing to the expansion of e-mobility. Key areas of progress include battery technology, charging infrastructure, electric motors, power semiconductors, and drivetrain control systems [3]. Operating vehicles in an energy

efficient manner remains essential for reducing emissions. The pursuit of sustainability in vehicle development is imperative, given that the transport sector is a major contributor to global greenhouse gas emissions—carbon dioxide (CO_2) alone accounts for approximately 20% of total global emissions [4]. Lightweighting is a key strategy in reducing vehicle energy consumption and emissions, typically evaluated through longitudinal dynamic models [5]. Although most studies emphasize vehicle design, efficient operation is equally important, as even well-designed vehicles can perform poorly if mismanaged. Efficient vehicle operation can be achieved through the integration of validated model-based approaches [6], adaptive data-driven modeling techniques [7], and advanced control methods [8,9].

Given the increasing emphasis on sustainability and the development of lightweight electric vehicles, the relevance of the Shell Eco-marathon (SEM) has become more significant than ever. SEM is an internationally recognized competition that challenges university teams to design and operate highly energy efficient experimental vehicles. According to SEM regulations, vehicles may be powered by internal combustion engines, electric drives, or hydrogen fuel cells. Across all categories, the core objective is to complete a predefined distance within a specified time while minimizing energy consumption. Achieving high efficiency requires not only an optimized vehicle design but also a well-planned driving strategy, as energy minimization is unfeasible without coordinated control.

Urban Concept (UC) vehicles have been widely studied using combined modeling and optimization techniques. In Ref. [10], a battery electric UC vehicle model was developed by integrating theoretical estimations with experimental measurements. Ref. [11] presents a detailed multi-physics model of a hydrogen-powered UC vehicle, where Particle Swarm Optimization (PSO) is used to optimize motor current, gear ratio, and vehicle speed bounds. The work in Ref. [12] describes a model-based optimization approach for an electric prototype vehicle, formulated using experimental data. Driving strategy was optimized using a Genetic Algorithm (GA), leading to a 30% improvement in energy efficiency compared to a human-driver. In Ref. [13], a hydrogen-powered prototype vehicle was analyzed with a focus on optimizing powertrain components to minimize fuel consumption across the track. Several metaheuristic optimization algorithms were compared in a similar prototype application and found that traditional gradient-based methods, such as sequential quadratic programming, were ineffective, highlighting the advantage of metaheuristic approaches in handling complex, nonlinear problems [14].

An energy consumption sensitivity analysis for an SEM vehicle conducted in Ref. [15] revealed that reducing vehicle mass provides the most significant savings: a 10% reduction in mass resulted in a 5.5% to 8% decrease in energy usage, depending on the track. The simulation also accounted for track aggressiveness, with cornering losses identified as a major contributor to power losses—ranging from 5% to 12%, depending on track layout. In a related study [16], a digital twin of the same vehicle was validated and used to further minimize energy consumption through simulation. Machine learning-based model was introduced in Ref. [17] along with a real-time telemetry system to evaluate the influence of driving techniques on the energy efficiency of a battery electric UC vehicle.

During SEM competitions, although human drivers remain in control, predefined strategies and advanced control techniques can support energy efficient operation. The Linear Quadratic Regulator (LQR), which minimizes a quadratic cost function while ensuring closed-loop stability, is widely used for such purposes due to its robustness and flexibility. It has also been extended to complex tasks, such as water level regulation, where Hybrid LQR (HLQR) outperforms Distributed Control LQR (DCLQR) in reducing error and transition time in both single- and multi-pool systems [18]. Digital LQR control has shown high effectiveness, as demonstrated in Ref. [19], where a feedforward LQR improved performance for non-minimum phase boost converters compared to traditional digital methods.

LQR is also often integrated into higher-level vehicle control systems. A logical framework and operation of a vehicle lateral control system is proposed in Ref. [20], combining LQR with feedforward and predictive control elements to enable proactive, context-aware path following. LQR-based strategies are also applied in hybrid vehicles [21], where an LQR controller with Kalman filtering ensures robust battery state of charge (SOC) estimation under varying driving conditions. Similarly, a predictive energy-saving control strategy for commercial vehicles is proposed in Ref. [22]. Road slope information is integrated to enhance energy efficiency and driving comfort. The proposed method outperforms traditional PID control, showing improved disturbance rejection and robustness in both simulated and real-world scenarios.

Energy efficiency is a recurring theme across many recent developments. A model predictive control approach is used for car-following, incorporating power-based energy estimation into a multi-stage cost function [21]. A complementary approach is detailed in Ref. [23], where an adaptive cruise control system combines a Sage-Husa adaptive cubature Kalman filter with a neural network and predictive speed models to minimize unnecessary acceleration and braking, resulting in measurable energy improvements. Lateral control has also seen energy efficient improvements. In Ref. [24], a β–$\dot{\beta}$ plane method is combined with dynamic gain-scheduled LQR controllers to distinguish between handling- and stability-oriented modes, achieving up to 9.68% energy savings compared to Shino's controller under various maneuvering conditions. In the context of control under uncertainty and external disturbances, LQR continues to be a strong foundation. For helicopter structural vibration minimization, Ref. [25] presents the LMS-IOBR algorithm that combines $\mathcal{H}_\infty$ control and feedforward reconstruction based on piezo-actuator data. Further expanding to energy-sharing systems, Ref. [26] proposes a disturbance observer-based sliding mode control for a new power converter that enables electric vehicle-to-vehicle energy transfer.

The solution maintains robust and accurate performance under varying conditions, supporting shared mobility applications. Vehicle-to-Infrastructure (V2I) communication enhances LQR-based systems by providing external data for proactive control. Real-time traffic information enables better decision-making, reducing unnecessary stops and starts and ultimately extending vehicle range [27].

The problem of minimizing energy consumption is reformulated as an LTV-LQG control problem through trajectory linearization. Although the proposed method represents a relatively simple control strategy, it provides a practical balance between implementation complexity and performance. More advanced techniques, such as MPC or $\mathcal{H}_\infty$ control, could also be applied. However, the selection among these methods should be guided by specific application requirements, such as robustness, constraint handling, and computational demands. These characteristics were assessed in Table 1.

The $\mathcal{H}_\infty$ approach is well known for its strong guarantees of robustness. However, robustness is not the primary focus of the problem under consideration. Therefore, the MPC framework could serve as a natural extension of the proposed LQG solution, offering improved constraint handling and flexibility. Nevertheless, its significantly higher computational burden must be carefully considered for real-time implementation.

This paper focuses on the design of an LTV-LQG controller for an energy efficient electric vehicle, using a predetermined driving strategy as the reference trajectory. This framework provides a computationally efficient alternative to MPC, making it particularly suitable for implementation in embedded systems in energy-efficient vehicle applications. The paper is organized as follows. First, the applied modeling methodology is introduced, which leads to the construction of a non-linear vehicle model based on defined subsystems. This structured model enables an accurate estimate of the vehicle's energy consumption with minimal deviation from measurements, making it suitable for driving strategy op-

timization. The optimization process is also described, in which a near-optimal driving trajectory is obtained. The nonlinear vehicle model is then linearized along this predefined trajectory to enable control design. The linearization procedure is presented, followed by the development of a control strategy that compensates for estimated external disturbances. Finally, the designed control system is evaluated through simulations and compared to a model reproducing the driver's switching-control behavior.

Table 1. Comparison of LQG, MPC, and $\mathcal{H}_\infty$ control methods.

Feature	LQG	MPC	H_∞
Handling of non-linearities	Trajectory linearization	Linearization-free or successive linearization	Set-point linearization or LPV methods
Objective	Infinite-horizon quadratic cost minimization	Finite-horizon cost minimization	Worst-case induced $\mathcal{L}_2$ gain minimization
Hard constraints	Not guaranteed	Guaranteed	Not guaranteed
Disturbance type	Gaussian	Bounded	Bounded
Robustness to model uncertainty	No explicit robustness	Tube-based or stochastic MPC	Explicit robustness
Computational load	Very light	Requires real-time optimization	Light
Disturbance rejection	Strong in $\mathcal{H}_2$ sense	Guaranteed via tube/stochastic formulation	Strong in $\mathcal{H}_\infty$ sense

2. Applied Simulation Model

This study focuses on a battery-electric Urban Concept vehicle, illustrated in Figure 1, which secured first place in its category at the 2024 Shell Eco-marathon. The winning vehicle achieved a remarkable energy consumption of 309 km/kWh, representing the best result in the Battery Electric Urban Concept class.



Figure 1. SZEmission—energy efficient battery electric vehicle.

The mathematical model of the experimental vehicle model captures the electric energy conversion within the powertrain, while excluding losses from the energy grid and battery. The converted electrical energy is used to overcome road loads and track-induced resistances in order to complete the required trajectory. To enable energy optimization

along this path, a precise mathematical representation of the vehicle dynamics is essential. The governing equation of motion, based on mechanical fundamentals, is formulated in Equation (1).

$$m\ddot{x}(t) = F_T(t) + F_R(t) + F_S(t), \tag{1}$$

Traction (F_T), resistance (F_R), and slope (F_S) represent the forces acting on the vehicle. These three primary force components must be carefully characterized for accurate vehicle modeling. The resistance force contains the combined effect of the F_{air}, $F_{cornering}$, $F_{rolling}$ and $F_{inertia}$. The created submodels were developed on the basis of systematic measurements, these measurements were conducted on either the test field (vehicle resistance) or the laboratory environment (powertrain).

The mathematical model of the electric vehicle is structured using a subsystem-based approach. The specific characteristics of the vehicle are captured through the powertrain and resistance subsystems, which are integrated with the track model. The subsequent subsections provide further detail on these components.

2.1. Powertrain Model

The first subsystem of the vehicle model is the powertrain, which describes the traction force that acts on the vehicle. Measurement-based approach was used to consider the losses of the motor, the motor controller, and the gear, resulting in a complex powertrain model which is suitable for calculating energy consumption. The traction force is calculated from the current state of the powertrain, which includes a permanent magnet synchronous motor (PMSM) connected to the left wheel through a synchronous belt drive. The belt drive provides an adjustable reduction ratio (i = 2.77 to 4) between the motor and the driven wheel. Measurements incorporate the effects of belt tension and the number of engaged teeth, as these factors are influenced by the actual gear ratio. This approach ensures that the specific impact of gear ratio variations is accurately considered, rather than being assumed constant. Accordingly, the traction force is given by the following equation:

The relationship between the reference torque (T_{ref}), vehicle speed ($\dot{x}(t)$), actual torque (T_{act}), and drive efficiency (η_{drive}) is defined in Equation (2).

$$\begin{bmatrix} T_{act} \\ \eta_{drive} \end{bmatrix} = f_{PT}\Big(T_{ref}, \dot{x}(t)\Big), \tag{2}$$

where f_{PT} represents the function that describes the characteristics of the motor vehicle.

The traction force (F_T) is calculated from the actual torque (T_{act}) by dividing it by the wheel radius as described in Equation (3).

$$F_T(t) = \frac{T_{act}(t)}{R_{wheel}}. \tag{3}$$

2.2. Resistance and Track Model

The resistance model characterizes the total road load acting on the vehicle under two primary operating conditions: straight-line motion and cornering.

For straight-line motion, the resistance forces are obtained from coast-down tests on level ground. The vehicle is accelerated to its maximum speed and allowed to decelerate freely with the drive disengaged. Environmental disturbances are mitigated by averaging multiple repetitions, and a fifth-order polynomial is fitted to the measured speed profile, from which the total resistance force is calculated. Although aerodynamic drag is typically dominant at higher speeds, the vehicle's low drag coefficient makes rolling resistance a significant factor even in this region.

Cornering resistance is assessed under steady-state conditions using controlled speed tracking. The vehicle performs repeated laps on a closed track with fixed steering angles, in both clockwise and counterclockwise directions, to capture asymmetries arising from the single driven rear wheel. For each configuration, average speed and traction force are recorded, allowing resistance values to be mapped to turning radius and speed.

The collected data are used to construct a three-dimensional resistance surface as a function of vehicle speed and cornering radius. The radius ranges from -200 m (left turns) to 200 m (right turns); outside this range, motion is considered straight, and resistance values default to those from the coast-down tests. This combined resistance map captures both symmetric and asymmetric effects linked to vehicle geometry and drivetrain layout.

Although aerodynamic and rolling resistance could be modeled separately, they are combined into a single effective resistance term, aligned with the modeling approach used in the powertrain. This simplification facilitates integration into simulation environments while preserving the essential dynamics for control and optimization tasks. The resistance model, based on free-rolling and steady-state cornering tests, thus provides an empirical foundation for accurate energy modeling and the development of eco-driving strategies, which is described in Equation (4).

$$F_R(t) = -f_R(\dot{x}(t), R(X)) \tag{4}$$

One of the other key components of the simulation model is the track model, which contains information about the topology of the racetrack.

Detailed information of the track was obtained using high-precision GNSS measurements with RTK correction, providing height values with an accuracy of 8–15 cm. The track was measured three times using a measurement system developed by our team. The resulting data was averaged and processed using a custom algorithm to obtain and store the x, y, and z coordinates of the track.

The track was modeled as a single lane and subdivided into N segments of uniform length. Each segment was assigned an index $i = 1, \ldots, N$. The cornering radius and distance of each segment from the start were recorded and stored in the track model. This information was used to calculate the cornering radius and slope force F_S at each point on the track as defined in Equation (5), where α is the elevation angle. Linear interpolation was applied between discrete segments to estimate values for the model. Further control-oriented modeling details of the experimental vehicle were provided in [28].

$$F_S(t) = -m \cdot g \cdot \sin(\alpha), \tag{5}$$

3. Vehicle Model-Based Driving Strategy Optimization

The 2024 Shell Eco-marathon competition took place at the Paul Armagnac racecourse near Nogaro, France. This track is relatively flat, with an elevation difference of approximately 5 m between its highest and lowest points, excluding the nearly 950-meter-long straight section. The Caupenne layout was used in the competition, which is 1535 m long and represents the shortest configuration of the racetrack, as shown in Figure 2.

The strategy was optimized for a single lap, where the vehicle starts from rest and must cover at least $s_{\max} - 2$ m to ensure valid completion, allowing room for maneuvering near the congested finish area. Although optimization does not enforce a complete stop, the final speed must be less than 8 km/h to enable driver-initiated stopping. The total duration must also remain within the maximum allowed time $T_{\max}$.

The driving strategy was optimized using a Genetic Algorithm (GA), which determines key control parameters such as the drive state (active or inactive) and torque values as a function of track position, to produce an optimized speed profile without requiring

gradient information. GA operates by evolving a population of candidate solutions. In each iteration, the fittest individuals are selected, recombined (crossover), and randomly modified (mutation) to explore new solutions. The best result is retained for the next generation. This process is repeated until a termination condition is met, yielding a near-optimal solution. The optimization model considers both the vehicle's resistance forces and the slope force caused by the track elevation. Accurate modeling requires the cornering radius and slope force data, which are presented in Figure 3.



Figure 2. Nogaro track—Caupenne layout.

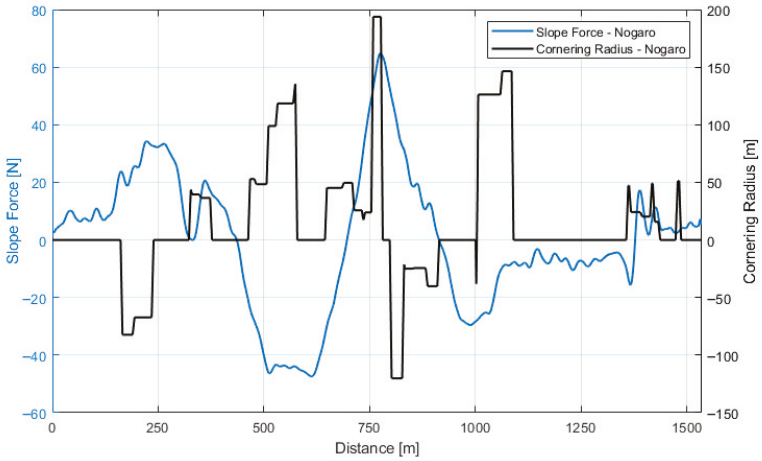

Figure 3. Slope force and cornering radius values of the Nogaro track Caupenne layout.

The constrained optimization problem is formulated in Equations (6)–(8).

$$\underset{T_{\text{ref}}}{\text{Minimize}} \quad E(\tau, T_{\text{ref}}) = \int_0^{\tau} \frac{F_T(t)\,\dot{x}(t)}{\eta_{\text{drive}}(t)}\,\mathrm{d}t \tag{6}$$

$$\text{subject to} \quad s_{\max} - 2 \;\leq\; \int_0^{\tau} \dot{x}(t)\,\mathrm{d}t \;\leq\; s_{\max} \tag{7}$$

$$\tau \;\leq\; \tau_{\max} \tag{8}$$

The energy consumption during vehicle operation can be calculated using the vehicle model, where τ is the simulation time horizon and T_{ref} is the applied reference torque. The energy is computed at each simulation step, and the integral yields the total energy consumption. The optimization process is primarily driven by these two parameters. The standby consumption of auxiliary electrical components is neglected in the current model. The optimized driving strategy is shown in Figure 4. A comprehensive overview of the optimization of the driving strategy is provided in [29].

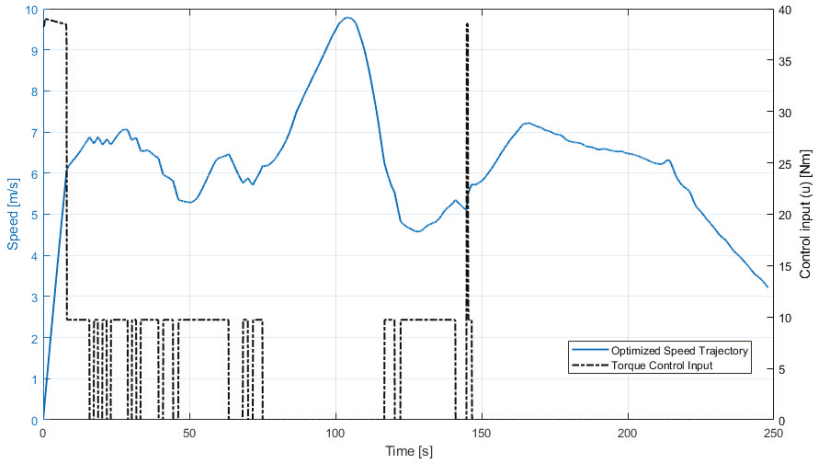

Figure 4. Result of driving strategy optimization: Speed profile and torque input.

The optimized strategy provides guidance for the driver, whose task is to follow the speed profile despite disturbances. A recent analysis of driver measurement data was carried out, focusing on the distribution of lap times and final energy consumption. Figure 5 illustrates the distribution of lap energy versus lap time, based on 69 laps recorded during the latest Shell Eco-marathon in Poland at the Silesia Ring. The scatter points show the raw data, while high-density region (HDR) contours from a two-dimensional kernel density estimation (KDE) at 20%, 40%, 60%, and 80% highlight the regions containing the corresponding share of the data. The innermost contour (HDR 20%) indicates that 20% of the laps are concentrated around the target lap time of 191 s, within an approximate 3 s range. It can also be observed that around 80% of the laps were completed within a 10 s range, while extreme deviations extend the overall range of human driving performance to 17.3 s. The lap energy consumption shows higher variability (coefficient of variation 7.3%), primarily caused by external disturbances. This analysis indicates that the experienced driver maintains the target lap time with a standard deviation of 3.41 s, suggesting that a properly designed controller could both respect the lap time target and exploit favorable external conditions. These findings motivated the research towards the design of a practically applicable controller.

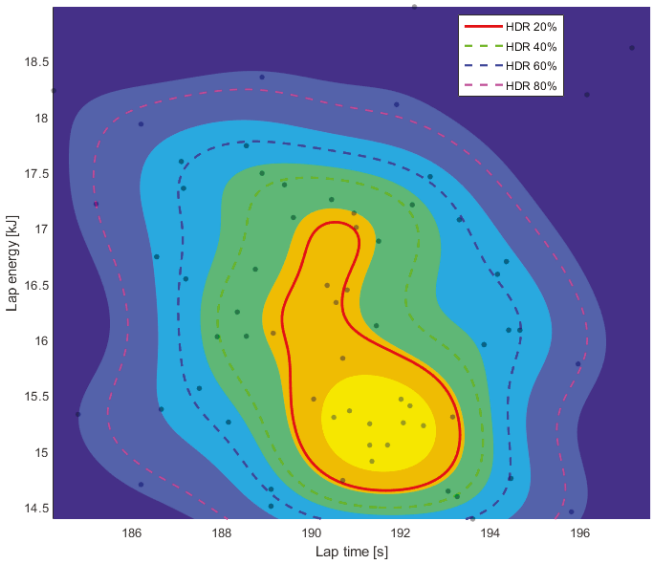

Figure 5. 2D density contours of lap time [s] and lap energy [kJ] for human-driven laps (shows as dots), Shell Eco-marathon, Silesia Ring 2025.

4. LTV Model and LQG Control of Energy Efficient Electric Vehicle

The developed nonlinear model is well-suited for the presented offline driving strategy optimization, which enables the definition of a predetermined near-optimal speed trajectory. Until now, the implementation of energy efficient control has been entirely manual, relying on the driver to follow the predefined driving strategy. This is a highly demanding task, as the driver must not only react to real-time events on the track, but also precisely track the speed profile.

Driver assistance is currently implemented through a simplified interface, where the driver is only required to press an accelerator button at predefined positions displayed during operation. This approach helps to follow the optimal speed trajectory. A straightforward and reliable control strategy proves to be more effective, particularly when the dynamics of the system can be expressed in a linearized framework.

4.1. LTV Vehicle Model

In the development of the trajectory-based Linear Time-Varying (LTV) model, a trajectory linearization approach was applied. By collecting the equations introduced in Section 2, the nonlinear system can be represented in the general discretized in Equations (9) and (10).

$$x_{k+1} = f(x_k, u_k, d_k) \tag{9}$$

$$y_k = h(x_k, u_k) \tag{10}$$

where $x(k)$, $u(k)$, and $y(k)$ denote the discretized state, input, and output vectors, respectively. In this formulation, the state vector $x(k)$ includes the speed of the vehicle $\dot{x}$ and the distance traveled x, while the input $u(k)$ comprises the control variables: the reference torque T_{ref} and the actual cornering radius $R(X)$. The term $d(k)$ denotes external disturbances acting on the system. The functions $f(\cdot,\cdot)$ and $h(\cdot,\cdot)$ describe the nonlinear state transition and output measurement functions, respectively, capturing the system's dynamics and its observable behavior.

In nonlinear trajectory tracking, we assume a nominal trajectory $\{x_0^*, x_1^*, \ldots, x_H^*\}$, which is feasible if there exists a corresponding input sequence $\{u_0^*, u_1^*, \ldots, u_{H-1}^*\}$ such that in Equation (11).

$$x_{k+1}^* = f(x_k^*, u_k^*) \qquad \forall\, k \in \{0, \ldots, H-1\}. \tag{11}$$

This trajectory results from solving the optimization problem of the driving strategy adapted to the specific track. The tracking problem then becomes minimizing the deviation from this as proposed in Equations (12) and (13).

$$\min_{u_0,\ldots,u_{H-1}} \quad \sum_{k=0}^{H-1} \left[(x_k - x_k^*)^\top Q (x_k - x_k^*) + (u_k - u_k^*)^\top R (u_k - u_k^*) \right] \tag{12}$$

$$\text{subject to} \quad x_{k+1} = f(x_k, u_k) \tag{13}$$

Here, x_k^* and u_k^* denote the state and input reference values along the predetermined trajectory, while x_k and u_k are the actual state and input of the system. The matrix Q is symmetric positive semi-definite and penalizes deviation from the reference trajectory, while R is symmetric positive definite and penalizes excessive control effort. The optimal control input minimizes the total cost by balancing trajectory tracking accuracy and energy usage. In this setup, the reference trajectory (x_k^*, u_k^*) is generated offline using a Genetic Algorithm (GA), which optimizes energy efficient vehicle operation. The LQ controller then computes the input sequence that best tracks this trajectory in the presence of model uncertainties or disturbances, enabling robust and energy-aware operation.

To solve this problem using linear control methods, we linearize the nonlinear dynamics around the nominal trajectory according to Equation (14).

$$x_{k+1} \approx f(x_k^*, u_k^*, 0) + A_k(x_k - x_k^*) + B_k(u_k - u_k^*) + E_k d_k, \tag{14}$$

where the Jacobians are defined based on Equation (15).

$$A_k = \frac{\partial f}{\partial x}(x_k^*, u_k^*, 0), \qquad B_k = \frac{\partial f}{\partial u}(x_k^*, u_k^*, 0), \qquad E_k = \frac{\partial f}{\partial d}(x_k^*, u_k^*, 0). \tag{15}$$

This approach eliminates the need for steady-state or equilibrium-based linearization and enables a local linear model to remain valid at any operating point along the trajectory. As a result, the nonlinear dynamics are embedded into a time-varying linear structure, making it possible to apply LTV control techniques. The state and input vectors of the LTV model are consistent with those of the original nonlinear system.

Since the LTV model is constructed along a predefined reference trajectory, the system matrices $A(k)$, $B(k)$, $C(k)$, and $D(k)$ are time-dependent but known in advance. Their temporal variation reflects the dynamic changes in the vehicle's operating conditions—such as speed, torque demand, and turning radius—encountered along the trajectory. As the entire reference trajectory is available offline, both the time-varying model and the corresponding controller gains (e.g., from LTV-LQG synthesis) can be precomputed. These gains can then be applied in real time based only on timing information, without requiring online measurement or estimation of any scheduling signals. This formulation enables the use of linear control design techniques adapted to time-varying dynamics, allowing accurate control of nonlinear vehicle behavior along complex trajectories.

4.2. Linear Time-Varying Linear Quadratic Gaussian (LTV–LQG) Control

The LTV–LQG (Linear Time-Varying–Linear Quadratic Gaussian) controller generalizes the classical LQR/LQG framework to systems with time-varying parameters, such as state transition, input, and noise-weighting matrices. This approach maintains optimal performance under dynamic conditions by continuously updating both feedback and estimation gains based on the system's evolution and uncertainty.

System dynamics and sensor measurements are subject to uncertainties and disturbances, which are modeled using stochastic noise variables according to Equation (16).

$$x_{k+1} = A_k x_k + B_k u_k + w_k, \qquad y_k = C_k x_k + v_k, \tag{16}$$

where w_k represents the process noise and v_k denotes the measurement noise. The process noise w_k captures model uncertainties and unmodeled dynamics, while the measurement noise v_k refers to sensor inaccuracies arising from real-world measurements (e.g., rotary sensors). These noise terms are modeled as zero-mean Gaussian distributions as described in Equation (17).

$$w_k \sim \mathcal{N}(0, W_k), \qquad v_k \sim \mathcal{N}(0, V_k). \tag{17}$$

where W_k and V_k are the respective covariance matrices that define the magnitude and correlation structure of the uncertainties and sensor noise.

Applying backward dynamic programming for finite-horizon LQR, and initializing $P_0 = 0$, the recursions described in Equations (18) and (19) are used for $k = 1, \ldots, H$.

$$K_k = -\left(R_k + B_k^\top P_{k+1} B_k\right)^{-1} B_k^\top P_{k+1} A_k \tag{18}$$

$$P_k = Q_k + K_k^\top R_k K_k + (A_k + B_k K_k)^\top P_{k+1} (A_k + B_k K_k) \tag{19}$$

The resulting feedback policy is given by Equation (20).

$$u_{H-k} = u^*_{H-k} + K_k (x_{H-k} - x^*_{H-k}), \tag{20}$$

and the corresponding cost-to-go function is described in Equation (21).

$$J_k(x) = x^\top P_k x \tag{21}$$

Within the trajectory-linearization scheme, the system variables represent deviations from the nominal trajectory, and therefore the penalty factors can be determined based on the maximum allowable tracking error. This can be expressed by introducing a diagonal Q matrix for the states, where each diagonal element corresponds to the penalty of a given state, as proposed in Equation (22).

$$q_{i,i} = \frac{1}{\max \tilde{e}_i^2} \tag{22}$$

In other words, the Q weighting matrix normalizes the states by the corresponding desired tracking accuracy. A similar principle applies to the input weighting matrix R, which serves to limit the control effort.

This formulation corresponds to a linear-quadratic (LQ) state feedback controller, which requires knowledge of the current system state x_{H-k}. Although in practice the states may be indirectly observable through noisy measurements, the control law assumes access to the true state values. Therefore, to obtain a reliable estimate of the internal state in real-time, a Kalman filter is used. The Kalman filter combines the available noisy measurements with the system model to provide an optimal estimate $\hat{x}_k$ of the actual state x_k, which is then used in the feedback law to compute the control input.

4.3. Disturbance Estimation

The Kalman filter estimates the internal state of the system by recursively applying a prediction–correction procedure at each time step. In the prediction step, the prior state estimate $\hat{x}_k^-$ and the corresponding error covariance P_k^- are propagated through the system model. In the update step, the prediction is corrected using the latest measurement y_k, where the Kalman gain L_k determines the relative influence of the measurement and the prediction. The discrete-time filter equations are listed in Equations (23)–(27).

$$\text{Prediction:} \quad \hat{x}_k^- = A_{k-1}\, \hat{x}_{k-1}^+ + B_{k-1}\, u_{k-1}, \tag{23}$$

$$P_k^- = A_{k-1}\, P_{k-1}^+\, A_{k-1}^\top + W_{k-1}, \tag{24}$$

$$\text{Update:} \quad L_k = P_k^-\, C_k^\top \left(C_k\, P_k^-\, C_k^\top + V_k\right)^{-1}, \tag{25}$$

$$\hat{x}_k^+ = \hat{x}_k^- + L_k \left(y_k - C_k\, \hat{x}_k^-\right), \tag{26}$$

$$P_k^+ = (I - L_k\, C_k) P_k^-. \tag{27}$$

Here, $\hat{x}_k^-$ is the predicted state estimate at time step k, and $\hat{x}_k^+$ is the updated estimate after incorporating the measurement y_k. The matrices P_k^- and P_k^+ represent the prior and posterior error covariances, respectively. The Kalman gain L_k balances model-based prediction with measurement correction. The time-varying system matrices A_k, B_k, and C_k are derived from the linearized trajectory-based model. The matrices W_k and V_k denote the covariance of the process and measurement noise, respectively, capturing system uncertainty and sensor inaccuracy.

In the considered system, the vehicle is influenced by unknown external disturbances, such as wind forces, which are not directly measured but affect the system dynamics. To enable real-time estimation of such disturbances, we introduce a co-state d_k representing the disturbance, and model it as a slowly varying process using a random-walk dynamic as described in Equation (28).

$$d_{k+1} = d_k + w_k^d, \qquad w_k^d \sim \mathcal{N}(0, W_k^d), \tag{28}$$

where w_k^d is a zero-mean Gaussian noise that captures the slow variation of the disturbance over time. This formulation assumes that the disturbance is smooth and time-correlated, and can therefore be included as an additional state variable in the Kalman filter.

The augmented state vector is defined according to Equation (29) to estimate both the system state and the disturbance.

$$x_k^{\text{aug}} = \begin{bmatrix} x_k \\ d_k \end{bmatrix} \tag{29}$$

The linearized system in discrete time with disturbance is compactly rewritten in an augmented form as proposed in Equations (30) and (31).

$$x_{k+1}^{\text{aug}} = \underbrace{\begin{bmatrix} A_k & F_k \\ 0 & I \end{bmatrix}}_{A_k^{\text{aug}}} x_k^{\text{aug}} + \underbrace{\begin{bmatrix} B_k \\ 0 \end{bmatrix}}_{B_k^{\text{aug}}} u_k + \underbrace{\begin{bmatrix} w_k \\ w_k^d \end{bmatrix}}_{w_k^{\text{aug}}}, \tag{30}$$

$$y_k = \underbrace{\begin{bmatrix} C_k & 0 \end{bmatrix}}_{C_k^{\text{aug}}} x_k^{\text{aug}} + v_k, \tag{31}$$

where w_k^{aug} is the combined process noise and $v_k \sim \mathcal{N}(0, V_k)$ is the measurement noise. The process noise covariance is described in Equation (32).

$$W_k^{\text{aug}} = \begin{bmatrix} W_k & 0 \\ 0 & W_k^d \end{bmatrix}. \tag{32}$$

The Kalman filter applied to this augmented system recursively estimates both the vehicle state and the unknown disturbance, enabling disturbance-aware feedback control.

The proposed LTV-LQG control framework for the investigated energy efficient vehicle is illustrated in Figure 6. The predefined driving strategy serves as the primary reference input to the controller, which is then adjusted by the LTV-LQG algorithm using the precomputed gains associated with the trajectory. This control block generates the modified torque command, which serves as the input to the vehicle. The Kalman filter estimates the internal states of the system, including the augmented disturbance states, which are also used in the feedforward control loop. This classical control architecture, tailored to the specific vehicle and trajectory, also enables the integration of simple and easily implementable strategies, such as the rule-based switching control described above. The MATLAB R2024a Simulink environment was used to implement both control frameworks.

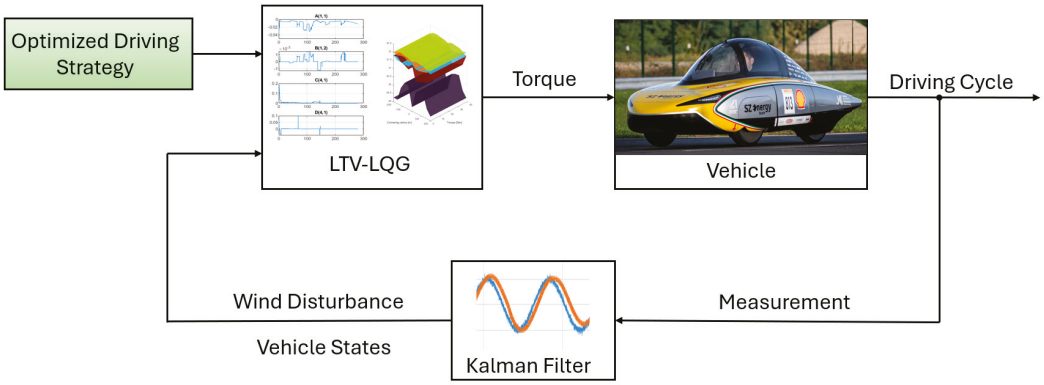

Figure 6. Block diagram of the control system.

5. Simulation Results

The developed rule-based switching control strategy describes the behavior of an ideal human driver operating the vehicle in accordance with the optimized driving strategy. During vehicle operation, the driver can monitor key parameters through a dedicated driver-assistant interface. This interface displays both the predetermined driving strategy and the actual speed profile in real time.

Theoretically, if no external disturbances occur, operating the vehicle according to the predefined reference torque T_{ref} will result the optimized speed profile as calculated in simulation. However, in real-world conditions, various disturbances, notably wind, affect vehicle motion, especially in the context of energy efficient vehicles with low driving resistances. Due to these disturbances, strictly following the reference torque does not necessarily result in the ideal speed trajectory that satisfies both the time limit and minimum energy consumption.

In practice, the driver compensates for disturbances by adding acceleration or deceleration. The vehicle control unit (VCU) determines the applied torque based on two torque levels: an acceleration torque T_{acc} and a cruising torque T_{cr}, which are defined during the optimization process. Switching between these torque levels depends on the vehicle's actual speed relative to a threshold called the switching speed v_{sw}, as well as the input of the driver (drive state).

This control mechanism supports the driver by allowing speed adjustments through a single button press and applying discrete torque values without manual modulation. Since torque levels T_{acc} and T_{cr} are derived from the powertrain model, this strategy is not only convenient from a software implementation perspective, but also relatively energy efficient. In the current implementation, the values are $T_{\text{acc}} = 40$ Nm and $T_{\text{cr}} = 10$ Nm.

This control strategy is implemented in simulation as a reference driver model, representing a perfectly responsive human driver, and is governed by Equation (33), where error is calculated based on the deviation from the speed trajectory.

$$T_{mod} = \begin{cases} -T_{acc}, & \text{if error} > 0.5 \text{ and } v < v_{\text{sw}} \\ -T_{cr}, & \text{if error} > 0.5 \text{ and } v \geq v_{\text{sw}} \\ T_{acc}, & \text{if error} < -0.5 \text{ and } v < v_{\text{sw}} \\ T_{cr}, & \text{if error} < -0.5 \text{ and } v \geq v_{\text{sw}} \\ 0, & \text{otherwise} \end{cases} \tag{33}$$

Varying wind conditions were simulated in the test scenarios using sinusoidal disturbance signals with Gaussian random noise, which provided an easily parameterized

and computationally convenient way to represent different magnitudes and frequencies for benchmarking the models. Although this configuration offers a useful reference, it is rarely encountered in real-world conditions and represents a limitation, as it excludes the sudden, gust-like effects of wind. In this study, the direction of the wind was not explicitly modeled, but only its net effect on the longitudinal motion was considered. These scenarios are classified as neutral(Bias = 0), headwind-dominant (Bias > 0), and tailwind-dominant (Bias < 0). In the neutral case, the wind force alternates symmetrically around zero, periodically assisting and resisting the vehicle with equal intensity.

Headwind-dominant scenarios introduce a consistent opposing force, increasing energy demand, whereas tailwind-dominant cases generate a net propelling force, leading to lower energy consumption. Since real environments typically exhibit biased wind conditions, these two cases offer a more realistic evaluation of vehicle behavior under disturbances. Table 2. summarizes the disturbance signal parameters used for each scenario.

Table 2. Parameter settings for Cases 1–20. Amplitude and bias are given in newtons (N), frequency in hertz (Hz).

Case	Amplitude [N]	Bias [N]	Frequency [Hz]
1	15	0	1.0
2	15	10	1.0
3	15	−10	1.0
4	15	20	1.0
5	15	−20	1.0
6	30	0	1.0
7	30	10	1.0
8	30	−10	1.0
9	30	20	1.0
10	30	−20	1.0
11	15	0	0.1
12	15	10	0.1
13	15	−10	0.1
14	15	20	0.1
15	15	−20	0.1
16	30	0	0.1
17	30	10	0.1
18	30	−10	0.1
19	30	20	0.1
20	30	−20	0.1

The cumulative effects of headwind-dominant scenarios are visualized in Figures 7 and 8, where the envelope curves represent the full range of simulated vehicle speed and energy consumption values. These visualizations highlight the controllers' behavior under adverse wind conditions. The envelope is defined by the area between the reference curve (solid black line), derived from the optimized driving strategy, and the corresponding simulation results. The position and shape of this shaded region convey the aggregated deviation from the reference trajectory due to external disturbances.

It is clearly visible that headwind-dominant cases are not adequately handled by the Switching algorithm, as it tends to exceed the time limit and shows greater variance compared to the reference. In contrast, the LTV-LQG controllers easily follow the predefined time constraint. Although the Switching strategy may result in lower energy consumption in some cases, these simulation attempts fail to meet the timing requirements.

Similarly, the tailwind-dominant scenarios are shown in Figures 9 and 10. It is immediately apparent that the deviations from the reference speed are significantly larger compared to the headwind cases. This behavior is due to the supportive nature of tailwind,

which provides additional propulsion that the controller does not counteract, as it assists the vehicle's motion.

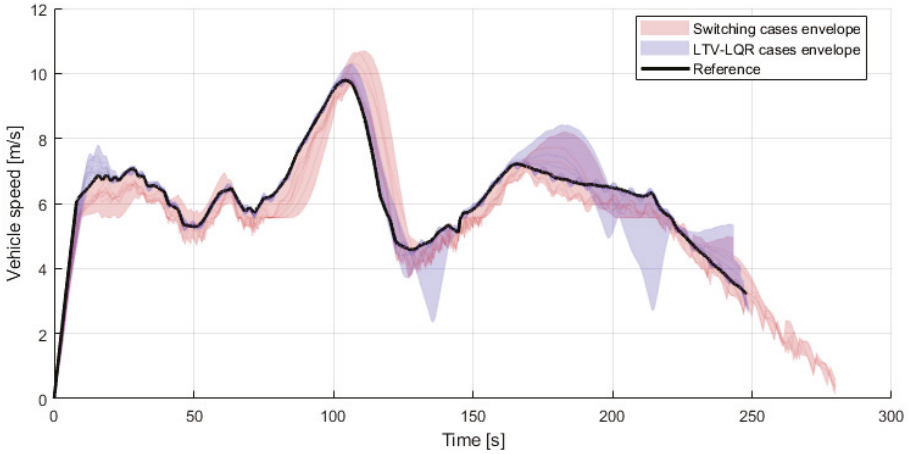

Figure 7. Headwind dominant scenarios—Vehicle Speed.

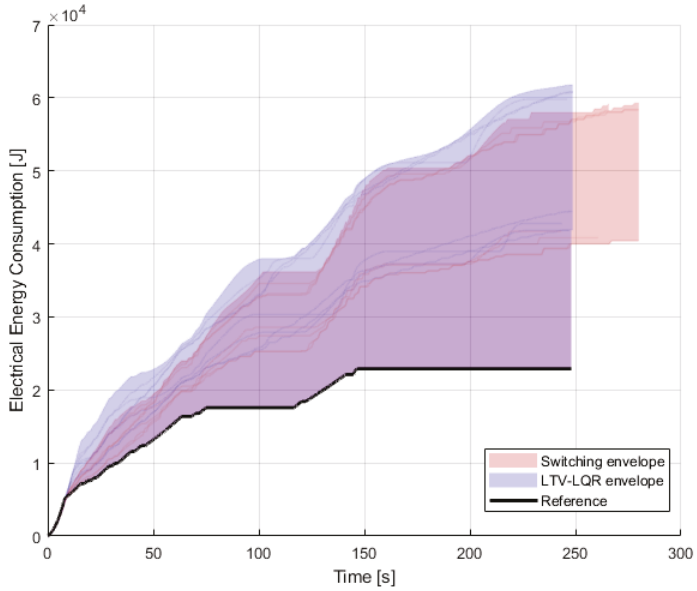

Figure 8. Headwind dominant scenarios—Electric Energy Consumption.

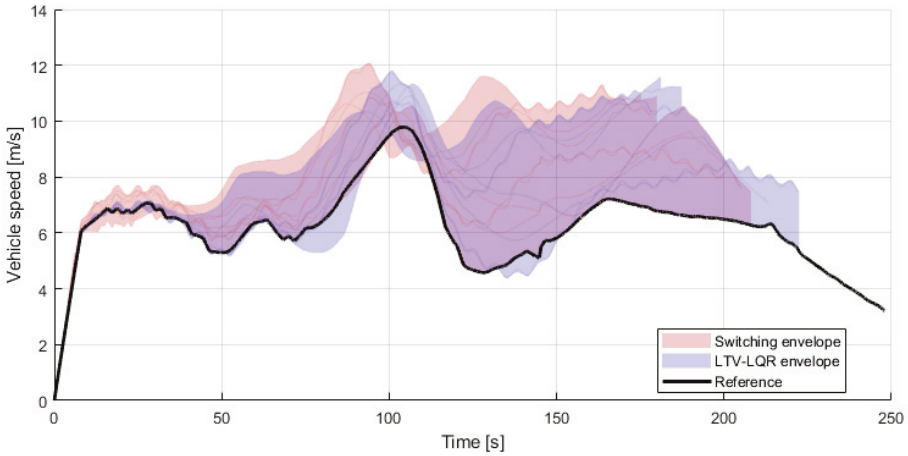

Figure 9. Tailwind dominant scenarios—Vehicle Speed.

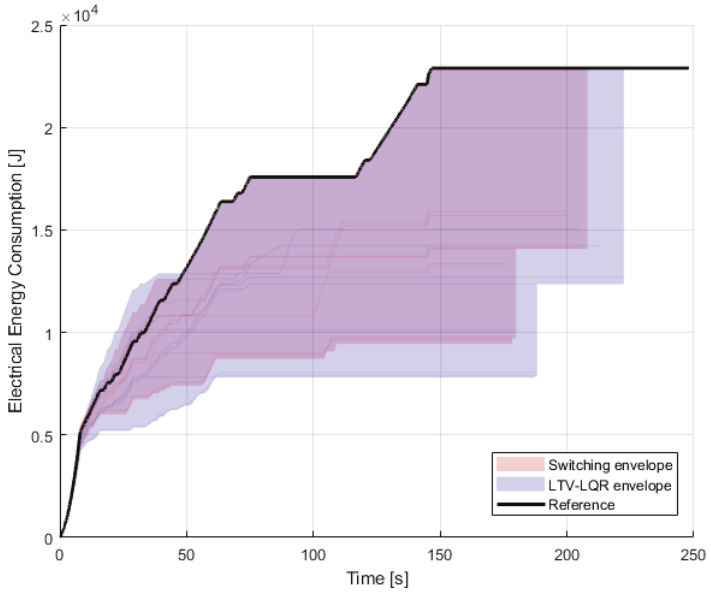

Figure 10. Tailwind dominant scenarios—Electric Energy Consumption.

The beneficial effect of tailwind is reflected in energy consumption, which is consistently lower than in the reference case for both control strategies. The energy savings depends on how effectively the control algorithm takes advantage of the wind assistance. In this regard, the advantage of the LTV-LQG approach is evident. Due to the Kalman filter-based disturbance estimation and the inherently more accurate and smoother control it provides, the LTV-LQG controller achieves better utilization of the tailwind.

This is also demonstrated by the envelope curves, where the LTV-LQG results exhibit a broader spread and lower energy values, indicating improved performance in tailwind-dominant conditions compared to the simpler switching strategy.

The detailed results of the simulation cases are presented in Table 3, where the two main indicators are the final simulation time, which should stay within one percent of the allowed time limit (248 s), and the total electric energy consumption for each case. The simulation was terminated at 280 s if the trajectory's end distance value was not reached. In scenarios with strong headwinds, this issue could occur with the switching control approach.

A more illustrative visualization is provided in Figure 11, where the deviations from the reference values are presented in the form of a heatmap, allowing for a clearer interpretation of the relationship between the time deviation and the energy deviation. The simulation was terminated at 280 s if the trajectory end-distance value was not reached. In scenarios with strong headwinds, this issue could occur with the switching control approach. The LTV-LQG controller achieved up to 15.4% lower energy consumption compared to the switching control in tailwind dominant scenarios (case 3).

Additional sensitivity tests were carried out following the main simulation studies. In the first test, the feedforward component of the controller was deactivated by setting it to zero, thereby emulating a scenario in which the Kalman filter is used solely for filtering the measurement signal to suppress noise, but the disturbance compensation is omitted. Under this condition, the energy consumption increased by up to 0.696% compared to the fully functioning framework. In a second test, the feedback gain was set to zero while the raw, unfiltered measurement signal was used directly. This emulates the effect of disabling the Kalman filter entirely. In this case, the framework exhibited degraded performance, with energy consumption increasing by up to 5.91% compared to the nominal

case. These sensitivity analyses highlight the importance of proper tuning and integration of the Kalman filter in the proposed LTV-LQG control architecture.

Table 3. Final time and energy values for each control method (LTV-LQG and Switching) for Cases 1–20.

Case	Final Time [s] (LTV-LQG)	Final Time [s] (Switching)	Final Energy [J] (LTV-LQG)	Final Energy [J] (Switching)
1	248.34	253.07	23,590	22,843
2	248.66	280.00	44,448	40,397
3	222.43	199.85	12,370	15,893
4	248.87	280.00	60,834	58,402
5	187.99	177.87	8030	9634
6	248.02	250.41	23,453	23,303
7	248.66	280.00	41,933	40,428
8	221.99	200.73	12,696	15,712
9	248.92	280.00	60,723	58,329
10	188.20	178.41	7875	9460
11	239.53	239.83	25,822	24,516
12	247.12	260.67	41,841	40,850
13	213.23	208.06	14,236	14,094
14	248.66	280.00	61,785	59,284
15	187.40	179.93	7820	9736
16	237.09	228.87	25,581	26,818
17	243.52	243.32	42,801	41,717
18	204.56	205.19	15,029	14,123
19	246.03	265.72	59,801	59,185
20	181.19	175.23	10,126	13,340

The scope of the present study is limited to simulation-based validation of the proposed controller. Hardware-in-the-loop and real-vehicle tests are planned as the next step to further strengthen the practical relevance of the proposed method.

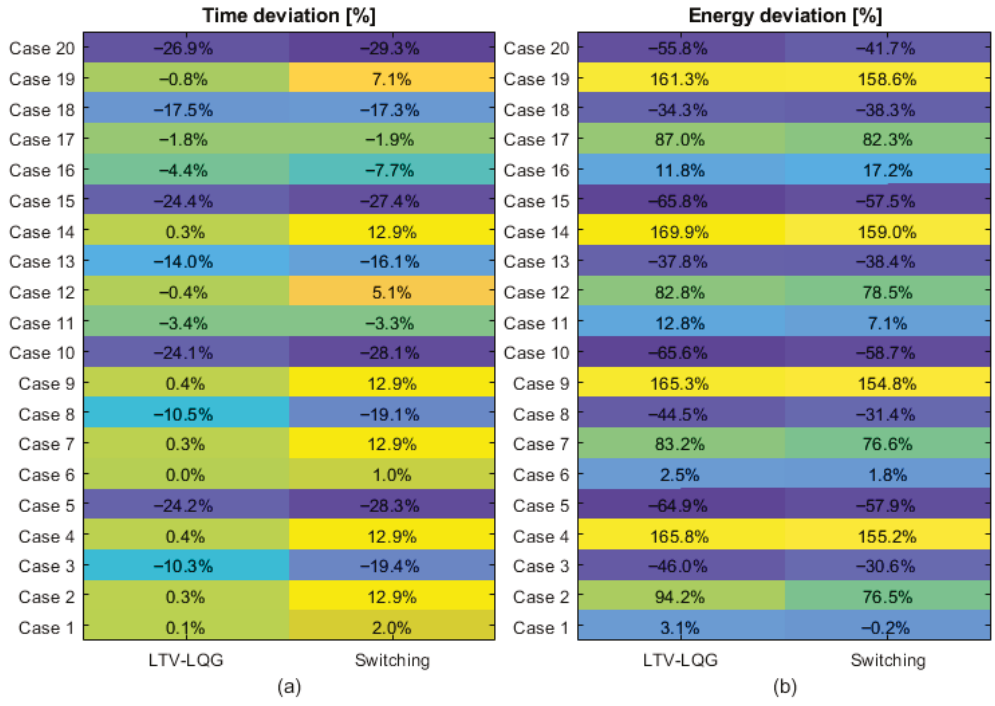

Figure 11. Comparison of simulation results for cases 1–20 with the reference trajectory: (**a**) Heatmap illustrating the deviation in final time, (**b**) Heatmap illustrating the deviation in energy consumption.

6. Conclusions

This paper presents a practical and effective control strategy for improving energy efficiency in electric vehicles through a Linear Time-Varying Linear Quadratic Gaussian (LTV-LQG) approach. The method relies on trajectory linearization around a predetermined driving strategy, which is generated offline using a genetic algorithm (GA) to optimize energy consumption based on a nonlinear vehicle model. Although the reference trajectory assumes disturbance-free conditions, the proposed controller accounts for real-world uncertainties by incorporating external disturbances into the model. The LTV-LQG controller applies precomputed, trajectory-dependent gains to generate modified torque input, while a Kalman filter estimates both the internal system states and the disturbance states for feedforward compensation. The controller's performance is evaluated by comparing it to a rule-based switching strategy, which describes ideal human-driver behavior. Simulations in various wind disturbance scenarios demonstrate that the LTV-LQG approach outperforms the switching controller by reliably maintaining time constraints and achieving up to 15.4% lower energy consumption. Future work will investigate the extension of this framework to further enhance performance. The present study has some limitations.

As this work has been carried out in a simulation environment, the next phase of the research will focus on hardware-in-the-loop and real-vehicle testing to confirm the practical feasibility of the proposed approach. This will address the main limitation of the present study by validating the LTV-LQG controller under real operating conditions. The controller requires only vehicle speed measurement, and preliminary calculations confirm that the applied VCU hardware (dsPIC33EV256GM106) can reliably execute the proposed LTV-LQG framework at 100 Hz, ensuring real-time feasibility. After successful vehicle testing, the theoretical next step will be the extension of the methodology towards MPC-based control, which may also necessitate additional hardware developments. In general, the proposed LTV-LQG control algorithm provides a robust and practical solution, easily implementable in the experimental electric vehicle, with clear potential for extension to other vehicle applications.

Author Contributions: Conceptualization, Z.P. and T.G.L.; methodology, Z.P. and T.G.L.; formal analysis, Z.P. and T.G.L.; writing—original draft preparation, Z.P.; writing—review and editing, T.G.L.; visualization, Z.P.; supervision, T.G.L. and F.F.; project administration, F.F.; funding acquisition, Z.P. and F.F. All authors have read and agreed to the published version of the manuscript.

Funding: The study was supported by EKÖP-24-4-I-SZE-142 University Research Fellowship Program of the Ministry for Culture and Innovation from the source of the National Research, Development and Innovation Fund.

Institutional Review Board Statement: Not applicable.

Informed Consent Statement: Not applicable.

Data Availability Statement: The datasets presented in this article are not readily available because they are part of an ongoing study.

Acknowledgments: This research was supported by the Research Center of Vehicle Industry (SZE-JKK) and the SZEnergy Team, whose contributions included providing the experimental platform and measurement data.

Conflicts of Interest: The authors declare no conflicts of interest.

Abbreviations

The following abbreviations are used in this manuscript:

LTV-LQG	Linear Time-Varying Linear Quadratic Gaussian
LTV	Linear Time Varying
GA	Genetic Algorithm
SEM	Shell Eco-marathon
CO_2	Carbon Dioxide
UC	Urban Concept
PSO	Particle Swarm Optimization
LQR	Linear Quadratic Regulator
HLQR	Hybrid Linear Quadratic Regulator
DCLQR	Distributed Control Linear Quadratic Regulator
SOC	State of Charge
MPC	Model Predictive Control
PID	Proportional–Integral–Derivative controller
LMS-IOBR	Least Mean Square-Input-Output-Based Robust
V2I	Vehicle-to-Infrastructure
PMSM	Permanent Magnet Synchronous Motor
RTK	Real Time Kinematic
GNSS	Global Navigation Satellite system
LQ	Linear Quadratic
HDR	High-Density Region
KDE	Kernel Density Estimation
VCU	Vehicle Control Unit

References

1. Li, M.J.; Tao, W.Q. Review of methodologies and polices for evaluation of energy efficiency in high energy-consuming industry. *Appl. Energy* **2017**, *187*, 203–215. [CrossRef]
2. Kobayashi, S.; Plotkin, S.; Ribeiro, S.K. Energy efficiency technologies for road vehicles. *Energy Effic.* **2009**, *2*, 125–137. [CrossRef]
3. Rahman, K.; Hiti, S. Trends in EV propulsion components and systems [about this issue]. *IEEE Electrif. Mag.* **2017**, *5*, 23. [CrossRef]
4. Albuquerque, F.D.B.; Maraqa, M.A.; Chowdhury, R.; Mauga, T.; Alzard, M. Greenhouse gas emissions associated with road transport projects: Current status, benchmarking, and assessment tools. *Transp. Res. Procedia* **2020**, *48*, 2018–2030. [CrossRef]
5. Candela, A.; Sandrini, G.; Gadola, M.; Chindamo, D.; Magri, P. Lightweighting in the automotive industry as a measure for energy efficiency: Review of the main materials and methods. *Heliyon* **2024**, *10*, e29728. [CrossRef] [PubMed]
6. Malozyomov, B.; Martyushev, N.; Sorokova, S.; Efremenkov, E.; Valuev, D.; Qi, M. Mathematical Modelling of Traction Equipment Parameters of Electric Cargo Trucks. *Mathematics* **2024**, *12*, 577. [CrossRef]
7. Schäfers, L.; Silber, D.; Savelsberg, R.; Pischinger, S. Efficient Determination of Driving Resistance through System Identification Based on Driving Route Information and Weather Data. *Expert Syst. Appl.* **2023**, *232*, 120755. [CrossRef]
8. Jin, L.; Tian, D.; Zhang, Q.; Wang, J. Optimal Torque Distribution Control of Multi-Axle Electric Vehicles with In-wheel Motors Based on DDPG Algorithm. *Energies* **2020**, *13*, 1331. . [CrossRef]
9. Yin, D.; Wang, J.; Du, J.; Chen, G.; Hu, J.S. A New Torque Distribution Control for Four-Wheel Independent-Drive Electric Vehicles. *Actuators* **2021** , *10*, 122. [CrossRef]
10. Carmeli, M.; Castelli-Dezza, F.; Galmarini, G.; Mastinu, G.; Mauri, M. A urban vehicle with very low fuel consumption: Realization, analysis and optimization. In Proceedings of the 2014 Ninth International Conference on Ecological Vehicles and Renewable Energies (EVER), Monte-Carlo, Monaco, 25–27 March 2014 ; pp. 1–6. [CrossRef]
11. Olivier, J.C.; Wasselynck, G.; Chevalier, S.; Auvity, B.; Josset, C.; Trichet, D.; Squadrito, G.; Bernard, N. Multiphysics modeling and optimization of the driving strategy of a light duty fuel cell vehicle. *Int. J. Hydrogen Energy* **2017**, *42*, 26943–26955. [CrossRef]
12. Targosz, M.; Skarka, W.; Przystałka, P. Model-Based Optimization of Velocity Strategy for Lightweight Electric Racing Cars. *J. Adv. Transp.* **2018**, *2018*, 3614025. [CrossRef]
13. Carello, M.; Bertipaglia, A.; Messana, A.; Airale, A.G.; Sisca, L. Modeling and Optimization of the Consumption of a Three-Wheeled Vehicle. *SAE Tech. Pap.* **2019**, *2019*, 1–9. [CrossRef]

14. Sawulski, J.; Ławryńczuk, M. Optimization of control strategy for a low fuel consumption vehicle engine. *Inf. Sci.* **2019**, *493*, 192–216. [CrossRef]
15. Stabile, P.; Ballo, F.; Mastinu, G.; Gobbi, M. An Ultra-Efficient Lightweight Electric Vehicle—Power Demand Analysis to Enable Lightweight Construction. *Energies* **2021**, *14*, 766. [CrossRef]
16. Stabile, P.; Ballo, F.; Previati, G.; Mastinu, G.; Gobbi, M. Eco-Driving Strategy Implementation for Ultra-Efficient Lightweight Electric Vehicles in Realistic Driving Scenarios. *Energies* **2023**, *16*, 1394. [CrossRef]
17. Rao, A.; Gupta, H.; Singh, P.; Mittal, S.; Singh, U.; Vishwakarma, D.K. Optimizing Electric Vehicle Efficiency with Real-Time Telemetry using Machine Learning. In Proceedings of the 2024 10th International Conference on Mechatronics and Robotics Engineering (ICMRE), Milan, Italy, 27–29 February 2024; pp. 213–219. [CrossRef]
18. Li, X.; Guan, G.; Tian, X.; Luo, Y.; Huang, Y.; Yang, J. Hybrid feedforward-feedback LQR controller based on model prediction for open channel water level control. *J. Hydroinform.* **2024**, *27*, 33–50. [CrossRef]
19. Zhang, M.; Li, X.; Liu, J.; Su, H.; Song, J. Digital LQR steady-state optimal control with feedforward for nonminimum phase boost DC-DC converter. In Proceedings of the 2016 Chinese Control and Decision Conference (CCDC), Yinchuan, China, 28–30 May 2016; pp. 384–389. [CrossRef]
20. Yang, T.; Bai, Z.; Li, Z.; Feng, N.; Chen, L. Intelligent Vehicle Lateral Control Method Based on Feedforward + Predictive LQR Algorithm. *Actuators* **2021**, *10*, 228. [CrossRef]
21. Haitao, Y.; Yulan, Z.; Zunnian, L.; Kui, H. LQR-Based Power Train Control Method Design for Fuel Cell Hybrid Vehicle. *Math. Probl. Eng.* **2013**, *2013*, 968203. [CrossRef]
22. Ren, X.; Lv, X.; Zhang, L.; Chen, L.; Chu, H.; Gao, B. LQR-based Predictive Energy-saving Control for Commercial Vehicles Based On Slope Information. In Proceedings of the 2022 6th CAA International Conference on Vehicular Control and Intelligence (CVCI), Nanjing, China, 28–30 October 2022; pp. 1–6. [CrossRef]
23. Li, Y.; Hao, G. Energy-Optimal Adaptive Control Based on Model Predictive Control. *Sensors* **2023**, *23*, 4568. [CrossRef]
24. Han, Z.; Xu, N.; Chen, H.; Huang, Y.; Zhao, B. Energy-efficient control of electric vehicles based on linear quadratic regulator and phase plane analysis. *Appl. Energy* **2018**, *213*, 639–657. [CrossRef]
25. Qin, Y.; Lu, Y.; Yue, H. An Improved Feedforward-Robust Algorithm for Active Vibration Control of Helicopter Maneuver Flight. *Int. J. Aerosp. Eng.* **2023**, *2023* , 3610865. [CrossRef]
26. Wang, R.; Sun, Q.; Sun, C.; Zhang, H.; Gui, Y.; Wang, P. Vehicle-Vehicle Energy Interaction Converter of Electric Vehicles: A Disturbance Observer Based Sliding Mode Control Algorithm. *IEEE Trans. Veh. Technol.* **2021**, *70*, 9910–9921. [CrossRef]
27. Bo, Z.; Di, W.; MinYi, Z.; Nong, Z.; Lin, H. Electric vehicle energy predictive optimal control by V2I communication. *Adv. Mech. Eng.* **2019**, *11*, 1687814018821523. [CrossRef]
28. Pusztai, Z.; Luspay, T.; Friedler, F. Control-Oriented Model for Energy-Efficient Electric Vehicle. In Proceedings of the 2025 IEEE 23rd World Symposium on Applied Machine Intelligence and Informatics (SAMI), Stará Lesná, Slovakia, 23–25 January 2025; pp. 000299–000304. [CrossRef]
29. Pusztai, Z.; Kőrös, P.; Szauter, F.; Friedler, F. Vehicle Model-Based Driving Strategy Optimization for Lightweight Vehicle. *Energies* **2022**, *15*, 3631. [CrossRef]

Disclaimer/Publisher's Note: The statements, opinions and data contained in all publications are solely those of the individual author(s) and contributor(s) and not of MDPI and/or the editor(s). MDPI and/or the editor(s) disclaim responsibility for any injury to people or property resulting from any ideas, methods, instructions or products referred to in the content.

vehicles

MDPI

Article

Defining the Optimal Characteristics of Autonomous Vehicles for Public Passenger Transport in European Cities with Constrained Urban Spaces

Csaba Antonya, Radu Tarulescu, Stelian Tarulescu and Silviu Butnariu *

Department of Automotive and Transport Engineering, Transilvania University of Brasov, 29 Eroilor Blvd, 500036 Brasov, Romania; antonya@unitbv.ro (C.A.); radu.tarulescu@unitbv.ro (R.T.); s.tarulescu@unitbv.ro (S.T.)
* Correspondence: butnariu@unitbv.ro

Abstract

This research addresses the complex challenge of integrating modern public transport into historic medieval city centers. These unique urban environments are characterized by narrow streets, protected heritage status, and topographical constraints, which are incompatible with conventional transit vehicles. The introduction of standard bus routes often aggravates traffic congestion and fails to meet the specific mobility needs of residents and visitors. This paper suggests that autonomous electric buses represent a viable and sustainable solution, capable of navigating these constrained environments while aligning with modern energy efficiency goals. The central challenge lies in the optimal selection of an autonomous electric bus that can operate safely and efficiently within the tight streets of historic city centers while satisfying the travel demands of passengers. To address this, a comprehensive study was conducted, analyzing resident mobility patterns—including key routes and hourly passenger loads—and the specific geometric constraints of the road network. Based on this empirical data, a vehicle dynamics model was developed in Matlab®. This model simulates various operational scenarios by calculating the instantaneous forces (rolling resistance, aerodynamic drag, inertial forces) and the corresponding power required for different electric bus configurations to follow pre-established speed profiles. The core of this research is an optimization analysis, designed to identify the balance between minimizing total energy consumption and maximizing the quality of passenger service. The findings provide a quantitative framework and clear procedures for urban planners to select the most suitable autonomous transit system, ensuring that the chosen solution enhances mobility and accessibility without compromising the unique character of historic cities.

Keywords: autonomous vehicle; public passenger transport; constrained urban spaces

1. Introduction

Autonomous vehicles (AVs) are of significant interest to the public transport sector due to their potential to revolutionize urban mobility. Their implementation promises several benefits that address many of the challenges in city transit, including operational efficiency through optimized routes and continuous service, enhanced safety by mitigating human error, and improved accessibility for individuals with mobility limitations. Furthermore, the transition to autonomous transit systems presents opportunities for reduced operational costs by eliminating driver expenses and optimizing energy consumption, which in turn reduces the environmental impact by decreasing greenhouse gas emissions and air pollution.

However, for a large portion of European cities, the integration of modern transport solutions is severely constrained by historic infrastructure. Many urban centers, particularly those with medieval origins, are characterized by narrow streets, protected heritage buildings, and dense populations. These environments were not designed for contemporary vehicle traffic, and the introduction of standard-sized buses often leads to severe traffic congestion, inefficient service, and a deterioration of the urban scenery. This creates a fundamental conflict between the mobility needs of citizens and the preservation of cultural heritage.

Technical and economic effectiveness of transport systems on the basis of autonomous cars is a barrier to mass adoption and integration into existing public transport networks. Further data from different European cities are needed to close gaps in the integration of electric cars into transport services. Another barrier is data protection and privacy (vulnerability to cyberattacks that pose risks to users and operators). Experimental data on the danger of cyberattacks would be a body of evidence from pilot projects adding AVs to old cities. Such data would form the basis of deciding remedies to counter such threats. There are loopholes in European law addressing the use and ownership of autonomous cars as well. These legislative uncertainties complicate the integration of AVs into existing transportation infrastructure (problem of civil liability in the case of accidents—legislation in every European state). Lack of proper data and studies on adaptation by users to the autonomous vehicle transportation system is an incomplete link to popularization of such transportation systems. It will take a long period before users would fully trust the transport service with Autonomous Vehicles (integration and acceptance problems). The solution is to automate public transport step by step so that users would get used to and trust the services. Statistics would drastically reduce the time spent in accepting and integrating AVs in ancient cities [1].

Problems of implementing AVs in transport services are explored in projects and publications. There are data on: period of car life; location map of implementation cities; power supply systems; Users; adaptation of public transport services; national legislation and policies; rush hour speed [2].

There are also needs for data gaps in optimal balance among vehicle size, passenger capacity, and service frequency to achieve maximum energy efficiency as well as maximum passenger satisfaction. There are also needs for data gaps in the features needed to enable an autonomous vehicle to drive efficiently in a historic city center.

In this context, the deployment of compact, autonomous electric buses emerges as a promising solution. This paper explores the operability and viability of such a system by addressing several key questions:

- What are the critical physical and operational characteristics required for an autonomous vehicle to navigate a historic city center effectively?
- Do existing autonomous vehicle technologies adequately address these unique challenges?
- What is the optimal balance between vehicle size, passenger capacity, and service frequency to maximize both energy efficiency and passenger satisfaction?

The scientific literature and existing pilot projects indicate that for successful operation in constrained environments, AVs must possess compact dimensions to minimize congestion, as well as superior maneuverability enabled by advanced steering systems. This, however, introduces a critical optimization problem: is it more effective to deploy a larger AV that meets the maximum dimensional limits of the infrastructure but operates at a low frequency, or to use smaller AVs that run at a higher frequency? Answering this question requires a multi-objective analysis that weighs criteria such as energy consumption, operational costs, and passenger service quality.

Technologically, the safe operation of these vehicles is very important. The deployment of AVs in pedestrian-heavy zones necessitates a sophisticated and redundant sensor suite—including lidar, radar, and cameras—to ensure complete perception of the surrounding environment, even in adverse conditions. To align with sustainability goals, an electric propulsion system is the preferred choice, requiring sufficient battery autonomy and fast-charging capabilities to meet the demands of public transport routes. Operationally, this is supported by precise navigation, V2X (Vehicle-to-Everything) communication, and seamless integration with existing transit networks.

To ground this research in a real-world scenario, the city of Brașov, Romania, was selected as a case study. Brașov's historic center, originating in the 14th century, retains its medieval street plan, which now serves as a major tourist destination and a critical transit zone for approximately 10,000 residents. The area contains roadways and intersections that are too narrow for conventional public or private transport, creating significant traffic bottlenecks and limiting mobility (Figure 1a—narrow streets, Figure 1b—Piața Unirii intersection).

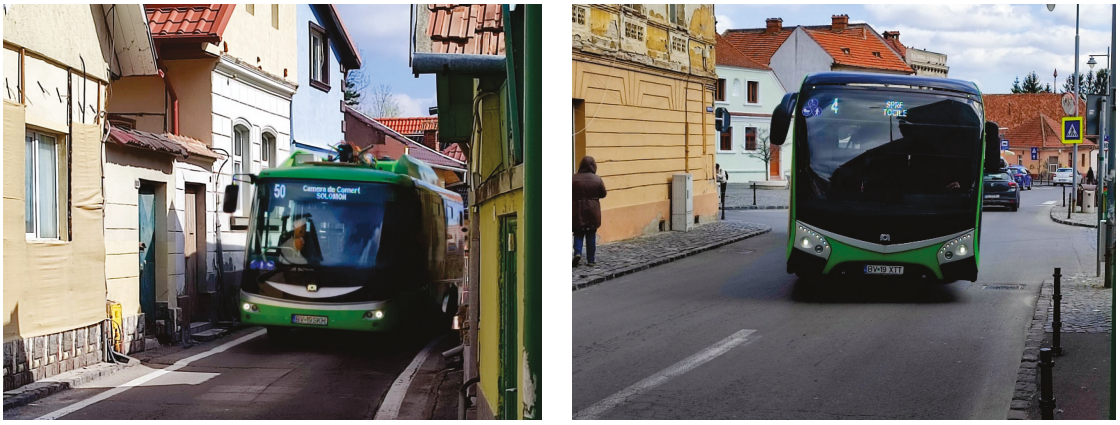

(**a**) (**b**)

Figure 1. Narrow streets of Brașov city (**a**) Pe Tocile St., the bus has difficulty squeezing through the houses; (**b**) Piata Unirii intersection, the bus turning right at 90 degrees violates the lane in the opposite direction of travel.

To address the primary purpose of this work, the following operational objectives have been established:

- Identify the required vehicle dimensions and maneuverability for a specific route.
- Evaluate the impact on existing infrastructure and traffic flow.
- Model and compare the energy consumption of different vehicle configurations.
- Propose a solution that resolves the transport needs of the area's inhabitants.

This paper is structured as follows: Section 2 presents the current state of the art in the field. Section 3 details the work methodology, including the identification of key vehicle characteristics and the criteria for comparison. Section 4 is dedicated to the simulation and data analysis. Finally, Section 5 presents a discussion of the results, followed by conclusions and recommendations.

2. State of the Art

2.1. Autonomous Vehicle Technology

Autonomous vehicles are built on three technological pillars that enable their autonomy: advanced sensor systems for perception, precise navigation and mapping technologies for localization, and decision-making and control algorithms for action.

2.1.1. Sensor Systems

The sensor systems of an autonomous vehicle enable it to perceive and interpret its surroundings in real-time. These sensors gather multi-dimensional data used for localization, object detection, and tracking.

- LiDAR (Light Detection and Ranging) systems use laser pulses to generate dense, three-dimensional point clouds, providing precise spatial data about surrounding objects. Recent studies by Yuan et al. [3] demonstrate how LiDAR data fusion improves object recognition and depth estimation, particularly under poor lighting conditions. However, the cost of LiDAR and its performance in adverse weather remain active research topics [4].
- Radar systems are highly effective for long-range object detection and velocity estimation, proving especially useful in conditions of poor visibility such as rain or fog. Operating in the millimeter-wave spectrum, they are less sensitive to environmental interference. Newer 4D radar systems enhance spatial resolution, supporting more robust object tracking in complex, multi-object scenarios [5,6].
- Cameras are indispensable for tasks requiring semantic interpretation, such as traffic light detection, lane marking identification, and traffic sign recognition. Monocular, stereo, and fisheye camera arrays are commonly mounted around the vehicle to provide a 360-degree visual field. Deep learning models are widely used for object detection and classification from visual inputs [7,8].

The fusion of data from these diverse sensors is critical for robust performance. Sensor fusion frameworks—ranging from traditional Kalman filtering to advanced deep fusion networks—enable the system to synthesize multiple data streams for greater accuracy, resilience, and redundancy [9].

2.1.2. Navigation and Mapping Technologies

Navigation and localization systems are important for guiding the vehicle's movement by determining its precise position and path within the environment.

- GPS (Global Positioning System) is a foundational technology, but its standard accuracy of approximately five meters is inadequate for the lane-level navigation required by AVs. Augmenting GPS with Inertial Measurement Units (IMUs) and Real-Time Kinematic (RTK) positioning can reduce error margins to centimeter levels.
- HD Maps (High-Definition Maps) are highly detailed, multi-layered digital representations of the road network that include semantic elements like curbs, traffic signs, and crosswalks. They are essential for predictive path planning and precise vehicle localization [10,11].
- SLAM (Simultaneous Localization and Mapping) algorithms allow AVs to build and update maps in real-time while navigating, which is critical for operation in unknown or dynamically changing areas. Visual SLAM and LiDAR SLAM are the most studied variants [12,13].

Hybrid approaches that combine global positioning, local odometry, and pre-built HD maps provide the most robust navigation solution, particularly in complex urban environments.

2.1.3. Decision-Making and Control Algorithms

Decision-making systems coordinate autonomous vehicles' responses to a complex and dynamic environment, including route planning, behavioral modeling, and motion control.

- Path Planning in modern AVs typically uses a hierarchical framework. Global planners determine the overall route to a destination, while local planners calculate safe,

collision-free trajectories in the immediate vicinity. Algorithms such as Hybrid A*, D*, and RRT* are widely used for generating smooth, drivable paths [14].

- Behavior Planning involves context-aware decision-making under uncertainty. Methodologies such as Finite State Machines (FSMs), Partially Observable Markov Decision Processes (POMDPs), and reinforcement learning models are deployed to select appropriate driving behaviors in response to traffic conditions and interactions with other road users [15,16].
- Control Systems transform planned trajectories into real-time steering, acceleration, and braking commands. Model Predictive Control (MPC), Linear Quadratic Regulators (LQR), and PID controllers are extensively used for longitudinal and lateral vehicle control. Research indicates that MPC is particularly effective for managing constraints related to road curvature and vehicle dynamics [17,18].

An emerging trend is the development of end-to-end learning models, where perception, planning, and control are jointly optimized within a single neural network [19]. However, the safety validation and interpretability of these systems remain significant ongoing challenges.

2.2. Urban Mobility and Public Transport

Urban mobility is undergoing a significant transformation driven by rapid urbanization, technological advancements, and evolving societal expectations. Historic city centers, such as that of Brașov, face a unique set of challenges related to infrastructure limitations and heritage preservation. In these contexts, the demand for efficient connectivity and the integration of emerging technologies like autonomous vehicles have become critical components of modern urban transport strategies.

Deploying AVs in public transit settings is challenging, especially in dense urban environment with mixed traffic, regulatory constraints, and safety expectations [20]. Several projects now operate at Level 4 (without driver) or Level 3 (supervised autonomy) in controlled areas or geofenced corridors. These pilots explore use cases including shuttles, feeders, and integrated network augmentation. The most important project, AVENUE (in France, Luxembourg, Italy and United Kingdom) deployed automated buses in four European cities, using shared, electric autonomous shuttles integrated into urban transport networks. It studied user acceptance, operations in mixed traffic, and safety protocols [21]. Cities like Lyon (France), Helsingborg (Sweden), and Berlin have tested the NAVYA project or EasyMile autonomous shuttles on short fixed routes. These vehicles typically carry 8 to 12 passengers, run at low speeds (less than 25 km/h), and operate in controlled conditions (e.g., separated lanes, pedestrian zones) [22]. Another project, LogiSmile, exemplifies AV deployment in urban logistics. It pilots autonomous delivery vehicles in European cities to optimize last mile flows, which has parallels for AV public transport [23].

High-definition maps, reliable localization, and V2X (vehicle-to-infrastructure) communication are essential. Pilots require roadway modifications or sensor infrastructure to support AV operations. Low speeds, limited range, and cautious acceleration are common constraints. Many pilots restrict AVs to controlled conditions or off-peak hours to minimize risk. Pilots are expensive, require specialized oversight, and often rely on subsidies or research funding. Scaling to full public transport networks is still aspirational. Despite challenges, pilots provide valuable lessons in human–machine interaction, system reliability, and incremental integration.

2.2.1. Challenges of Public Transport in Historical City Centers

Historical urban cores are characterized by narrow streets, strict heritage preservation requirements, and high pedestrian density. These constraints often prevent the implemen-

tation of large-scale public transport infrastructure [24]. Traditional buses and trams may be too large or disturbing for these settings, leading to traffic congestion, inefficient service, and accessibility issues. In many European cities, attempts to retrofit transit systems in historical centers have created conflicts between mobility demands and conservation efforts [25]. Furthermore, issues of traffic congestion, air pollution, and noise are amplified in these dense areas. Researchers like Banister [26] argue that urban sustainability in such areas depends on shifting from car-dominant paradigms to integrated, low-impact transport solutions.

2.2.2. Existing Solutions for Last-Mile Connectivity

Last-mile connectivity refers to the final part of a journey from a transit hub to a destination. This is a persistent barrier in achieving door-to-door mobility, particularly in cities with fragmented networks. According to [27], shared mobility services, such as bike-sharing, e-scooters, and demand-responsive shuttles, offer scalable last-mile options. The integration of active transport (walking and cycling) with mass transit improves both health and environmental outcomes [28]. Transit-oriented development (TOD) strategies that prioritize walkable neighborhoods and mixed land use have been shown to reduce last-mile barriers [29].

Digital platforms that enable multimodal trip planning and ticketing, like Mobility-as-a-Service (MaaS), are also key enablers. Studies in Helsinki and Vienna have demonstrated the potential of MaaS in reducing car dependency by streamlining travel experiences [30].

2.2.3. Studies on the Integration of Autonomous Vehicles in Urban Environments

Autonomous vehicles are increasingly seen as a transformative force in urban mobility. Their deployment in shared public transport modes, such as the autonomous shuttle pilots in cities like Lyon, Las Vegas, and Geneva, has demonstrated their potential [31]. Research indicates that shared AVs could enhance safety, reduce operational costs, and support low-emission mobility if properly integrated with public transport networks [32]. However, concerns regarding curb management, drop-off positions, safe interaction with pedestrians in crowded zones, and data control remain unresolved. Studies emphasize that policy frameworks must promote inclusive design and ensure that autonomous vehicle deployment complements, rather than competing with existing mass transit systems [33].

2.3. Urban Planning and Infrastructure

The introduction of autonomous vehicles into urban environments has the potential to significantly reshape city planning, infrastructure, and transportation policies. The integration of AVs necessitates changes in urban areas, such as a reduced need for parking, which could alter land use and support economic growth.

2.3.1. The Impact of Autonomous Vehicles on Street Design and Traffic Flow

AVs necessitate a rethinking of traditional street layouts. Their capacity for precise navigation and responsive driving behaviors may allow for narrower lanes and reduced spacing between vehicles, potentially reclaiming urban space for pedestrians, cyclists, and green infrastructure [34]. In terms of traffic flow, AVs are expected to reduce congestion by maintaining consistent speeds and minimizing reaction time delays. Coordinated AV movements can mitigate bottlenecks and optimize traffic signal performance [33]. However, the overall impact depends heavily on the ownership model; privately owned AVs may increase vehicle kilometers traveled (VKT), whereas shared autonomous vehicles (SAVs) can support more efficient usage patterns. Infrastructure sensors, vehicle-to-everything (V2X) communication, and dynamic signage are also likely to become integral to future street design, requiring digital as well as physical infrastructure planning [31].

2.3.2. Challenges in Adapting Existing Infrastructure

Legacy infrastructure was not designed for autonomous navigation. Retrofitting roads, intersections, and signage to accommodate AVs presents significant logistical and financial challenges, especially in historic urban areas where physical alterations are often restricted [32]. Planners must also manage the transitional period where AVs and conventional vehicles share the road, a mixed-traffic environment that poses safety and predictability challenges [35]. Furthermore, the operational dependence of AVs on high-definition maps and real-time data highlights the need for robust ICT infrastructure, making the deployment of 5G and edge computing critical for enabling low-latency data exchange [36].

2.3.3. Regulations and Policies for the Implementation of Autonomous Vehicles

The policy environment surrounding AVs is still evolving. Key considerations include data privacy, cybersecurity, insurance liability, and the ethical frameworks governing decision-making algorithms. Establishing clear lines of accountability in the event of an accident is one of the most pressing legal challenges [37]. Successful implementation requires close coordination among transport authorities, technology providers, and the public to ensure that the benefits of autonomous mobility are distributed equitably [33].

In June 2022, Regulation (EU) 2022/2236 [38] on the technical requirements for vehicles produced in unlimited series, also integrated autonomous vehicles produced in small series and special-purpose vehicles, and the specifications on the software update.

Regulation (EU) 2022/1426 entered into force on 5 August 2022 [39]. It lays down detailed rules for the application of Regulation (EU) 2019/2144 proposed by the European Parliament and the Council of the European Union laying down the procedures and technical specifications for the approval of automated driving systems (ADS) for autonomous vehicles [40].

According to the mentioned regulations, three autonomous vehicle architectures were considered:

- Dual vehicles: manual driving and fully automated driving.
- Fully automated vehicles of categories N1, N2, N3, M1, M2, M3 without a driver's seat, with passengers.
- Fully automated vehicles in categories N1, N2 and N3 without driver seat and without occupants.

Cybersecurity and Software Updates legislation articles are as follows:

- UNECE Reg. 155 [41] for the approval of vehicles with regard to cybersecurity and the cybersecurity management system.
- UNECE Reg. 156 [42] for the approval of vehicles with regard to the software update management system.

Deployment of ITS legislation articles are as follows:

- Directive 2010/40/EU of the European Parliament and of the Council of 7 July 2010 [43] governing the framework for the deployment of intelligent transport systems in road transport and for interfaces with other modes of transport.
- 2017/2380 Decision amending Directive 2010/40/EU [44]. The decision requires compliance with the specifications necessary to ensure compatibility, interoperability and continuity of the deployment and operational use of Intelligent Transport Systems for priority actions for a further period of five years starting with 27 August 2017.

2.4. Social Acceptance and User Experience of Autonomous Vehicles as Means of Transport

The social integration of autonomous vehicles requires not only technological maturity but also public perception, user expectations, and equitable access. Following studies

and theoretical models from transport psychology and human–computer interaction, this section examines public attitudes, behavioral intentions, and inclusivity concerns related to autonomous public transport.

2.4.1. Public Perception of Autonomous Vehicle Technology

Public perception plays a pivotal role in the adoption and policymaking surrounding autonomous vehicle technologies. According to [45], surveys indicate that while many respondents express cautious optimism, they remain concerned about safety, cybersecurity, and the loss of human control. Trust in autonomous vehicles often varies by demographic, with younger populations and individuals with higher technological literacy being more open to the concept [46].

Media portrayals and real-world testing incidents significantly influence attitudes. For instance, a study by Nordhoff [47] shows that direct exposure to autonomous vehicles, such as riding in a pilot shuttle, improves trust and willingness to adopt. Similarly, Kyriakidis [48] found that the willingness to use autonomous vehicles increases when users are provided with comprehensive information about the system's limitations and operational procedures.

Socio-cultural factors also impact acceptance. In collectivist cultures, trust in governmental oversight may correlate with higher acceptance levels [49], whereas in others, concerns about personal safety and freedom of choice dominate perceptions. Public education campaigns, interactive demonstrations, and transparent communication regarding AV capabilities and limitations are essential for building long-term public confidence. Additionally, the perceived value of AVs in improving safety, reducing traffic congestion, and providing mobility to underserved populations plays a significant role in getting public support [50].

2.4.2. User Needs and Expectations for Public Transportation Using Autonomous Vehicles

Understanding user expectations is critical to developing autonomous vehicle-based public transport systems that are user-centric, efficient, and widely accepted. According to Kröger [51], key user expectations include reliability and punctuality, affordable pricing, seamless integration with existing transport modes, and safe operation in mixed-traffic conditions. In a cross-national study, Haboucha [52] found that many users prefer autonomous vehicles when they enhance comfort, reduce travel-related stress, and improve time efficiency. Preferences for shared versus private AVs differ based on factors such as income level, urban density, and commuting patterns [53].

Users are particularly sensitive to how autonomous vehicles handle dynamic environments, such as interactions with pedestrians and cyclists. Perceived competence in such scenarios significantly affects user confidence [54]. Moreover, trust is influenced by human–machine interaction features, such as voice interfaces, visual feedback, and emergency override options [55]. For AVs to become a mainstream public transport option, they must also support intermodal travel planning, facilitate digital payment systems, and provide real-time updates.

2.4.3. Accessibility and Inclusion Considerations

To ensure the equitable distribution of benefits from AV technology, systems must be designed with inclusiveness as a core principle. Autonomous public transport holds significant potential for increasing mobility for people with disabilities, the elderly, and those in underserved areas. However, early deployments have shown that inclusion is often an afterthought in AV development [56].

Designing AVs for accessibility requires adherence to universal design principles, including low-floor boarding, tactile surfaces, auditory announcements, visual cues, and

user-friendly applications that support multiple languages and accessibility settings [57]. Furthermore, inclusive service planning must address spatial and temporal coverage to ensure that AVs serve low-income neighborhoods and operate outside of peak hours. Regulatory mandates should guide public-sector AV investments to promote transport equity [58]. Community co-design and stakeholder engagement are crucial for enhancing inclusivity, ensuring that AV services address diverse needs and foster a sense of public ownership [31,59].

2.5. Dimensions and Maneuverability of Electric Buses

Electric buses (e-buses) are central to the transition toward cleaner and more sustainable urban transport. This section addresses the critical issues of vehicle dimensions and maneuverability, the use of articulated or modular structures, and the inherent advantages of electric propulsion in reducing urban noise and emissions.

2.5.1. Optimal Bus Width and Turning Radius

The physical dimensions of electric buses significantly influence their operability within constrained city streets. The optimal width of a bus typically ranges from 2.4 to 2.6 m, which provides sufficient interior space for passengers while maintaining compatibility with standard traffic lanes [60]. Buses that exceed this range can face difficulties in older urban districts with narrow roads.

Turning radius is another critical factor, especially in dense cities with tight intersections. Highway and street design vehicles standard [61] gives the typical dimensions for all types of transport vehicles. Standards for turning radius can vary depending on the effective radius of each bus and other factors, such as whether a bicycle lane or parking lane is available, or if traffic volumes are so low as to allow transit vehicles to make full use of either departure or receiving lanes.

Ref. [45] According to [61], a typical 12 m standard bus requires a turning radius of around 12 m, though modern steering systems and electric drive configurations allow tighter turning capabilities.

Small electric buses, typically 6 to 8 m in length, are increasingly deployed on low-demand routes and in areas with narrow streets, such as historic districts. Their compact dimensions allow for a much tighter turning radius (often less than 8 m), making them ideal for first- and last-mile connections where full-size buses are impractical. Electric powertrains offer advantages in weight distribution and vehicle architecture, which can enhance maneuverability. A study by [62], Gori shows that the placement of electric drive units can lower the center of gravity, improve stability, and increase turning efficiency.

2.5.2. Considerations Regarding Articulation and Modularity

Articulated and modular bus configurations are increasingly used to manage growing urban transit demands. Articulated buses, often exceeding 18 m in length, offer higher passenger capacity without a proportional increase in their operational footprint. They typically include a flexible joint and multiple axles to help navigate tighter turns.

Modularity in bus design allows for a more adaptable fleet composition, with configurations that can include interchangeable power modules, battery packs, or passenger units, as outlined by [47].

Both articulated and modular designs must balance capacity, energy efficiency, and drivability. Electric articulation systems benefit from precise torque control and regenerative braking systems, enhancing stability in curves and during deceleration [60].

Recent developments in small bus design include modular chassis systems that allow the same base vehicle to serve multiple purposes, from passenger shuttle to cargo

transport. This is particularly advantageous for cities seeking multipurpose fleets and cost efficiency [63].

2.5.3. Electric Propulsion for Reduced Noise and Emissions

A primary advantage of electric propulsion in public transport is the significant reduction in noise and emissions. Unlike internal combustion engine (ICE) buses, e-buses generate minimal operational noise, especially at low speeds, which improves the urban soundscape [64]. The elimination of tailpipe pollutants, such as nitrogen oxides (NOx) and particulate matter (PM), is crucial for improving air quality in congested city centers. According to [65], when paired with clean electricity sources, the shift to e-buses can reduce local emissions by over 90%.

Electric drivetrains also support smoother acceleration and deceleration, which reduces mechanical wear and enhances rider comfort, contributing to a longer service life and lower operational costs, as confirmed by case studies from the European Clean Bus Deployment Initiative [66]. Small electric buses are especially valuable in cities with environmental protection zones, where noise and air quality standards are most stringent. Their low operational weight and battery consumption contribute to energy efficiency and extended range, making them suitable for inner-city loops and community transport [60].

3. Materials and Methods

3.1. Assessing European Urban Contexts for Narrow-Street Electric Buses Deployment

European cities with historic, narrow street networks offer valuable real-world laboratories for testing and deploying autonomous public transport due to their inherent spatial constraints and high pedestrian presence. Prototypical environments for such a deployment include the historic centers of Lucca, Italy; the canalized roads of Bruges, Belgium; the winding alleyways of Toledo, Spain; and the heritage districts of Salzburg, Austria. The selection of a representative city for a case study must, however, be based on a strategic and evidence-based framework.

3.1.1. Criteria for Selecting a Representative European City with Narrow Streets

To ensure the relevance and broader applicability of the findings, the selection of a city for piloting autonomous electric buses should be guided by several core criteria:

(a) Historical urban fabric: The city should feature a well-preserved historic urban form with a compact street grid and narrow passages that challenge conventional vehicle navigation [67] (b) Street width profile: The city must have a significant number of streets, particularly in central areas, that are narrower than 3.5 m, thereby necessitating the use of smaller, more agile vehicles [24]. (c) Transport system maturity: An ideal candidate will have an established yet flexible public transport system that can support the integration of a new autonomous service [29]. (d) Supportive policy environment: The city should demonstrate a commitment to sustainable mobility through policies such as Low Emission Zones (LEZs) or congestion charging [68]. (e) Demographic and pedestrian considerations: high-density pedestrian areas, particularly in cities with significant tourist influxes or aging populations, stand to benefit most from quiet, zero-emission transport modes [26].

3.1.2. Archetype of a Suitable European City: Lucca, Italy

The city of Lucca, Italy, offers a compelling archetype of a European city suitable for narrow-street autonomous bus deployment. Its characteristics provide a representative model for identifying similar locations:

1. Urban morphology: the inner city is defined by its Renaissance-era walls and a network of compact streets, many of which are less than 3 m wide. Cobblestone

surfaces and historic building facades limit infrastructural modifications, requiring vehicle-based innovation [69].

2. Traffic regulations: the city enforces a Limited Traffic Zone (Zona a Traffico Limitato—ZTL), which restricts car access and prioritizes pedestrians, bicycles, and electric minibuses [70].
3. Mobility demand and flow; as a UNESCO cultural heritage site, Lucca receives large numbers of seasonal tourists. Daily pedestrian counts within the city center frequently exceed 10,000 in peak months. This creates a clear demand for small-scale, quiet transit that complements foot traffic without disrupting the historical ambiance [71].
4. Policy and planning alignment; Lucca's inclusion in Tuscany's Sustainable Urban Mobility Plan (SUMP) positions it as a forward-thinking municipality focused on multimodal, clean transport solutions.
5. AV readiness: Lucca already operates a fleet of electric minibuses on its narrowest routes. The city has also begun implementing intelligent traffic systems and vehicle-to-infrastructure (V2I) trials, suggesting a strong readiness for limited-autonomy operations within its geofenced ZTL [69].

Together, these characteristics make Lucca not only representative of many compact European cities but also an ideal candidate for deeper research and experimentation with next-generation electric and autonomous public transport systems.

3.2. Case Study: Brașov, Romania

3.2.1. Description of the Study Area: Urban Planning and Road Infrastructure

As outlined in the introduction, the historic center of Brașov was chosen for this case study due to its significant infrastructural challenges. The area concentrates numerous functions, serving as a hub for administrative, educational, cultural, commercial, and tourism activities [72] which generates significant pedestrian and vehicular traffic.

The geometric particularities of the street network reflect the city's medieval origins (Figure 2). The Prund-Șchei district and the Old Center are characterized by a traditional, irregular street grid with narrow profiles, which is not favorable to modern traffic volumes. The core of the historic center is managed by a one-way ring system that utilizes a series of collector streets (e.g., Mureșenilor Street, Poarta Șchei Street, Castelului Street) to facilitate traffic flow. Public transport currently operates on these streets, where speeds are limited to 30 km/h. However, the network's capacity is insufficient.



(**a**) (**b**)

Figure 2. Brasov's old (historical) center: (**a**) Parking of vehicles on the second lane on N. Balcescu Street; (**b**) Poarta Schei area with a roundabout near a secondary school.

The main dysfunction in this area arises from the conflict between vehicular traffic and pedestrian activity. On key streets open to cars, such as Poarta Șchei and Castelului, the sidewalks are dangerously narrow. This forces pedestrians into close proximity with moving vehicles, creating safety risks and degrading the quality of the urban environment, particularly given the area's significant role as a tourist and leisure destination.

3.2.2. Analysis of Road Flows in the Implementation Area

To enhance the quality of life for urban residents in line with European Union standards, the challenges posed by the transport sector must be systematically assessed and addressed. The primary objectives of sustainable urban mobility—improving accessibility, safety, economic efficiency, and environmental quality—serve as the guiding principles for this analysis. Sustainable transport includes not only vehicles and energy but also the infrastructure and operational logistics that support them. Its success is measured by the efficiency of the transport system and its overall environmental impact.

Any modifications to public transport networks or the implementation of new services must be grounded in rigorous analysis, including traffic studies, impact assessments, and feasibility studies, while also aligning with regional development strategies and sustainable urban mobility plans.

In the context of Brașov, traffic flow in and around the historic Old Center is a significant and persistent problem. During the morning, noon, and evening peak hours, the area experiences high volumes of vehicular traffic. The concentration of public institutions, educational facilities, tourist attractions, and commercial areas within this perimeter leads to frequent traffic congestion on both weekdays and weekends.

For this study, a critical intersection was selected for detailed analysis: the junction of Gheorghe Baritiu Street, Șirul Beethoven Street, and Șirul Gheorghe Dima Street, located near the Maternity Hospital (Figure 3). This intersection is a significant bottleneck during rush hour, serving key destinations such as the Andrei Șaguna National College, Transilvania University, and access points to the old citadel walls. It consistently experiences traffic jams that delay both vehicular and pedestrian access to these areas of interest.

The following table (Table 1) presents the road flow data collected during the afternoon peak hour (13:40–14:40) for vehicles traveling inbound on Gheorghe Baritiu Street toward the Șchei neighborhood.

The data reveals that a total of 659 vehicles entered the intersection from Gheorghe Baritiu Street during the one-hour observation period. In the same period, seven vehicles came from Cibinului Street and headed towards Schei, and 40 came from Ludwig van Beethoven Street, with the same destination—the Schei neighborhood. Analysis of turning movements shows that 321 of these vehicles proceeded toward the Șchei neighborhood. Assuming an average vehicle occupancy, this corresponds to an estimated passenger volume of approximately 500 people traveling in private vehicles toward this specific destination.

In parallel, data for the existing public transport route (Line 50) traveling in the same direction was analyzed. By examining bus schedules, vehicle types, and observed passenger loads, the public transit load was calculated. This analysis revealed a demand ranging from 40 passengers per hour during off-peak times to 120 passengers per hour during peak periods (e.g., 07:30–08:30 and 15:00–16:00).

By combining these two data streams, a comprehensive demand profile can be established. The minimum baseline demand for a public transport service is 120 passengers per hour, based on existing transit load. However, to fully address the mobility needs of the area and attract users from individual transport, the service must be designed to accommodate a potential peak demand of up to 620 passengers per hour (120 from current

transit +500 from private vehicles). These demand figures serve as the primary input data for the subsequent public transport simulations.



Figure 3. Gheorghe Baritiu St. + Şirul Beethoven St. + Șirul Gheorghe Dima Street + Cibinului St. (Maternity Hospital), source Google Maps.

Table 1. Vehicle counts at the Maternity Hospital intersection.

	Intersection: Maternity Roundabout															
Vehicle Type	**Cars**				**Utility Vehicles**				**Buses**				**Trucks**			
Direction [1]	←	↑	→	↻	←	↑	→	↻	←	↑	→	↻	←	↑	→	↻
13:40–13:55	70	73	6	20	0	1	0	2	0	4	0	1	0	0	0	0
13:55–14:10	57	64	8	35	3	1	0	1	0	5	0	0	1	0	0	0
14:10–14:25	56	60	9	30	0	1	0	1	0	2	0	0	0	0	0	0
14:25–14:40	56	57	4	23	0	1	0	1	0	5	0	1	0	0	0	0
Total 13:40–14:40	239	254	27	108	3	4	0	5	0	16	0	2	1	0	0	0
Total	628				24				54				4			

[1] The arrows indicate the direction of movement of vehicles in the roundabout: ↑ forward, ← left, → right or ↻ turn. Same for the following tables.

	Vehicles	**Etalon Vehicles**
Total Left ←	243	249
Total Forward ↑	274	310
Total Right →	27	27
Total Turn ↻	115	124
Total for Access	659	710

3.2.3. Description of Infrastructure Problems

The primary infrastructural challenge within Brașov's Historic Center is the intense competition for limited space. This spatial conflict is aggravated by historical urban planning decisions that prioritized personal vehicle mobility, leading to significant accessibility and safety issues for other road users. These existing deficiencies create a complex environment for implementing an autonomous public transport service. The following specific problems have been identified as critical barriers:

- P1. Constrained vehicle access on narrow streets (Figure 4): The historic center's canyon streets physically restrict vehicle dimensions. In many sections, the road is too narrow for vehicles to pass one another, and tight intersection radii make turning difficult for any vehicle larger than a standard car. This requires any autonomous shuttle to be compact and highly maneuverable.



Figure 4. Castelului Street, Brasov.

- P2. Hazardous parking configurations (Figure 5): Parking is organized both laterally and obliquely along the roadways. While lateral parking presents a lower risk, oblique parking spaces force drivers to reverse into active traffic lanes with severely limited visibility. This creates unpredictable and high-risk scenarios that are challenging for an autonomous vehicle's prediction and decision-making algorithms.



(**a**) (**b**)

Figure 5. Side parking (**a**) and oblique parking (**b**).

- P3. Illegal parking and obstruction (Figure 6): Insufficient parking capacity leads to frequent illegal parking on roadways and sidewalks. These static and dynamic obstructions reduce the effective width of the street, block sightlines, and create unexpected obstacles that an autonomous system must be able to safely navigate or circumvent.



(**a**) (**b**)

Figure 6. Situations of illegal parking (**a**) on the secondary street C. Lacea or (**b**) on the main street Prundului.

- P4. High-density pedestrian flow (Figure 7): As a major tourist and commercial hub, the historic center experiences extremely high pedestrian flows. Pedestrians often spill off the narrow sidewalks into the street, creating a complex and fluid environment that is difficult for autonomous sensors to interpret and predict safely, especially in crowded conditions.



(**a**) (**b**)

Figure 7. Pedestrian flows on (**a**) pedestrian crossings and (**b**) sidewalks at peak hours.

- P5. Unpredictable traffic from school-related activity (Figure 7): The morning and afternoon peaks are characterized by chaotic traffic patterns around schools, with frequent stopping, double-parking, and sudden maneuvers from vehicles dropping off or picking up students. This type of unpredictable human driver behavior represents a significant "edge case" that poses a major safety and operational challenge for current autonomous driving systems.

3.3. Methodology—Optimizing Autonomous Public Transport in the Historic Center of Brașov

This chapter details the methodology for optimizing an autonomous public transport route within a constrained urban environment. The analysis is built upon a multi-objective

optimization framework that considers three essential pillars: the minimization of travel time, the maximization of passenger comfort, and the minimization of energy consumption. This framework is applied to a case study involving four distinct types and sizes of autonomous electric vehicles operating on a designated route in Brașov's historic center.

1. Travel time: Minimizing travel time is a fundamental objective for any public transport system. For autonomous vehicles, this is achieved not by maximizing speed, but through intelligent management of velocity and acceleration to maintain a consistent and efficient flow while adhering to all traffic regulations and operational constraints.
2. Passenger comfort: This is quantified by limiting longitudinal and lateral accelerations. To prevent motion sickness and ensure a comfortable ride, the simulation enforces strict limits on acceleration, typically within the range of 0.1 g to 0.2 g (where g is gravitational acceleration).
3. Energy consumption: The model calculates the total energy required for propulsion to overcome rolling resistance, aerodynamic drag, and grade resistance.

The deployment of autonomous vehicles in the environment presents significant benefits, from reducing human error to optimizing traffic flow and improving air quality. However, realizing these benefits requires meticulous planning and optimization. The following methodology was developed for a case study on Brașov's existing public transport route, Line 50 (Livada Poștei—Pietrele lui Solomon).

The proposed methodology involves the following key steps:

1. Detailed mapping and digitalization of the route: The geometry of the route (width, curvature, slopes), traffic restrictions (speed limits, one-way streets), and the location of fixed obstacles and high-pedestrian-traffic zones were digitized to create a high-fidelity model of the operational environment.
2. Modeling of vehicle dynamics and autonomous behavior: A dynamic model was developed for each vehicle type to reflect its behavior in real-world conditions. The autonomous driving behavior was modeled using trajectory planning and rule-based adaptive control algorithms, assuming the vehicles can maintain constant speeds and optimize acceleration and deceleration profiles within safety and comfort limits.
3. Calculation of minimum travel time: The minimum travel time for each vehicle was calculated while strictly adhering to traffic laws, mandatory stops at stations, and the pre-defined passenger comfort constraints.
4. Fleet size calculation: Based on the travel time for each vehicle type, the number of vehicles required to meet the estimated passenger demand (as presented in the previous chapter) was calculated.
5. Energy efficiency analysis: The total energy consumption for each vehicle type was calculated and normalized by the number of passengers to determine the energy consumed per passenger transported, providing a key metric for comparing the overall efficiency of the different solutions.

3.3.1. Generating the Vehicle Trajectory in Constrained Urban Spaces

For the case study, bus route Line 50 was selected. The route's path was exported from OpenStreetMap (Figure 8). The raw geospatial data, consisting of a series of waypoints, was then imported into the MathWorks Driving Scenario Designer. In this environment, the data was processed and refined to create an accurate digital representation of the route, including features such as the "Livada Poștei" bus station (Figure 9).



Figure 8. Route of line 50 crossing the historic center of Brasov, where the symbols represent tourist destinations (historical, architectural monuments or natural reserves), source Google Map.

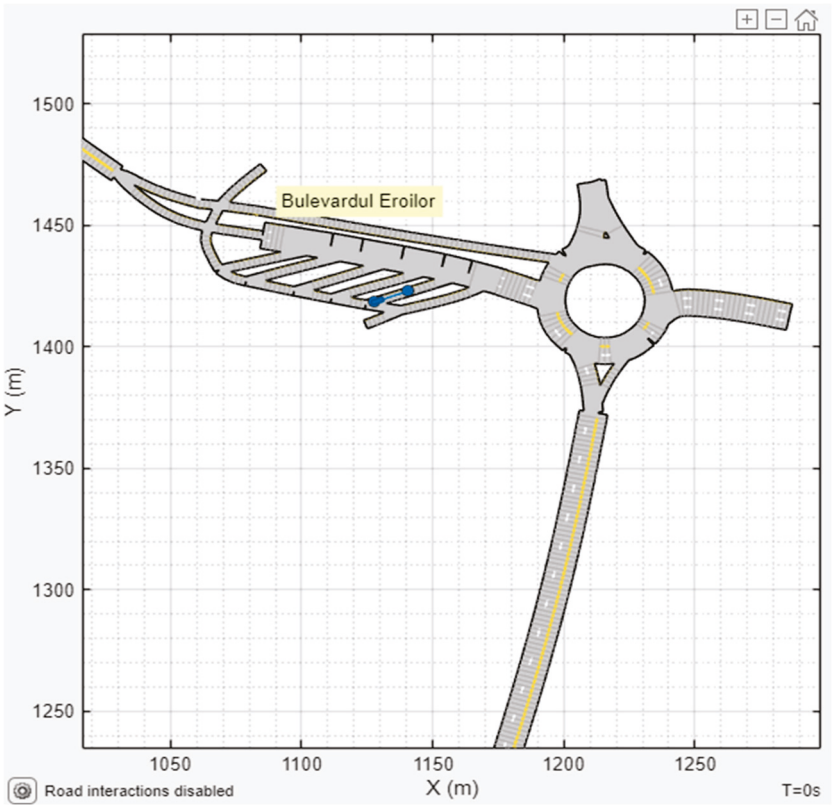

Figure 9. Digitized representation of the "Livada Postei" bus station with details regarding passenger boarding platforms and the first segment of the route of line 50 created with Driving Scenario Designer.

The initial set of points primarily marked the beginning and end of road segments. To create a continuous, high-resolution path suitable for dynamic simulation, spline interpolation was used to generate points along the entire route at approximately 0.1 m intervals (Figure 10). From this high-resolution path, the curvature at each point was computed. This curvature value is a critical input, as it directly determines the maximum velocity the bus can maintain in a turn without exceeding the acceptable lateral acceleration limit for passenger comfort.

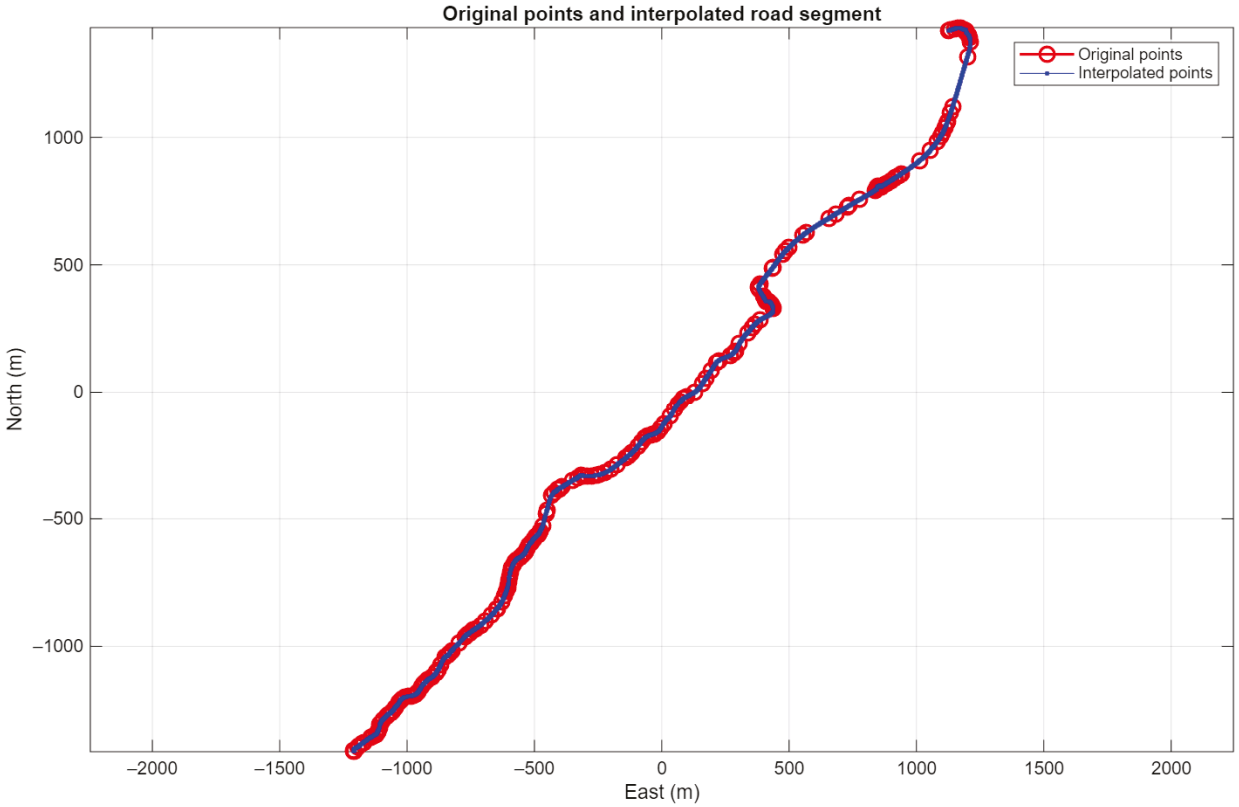

Figure 10. Route of line 50 reconstructed based on points (marked with red circles) and segments (blue color) generated by interpolation.

Along this route, several points require the vehicle to either stop or slow down. These constraints were mapped by their distance from the starting point (in meters):

- Bus station locations = [0, 782, 1028, 1503, 2058, 2371, 2672, 2887, 3077, 3357, 3537, 4044];
- Crosswalk locations = [770, 850, 1000, 1170, 1350, 1870, 2860];
- Traffic light locations = [192, 402].

The chosen route is geometrically complex, traversing a dense urban and tourist area with tight curves, a small-radius roundabout, and multiple pedestrian crossings. Figure 11 presents the curvature values (in 1/m) along the entire route, highlighting the sections with a small turning radius that impose the most significant speed constraints.

The vehicle is modeled as a 4×2, rear-wheel-drive vehicle with Ackerman steering. It is assumed that the rear axle wheels rotate around the center of the road's curve (Figure 12). Under these assumptions, the point of maximum lateral acceleration occurs at the outer front corner of the vehicle. This critical point is therefore used to calculate and enforce the passenger comfort limits throughout the simulation.

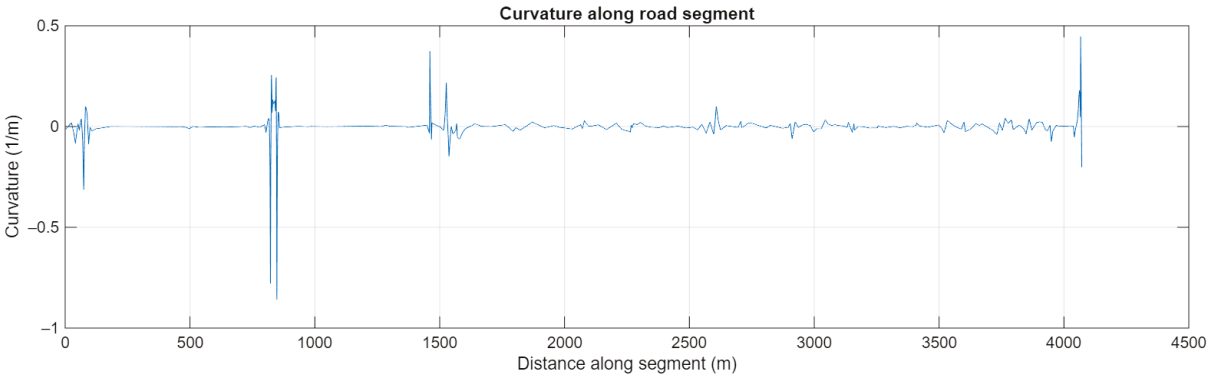

Figure 11. Curvature along road segment.

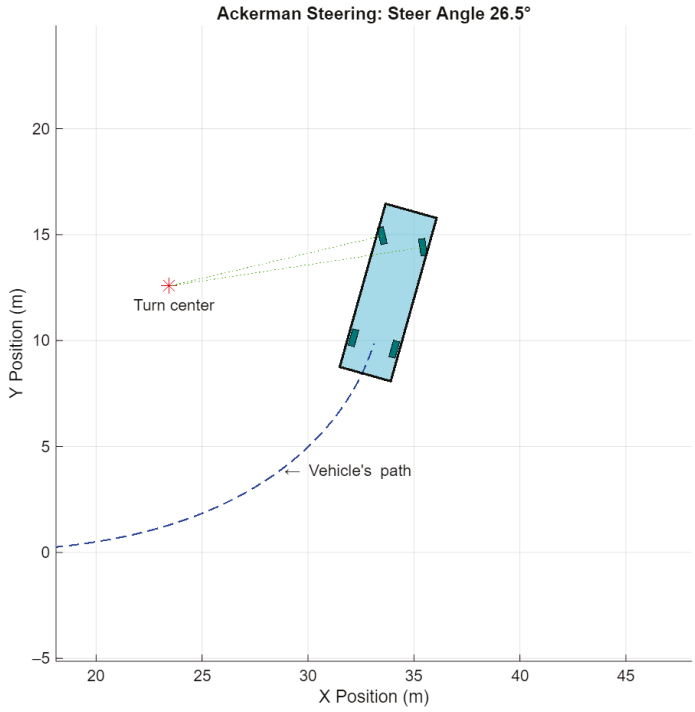

Figure 12. Vehicle trajectory, with blue dashed line, around the center of rotation marked in red, with Ackerman steering.

3.3.2. Simulating the Movement of Different Autonomous Public Transport Vehicles

This study develops a computational and analytical model to evaluate the suitability of various autonomous public transport vehicles for meeting passenger demand in cities with constrained urban spaces. The analysis is benchmarked against electric passenger transport vehicles that are already in operation in such environments, although with human drivers.

Vehicle Selection

Six distinct electric vehicles were identified for this comparative analysis. The selection includes a range of sizes, from compact vans to full-sized 12 m buses, to assess the trade-offs between passenger capacity and maneuverability. The final four vehicles in the list are currently part of the operational fleet of the local transport authority in Brașov, providing a direct real-world baseline for the case study. The main characteristics of the selected electric vehicles are presented in Table 2 [73–75].

Table 2. Types of electric buses proposed for analysis.

Brand	Model	Wheelbase (mm)	Length (mm)	Width (mm)	Height (mm)	Seats	No. of Access Doors	Weight (kg)
Zhongthong	Electric Van	4750	5930	2040	2720	8	1	5000
Yutong	E7S	5240	6960	2280	2970	10	2	6350
SOR	EBN 8	3950	8000	2525	2920	16	2	8600
SOR	EBN 9.5	5740	9790	2525	2920	23	2	9050
SOR	EBN 11	6320	11,100	2525	2920	27	3	9700
SOR	NS 12	5900	12,000	2550	3150	35	3	12,000

Simulation Parameters

To configure the MATLAB R2025a simulation, key parameters governing vehicle dynamics, passenger comfort, and energy efficiency were established based on a review of the specialized literature.

- Longitudinal Acceleration (=0.9 m/s^2): While human drivers can exhibit accelerations up to 4.8 m/s^2, studies show that 90% of observed accelerations fall within a much narrower range, typically below 1.0 m/s^2 [76,77]. Furthermore, public transport systems like light rail transit (LRT), which are considered a benchmark for passenger comfort, operate with a longitudinal acceleration of approximately 1.34 m/s^2 [76,78]. To prioritize a smooth and comfortable ride, a conservative value of 0.9 m/s^2 was selected for the simulation.
- Lateral Acceleration (=1.2 m/s^2): Passenger comfort is highly sensitive to lateral acceleration in curves [79]. Guidelines for driver comfort and safety set tolerance limits between 1.47 m/s^2 and 1.96 m/s^2 [80]. Prediction models for electric buses often use a threshold of 1.5 m/s^2 [81]. To ensure a high degree of passenger comfort, especially in the tight turns of the historic center, a maximum lateral acceleration of 1.2 m/s^2 was chosen.
- Deceleration (=-1.0 m/s^2): Similarly to acceleration, comfortable deceleration is critical. The LRT benchmark for comfortable deceleration is -1.34 m/s^2 [76], while some energy consumption models for electric buses use a limit of -0.8 m/s^2 [81]. A value of -1.0 m/s^2 was selected as a balanced parameter that ensures a smooth, comfortable stop without being overly conservative.
- Powertrain and regenerative braking efficiency (=0.85 and 0.70): The efficiency of an electric powertrain varies with operating conditions, but comprehensive vehicle tests show that it can reach up to 91% [81]. An average efficiency of 0.85 from the battery to the wheels was adopted for propulsion. For regenerative braking, which captures kinetic energy and returns it to the battery, a round-trip efficiency of 0.70 was used [82].
- Vehicle resistance parameters:
    a. Effective mass factor (=1.02): To account for the rotational inertia of the wheels and transmission, an effective mass factor of 1.02 was applied, meaning the inertial mass is considered to be 102% of the vehicle's static mass [81].
    b. Drag coefficient (=0.36): Based on coast-down tests for modern electric vehicles [81], an average aerodynamic drag coefficient of 0.36 was used.
    c. Rolling resistance coefficient (=0.01): This coefficient varies with road surface quality. Measured values for electric buses range from 0.0088 on good asphalt

to 0.0112 on poor asphalt [81,83]. An intermediate value of 0.01 was selected for the simulation.

Behavioral Rules and Constraints

The behavioral patterns of human drivers serve as the basis for the simulation program, which operates on three levels: strategic, tactical, and control. Behavior is defined as a sequence of actions taken in response to a driving situation. The strategic level establishes the overall objective, the tactical level manages these tasks through rule-based or knowledge-based behaviors, and the control level is responsible for their execution [84,85]. In [86], Wang et al. demonstrated that a multi-agent system strategy can integrate multiple criteria to assess the energy efficiency of vehicle behavior in real-time, enabling the selection of optimal driving strategies. The simulated bus was programmed to adhere to the following operational rules:

- The maximum speed is limited to 30 km/h, in accordance with local regulations for the historic center.
- When approaching pedestrian crossings, the vehicle decelerates to 20 km/h over a distance of 20 m.
- In all curves, the vehicle's speed is dynamically adjusted to ensure that the lateral acceleration experienced by the outermost passenger does not exceed the comfort limit of 1.2 m/s^2.

4. Results

4.1. Calculation of Velocity Profiles

Using the parameters, behavioral rules, and vehicle characteristics defined in the previous chapter, the simulation program calculated the optimal velocity profile for each of the six electric bus types. The primary objective was to determine the minimum possible travel time for each vehicle along the designated route, while strictly adhering to all constraints, including regulatory speed limits, mandatory stops, and passenger comfort limits (i.e., maximum longitudinal and lateral acceleration).

The resulting velocity profiles for Bus #1 (the most compact vehicle) and Bus #6 (the largest vehicle) are presented in Figures 13 and 14, respectively. These two cases were selected as they represent the minimum and maximum limits of the dimensional and capacity range of the vehicles under consideration.

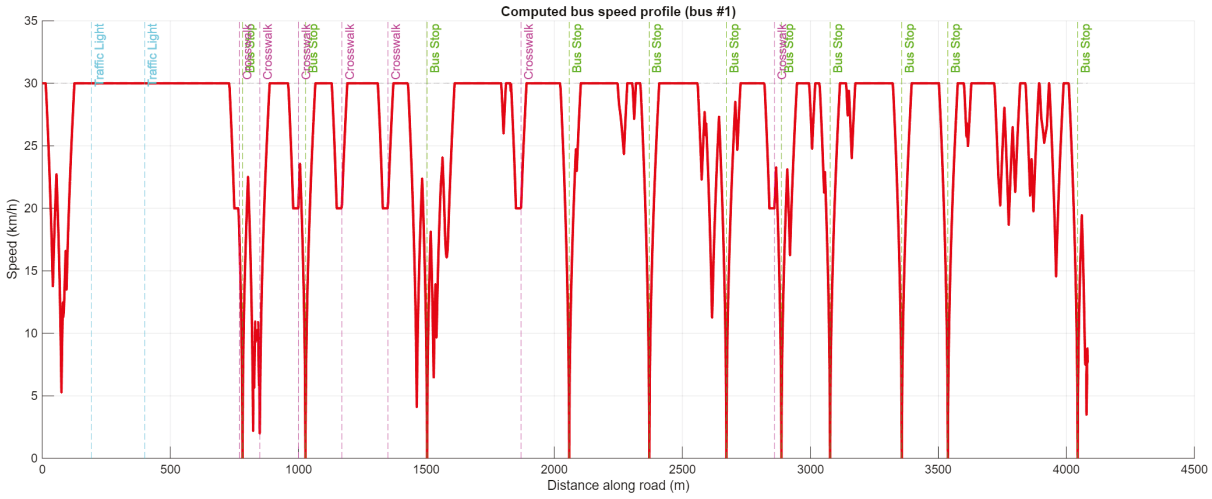

Figure 13. Speed profile along the route for Bus#1.

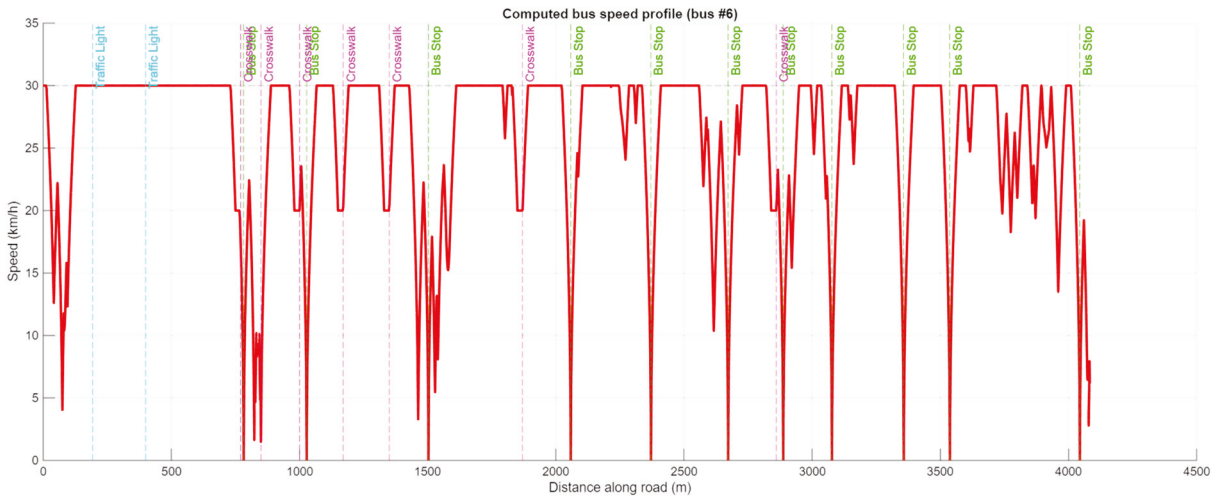

Figure 14. Speed profile along the route for Bus#6.

The graphs clearly illustrate the vehicle's behavior along the route. The velocity drops to zero at designated bus stops, as required. At signalized pedestrian crossings, the model assumes a green light, and thus the vehicle does not stop. At unsignalized pedestrian crossings, the vehicle proactively decelerates to a safe, lower speed to mitigate the risk posed by unexpected pedestrian movements.

A comparison of the two graphs reveals that the speed profiles are nearly identical on straight segments of the route. In these sections, both vehicles accelerate to the maximum permitted speed of 30 km/h and maintain it.

The significant differences emerge in sections with non-zero curvature, particularly in curves with small turning radii. In these segments, the dimensional characteristics of the vehicles directly influence the maximum safe speed. To stay within the passenger comfort limit for lateral acceleration, longer and wider vehicles must navigate these tight turns at a considerably lower speed than their smaller, more agile counterparts. This dynamic speed adjustment based on vehicle geometry is a key factor influencing the overall travel time and energy consumption for each bus type.

4.2. Bus Energy Consumption Calculation

Based on the parameters presented in Section 3.3.2, the constructive characteristics of the electric buses presented in Table 2 (length, wheelbase, width, height, self-weight, weight with passengers within the limit of seats), respecting the traffic rules on the chosen route as well as the imposed rules of behavior, we calculated for all six types of electric buses the forces and powers of the engines necessary to travel with the previously established speed profiles.

The total energy consumed by the bus over its operational route was determined using a backward quasi-static model, based on the principles of longitudinal vehicle dynamics. This approach uses the known velocity profile to calculate the instantaneous tractive force required at the wheels, which is then used to compute the power demand from the energy source (battery) by taking into account the powertrain efficiencies.

The principle of the model is the longitudinal force balance equation, where the total tractive force, $F_{tractive}$, must overcome the sum of all resistive forces to produce the required acceleration:

$$F_{tractive}(t) = F_{rr}(t) + F_{ad}(t) + F_g(t) + F_i(t), \quad (1)$$

where F_{rr} is the rolling resistance, F_{ad} is the aerodynamic drag, F_g is the gradient resistance, and F_i is the inertial force.

Each resistive force component is calculated at every time step of the simulation as follows:

1. Rolling resistance (F_{rr}): This force arises from the deformation of the tires and contact with the road surface. It is calculated as a function of the vehicle's mass and the road surface characteristics:
$$F_{rr} = C_{rr} \cdot m \cdot g \cdot \cos(\theta), \tag{2}$$
where m is the vehicle mass, g is the gravitational acceleration, θ is the road grade angle, and C_{rr} is the dimensionless rolling resistance coefficient.
2. Aerodynamic drag (F_{ad}): This is the force of air resistance acting on the vehicle and it is proportional to the square of the vehicle's velocity:
$$F_{ad} = \frac{1}{2}\rho A C_d v^2. \tag{3}$$
Here, ρ is the air density, A is the vehicle's frontal cross-sectional area, v is the vehicle velocity, and C_d is the dimensionless drag coefficient.
3. Gradient resistance (F_g): The gravitational force component on a slope, given by $F_g = m \cdot g \cdot \sin(\theta)$. For this analysis, the road was assumed to be perfectly flat ($\theta = 0$) at all points along the route. This simplification was made to establish a baseline energy consumption profile, isolating the energy impacts of the vehicle's mass, aerodynamic profile, and the kinetic demands of the speed profile itself, independent of topographical variations.
4. Inertial Force (F_i): This is the force required to accelerate the vehicle. The calculation includes an effective mass factor, y_m, to account for the rotational inertia of the wheels and powertrain components.

$$F_i = (m \cdot y_m) \cdot a, \tag{4}$$

where *a* is the longitudinal acceleration of the vehicle.

From the total tractive force, the mechanical power required at the wheels, P_{wheels}, is calculated:

$$P_{wheels}(t) = F_{tractive}(t) \cdot v(t). \tag{5}$$

To determine the power drawn from the energy source, P_{source}, the model accounts for the overall efficiency of the powertrain (η_{pt}). During propulsion ($P_{wheels} > 0$), the power drawn is greater than the power delivered. During deceleration ($P_{wheels} < 0$), the electric vehicle can recover a portion of the vehicle's kinetic energy through regenerative braking. This is particularly effective in urban driving, where frequent braking events occur. The power from the source is thus determined by

$$P_{source}(t) = \begin{cases} P_{wheels}(t)/\eta_{propulsion}, & \text{if} P_{wheels}(t) > 0 \\ P_{wheels}(t) \cdot \eta_{regeneration}, & \text{if } P_{wheels}(t) < 0 \\ 0, & \text{if} P_{wheels}(t) = 0 \end{cases}. \tag{6}$$

The efficiencies for propulsion and regeneration, $\eta_{propulsion}$ and $\eta_{regeneration}$, can be derived from component efficiency maps but can be represented by average values for a quasi-static analysis.

Finally, the total energy consumed, E_{total}, over the entire route is calculated by numerically integrating the source power over the duration of the trip:

$$E_{total} = \int P_{source}(t)\, dt. \tag{7}$$

This computational approach provides a robust and repeatable method for estimating the energy consumption of a vehicle over any given drive cycle for which position and speed data are available.

Figure 15 illustrates the calculated tractive forces for Bus #1, Bus #3, and Bus #6. A significant difference is observable between the maximum force values. Bus #6, being the largest and heaviest vehicle, requires substantially higher forces to accelerate and overcome resistance compared to the much smaller Bus #1 minibus. Bus #3, with its intermediate size, exhibits force values that fall between these two extremes.

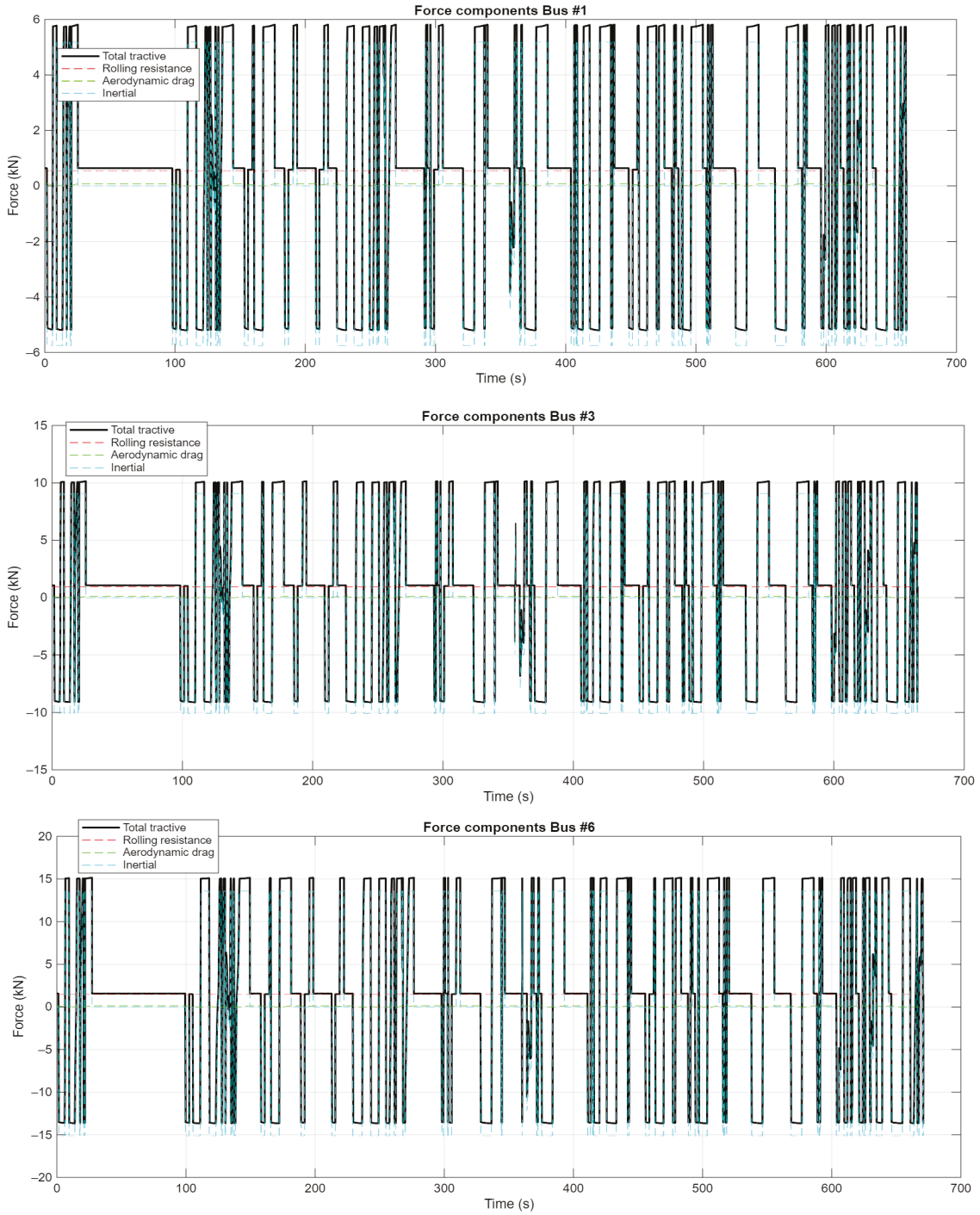

Figure 15. Calculated forces.

This difference in required force translates directly to the power demand, as shown in Figure 16. The larger mass and frontal area of Bus #6 necessitate a much higher power output from the electric motor to follow the same speed profile as the smaller vehicles.

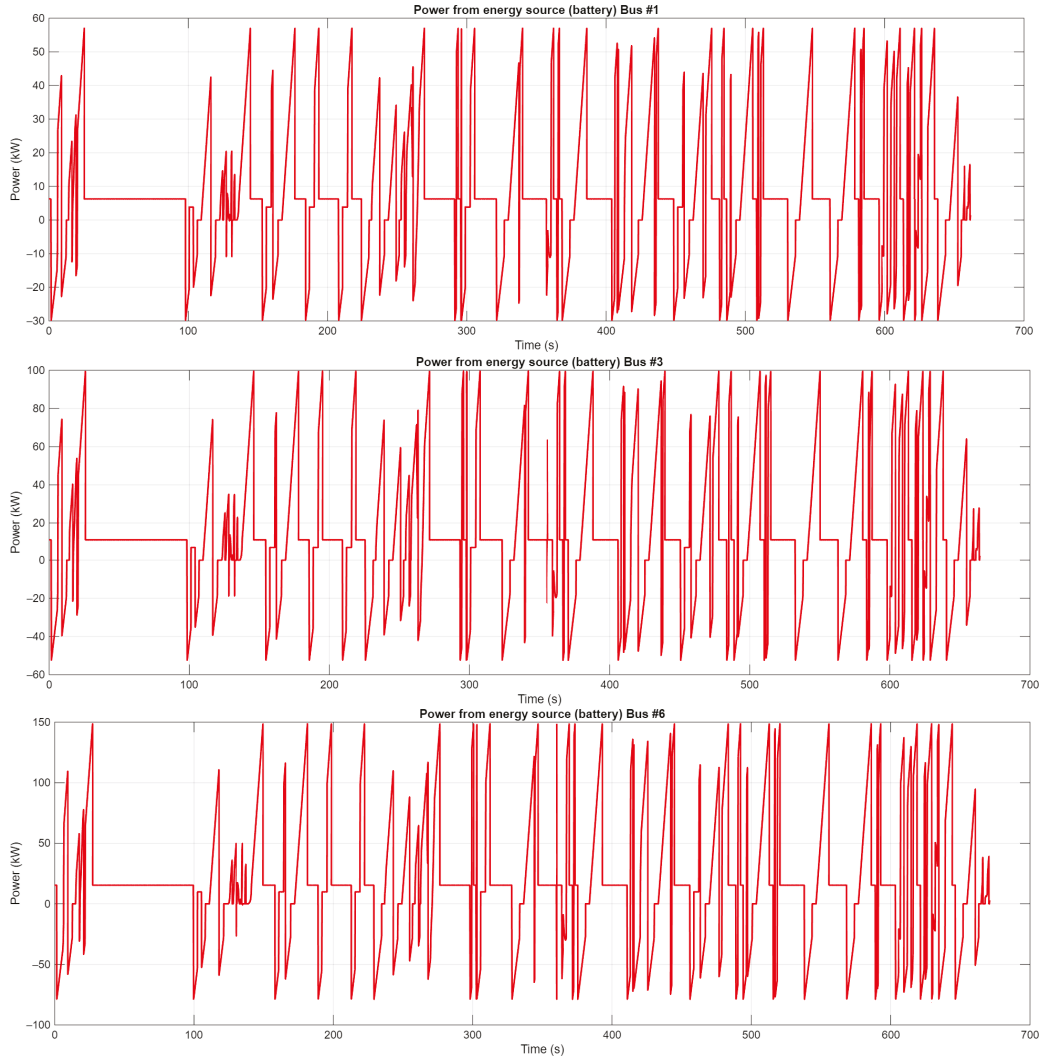

Figure 16. Calculated power.

The final calculated travel times and energy consumption metrics for all six cases are presented in Table 3. The data was then used to calculate the energy consumption rate per kilometer and, crucially, the energy consumed per passenger, which normalizes the results based on the transport capacity of each vehicle.

Table 3. Calculated energies by each type of bus (six cases) along the route.

Case	Total Time (s)	Total Energy Consumed (kWh)	Energy Consumption Rate (kWh/km)	Bus Capacity (Seats)	Energy Consumption Per Passenger (kWh/Pers)
1	661.56	1.40	0.34	8	0.175
2	663.88	1.77	0.43	10	0.177
3	664.20	2.41	0.59	16	0.1506
4	667.14	2.65	0.65	23	0.1152
5	670.12	2.88	0.71	27	0.1067
6	671.03	3.58	0.88	35	0.1023

The results reveal a clear trend. While larger buses consume more total energy and have slightly longer travel times due to their need to slow down more in curves, they are significantly more efficient on a per-passenger basis. The energy consumption per passenger decreases steadily as the vehicle size and capacity increase, with the largest vehicle (Bus #6) demonstrating the highest efficiency in terms of moving people. This highlights the critical trade-off between the absolute energy consumption of a vehicle and its overall transport efficiency

4.3. Validation of Simulation Results

To verify the accuracy of the simulation model, a comparative analysis was conducted between the simulated velocity profile and real-world operational data. The velocity profile for Bus #4 (SOR EBN 9.5) (see Table 2, Figure 1a) was selected for this validation, as it corresponds to a vehicle currently in operation. Real-world data was collected by recording a complete trip along the Line 50 route aboard an operational SOR EBN 9.5 electric bus, using the Matlab Mobile application to capture GPS and speed data.

The two datasets—simulated and real—were superimposed for a direct comparison, as shown in Figure 17. The analysis reveals several key differences between the idealized simulation and the real-world operation. The human-driven bus (blue curve) occasionally exceeded the legal speed limit on straight sections, a behavior not permitted in the simulation's rule-based system. Also, the real bus was subject to unpredictable traffic conditions, necessitating decelerations and stops not accounted for in the baseline simulation, such as stops at two pedestrian crossings.

To create a meaningful comparison of the net travel time, it is necessary to account for the time the real bus spent stationary. The total measured trip time for the real bus was 739 s (12 min and 19 s). This included a cumulative 80 s of dwell time at bus stops (as detailed in Table 4) and 18 s stationary at pedestrian crossings.

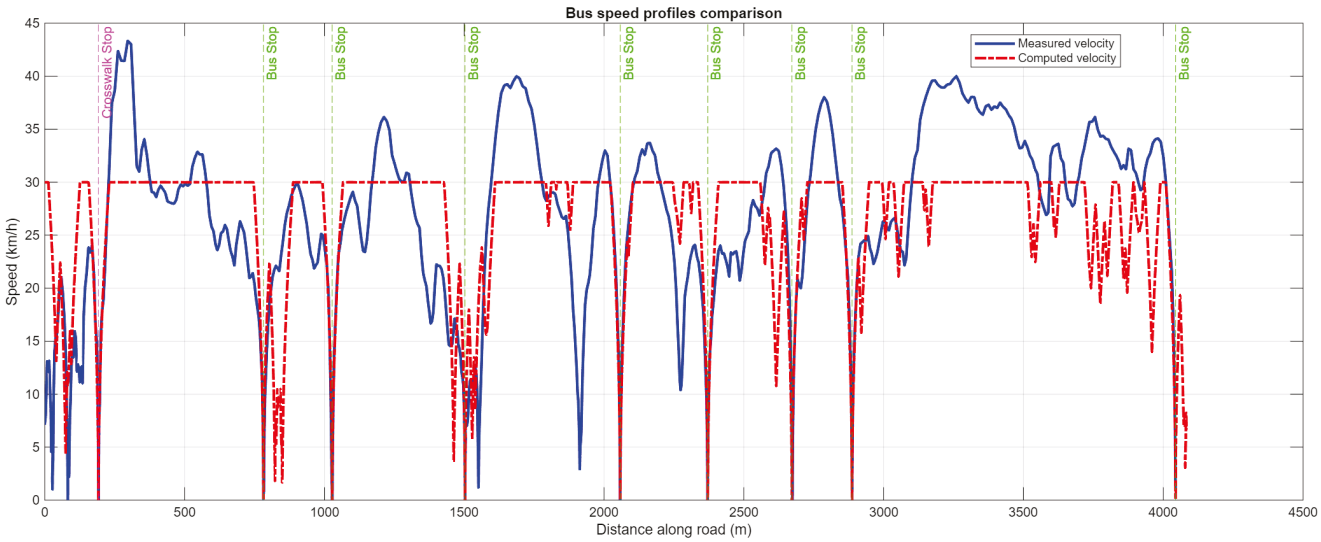

Figure 17. Speed profiles of the real bus (solid blue line) and the virtual one (dashed red line).

Table 4. Bus stops on line 50.

Nr	Bus Stop Name	Distance from Start [m]	Dwell Time/Getting on and Off [s]
0	Livada Postei	0	0
1	Biserica Neagra	782	11
2	Brancoveanu	1028	8
3	Piata Unirii	1503	13
4	Tocile	2058	19
5	Egalitatii	2371	9
6	Varistei	2672	8
7	Invatatorilor	2887	12
8	Podul Cretului	3077	0
9	La moara	3357	0
10	Graft	3537	0
11	Solomon	4044	0

By subtracting these stationary periods from the total trip duration, the net travel time for the real bus is calculated:

$$\text{Net Real Travel Time} = 739\ \text{s (Total)} - 80\ \text{s (Bus Stops)} - 18\ \text{s (Crossings)} = 641\ \text{s}.$$

This net travel time of 641 s is remarkably close to the simulated travel time of 640 s for the virtual bus under the same stopping conditions. This strong correlation, with a deviation of less than 0.2%, validates the accuracy of the vehicle dynamics model and confirms that the simulation provides a reliable and realistic prediction of the vehicle's performance along the specified route.

4.4. Analysis of Optimal Fleet Configuration

The final goal of this analysis is to propose an optimal autonomous vehicle fleet for Line 50, one that meets the established passenger demand while balancing operational efficiency, energy consumption, and passenger service quality. The simulation results provide the necessary data to evaluate the trade-offs between deploying different vehicle types. This analysis considers six key dimensions: (i) the balance between energy consumption and passenger service, (ii) infrastructural compatibility, (iii) total costs, (iv) social acceptance, (v) operational flexibility, and (vi) integration with broader urban mobility strategies.

(i) The trade-off: energy efficiency and passenger waiting time

As established in Section 3.2.2, the public transport service on Line 50 must accommodate a baseline demand of 120 passengers per hour. Currently, the operator uses three different bus types (SOR EBN 8, 9.5, and 11) at different times of the day to manage this demand (see Table 2). This raises a classic public transport optimization problem: is it more effective to use small buses with a high frequency or large buses with a low frequency?

To answer this, the number of vehicles required per hour to meet the 120-passenger demand was calculated for each of the three SOR bus types. The results, along with the corresponding total energy consumption and maximum passenger waiting time, are presented in Table 5.

Table 5. Fleet requirements and performance metrics for a 120 passenger/h demand.

Vehicle Type	Energy Per Bus (kWh/trip)	Buses Required Per Hour (Calculated)	Buses Required Per Hour (Rounded)	Bus Capacity (Seats)	Total Fleet Energy (kWh)	Maximum Waiting Time (min)
EBN 8	2.41	7.50	8.00	16	19.28	7.5
EBN 9.5	2.65	5.22	6.00	23	15.90	10
EBN 11	2.88	4.44	5.00	27	14.40	12

The analysis reveals a clear conflict between two primary objectives. From an energy consumption perspective, the largest buses (EBN 11) are the most efficient, resulting in the lowest total fleet energy consumption (14.40 kWh). However, this efficiency comes at the cost of reduced service frequency, leading to the longest maximum waiting time for passengers (12 min). Conversely, the smallest buses (EBN 8) offer the best passenger service with a short waiting time of just 7.5 min, but this requires a larger fleet and results in the highest total energy consumption (19.28 kWh). This demonstrates a classic multi-objective optimization challenge where a balance must be struck between operational efficiency and quality of service.

(ii) Infrastructural compatibility

The physical constraints of the historic city center are a critical factor. As the simulation results showed, larger vehicles are forced to travel at lower speeds in tight curves to maintain passenger comfort, which slightly increases their overall journey time. Smaller vehicles, with their superior maneuverability and tighter turning radii, are inherently better suited to the "canyon streets" and non-standard intersections of Brașov. The current use of the SOR EBN 8, 9.5, and 11 buses on Line 50 already highlights a practical compromise, demonstrating their adaptability to the local conditions.

(iii) Total cost of ownership

While this study focuses on energy consumption, a comprehensive decision-making process must consider the total cost of ownership (TCO). This includes the initial investment value, maintenance, and other operational costs. A TCO analysis comparing the cost of operating a larger fleet of small buses versus a smaller fleet of large buses would be essential for a final implementation decision.

(iv) Social acceptance and user experience

Public acceptance is essential for large-scale adoption. In Romania, citizens' perceptions and attitudes toward AVs remain underexplored, particularly in medium-sized cities like Brașov, which present specific challenges: urban density, street layout, population's tech literacy, and public transport experience. Romanian citizens have limited knowledge about Avs and they still lean toward private mobility solutions over shared autonomous transport systems. However, Brașov is a university center with a substantial student population (Romanian students show positive attitudes toward Avs, especially due to safety and comfort), potentially increasing familiarity and openness to emerging mobility technologies. If current public transport systems are perceived as inefficient, citizens may be more receptive to AV alternatives that promise reliability, comfort, and punctuality.

As detailed in Section 2.4.2, passenger satisfaction is driven by factors such as reliability, punctuality, comfort, and short waiting times. The higher frequency offered by smaller buses directly addresses the critical issue of waiting time, which is a major determinant of passenger satisfaction. Furthermore, different bus models may offer varying levels of accessibility for people with disabilities, another crucial factor for social acceptance.

Public perception of autonomous vehicle technology in Romanian cities like Brașov remains under-researched but critical for future implementation.

(v) Adapting to fluctuating demand

Tourist cities like Brașov experience significant fluctuations in transport demand, driven by seasonal visitor numbers, special events, and the daily mobility of students. A flexible and modular fleet offers the most effective way to manage these variations. For instance, a strategy could involve deploying larger buses during peak tourist and commuter hours, while using smaller, more frequent buses during off-peak periods to maintain a high level of service without operating large, empty vehicles.

(vi) Integration with urban mobility strategies

The choice of vehicle type must align with the city's broader sustainable urban mobility plan. The use of compact autonomous vehicles can support strategic goals by reclaiming urban space for pedestrians and cyclists. However, the successful operation of AVs also depends on a robust ICT infrastructure (e.g., 5G, edge computing) to support the real-time data exchange and high-definition mapping they require.

(vii) Legal framework for integrating an AV transport system in Brașov city

Implementing an autonomous vehicle (AV) transport system in Brașov requires navigating a complex and evolving legal environment. At present, Romania lacks specific AV legislation, and the regulatory impetus comes largely from European Union rules. AVs are not separately regulated, so they must rely on existing traffic and vehicle laws. There are no tailored insurance or liability rules for Avs, and general third-party liability and product liability frameworks apply. Romanian civil law adheres to fault-based liability (culpa) as a basic principle. However, in AV contexts, the fault-based approach may be insufficient, as computing what failed can be complex. Since AVs are not yet legally recognized, no specific mandatory insurance regime for AV operation exists, so standard compulsory motor insurance remains in place.

However, Romania participates in broader European Union level frameworks to authorize testing of automated driving systems. So, national implementation and enabling administrative procedures remain limited. For Brașov to integrate an AV public transport system, the legal framework must fill existing gaps and adapt European Union rules to local context. Brașov City Council should create by-laws or municipal regulations designating geofenced zones where AV transit can operate (historic center, corridors, limited zones). ocal traffic regulations must be modified to allow AVs to deviate from normal traffic rules under controlled conditions (e.g., priority, signals, turning permissions).

4.5. Economic Considerations to Bring Autonomous Vehicles to Constrained Urban Settings

It takes more than addressing technology requirements to implement autonomous public transport solutions—there is an overall economic consideration as well. To assist with informed decision-making on the part of city governments, we recommend the following primary areas of analysis be considered:

- Capital Expenditure (CAPEX): Initial outlays for purchasing and installing vehicles and supporting infrastructure, including autonomous technology, charging stations, and environmental sensors.
- Operational Expenditure (OPEX): Recurring costs such as energy or fuel, maintenance, insurance, communication networks, software, and staff for monitoring and maintenance.
- Lifecycle Costs and Depreciation: Predicted operating lifespan of the vehicle and forecasted residual value.

- Other Costs in Densely Packaged Environments: Such as costs unique to densely populated urban environments, i.e., modifying road infrastructure, new signs or signals, and the operational impacts of using smaller, more intense groups of vehicles.

Current studies provide benchmark cost estimates to guide financial planning. Autonomous micro shuttles (6–12 passengers) used in pilot operations typically cost in the order of USD 100,000 per vehicle. Overall costs per route in terms of both CAPEX and OPEX are tens of thousands to several hundred thousand USD in context-dependent and scale-dependent variations.

Electric buses (9–12 m), based on study and buying data, generally run from around USD 200,000 to over USD 500,000, depending on options and market dynamics in a region.

While removing the driver would greatly decrease some operating costs, other ongoing expenses—maintenance, infrastructure, and long-distance monitoring, for instance—remain [87].

Simple Total Cost of Ownership (TCO) model. The table below (Table 6) presents some illustrative calculations from published sources [88–93].

Table 6. Total Cost of Ownership (TCO) model.

Subject	Small Shuttle (6–12 Locuri)	Electric Bus 9–12 m
CAPEX vehicle	USD 80,000–200,000 [1]	USD 200,000–500,000+ [8]
Infrastructure (charging stations/depots per vehicle)	USD 5000–25,000	USD 20,000–100,000 per bus (depends on the fast power required) [94]
Energy/combustible (EUR/km or USD/km)	USD 0.05–0.25/km (electric, depends on efficiency and energy price)	USD 0.10–0.50/km (electric, depends on load and conditions) [95]
Maintenance and service (parts and software)	USD 0.05–0.30/km	USD 0.3–1.0/km
Staff and supervision (remote attendants/technicians)	variable—automation reduces driver costs but supervisors/assistant operators may remain; studies report savings depending on scenario [68]	
Total operating cost (indicative)	USD 0.2–1.0/km	USD 1.0–3.5/km (depends on depreciation, energy, personnel) [96]

Recommended analyses for decision makers

- Cost per seat-km and per vehicle-km analysis—determine the cost per seat-kilometer and compare it with traditional alternatives (such as conventional diesel or electric buses), taking into account the additional expenses related to operating on constrained routes.
- Sensitivity analysis—adjust key variables such as energy prices, annual mileage (km/year), battery lifespan, capital costs, and level of automation (e.g., L4 vs. L2+ with an onboard operator). Research indicates that the primary factors affecting TCO are vehicle/AV equipment costs and labor expenses; while lowering labor costs can make certain projects more viable, this typically requires time and adjustments to contractual frameworks [95].
- Additional costs in confined environments—operations on narrow streets may necessitate smaller vehicles, increased service frequency, and infrastructure modifications, which can lengthen cycle times and raise OPEX per passenger.
- Contractual frameworks—models such as leasing, public–private partnerships, or "gross cost" vs. "net cost" contracts can redistribute financial risks between public authorities and operators (for example, the Noida project illustrates per-kilometer tariff structures in tenders) [97].

5. Discussion and Conclusions

Europe's historic cities often feature small floor plans, winding streets, and infrastructure that respects cultural heritage. These characteristics challenge traditional buses and large transport vehicles, but also create opportunities for autonomous, electric, and small shuttles.

The morphology of the historic core and street width should be considered when determining which cities are suitable for AV-based public transportation in narrow-street settings. Criteria include:

- City layout (cities with medieval cores featuring streets less than 4 m wide);
- Traffic and access restrictions (cities with low-emission zones or limited traffic zones in their old towns);
- Pedestrian density and tourism pressure (high footfall areas where quieter, cleaner AVs could enhance the urban experience);
- Existing mobility policies and smart infrastructure (municipal support for sustainable mobility, readiness for digital infrastructure, and openness to innovation);
- Precedent for small-scale transit or shuttle solutions (cities already running electric minibuses or pilot mobility systems).

The findings from the Brașov case study provide a transferable framework that can be applied to other European cities facing similar challenges, particularly those with historically significant and spatially constrained urban cores. Cities such as Lucca, Italy; Bruges, Belgium; and Toledo, Spain, exhibit comparable infrastructural and mobility characteristics, making the lessons learned from this analysis broadly applicable. The discussion below synthesizes the key findings and their implications.

5.1. Vehicle Selection and Infrastructural Compatibility

The results strongly support the conclusion that compact, electric-powered vehicles, like Zhongthong Electric Van, Yutong E7S and SOR EBN 8, are the most suitable option for navigating the "canyon streets" typical of historic city centers. Their smaller dimensions and superior maneuverability are important for minimizing traffic disruption and safely operating within the existing infrastructure. The simulation demonstrated that larger vehicles like SOR EBN 9.5, SOR EBN 11 and SOR NS 12 are forced to operate at lower speeds in curves to maintain passenger comfort, which negatively impacts their overall journey time and the operational frequency of the service. This finding reinforces the principle that in environments with tight geometric constraints, vehicle agility is a primary determinant of operational efficiency. Furthermore, the choice of electric vehicles is also important for addressing the environmental concerns in these high-density pedestrian zones, as their zero-emission and low-noise operation aligns with sustainable mobility objectives.

5.2. The Central Optimization Challenge: Capacity, Efficiency, and Service Quality

The analysis revealed a direct trade-off between energy efficiency and passenger service quality. Larger buses, like SOR EBN 9.5, SOR EBN 11 and SOR NS 12, while consuming more energy in absolute terms, are significantly more efficient on a per-passenger basis. However, this efficiency is achieved at the cost of lower service frequency and longer waiting times for passengers. On the other hand, smaller vehicles like Zhongthong Electric Van and Yutong E7S provide a superior level of service with short travel time but result in higher total fleet energy consumption.

This highlights that there is no single "optimal" vehicle. The ideal solution lies in a carefully balanced fleet configuration that is tailored to the specific mobility patterns of the city. This requires a data-driven approach, using detailed mobility studies to understand passenger demand across different times of the day and days of the week. For instance, a

hybrid strategy could be employed, deploying larger, high-capacity vehicles during peak commuter and tourist hours, while using smaller, more frequent shuttles during off-peak periods to maintain a high level of service without operating underutilized vehicles.

5.3. A Data-Driven Framework for Urban Planning

This study demonstrates the value of a simulation-driven planning methodology. By creating a digital twin of the road infrastructure and modeling vehicle dynamics, it is possible to conduct an analysis of various transport scenarios. This approach allows urban planners to calculate key performance indicators, such as travel times, fleet requirements, and energy consumption per passenger, for different vehicle types before making significant capital investments.

5.4. Addressing Broader Urban Challenges

The deployment of a well-designed autonomous public transport service can be a catalyst for addressing broader urban challenges. The specific issues identified in Brașov, such as illegal parking, high-density pedestrian flows, and school-related traffic congestion, are common to many historic cities. A reliable, high-frequency autonomous shuttle service can reduce dependency on private vehicles, thus improving parking pressure and congestion. When integrated with local policies such as limited traffic zones and congestion charging, compact AVs can help reclaim urban space, enhancing the environment for pedestrians and cyclists and improving the overall quality of life in the historic center.

5.5. Social Inclusion and User Experience

The success of any public transport system depends on its acceptance by the public. The operational frequency, which is directly linked to vehicle size and fleet configuration, has a significant impact on waiting times and perceived reliability—two critical factors for passenger satisfaction. Furthermore, autonomous public transport systems must be designed with inclusivity at their core. By adhering to universal design principles, these services have the potential to dramatically improve accessibility for the elderly, people with disabilities, and other underserved groups, ensuring that the benefits of modern mobility are distributed equitably.

In summary, the Brașov case study provides a robust framework for understanding the complex variables involved in implementing autonomous public transport in historic cities. The simulation model, validated against real-world operational data from an existing bus line, proved to be a highly accurate tool for predicting vehicle performance and energy consumption. In this analysis, the objective was to evaluate whether an autonomous vehicle can exhibit operational behavior comparable to that of a conventional vehicle operated by a human driver. To ensure a controlled comparison between the two configurations, a simplified route was selected—one devoid of stochastic elements such as uncertainties or unexpected obstacles. Key operational parameters, including acceleration profiles, maximum velocities, and station dwell times, were constrained based on established standards and values cited in the specialized literature. Although the autonomous model has been trained to handle certain levels of uncertainty, for the purposes of this phase of the study, such factors were assumed to impact the digital simulation outcomes to a similar extent as they would affect real-world vehicle behavior.

The central conclusion is that a comprehensive, multi-objective analysis—balancing vehicle size, operational frequency, energy consumption, and passenger comfort—is essential for tailoring a solution to the unique characteristics of each urban environment. This study was subject to some simplifying assumptions that provide clear directions for future research. Firstly, the energy consumption model assumed a flat road network. While this established a crucial baseline, road grade is known to have a major impact on the

energy consumption of electric vehicles. The inclusion of topographical data would be particularly important for modeling regenerative braking, where energy recovered during descents can significantly compensate the energy consumed during climbs. Secondly, the analysis was based on a static passenger demand profile. Real-world passenger flow is dynamic and can fluctuate significantly, a factor that would be better captured by more advanced modeling techniques. Future studies must be supported by precise local data and dynamic simulations to move beyond theoretical models and toward practical, effective, and sustainable urban mobility solutions. In this article, we aimed to identify specific challenges that may arise in cities with limited urban space and to assess the potential use of autonomous vehicles for future public transportation systems. Naturally, several challenges were not addressed in this study, including those related to vehicle performance under special operating conditions—such as winter environments, areas with high pedestrian density, or emergency scenarios. Consequently, the proposed analytical model has certain limitations and can be further refined. Future work may expand this model by incorporating additional external and internal factors related to operation, profitability, safety, and social acceptance.

Author Contributions: Conceptualization, S.B.; data curation, S.T. and R.T.; formal analysis, C.A.; investigation, S.T. and R.T.; methodology, S.B. and C.A.; project administration, S.B.; software, C.A.; supervision, S.B. and C.A.; validation, S.B. and C.A.; visualization, C.A.; writing—original draft, S.T. and R.T.; writing—review and editing, S.B. All authors have read and agreed to the published version of the manuscript.

Funding: This work is supported by the Ministry of Education of Romania, Executive Unit for Financing Higher Education, Research, Development and Innovation (UEFISCDI), under the project titled "Intelligent Connected Vehicle Cooperative System for Enhanced Driving Experience" (iDrive), project code PN-IV-P2-2.1-TE-2023-1434.

Data Availability Statement: The original contributions presented in this study are included in the article. Further inquiries can be directed to the corresponding author.

Conflicts of Interest: The authors declare no conflicts of interest.

References

1. Hafiz, D.; AlKhafagy, M.; Zohdy, I. Autonomous Public Transport: Evolution, Benefits, and Challenges in the Future of Urban Mobility. *World Electr. Veh. J.* **2025**, *16*, 482. [CrossRef]
2. Konstantas, D.; Fournier, G. Fully automated public transportation mobility: The hidden challenges for a commercial deployment. *Open Res. Eur.* **2023**, *3*, 71. [CrossRef]
3. Yuan, Y.; Liu, Y. BEVEFNet: A Multiple Object Tracking Model Based on LiDAR-Camera Fusion. *Procedia Comput. Sci.* **2024**, *242*, 560–567. [CrossRef]
4. Chen, X.; Ma, H.; Wan, J.; Li, B.; Xia, T. Multi-View 3D Object Detection Network for Autonomous Driving. In Proceedings of the 2017 IEEE Conference on Computer Vision and Pattern Recognition (CVPR), Honolulu, HI, USA, 21–26 July 2017.
5. Paek, D.-H.; Kong, S.-H.; Wijaya, K.T. K-Radar: 4D Radar Object Detection for Autonomous Driving in Various Weather Conditions. In Proceedings of the Neural Information Processing Systems Track on Datasets and Benchmarks, New Orleans, LA, USA, 10–16 November 2023.
6. Yao, S.; Guan, R.; Huang, X.; Li, Z.; Sha, X.; Yue, Y.; Lim, E.G.; Seo, H.; Man, K.L.; Zhu, X.; et al. Radar-Camera Fusion for Object Detection and Semantic Segmentation in Autonomous Driving: A Comprehensive Review. *IEEE Trans. Intell. Veh.* **2024**, *9*, 2094–2128. [CrossRef]
7. Redmon, J.; Divvala, S.; Girshick, R.; Farhadi, A. You Only Look Once: Unified, Real-Time Object Detection. In Proceedings of the 2016 IEEE Conference on Computer Vision and Pattern Recognition (CVPR), Las Vegas, NV, USA, 27–30 June 2016; pp. 779–788.
8. Geiger, A.; Lenz, P.; Urtasun, R. Are We Ready for Autonomous Driving? The KITTI Vision Benchmark Suite. In Proceedings of the 2012 IEEE Conference on Computer Vision and Pattern Recognition, Providence, RI, USA, 16–21 June 2012; pp. 3354–3361.
9. Fayyad, J.; Jaradat, M.A.; Gruyer, D.; Najjaran, H. Deep Learning Sensor Fusion for Autonomous Vehicle Perception and Localization: A Review. *Sensors* **2020**, *20*, 4220. [CrossRef]

10. Ziegler, J.; Bender, P.; Schreiber, M.; Lategahn, H.; Strauss, T.; Stiller, C.; Dang, T.; Franke, U.; Appenrodt, N.; Keller, C.G.; et al. Making Bertha Drive—An Autonomous Journey on a Historic Route. *IEEE Intell. Transport. Syst. Mag.* **2014**, *6*, 8–20. [CrossRef]
11. Levinson, J.; Thrun, S. Robust Vehicle Localization in Urban Environments Using Probabilistic Maps. In Proceedings of the 2010 IEEE International Conference on Robotics and Automation, Anchorage, AK, USA, 3–7 May 2010; pp. 4372–4378. [CrossRef]
12. Cadena, C.; Carlone, L.; Carrillo, H.; Latif, Y.; Scaramuzza, D.; Neira, J.; Reid, I.; Leonard, J.J. Past, Present, and Future of Simultaneous Localization and Mapping: Towards the Robust-Perception Age. *IEEE Trans. Robot.* **2016**, *32*, 1309–1332. [CrossRef]
13. Thrun, S.; Burgard, W.; Fox, D. *Probabilistic Robotics*; Intelligent Robotics and Autonomous Agents series; MIT Press: Cambridge, MA, USA, 2005; ISBN 978-0-262-20162-9.
14. Dolgov, D.; Thrun, S.; Montemerlo, M.; Diebel, J. Practical Search Techniques in Path Planning for Autonomous Driving. *Ann. Arbor* **2008**, *1001*, 18–80.
15. Sadigh, D.; Sastry, S.; Seshia, S.A.; Dragan, A.D. Planning for Autonomous Cars That Leverage Effects on Human Actions. In Proceedings of the Robotics: Science and Systems XII, Robotics: Science and Systems Foundation, Ann Arbor, MI, USA, 18–22 June 2016.
16. Paden, B.; Čáp, M.; Yong, S.Z.; Yershov, D.; Frazzoli, E. A Survey of Motion Planning and Control Techniques for Self-Driving Urban Vehicles. *IEEE Trans. Intell. Veh.* **2016**, *1*, 33–55. [CrossRef]
17. Falcone, P.; Borrelli, F.; Asgari, J.; Tseng, H.E.; Hrovat, D. Predictive Active Steering Control for Autonomous Vehicle Systems. *IEEE Trans. Contr. Syst. Technol.* **2007**, *15*, 566–580. [CrossRef]
18. Gao, Y.; Lin, T.; Borrelli, F.; Tseng, E.; Hrovat, D. Predictive Control of Autonomous Ground Vehicles with Obstacle Avoidance on Slippery Roads. In Proceedings of the ASME 2010 Dynamic Systems and Control Conference, ASMEDC, Cambridge, MA, USA, 12–15 September 2010; Volume 1, pp. 265–272.
19. Bojarski, M.; Testa, D.D.; Dworakowski, D.; Firner, B.; Flepp, B.; Goyal, P.; Jackel, L.D.; Monfort, M.; Muller, U.; Zhang, J.; et al. End to End Learning for Self-Driving Cars. *arXiv* **2016**, arXiv:1604.07316. [CrossRef]
20. Gavanas, N.; Anastasiadou, K.; Nathanail, E.; Basbas, S. Transport Policy Pathways for Autonomous Road Vehicles to Promote Sustainable Urban Development in the European Union: A Multicriteria Analysis. *Land* **2024**, *13*, 1807. [CrossRef]
21. Nemoto, E.H.; Jaroudi, I.; Duffner-Korbee, D.; Viere, T.; Naderer, G.; Boos, A.; van den Boom, N.; Fournier, G. Sustainability Assessment of the Integration of Automated Minibuses in Urban Mobility Systems: Learnings from the AVENUE Project. In *Automated Vehicles as a Game Changer for Sustainable Mobility: Learnings and Solutions*; Fournier, G., Boos, A., Konstantas, D., Attias, D., Eds.; Springer Nature: Cham, Switzerland, 2024; pp. 413–426, ISBN 978-3-031-61681-5.
22. Debbaghi, F.-Z.; Rombaut, E.; Vanhaverbeke, L. Lessons Learned from Shared Automated Vehicles Pilots in Europe: An Evaluation of Safety, Traffic, and User Acceptance. *Case Stud. Transp. Policy* **2025**, *20*, 101447. [CrossRef]
23. Lemardelé, C.; Baldó, A.; Aniculaesei, A.; Rausch, A.; Conill, M.; Everding, L.; Vietor, T.; Hegerhorst, T.; Henze, R.; Mátyus, L.; et al. The LogiSmile Project—Piloting Autonomous Vehicles for Last-Mile Logistics in European Cities. *Transp. Res. Procedia* **2023**, *71*, 180–187. [CrossRef]
24. Gehl, J. *Cities for People*; Island Press: Washington, DC, USA, 2010; ISBN 978-1-59726-573-7.
25. Wheeler, S.M. The Transit Metropolis: A Global Inquiry by Robert Cervero. *Berkeley Plan. J.* **2000**, *14*, 202. [CrossRef]
26. Banister, D. *Unsustainable Transport: City Transport in the New Century*; Routledge: London, UK, 2005; ISBN 978-0-203-00388-6.
27. Shaheen, S.; Cohen, A.; Zohdy, I.; United States Federal Highway Administration. *Shared Mobility: Current Practices and Guiding Principles*; Federal Highway Administration: Washington, DC, USA, 2016. Available online: https://ops.fhwa.dot.gov/publications/fhwahop16022/index.htm (accessed on 6 September 2025).
28. Koglin, T. City Cycling by John Pucher & Ralph Buehler. *Eur. Plan. Stud.* **2013**, *22*, 227–228. [CrossRef]
29. Cervero, R.; Suzuki, H.; Iuchi, K. *Transforming Cities with Transit: Transit and Land-Use Integration for Sustainable Urban Development*; World Bank Publications—Books: Washington, DC, USA, 2013.
30. Sochor, J.; Arby, H.; Karlsson, M.; Sarasini, S. A Topological Approach to Mobility as a Service: A Proposed Tool for Understanding Requirements and Effects, and for Aiding the Integration of Societal Goals. In Proceedings of the 1st International Conference on Mobility as a Service (ICoMaaS), Tampere, Finland, 28–29 November 2017; pp. 187–201.
31. Milakis, D.; Snelder, M.; van Arem, B.; van Wee, B.; Correia, G.H.d.A. Development and Transport Implications of Automated Vehicles in the Netherlands: Scenarios for 2030 and 2050. *Eur. J. Transp. Infrastruct. Res.* **2017**, *17*, 5. [CrossRef]
32. Fagnant, D.J.; Kockelman, K. Preparing a Nation for Autonomous Vehicles: Opportunities, Barriers and Policy Recommendations. *Transp. Res. Part A Policy Pract.* **2015**, *77*, 167–181. [CrossRef]
33. Litman, T. Autonomous Vehicle Implementation Predictions. Implications for Transport Planning. Available online: https://www.scirp.org/reference/referencespapers?referenceid=2466795 (accessed on 6 September 2025).
34. Anderson, J.M.; Nidhi, K.; Stanley, K.D.; Sorensen, P.; Samaras, C.; Oluwatola, O.A. *Autonomous Vehicle Technology: A Guide for Policymakers*; Rand Corporation: Santa Monica, CA, USA, 2014; ISBN 978-0-8330-8437-8.
35. Rahman, M.d.M.; Thill, J.-C. Impacts of Connected and Autonomous Vehicles on Urban Transportation and Environment: A Comprehensive Review. *Sustain. Cities Soc.* **2023**, *96*, 104649. [CrossRef]

36. Kovačić, M.; Mutavdžija, M.; Buntak, K. New Paradigm of Sustainable Urban Mobility: Electric and Autonomous Vehicles—A Review and Bibliometric Analysis. *Sustainability* **2022**, *14*, 9525. [CrossRef]
37. Gurney, J.K. Crashing into the Unknown: An Examination of Crash-Optimization Algorithms Through the Two Lanes of Ethics and Law, 79 Albany Law Review (2016). Available online: https://www.albanylawreview.org/article/69727-crashing-into-the-unknown-an-examination-of-crash-optimization-algorithms-through-the-two-lanes-of-ethics-and-law (accessed on 6 September 2025).
38. European Comission Commission Delegated Regulation (EU) 2022/2236. Available online: https://eur-lex.europa.eu/eli/reg_del/2022/2236/oj/eng (accessed on 15 October 2025).
39. European Commission, Commission Implementing Regulation (EU) 2022/1426. Available online: https://eur-lex.europa.eu/eli/reg_impl/2022/1426/oj/eng (accessed on 15 October 2025).
40. EU-Level—Connected Automated Driving. Connected Automated Driving—Just Another WordPress Site 2019. Available online: https://www.connectedautomateddriving.eu/regulation-and-policies/eu-level/ (accessed on 15 October 2025).
41. UN Regulation No. 155—Uniform Provisions Concerning the Approval of Vehicles with Regards to Cyber Security and Cyber Security Management System [2025/5]. 2025. Available online: https://eur-lex.europa.eu/legal-content/EN/TXT/PDF/?uri=OJ:L_202500005 (accessed on 15 October 2025).
42. UN Regulation No. 156—Uniform Provisions Concerning the Approval of Vehicles with Regards to Software Update and Software Updates Management System, E/ECE/TRANS/505/Rev.3/Add.155. Available online: https://unece.org/sites/default/files/2024-03/R156e%20%282%29.pdf (accessed on 15 October 2025).
43. European Union. Directive 2010/41/EU of the European Parliament and of the Council of 7 July 2010. *Off. J. Eur. Union* **2015**, *207/1*, 352–355. Available online: https://eur-lex.europa.eu/eli/dir/2010/41/oj/eng (accessed on 15 October 2025).
44. European Union. Decision (EU) 2017/2380 of the European Parliament and of the Council—Of 12 December 2017—Amending Directive 2010/40/EU as Regards the Period for Adopting Delegated Acts. *Off. J. Eur. Union* **2017**, *340/1*, 1–3. Available online: https://eur-lex.europa.eu/eli/dec/2017/2380/oj/eng (accessed on 15 October 2025).
45. Schoettle, B.; Sivak, M. A Survey of Public Opinion about Connected Vehicles in the U.S., the U.K., and Australia. In Proceedings of the 2014 International Conference on Connected Vehicles and Expo (ICCVE), Vienna, Austria, 3–7 November 2014; pp. 687–692.
46. Kaur, K.; Rampersad, G. Trust in Driverless Cars: Investigating Key Factors Influencing the Adoption of Driverless Cars. *J. Eng. Technol. Manag.* **2018**, *48*, 87–96. [CrossRef]
47. Nordhoff, S.; de Winter, J.; Kyriakidis, M.; van Arem, B.; Happee, R. Acceptance of Driverless Vehicles: Results from a Large Cross-National Questionnaire Study. *J. Adv. Transp.* **2018**, *2018*, 5382192. [CrossRef]
48. Kyriakidis, M.; Happee, R.; de Winter, J.C.F. Public Opinion on Automated Driving: Results of an International Questionnaire among 5000 Respondents. *Transp. Res. Part F Traffic Psychol. Behav.* **2015**, *32*, 127–140. [CrossRef]
49. Charness, N.; Yoon, J.S.; Souders, D.; Stothart, C.; Yehnert, C. Predictors of Attitudes Toward Autonomous Vehicles: The Roles of Age, Gender, Prior Knowledge, and Personality. *Front. Psychol.* **2018**, *9*, 2589. [CrossRef] [PubMed]
50. Payre, W.; Cestac, J.; Delhomme, P. Intention to Use a Fully Automated Car: Attitudes and a Priori Acceptability. *Transp. Res. Part F Traffic Psychol. Behav.* **2014**, *27*, 252–263. [CrossRef]
51. Kröger, L.; Kuhnimhof, T.; Trommer, S. Does Context Matter? A Comparative Study Modelling Autonomous Vehicle Impact on Travel Behaviour for Germany and the USA. *Transp. Res. Part A Policy Pract.* **2019**, *122*, 146–161. [CrossRef]
52. Haboucha, C.J.; Ishaq, R.; Shiftan, Y. User Preferences Regarding Autonomous Vehicles. *Transp. Res. Part C Emerg. Technol.* **2017**, *78*, 37–49. [CrossRef]
53. Levin, M.W.; Kockelman, K.M.; Boyles, S.D.; Li, T. A General Framework for Modeling Shared Autonomous Vehicles with Dynamic Network-Loading and Dynamic Ride-Sharing Application. *Comput. Environ. Urban Syst.* **2017**, *64*, 373–383. [CrossRef]
54. Rödel, C.; Stadler, S.; Meschtscherjakov, A.; Tscheligi, M. Towards Autonomous Cars: The Effect of Autonomy Levels on Acceptance and User Experience. In Proceedings of the 6th International Conference on Automotive User Interfaces and Interactive Vehicular Applications, Seattle, WA, USA, 17–19 September 2014; Association for Computing Machinery: New York, NY, USA; pp. 1–8.
55. Verberne, F.M.F.; Ham, J.; Midden, C.J.H. Trust in Smart Systems: Sharing Driving Goals and Giving Information to Increase Trustworthiness and Acceptability of Smart Systems in Cars. *Hum. Factors* **2012**, *54*, 799–810. [CrossRef]
56. Dianin, A.; Ravazzoli, E.; Hauger, G. Implications of Autonomous Vehicles for Accessibility and Transport Equity: A Framework Based on Literature. *Sustainability* **2021**, *13*, 4448. [CrossRef]
57. Rosenbloom, S. The Mobility Needs of Older Americans: Implications for Transportation Reauthorization, The Brookings Institution—Series on Transportation Reform. Available online: https://www.brookings.edu/wp-content/uploads/2016/06/20030807_Rosenbloom.pdf (accessed on 8 September 2025).
58. Schweitzer, L.; Valenzuela, A., Jr. Environmental Injustice and Transportation: The Claims and the Evidence. *J. Plan. Lit.* **2004**, *18*, 383–398. [CrossRef]

59. Binns, R. Fairness in Machine Learning: Lessons from Political Philosophy. In Proceedings of the 1st Conference on Fairness, Accountability and Transparency, New York, NY, USA, 23–24 January 2018; pp. 149–159.
60. UITP Global Urban Mobility Indicators. Public Transport Metrics from 53 Cities Worldwide in 2023. Available online: https://mylibrary.uitp.org/GED_V14/298938001611/20250812_Global-Urban-Mobility-Indicators-GUMI_Statistics_Brief_WEB.pdf (accessed on 8 September 2025).
61. Potts, I.B.; Harwood, D.W.; Cook, D.J.; Moran, R.A.; Busenbark, L. *Highway and Street Design Vehicles: An Update*; Transportation Research Board: Washington, DC, USA, 2023; ISBN 978-0-309-69897-9.
62. Gori, V.; Hendrix, W.; Das, A.; Sun, Z. Effect of Weight Distribution and Active Safety Systems on Electric Vehicle Performance. *Sensors* **2024**, *24*, 3557. [CrossRef]
63. Hatzenbühler, J.; Jenelius, E.; Gidófalvi, G.; Cats, O. Modular Vehicle Routing for Combined Passenger and Freight Transport. *Transp. Res. Part A Policy Pract.* **2023**, *173*, 103688. [CrossRef]
64. Martini, D.; Bezzini, P.; Longo, M. Environmental Impact of Electrification on Local Public Transport: Preliminary Study. *Energies* **2024**, *17*, 5886. [CrossRef]
65. Buekers, J.; Van Holderbeke, M.; Bierkens, J.; Int Panis, L. Health and Environmental Benefits Related to Electric Vehicle Introduction in EU Countries. *Transp. Res. Part D Transp. Environ.* **2014**, *33*, 26–38. [CrossRef]
66. European Commission European Clean Bus Deployment Initiative. Available online: https://transport.ec.europa.eu/transport-themes/clean-transport/european-clean-bus-deployment-initiative_en (accessed on 5 September 2025).
67. Jensen, J.O.; Christensen, T.H.; Gram-Hanssen, K. Sustainable Urban Development—Compact Cities or Consumer Practices? *Dan. J. Geoinform. Land Manag.* **2011**, *119*, 50–64. [CrossRef]
68. European Commission Fit for 55: Delivering the EU's 2030 Climate Target, 2021. Available online: https://eur-lex.europa.eu/legal-content/EN/TXT/HTML/?uri=CELEX:52021DC0550 (accessed on 5 September 2025).
69. Comune di Lucca Piano Della Mobilità Sostenibile—Relazione Generale, Atto Normative. Available online: https://www.comune.lucca.it/documento_pubblico/piano-della-mobilita-sostenibile-relazione-generale/ (accessed on 5 September 2025).
70. DeRobertis, M.; Tira, M. The Most Widespread Traffic Control Strategy You've Never Heard of: Traffic-Restricted Zones in Italy. *Ite J. Inst. Transp. Eng.* **2016**, 44–49. Available online: https://www.semanticscholar.org/paper/The-Most-Widespread-Traffic-Control-Strategy-You%27ve-DeRobertis-Tira/42bef80ce5226254b7814b10423d479db448a5f1 (accessed on 5 September 2025).
71. Comune di Viareggio Piano Urbano della Mobilità Sostenibile (P.U.M.S.). Available online: http://viareggio-pnrr.web.kibernetes.net/home/amministrazione/Strumenti-urbanistici-di-Governo-del-Territorio/Piani-di-settore/Piano-Urbano-Mobilita{-}{-}Sostenibile.html (accessed on 5 September 2025).
72. Traffic Study for Municipality of Brasov. Available online: https://www.brasovcity.ro/file-zone/transport-public/studiu-trafic/Actualizare%20studiu%20de%20trafic%20Brasov_Livrabil4_v6_15.03.2021.pdf (accessed on 6 September 2025).
73. Electric Van | New Energy Vehicle Manufacturer | Zhongtong Bus. Available online: http://zhongtongbuses.com/5-3-electric-van.html (accessed on 24 September 2025).
74. 12 Seater Electric Mini Coach Bus for Trip-Yutong. Available online: https://en.yutong.com/products/E7S.shtml (accessed on 24 September 2025).
75. SOR EBN—SOR Libchavy s.r.o. Available online: https://www.sor.cz/en/ebn/ (accessed on 24 September 2025).
76. Karjanto, J.; Yusof, N.M.; Terken, J.; Delbressine, F.; Hassan, M.Z.; Rauterberg, M. Simulating Autonomous Driving Styles: Accelerations for Three Road Profiles. *MATEC Web Conf.* **2017**, *90*, 01005. [CrossRef]
77. Bosetti, P.; Da Lio, M.; Saroldi, A. On the Human Control of Vehicles: An Experimental Study of Acceleration. *Eur. Transp. Res. Rev.* **2014**, *6*, 157–170. [CrossRef]
78. de Winkel, K.N.; Irmak, T.; Happee, R.; Shyrokau, B. Standards for Passenger Comfort in Automated Vehicles: Acceleration and Jerk. *Appl. Ergon.* **2023**, *106*, 103881. [CrossRef]
79. Pigeon, C.; Alauzet, A.; Paire-Ficout, L. Factors of Acceptability, Acceptance and Usage for Non-Rail Autonomous Public Transport Vehicles: A Systematic Literature Review. *Transp. Res. Part F Traffic Psychol. Behav.* **2021**, *81*, 251–270. [CrossRef]
80. Antonios, T.E.; Konstantinos, A.; Basil, P. Vehicles Lateral Acceleration and Speed Profiles Investigation at the Entry Area of Interchange Ramps as a Criterion of Geometric Road Design. *Transp. Res. Procedia* **2023**, *69*, 13–20. [CrossRef]
81. Beckers, C.J.J. Energy Consumption Prediction for Electric City Buses: Using Physics-Based Principles. Ph.D. Thesis, Technische Universiteit Eindhoven, Eindhoven, The Netherlands, 2022.
82. Berjoza, D.; Jurgena, I.; Millers, R. Effect of electric vehicle mass change on energy consumption and the range. *Agronomy Res.* **2024**, *22*, 1089–1097. [CrossRef]
83. Wu, X.; Freese, D.; Cabrera, A.; Kitch, W.A. Electric Vehicles' Energy Consumption Measurement and Estimation. *Transp. Res. Part D Transp. Environ.* **2015**, *34*, 52–67. [CrossRef]
84. Pozna, C.R.; Antonya, C.; Horváth, E. Case Study on the Tactical Level of an Autonomous Vehicle Control. In Proceedings of the 2021 International Conference on Electrical, Computer, Communications and Mechatronics Engineering (ICECCME), Mauritius, Mauritius, 7–8 October 2021; pp. 1–6.

85. Pozna, C.R.; Antonya, C. Proposal of an Autonomous Vehicle Control Architecture. In Proceedings of the 2021 IEEE 25th International Conference on Intelligent Engineering Systems (INES), Budapest, Hungary, 7–9 July 2021; pp. 000037–000042.
86. Wang, X.; Qi, X.; Wang, P.; Yang, J. Decision Making Framework for Autonomous Vehicles Driving Behavior in Complex Scenarios via Hierarchical State Machine. *Auton. Intell. Syst.* **2021**, *1*, 10. [CrossRef]
87. ITS The Total Deployment Cost for an Automated Shuttle Pilot Project in Utah Was Estimated at $627,000.|ITS Deployment Evaluation. Available online: https://www.itskrs.its.dot.gov/2022-sc00509 (accessed on 15 October 2025).
88. ITS Autonomous Vehicle Fleet Ownership and Operating Costs Are Expected to Be Half That of Traditional Vehicles by 2030–2040.|ITS Deployment Evaluation. Available online: https://www.itskrs.its.dot.gov/2018-sc00406 (accessed on 15 October 2025).
89. Wadud, Z.; Mattioli, G. Fully Automated Vehicles: A Cost-Based Analysis of the Share of Ownership and Mobility Services, and Its Socio-Economic Determinants. *Transp. Res. Part A Policy Pract.* **2021**, *151*, 228–244. [CrossRef]
90. Tirachini, A.; Antoniou, C. The Economics of Automated Public Transport: Effects on Operator Cost, Travel Time, Fare and Subsidy. *Econ. Transp.* **2020**, *21*, 100151. [CrossRef]
91. Foresights, M. Global Autonomous Shuttle Market 2024–2030. Available online: https://mobilityforesights.com/product/autonomous-shuttle-market (accessed on 15 October 2025).
92. Robot Shuttles and Autonomous Buses Market Report|Forecast [2033]. Available online: https://www.marketgrowthreports.com/market-reports/robot-shuttles-and-autonomous-buses-market-114251 (accessed on 15 October 2025).
93. Gusev, M.; Gilroy, S. The Effectiveness of Autonomous Public Transport Systems in Densely Populated Urban Areas. *Transp. Econ. Manag.* **2025**, *3*, 1–8. [CrossRef]
94. Steinvorth, A.; Gutiérrez, K.; Campos, E.; Macêdo, B.; Batista, M.; Tenenbaum, G.; Maltese, T.; Rosa, A.; Galarza, S.; Acevedo, H. *Pipeline of Electric Bus Projects in Latin America an Overview of 32 Cities*; 2023. Available online: https://www.c40.org/wp-content/uploads/2023/04/FINAL-Pipeline-of-Electric-Bus-Projects-in-Latin-America-compressed.pdf?utm_source=chatgpt.com (accessed on 15 October 2025).
95. Quarles, N.; Kockelman, K.M.; Mohamed, M. Costs and Benefits of Electrifying and Automating Bus Transit Fleets. *Sustainability* **2020**, *12*, 3977. [CrossRef]
96. Bösch, P.M.; Becker, F.; Becker, H.; Axhausen, K.W. Cost-Based Analysis of Autonomous Mobility Services. *Transp. Policy* **2018**, *64*, 76–91. [CrossRef]
97. Dev, A. Government Hires Two Agencies to Run 500 Electric Buses for 12 Years. The Times of India. 2025. Available online: https://timesofindia.indiatimes.com/city/noida/government-hires-two-agencies-to-run-500-electric-buses-for-12-years/articleshow/122032583.cms?utm_source=chatgpt.com (accessed on 15 October 2025).

Disclaimer/Publisher's Note: The statements, opinions and data contained in all publications are solely those of the individual author(s) and contributor(s) and not of MDPI and/or the editor(s). MDPI and/or the editor(s) disclaim responsibility for any injury to people or property resulting from any ideas, methods, instructions or products referred to in the content.

vehicles

MDPI

Article

Investigation of Bearing Condition by Means of Robust Linear Regression and Informative Predictors

Ramona-Monica Stoica *, Daniela Voicu and Radu Vilău

Faculty of Aircraft and Military Vehicles, Military Technical Academy "Ferdinand I", 39-49 George Cosbuc Av., 050141 Bucharest, Romania; daniela.voicu@mta.ro (D.V.); radu.vilau@mta.ro (R.V.)
* Correspondence: ramona.stoica@mta.ro

Abstract

This study addresses the condition monitoring of rolling bearings by applying robust linear regression to statistically derived features from vibration data. Four datasets of acceleration signals were collected under varying operating conditions: aligned and misaligned bearings at rotational speeds of 1000 rpm and 1500 rpm. From each signal, key statistical indicators were extracted, including root mean square (RMS), skewness, kurtosis and crest factor, to capture signal characteristics that were relevant to fault detection. To follow-up, we applied the Kolmogorov–Smirnov test to assess data normality and the results confirmed significant deviations from a Gaussian distribution, motivating the use of robust regression techniques for further investigations. The regression model created incorporated rotational speed and alignment conditions as predictors of acceleration and the results indicated that while the coefficient associated with misalignment suggested a possible increase in acceleration (~1.115 units), statistical testing (p = 0.5233) indicated that neither speed nor alignment had a significant influence on the measured vibration levels within the dataset. The findings suggest that under the tested conditions, misalignment does not manifest as a strong linear change in acceleration magnitude, and the study underscores the importance of robust modeling techniques and feature selection in the condition monitoring of rotating machinery.

Keywords: robust linear regression; Kolmogorov–Smirnov test; statistical indicators; kurtosis; root mean square; advanced analysis techniques; bearing fault detection

1. Introduction

Bearings are one of the most important constituents of a mechanical transmission, and are used to support rotating parts and reduce friction. Most of the studies related to bearing functioning study load capacity, lubrication techniques, wear resistance and noise generation. The lubrication regime is often a focus, including studies on oil flow and temperatures. Because most of the damages to roller bearings are due to wear, whether they are determined by lubricant failure or contamination or by normal fatigue, now, studies focus on predicting bearing failures in advance, with the use of vibration or temperature analysis, advanced techniques such as deep learning and neural networks or advanced mathematical tools, such as multiple linear regression (MLR), with the use of statistical inference and model building.

Linear regression models have long been used in statistical analysis for their simplicity and interpretability. In the context of bearing condition monitoring, linear regression can offer valuable insights into the relationships between vibration characteristics

and bearing health. However, traditional linear regression models often struggle with outliers, multicollinearity and noise, which are common in vibration datasets. As a result, a robust regression framework is required to address these issues and improve the model's performance.

Over the past few decades, numerous studies have explored the use of vibration-based techniques for bearing fault detection. Early research focused on the extraction of simple features, such as root mean square (RMS) and peak-to-peak amplitude, with a view to detecting major faults such as outer race, inner race and ball bearing defects. More recently, studies have moved towards advanced techniques such as wavelet transform [1,2], empirical mode decomposition [3,4] and deep learning-based methods, according to [5–8]. However, despite significant progress in the area, the challenge of selecting the right features and developing models that are both accurate and computationally efficient remains. Recent advancements in robust regression techniques, such as least absolute deviations (LAD) regression and weighted regression models, have shown promise in providing more reliable estimates in the presence of noise and outliers.

Several studies have highlighted the limitations of standard regression techniques when applied to vibration-based fault detection. For instance, Daoud (2017) [9] noted that traditional regression methods are often hindered by multicollinearity in high-dimensional vibration datasets. Other researchers, such as Giloni et al. (2006) [10] and Tian and Wang (2021) [11], have explored the use of robust regression methods, such as LAD regression, that offer improved resistance to the effects of noise and outliers. Despite these advancements, there remains a lack of comprehensive studies that systematically investigate the effectiveness of robust regression in bearing condition monitoring, particularly when compared to more traditional approaches.

Yan et al. [12] proposed an adaptive regression model to estimate the remaining life of a bearing, by using an elbow point detection design to improve the prognostic performance. The paper showed that the suggested method can effectively determine the time to start the prediction and can calibrate the degradation regression model dynamically, according to the evolving degradation trend in the health indicator (HI).

While there is a wide array of anomaly detection algorithms for bearing fault identification, few studies utilize the specific, simple setup presented in our work. The decision to use one analysis method or another is difficult, as it is amplified by the varying experimental setups, which often do not allow for a direct comparison of results under consistent conditions.

In terms of methodology, our study aims to determine whether bearing faults can be detected using simple, computationally efficient models and what the difficulties in applying an appropriate analysis method are. This is particularly important, given that numerous studies have shown that bearing operation is a nonlinear and non-stationary process, which makes it challenging to accurately assess their performance and functional condition [13,14]. To this end, we chose to investigate the limitation of applying robust regression analysis, as statistical methods are among the widely recognized approaches. Therefore, regression techniques are one of the most used methods to evaluate bearing functioning, its remaining life cycle or high influence parameters [15,16]. To that end, the use of multiple regressions, as an extension of linear regression, takes into account more than one independent variable as input, to predict a single output variable. Such a technique can only be effectively applied if the deviation of any data point from the fitted line exceeds the maximum allowable error for the measured variable. To that end, the first step is to perform a baseline diagnosis with the use of informative predictors such as RMS (root mean square), kurtosis, skewness and crest factor, as part of the vibration analysis and condition monitoring goals, highlighting the comparative values between aligned and

misaligned functional bearing, while running at 1000 rpm and 1500 rpm. The use of time domain analysis contributed to the overall measure of the signal's energy, detection of impulsive events in the endogenous variable, like pitting, spalling or a crack in the bearing, or detection of non-uniform loading or misalignment.

Given that feature extraction introduces numerical complexity, our study also highlights the challenges derived from the data processing on fault detection performance. Our findings show that, for certain experimental methods, choosing the appropriate method is challenging and the results can be inconclusive for pointing out certain statements, such as the effect of certain degrees of misalignment on bearing functioning.

The second step was to inspect the variable variation, then proceed with the linear regression itself. There were several attempts to identify a suitable regression method, taking into account the Gaussian or non-Gaussian distribution of data. It was assumed to be a normal distribution of acceleration; it was verified and, in the follow-up, we chose a more appropriate regression model.

Hence, the main purpose of this study is to investigate the application of robust linear regression for bearing condition monitoring, focusing on identifying key predictors for fault detection under different operational conditions. Specifically, we examine the bearing behavior in both aligned and misaligned states at two distinct rotational speeds (1000 rpm and 1500 rpm). By employing robust regression techniques, we aim to model how changes in bearing misalignments and functioning speed affect the acceleration values. Hence, the acceleration is considered to be the dependent variable, and misalignment and speed are the independent ones: the former is a quantitative parameter and the latter is the continuous variable. This research contributes to the growing body of knowledge on predictive maintenance, offering valuable insights for industries such as automotive, aerospace and manufacturing, where bearing health is critical to operational performance.

The study is situated within recent advancements in machine learning and statistical methods for condition monitoring, where feature extraction and model robustness are key to improving fault diagnosis accuracy, and it concluded that the datasets used for analysis showed a faulty bearing submitted to tests, with problems caused by wear and the low-to-minimal influence of bearing alignment and functional speed on the resulting acceleration values. Also, the absence of strong linear effects highlights the complexity of fault diagnosis in bearing systems, suggesting that additional nonlinear or time-series methods could be explored in future work. Our findings emphasize the importance of carefully chosen methodologies and the selection of relevant features in condition monitoring tasks, contributing to the ongoing evolution of data-driven predictive maintenance strategies.

2. Materials and Methods

The physical configuration used during experimental tests comprises a control unit, a mechanical assembly and a computer, as depicted in Figure 1.

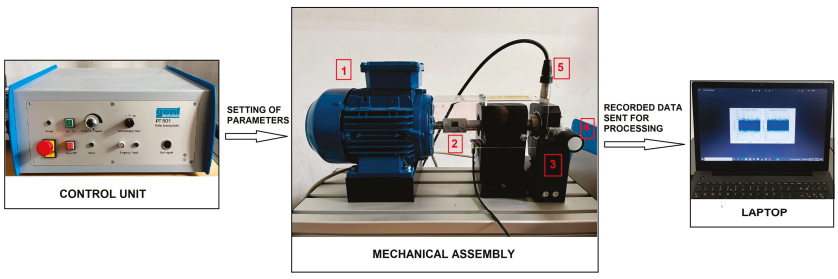

Figure 1. Configuration of experimental setup and constituent elements.

The control unit was used to vary the functioning speed of the mechanical transmission, generating the first independent variable. The mechanical assembly comprised an electric motor (1), a flexible jaw coupling (2), a bearing seat (3) with a roller bearing, loading knob for radial forces (4) and a piezoelectric accelerometer with integral electronics (IEPE sensor), mounted in a vertical position on a threaded bore. The main characteristics of the piezoelectric accelerometer and the roller bearing are presented in Table 1.

Table 1. Characteristics of the main elements of the mechanical assembly.

Accelerometer		**Bearing**	
Type	Piezoelectric sensor	Type	NU 204 E TVP2
Resonance frequency	25 kHz	Number of rollers	12
Measuring range (3 dB)	0.5–10 kHz	Limiting speed	22,000 rpm
Nonlinearity	1%	Basic dynamic load rating, radial	32.500 N
Measuring range	490 m/s^2 or 50 g	Temperature range	−30–120 °C
Temperature range	−54–121 °C	-	-

Different types of experimental tests were conducted, wherein the functioning speeds and statuses of bearing were varied, resulting in the following four cases:

- Functioning speed of 1000 rpm, aligned roller bearing;
- Functioning speed of 1000 rpm, misaligned roller bearing;
- Functioning speed of 1500 rpm, aligned roller bearing;
- Functioning speed of 1500 rpm, misaligned roller bearing.

The misalignment of the bearing was set through the loading knob of the mechanical assembly by applying a constant static load, depicted on the scale as 2.5 mm, which corresponds to a force of 100 N. Each test lasted 120 s, during which the measured data from the accelerometer (namely acceleration values) were transmitted to the laptop for further processing and analysis.

Prior to conducting the linear regression analysis, we established the physical status of the analyzed bearing, meaning whether there are damages on either of the characteristic elements, by means of time domain analysis. To that purpose, four statistical features of the measured acceleration series were determined, which are depicted in Table 2.

Table 2. Statistical indicators used for the analysis of bearing functioning.

No.	**Statistical Indicator**	**Units**	**Purpose**
1	RMS (root mean square)	m/s^2	Quantifies the overall magnitude of the vibration signal
2	Kurtosis	-	Measures the asymmetry of the vibration signal distribution
3	Skewness	-	Is a key indicator in fault detection
4	Crest Factor	-	Identifies potential failure mechanisms like surface damage

The details about the formulas that are used to calculate each statistical indicator within Table 2 are presented in Appendix A.

After obtaining the results for each baseline indicator, in order to assess the overall shape of the data distribution and ensure more accurate analysis, the Kolmogorov–Smirnov (KS) test was applied. This statistical test evaluates whether the dataset follows a normal distribution by defining the null hypothesis (H_0), running the test itself and then interpreting the results.

To that end, we considered the sample of data: namely, acceleration values such as $x_1, x_2, x_3, \ldots, x_n$. To test the hypothesis that the sample comes from a specific distribution,

denoted F_0 (e.g., normal distribution), against the alternative that it is from another distribution, denoted F (the empirical distribution derived from sample), where $F(x_i) \neq F_0(x_i)$ for some $x_i \in R$, it is calculated that the Kolmogorov–Smirnov statistic is the maximum absolute difference between the empirical cumulative distribution function (ECDF) and the theoretical cumulative distribution function (CDF) [17]:

$$D_n = \max_{1 \leq i \leq n} \| F_n\left(x_{(i)}\right) - F\left(x_{(i)}\right) \|, \tag{1}$$

Empirical CDF at point $x_{(i)}$ (where $x_{(i)}$ represents the i-th ordered observation) is as follows:

$$F_n\left(x_{(i)}\right) = \frac{i}{n}, \tag{2}$$

where

$$x_i = \frac{x_i - \mu}{s}, \tag{3}$$

and data were sorted in ascending order as follows: $x_{(1)} \leq x_{(2)} \leq \cdots \leq x_{(n)}$.

The theoretical CDF is the following:

$$F\left(x_{(i)}\right) = \Phi(x_{(i)}) \tag{4}$$

where Φ represents the cumulative distribution function of the normal distribution.

In the absence of normality, multiple data transformations were performed, such as power and square root. The results were not favorable. As a consequence, taking into account the lack of Gaussian fit of data and residuals, even after several attempts to apply transformations, it was chosen to continue the study of bearing functioning by means of robust regression, which is more suitable for considering the characteristics of acceleration values.

Robust regression is also a linear regression technique that relaxes assumptions regarding outliers, handling heteroscedasticity and non-normal residuals, and it fits the model by minimizing weighted errors, using functions like bisquare.

The general equation used was as follows:

$$Y = \beta_0 + \beta_1 \cdot x_1 + \beta_2 \cdot x_2 + \beta_3 \cdot x_1 \cdot x_2 + \varepsilon, \tag{5}$$

where y is the dependent variable (acceleration), x_1 is the first independent variable (speed), x_2 is the second independent variable (alignment), x_1x_2 is the interaction term between speed and alignment and ε represents the error term.

Assuming that the regression output includes coefficients (denoted β_0, β_1, β_2, β_3) for the intercept, main effects and interaction, the regression equation can be written as follows:

$$\text{Acceleration} = \beta_0 + \beta_1 \cdot \text{speed} + \beta_2 \cdot D_{\text{alignment}} + \beta_3 \cdot (\text{speed} \times D_{\text{alignment}}) + \varepsilon, \tag{6}$$

where β_0 is the intercept term (baseline acceleration when speed = 0 and alignment = "aligned"), β_1 is the coefficient for speed (the effect of speed on acceleration), β_2 is the coefficient for alignment (the effect of alignment on acceleration), β_3 is the coefficient for the interaction between speed and alignment, $D_{\text{alignment}}$ has a value of 0 for "aligned" and 1 for "misaligned" and ε represents the error term (residuals).

3. Results

3.1. Time Domain Analysis Results

The results of RMS, as depicted in the calculation, indicated a value of 16.62 m/s^2 in the case of the aligned bearing and 38.96 m/s^2 for the misaligned one, for a functioning speed of 1000 rpm, and 31.77 m/s^2 and 70.00 m/s^2, respectively, for the aligned and misaligned bearings, for a functioning speed of 1500 rpm. In the case of mechanical parts, RMS values are a measure of signal magnitude, which is useful to determine, especially when dealing with time-varying parameters like acceleration. In the absence of manufacturing guidelines for the specific roller bearing, one can compare the values measured in the cases of aligned and misaligned bearings, which revealed that the misalignment condition caused an increase in RMS by more than 2.34 times at 1000 rpm and 2.2 times at 1500 rpm. At 1000 rpm, misalignment increases the RMS by a greater factor compared to 1500 rpm, even though the absolute RMS values are higher at 1500 rpm. The result here indicates that the system is more sensitive to misalignment at lower speeds in terms of the RMS increase, potentially because of the specific operating characteristics of the bearing or the system.

In terms of the calculated values of kurtosis, it resulted that β is 4.15 in the case of the aligned bearing and 3.69 for the misaligned one while running at 1000 rpm, and the values at 1500 rpm are 4.33 and 3.39, respectively. According to the literature, a kurtosis value above three indicates a leptokurtic sample that is greater than that of a normal distribution, which is consistent with heavier tails, a sharp peak around the mean and more extreme outlier or impulsive values. This implies that the bearing's vibration signal contains spikes and impulses, possibly indicating early-stage faults on bearing elements due to the wear phenomenon.

Also, the comparative display of the detailed statistical indicators before, as well as for skewness and crest factor, which are detailed in the follow-up, is depicted in Figures 2 and 3.

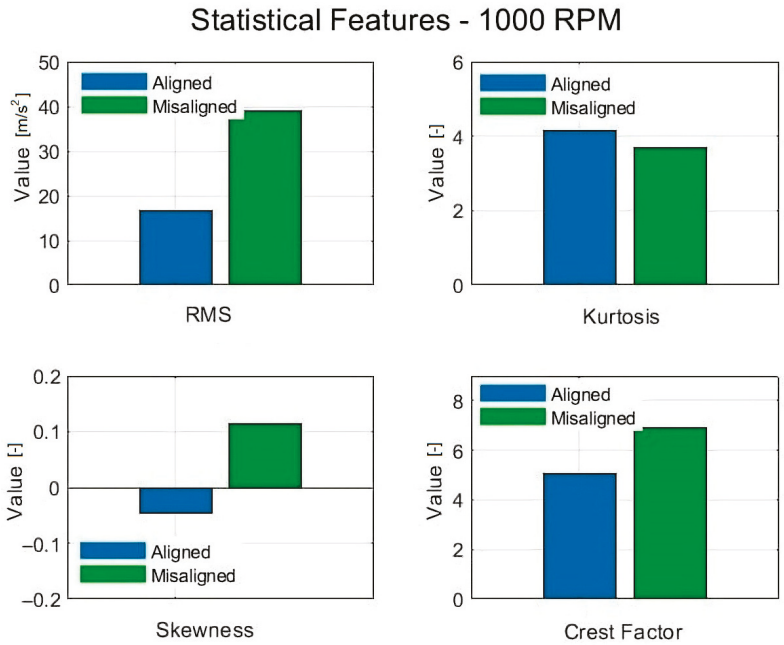

Figure 2. Comparative statistical features (RMS, kurtosis, skewness and crest factor) for aligned and misaligned bearings at 1000 RPM.

From Figures 2 and 3, it can be observed that the RMS values are higher in the case of the misaligned bearing, which is known due to the fact that this condition increases non-Gaussian characteristics. Higher values of RMS indicate larger amplitude values on

average. Regarding kurtosis, the two figures show higher values for the aligned bearing, which is counterintuitive. Possible causes can reside in the type of misalignment, which determines the type of vibration response; the introduction of additional frequency components into the vibration spectrum, which might be more regular or sinusoidal; or the fact that misalignment can create a smoother and more consistent vibration pattern where periodic vibrations can be present.

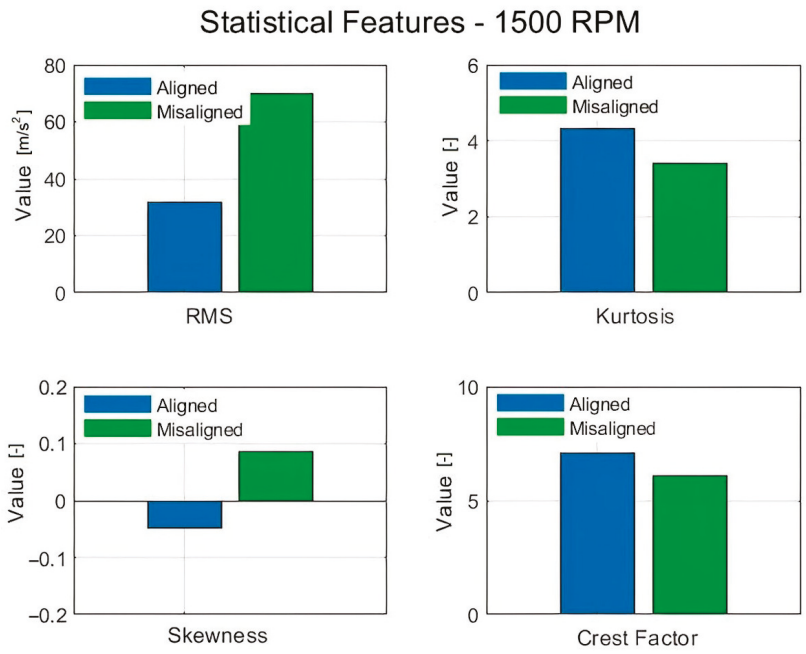

Figure 3. Comparative statistical features (RMS, kurtosis, skewness and crest factor) for aligned and misaligned bearings at 1500 RPM.

From the calculation, it was determined that for the aligned and misaligned bearings, the sw is −0.04 and 0.11 while functioning at 1000 rpm, and −0.04 and 0.08 while functioning at 1500 rpm. According to [14,15], the values between −0.5 and 0.5 indicate an approximately symmetric distribution, characterized by moderate skewness, which represents an advantage for applying further regression analysis. The visual representation of acceleration distribution is depicted in Figure 4.

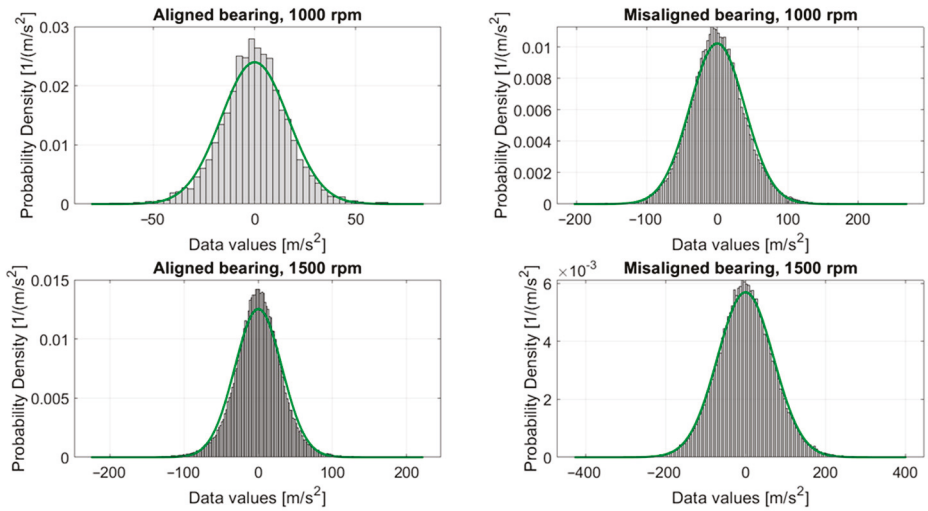

Figure 4. Overlay of normal distribution curve on the histogram of acceleration values.

Given the negligible skewness values, that are still different from 0, the results cannot indicate with certainty that the data follow a normal distribution. Hence, to check the overall shape of the distribution and obtain more relevant results, the Kolmogorov–Smirnov (KS) test was applied. This is used to check if the data follow a normal distribution, considering the null hypothesis (H0). If h = 0 (where h is the variable used to define the result when performing hypothesis tests), we fail to reject H0, meaning the data follow a normal distribution, and if h = 1, we reject H0, meaning the data do not follow a normal distribution. Considering that the critical value of 0.016 (for the aligned bearing, at 1000 rpm) and 0.0045 (for the other three tests), was calculated according to the sample size and the significance level $\alpha = 0.05$, they were compared with the determined KS statistic. Also, the empirical cumulative distribution function (ECDF) and theoretical cumulative distribution function (CDF) were displayed (Figure 5) to determine the degree of fitting of the acceleration series to the normal distribution.

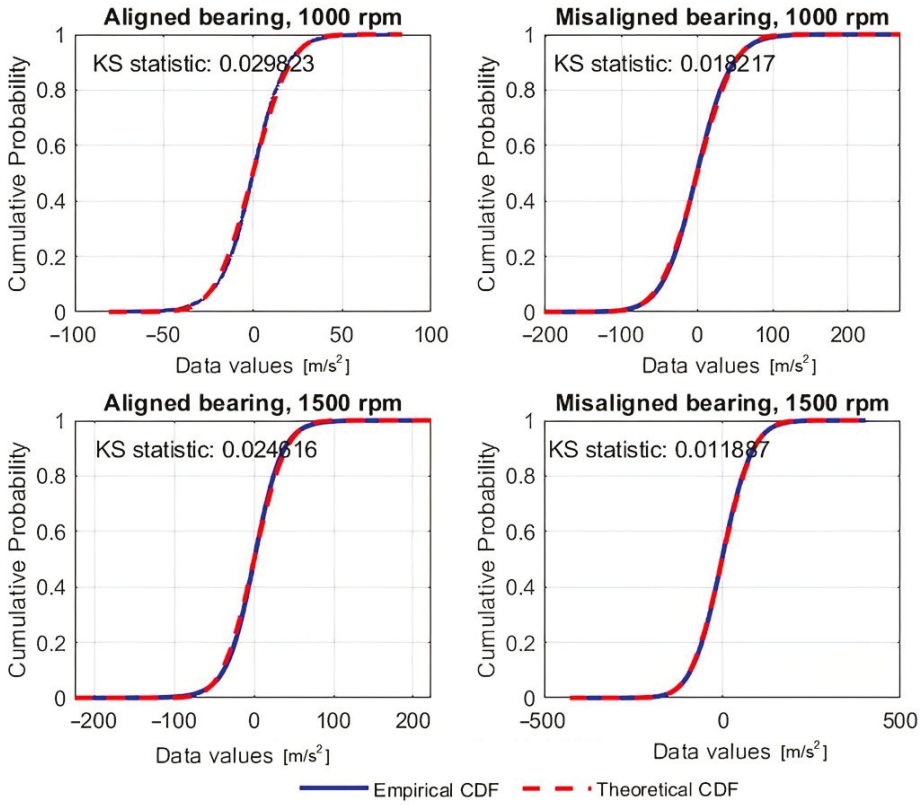

Figure 5. Comparison of empirical and theoretical cumulative distribution function for aligned and misaligned bearing, while functioning at 1000 rpm and 1500 rpm.

From the resulting values of the KS statistics displayed in Figure 5, it can be concluded that the acceleration values do not fit a normal distribution (all four KS statistics are higher than the corresponding critical values). Even if the acceleration values do not have a Gaussian fit, one can check the residual distribution for normality in order to apply multiple linear regression analysis in the follow-up. Considering this, the Kolmogorov–Smirnov statistical method was also applied to test the residuals. The method was chosen due to the large dataset of values, and it applied a regression model to the known data (to calculate the residuals). The results also indicated that the test result was 1, which suggests that the null hypothesis (H0) is rejected and the data do not fit a normal distribution. Also, the *p*-value, which was used to represent the probability of observing data under the assumption of the null hypothesis, was 0.0000, which implies that it strongly rejects H0.

In the case of the fourth indicator, the crest factor, the resulting values were 5.03 and 7.10 for the aligned and misaligned bearing while functioning at 1000 rpm and, while functioning at 15,000 rpm, the crest factors were 6.92 and 6.10. Generally, the misalignment typically increases the dynamic forces on the bearing, leading to more sudden peaks in vibration, hence the higher crest factor while functioning at 1000 rpm. Also, while functioning at 1500 rpm, there were lower values observed than in the misaligned condition at 1000 rpm. This could suggest that at higher speeds, the bearing experiences slightly more transient events, due to factors like increased centrifugal forces or slight operational changes, but the bearing is still operating relatively smoothly.

3.2. Robust Regression Analysis Results

Substituting Formula (6) with the calculated values, the regression model becomes the following:

$$\text{acceleration} = -0.0523 + 0.00009 \cdot \text{speed} + 1.1150 \cdot D_{\text{alignment}} - 0.0015 \cdot (\text{speed} \times D_{\text{alignment}}) \quad (7)$$

All the estimated coefficients are presented in Table 3, and the graphical representations of residual distribution are depicted in Figures 6 and 7.

Table 3. Estimated coefficients after applying linear regression model (robust fit).

Term	Estimate	Standard Error	t-Statistic	*p*-Value
Intercept	−0.0523	1.6653	−0.0314	0.9749
Speed	0.00009	0.0011	0.0797	0.9365
Aligned/ Misaligned	1.1150	1.7468	0.6383	0.5233
Speed: Alignment	−0.0015	0.0012	−1.2653	0.2057
RMS Error: 43.9				
F-statistic versus constant model: 20.8				
Number of observations: 276,453				

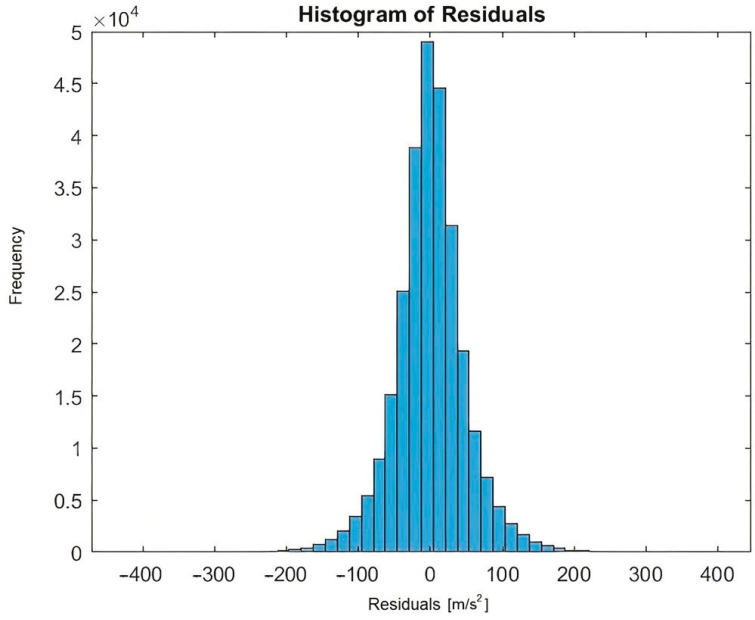

Figure 6. Histogram of residuals after applying robust regression for aligned and misaligned bearings, while functioning at 1000 rpm and 1500 rpm.

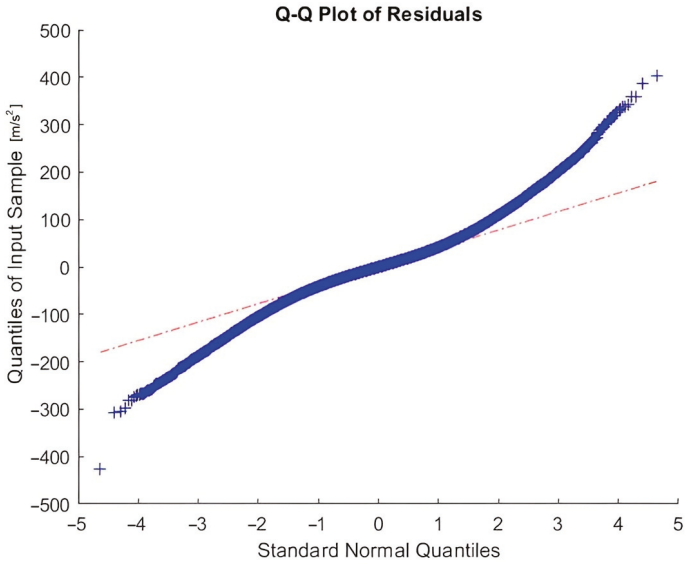

Figure 7. Q-Q plot of residuals after applying robust regression for aligned and misaligned bearings, while functioning at 1000 rpm and 1500 rpm.

From Table 2, it can be observed that all *p*-values indicate the results, and predictors are not statistically significant; for example, the coefficient for speed indicates that the effect of speed on acceleration is very small (0.00009). The high *p*-value (0.9365) indicates that speed is not a significant predictor of acceleration in this model. Essentially, changes in speed do not have a statistically significant effect on the acceleration values, based on the current data.

Also, the coefficient for alignment status (aligned versus misaligned) suggests that, on average, misalignment might increase the acceleration by around 1.115 units. However, the *p*-value (0.5233) is much higher than 0.05, which indicates that the alignment condition does not have a statistically significant effect on the acceleration, considering the recorded variable at constant functioning speed.

Yet again, the small number of variables that are taken into account generated results showing that the model has a high residual error (RMS = 43.9), indicating that most of the variation in the acceleration remains unexplained by these variables and the model does not fit well. Still, the model is better than using a simple mean as a prediction, according to the F-statistic versus the constant model: 20.8.

The results regarding the degree of influence of the alignment status on acceleration values, or whether there is any, are also confirmed by means of ANOVA applied to the dataset, where it was determined that there is no significant difference between the values recorded while the bearing was aligned and misaligned. Characteristic values are presented in Table 4, and the boxplot representation of the acceleration is depicted in Figure 8.

Table 4. ANOVA table.

Source	SS (Sum of Squares)	DF (Degrees of Freedom)	MS (Mean Square)	F (F-Statistic)	Prob > F (*p*-Value)
Groups	4.314	3	1.44	0	1
Error	670,400,309.33	276,449	2425.04		
Total	670,400,313.65	276,452			

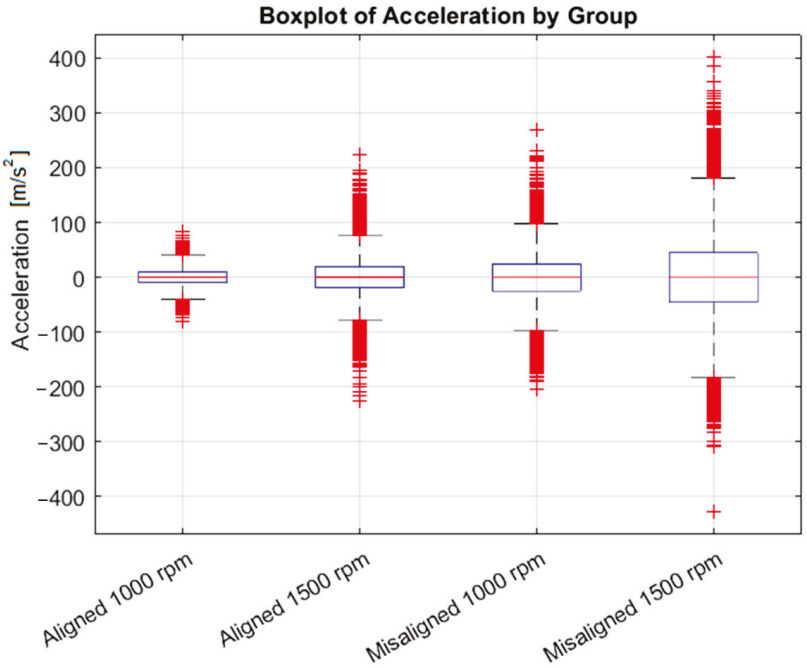

Figure 8. ANOVA results in the form of a boxplot of acceleration for aligned and misaligned bearings, while functioning at 1000 rpm and 1500 rpm.

From Table 4, it can be interpreted that the differences between the group means are not statistically significant, given the value of 1.44. Also, the sum of squares value for the groups (SS = 4.314) indicates that the variability between the groups is very small compared to the huge variability within the groups (Error SS = 670,400,309.33). This further supports the conclusion that there are no meaningful differences between the group means, meaning there is no significant difference between the groups in terms of the acceleration data. The results suggest that the speed and alignment conditions have little to no effect on the acceleration measurements, based on this particular dataset. To strengthen the generalization and reproducibility of the results, the proposed condition-monitoring method of computing baseline statistical indicators, followed by robust regression analysis, was validated using the publicly available CWRU bearing dataset [17]. Specifically, we utilized four distinct datasets: two sets representing a healthy bearing, of which one was running at 1750 rpm with a load of 2HP, and the other was running at 1730 rpm with a load of 3HP, and two sets of bearings exhibiting an inner race fault, of which one was running at 1750 rpm with a load of 2HP, and the other was running at 1730 rpm, with a load of 3HP. This validation process was undertaken to assess the robustness and generalization of the proposed methodology, ensuring its applicability to real-world scenarios with varying fault conditions. The inclusion of both healthy and faulty bearing data strengthens the reproducibility of the results and provides further empirical evidence of the method's effectiveness in condition monitoring and fault detection.

The method of analysis proposed within the current paper—namely, the use of statistical indicators, followed by a robust regression model—is validated by the results depicted in Table 5, where it is indicated that the bearing state (normal versus inner race faults) has a statistically significant impact on the acceleration signal ($p < 0.001$). The positive coefficient associated with the "faulty" condition suggests that defective bearings exhibit significantly higher vibration levels compared to healthy bearings.

Table 5. Robust regression coefficients for applying the proposed method to the CWRU dataset.

Term	Estimate	*p*-Value	95% CI	Interpretation
Intercept	−0.0160	0.5915	[−0.0743, 0.0424]	Not statistically significant
RPM	0.0000	0.1049	[−0.0000, 0.0001]	Weak effect of rotational speed
Bearing status (faulty)	0.1464	0.0005	[0.0639, 0.2289]	Strong and significant effect of bearing defect
RPM × status (faulty)	−0.0001	0.0000	[−0.0001, −0.0001]	Significant interaction effect

Also, although the RPM coefficient is not significant at the 95% confidence level, the interaction between RPM and alignment is significant, indicating that the effect of rotational speed differs between healthy and defective bearings. Specifically, in the faulty state, increasing RPM is associated with a slight but statistically significant change in vibration amplitude.

The statistical indicators were as follows: RMS = 0.0880 m/s^2, skewness = −0.1674, kurtosis = 3.5176 and crest factor = 4.2463.

In addition, to assess the statistical significance of the results, we computed the 95% confidence intervals (CIs) for each coefficient, following the robust linear regression analysis. This step is vital for a more comprehensive evaluation of the relationships between the variables, as CIs provide a range of plausible values for the coefficients, thereby quantifying the uncertainty of the estimates. By incorporating confidence intervals, we enhanced the robustness of our findings, offering a more thorough understanding of the effect sizes and further supporting the conclusion that neither alignment nor speed significantly influences acceleration, considering the analyzed data and experimental setup. The results are visible in Table 6.

Table 6. Confidence interval values, computed for the robust regression coefficients.

Term	Estimates	95% Confidence Interval (CI)
Intercept	−0.0523	[−3.3163, 3.2117]
Speed	0.00009	[−0.0020, 0.0022]
Alignment	1.1150	[−2.3080, 4.5387]
Speed: Alignment	−0.0015	[−0.0039, 0.0009]

From the results, it can be observed that the 95% confidence interval for the intercept is [−3.3163, 3.2117], which includes zero, suggesting that the baseline value of acceleration is uncertain and could be close to zero. This wide interval indicates a high degree of variability in the intercept estimate. Also, the 95% CI suggests that speed, alignment and their interaction do not significantly influence acceleration in the context of this model. The wide intervals for each term highlight substantial uncertainty, indicating that the effects, if present, are likely very small or non-existent.

The lack of significant influence from misalignment and rotational speed could be attributed to several factors. First, the misalignment tested may have been too mild to induce noticeable changes in vibration, particularly because the bearing was operating within its tolerance limits. Additionally, the narrow speed range (1000 rpm and 1500 rpm) may not have been sufficient to capture nonlinear behaviors or resonance effects, which are often more pronounced at higher or more variable speeds. The results can also be explained by the limited range of operating conditions tested in this study, which might not fully capture the range of dynamics that could be observed in more complex scenarios.

Ultimately, while the findings suggest that, under the tested conditions, neither speed nor alignment significantly affected the acceleration measurements, we caution against

broad generalizations. This study serves as an initial exploratory analysis, and future research, with a wider range of experimental conditions, including varying misalignment levels, additional fault scenarios and more extensive speed variations, would be crucial to assess whether these variables have a more pronounced effect under different operating circumstances.

4. Conclusions

Regression analysis is a valuable tool for evaluating the degree of influence of different factors on bearing condition, particularly in predictive maintenance applications. The results of this study suggest that, within the specific conditions of the tested dataset, speed and alignment may have little to no significant effect on the acceleration measurements. This implies that, in this particular scenario, these variables may not serve as strong predictors for fault detection. However, given the limited experimental setup, which includes only two rotational speeds and one level of misalignment, these findings should be viewed as preliminary and not broadly generalizable, and the study may be seen as being limited to the chosen experimental framework and serves as an exploratory analysis. Future research incorporating a wider range of operating conditions might lead to more extensive conclusions. Instead, the vibration signal itself, with its characteristic spikes and impulses, emerges as a suitable informative predictor for faulty bearings, highlighting the usefulness of statistic indicators such as skewness, crest factor or RMS. Still, while this study focused on the analysis of bearing performance using time-domain features, it is acknowledged that these indicators, although useful, may have limitations in capturing more complex fault characteristics. Time-domain features primarily reflect the statistical properties of the vibration signal, which may not always provide sufficient discriminative power for detecting subtle or early-stage faults. Frequency-domain and time-frequency domain features, such as spectral kurtosis, wavelet features, and entropy, are known to provide a more comprehensive analysis by capturing information about signal behavior across different frequencies and time intervals. These features are often more sensitive to transient changes and can enhance fault detection, particularly in more complex or dynamic conditions. As a result, future work could explore the integration of these advanced features to improve diagnostic accuracy. Additionally, a hybrid approach combining both time-domain and frequency-domain features could be considered for a more robust fault analysis on bearing systems and could improve diagnostic accuracy and reliability.

It is also important to acknowledge that the dataset used in this study includes only two rotational speeds and a binary alignment condition (aligned/misaligned). While this simplification allows for a more focused analysis, it limits the extension of the findings to real-world bearing operating conditions, where the bearing could experience a wider range of speeds and more complex alignment scenarios. In real-world applications, bearings are subject to varying operational conditions that may involve continuous changes in speed and potentially more intricate alignment variations. Therefore, future research might consider datasets with a broader range of speeds and alignment conditions, and possibly other factors, such as load and temperature, thus reducing the uncertainty in the generalizability of the findings and providing a more comprehensive understanding of the factors influencing bearing vibration behavior under real-world operational conditions. This would help to enhance the robustness and applicability of the results to real-world scenarios.

In this study, we applied robust linear regression analysis that is particularly beneficial in handling non-normal data distributions, which is common in industrial applications where noise and outliers can significantly impact analysis. This approach allowed for more reliable results compared to traditional regression methods that assume normality in data. However, it is important to note that while robust regression can mitigate the influence

of outliers and non-normality, it may not capture subtle effects when the predictor set is limited. The findings suggest that neither alignment nor speed significantly influenced acceleration values in this case, but the methodology's ability to handle complex data structures could be particularly useful in other scenarios where more complex relationships may exist. Future work should consider exploring alternative features or expanding the predictor set to further evaluate the applicability of robust regression in fault diagnosis under varying operational conditions.

Author Contributions: Conceptualization, R.-M.S.; methodology, R.-M.S., D.V. and R.V.; software, R.-M.S., D.V. and R.V.; validation, R.-M.S.; formal analysis, R.-M.S.; investigation, R.-M.S., D.V. and R.V.; resources, R.V.; data curation, R.-M.S., D.V. and R.V.; writing—original draft preparation, R.-M.S.; writing—review and editing, R.-M.S., D.V. and R.V.; supervision, R.V.; project administration, R.-M.S.; funding acquisition, R.-M.S., D.V. and R.V. All authors have read and agreed to the published version of the manuscript.

Funding: This research received no external funding.

Data Availability Statement: The authors confirm that the data supporting the findings of this study are available within the article.

Conflicts of Interest: The authors declare no conflicts of interest.

Abbreviations

The following abbreviations are used in this manuscript:

MLR	Multiple Linear Regression
HI	Health Indicator
RMS	Root Mean Square
ECDF	Empirical Cumulative Distribution Function
CDF	Theoretical Cumulative Distribution Function
EMD	Empirical Mode Decomposition
LAD	Least Absolute Deviations

Appendix A

The first statistical feature, root mean square indicator, was determined in order to measure the overall intensity and magnitude of vibrations in the analyzed bearings, considering the experimental dataset.

For determining kurtosis values for both series, it was used in the following formula [18]:

$$k = \frac{E(X - \mu)^4}{\sigma^4} \tag{A1}$$

where E(t) represents the expected values of the quantity t, μ is the mean of analised series, σ represents the standard deviation and X will take each value of the set.

When the series observations are x_1, x_2, x_3, ..., x_n, the coefficient of kurtosis is expressed as the arithmetic mean of the fourth powers of distances, where the latter are calculated between each observation and its variable mean value, denoted by β:

$$\beta = \frac{\frac{1}{N}\sum_{n=1}^{N}(x_n - \mu)^4}{\sigma^4} \tag{A2}$$

Derived from the kurtosis indicator, in statistics, there is another measure in the form of excess kurtosis, noted γ, which is used to describe if a sample is flatter or more peaked in nature than the normal distribution and it is calculated with the following formula:

$$\gamma = \beta - 3 \tag{A3}$$

In the context of bearing health, high kurtosis (greater than three) often indicates that there are impulsive events in the acceleration signal. This is typically associated with faults such as pitting, cracks, or spalling on bearing surfaces.

The analysis continued with the calculation of skewness to determine the third moment of the distribution. Because most of the statistical techniques used in mechanical fields assume a normal distribution of data, determining whether a set is positively or negatively skewed is useful for improved results. The coefficient of skewness is determined with the following formula:

$$sw = \frac{\mu_3}{{\mu_2}^{3/2}} \tag{A4}$$

where μ_3 is the third central moment, used to measure skewness asymmetry, and μ_2 is the variance, defined by the following formula:

$$\mu_2 = E\left[(X - \mu)^2\right] \tag{A5}$$

The last baseline indicator used to analyze the tested bearings, the crest factor, can give a fast insight into the waveform and the amount of impact that is associated with roller bearing wear. The crest factor can be determined with the following formula [19,20]:

$$CF = \frac{A_{max}}{A_{RMS}}, \tag{A6}$$

where A_{max} is the maximum amplitude of the signal and A_{RMS} is its RMS value.

References

1. Li, C.; Yin, X.; Chen, J.; Yang, H. Bearing Fault Diagnosis Based on Wavelet Transform and Convolutional Neural Network. *Open Access Libr. J.* **2022**, *9*, 1–14. [CrossRef]
2. Li, J.; Wang, H.; Wang, X.; Zhang, Y. Rolling bearing fault diagnosis based on improved adaptive parameterless empirical wavelet transform and sparse denoising. *Measurement* **2020**, *152*, 107392. [CrossRef]
3. Damine, Y.; Bessous, N.; Pusca, R.; Megherbi, A.C.; Romary, R.; Sbaa, S. A New Bearing Fault Detection Strategy Based on Combined Modes Ensemble Empirical Mode Decomposition, KMAD, and an Enhanced Deconvolution Process. *Energies* **2023**, *16*, 2604. [CrossRef]
4. Li, W.; Wang, L.; Lu, P.; Hua, L. Bearing Fault Diagnosis Research Based on Empirical Mode Decomposition and Deep Learning. In Proceedings of the 35th Youth Academic Annual Conference of Chinese Association of Automation (YAC), Zhanjiang, China, 16–18 October 2020; pp. 32–37. [CrossRef]
5. He, M.; He, D. Deep Learning Based Approach for Bearing Fault Diagnosis. *IEEE Trans. Ind. Appl.* **2017**, *53*, 3057–3065. [CrossRef]
6. Zhang, W.; Li, C.; Peng, G.; Chen, Y.; Zhang, Z. A deep convolutional neural network with new training methods for bearing fault diagnosis under noisy environment and different working load. *Mech. Syst. Signal Process.* **2018**, *100*, 439–453. [CrossRef]
7. Yuan, B.; Lu, L.; Chen, S. Research on Bearing Fault Diagnosis Based on Vibration Signals and Deep Learning Models. *Electronics* **2025**, *14*, 2090. [CrossRef]
8. Wang, Y.; Li, D.; Li, L.; Sun, R.; Wang, S. A novel deep learning framework for rolling bearing fault diagnosis enhancement using VAE-augmented CNN model. *Heliyon Sci.* **2024**, *10*, e35407. [CrossRef] [PubMed]
9. Daoud, J. Multicollinearity and Regression Analysis. *J. Phys. Conf. Ser.* **2017**, *49*, 012009. [CrossRef]
10. Giloni, A.; Simonoff, J.S.; Sengupta, B. Robust weighted LAD regression. *Comput. Stat. Data Anal.* **2006**, *50*, 3124–3140. [CrossRef]
11. Tian, Q.; Wang, H. Predicting Remaining Useful Life of Rolling Bearings Based on Reliable Degradation Indicator and Temporal Convolution Network with the Quantile Regression. *Appl. Sci.* **2021**, *11*, 4773. [CrossRef]
12. Yan, M.; Xie, L.; Muhammad, I.; Yang, X.; Liu, Y. An effective method for remaining useful life estimation of bearings with elbow point detection and adaptive regression models. *ISA Trans.* **2022**, *128*, 290–300. [CrossRef] [PubMed]
13. Wang, S.; Xiang, J.; Zhong, Y.; Zhou, Y. Convolutional neural network-based hidden Markov models for rolling element bearing fault identification. *Knowl.-Based Syst.* **2018**, *144*, 65–76. [CrossRef]

14. Băltoiu, A.; Dumitrescu, B. Bearing Semi-Supervised Anomaly Detection Using Only Normal Data. *Appl. Sci.* **2025**, *15*, 10912. [CrossRef]
15. Chen, Y.; Chen, Q.; Wang, R. Bearing Fault Diagnosis Based on Vibration Envelope Spectral Characteristics. *Appl. Sci.* **2025**, *15*, 2240. [CrossRef]
16. Selvamuthu, D.; Das, D. *Introduction to Statistical Methods, Design of Experiments and Statistical Quality Control*, 1st ed.; Springer: New Delhi, India, 2018.
17. Case Western Reserve University. Case School of Engineering. Bearing Data Center. Available online: https://engineering.case.edu/bearingdatacenter/12k-drive-end-bearing-fault-data (accessed on 16 October 2025).
18. Johnson, R.; Wichern, D. *Applied Multivariate Statistical Analysis*, 6th ed.; Pearson: Upper Saddle River, NJ, USA, 2007.
19. Martinez, W.L.; Martinez, A.R. *Computational Statistics Handbook with MATLAB*; Chapman&Hall/CRC: Boca Raton, FL, USA, 2002.
20. Althoff, H.; Eberhardt, M.; Geinitz, S.; Linder, C. Advances in Crest Factor Minimization for Wide-Bandwidth Multi-Sine Signals with Non-Flat Amplitude Spectra. *Comput. Sci. Math. Forum* **2022**, *2*, 11. [CrossRef]

Disclaimer/Publisher's Note: The statements, opinions and data contained in all publications are solely those of the individual author(s) and contributor(s) and not of MDPI and/or the editor(s). MDPI and/or the editor(s) disclaim responsibility for any injury to people or property resulting from any ideas, methods, instructions or products referred to in the content.

vehicles

MDPI

Article

Investigation on the Manufacturing, Testing, and Simulation Processes of the Hood Hinge Assembly

Mihai Stirosu [1,2,*], Stefan Tabacu [1,*] and Gabriel Cimpeanu [2]

[1] Faculty of Mechanics and Technology, National University of Science and Technology POLITEHNICA Bucharest, Pitesti University Centre, Târgu din Vale, no. 1, Arges, 110040 Piteşti, Romania
[2] AKA Automotiv SRL, Văleni-Podgoria, 364A, Argeş, 117207 Călineşti, Romania; gcimpeanu@akaoto.com.tr
* Correspondence: mstirosu@akaoto.com.tr (M.S.); stefan.tabacu@upb.ro (S.T.)

Abstract

The automotive industry is currently undergoing significant transformations driven by challenges such as fierce competition, supply chain disruptions, and stringent legislative regulations aimed at reducing pollutant emissions. The research employs a combination of theoretical analysis and numerical modeling to investigate the manufacturing processes of stamped automotive components. Data collection methods include experimental testing of materials, LS-DYNA simulations, and non-contact scanning for dimensional analysis. The study also utilizes a workflow diagram to illustrate the various phases involved in the design and validation of automotive assemblies. The findings detail the critical role of digital transformation in the automotive industry, particularly in enhancing the accuracy and reliability of manufacturing processes. Implementing digital twins improves product quality and reduces product development time. The experimental results were compared with simulation data, and a good correlation was identified, showing, for the numerical model with complete history (thickness and stress), a difference of 1.6%. Furthermore, to simplify the process of developing the numerical models for the initial iterations, a scale factor of $\sim$ 1.1 is proposed for the testing load. This factor is not limited to the current design, as the manufacturing stages are similar for this range of products.

Keywords: hood hinge assembly; digital twin; manufacturing process; structural performance

1. Introduction

The automotive industry, over the past 20 years, has probably been going through its most dynamic period of transformation and adaptation. Every day, new market challenges from stakeholders [1], energy efficiency [2], new requirements, advanced manufacturing solutions [3], and legislative regulations emerge. Car manufacturers have to implement these updates during development or, sometimes, on the fly, even after the start of series production. Currently, referring to the car manufacturing industry [1] there are new technologies and terms that making their presence: Industry 4.0 and use of machine learning instruments [2], advance to Industry 5.0 [3], development of high end robots [4], interconnecting machines by Internet of Things [5], 3D printing for prototypes and some industrial application [6], emerging industrial processes [7], automated production [8], lean manufacturing, electrification, and autonomous vehicles [9]. For European manufacturers, new challenges arise every day, dictated by market requirements, the legislation in force, and global competition.

The concept of "Industry 4.0" was first introduced in an article published by the German Government in 2011 to define a high-tech strategy for 2020. Industry 4.0 is a complex technological system that has been widely discussed and researched, with a significant influence on the industrial sector, and which introduces new concepts and technologies in industrial development: Internet of Things (IoT), Internet of Services (IoS), Augmented Reality (AR), robotics, virtual manufacturing (Cloud Manufacturing) [10,11].

One of the biggest challenges in the automotive industry is reducing pollutants and greenhouse gas emissions. Currently, the legislative norms in force impose increasingly stringent carbon-emission limits, leading manufacturers to seek a balance between a vehicle's mass and its dynamic performance and fuel consumption by updating powertrains' performances while simultaneously reducing the vehicle's own mass [12,13].

This is how the concept of digitalization or digital transformation emerged [3] in terms of products and their related processes. The Digital Twin was first defined in aeronautics in 2010 as an integrated, probabilistic, multi-physics, multi-scale simulation of a vehicle or system that uses the best physical models, up-to-date sensors, and fleet history to provide a virtual mirror of the real twin's life. The digital twin is ultra-realistic and can model one or more critical, interdependent systems of the vehicle, including propulsion, energy storage, safety devices, vehicle structure, thermal management, etc. [10,14]. The benefits of using a digital twin are numerous, including higher quality, rapid integration into master planning, reduced development time, reduced project complexity, and the adaptation of manufacturing processes to new models with minimal changes to production systems.

All these challenges affect the less visible domain for the end customer: suppliers of components, manufacturing equipment, or various services. A significant impact is on the level of suppliers developing parts and components: the time allocated to the product development and validation stages has decreased, new security and regulatory requirements have been imposed, and together with a significant trend of reducing all costs [5].

Finite element simulation [15–17] of mechanical processes play a crucial role in engineering. From an economic point of view, finite element simulation brings a considerable reduction in associated expenses through optimal component design [18]. Numerical models are an effective tool for performance evaluation, structure monitoring, and damage detection [19], lifetime estimation [20,21] and identification of optimal maintenance methods [22].

Numerical tools are helpful for better understanding the physical mechanisms that control the strength, ductility, and failure mode of threaded assemblies. The current progress in numerical modeling tools and methods requires that numerical models meet the accuracy and reliability requirements for their results. The use of simple design and evaluation procedures cannot fully capture the behavior of many structures unless they are updated and calibrated using large models.

The success of these numerical predictions depends on the quality of the constitutive model adopted, including the identification of the material parameters [20]. The manufacturing process analysis plays a significant role as it provides the input data for structural analyses. In this paper, a complex procedure is presented that shows, step by step, the prerequisites for accurate numerical simulations. To allow rapid analyses, the use of scale factors is discussed, and a solution is proposed for components of the hood-hinges family.

2. Materials

2.1. Hood Hinge Assembly

Developing a mechanism to open a vehicle hood is a complex task that requires specific engineering skills. Previous practical experience, cost orientation, weight reduction, and performance are some key elements considered in the design activities. Hood hinges are usually simple mechanisms made up of three main elements: a fixed element, in contact

with the vehicle body, a movable element in contact with the hood, and a rotation axis to ensure the rotation of the hood during maneuvering [23]. First, their role is to facilitate access to the engine compartment (for periodic maintenance performed by the user or for more complex work carried out in service units). Additional constraints are defined by the assembly process, which requires precise tolerances and significant effort. Regarding the vehicle, passive safety measures require that, in the event of an impact, the consequences be minimal. The most common road accidents are those in which the vehicle collides with the front end [24,25]. Therefore, the need for special constructions with multiple functions is identified [26–28].

Thus, it is necessary to maintain the hood in the closed position when considering the vehicle's passengers and to define a deformation space when vulnerable road users (pedestrians, cyclists, or moped users) are involved.

The car manufacturer documents the mechanical system's operating requirements and further analyzes and validates them with the supplier. Figure 1 presents the component elements of the hood hinge assembly.

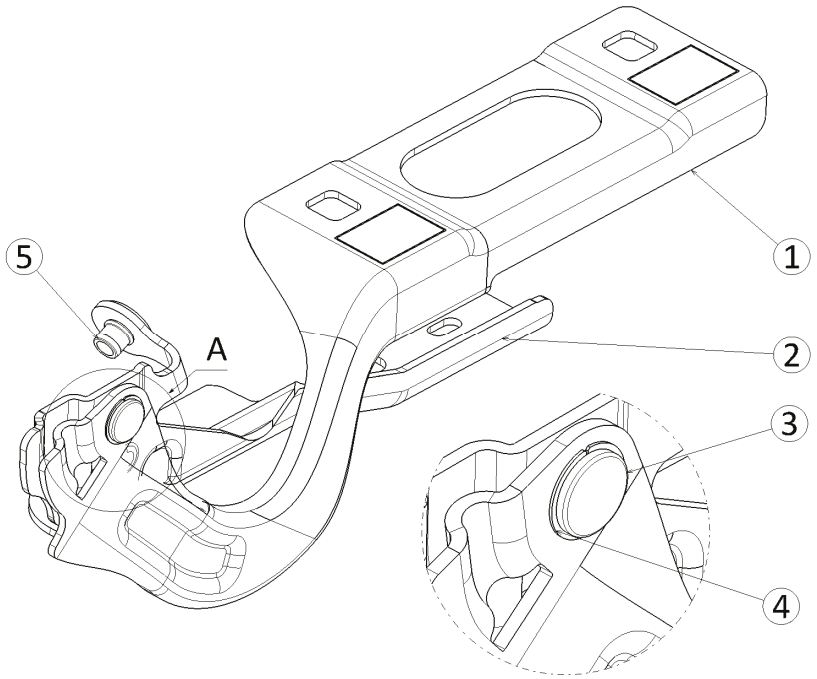

Figure 1. Hood hinge assembly: (**1**)—mobile part; (**2**)—fixed part; (**3**)—shaft; (**4**)—friction seal (detail A); (**5**)—link (detail A).

The initial model includes the necessary functional elements. The level of detail of the initial model depends on the information available to the supplier during the technical solution development phase.

The complex tasks that will be performed simultaneously during the design process and product validation are related (and not limited) to the following stages: (Figure 2):

- functional definition of the assembly;
- geometric definition of the assembly;
- manufacturing process analysis;
- material selection;
- usage performance validation;
- structural performance validation.

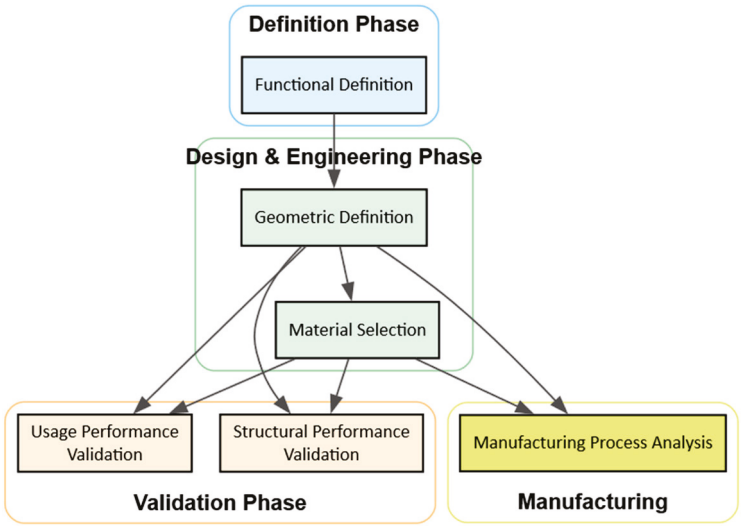

Figure 2. Workflow. The diagram presents the workflow and the connections between operations.

Figure 2 shows that the process is not linear and that design loops are necessary to develop a functional and reliable product.

The functional definitions of the assembly are related to the following requirements:

- to guarantee the hood functionality in opening/closing durability;
- ensure a maximum angle of hood opening;
- no radial and axial gap;
- lateral stiffness;
- hood maintained on hinges stop;
- resist the exceptional forces: Strong wind on the hood maintained on the hinges stop;
- resist the exceptional forces: **High speed frontal crash**;
- repairability crash;
- temperature in the current rolling conditions;
- thermal and climatic behavior;
- guarantee the maintenance of the security position;
- maintaining the hinge during the mounting.

Given the limited information, a basic model (Figure 3a) is selected for design optimization. Technical validation is the supplier's responsibility, so intervention was necessary to reinforce the part's structure.

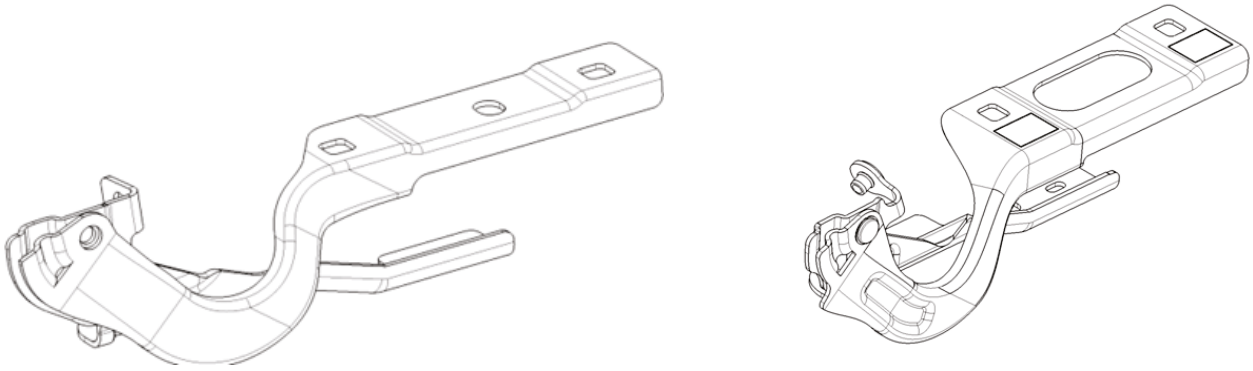

(**a**) (**b**)

Figure 3. Design of the assembly: (**a**) preliminary design; (**b**) final design.

The final shape of the assembly indicates the addition of reinforcement elements and dome cutouts to optimize the part's mass (Figure 3b).

To match current design trends and safety requirements, the mobile part of the assembly features a critical feature: a goose-neck-like shape between the connecting plate and the rotation axis. This design feature is not structurally favorable; thus, it requires multiple actions to define a functional part. To stiffen the structure, it is designed as a C-shaped section. Although intended to increase structural capacity, these added design features should be implemented with care, as they can affect thickness during manufacturing. The loads are bending dominant, and thickness determines the formation of plastic hinges, leading to structural failure [29]. At the same time, material selection is a critical step in the design process. The material is also challenging for the manufacturing process, as it determines the forming capability.

2.2. Material Modeling

The material was selected based on previous experience and following simple numerical simulations. The required mechanical response was achieved using S460 structural steel [30,31].

From the actual blanks used in the manufacturing process, a series of samples was extracted. As the blank's rolling direction is unknown, the specimens were extracted according to the configuration shown in Figure 4a. Figure 4b presents the set of samples prepared, while Figure 4c presents the results of the tensile tests.

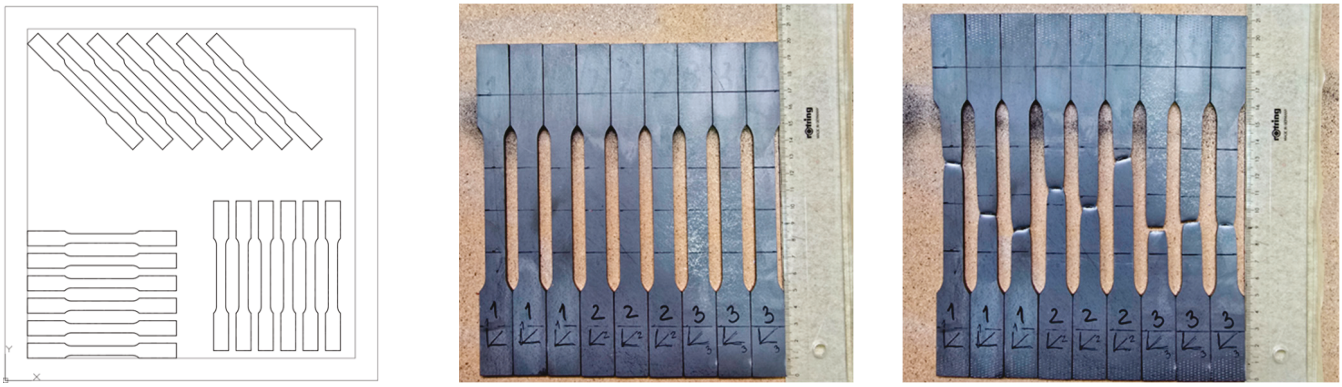

(**a**) (**b**) (**c**)

Figure 4. Samples for the tensile tests: (**a**) cutting solutions; (**b**) collection of samples; (**c**) tested samples (the corresponding set ID is marked on the sample).

The specimens were tested using a computer-controlled universal testing machine (Figure 5a). A mechanical extensometer was fitted to the specimens for direct measurement of elongation (Figure 5b). The testing protocol follows the mechanical characterization specification for the materials and includes three stages: pre-load, loading, and high-speed separation. The results were cumulated and compared to the reference values specific to S460 steel. As can be noticed (Figure 5c), in all cases the values of $R_{p0,2}$—proportionality limits and R_m—maximum stress is within the prescribed range.

Equations set (1) are used to convert measured (engineering) stress—strain data to the true values:

$$\begin{aligned} \varepsilon_t &= \log(1+\varepsilon_e) \\ \sigma_t &= \sigma_e \cdot (1+\varepsilon_e) \end{aligned} \tag{1}$$

where:

- $(\varepsilon_e, \sigma_e)$ define the measure dataset;
- $(\varepsilon_t, \sigma_t)$ define the true stress strain dataset.

The maximum stress was identified from the curves, and the data were subsequently extracted before degradation. Figure 6 presents the resulting stress–strain curves.

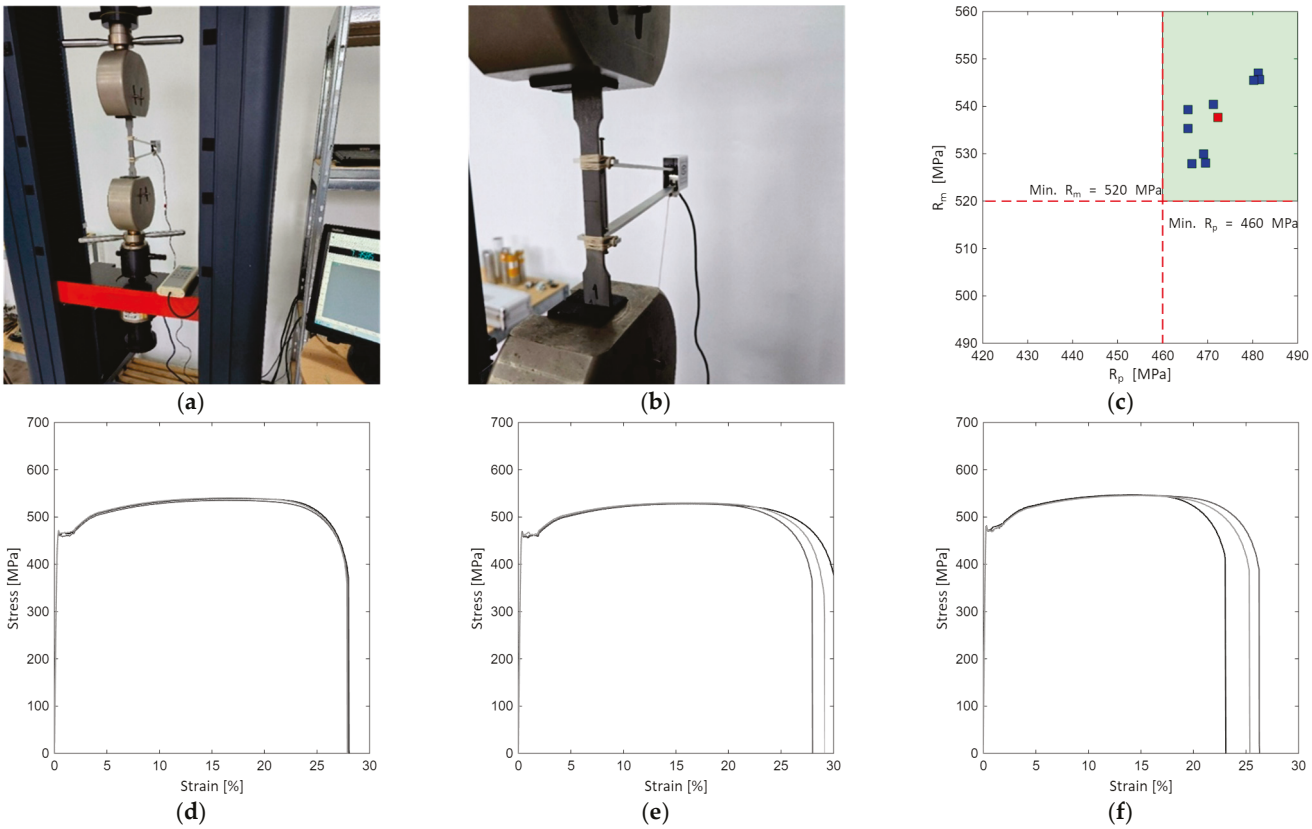

Figure 5. Testing of samples: (**a**) universal testing machine; (**b**) extensometer fitted on the sample; (**c**) collection of $R_{p0,2}$ and R_m; (**d**) engineering stress-strain curves for set 1; (**e**) engineering stress-strain curves for set 2; (**f**) engineering stress-strain curves for set 3.

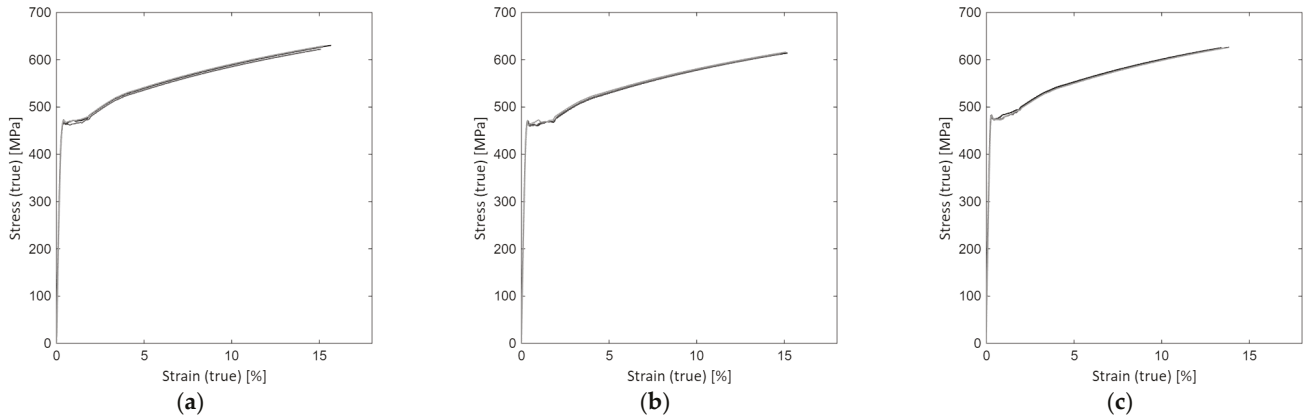

Figure 6. True stress—strain curves: (**a**) set 1; (**b**) set 2; (**c**) set 3.

A numerical model of the samples (Figure 7a) for calibrating the material model was developed, following the LS-Dyna nomenclature. Material *MAT_PIECEWISE_LINEAR_PLASTICITY was selected due to its versatility [32]. The material model can also be adapted to capture the degradation phase following the maximum stress [33].

The implicit solver (*CONTROL_IMPLICIT) was used to solve the numerical model. The clamped ends were modeled as rigid bodies to impose both fixed and moving sections. To measure the force, a set of nodes located in the vicinity of the fixed end was constrained (*BOUNDARY_SPC). Two nodes on the calibrated section of the specimen, at the same distance as the extensometer opening, were selected to measure elongation during tensile loading. The simulation results (Figure 7b) were compared with the measured dataset to

evaluate the performance of the implemented material model. A summary of the physical and mechanical properties of S460 is presented in Table 1.

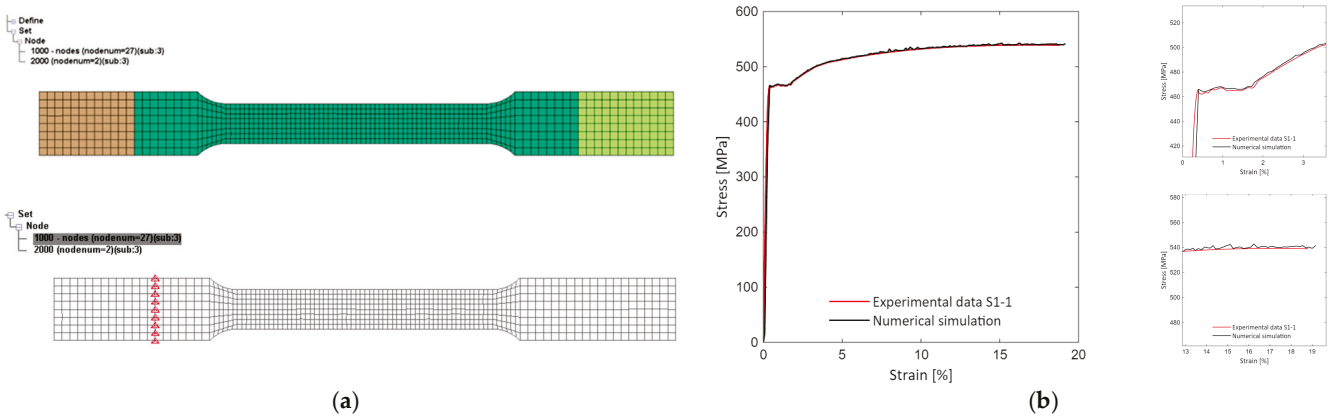

Figure 7. Model for the calibration of the material: (**a**) numerical model of the sample; (**b**) experimental vs. numerical results.

Table 1. S460 structural steel. Physical and mechanical properties.

Parameter	Symbol	Value	Units
Density	ρ	7800	kg/m^2
Young modulus	E	21,000	MPa
Yield stress	R_p	min. 460	MPa
Tensile strength *	R_m	min. 520	MPa
Tensile strength $^+$	σ_m	min. 610	MPa
Elongation	A	min. 20	%

* The value refers to the engineering stress /$^+$ The value refers to the true stress.

Cross-analysis of experimental and numerical results is an essential step in validating the material model. If differences between the two sets of results are identified, the material model requires revision, or the experimental setup was unable to provide accurate data.

3. Manufacturing Process and Simulation

3.1. Industrial Process

The manufacturing process for the assembly's components involves a multi-step forming process. Figure 8 presents the press equipped with the dies for the forming operations. The initial shape presented in Figure 8 was previously cut from a blank sheet to match the final shape of the part.



Figure 8. Press equipped with the forming dies.

Figure 9 shows the part after each forming operation. The process begins with the workpiece being extracted from the blank sheet (Figure 9a), followed by four stages of forming (Figure 9b–e). To ensure accurate positioning of the part during forming, circular cutouts are required for the guidance pins (Figure 9a–e). The final stage involves trimming to obtain the finished part (Figure 9f).



(**a**) (**b**) (**c**) (**d**) (**e**) (**f**)

Figure 9. Forming stages: (**a**) workpiece; (**b**) stage I—construction of reinforced area and one edge of the C shape of the goose-neck section; (**c**) stage II—construction of second edge of the C shape; (**d**) stage III—90° bend; (**e**) stage IV—cuts in the stopper area and the axis; (**f**) stage V—cuts in the fixation area.

3.2. Numerical Simulation of the Forming Process

In most cases, the evaluation of the assembly's structural performance is based on the nominal geometric definitions of the components. Thus, there are no changes in the material thickness or residual stress due to the manufacturing process that affect performance. Furthermore, performing complex analyses during design iterations is time-consuming and not justified during the design phase. A complete chain of design–manufacture–testing processes provides an opportunity to investigate the methods used during the design activity. Figure 10 gives a global perspective of simulation models developed for the forming process.

The numerical models for the workpiece, die, punch, and pins were constructed by extracting specific features from the geometrical model. Figure 10a presents the forming set-up for the shape presented in Figure 9b, while Figure 10b presents the thickness of the part. Figure 10c presents the forming setup for the shape shown in Figure 9c, along with the estimated thickness (Figure 10d). The final numerical setup (Figure 10e) was defined for the shape shown in Figure 9d. The resulting thickness distribution is presented in Figure 10f. The numerical simulation process was limited to stage III, as at this step, all the operations involved in forming were performed.

The numerical models were developed using ANSYS Forming 2025R1, which uses the LS-Dyna [34] as a solver. Thus, the entire simulation process is integrated into a single solver to facilitate the data exchange between various simulation stages [35,36].

The forming analysis includes, by default, mesh adaptation and refinement options. Thus, the number of elements increases substantially at the end of the simulation. The final step is a springback analysis for the stress release [37–39]. The solver facilitates the export of simulation results in a.dynain file in ASCII format.

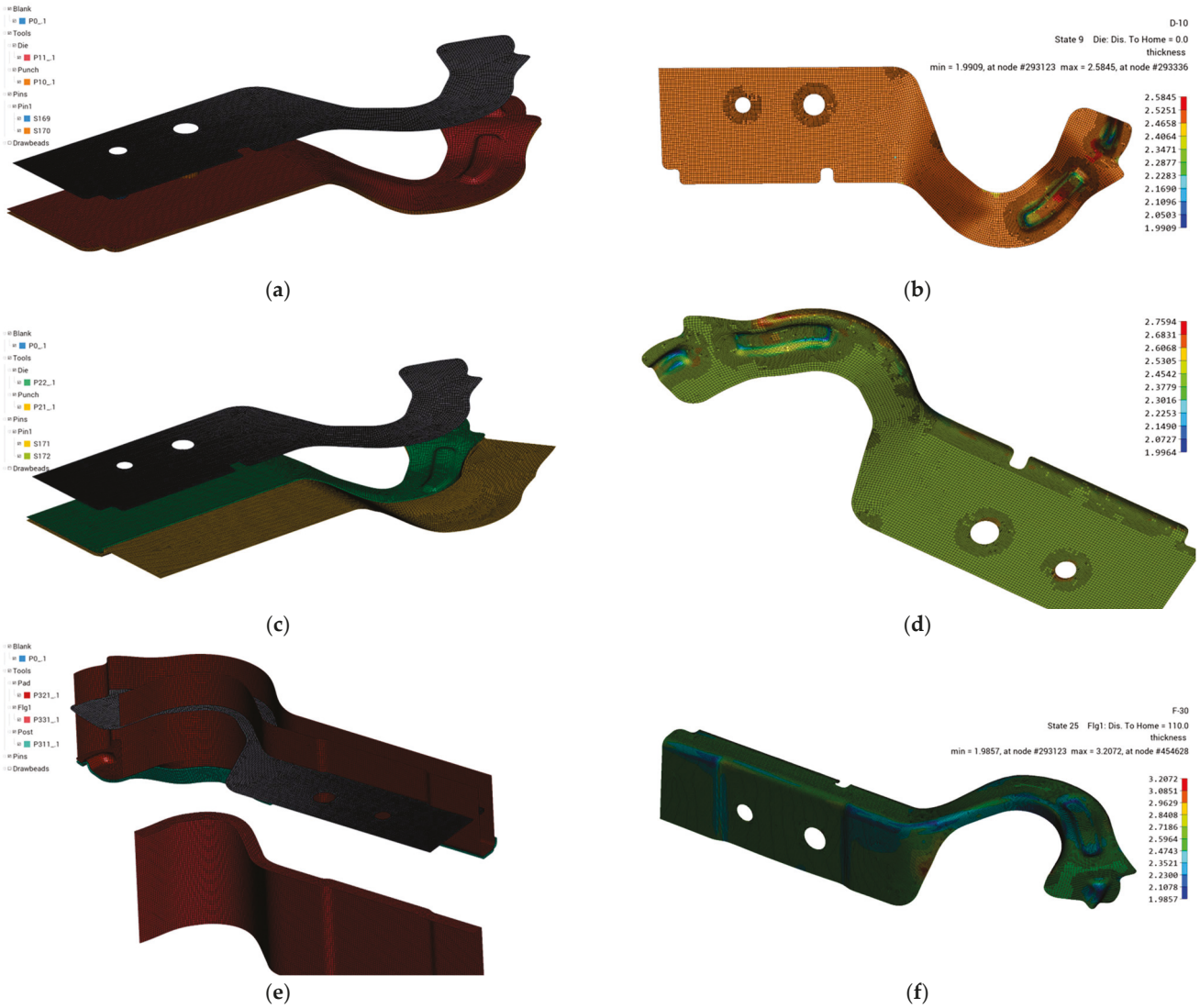

Figure 10. Forming set-ups for numerical simulation: (**a**) stage I tooling; (**b**) stage I—thickness distribution; (**c**) stage II tooling; (**d**) stage II—thickness distribution; (**e**) stage III tooling; (**f**) stage III—thickness distribution.

3.3. Scan from the Manufactured Part

Dimensional control is performed only on the finished part; thus, during manufacturing, there are no intermediate steps to verify the part's dimensional accuracy. Non–contact scanning methods are versatile tools for dimensional analysis and surface reconstruction. The physical shape obtained from stage III of the manufacturing process was scanned using a laser device. The geometrical model [40] was cleaned and checked for errors. To facilitate further manipulation, the STL (Stereolithography) geometry was saved in.ply (Polygon File Format) format.

Figure 11 presents the geometrical model of the scanned shape.

The scanning process was performed in a floating reference system. Therefore, a method is necessary to align the scanned model with the nominal geometry. A MATLAB application was developed to manipulate geometrical data. The first step was to evaluate the surface normals. Equation set (2) provides the data required to determine the components of the normal vector starting from the cross product of two vectors defined by two edges of a triangle.

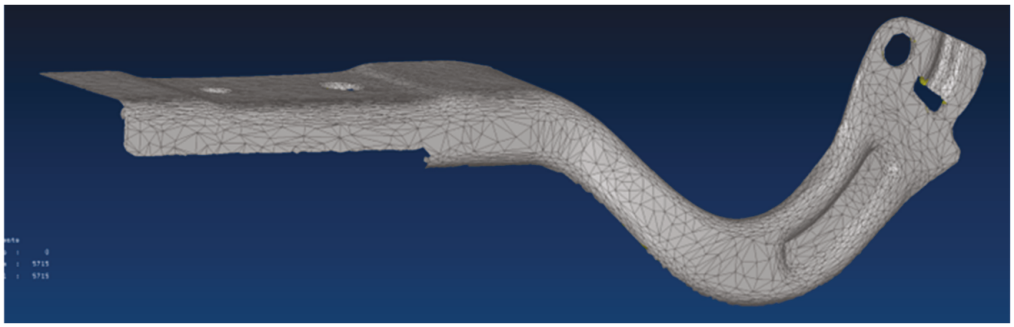

Figure 11. Scan of the manufactured part after stage III of the process.

$$\begin{gathered} \overline{n} = \begin{bmatrix} \overline{i} & \overline{j} & \overline{k} \\ u_{12} & v_{12} & w_{12} \\ u_{13} & v_{13} & w_{13} \end{bmatrix} \\ u_{ij} = \frac{x_i - x_j}{d_{ij}} \\ v_{ij} = \frac{y_i - y_j}{d_{ij}} \\ w_{ij} = \frac{z_i - z_j}{d_{ij}} \\ d_{ij} = \sqrt{(x_i - x_j)^2 + (y_i - y_j)^2 + (z_i - z_j)^2} \end{gathered} \tag{2}$$

Figure 12a presents the scanned part and the normal of the triangular entities. The algorithm operates with directional vectors computed for a specific element. Subsequently, all triangular elements were interrogated to create sets of elements with common normals (Figure 12b). The user can select a set to serve as the reference for the geometrical operations (Figure 12c).

From the selected set, the element with the largest area is chosen to display the local and global coordinate frames (Figure 12d). The geometrical operations follow the pattern $RZ - RY - RX$ to align the geometrical data to the reference system (Figure 12e). Figure 13a displays the scanned model and the nominal CAD model. The MATLAB application includes a tool for the definition of a sectioning place (Figure 13b) to allow a comparison of the scanned model to the nominal model (Figure 13c) [41].

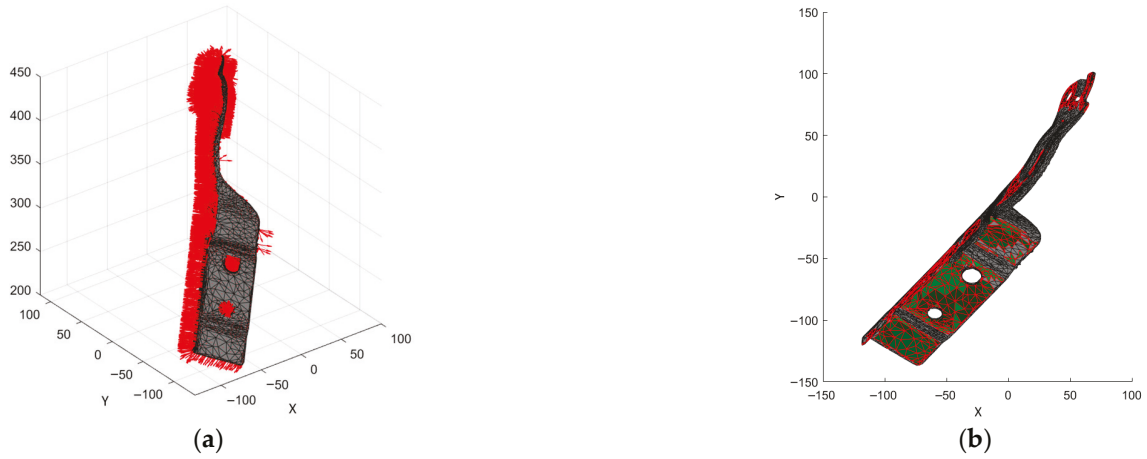

(**a**) (**b**)

Figure 12. *Cont.*

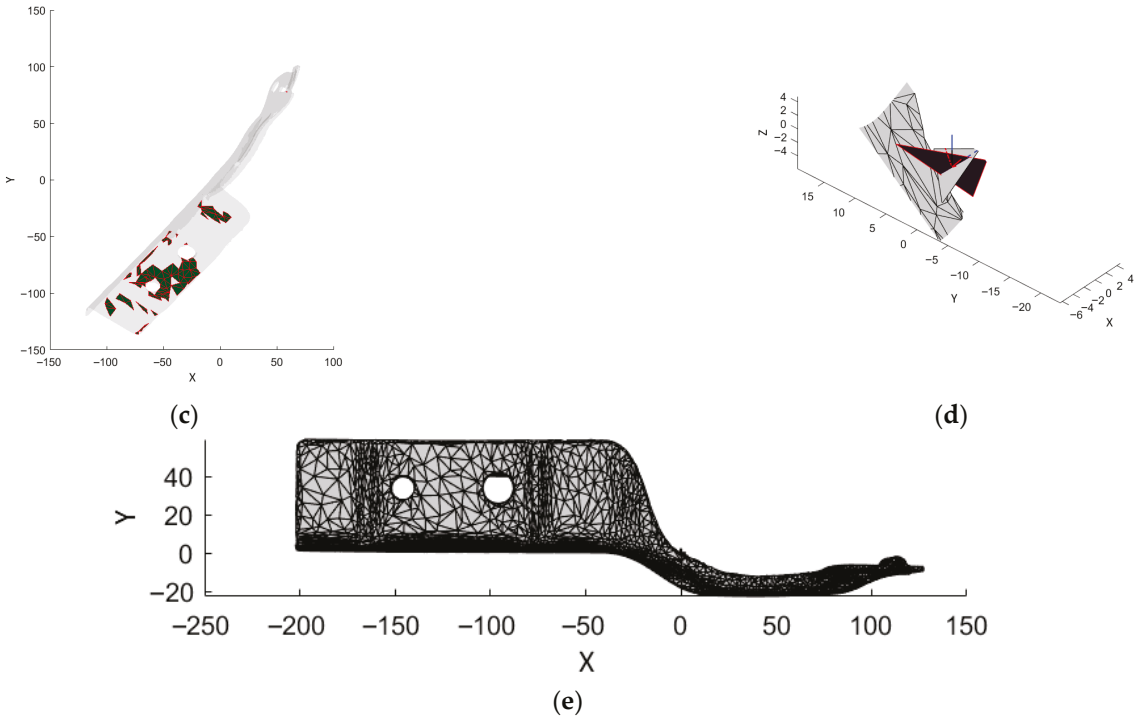

Figure 12. Geometrical operations (dimensions are represented in mm): (**a**) normals; (**b**) definition of triangles' sets; (**c**) reference set for alignment; (**d**) local vs. global coordinate systems; (**e**) aligned model.

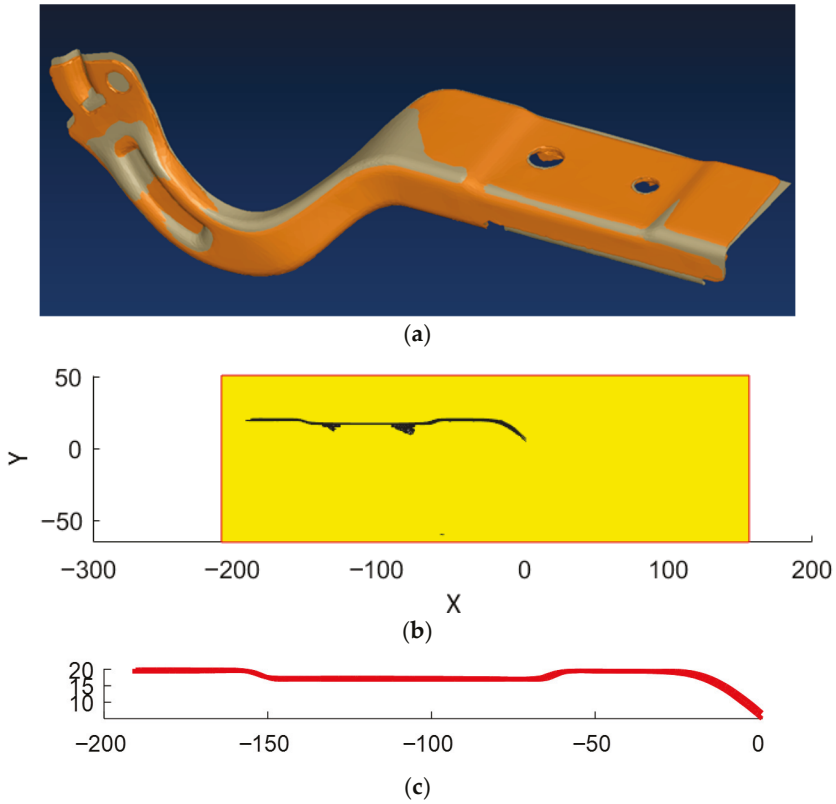

Figure 13. Comparison of the geometrical models (dimensions are represented in mm): (**a**) nominal vs. scanned model; (**b**) definition of the sectioning plane; (**c**) evaluation of the shapes of the nominal and scanned model.

3.4. Mapping Method of the Forming Simulation

Results from the simulation forming are available as a direct output. The file is structured, so the data is easily accessible for reading and analysis. Because adaptive meshing was enabled during the forming simulation, the number of elements increased significantly. Further simulation using the current numerical definition is difficult to implement and requires increased computational resources.

To overcome this issue, a user-defined MATLAB application was developed to map the results for different mesh sizes.

Figure 14a presents two sample meshes. On top, the current mesh used for simulation (receiving model) is shown. Behind is the mesh of the structure after the forming simulation (donor model). Figure 14b presents the thickness distribution after the forming simulation.

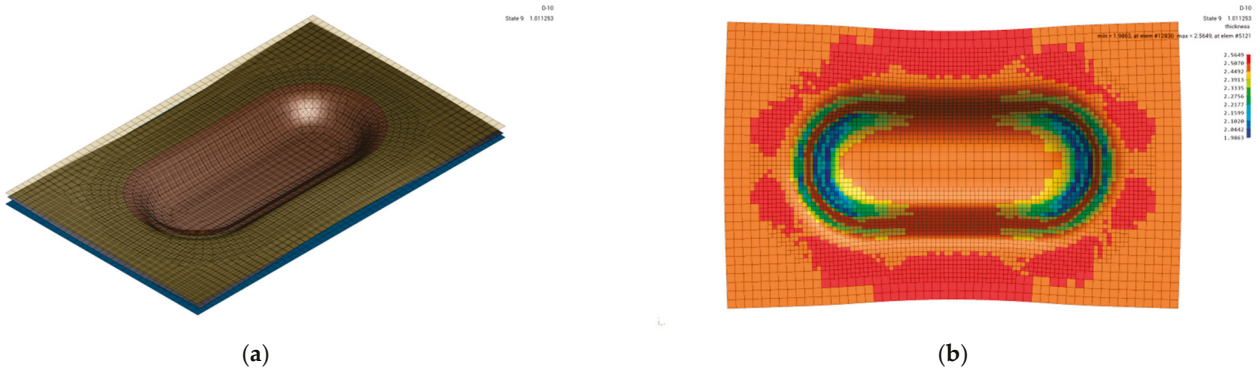

(**a**) (**b**)

Figure 14. Mapping simulation results: (**a**) reference and forming meshes; (**b**) map of the thicknesses.

As a first step of the mapping process, the mesh definitions of the models are interpreted by the MATLAB application. For each finite element in the donor mesh, the coordinates of the centroid are determined as presented in equation set (3).

$$\begin{aligned} x_{c,e} &= \tfrac{1}{4}\textstyle\sum n_{i,x} \\ y_{c,e} &= \tfrac{1}{4}\textstyle\sum n_{i,y} \\ z_{c,e} &= \tfrac{1}{4}\textstyle\sum n_{i,z} \end{aligned} \tag{3}$$

The algorithm uses a 3D search domain to collect and average the input data. The 3D domain is defined by a parameter—search distance s_d—defined by the user. This parameter (Equation (4)) defines a cuboid with its center at the center of the finite element on the donor mesh.

$$\begin{aligned} x &\in [x_{c,e} - s_d \ldots x_{c,e} + s_d] \\ y &\in [y_{c,e} - s_d \ldots y_{c,e} + s_d] \\ z &\in [z_{c,e} - s_d \ldots z_{c,e} + s_d] \end{aligned} \tag{4}$$

Based on this search zone, the elements from the donor model and the simulation results are collected. Results are averaged and associated with the current finite element of the receiving model (Equation (5)).

$$t_{e,ref} = \frac{1}{n_{e,s_d}} \sum t_{e,dynain} \tag{5}$$

Figure 15 presents the results of the mapping algorithm for different values of the search distance.

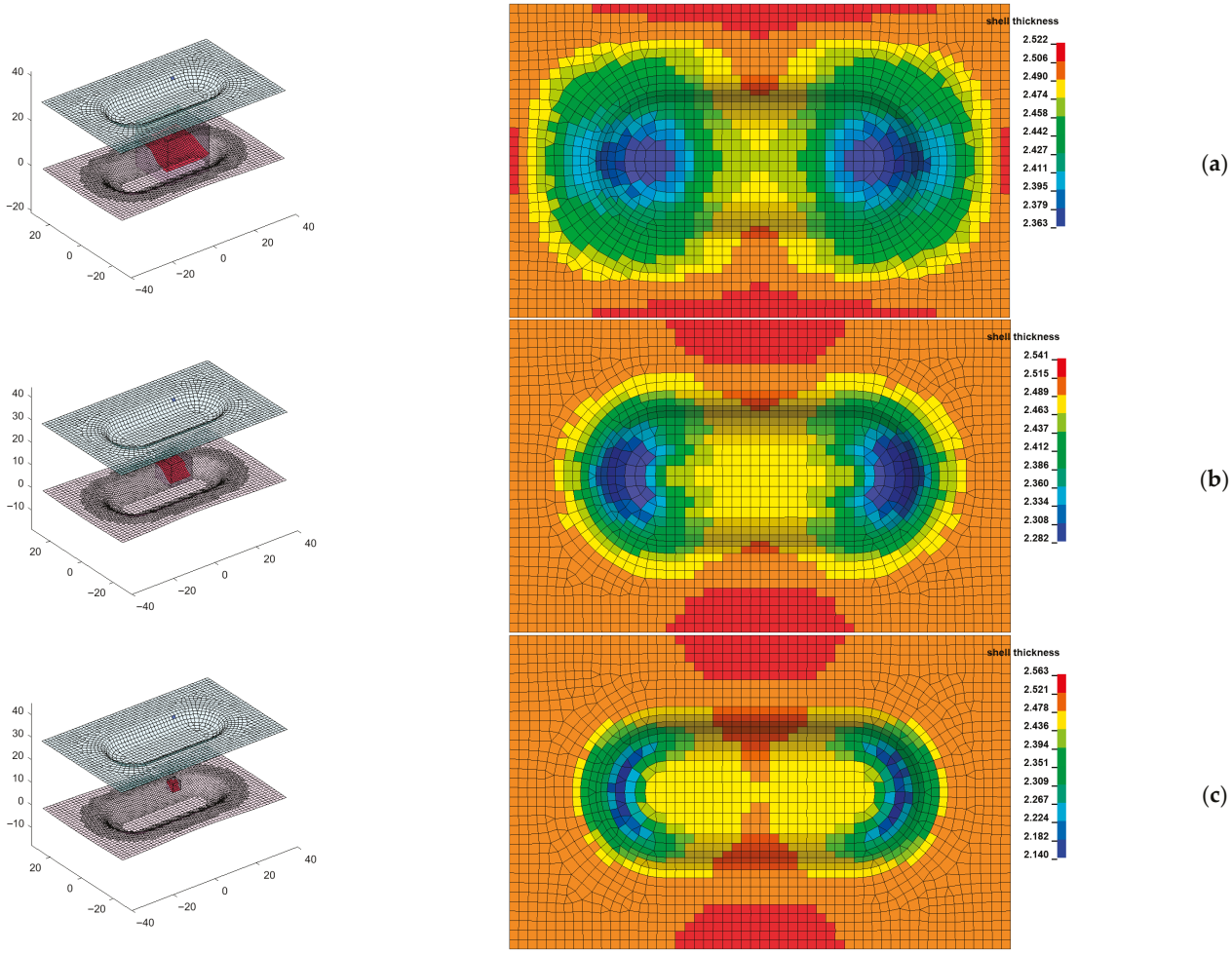

Figure 15. Results of the mapping method (dimensions are represented in mm): (**a**) $s_d = 10$ mm; (**b**) $s_d = 5$ mm; (**c**) $s_d = 2$ mm.

Results presented in Figure 15 reveal that increasing the value of s_d Parameter results are influenced by the average operator, as evidenced by the minimum thickness value. Therefore, the parameter s_d should be selected with care, as local effects on the donor model may not be correctly transferred to the receiving model.

Figure 16 presents the mapping algorithm used for the mobile part. Thanks to the centroid-matching method, the mapping algorithm is robust; thus, it is not necessary to have a one–to–one matching of elements. This is the actual reason the forming simulation was finished after stage III.

3.5. Results Mapping for 3D Elements

The structural analysis model is defined using 3D solid elements. Forming results are available for 2.5D shell elements. Therefore, the thickness associated with the shell elements must be converted to the dimensions of the 3D solid element. Figure 17a presents the definition of the finite elements for the middle surface [42].Two layers of solid elements are defined from the support surface as presented in Figure 17b. A layer is constructed in the positive direction of the normal, while the other is built in the negative direction. Figure 17c presents the 3D model with updated thickness.

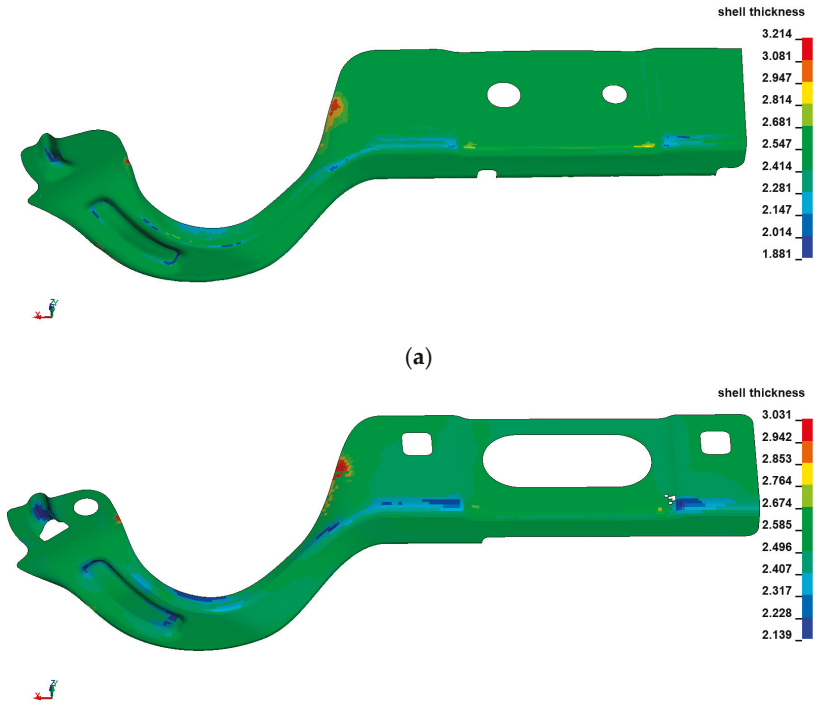

Figure 16. Results mapping for the mobile part: (**a**) forming analysis results; (**b**) model for structural analysis.

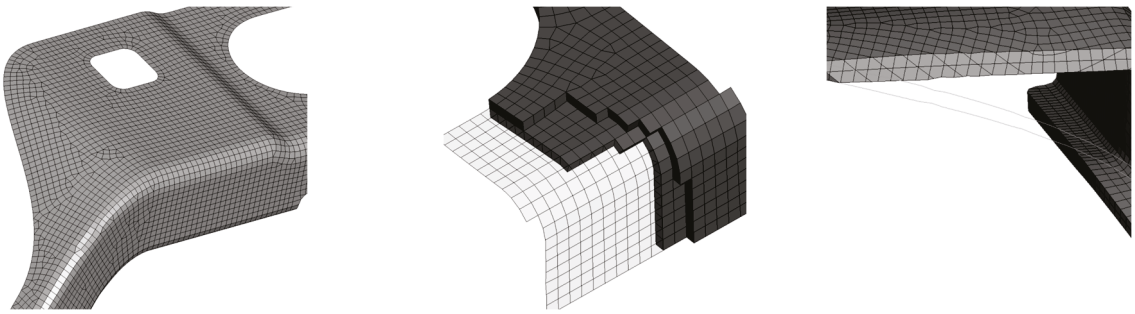

Figure 17. Numerical models: (**a**) mesh associated to the middle surface; (**b**) construction of the 3D solid elements; (**c**) updated 3D model.

To map the thickness determined from the forming analysis, it is necessary to update the dimensions of the 3D elements [43]. For each element, the edges that point toward the support surface are identified. The length of the edge is computed, and subsequently the components of the support vector of the edge (Equation (6)).

$$\begin{aligned} d_{ij} &= \sqrt{(x_i - x_j)^2 + (y_i - y_j)^2 + (z_i - z_j)^2} \\ \bar{i} &= \frac{x_j - x_i}{d_{ij}} \\ \bar{j} &= \frac{y_j - y_i}{d_{ij}} \\ \bar{k} &= \frac{z_j - z_i}{d_{ij}} \end{aligned} \tag{6}$$

The support vector is defined on the support surface. Using the thickness data stored by the shell element the length of the solid element is updated (Equation (7)).

$$\begin{aligned} x_j^* &= x_i + \bar{i} \cdot t \\ y_j^* &= y_i + \bar{i} \cdot t \\ z_j^* &= z_i + \bar{i} \cdot t \end{aligned} \tag{7}$$

The elements' residual stresses [44–46] determined after the forming simulation are exported via the ASCII file and associated with the 3D model. To simplify data processing, the results from the forming model, available for each through–thickness integration point, were averaged. The residual stresses are presented in Figure 18.

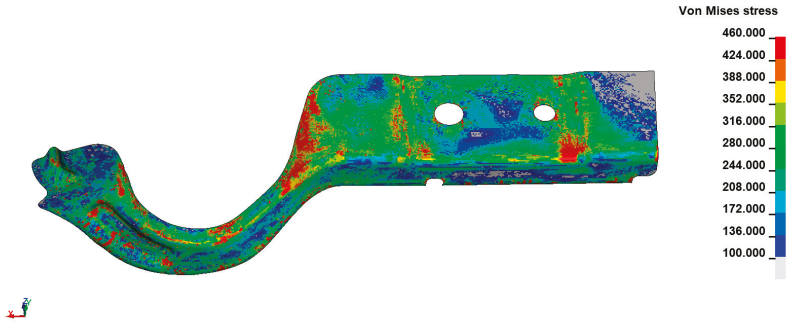

(**a**)

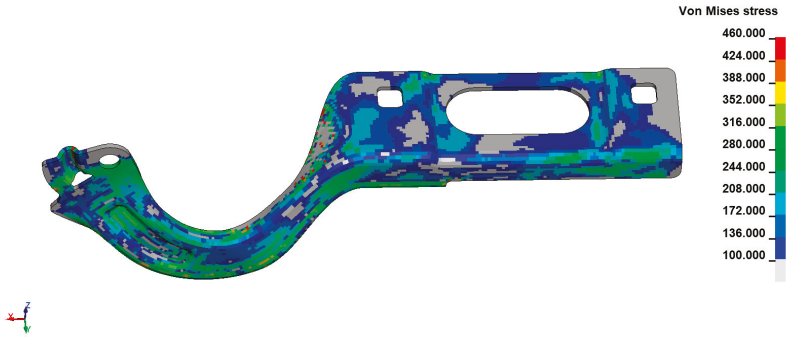

(**b**)

Figure 18. Residual stress: (**a**) results obtained from the forming simulation; (**b**) mapped data for the 3D model.

Mapping methods facilitate the use of various techniques and simulation results to develop detailed numerical models [47,48] capable of providing accurate results using reasonable resources.

4. Structural Performance Analysis

The numerical model developed to evaluate the structural performance of the assembly was created to mimic the fixtures used to support the actual parts during the experiments. Figure 19a shows the complete numerical model. The parts were clamped using a set of elements defined as rigids (*MAT_RIGID). The axes between the mobile and fixed parts were defined using joints (*CONSTRAINED_JOINT_REVOLUTE) as presented in Figure 19b. A very small amount of mobility is permitted at the bottom clamp of the testing machine. To account for the possibility of influencing the results, the clamp, modeled as a rigid body, was connected to the mobile part via a joint with a limited range of motion (*CONSTRAINED_JOINT_STIFFNESS_GENERALIZED). The load entry for the mobile part is located at the bolt holes.

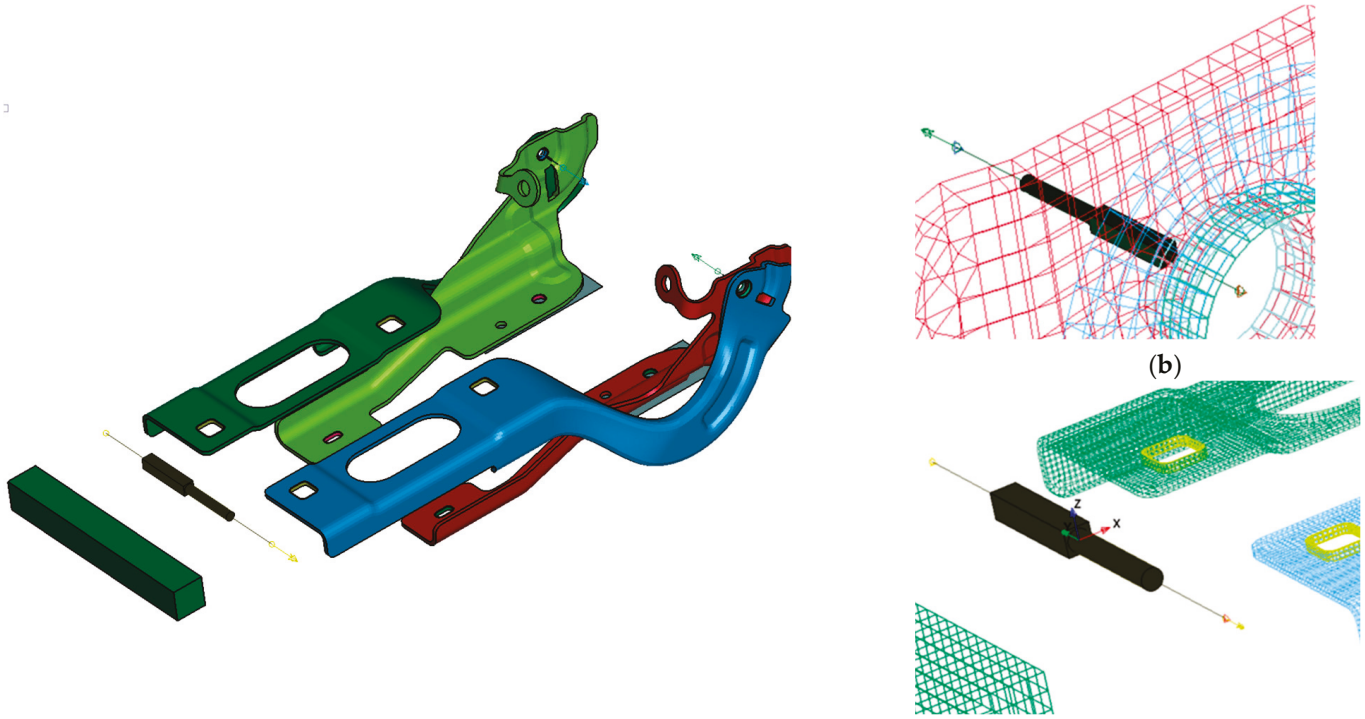

Figure 19. The numerical model: (**a**) global view; (**b**) definition of the axes; (**c**) loading components.

The advantage of using the implicit solver is that the simulation time can be adapted to match the computational resources, without affecting the results (inertia).

4.1. Convergene Analysis

Previously, it was discussed that the hinge numerical model was built using two layers of 3D elements. To justify this approach, a convergence analysis was conducted. In Figure 20a, the reference model (RM) is shown. A simplified model (RM) with a single solid element through the thickness is illustrated in Figure 20b. The model is detailed with four elements through the thickness, as shown in Figure 20c. The number of solid elements through the thickness determines the overall size, as efforts are made during meshing to maintain cuboid shapes.

Figure 20a presents the displacement history of the load entry sections. The load path is determined by the load factor parameter defined over the simulation time. The load factor determines multiple stages:

− initialization with a value of zero;
− loading when ramping from zero to one;
− load keeping with a value of 0.

Initialization is required to apply gravity. During load ramping, the force is increased to the nominal value. The load-keeping stage is required to verify that no plastic hinges were formed. A constant value obtained during this stage indicated that the assembly can sustain the prescribed loads.

The displacement history shows that, in all cases, the solution converged. The maximum displacement recorded for the reference model is of 11.1 mm. The coarse model displays a value of 13.2 mm (+19%), while for the fine model, the results are identical to the reference model (11.1 mm).

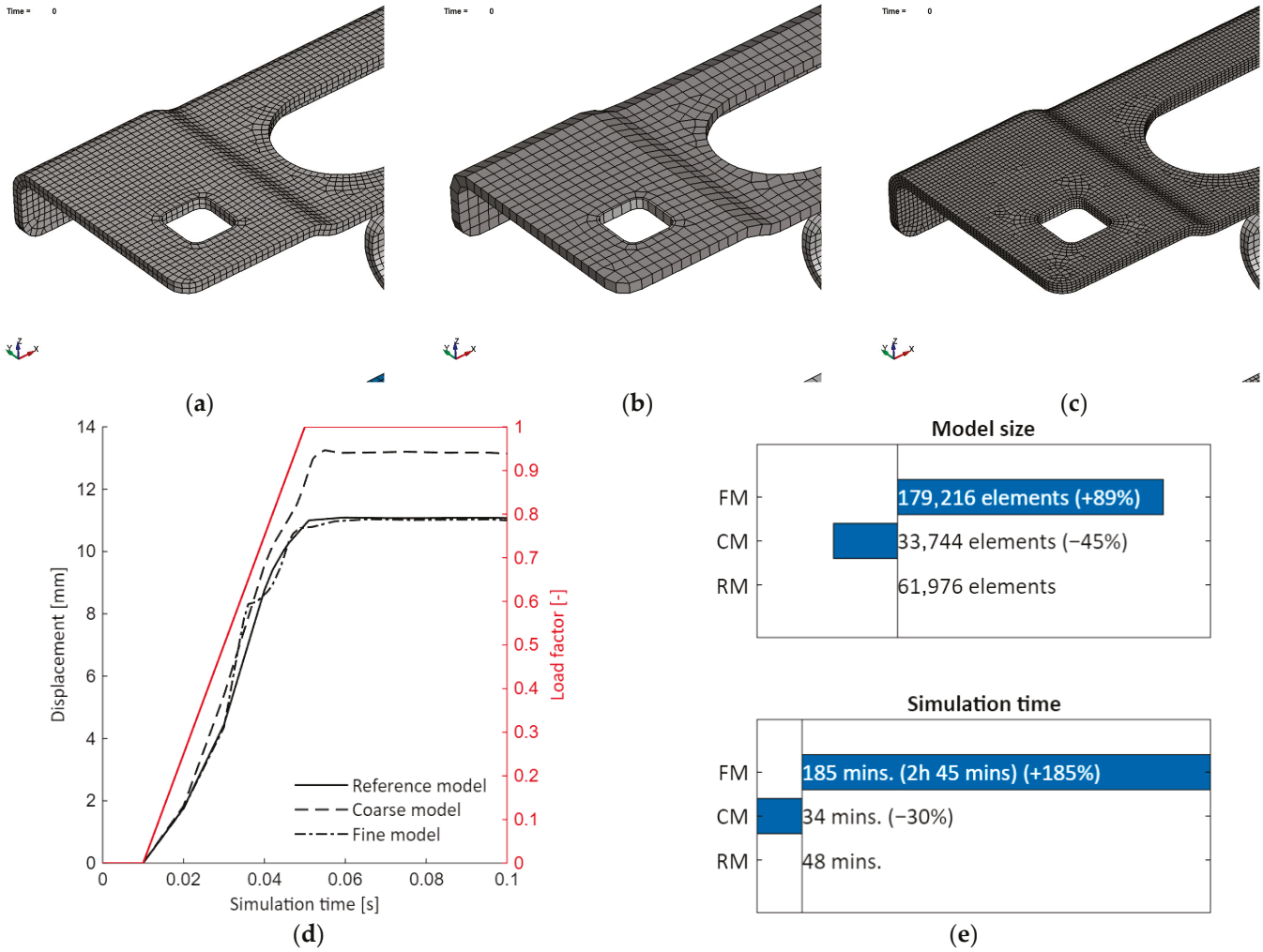

Figure 20. Convergence analysis: (**a**) Reference model—RM (two elements through thickness); (**b**) Coarse model—CM (one element through thickness); (**c**) Fine model—FM (four elements through thickness); (**d**) displacement plot; (**e**) performance plot.

The performance analysis reveals that, for the model using two elements through thickness, a total of 61,976 elements is obtained. The number decreases for the coarse model to 33,744 (−45%). The fine model requires an increased number of elements: 179,216 (+89%). The number of elements in a numerical model determines the time required to obtain a solution. To solve the numerical model, an Intel i7-8086 (4 GHz) machine with 32 GB of RAM was used. The solver was set to implicit in the SMP (Shared Memory Parallel) model, and it was using 4 CPUs.

For the reference model, a runtime of 48 min was obtained, which decreased to 34 min (−30%) for the coarse model. The fine model required a runtime of 2 h and 45 min (+185%). The runtime is not directly proportional to the number of elements, as it also accounts for nonlinear behavior (interfaces and materials).

These results reveal that the solution of two elements through thickness is a reliable and efficient method for developing the numerical model.

4.2. Experimental vs. Numerical Analysis

A specialized fixture was constructed for the assembly to evaluate the performance under an axial force of 12 kN corresponding to the load case **High speed frontal crash** (Figure 21).

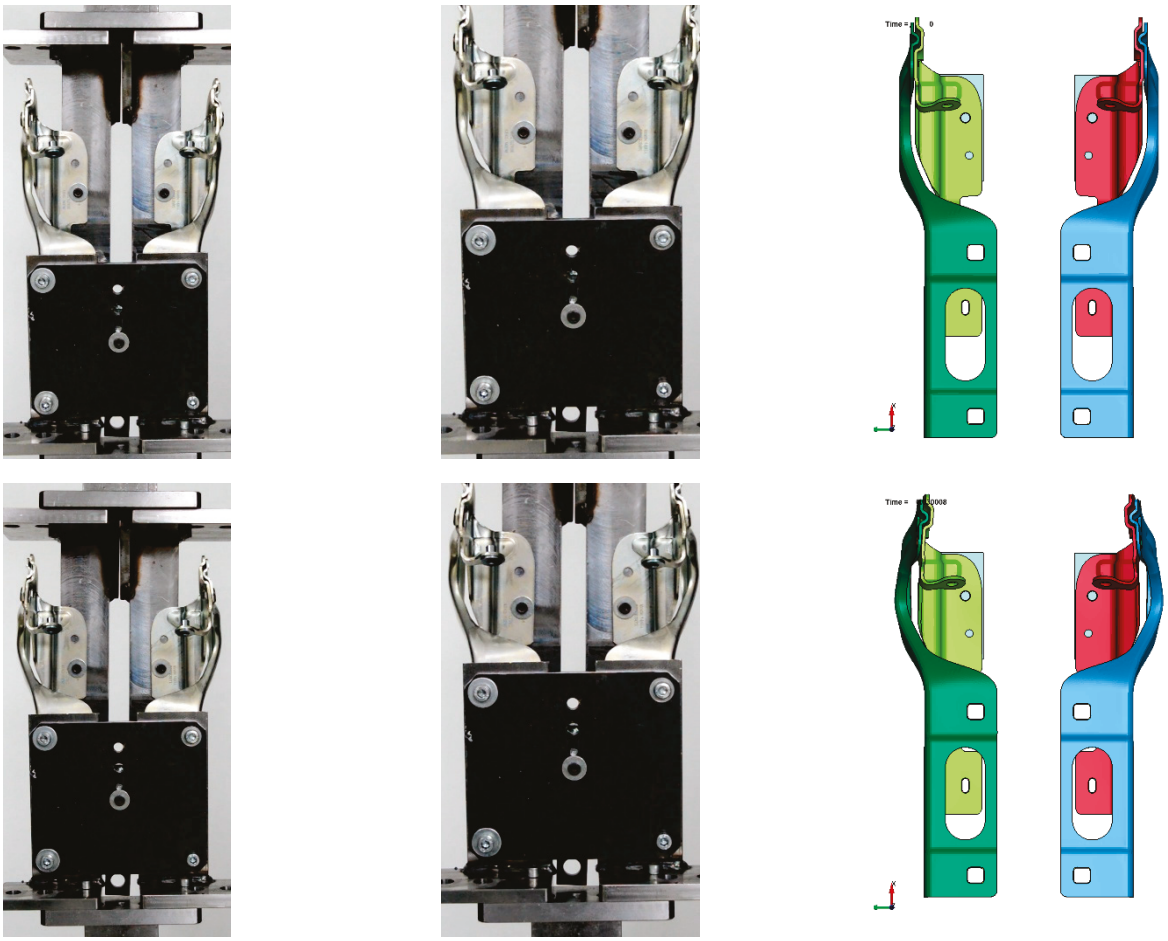

Figure 21. Experimental vs. simulation data (**top**—initial stage; **bottom**—final stage).

The experimental process was recorded using a digital camera [49]. The frames captured were processed to extract information related to the deformation of the structure [50–52]. Figure 22 illustrates the steps involved in processing the digital images.

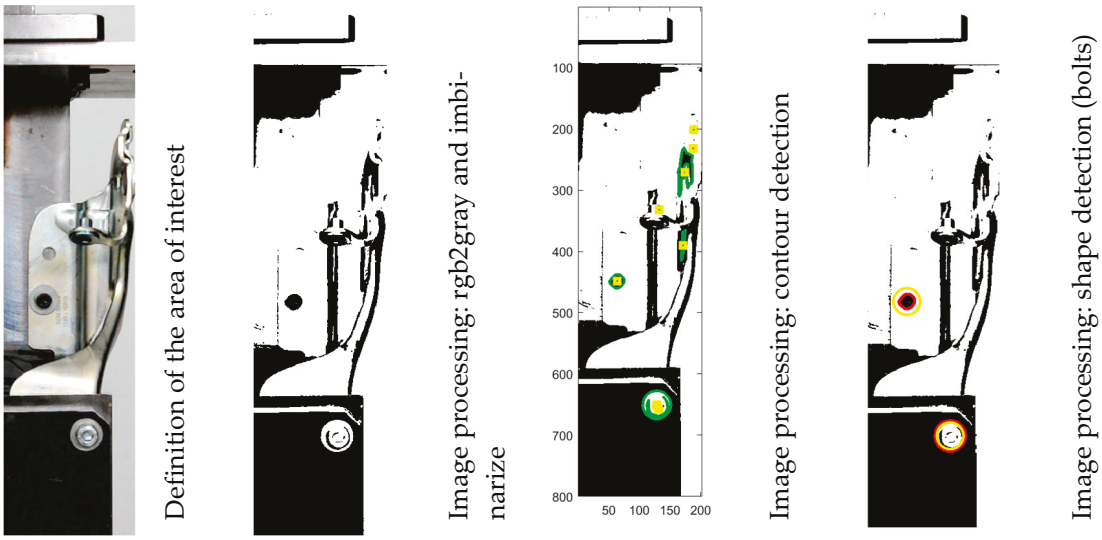

Figure 22. Digital image processing procedure: identification of the area of interest—conversion from RGB to grayscale and subsequently to black and white (binarize)—detection of contours (definition of a collection of edges)—detection of circular shapes (processing of edge information).

The algorithm used to detect the circular shapes from the collection of edges is defined by the equation set (8). The user corrects the selection of the shapes using the parameters R_{min} and R_{max}.

$$\begin{gathered} x_c = \frac{1}{n_p}\sum x_i \\ y_c = \frac{1}{n_p}\sum y_i \\ d_{i,c} = \sqrt{(x_i - x_c)^2 + (y_i - y_c)^2} \\ R_{min} \leq d_{i,c} \leq R_{max} \end{gathered} \tag{8}$$

For each frame, the location of the bolts was detected. Figure 23a presents the coordinates of the circles with reference to the image definition (pixels), while Figure 23b presents the deformation of the structure during the loading process.

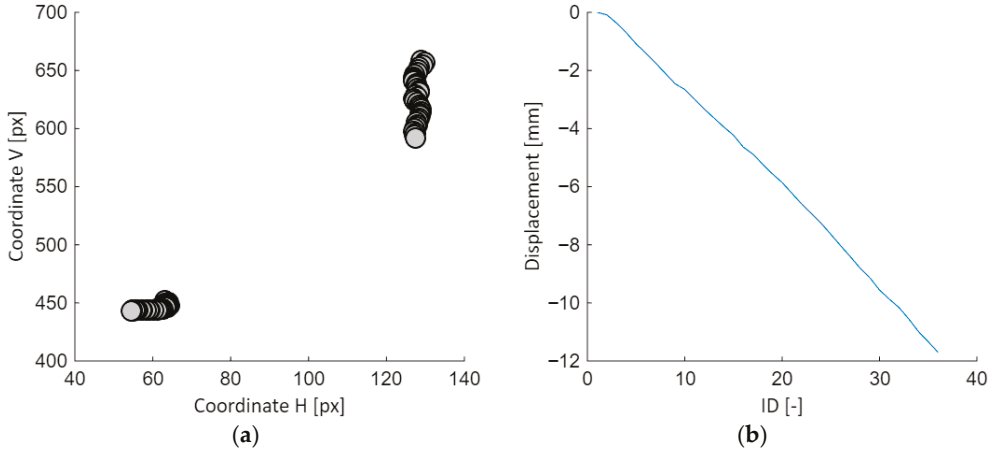

Figure 23. Digital image analysis: (**a**) image coordinates of the bolts; (**b**) deformation of the structure measured at the load entry.

5. Discussion

Three numerical models for the assembly were constructed. The first model–reference model–uses the nominal dimensions from the CAD file. For the second model, the finite elements were updated to capture the thickness changes resulting from the forming process. For the third model, both thickness changes and residual stress were included.

The loading history was extended with two additional stages: unloading, during which the load decreases to zero, and relaxation, to evaluate the residuals.

Figure 24a displays the displacement of the structure for each analysis case. As expected, the stiffest response is obtained for the model developed from the nominal model, with a maximum displacement of 11.1 mm. The thickness change has a minor influence on the results, with a maximum displacement of 11.4 mm (+2.7%). The full data mapping [53] shows an increase in the deformation of the structure [54] to 12.2 mm (+10%). This should be considered, as there is a load limit beyond which plastic hinges are developed, leading to the collapse of the structure.

Figure 24b shows displacement vs. force (the primary parameter for this load case is the applied force). The plot provides an alternate view showing the displacement at peak load and residual deformation.

The simulation results are compared with the experimental data shown in Figure 25. During initial loading, the simulation model is stiffer than the experimental model. As the peak load is reached, the curves converge. The displacement recorded during the experiment is of 12.4 mm, while for the numerical model, a value of 12.2 mm (−1.6%) was obtained.

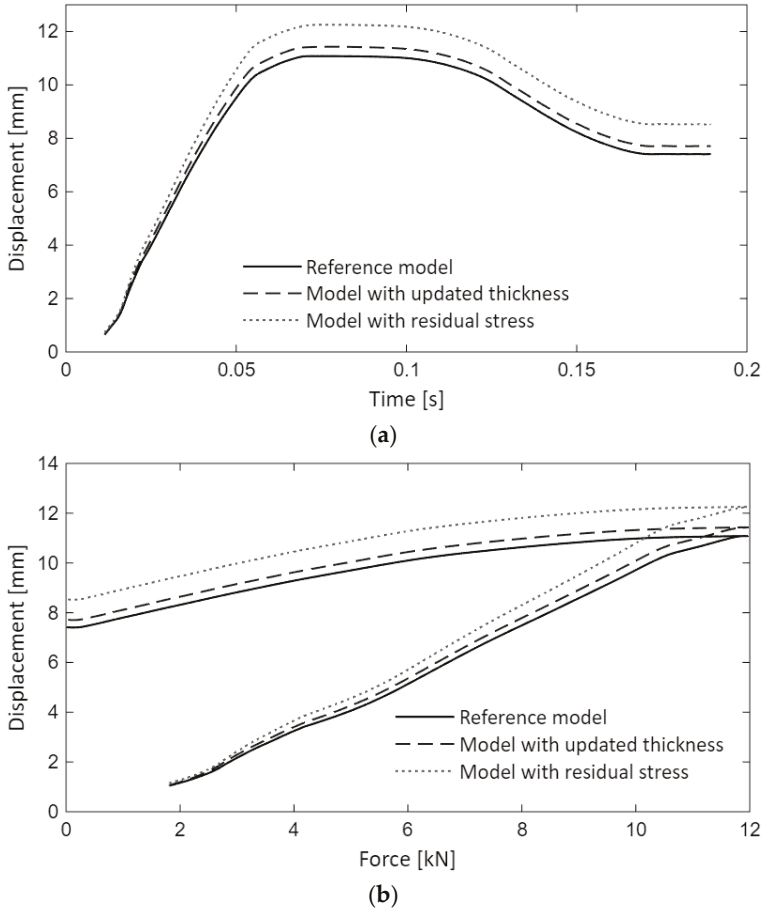

Figure 24. Results of the numerical simulation (history of the load entry): (**a**) displacement vs. simulation time; (**b**) displacement vs. load.

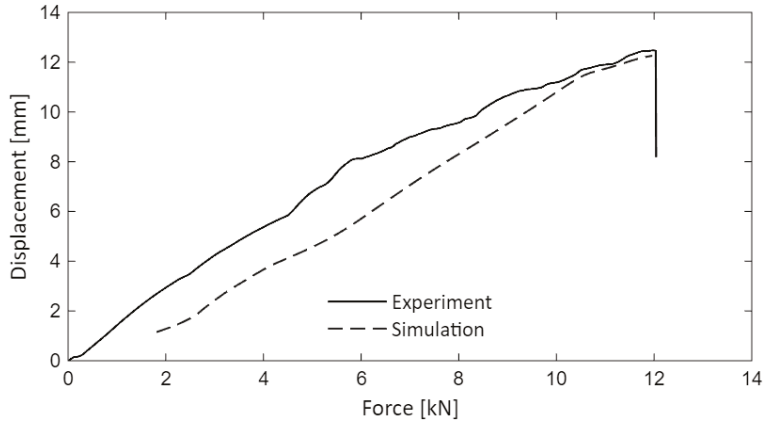

Figure 25. Experimental vs. numerical model–displacement at the load entry.

The stiffness of the testing machine and the fixture influences the behavior of experimental models during the initial loading stages.

A simple solution to improve the numerical model's reliability while reducing computational effort is to define scale factors for different structural families, which are applied to the numerical model derived from the nominal definition.

$$s_{f,i} = \frac{d_{max}}{d_{max,ref}} \tag{9}$$

The values of the scale factor as extracted from the results presented in Figure 24b are

$$\begin{aligned} s_{f,1-2} &= \frac{11.4}{11.1} = 1.03 \\ s_{f,1-3} &= \frac{12.2}{11.1} = 1.10 \end{aligned} \tag{10}$$

1—Reference model; 2—Model with updated thickness; 3—Model with residual stresses

The applied force was scaled for the nominal model with a factor of 1.10. The resulting displacement obtained from the simulation models is presented in Figure 26.

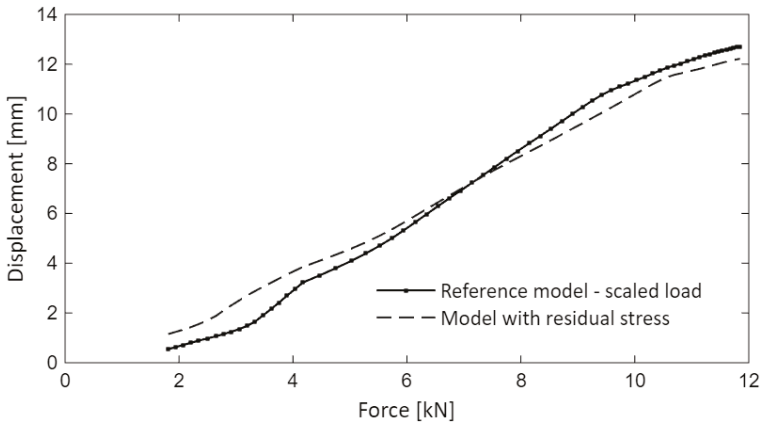

Figure 26. Simulation results (displacement at the load entry). Model with residual stresses vs. scaled model.

The maximum displacement for the model with scaled load (13.2 kN) is of 12.7 mm, showing a slight increase of 4% compared to the model with forming data, and a difference of +2.4% compared to the experiment.

The results from the scaled model agree with those from the model that includes residual stress.

6. Conclusions

In this work, a comprehensive analysis of a hood joint assembly was conducted. In this regard, the following stages were completed:

- analysis of the assembly and identification of the constructive elements;
- study of the technical specifications;
- a synthesis of the constructive and technical elements and identification of the correlation method for meeting the operating requirements;
- choice of material and mechanical characterization of the material;
- the technological process of manufacturing the moving part component was researched, and semi-finished parts were taken after each stage;
- the semi-finished parts corresponding to the stages of the technological process were investigated:
    - CAD models were created by 3D optical scanning;
    - a MATLAB application was developed that allows the geometric model to be aligned with the global reference;
    - CAD models of the scanned parts were compared with those obtained by numerical simulation of the manufacturing process.
- a numerical model of the manufacturing process of the moving part was developed using the ANSYS Forming program:
    - the CAD model of the finished product was analyzed;

- the stages of the numerical simulation process were developed in accordance with the stages of the technological process;
- for each stage, significant results that influence the structural performance of the product were presented.

- a numerical model of the product was developed to evaluate the structural performance:
  - the methods developed for processing the geometric model are presented;
  - the methods developed for creating the numerical model are presented;
- through numerical simulation of the manufacturing process, information is obtained regarding the change in thickness of the part as well as the residual stress state resulting from the technological process:
  - a method was developed for transposing (mapping) the results obtained from the simulation of the technological process for the structural model;
  - a method was developed for creating the 3D finite element model for structural analysis that includes specific results of the technological process;
- specific scenarios for numerical simulation were defined:
  - conventional model (reference);
  - variable thickness model (mapping);
  - residual stress model.
- the physical assembly was experimentally investigated, and the results were processed using digital tools.

The experimental results were compared with simulation data, and a good correlation was identified, showing, for the numerical model with complete history (thickness and stress), a difference of 1.6%. However, this method requires multiple numerical models and an algorithm for results mapping, making this solution less feasible during the design stages.

To further simplify the numerical simulation process, a parameter is defined to scale the reference quantity, enabling the use of a conventional simulation model.

The determined scale factor can be applied to similar products, provided the manufacturing process follows a similar set of forming stages.

The work can serve as a benchmark for future complex simulations that integrate results from manufacturing processes. Moreover, it presents solutions for developing in-house data-exchange code.

Author Contributions: Conceptualization, M.S. and S.T.; methodology, M.S.; software, S.T.; validation, M.S., S.T. and G.C.; formal analysis, S.T.; investigation, M.S., S.T. and G.C.; resources, M.S.; data curation, S.T.; writing—original draft preparation, M.S. and S.T.; writing—review and editing, M.S. and S.T.; visualization, S.T. and G.C.; supervision, M.S.; project administration, M.S. and S.T. All authors have read and agreed to the published version of the manuscript.

Funding: This research received no external funding.

Data Availability Statement: The numerical models presented in the paper are available on request.

Conflicts of Interest: Author Gabriel Cimpeanu was employed by AKA Automotiv SRL. The remaining authors declare that the research was conducted in the absence of any commercial or financial relationships that could be construed as a potential conflict of interest.

References

1. Giampieri, A.; Ling-Chin, J.; Ma, Z.; Smallbone, A.; Roskilly, A.P. A review of the current automotive manufacturing practice from an energy perspective. *Appl. Energy* **2020**, *261*, 114074. [CrossRef]

2. Dalzochio, J.; Kunst, R.; Pignaton, E.; Binotto, A.; Sanyal, S.; Favilla, J.; Barbosa, J. Machine learning and reasoning for predictive maintenance in Industry 4.0: Current status and challenges. *Comput. Ind.* **2020**, *123*, 103298. [CrossRef]
3. Bongomin, O.; Mwape, M.C.; Mpofu, N.S.; Bahunde, B.K.; Kidega, R.; Mpungu, I.L.; Tumusiime, G.; Owino, C.A.; Goussongtogue, Y.M.; Yemane, A.; et al. Digital twin technology advancing industry 4.0 and industry 5.0 across sectors. *Results Eng.* **2025**, *26*, 105583. [CrossRef]
4. D'Avella, S.; Avizzano, C.A.; Tripicchio, P. ROS-Industrial based robotic cell for Industry 4.0: Eye-in-hand stereo camera and visual servoing for flexible, fast, and accurate picking and hooking in the production line. *Robot. Comput.-Integr. Manuf.* **2023**, *80*, 102453. [CrossRef]
5. Al-Turjman, F.; Hussain, A.A.; Alturjman, S.; Altrjman, C. Vehicle Price Classification and Prediction Using Machine Learning in the IoT Smart Manufacturing Era. *Sustainability* **2022**, *14*, 9147. [CrossRef]
6. Zhao, N.; Parthasarathy, M.; Patil, S.; Coates, D.; Myers, K.; Zhu, H.; Li, W. Direct additive manufacturing of metal parts for automotive applications. *J. Manuf. Syst.* **2023**, *68*, 368–375. [CrossRef]
7. Hartley, W.D.; Garcia, D.; Yoder, J.K.; Poczatek, E.; Forsmark, J.H.; Luckey, S.G.; Dillard, D.A.; Yu, H.Z. Solid-state cladding on thin automotive sheet metals enabled by additive friction stir deposition. *J. Mater. Process Technol.* **2021**, *291*, 117045. [CrossRef]
8. Douimia, S.; Bekrar, A.; Cadi, A.A.E.; Hillali, Y.E.; Fillon, D. Machine learning and deep learning applications in the automotive manufacturing industry: A systematic literature review and industry insights. *Robot. Comput.-Integr. Manuf.* **2025**, *96*, 103034. [CrossRef]
9. Adnan Yusuf, S.; Khan, A.; Souissi, R. Vehicle-to-everything (V2X) in the autonomous vehicles domain–A technical review of communication, sensor, and AI technologies for road user safety. *Transp. Res. Interdiscip. Perspect.* **2024**, *23*, 100980. [CrossRef]
10. Tihanyi, V.; Rövid, A.; Remeli, V.; Vincze, Z.; Csonthó, M.; Pethő, Z.; Szalai, M.; Varga, B.; Khalil, A.; Szalay, Z. Towards Cooperative Perception Services for ITS: Digital Twin in the Automotive Edge Cloud. *Energies* **2021**, *14*, 5930. [CrossRef]
11. Fernandez De Arroyabe, I.; Watson, T.; Phillips, I. Cybersecurity Maintenance in the Automotive Industry Challenges and Solutions: A Technology Adoption Approach. *Future Internet* **2024**, *16*, 395. [CrossRef]
12. Özmerdivanlı, A.; Sönmez, Y. The Relationship Between Financial Development, Energy Consumption, Economic Growth, and Environmental Degradation: A Comparison of G7 and E7 Countries. *Economies* **2025**, *13*, 278. [CrossRef]
13. Palea, V.; Santhià, C. The financial impact of carbon risk and mitigation strategies: Insights from the automotive industry. *J. Clean. Prod.* **2022**, *344*, 131001. [CrossRef]
14. Li, X.; Niu, W.; Tian, H. Application of Digital Twin in Electric Vehicle Powertrain: A Review. *World Electr. Veh. J.* **2024**, *15*, 208. [CrossRef]
15. Ereiz, S.; Duvnjak, I.; Jiménez-Alonso, J.F. Review of finite element model updating methods for structural applications. *Structures* **2022**, *41*, 684–723. [CrossRef]
16. Thacker, J.G.; Reagan, S.W.; Pellettiere, J.A.; Pilkey, W.D.; Crandall, J.R.; Sieveka, E.M. Experiences during development of a dynamic crash response automobile model. *Finite Elem. Anal. Des.* **1998**, *30*, 279–295. [CrossRef]
17. Jayasinghe, S.C.; Mahmoodian, M.; Alavi, A.; Sidiq, A.; Shahrivar, F.; Sun, Z.; Thangarajah, J.; Setunge, S. A review on the applications of artificial neural network techniques for accelerating finite element analysis in the civil engineering domain. *Comput. Struct.* **2025**, *310*, 107698. [CrossRef]
18. Yokoyama, Y.; Nagasaka, K.; Masuda, I.; Sugiyama, H.; Okazawa, S. Simulation of Automobile Structural Member Deformation and Crash via Isogeometric Analysis. *Vehicles* **2024**, *6*, 967–983. [CrossRef]
19. Choi, S.; Park, T.; Kim, H.; Nam, B.; Ye, B.; Kim, D. Ductile fracture prediction in thin-walled structures through a novel damage model. *Heliyon* **2024**, *10*, e40849. [CrossRef]
20. Abebe, M.; Koo, B. Fatigue Life Uncertainty Quantification of Front Suspension Lower Control Arm Design. *Vehicles* **2023**, *5*, 859–875. [CrossRef]
21. Li, D.; Tian, J.; Shi, S.; Wang, S.; Deng, J.; He, S. Lightweight Design of Commercial Vehicle Cab Based on Fatigue Durability. *CMES-Comput. Model. Eng. Sci.* **2023**, *136*, 421–445. [CrossRef]
22. Chen, S.; Bekar, E.T.; Bokrantz, J.; Skoogh, A. AI-enhanced digital twins in maintenance: Systematic review, industrial challenges, and bridging research–practice gaps. *J. Manuf. Syst.* **2025**, *82*, 678–699. [CrossRef]
23. Suo, H.; Zhou, H.; Wei, Z.; Li, R.; Zhang, Y.; Guan, W.; Cheng, H.; Luo, B.; Zhang, K. Degradation mechanisms and mechanical behavior of composite-metal bolted/riveted joints in complex service conditions: A comprehensive review. *Eng. Fail. Anal.* **2025**, *182*, 110037. [CrossRef]
24. Lv, X.; Xiao, Z.; Fang, J.; Li, Q.; Lei, F.; Sun, G. On safety design of vehicle for protection of vulnerable road users: A review. *Thin-Walled Struct.* **2023**, *182*, 109990. [CrossRef]
25. Radu, A.-I.; Tolea, B.-A.; Trusca, D.-D. Validation of a virtual model for the kinematic and dynamic analysis of the impact of a pedestrian's head with a bonnet using experimental tests. *Ing. Automob.* **2025**. Available online: https://siar.ro/wp-content/uploads/2025/08/rIA_76.pdf (accessed on 2 October 2025).

26. Abbasi, M.; Reddy, S.; Ghafari-Nazari, A.; Fard, M. Multiobjective crashworthiness optimization of multi-cornered thin-walled sheet metal members. *Thin-Walled Struct.* **2015**, *89*, 31–41. [CrossRef]
27. Baroutaji, A.; Sajjia, M.; Olabi, A.G. On the crashworthiness performance of thin-walled energy absorbers: Recent advances and future developments. *Thin-Walled Struct.* **2017**, *118*, 137–163. [CrossRef]
28. Isaac, C.W.; Duddeck, F. Current trends in additively manufactured (3D printed) energy absorbing structures for crashworthiness application–a review. *Virtual Phys. Prototyp.* **2022**, *17*, 1058–1101. [CrossRef]
29. Jones, N. *Structural Impact*, 1st ed.; Cambridge University Press: Cambridge, UK, 1990; ISBN 978-0-521-30180-0.
30. Stirosu, M.; Tabacu, S. Experimental and numerical analysis and validation of S460 steel. *Univ. Pitesti Sci. Bull.-Automot. Ser.* **2024**, *34*, 1–9. [CrossRef]
31. Vormwald, M. Fatigue of Constructional Steel S460 under Complex Cyclic Stress and Strain Sequences. *Procedia Eng.* **2011**, *10*, 270–275. [CrossRef]
32. Xu, T.H.; Zhang, L.M. Numerical implementation of a bounding surface plasticity model for sand under high strain-rate loadings in LS-DYNA. *Comput. Geotech.* **2015**, *66*, 203–218. [CrossRef]
33. Woelke, P.B.; Londono, J.G.; Erhart, T.; Haufe, A.; Jurendic, S.; Anderson, D. Extension of the GISSMO fracture model for thin-walled structures under combined tensile and bending loads. *Eng. Fract. Mech.* **2024**, *311*, 110574. [CrossRef]
34. Hallquist, J.O. LS-DYNA ® THEORY MANUAL. Available online: https://ftp.lstc.com/anonymous/outgoing/jday/manuals/ls-dyna_theory_manual_2006.pdf (accessed on 1 July 2025).
35. Rust, W.; Schweizerhof, K. Finite element limit load analysis of thin-walled structures by ANSYS (implicit), LS-DYNA (explicit) and in combination. *Thin-Walled Struct.* **2003**, *41*, 227–244. [CrossRef]
36. Arriaga, A.; Pagaldai, R.; Zaldua, A.M.; Chrysostomou, A.; O'Brien, M. Impact testing and simulation of a polypropylene component. Correlation with strain rate sensitive constitutive models in ANSYS and LS-DYNA. *Polym. Test.* **2010**, *29*, 170–180. [CrossRef]
37. Narasimhan, N.; Lovell, M. Predicting springback in sheet metal forming: An explicit to implicit sequential solution procedure. *Finite Elem. Anal. Des.* **1999**, *33*, 29–42. [CrossRef]
38. Kim, H.-K.; Kim, W.-J. A Springback Prediction Model for Warm Forming of Aluminum Alloy Sheets Using Tangential Stresses on a Cross-Section of Sheet. *Metals* **2018**, *8*, 257. [CrossRef]
39. Ahmed, G.M.S.; Ahmed, H.; Mohiuddin, M.V.; Sajid, S.M.S. Experimental Evaluation of Springback in Mild Steel and its Validation Using LS-DYNA. *Procedia Mater. Sci.* **2014**, *6*, 1376–1385. [CrossRef]
40. Bénière, R.; Subsol, G.; Gesquière, G.; Breton, F.L.; Puech, W. A comprehensive process of reverse engineering from 3D meshes to CAD models. *CAD Comput. Aided Des.* **2013**, *45*, 1382–1393. [CrossRef]
41. Amaral, R.L.; Neto, D.M.; Wagre, D.; Santos, A.D.; Oliveira, M.C. Issues on the Correlation between Experimental and Numerical Results in Sheet Metal Forming Benchmarks. *Metals* **2020**, *10*, 1595. [CrossRef]
42. Gavalas, E.; Pressas, I.; Papaefthymiou, S. Mesh sensitivity analysis on implicit and explicit method for rolling simulation. *Int. J. Struct. Integr.* **2018**, *9*, 465–474. [CrossRef]
43. Tabacu, S.; Ducu, C. Numerical investigations of 3D printed structures under compressive loads using damage and fracture criterion: Experiments, parameter identification, and validation. *Extreme Mech. Lett.* **2020**, *39*, 100775. [CrossRef]
44. Acevedo, C.; Nussbaumer, A. Effect of tensile residual stresses on fatigue crack growth and S-N curves in tubular joints loaded in compression. *Int. J. Fatigue* **2012**, *36*, 171–180. [CrossRef]
45. Hassani-Gangaraj, S.M.; Carboni, M.; Guagliano, M. Finite element approach toward an advanced understanding of deep rolling induced residual stresses, and an application to railway axles. *Mater. Des.* **2015**, *83*, 689–703. [CrossRef]
46. Shang, D.; Liu, X.; Shan, Y.; Jiang, E. Research on the stamping residual stress of steel wheel disc and its effect on the fatigue life of wheel. *Int. J. Fatigue* **2016**, *93*, 173–183. [CrossRef]
47. Varedi, S.R.; Buffel, B.; Desplentere, F. Post-forming deformation and thermal residual stress prediction in vacuum thermoformed ABS sheets. *J. Manuf. Process* **2025**, *155*, 1162–1170. [CrossRef]
48. Sandin, O.; Larour, P.; Rodríguez, J.M.; Parareda, S.; Hammarberg, S.; Kajberg, J.; Casellas, D. Numerical modelling of shear cutting in complex phase high strength steel sheets: A comprehensive study using the Particle Finite Element Method. *Finite Elem. Anal. Des.* **2025**, *246*, 104331. [CrossRef]
49. Liu, T.; Zheng, P.; Bao, J. Deep learning-based welding image recognition: A comprehensive review. *J. Manuf. Syst.* **2023**, *68*, 601–625. [CrossRef]
50. Leonetti, D.; Baarssen, H.; Pucillo, G.P.; Snijder, B.H.H. Measurement of crack paths using digital image correlation. *Eng. Fract. Mech.* **2025**, *327*, 111391. [CrossRef]
51. Almazán-Lázaro, J.-A.; López-Alba, E.; Díaz-Garrido, F.-A. Indentation measurement of thin plates using 3D digital image correlation and experimental validation. *Results Eng.* **2025**, *25*, 104246. [CrossRef]
52. Li, D.; Cheng, B.; Shi, L.; Zhang, E.; Zhao, Q. Propagation measurement for visually thin fatigue crack using homography mapping error and digital image correlation. *Mech. Syst. Signal Process* **2024**, *220*, 111628. [CrossRef]

53. Wang, S.; Wu, Y.; Xu, Q.; Ma, Y.; Wang, T. Research on stamping formability and process simulation of AZ31 magnesium alloy based on deep learning. *Mater. Today Commun.* **2024**, *40*, 109807. [CrossRef]
54. Zeng, C.; Tian, W.; Liao, W.H. The effect of residual stress due to interference fit on the fatigue behavior of a fastener hole with edge cracks. *Eng. Fail. Anal.* **2016**, *66*, 72–87. [CrossRef]

Disclaimer/Publisher's Note: The statements, opinions and data contained in all publications are solely those of the individual author(s) and contributor(s) and not of MDPI and/or the editor(s). MDPI and/or the editor(s) disclaim responsibility for any injury to people or property resulting from any ideas, methods, instructions or products referred to in the content.

vehicles

MDPI

Article

Dynamic Finite Element and Experimental Strain Analysis of a Passenger-Car Rear Axle for Durable and Sustainable Suspension Design

Ionut Daniel Geonea [1,*], Ilie Dumitru [2], Laurentiu Racila [2] and Cristian Copilusi [1]

[1] Department of Applied Mechanics and Civil Engineering, Faculty of Mechanics, University of Craiova, 200478 Craiova, Romania; cristian.copilusi@edu.ucv.ro
[2] Department of Automotive, Transportation and Industrial Engineering, Faculty of Mechanics, University of Craiova, 200478 Craiova, Romania; ilie.dumitru@edu.ucv.ro (I.D.); laurentiu.racila@edu.ucv.ro (L.R.)
* Correspondence: ionut.geonea@edu.ucv.ro; Tel.: +40-727779866

Abstract

This paper proposes an integrated numerical–experimental methodology for the durability assessment and optimisation of a passenger-car rear axle. A dedicated rear-suspension durability test bench was designed to impose a controlled cyclic vertical excitation on a dependent axle, reproducing service-like translational and rotational amplitudes of the beam and stabiliser bar. A detailed flexible multibody model of the bench–axle system was developed in MSC ADAMS 2023 and used to tune the kinematic excitation and determine an equivalent design load at the wheel spindles, consistent with the stiffness of the suspension assembly. Experimental strain measurements at nine locations on the axle, acquired with strain-gauge instrumentation on the bench, were converted into stresses and used to validate an explicit dynamic finite element model in ANSYS. The FE predictions agree with the experiments within about 10% at the beam mid-span and correctly identify a critical region at the junction between the side plate and the arm, where peak von Mises stresses of about 104 MPa occur. The validated model then supports a response-surface-based optimisation of the safety-critical wheel spindle, yielding an optimised geometry in which spindle-fillet stresses remain around 180–185 MPa under a severe loading case corresponding to the maximum admissible wheel load at the bearings, while the associated increase in mass is modest and compatible with practical design constraints.

Keywords: rear axle; durability test bench; flexible multibody dynamics; explicit dynamic finite element analysis; strain-gauge measurements; response-surface optimisation; wheel spindle design

1. Introduction

The current state of research on the design, optimisation and testing of suspension components and rear axle assemblies in road vehicles shows a clear trend towards combining advanced numerical modelling with dedicated test rigs, as well as towards the use of modern multi-objective optimisation methods. A critical synthesis of optimisation methods used in road vehicle design—including deterministic algorithms, metaheuristics, response-surface-based techniques and multicriteria formulations—is provided by Gobbi et al. [1], who emphasise the need to couple vehicle dynamic models with structural, comfort and safety criteria. In the same direction, Yıldız et al. propose a metaheuristic equilibrium optimisation algorithm coupled with a response-surface-based metamodel for the structural

optimisation of vehicle components [2], demonstrating the potential of such approaches to reduce mass and computational cost while still satisfying strength constraints.

1.1. Structural and Fatigue Optimisation of Chassis and Axle Components

A significant part of the literature focuses on geometric and structural optimisation of components in the rear axle and chassis area, closely linked to fatigue phenomena and failures observed during development testing. Kumar and Kumaraswamidhas analyse the causes of failures occurring during developmental testing of a fabricated rear axle housing, and propose a geometry optimisation procedure aimed at eliminating stress concentrations identified by finite element analysis and increasing the durability of the assembly [3]. For heavy-duty vehicles, Zheng et al. apply both topology optimisation and multi-objective optimisation to a drive axle housing, seeking to reduce mass, increase stiffness and improve fatigue performance, based on advanced FEM models and iterative–evolutionary procedures [4].

At the level of connection subassemblies, Topaç et al. demonstrate, on a rear axle connection bracket for heavy commercial vehicles, that topology optimisation can lead to significant mass reduction without penalising stress levels and overall stiffness [5]. Park et al. use a Design of Experiments (DoE) approach to optimise several rear chassis components, combining FEM analysis with experimental design techniques to identify lightweight design variants that satisfy strength and natural frequency constraints [6].

Failure mode analysis and design improvement of severely loaded subassemblies is also addressed in the work of Topaç et al. on an eccentrically loaded connecting rod in a double front axle steering linkage prototype [7]. The authors combine stress analysis with fatigue assessment for different design variants, identifying geometric modifications that yield a more favourable stress distribution and increased service life. Jeong et al. focus on the shape optimisation of a torsion beam axle, correlating its geometric parameters with the handling performance of the vehicle and using an optimisation procedure that improves directional response while satisfying structural constraints [8].

In the field of safety components and steering elements, Balta et al. apply Pareto optimisation to the design of a heavy truck rear underrun protection system, simultaneously considering regulatory load cases and the mass of the structure [9]. Senniappan et al. address the optimisation of a steering tie rod arm for a commercial vehicle based on a strain-life fatigue criterion, calibrated by experimental testing and FEM analysis, in order to obtain a configuration robust against cyclic loading [10].

Adopting a system-level perspective, Zhou et al. propose a cooperative multi-objective optimisation algorithm for the design of a vehicle axle system, where objectives such as mass, stiffness and reliability are considered simultaneously [11]. With regard to torsional vibration, Hao et al. develop a coupled driveline–rear axle model and perform uncertainty analysis and parameter optimisation in order to limit driveline torsional vibration amplitudes [12]. Taken together, these studies show that modern rear axle and associated component design increasingly relies on the combination of detailed FEM models, fatigue assessment and advanced multi-objective optimisation techniques, often supported by metamodeling and evolutionary algorithms [1–6,8–12].

1.2. Test Benches for Suspension, Axles and Elastic Components

Complementary to numerical optimisation, a major research direction is the development of test benches for experimental validation of suspensions, elastic elements and axle assemblies. Early contributions focus on dedicated rigs for leaf springs and suspensions of commercial vehicles. Soares et al. describe a test bench for static and dynamic tests of suspension leaf springs, capable of reproducing conditions close to real operation and

https://doi.org/10.3390/vehicles8010009

providing data for numerical model calibration [13]. A subsequent work by the same group presents a multiaxial bench for testing the suspension of commercial vehicles, which enables the simultaneous application of vertical, longitudinal and lateral loads and highlights the advantages of bench testing compared to full-vehicle tests [14].

For suspension parameter identification and testing, quarter-car rigs form a distinct category. Mitra et al. use a quarter-car test rig to apply DoE methods to suspension optimisation, analysing the influence of key parameters on the dynamic response [15]. In a related paper, the same authors propose a derivative-free, DoE-based optimisation method for automotive suspension systems, which makes it suitable for nonlinear problems or computationally expensive numerical models [16]. Salah proposes the design, implementation and integration of a laboratory-scale automotive suspension test rig, intended for both research and teaching activities, where different control strategies and design configurations can be evaluated [17]. Alzughaibi et al. address the modelling of a passive suspension test rig, highlighting the role of nonlinear friction forces in system dynamics and the need for more sophisticated models for parameter identification [18]. Recent developments target the full automation of quarter-car test benches, including actuator control, data acquisition and processing, which increases repeatability and efficiency in testing campaigns [19].

There are also test benches focused on specific operating regimes. Liao et al. propose the design, modelling and verification of a test bench for braking simulation of a quarter vehicle, combining dynamic modelling with experimental tests for calibration [20]. From the standpoint of vibration isolation and the interaction between the bench and its foundation, Croce et al. analyse design criteria for automotive test benches and propose isolation solutions that reduce the transmission of vibrations to surrounding structures and improve measurement quality [21].

Beyond suspension and spring benches, Favilli et al. propose an innovative tyre–road test bench capable of using real asphalt surfaces and reproducing modern operating conditions (high speeds, varying contact conditions), which allows integrated assessment of tyre performance and, indirectly, of associated chassis elements [22]. These developments illustrate a trend from mono-axial or simplified test benches towards multiaxial rigs with advanced control and instrumentation capabilities, intended to reproduce real driving conditions as closely as possible [13–20].

1.3. Test Benches and Virtual Concepts for Powertrain and Steering–Suspension Systems

In parallel with suspension and axle testing, the literature also addresses test benches for powertrains and integrated vehicle systems. Mántaras and Luque introduce the concept of a "virtual test rig" for steering and suspension systems, based on multibody modelling, which enables the evaluation and optimisation of geometric and elastokinematic parameters prior to physical prototyping, thus reducing development time and cost [23]. In the field of electric powertrains, El Hadraoui et al. propose a customizable test bench for an electric vehicle powertrain, developed using a Model-Based Systems Engineering (MBSE) methodology, with emphasis on flexibility, modularity and use for educational and research purposes [24].

Andert et al. present the "virtual shaft" concept, a synchronised motion control strategy for real-time testing of automotive powertrains, in which real and virtual components are coupled in a hardware-in-the-loop configuration, allowing faithful reproduction of operating conditions and dynamic interactions in the driveline [25]. These approaches show that the development of modern test benches tends to be integrated with real-time modelling and closed-loop coupling with numerical models, going beyond the paradigm of purely experimental rigs.

https://doi.org/10.3390/vehicles8010009

1.4. Integration of Optimisation Methods with Bench Testing and Current Trends—Implications for the Rear Axle

Overall, the reviewed literature indicates two major directions that are still insufficiently integrated: on the one hand, structural and fatigue optimisation of rear-axle-related components based on FEM, fatigue assessment and multi-objective optimisation [1–12], and, on the other hand, the development of test benches for suspensions, springs and chassis subassemblies, including automated quarter-car rigs and multiaxial benches for commercial vehicles [13–20]. Although some studies employ experimental methods for calibrating numerical models or for partial validation of optimised solutions, relatively few works propose a fully integrated methodology combining multibody modelling for load generation, detailed FEM analysis of a real rear axle, dedicated test benches for rear suspension testing and explicit durability assessment under representative operating conditions.

Building on the earlier literature, several recent contributions highlight current trends in the design and use of test benches for automotive components and subsystems. At component level, increasingly detailed finite element models are validated against dedicated rigs, as shown by Fathi et al., who developed and experimentally validated a passenger-car tyre model for combined stiffness and durability assessment [26], and by Patil et al., who combined strain measurements on a reinforced composite front drive axle with FE simulations to evaluate strength and stiffness improvements [27]. For wheels, Lockett et al. proposed a digital testing framework in which three-piece alloy wheels are iteratively redesigned using FE analysis before being verified on a cornering-fatigue test bench [28], while Poungkom and Pimsarn compared several FE formulations specifically for reproducing the dynamic cornering fatigue test of an automotive wheel [29]. Similar digital-twin concepts are applied to suspension members: Do et al. reported the development of a rear coupled torsion-beam axle where deformation compensation is achieved through FE-based refinement of the beam geometry [30], and Lozia reviewed the role of modelling and simulation in planning and interpreting durability tests for vehicles and their components, emphasising the tight coupling between road-load spectra, test rigs and virtual models [31]. At the same time, advanced dynamic FE techniques originally developed for safety applications—such as nonlinear analyses of vehicle impacts into road restraint systems [32] and combined experimental–numerical approaches for crashworthiness of automotive bodies [33] or rail-vehicle interiors with multibody dummies and FE seat models [34]—are increasingly being transferred to the durability domain, where they support the definition of multiaxial loading on test benches. System-level developments move toward vehicle-in-the-loop testing, in which hardware test rigs are integrated with real-time simulation environments for autonomous and connected vehicles, as surveyed by Cheng et al. [35]. Finally, several studies underline that suspension performance and vehicle stability [36], as well as the ongoing push toward lightweight materials and structures [37], make accurate durability assessment of chassis components even more critical, reinforcing the need for integrated experimental–numerical test-bench methodologies such as the one adopted in the present work.

In a recent contribution, Stirosu et al. [38] investigated the manufacturing, testing and simulation processes of a hood hinge assembly, combining detailed finite element analysis with experimental validation to support the structural assessment of a safety-relevant body component. This type of integrated workflow at component level is in line with the present study, where we extend a similar numerical–experimental philosophy to a welded torsion-beam rear axle, with a specific focus on fatigue-critical regions and the optimisation of the wheel spindle.

Furthermore, most of the analysed test benches are either oriented toward simplified suspension representations (quarter-car), elastic components (leaf springs), or powertrain

https://doi.org/10.3390/vehicles8010009

subsystems, without explicitly targeting a passenger-car rear axle as the central object of evaluation. In the current context, characterised by stringent mass reduction requirements, increased durability demands and the need to adapt to electrified vehicles (with different masses and load distributions), there is a clear need for an integrated methodology and a dedicated test bench that enable rear axle durability testing directly correlated with advanced numerical modelling and modern structural optimisation procedures. This intersection between test bench development, multibody modelling, FEM analysis and multi-objective optimisation defines the gap that the proposed work aims to address.

In this context, the present work contributes an integrated methodology in which: (i) a dedicated rear-suspension durability test bench is used to impose a controlled cyclic excitation on a passenger-car rear axle; (ii) a flexible multibody model of the complete bench–axle system in MSC ADAMS is employed to tune the kinematic excitation and to define an equivalent design load at the wheel spindles that is consistent with the stiffness of the suspension assembly; (iii) an explicit dynamic FE model of the real rear axle in ANSYS is validated against strain-gauge measurements on the test bench; and (iv) the validated model is finally used as the basis for a response-surface-based optimisation of the safety-critical wheel spindle. This combination of test bench development, flexible multibody analysis, explicit FE simulation and spindle optimisation distinguishes the present study from previous approaches, which typically address only part of this chain, by linking bench testing, dynamic modelling and component optimisation into a single workflow for rear axle durability. The proposed workflow can be directly implemented in industrial rear-axle development to identify fatigue-critical regions, virtually assess design changes and reduce the number of physical prototypes and test iterations needed to achieve a durable and lightweight suspension design.

2. Experimental Test Bench for Rear Suspension Durability Testing

This section presents the dedicated test bench developed for the durability assessment of a passenger-car rear suspension. The rig has been conceived to reproduce, in a controlled and repeatable manner, the cyclic loading acting on a dependent rear axle and its associated elastic elements, while allowing direct comparison between numerical predictions and experimental measurements of stresses and strains.

2.1. Concept and Kinematic Layout

The test bench is designed to excite the rear suspension through a crank–rocker mechanism that converts the rotary motion of an electric drive into a nearly harmonic vertical motion at the wheel spindle. The kinematic chain consists of a crank mounted on the motor shaft, an adjustable-length connecting rod and a rocker arm pivoted to the bench frame. The distal end of the rocker is connected to the rear axle assembly through a bushing, so that the imposed motion generates a cyclic vertical force on one wheel side of the axle.

The rear axle, complete with helical coil springs and stabiliser bar, is installed on the rig using mounting conditions that reproduce as closely as possible the actual interfaces on the vehicle body. The bench frame provides rigid supports for the axle trailing arms and spring seats, while the crank–rod–rocker mechanism excites the right wheel side. This arrangement enables the investigation of both global bending of the axle beam and local stress concentrations in critical regions, under a loading pattern representative of service conditions.

The stroke of the rocker and the amplitude of the imposed load can be adjusted by modifying the effective length of the connecting rod and the crank radius. In this way, the

https://doi.org/10.3390/vehicles8010009

same bench can be used to test different rear axle geometries and to reproduce various severity levels of service loading.

2.2. CAD Model and Virtual Prototyping

A detailed three-dimensional model of the test bench and rear suspension has been created in SolidWorks 2024. The CAD assembly includes the bench frame, crank–rod–rocker drive mechanism, bushings, rear axle beam, helical coil springs, stabiliser bar and the auxiliary fixtures required for mounting the axle on the rig.

The CAD model serves a dual purpose. First, it provides the geometric basis for manufacturing the bench components and for verifying assembly clearances and ranges of motion. Second, it is used as input for the multibody dynamic model developed in MSC ADAMS, in which the crank–rod–rocker mechanism and the rear axle are represented as a system of rigid and flexible bodies connected by kinematic joints and compliant elements.

Within the ADAMS environment, the stabiliser bar and the rear axle beam are modelled as deformable solids, allowing the computation of displacements, deformations and internal forces in these components under cyclic excitation. The simulation results are subsequently used to define the load cases for the finite element analysis and to support the design of the experimental test programme.

The kinematic scheme of the test bench is shown in Figure 1a, while the corresponding 3D CAD model developed in SolidWorks is presented in Figure 1b. In the kinematic sketch, the rear axle assembly is represented in its test position between the vertical uprights of the bench. The lower oscillating beam (3) acts as a rocker that transforms the input motion into a vertical displacement of the right wheel side. The excitation is introduced with a prescribed eccentricity e indicated by item (1), so that the imposed rotation of the rocker generates an alternating vertical motion at its ends.

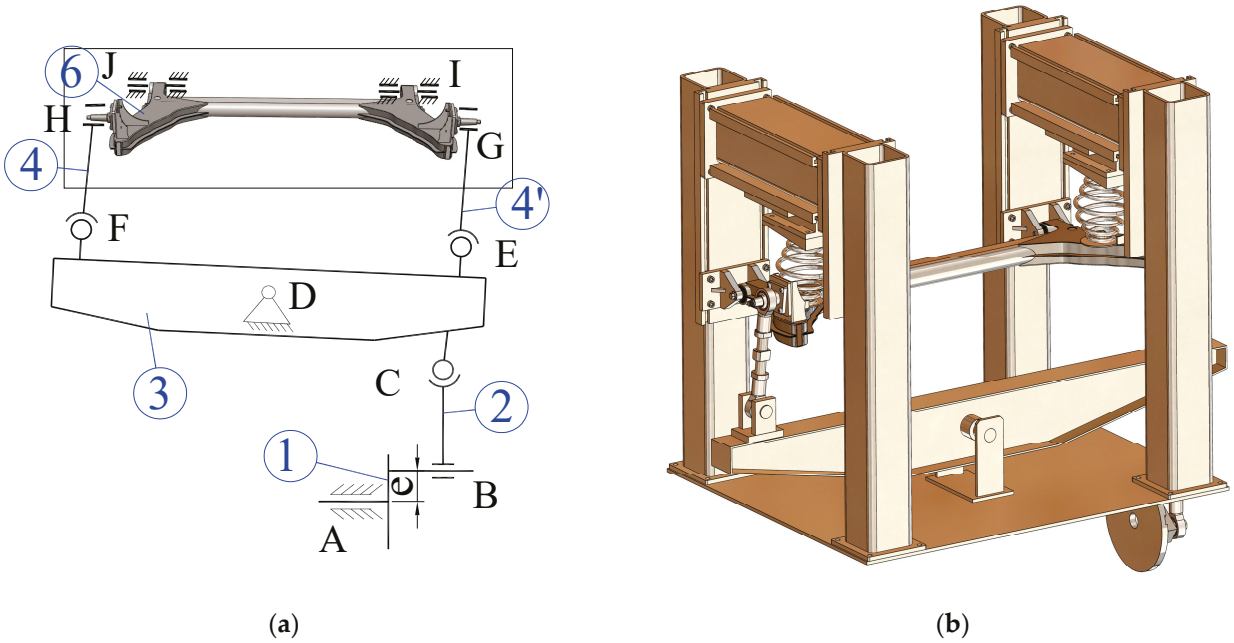

Figure 1. Kinematic scheme and CAD model of the rear suspension durability test bench: (**a**) kinematic scheme of the excitation mechanism and rear axle assembly (1—eccentricity e; 2—connecting link; 3—rocker beam; 4, 4′—vertical links; 6—rear axle with coil springs); (**b**) SolidWorks model of the test bench.

This motion is transmitted through link 2 (item 2) and the vertical links (4) and (4′) to the axle and to the coil springs (6), reproducing the relative vertical displacement between

https://doi.org/10.3390/vehicles8010009

the axle and the vehicle body. Link 4 provides the mechanical connection between the rocker beam (3) and the right side of the axle, and therefore concentrates the main load path from the drive mechanism to the axle assembly.

The SolidWorks model (Figure 1b) details the actual geometry of the test bench built according to this kinematic scheme. The structure consists of a base frame and two stiff vertical portals, assembled from rectangular profiles using threaded joints and bolted connections, rather than welded joints. The dependent rear axle is mounted between the portals, with its trailing arms clamped to brackets on the frame and the helical coil springs installed between the axle seats and the adjustable upper supports attached to the uprights. The lower rocker beam is pivoted to the base frame at its centre and connected to the axle on the right-hand side via link 2 and the vertical linkage, in accordance with the schematic in Figure 1a.

The 3D model includes all functional components of the bench—frame, rocker, links, spring seats, guides and fastening elements—and has been used both to check assembly clearances and to export geometry to the multibody and finite element models employed in the subsequent numerical analysis.

2.3. Mounting of the Rear Axle Assembly on the Bench

The dependent rear axle considered in this study consists of a central beam, two trailing arms made of bent sheet metal, end plates, spring seats and brackets for the stabiliser bar. In the vehicle, the axle is connected to the body through flexible bushings and supported by helical coil springs.

On the test bench, the axle is mounted in a configuration that reproduces the kinematic boundary conditions of the vehicle installation. The trailing arms are clamped to rigid supports that mimic the body brackets, and the coil springs are mounted between the axle seats and fixed upper seats attached to the frame. The stabiliser bar is installed in its operational position, with its ends connected to the axle through links and bushings.

The right wheel spindle location is connected to the rocker arm via a bushing and a short link. The excitation force is thus transmitted directly to the spindle region, generating bending of the axle beam and relative motion in the suspension joints similar to those encountered in service. By acting on both wheel sides, a symmetric loading condition is created, which is particularly demanding for the beam and the welded joints near the wheel spindles.

2.4. Loading System and Test Conditions

The stand is driven by an electric motor operating at a constant speed, which imposes a cyclic motion of the crank and, consequently, of the rocker arm. For the present study, the operating parameters of the rig have been selected such that the maximum dynamic force transmitted to the right wheel spindle is of the order of 1 kN, in line with the values obtained from the flexible multibody simulations for the chosen fatigue loading case.

The resulting operating cycle consists of repeated load reversals over a given number of cycles, corresponding to an accelerated durability test. After a short run-in period, the system reaches a steady-state regime in which the force in the connecting rod and the stresses in the axle structure exhibit nearly periodic behaviour. This regime is used for both numerical–experimental correlation and fatigue-related assessment.

The test bench is designed to allow variation in the excitation frequency, stroke and mean position of the rocker arm, so that different duty cycles can be imposed on the same axle configuration. This flexibility is essential for studying the influence of loading severity and spectrum on the stress distribution and on the anticipated fatigue life of the axle.

https://doi.org/10.3390/vehicles8010009

It should be noted that, in its current configuration, the test bench applies predominantly vertical cyclic loading; lateral and longitudinal load components associated with braking and cornering are not reproduced and are therefore outside the scope of the present experimental campaign.

The selected load amplitude corresponds to a severe vertical bending case representative of driving over rough, uneven surfaces (e.g., cobblestone or pothole-type irregularities), rather than to the absolute worst-case impact loads.

3. Dynamic Simulation of the Test Bench in ADAMS

The kinematic scheme and CAD model presented in Section 2 were used as a basis to build a detailed multibody model of the test bench in MSC ADAMS. The objective of this model is twofold: (i) to evaluate the kinematic amplitudes and dynamic loads transmitted to the rear axle and stabiliser bar during fatigue testing, and (ii) to provide design loads for the subsequent finite element analysis of the rear axle assembly.

3.1. Multibody Modelling Strategy

The CAD assembly created in SolidWorks was exported in Parasolid format and imported into ADAMS/View. The rigid parts of the stand (base frame and vertical uprights) were merged into a single body and fixed to ground. The driving mechanism is modelled as a planar four-bar linkage, consistent with the kinematic scheme in Figure 1a:

In the kinematic scheme of the test bench (Figure 1a), the kinematic pairs are labelled A–J and are defined as follows:

- Joint A—revolute joint between the fixed frame (ground) and the crank (link 1), corresponding to the motor shaft.
- Joint B—revolute joint between the crank (link 1) and the adjustable connecting link (link 2).
- Joint C—spherical joint between the connecting link (link 2) and the rocker beam (link 3), which accommodates the relative angular misalignment between the two members.
- Joint D—revolute joint between the rocker beam (link 3) and the fixed frame.
- Joints E and F—spherical joints between the rocker beam (link 3) and the vertical connecting links (links 4′ and 4, respectively), allowing the links to follow the motion of the axle without overconstraining the mechanism.
- Joints G and H—cylindrical (revolute) joints between the upper ends of the vertical connecting links (4′ and 4) and the wheel-spindle regions of the rear axle (link 6), transmitting the vertical load from the mechanism to the axle while allowing rotation about the spindle axis.
- Joints I and J—cylindrical (revolute) joints between the rear axle (link 6) and the test-bench frame. These joints represent the bushings through which the axle is guided relative to the uprights of the stand and ensure that the axle is constrained to move according to the bench kinematics. The helical coil springs are modelled separately as spring–damper force elements acting between markers on the axle, located in the vicinity of joints I and J, and corresponding markers on the upper supports of the frame.

This explicit definition of the kinematic pairs A–J is used consistently in the ADAMS model, ensuring a one-to-one correspondence between the schematic representation in Figure 1a and the multibody model.

In the ADAMS model, the mechanism is driven by a single independent degree of freedom, namely the crank rotation at joint A. The motion of the rear axle assembly is then fully determined by the kinematic constraints at joints I and J, which guide the axle in

https://doi.org/10.3390/vehicles8010009

a predominantly vertical translation combined with a small torsional rotation about its longitudinal axis.

The crank is prescribed a periodic rotational motion about its axis. In the simulations reported here a harmonic law is used, with angular position $\phi(t) = \phi_0 + \Delta\phi\sin(2\pi ft)$, where ϕ_0 is the mean angle, $\Delta\phi$ the amplitude and f the test frequency. These parameters are selected such that the vertical displacement at the wheel spindle reproduces the target fatigue loading conditions of the rear axle. Gravity acts along the global negative Z-direction; the global X-axis is aligned with the longitudinal direction of the axle beam.

Contact between the stand and the floor is neglected, because the base frame is bolted to the foundation in the real installation and its motion is negligible. The clearance in revolute joints is also neglected; joints are assumed ideal without friction. This leads to a conservative estimate of the internal forces in the rear axle and stabiliser bar.

3.2. Flexible Representation of the Rear Axle and Stabiliser Bar

To correctly evaluate stress-related quantities and local deformations, the rear axle beam and stabiliser bar cannot be treated as perfectly rigid. Therefore, these components are introduced as flexible bodies using the dedicated functionality available in ADAMS (Figure 2).

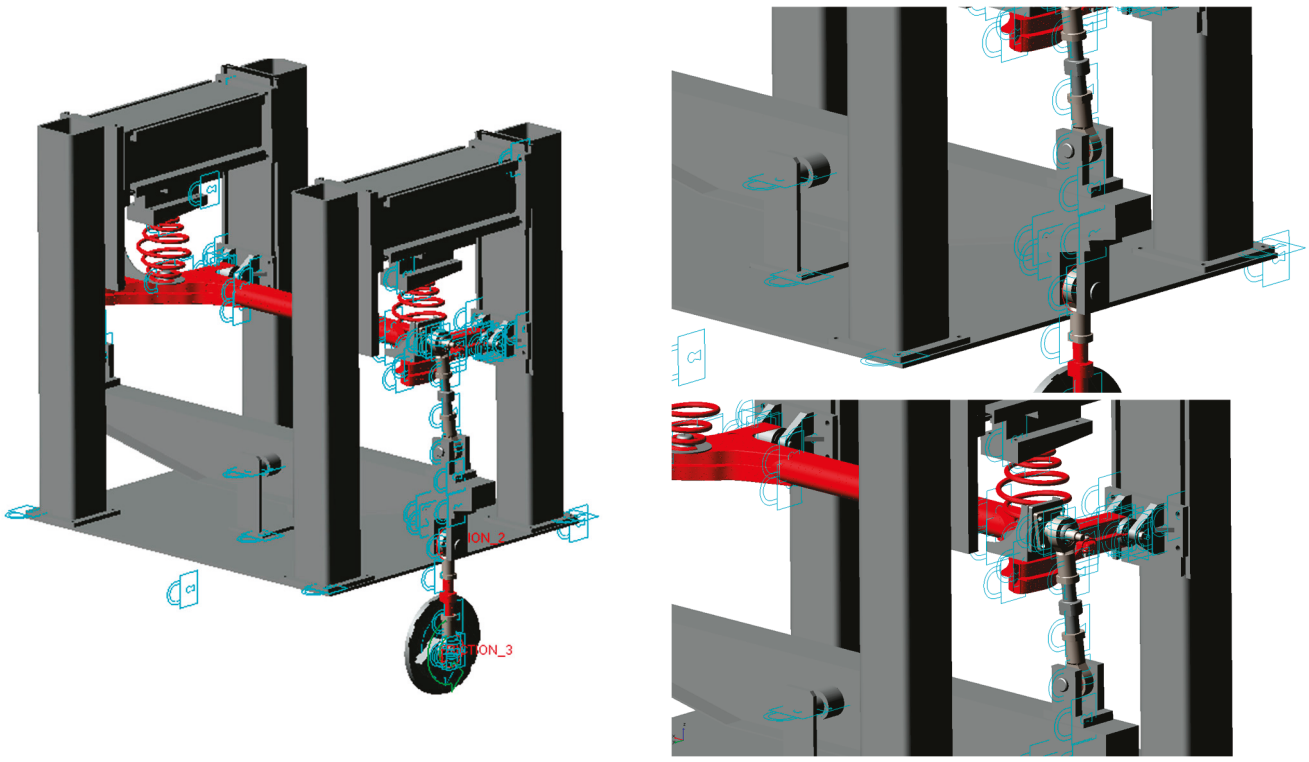

(**a**) (**b**)

Figure 2. Multibody model of the rear suspension durability test bench in MSC ADAMS: (**a**) overall dynamic model including the flexible rear axle, stabiliser bar, springs and driving mechanism; (**b**) detail of the vertical connecting link (4) showing the spherical joint E to the rocker beam and the cylindrical joint G to the wheel-spindle region of the axle.

A finite element model of the rear axle–stabiliser-bar assembly is first generated starting from the CAD geometry and the nominal material properties of the steel. The mesh combines shell and solid elements in the regions with complex geometry (such as the bent side plates and welded brackets). This FE model is then reduced to a modal

https://doi.org/10.3390/vehicles8010009

neutral file (MNF), retaining the lowest natural modes that are relevant for the operating frequency range of the stand. The MNF is imported into ADAMS/Flex and replaces the corresponding rigid body. The locations of all joints, bushings and load application points are mapped to interface nodes of the flexible body.

A reference marker is placed at the centre of mass of the stabiliser bar. The translational displacements and elastic deformations of this point along the global X- and Y-axes are later used both for evaluating the dynamic behaviour of the stand and for comparison with experimental measurements.

3.3. Simulation Scenarios and Post-Processing

Dynamic simulations are performed in the time domain for a sequence of crank revolutions, starting from rest. An initial transient interval is discarded so that the analysis focuses on the steady-state response under periodic loading. The integration is carried out with a variable-step algorithm with error control adequate for flexible multibody systems; the maximum step size is limited in order to capture the higher-frequency modes of the axle–stabiliser assembly.

In all simulations, the crank at joint A is driven with a constant angular velocity of ω = 15.5 rad/s (corresponding to an excitation frequency of approximately 2.47 Hz), matching the operating speed used in the experimental tests.

The main output quantities used in the subsequent analysis are:

- translational displacements, velocities and accelerations of the marker at the stabiliser bar centre of mass along the global X- and Y-directions;
- relative rotations of the stabiliser bar about its longitudinal axis, which correlate with the torsional deformation of the bar;
- reaction forces in the vertical connecting links (links 4 and 4′), transmitted through the spherical joint on the rocker beam and the cylindrical joint on the wheel spindle region, which indicate how the excitation is transmitted from the mechanism to the axle;
- internal forces at the wheel spindles, obtained by defining force sensors at the connection between the axle and the wheel-hub region.

Figure 2 illustrates the multibody model of the rear suspension durability test bench implemented in MSC ADAMS, highlighting both the overall assembly and, in particular, the vertical connecting link (4) with its spherical joint E to the rocker beam and cylindrical joint G to the wheel-spindle region of the rear axle.

The multibody simulation also provides the reaction forces in joint E, which represents the main load path through which the excitation of the mechanism is transmitted to the right side of the rear axle. Figure 3 shows the time histories of the force components F_X, F_Y and F_Z in this joint (Joint 86 in ADAMS). It can be observed that the dominant component is the vertical force F_Z, whereas the longitudinal and lateral components F_X and F_Y remain comparatively small, confirming that the stand primarily excites the axle in vertical bending with only minor parasitic loads in the other directions.

In addition to joint E, the reaction forces were evaluated in joint G, which represents the cylindrical connection between the upper end of the vertical connecting link (4) and the right wheel-spindle region of the rear axle. Figure 4 shows the time histories of the three force components F_X, F_Y and F_Z in this joint (Joint 95 in ADAMS), while panel (d) presents the magnitude of the reaction force $|F|$. After a short transient in the first second of simulation, the response becomes strictly periodic. The dominant contribution is given by the F_Z component, which reaches peak values close to $\pm$800–$\pm$1000 N, whereas the F_X and F_Y components remain below about $\pm$60–$\pm$70 N. This confirms that the connection between link 4′ and the wheel spindle is loaded predominantly in the direction that is approximately

https://doi.org/10.3390/vehicles8010009

aligned with the vertical motion imposed by the test bench, while the longitudinal and lateral force components are comparatively small.

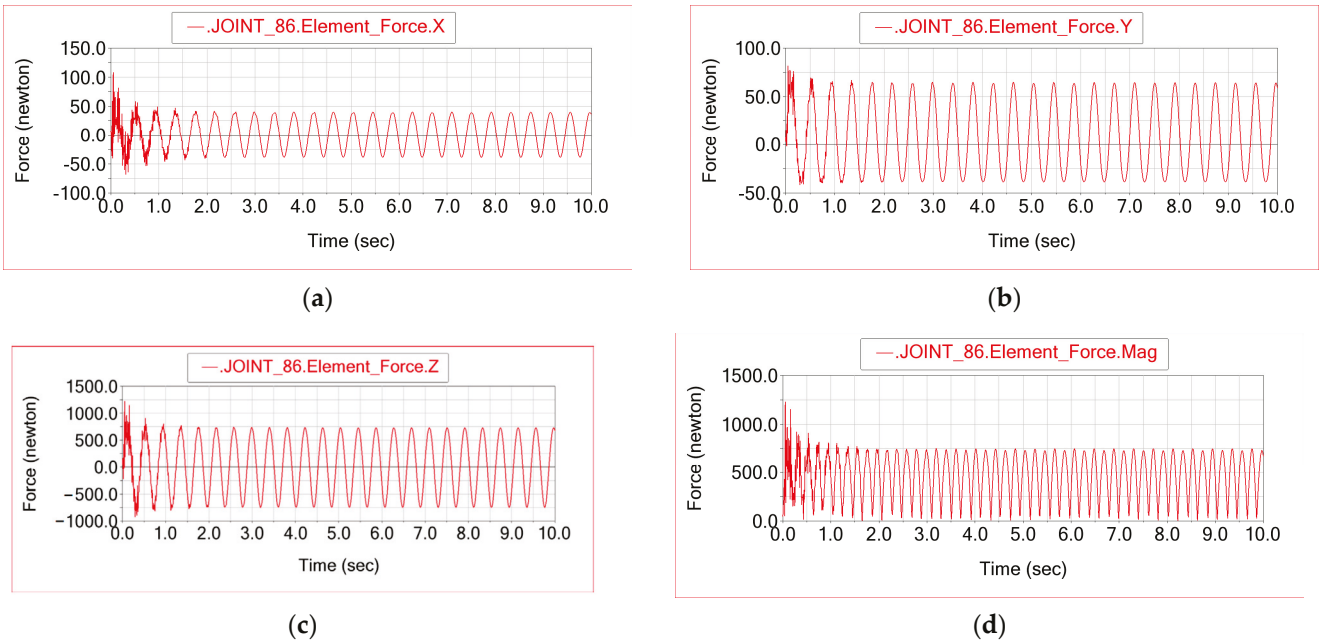

Figure 3. Time histories of the reaction force components F_X, F_Y and F_Z in joint E (Joint 86 in ADAMS), corresponding to the cylindrical connection between the vertical connecting link (4′) and the right wheel-spindle region of the rear axle: (**a**) F_X, (**b**) F_Y, (**c**) F_Z and (**d**) Magnitude Force.

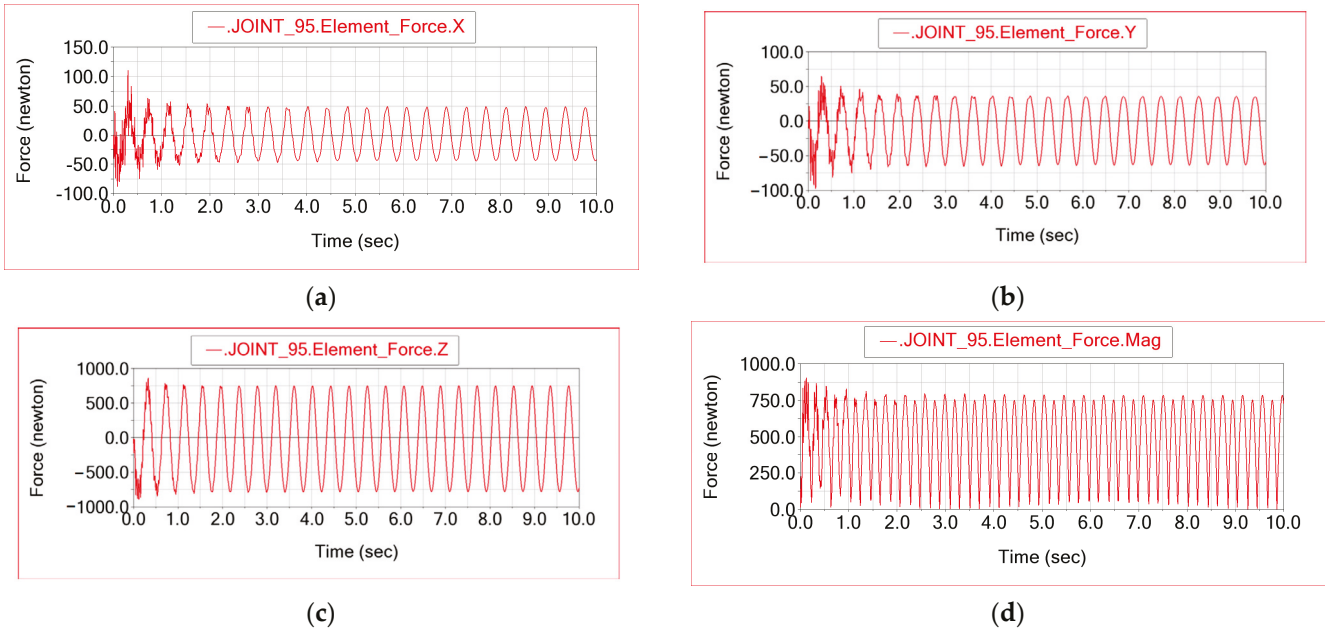

Figure 4. Time histories of the reaction force components at joint G (Joint 95 in ADAMS) between the vertical connecting link (4′) and the right wheel-spindle region of the rear axle: (**a**) F_X, (**b**) F_Y, (**c**) F_Z, and (**d**) magnitude of the reaction force.

Besides the reaction forces in the kinematic joints, the dynamic simulation provides the translational displacements, velocities and accelerations of any marker in the model, as well as the corresponding elastic deformations of the flexible rear stabiliser bar.

In order to characterise the global motion of the rear stabiliser bar during the test cycle, the translational displacements of its centre of mass were monitored in the ADAMS model.

https://doi.org/10.3390/vehicles8010009

Figure 5 shows the time histories of the three Cartesian components and of the displacement magnitude. After the initial transient, the response becomes clearly periodic, with small-amplitude oscillations of the order of a few millimetres. The longitudinal displacement component remains very small compared with the other two components, indicating that the stabiliser bar is mainly subjected to vertical and lateral motion, consistently with the intended loading mode of the test bench.

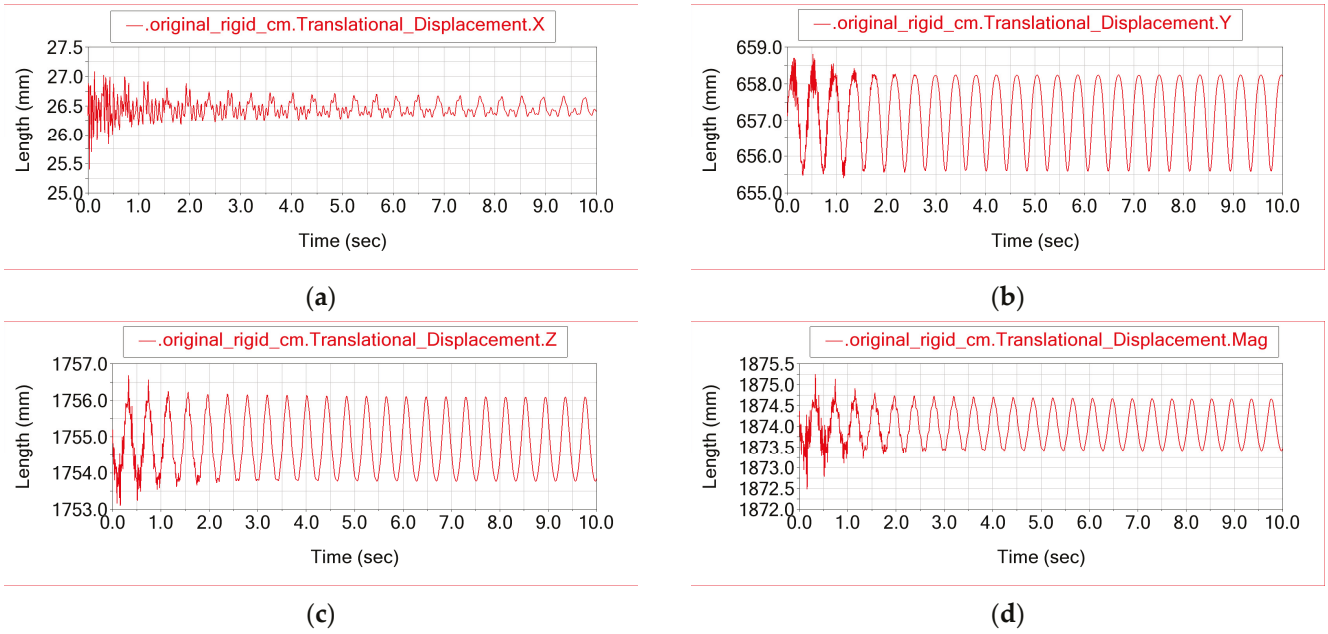

Figure 5. Time histories of the translational displacements of the centre of mass of the rear stabiliser bar in the global coordinate system: (**a**) displacement u_X; (**b**) displacement u_Y; (**c**) displacement u_Z; (**d**) magnitude of the displacement $|u|$.

To distinguish between rigid-body motion and elastic behaviour, the translational deformations of the centre-of-mass marker of the rear stabiliser bar with respect to its reference node were also monitored. Figure 6 shows the time histories of the three Cartesian components of this deformation and of its magnitude. After the initial transient, the response becomes purely periodic. The δ_X component remains almost negligible, while δ_Y and δ_Z reach amplitudes of the order of 1 mm, indicating that the stabiliser bar mainly deforms in the vertical and lateral directions under the imposed excitation.

In the ADAMS/Flex model, the motion of the marker attached to the centre of mass of the stabiliser bar can be decomposed into a rigid-body contribution and an elastic contribution. The translational displacement outputs (Figure 5) represent the total motion of the marker in the global reference frame, i.e., the sum of the rigid-body motion of the bar and its local elastic deflection. By contrast, the translational deformation outputs (Figure 6) represent only the elastic part of the motion, measured with respect to the reference node of the flexible body. Consequently, the deformation amplitudes are much smaller than the corresponding displacements and directly reflect the bending and torsional flexibility of the stabiliser bar under the imposed excitation.

In addition to the translational deformations, the ADAMS/Flex model provides the rotational elastic deformations of markers attached to the flexible stabiliser bar. Figure 7 shows the time histories of the rotational deformation components θ_X, θ_Y and θ_Z for a marker located in the vicinity of the bar's centre of mass, together with the magnitude of the rotation $|\theta|$. These quantities describe the local twist and bending rotations of the stabiliser bar relative to its reference configuration. After the initial transient, the response becomes

https://doi.org/10.3390/vehicles8010009

periodic, with the dominant contribution associated with the rotation about the bar's longitudinal axis (X), confirming that the excitation applied by the test bench produces a significant torsional deformation of the stabiliser bar superimposed on its bending motion.

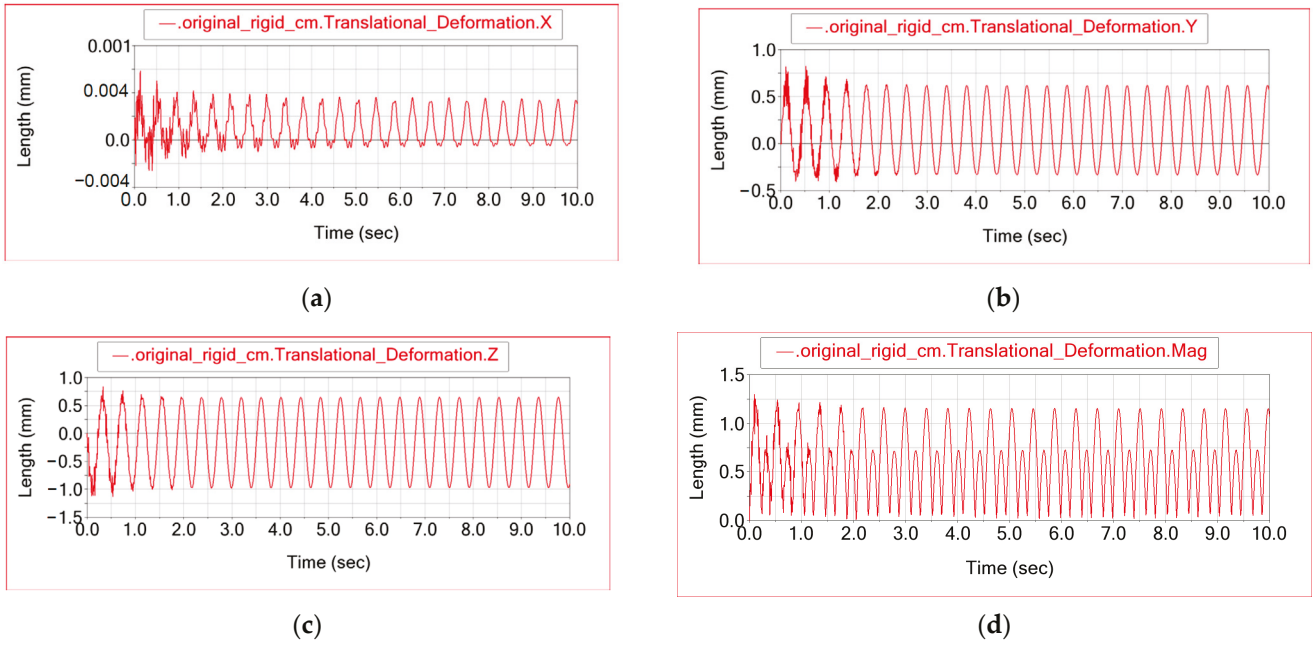

Figure 6. Time histories of the translational elastic deformations of the centre of mass of the rear stabiliser bar: (**a**) deformation δ_X; (**b**) deformation δ_Y; (**c**) deformation δ_Z; (**d**) magnitude of the deformation $|\delta|$.

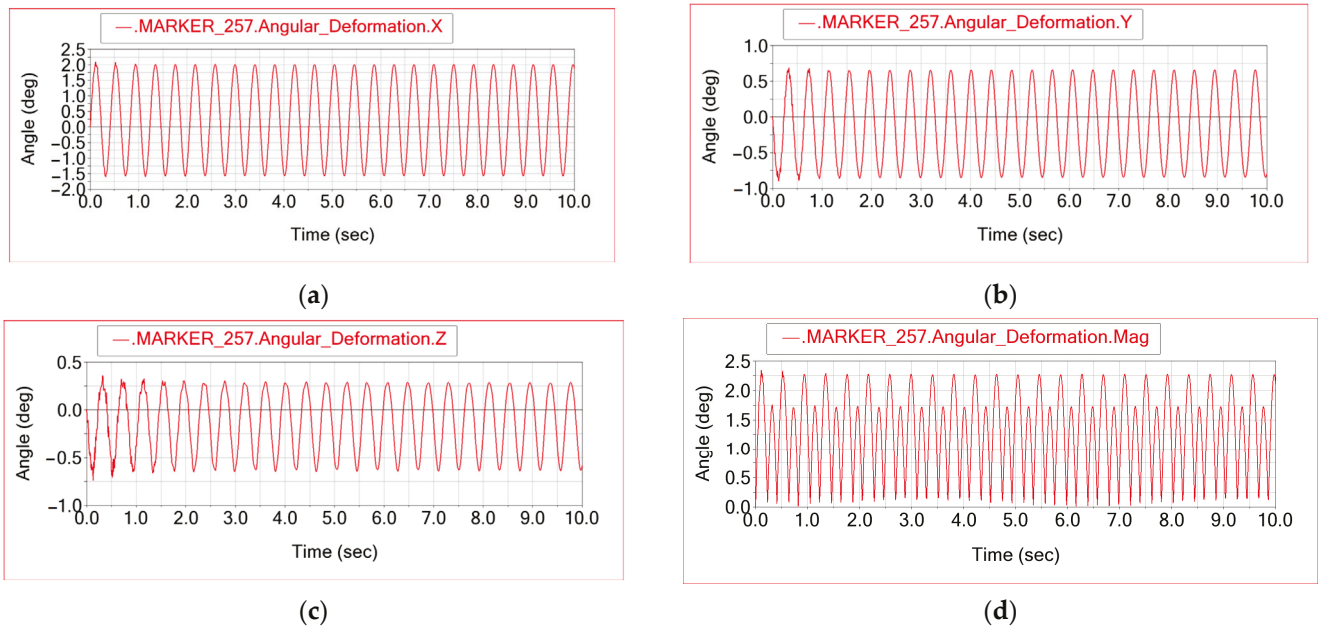

Figure 7. Time histories of the rotational elastic deformations of a marker located near the centre of mass of the rear stabiliser bar: (**a**) θ_X; (**b**) θ_Y; (**c**) θ_Z; (**d**) magnitude of the rotation $|\theta|$.

The ADAMS/Flex model also enables a direct three-dimensional visualisation of the deformation of the flexible components. As illustrated in Figure 8, deformed shapes corresponding to different vibration modes or to selected instants of the transient response can be displayed for the rear stabiliser bar and the rear axle assembly. In addition, coloured contour plots of the deformation field and full 3D animations of the simulated motion have

https://doi.org/10.3390/vehicles8010009

been generated; these are provided as Supplementary Materials Videos to better illustrate the dynamic behaviour of the test bench and of the rear suspension components.

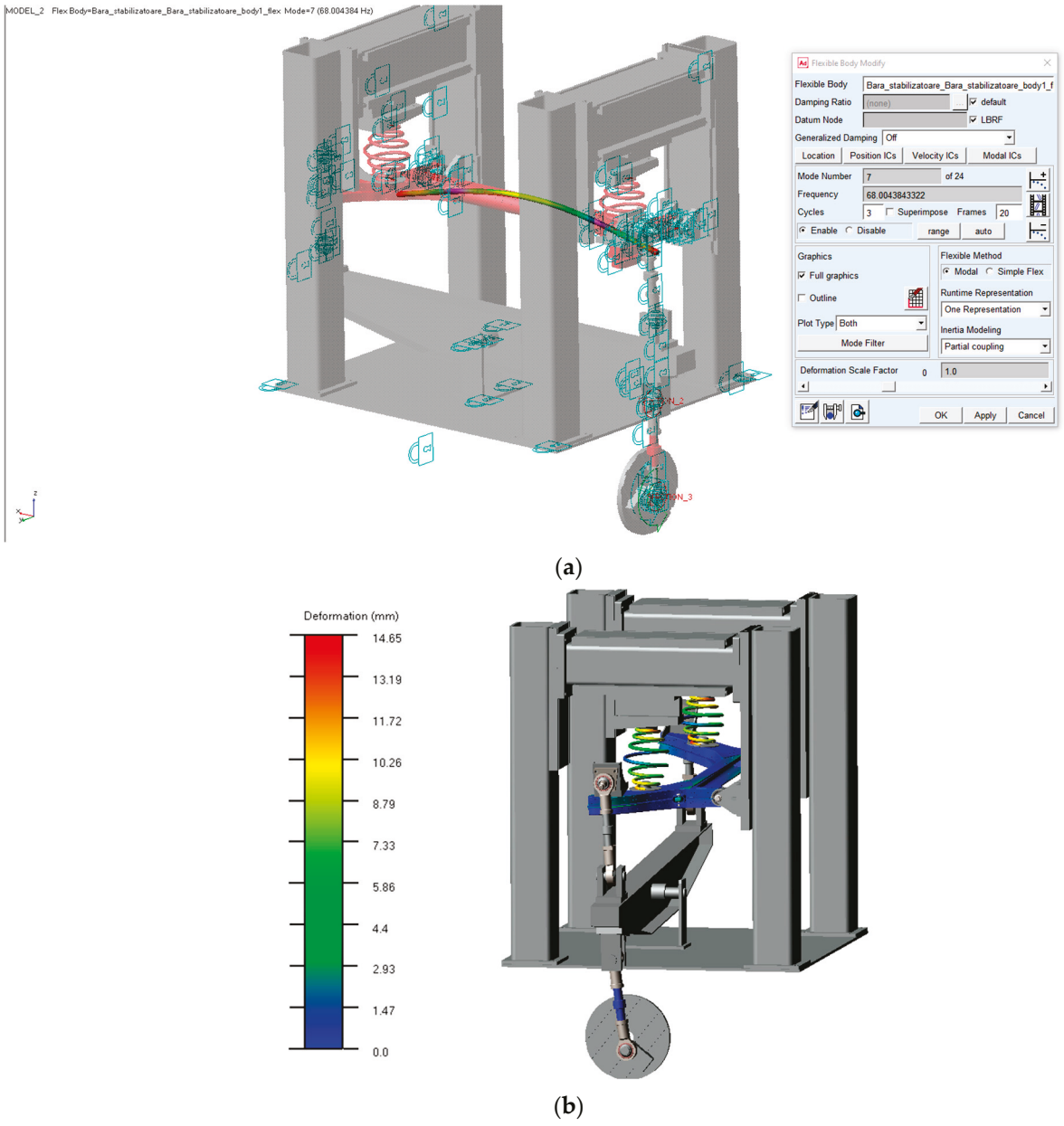

Figure 8. Visualisation of the flexible multibody model in MSC ADAMS: (**a**) definition and display of the deformed shape of the rear stabiliser bar as a flexible body; (**b**) contour plot of the deformation field of the rear axle–stabiliser assembly during dynamic excitation.

3.4. Discussion of Dynamic Response

The ADAMS model confirms that the test bench reproduces the intended loading mode of the rear axle. The crank at joint A, driven at a constant angular velocity of ω = 15.5 rad/s, imposes a nearly harmonic motion on the rocker beam (link 3), which in turn drives the vertical connecting links (4 and 4′) through the spherical joints E and F. The loads are then transmitted to the rear axle through the cylindrical joints G and H, exciting the axle beam and the stabiliser bar in a combined bending–torsion mode. After a short transient, all relevant kinematic and kinetic quantities exhibit a purely periodic response. The time histories of displacement and deformation at the stabiliser-bar centre of mass

https://doi.org/10.3390/vehicles8010009

are nearly sinusoidal, as expected from the harmonic drive, while small higher-frequency components are associated with the flexible modes of the axle assembly.

Besides the reaction forces in the joints, the dynamic simulation provides the translational displacements, velocities and accelerations of any marker in the model. Figures 5 and 6 illustrate, respectively, the total translational displacements and the translational elastic deformations of the marker located at the centre of mass of the rear stabiliser bar. The displacement histories in Figure 5 describe the global oscillatory motion imposed by the test bench, whereas the deformation histories in Figure 6 represent only the elastic part of this motion, relative to the reference node of the flexible body. The deformation amplitudes are significantly smaller than the corresponding displacements and are mainly associated with the lateral and vertical components, indicating that the stabiliser bar undergoes modest but clearly periodic bending and torsional deflection under the imposed excitation. The associated velocity and acceleration histories (displayed in paper) follow the same pattern, with smooth, nearly sinusoidal steady-state behaviour.

The reaction forces transmitted along the load path are quantified in joints E and G. Figures 3 and 4 show the time histories of the three Cartesian components and of the magnitude of the reaction force in these joints. After the initial transient, the resultant forces stabilise to nearly constant amplitudes and remain strongly dominated by a single component (here aligned with the global Z-direction), while the other two components are much smaller. This confirms that the mechanism primarily excites the rear axle in the intended loading direction, with only minor parasitic loads in the orthogonal directions, and that no undesirable kinematic amplification or spurious constraints are introduced by the joint configuration.

In addition, the flexible multibody model allows three-dimensional visualisation of the deformed shapes of the axle and stabiliser bar. As illustrated in Figure 8, deformed configurations and contour plots of the deformation field can be displayed for selected instants of the response, providing an intuitive picture of the bending and twisting of the flexible components. Animations obtained from these simulations are supplied as Supplementary Materials Videos, offering further insight into the dynamic behaviour of the test bench and the rear suspension assembly.

Finally, a dedicated force sensor located in the region of the right wheel spindle is used to record the reaction force transmitted by the test bench during the fatigue loading cycle. The resulting periodic signal exhibits a peak value of about 1 kN, which does not represent the maximum service load acting on the wheel, but the reaction corresponding to the prescribed displacement imposed by the bench, given the stiffness of the rear axle and suspension components. This peak value of the simulated reaction force is then adopted as an equivalent design load in the finite element analysis of the rear axle assembly, so that the boundary conditions in the structural model are fully consistent with the kinematic excitation and stiffness distribution represented in the multibody model.

The combination of multibody dynamics with flexible bodies therefore provides a comprehensive picture of the dynamic behaviour of the test bench. It allows the designer to verify that the mechanism operates without excessive kinematic amplification or undesired resonance, and at the same time supplies consistent internal force histories to be used as input for the subsequent explicit-dynamics finite element simulations of the rear axle housing and stabiliser bar.

4. Experimental Strain Analysis of the Rear Axle on the Test Bench

The numerical investigations presented in the previous sections were complemented by an experimental strain analysis carried out on the rear axle mounted on the durability test bench. The main objectives of this analysis were (i) to measure the strain and stress

https://doi.org/10.3390/vehicles8010009

state in critical regions of the rear axle during the imposed fatigue loading cycle, and (ii) to provide reference data for the validation of the finite element model of the axle assembly.

4.1. Strain-Gauge Instrumentation and Measuring Points

The instrumentation layout on the rear axle is shown schematically in Figure 9. A total of nine measuring points were selected based on the fatigue-sensitive regions identified in previous studies and on the expected bending and torsion modes of the axle beam.

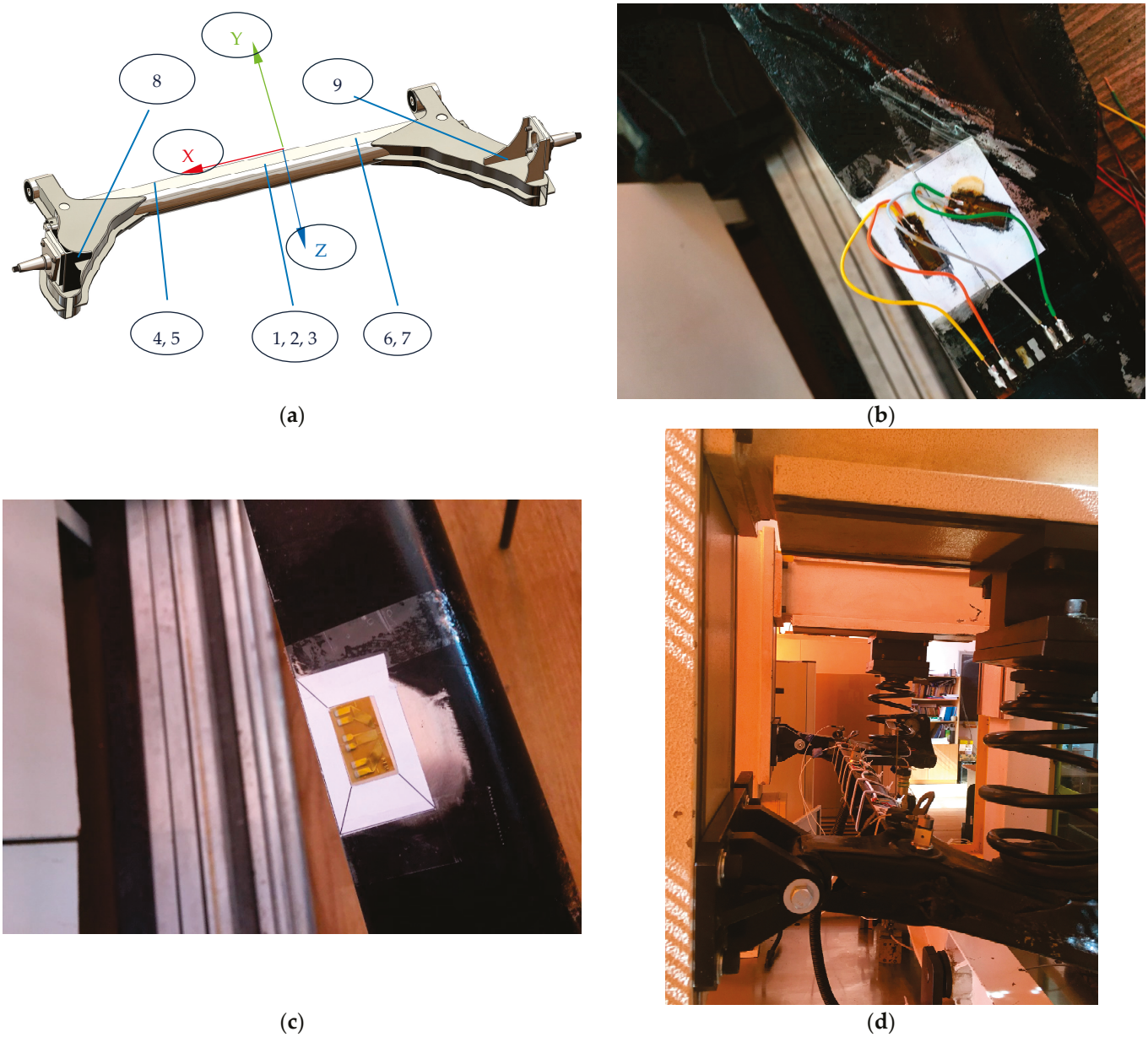

Figure 9. Experimental strain-gauge instrumentation of the rear axle: (**a**) CAD model of the axle with the global *X*-*Y*-*Z* axes and the locations of the nine measuring points (1–9); (**b**) single strain gauge mounted on the axle beam/head; (**c**) strain-gauge rosette bonded at mid-span of the axle beam; (**d**) rear axle installed on the test bench, with the instrumented regions and wiring visible.

In the central portion of the axle beam, a strain-gauge rosette consisting of three grids was bonded on the tensile side of the beam (points 1, 2 and 3). The grids are oriented at different angles with respect to the longitudinal axis *X* of the beam so as to enable

https://doi.org/10.3390/vehicles8010009

the reconstruction of the local principal strains and stresses under combined bending and torsion.

Additional single strain gauges were mounted in the following locations:

- Left beam head (points 4 and 5), in the vicinity of the left wheel-spindle region, to capture the local bending and torsional effects close to the left support;
- Right beam head (points 6 and 7), in a position geometrically symmetric to points 4 and 5 with respect to the mid-span of the axle beam, so that the stress state at both beam ends can be compared under the symmetric loading generated by the test bench;
- Left and right trailing arms (points 8 and 9), at the transitions between the bent sheet-metal arms and the axle beam, where geometric discontinuities may induce stress concentration even under globally symmetric excitation.

The X-axis of the local coordinate system is aligned with the longitudinal axis of the axle beam, while the Y-axis is oriented transversely, as indicated in Figure 9a. This convention is consistent with the multibody and finite element models, which simplifies the comparison between measured and simulated stress components.

The layout of the nine strain-gauge measuring points on the rear axle and several details of the instrumentation are shown in Figure 9a.

A photograph of the rear axle mounted on the test bench, with the strain-gauge positions indicated, is presented in Figure 9d.

A detailed view of the strain-gauge rosette bonded near the transition between the axle beam and the trailing arm is shown in Figure 9b. The three grids are oriented at different angles with respect to the beam axis and are protected with adhesive and epoxy coating, while the colour-coded lead wires are routed towards the data acquisition system.

4.2. Data Acquisition System and Measured Channels

The strain gauges were connected to an HBM MGCplus data acquisition system (HBM, Darmstadt, Germany) equipped with CANHEAD modules, providing stable bridge excitation, high-accuracy amplification and simultaneous multi-channel recording. The measurement setup was configured to record both the input force in the driving mechanism and the mechanical stresses derived from the strain-gauge signals.

The experimental setup employed the following instrumentation:

- Force transducer S9M-50 kN (HBM, serial no. 31421930/2016, Darmstadt, Germany), nominal force range $\pm$50 kN, nominal sensitivity 2 mV/V, accuracy class 0.1, linearity $\leq$0.1%. The sensor was conditioned by strain-gauge input modules SCM5B38-37 (Dataforth, Tucson, AZ, USA) with $\pm$5 V output, nominal sensitivity 2 mV/V, 4 Hz bandwidth, linearity 0.01% and continuous isolation of 240 Vrms.
- Reference force transducer U2B-50 kN (HBM, serial no. 168854/013481), nominal force range $\pm$50 kN, nominal sensitivity 2 mV/V, accuracy class 0.5, coupled with an electronic indicator SCOUT55 (HBM, serial no. 827419902), used for calibration of the main force channel.
- Precision vernier calliper (MIB, New York City, NY, USA), measuring range 0–300 mm, resolution 0.01 mm (serial no. GX 140110211), used for checking geometric dimensions and sensor positioning.
- Portable data acquisition system SoftronicDataAcquisition, Craiova, Romania, based on LAN-XI 3053B120 and LAN-XI 3160A042 modules, providing 16 analogue input channels, 2 analogue output channels (signal generator), one LAN port, one stabilised 5 V DC output and one stabilised 24 V DC output, with battery operation for up to 5 h with all acquisition systems active.

https://doi.org/10.3390/vehicles8010009

- Strain gauges LY6-10/350 (HBM), resistance 350 Ω, gauge length 10 mm, gauge width 5 mm, polyamide backing, constantan grid, gauge factor $k = 2$, used in quarter-bridge configurations.
- MGCplus data acquisition system (HBM), 15 measurement channels, maximum sampling frequency 19.2 kHz, accuracy 0.0025, used as the main multi-channel bridge amplifier.
- CANHEAD Data Acquisition System (HBM), strain-gauge measurement system in quarter-bridge configuration, 10 input channels, accuracy class 0.1, maximum sampling frequency 100 Hz.

Data acquisition and online signal processing were performed using Catman 5.6.4 software (HBM), which provides real-time control, visualisation and multi-channel processing for MGCplus and CANHEAD systems.

The following quantities were recorded during the tests:

- Longitudinal force in the connecting link 2: F_link2 (N);
- Normal stress at mid-span of the axle beam, gauge oriented at $-90°$ with respect to the *OX* axis: Sigma 1 (MPa);
- Normal stress at mid-span of the axle beam, gauge oriented at $-135°$ with respect to the *OX* axis: Sigma 2 (MPa);
- Normal stress at mid-span of the axle beam, gauge oriented at $-45°$ with respect to the *OX* axis: Sigma 3 (MPa);
- Normal stress at the left beam head, gauge oriented at $0°$ with respect to the *OX* axis: Sigma 4 (MPa);
- Normal stress at the left beam head, gauge oriented at $-135°$ with respect to the *OX* axis: Sigma 5 (MPa);
- Normal stress at the right beam head, gauge oriented at $0°$ with respect to the *OX* axis: Sigma 6 (MPa);
- Normal stress at the right beam head, gauge oriented at $-135°$ with respect to the *OX* axis: Sigma 7 (MPa);
- Normal stress in the left axle arm, gauge oriented at $-45°$ with respect to the *OX* axis: Sigma 8 (MPa);
- Normal stress in the right axle arm, gauge oriented at $-135°$ with respect to the *OX* axis: Sigma 9 (MPa).

The sampling frequency was chosen to ensure a sufficiently dense discretisation of the loading cycle, given the excitation frequency imposed in the ADAMS model and on the test bench (Section 3). All signals were recorded simultaneously during the start-up and steady-state operation of the bench.

The complete experimental setup, including the rear axle mounted on the test bench and the data-acquisition chain, is shown in Figure 10.

4.3. Test Procedure and Data Processing

The experimental tests were carried out under the same operating conditions as those used in the multibody simulations, i.e., with the crank rotating at constant angular speed and the rocker beam imposing a periodic displacement on the right wheel-spindle region. After the stand was brought to operating speed, several consecutive cycles were recorded.

For the analysis, three load cycles (cycles 3, 4 and 5) were selected from the stabilised regime, after the decay of the initial transient. For each of these cycles and for each channel (F_Rod and Sigma 1–9), the following quantities were computed:

- mean value;
- root-mean-square (RMS) value;
- maximum value;

https://doi.org/10.3390/vehicles8010009

- minimum value.

The statistical processing was then extended across the three cycles:

- the average and standard deviation of the mean values and RMS values,
- the average and standard deviation of the maxima and minima,
- the peak-to-peak amplitude (difference between maximum and minimum) for each measured signal.

These results are summarised in Table 1, which reports the processed values for the connecting-rod force and for all nine stress channels. The relatively small standard deviations confirm the good repeatability of the measurements in the stabilised regime and indicate that the test bench operates under stable kinematic and loading conditions.

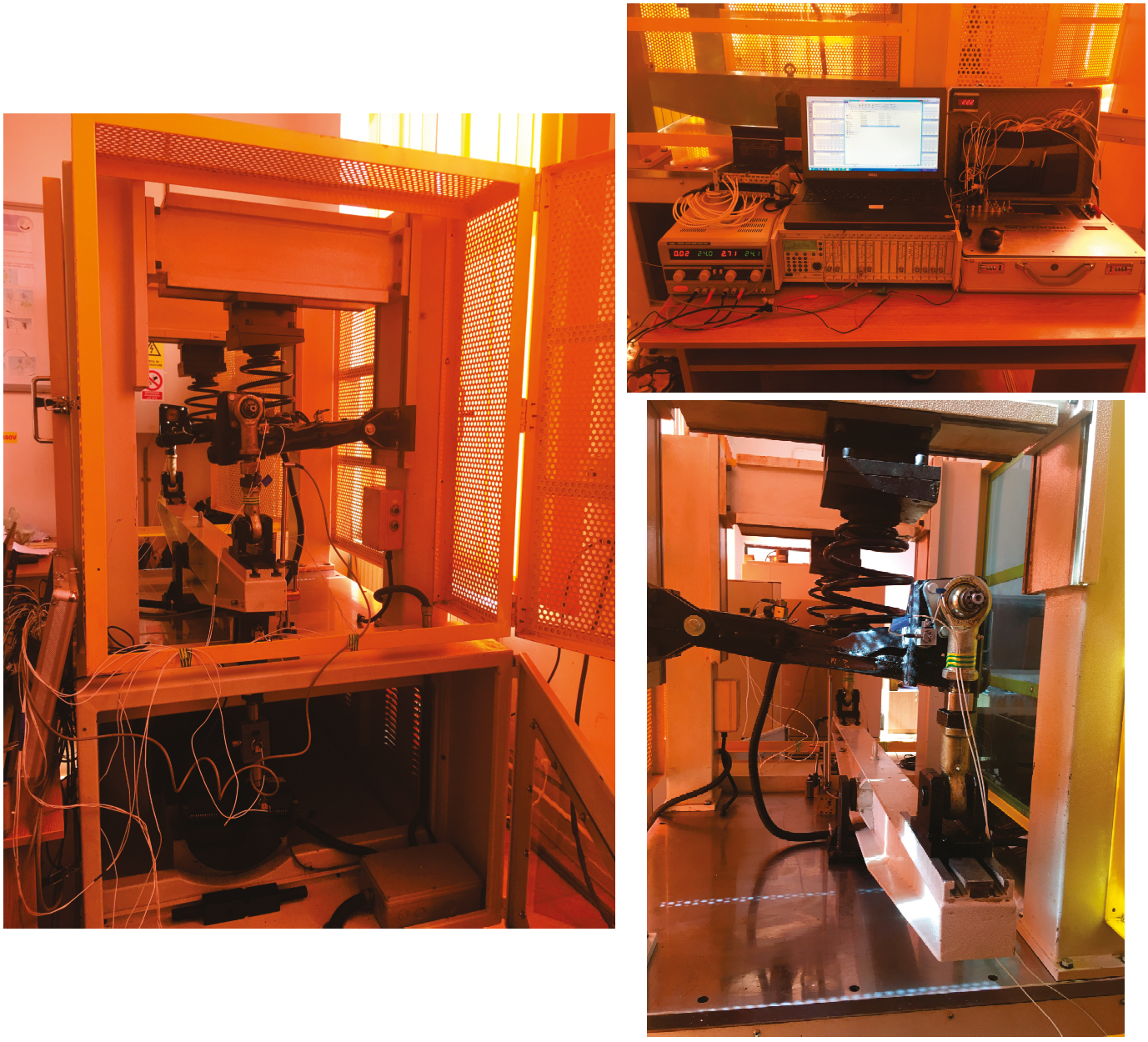

(**a**) (**b**)

Figure 10. Experimental setup for the strain measurements on the rear axle: (**a**) rear suspension durability test bench with the axle mounted and instrumented with strain gauges, inside the protective enclosure; (**b**) data acquisition and signal conditioning equipment together with a close-up view of the instrumented rear axle and coil springs inside the test bench.

https://doi.org/10.3390/vehicles8010009

Table 1. Processed experimental results for the connecting-link force and the measured stresses at the nine strain-gauge locations on the rear axle (averages and peak-to-peak values over cycles 3–5).

	F_Rod	Sigma-1	Sigma-2	Sigma-3	Sigma-4	Sigma-5	Sigma-6	Sigma-7	Sigma-8	Sigma-9
	(N)	(MPa)	(MPa)	(MPa)	(MPa)	(MPa)	(MPa)	(MPa)	(MPa)	(MPa)
					Medium value					
Cycle 3	230.66	0.25	−16.21	15.70	−6.24	2.11	12.11	7.53	5.48	−7.12
Cycle 4	232.41	0.25	−16.24	15.74	−6.25	2.12	12.14	7.54	5.49	−7.14
Cycle 5	230.65	0.25	−16.01	15.68	−6.21	2.11	12.10	7.52	5.48	−7.09
Average	231.24	0.25	−16.15	15.71	−6.24	2.11	12.12	7.53	5.48	−7.12
St.Dev	0.83	0.00	0.10	0.02	0.02	0.00	0.02	0.01	0.01	0.02
					Value (RMS efficacy)					
Cycle 3	976.07	0.37	29.26	28.92	11.69	3.94	21.92	12.24	11.46	11.67
Cycle 4	976.54	0.37	29.28	28.94	11.69	3.94	21.93	12.25	11.47	11.68
Cycle 5	974.90	0.37	29.12	28.88	11.66	3.94	21.89	12.22	11.45	11.65
Average	975.84	0.37	29.22	28.91	11.68	3.94	21.91	12.24	11.46	11.67
St.Dev	0.69	0.00	0.07	0.03	0.02	0.00	0.02	0.01	0.01	0.01
					Maximum value					
Cycle 3	1591.95	0.67	18.94	50.74	8.01	6.92	38.45	21.46	20.00	6.23
Cycle 4	1591.72	0.67	18.93	50.74	8.01	6.92	38.44	21.46	20.00	6.22
Cycle 5	1591.07	0.68	19.13	50.65	8.03	6.93	38.41	21.43	20.01	6.26
Average	1591.58	0.68	19.00	50.71	8.02	6.93	38.43	21.45	20.00	6.24
St.Dev	0.37	0.01	0.09	0.04	0.01	0.00	0.02	0.02	0.00	0.02
					Minimum value					
Cycle 3	−1131.29	−0.18	−51.44	−19.32	−20.56	−2.74	−14.25	−6.39	−9.10	−20.50
Cycle 4	−1131.29	−0.18	−51.40	−19.31	−20.55	−2.71	−14.23	−6.39	−9.07	−20.48
Cycle 5	−1131.59	−0.17	−51.15	−19.33	−20.46	−2.72	−14.25	−6.42	−9.06	−20.43
Average	−1131.39	−0.18	−51.33	−19.32	−20.52	−2.72	−14.25	−6.40	−9.08	−20.47
St.Dev	0.14	0.01	0.13	0.01	0.04	0.01	0.01	0.01	0.02	0.03
					Amplitude					
	2722.97	0.86	70.33	70.03	28.54	9.65	52.68	27.85	29.08	26.71

The strain-gauge bridges were configured and calibrated in Catman 5.6.4 using the nominal resistance and gauge factor of the LY6-10/350 sensors (350 Ω, k = 2) and the quarter-bridge wiring. The raw voltage signals were first converted into engineering strain $\varepsilon(t)$ for each channel. Assuming linear–elastic, isotropic behaviour of the axle material, the measured strains were then transformed into mechanical stresses by applying Hooke's law with a Young's modulus E = 210 GPa (Poisson's ratio ν = 0.3). For the single gauges, the stress in the gauge direction was obtained as $\sigma(t) = E\,\varepsilon(t)$, so that each channel Sigma 1–9 directly represents the normal stress in MPa along the orientation of the corresponding strain gauge. In the case of the strain-gauge rosette mounted at mid-span of the beam, the three measured strains were combined to reconstruct the in-plane strain components and the associated normal stresses in the chosen directions, which are likewise reported as Sigma 1–3.

Figure 11 shows the strain histories recorded by the three grids of the rosette mounted at mid-span of the axle beam. After an initial idle phase, the stand is brought to operating speed at about $t \approx 9$ s, where the signals quickly reach a steady-state, nearly sinusoidal regime that is maintained up to approximately $t \approx 38$ s. The subsequent increase and decay of the amplitudes correspond to the controlled run-down of the stand at the end of the test. It can be observed that channel 1 exhibits only small strain amplitudes, whereas channels 2 and 3 reach significantly higher values, indicating that the dominant bending and torsional stresses in the mid-span region are aligned closer to the −135° and −45° directions with respect to the beam axis. The stabilised part of these records (cycles 3–5 in the steady-state window) was used for the statistical processing summarised in Table 1.

https://doi.org/10.3390/vehicles8010009

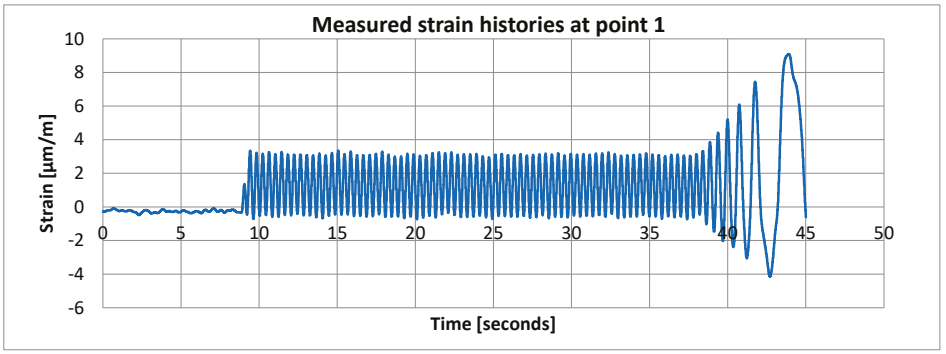

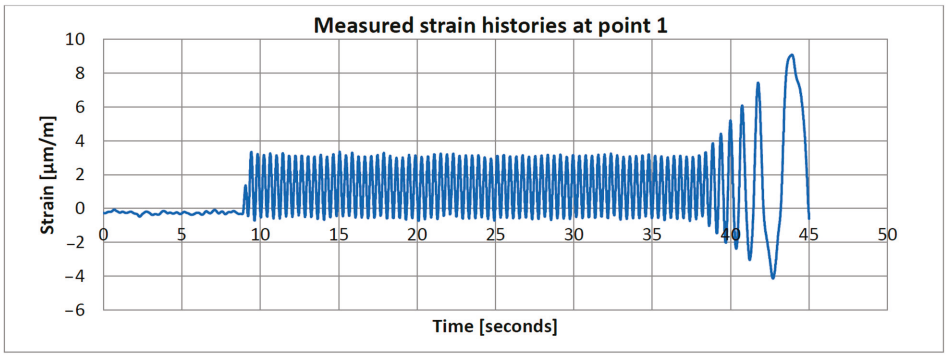

(**a**)

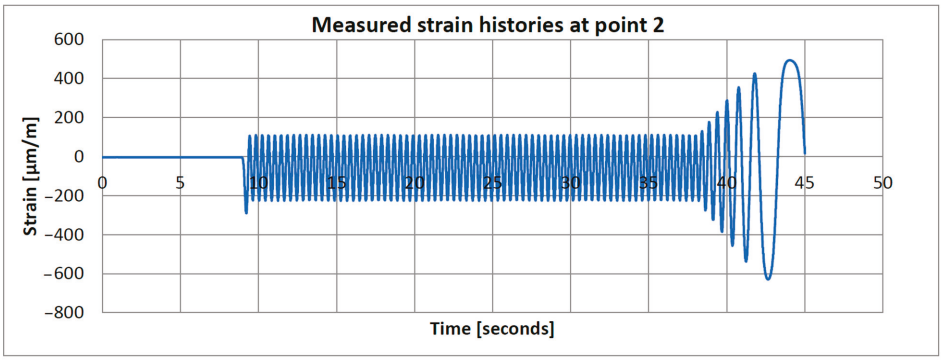

(**b**)

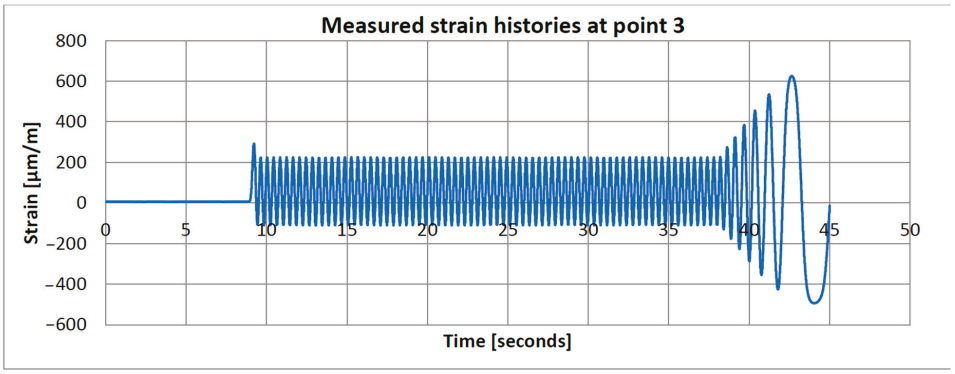

(**c**)

Figure 11. Time histories of the measured strains at mid-span of the axle beam (strain-gauge rosette): (**a**) point 1, gauge oriented at −90° to the *OX* axis; (**b**) point 2, gauge oriented at −135°; (**c**) point 3, gauge oriented at −45°.

To check the repeatability and stationarity of the loading cycle, the full time histories of the connecting-link force and of the nine stress channels were inspected in TestPoint. Figure 12 presents representative time windows taken from the beginning, from the middle and from the end of the measurement. In all three cases, the force and stress signals exhibit

https://doi.org/10.3390/vehicles8010009

the same waveform, frequency and amplitude within the steady-state portion of the test, confirming that the stand reproduces an identical motion and load cycle throughout the entire recording and that no significant drift or degradation of the excitation occurs.

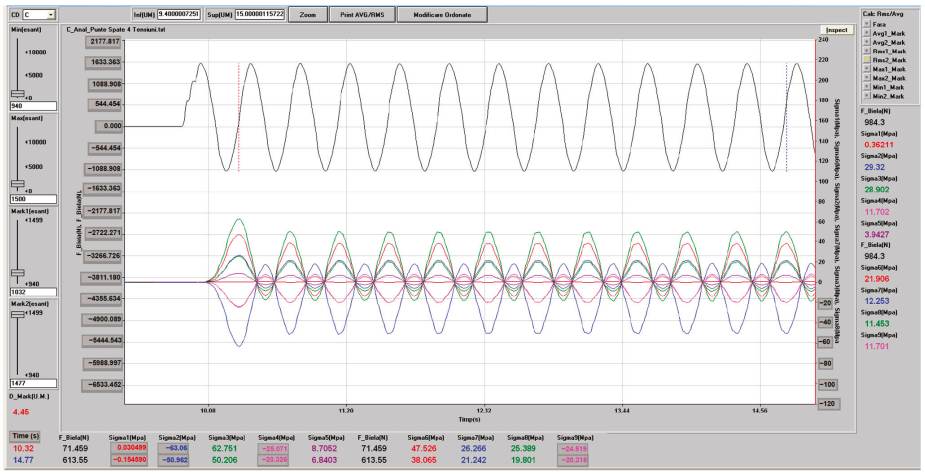

(**a**)

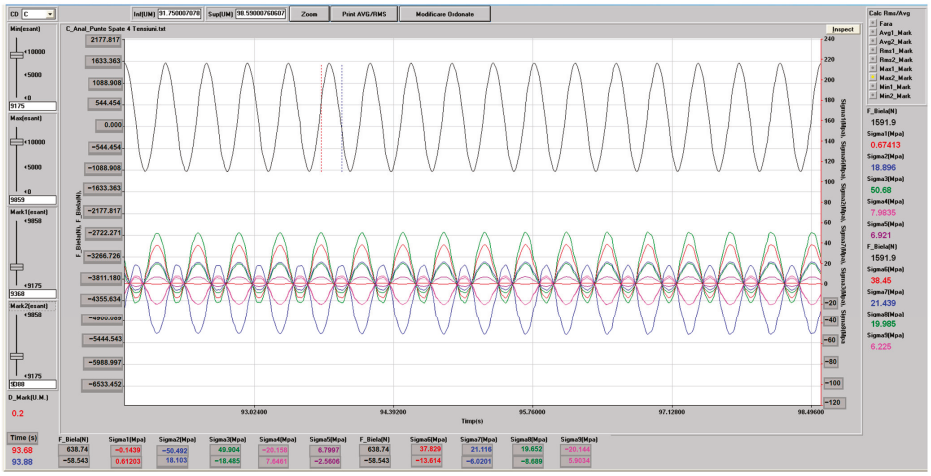

(**b**)

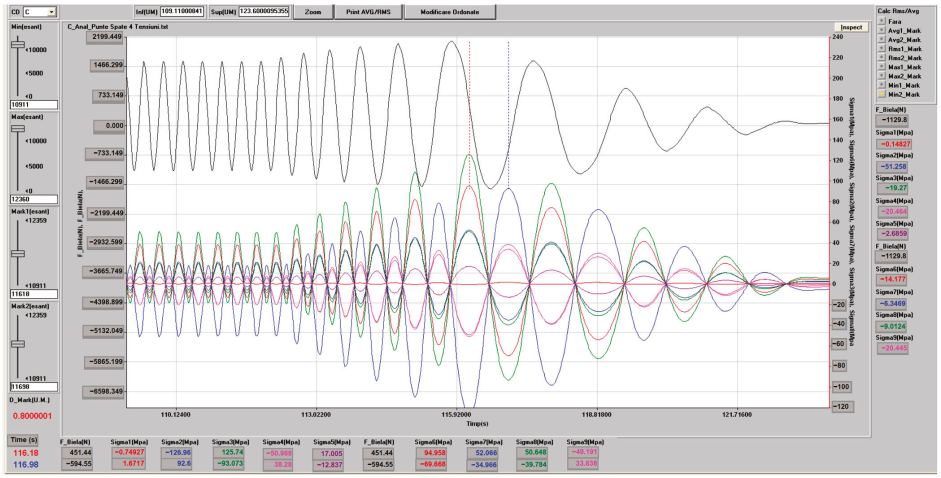

(**c**)

Figure 12. Multi-channel recordings from TestPoint 2021 for the rear axle fatigue test: (**a**) time window at the beginning of the stabilised regime; (**b**) time window in the middle of the recording; (**c**) time window at the end of the recording, including the stand run-down. The upper trace shows the connecting-link force, while the coloured curves represent the nine stress channels Sigma 1–9.

https://doi.org/10.3390/vehicles8010009

4.4. Measured Stress Levels and Identification of Critical Regions

Inspection of the recorded time histories shows that all stress channels exhibit a periodic variation consistent with the imposed cyclic loading. A typical example is provided in Figure 12b, which illustrates the rod force and selected stress components over a representative cycle in the steady-state regime.

From Table 1, it can be observed that:

- the maximum recorded stresses in the mid-span region (Sigma 3 channel) reach values of approximately 50–51 MPa in the most heavily loaded parts of the cycle;
- stresses at the beam heads and arms are somewhat lower in magnitude, with typical maxima in the range of 20–40 MPa, depending on the location and orientation of the gauge;
- the peak-to-peak amplitudes of the stress signals (last line of Table 1) provide a direct indication of the cyclic stress range experienced at each measuring point, which is particularly relevant for fatigue assessment.

Although only nine points on the axle were instrumented, the measured stress distribution already suggests that the most critical regions under the considered loading cycle are located in the central portion of the beam and in the vicinity of the right beam head, where the excitation is applied on the test bench. This observation is consistent with previous numerical studies and will be further quantified by the finite element analysis presented in the next section.

It should be emphasised that in the experimental campaign the stress field is sampled only at discrete locations, limited by the number of strain gauges that can reasonably be installed on the axle. By contrast, finite element analysis provides full-field maps of stresses and strains over the entire structure. The comparison between the measured stresses at the instrumented points and the corresponding values predicted by the FE model therefore constitutes a crucial step in the validation of the numerical model and in the subsequent identification of stress concentration zones and potential fatigue-critical details.

5. Finite Element Analysis of the Rear Axle Assembly

This section presents the finite element analysis of the rear axle assembly, which constitutes the third pillar of the proposed numerical–experimental methodology. Starting from the CAD geometry, a solid finite element model of the axle is built to reproduce the stress and deformation fields under the equivalent design load defined by the flexible multibody simulations. The aim is twofold: first, to obtain full-field maps of von Mises stress and deformation that complement the local strain-gauge measurements; and second, to provide a validated structural model that can be used for design optimisation of safety-critical details, such as the wheel spindle region. The section is organised as follows: Section 5.1 describes the geometry preparation and FE model; Section 5.2 details the boundary conditions and loading; Section 5.3 discusses the resulting stress distribution and critical regions; and Section 5.4 compares the numerical predictions with the experimental strain measurements.

5.1. Geometry Preparation and FE Model

The finite element analysis was carried out in ANSYS Workbench 19.2, using the CAD assembly of the rear axle previously created in SolidWorks. The geometry was first imported into DesignModeler, where a series of clean-up operations were performed to ensure a robust mesh and physically meaningful connections between parts. In particular, small fillets and chamfers not affecting the global stiffness were removed, artificial overlaps were corrected and several adjacent sheet-metal components (U-shaped cross member,

https://doi.org/10.3390/vehicles8010009

bent side arms and end brackets) were merged by Boolean operations into a single solid representing the rear axle beam.

The final model of the rear axle assembly contains the main torsion beam, the trailing arms, the wheel-spindle regions and the brackets for the springs and stabiliser bar. The components that are welded in the real structure are represented as a single continuous body, whereas components connected by bushings in the real suspension (e.g., body mounts) are modelled by appropriate boundary conditions. The mesh consists of 3D solid elements with local refinement in the vicinity of geometric discontinuities, such as the junction between the bent side plate and the bent arm, and around the locations of the strain gauges (points 1–9), in order to capture accurately the stress gradients in these critical regions.

The axle material is assumed to be structural steel with linear elastic behaviour, characterised by a Young's modulus E = 210 GPa and Poisson's ratio ν = 0.3. The rubber bushings that connect the axle to the vehicle body in service and to the stand in the laboratory are represented by equivalent linear springs and dashpots with stiffness and damping values consistent with the experimental stand. The Explicit Dynamics module of ANSYS Workbench was used in order to handle the contact conditions and the nonlinear stiffness of the bushings in a numerically stable way.

5.2. Boundary Conditions and Loading

The CAD geometry of the rear axle was imported into ANSYS DesignModeler as an assembly of solid bodies (torsion beam, side arms and spindle brackets). The parts that are welded in the real component were merged into a single continuous body, whereas those connected through bushings or supports were kept as separate entities to allow the definition of realistic boundary conditions. After this preprocessing step, the assembly was discretised with 3D solid elements, with mesh refinement in the vicinity of geometric discontinuities and in the wheel-spindle region (Figure 13b). The supports corresponding to the axle bushings and spring seats were constrained to reproduce the mounting conditions on the test bench, and a vertical force was applied at the wheel spindle (Figure 13a), consistent with the equivalent reaction obtained from the multibody simulation.

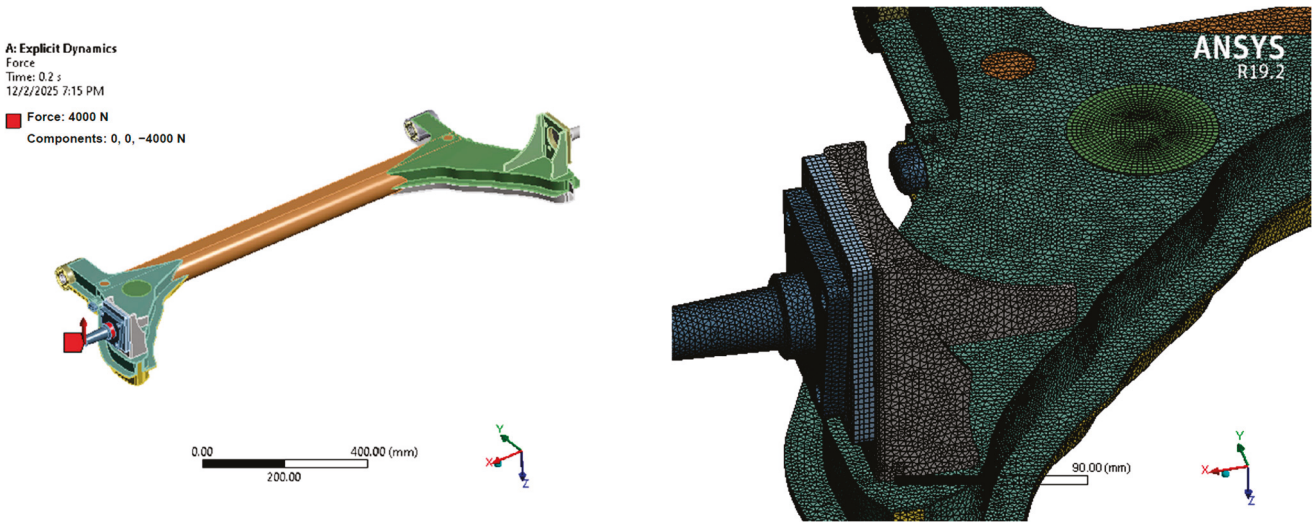

(**a**) (**b**)

Figure 13. Finite element model of the rear axle assembly in ANSYS Explicit Dynamics: (**a**) geometry of the axle and wheel-spindle region imported in DesignModeler, with the vertical force applied at the spindle; (**b**) detail of the solid finite element mesh in the right-hand arm and spindle area.

https://doi.org/10.3390/vehicles8010009

The explicit dynamic analysis was run over one complete loading cycle, with a time step automatically controlled by the stability criterion of the solver. The resulting time histories of displacements, strains and stresses were post-processed at the nodes corresponding to the experimental measuring points, as well as over the entire axle surface to obtain full-field stress maps.

5.3. Stress Distribution and Critical Regions

Figure 14 shows the von Mises equivalent stress distribution obtained from the ANSYS Explicit Dynamics analysis at the time instant corresponding to the peak value of the reaction force in the fatigue loading cycle. The model is solved as a fully transient dynamic problem, but for correlation purposes the stress field is sampled at this representative time step, after the initial transient has decayed and the response has reached a stable periodic regime. It should be emphasised that the finite element model of the rear axle is analysed using the Explicit Dynamics solver in ANSYS, i.e., as a transient dynamic problem rather than a quasi-static analysis. Figure 14 therefore represents one time instant of this dynamic solution.

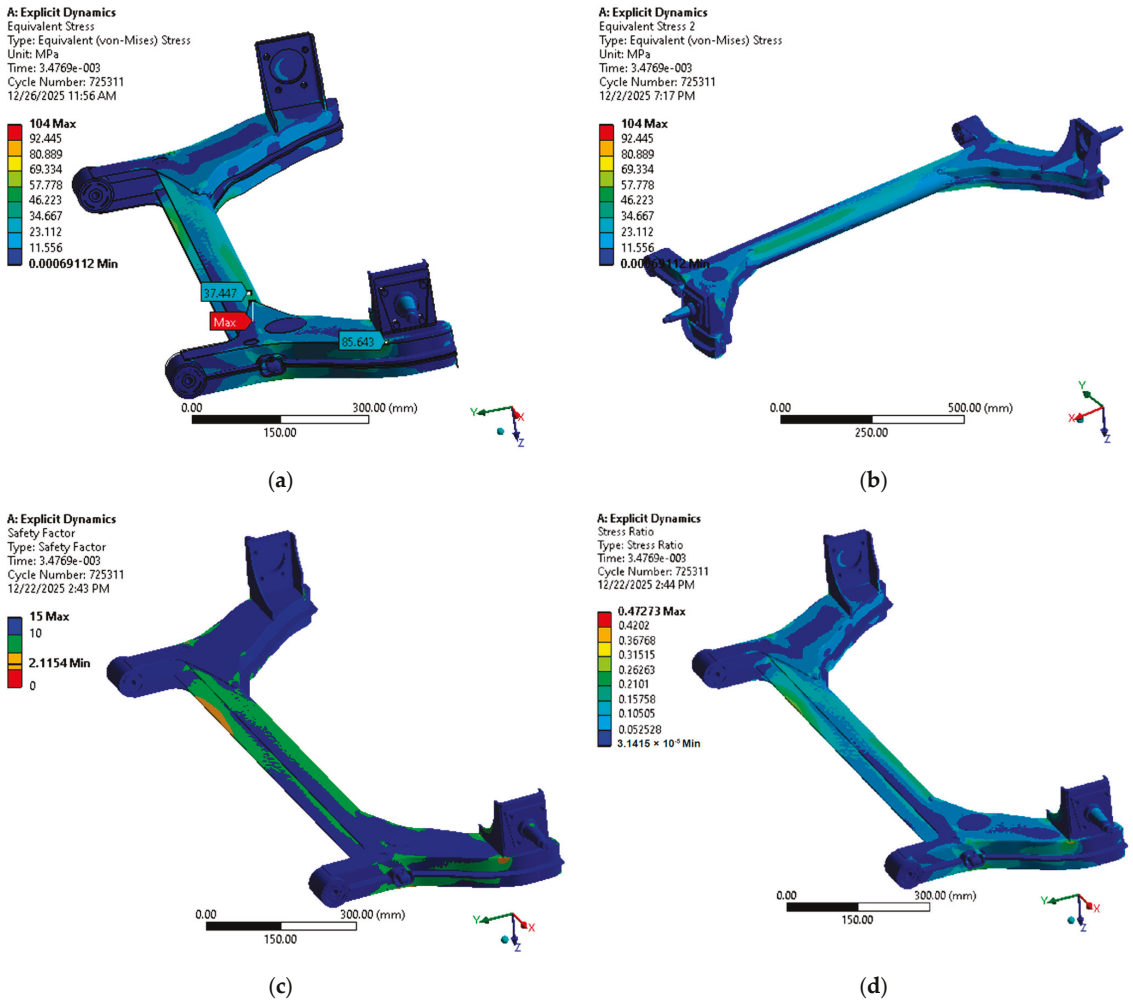

Figure 14. Equivalent (von Mises) stress in the rear axle at the instant of maximum applied load from the explicit dynamic analysis: (**a**) overall view of the axle; (**b**) enlarged view of the right-hand arm and spindle region, highlighting the local stress concentration; (**c**) distribution of the fatigue safety factor over the entire axle; (**d**) distribution of the stress ratio $R = \sigma_{min}/\sigma_{max}$ for the same loading cycle, showing that the most unfavourable stress ratio occurs in the same corner region as the peak von Mises stress and minimum safety factor.

https://doi.org/10.3390/vehicles8010009

The von Mises equivalent stress distribution at the instant of maximum load reveals that the most highly stressed region is the corner area where the bent side plate joins the bent side arm, on the side of the axle where the excitation is applied. In this region, the equivalent stress reaches a maximum of approximately 104 MPa, as illustrated in the contour plots of the FE results. This corner therefore represents a potential fatigue-critical detail and a prime candidate for design optimisation (e.g., by introducing larger radii or local stiffening).

In the central portion of the axle beam, the equivalent stresses are significantly lower but still non-negligible. The FE model predicts a maximum equivalent stress of about 54.6 MPa at the mid-span of the U-shaped cross member, decreasing to approximately 41 MPa in the adjacent areas. These values are consistent with the expectation that the central region is mainly subjected to global bending and torsion rather than to strong local stress concentrations.

The stress levels in the regions corresponding to the strain gauges at the beam heads (points 4–7) and in the trailing arms (points 8–9) are lower than in the aforementioned hot spots but still relevant to fatigue. In particular, the FE analysis yields equivalent stresses of about 27 MPa in the vicinity of points 4–5 and about 41 MPa near points 6–7. Although these locations are geometrically symmetric with respect to the beam mid-span, the local stress values differ because of the complex geometry of the brackets and the presence of additional stiffening features, which slightly modify the local stiffness and stress flow. The stresses in the trailing arms (points 8–9) are smaller, in line with the more compliant geometry and with the larger distance from the main load path.

Overall, all predicted stresses remain well below the yield strength of the axle material for the considered equivalent design load, indicating a comfortable static safety margin. However, the local maxima and the stress gradients identified by the FE analysis are highly relevant for assessing fatigue strength and for guiding possible design improvements.

The von Mises stress field at the instant of maximum applied load is shown in Figure 14. The overall view in Figure 14a indicates that the stress distribution is far from uniform: most of the axle beam is subjected to moderate equivalent stresses below about 60–70 MPa, while significantly higher values appear in the transition regions between the main beam and the side arms. The detailed view in Figure 14b reveals a pronounced local maximum in the corner where the right-hand arm joins the beam and spindle bracket, with a peak equivalent stress of approximately 104 MPa. This confirms that the welded junction between the bent side plate and the arm is the most critical area of the axle for the considered loading case and should be regarded as a potential fatigue hot spot in any subsequent design optimisation.

To evaluate the fatigue relevance of these stress levels, the equivalent stress history obtained from the explicit dynamic analysis was further processed to compute a fatigue safety factor for the axle material, using the nominal S–N curve of the structural steel and the stress range in the stabilised regime. The resulting safety-factor and stress-ratio maps are shown in Figure 14c,d. Figure 14c confirms that most of the axle beam operates with a comfortable fatigue safety margin, while the lowest safety factor is attained in the same corner region where the peak von Mises stress occurs. Figure 14d presents the corresponding stress ratio $R = \sigma_{\min}/\sigma_{\max}$ over the axle surface; the most unfavourable (i.e., lowest) values of R are likewise concentrated in the beam–arm–spindle junction region. This consistency between the von Mises stress field, the fatigue safety factor and the stress-ratio distribution reinforces the identification of this junction as the primary fatigue-critical detail for the considered loading case.

https://doi.org/10.3390/vehicles8010009

5.4. Correlation with Experimental Strain Measurements

To validate the finite element model, the stress results at the nodes corresponding to the strain-gauge locations were compared with the experimental values derived from the strain measurements presented in Section 4.

To quantify the agreement between the numerical model and the measurements, the absolute and relative errors of the peak stresses were evaluated for each strain-gauge location. The absolute error is defined as:

$$\Delta\sigma_{_abs,i} = |\sigma_{_FE,max,i} - \sigma_{_exp,max,i}| \quad (1)$$

The relative error (expressed as a percentage and taken with respect to the FE result) is:

$$\Delta\sigma_{_rel,i} = \Delta\sigma_{_abs,i} / \sigma_{_FE,max,i} \times 100\% \quad (2)$$

where $\sigma_{_exp,max,i}$ is the maximum experimental stress at point i, and $\sigma_{_FE,max,i}$ is the corresponding maximum stress predicted by the finite element model.

The quantitative comparison between experimental and numerical peak stresses is summarised in Table 2, which reports, for each of the nine strain-gauge locations, the maximum experimental stress, the corresponding FE prediction, and the absolute and relative errors. All relative errors remain within a moderate range (typically below about 10–15%), with the smallest discrepancies occurring at the beam mid-span and slightly larger differences in regions where local geometric details (e.g., weld toes, small fillets and local compliance) are necessarily simplified in the FE model. This quantitative agreement supports the earlier qualitative statement that the FE model reproduces both the absolute stress levels and their relative distribution along the axle with sufficient accuracy for design and optimisation purposes.

Table 2. Comparison between experimental and FE peak stresses at the nine strain-gauge locations on the rear axle.

Point No.	Channel	σ_exp,max [MPa]	σ_FE,max [MPa]	Δσ_abs [MPa]	Δσ_rel [%]
1	Sigma 1	0.67	0.55	0.12	21.8
2	Sigma 2	18.93	21.11	2.18	10.3
3	Sigma 3	50.74	54.78	4.04	7.4
4	Sigma 4	8.01	9.56	1.55	16.2
5	Sigma 5	6.92	7.65	0.73	9.5
6	Sigma 6	38.44	34.66	3.78	10.9
7	Sigma 7	21.46	23.11	1.65	7.1
8	Sigma 8	20.00	23.10	3.10	13.4
9	Sigma 9	6.22	7.20	0.98	13.6

For the central portion of the beam, the stresses obtained from the rosette gauges (channels Sigma 1–3) reach peak values of approximately 50.7 MPa during the stabilised cycles. This is in very good agreement with the FE prediction of about 54.7 MPa at the same location, the difference being within 7.4%.

At the beam heads, the experimentally derived stresses in points 4–7 are also of the same order of magnitude as those predicted numerically. The FE model tends to slightly overestimate the stresses on the side where stronger geometric discontinuities are present, which is expected for a model that neglects certain local compliance effects (e.g., small gaps, weld toe geometry). In the trailing arms (points 8–9), both experiment and simulation confirm relatively low stress levels, confirming that these regions are not critical for the current loading case.

https://doi.org/10.3390/vehicles8010009

The FE analysis is therefore used to extend the information obtained from the discrete strain-gauge measurements to the entire axle, identifying stress concentrations and critical regions that cannot be accessed experimentally and providing a reliable basis for fatigue assessment and design optimisation.

6. Design Optimisation of the Rear Axle Wheel Spindle

The results presented in the previous sections show that, for the considered loading case, the highest equivalent stresses are concentrated in the junction regions between the beam, side arms and spindle brackets. Among all components of the rear axle, the wheel spindle, which supports the hub and wheel bearings, is the most safety-critical part: a fracture of the spindle would lead to the loss of the wheel and therefore to a potentially catastrophic failure of the vehicle. For this reason, the spindle is selected as the primary target for design optimisation.

The purpose of this section is to use the validated finite element model as a basis for refining the geometry of the spindle region, with the dual objective of:

- reducing the maximum local stresses and stress gradients in the spindle and its immediate vicinity, thus increasing the fatigue strength and safety margin, and
- preserving the global stiffness and mass characteristics of the axle assembly, so that the overall kinematic and dynamic behaviour of the suspension is not adversely affected.

To this end, the FE model is restricted to the substructure containing the spindle, the adjacent portion of the arm and the beam–arm junction, while the boundary conditions are inherited from the full-axle model (displacements and reaction forces applied on the cut boundaries). The optimisation problem is formulated in terms of a small number of geometric design variables (for example, fillet radii, local thicknesses and transition angles around the spindle base), with the objective of minimising the peak von Mises stress in the spindle region, subject to constraints on mass, stiffness and manufacturability.

In the following subsections, the design variables, objective function and constraints are specified, and the numerical procedure adopted for the iterative FE-based optimisation of the spindle is described.

The optimisation is focused on the geometry of the wheel spindle, which was modelled as a separate, fully parametric component in ANSYS DesignModeler (Figure 15). The sketch defining the spindle profile includes a set of key dimensions—axial lengths $H11$–$H13$, diameters $V8$–$V10$ and fillet radius $R14$—that control the bearing seats, the transition between different sections and the connection to the mounting flange. These dimensions were exposed as design parameters in Workbench and subsequently used as design variables in the response-surface-based optimisation procedure.

The optimisation of the wheel spindle was performed in ANSYS Workbench using the parametric workflow illustrated in Figure 16. First, a Static Structural system (A) was setup, in which the spindle geometry, material data, boundary conditions and loads were defined as in the validated FE model, and a set of key geometric dimensions of the spindle region were promoted as design parameters. These parameters were collected in the Parameter Set and linked to a Response Surface system (B). A Design of Experiments (DoE) was then generated to sample the design space; for each design point, the static analysis was solved and the resulting maximum von Mises stress in the spindle and the corresponding mass were stored as responses.

Based on these results, ANSYS built a response surface metamodel, which was subsequently used in the Response Surface Optimisation system (C) to search for the best combination of design parameters. The optimisation objective was to minimise the peak von Mises stress in the spindle region, while imposing constraints on the component mass

https://doi.org/10.3390/vehicles8010009

and on selected stiffness-related quantities, so that the global behaviour of the rear axle remains compatible with the original design.

In the Design of Experiments module, five input parameters were defined, corresponding to the most influential geometric dimensions of the spindle (Figure 15d). Parameter P1 controls the axial blend length at the transition between the flange and the first bearing seat (Blend1.FD1). Parameters P2 and P3 correspond to the fillet radius *R*14 and to the diameter *V*10 of the central section of the spindle, respectively, while parameters P4 and P5 define the diameters *V*8 and *V*9 of the adjacent sections. These parameters were varied within practical bounds dictated by bearing dimensions, assembly requirements and manufacturability.

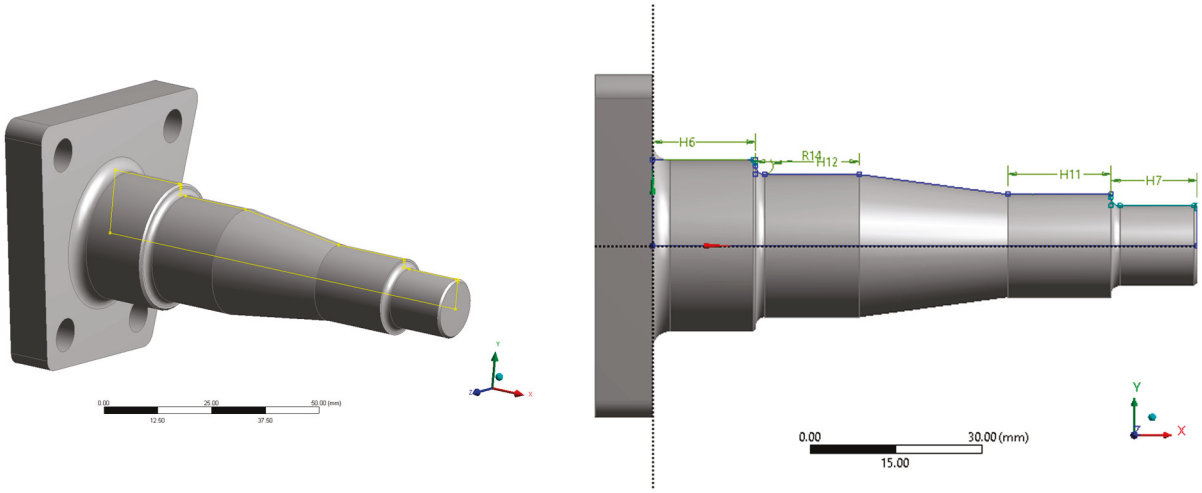

(**a**) (**b**)

Details View

Details of Sketch1	
Sketch	Sketch1
Sketch Visibility	Show Sketch
Show Constraints?	No
Dimensions: 9	
H11	18 mm
H12	18 mm
H13	95 mm
H6	18 mm
H7	15 mm
R14	1.5 mm
V10	12.5 mm
V8	9 mm
V9	15 mm
Edges: 14	
Line	Ln8
Line	Ln9
Line	Ln10
Line	Ln11
Line	Ln13
Line	Ln14
Line	Ln15
Line	Ln17
Line	Ln25
Line	Ln32
Circular Arc	Cr33
Circular Arc	Cr34

(**c**)

Outline of Schematic B2: Design of Experiments

	A	B
1		Enabled
2	Design of Experiments	
3	Input Parameters	
4	Static Structural (A1)	
5	P1 - FBlend1.FD1	☑
6	P2 - XYPlane.R14	☑
7	P3 - XYPlane.V10	☑
8	P4 - XYPlane.V8	☑
9	P5 - XYPlane.V9	☑
10	Output Parameters	
11	Static Structural (A1)	
12	P6 - Solid Mass	
13	P7 - Equivalent Stress Maximum	
14	P8 - Total Deformation Maximum	

(**d**)

Figure 15. Parametric setup of the wheel spindle in ANSYS Workbench: (**a**) 3D CAD model of the spindle with the bearing seats and mounting flange; (**b**) 2D profile sketch with the main dimensional constraints; (**c**) list of geometric parameters defined in Details of Sketch (diameters, fillet radius and axial lengths); (**d**) Design of Experiments table linking the input parameters (P1–P5) to the output responses (solid mass, maximum equivalent von Mises stress and maximum total deformation).

https://doi.org/10.3390/vehicles8010009

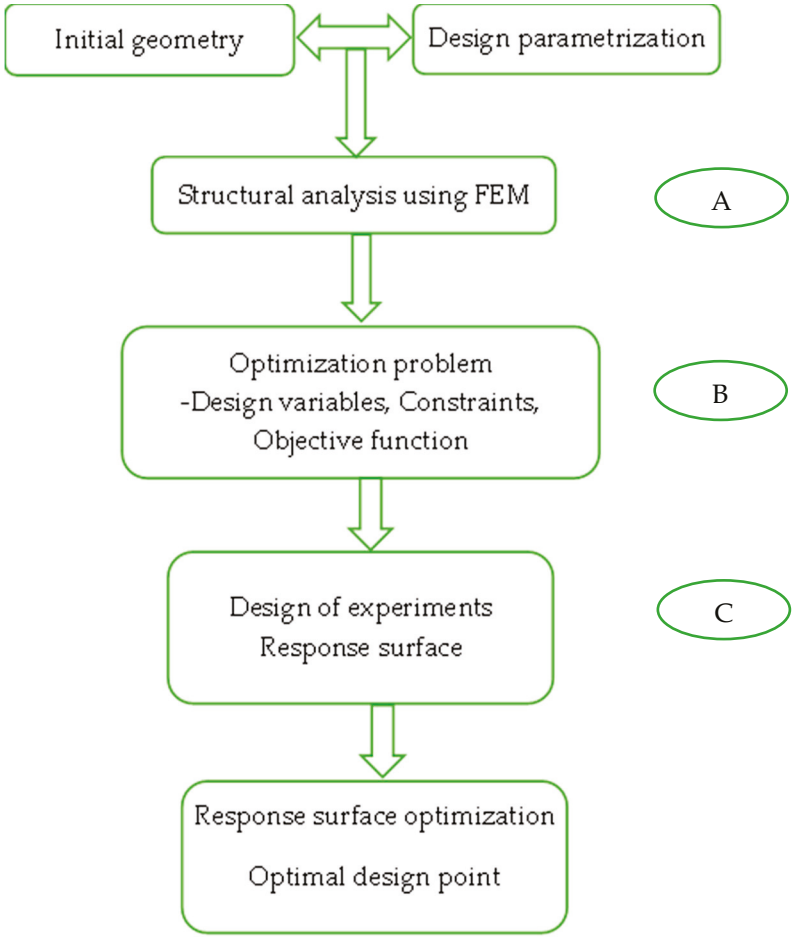

Figure 16. ANSYS Workbench workflow used for the wheel spindle optimisation: parametric Static Structural analysis (A), construction of the response surface based on a design of experiments (B) and response-surface-based optimisation (C).

For each design point in the DoE, the static analysis was solved and three output responses were recorded: P6—the solid mass of the spindle, P7—the maximum equivalent von Mises stress in the spindle region, and P8—the maximum total deformation at the critical nodes. In the subsequent response-surface optimisation, P7 was taken as the objective function to be minimised, while P6 and P8 were used as constraints to ensure that the optimised design does not lead to an unacceptable increase in mass or a reduction in stiffness with respect to the baseline spindle.

The design space explored in the optimisation is defined by the five geometric parameters listed in Table 3. Parameter *P*1 controls the axial length of the blend between the flange and the first bearing seat, while *P*2 specifies the fillet radius at the same junction. Parameters *P*3, *P*4 and *P*5 correspond to the diameters of the central, intermediate and outer spindle sections, respectively, and therefore govern both the local stiffness and the mass of the component. The minimum and maximum levels were selected around the nominal (central) values so as to respect bearing and seal fit requirements, available packaging space and manufacturing constraints, while still allowing sufficient variation to reveal the sensitivity of stress, deformation and mass to each parameter.

The response surfaces in Figure 17 show how the maximum total deformation of the spindle varies with the selected geometric parameters. In Figure 17a, a shallow minimum of *P*8 is observed close to the central values of the blend length *P*1 and fillet radius *P*2; moving towards the lower or upper bounds of these parameters leads to a slight increase in deformation, indicating that excessively small or large transition lengths and fillet

https://doi.org/10.3390/vehicles8010009

radii reduce the local stiffness of the spindle. Figure 17b highlights a stronger influence of the central diameter *P*3: decreasing *P*3 and *P*1 simultaneously produces the largest deformations, whereas combinations with larger diameters and longer blends yield a stiffer spindle. Overall, the surfaces confirm that the candidate design space contains a region where the deformation remains close to the baseline value, which is used as a constraint in the optimisation to avoid an undesirable loss of stiffness.

Table 3. Design-of-experiments (DoE) input parameters used for the wheel spindle optimisation.

Parameter	ANSYS Label	Central Value	Minimum Level	Maximum Level	Unit	Description
P1	Blend1.FD1	3.0	2.7	3.3	mm	Axial blend length at transition between flange and first bearing seat
P2	R14	1.5	1.35	1.65	mm	Fillet radius at junction between flange and spindle
P3	V10	12.5	12.146	12.854	mm	Diameter of the central spindle section
P4	V8	9.0	8.745	9.255	mm	Diameter of the section adjacent to the flange
P5	V9	15.0	13.5	16.5	mm	Diameter of the outer spindle section (near the wheel bearings)

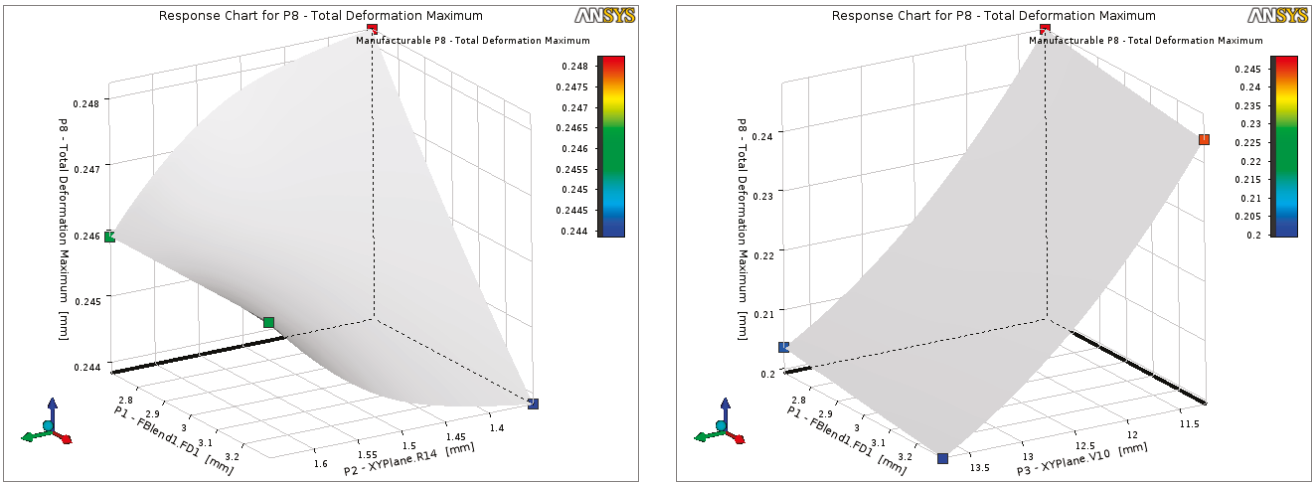

(**a**) (**b**)

Figure 17. Response surfaces for the maximum total deformation *P*8 of the wheel spindle obtained from the DoE: (**a**) effect of the axial blend length *P*1 (Blend1.FD1) and fillet radius *P*2 (R14); (**b**) effect of the axial blend length *P*1 and the central diameter *P*3 (V10).

The influence of the geometric parameters on the maximum equivalent von Mises stress is illustrated by the response surfaces in Figure 18. In Figure 18a, the stress level decreases when both the blend length *P*1 and the fillet radius *P*2 are increased, indicating that smoother and more gradual transitions between the flange and the spindle significantly reduce the local stress concentration. The lowest stresses are obtained near the upper bounds of *P*1 and *P*2, whereas the most compact geometry (short blend and small radius) leads to the highest stresses.

Figure 18b shows a pronounced dependence on the central diameter *P*3: increasing *P*3 results in a marked reduction in the maximum stress, while smaller diameters yield higher stress levels even if *P*1 is increased. This confirms that both the cross-sectional area and the transition geometry play an important role in controlling the peak stresses in the spindle region. Consequently, the optimisation process favours combinations with slightly larger

diameters and generous transition blends, within the constraints imposed by bearing fit and overall packaging.

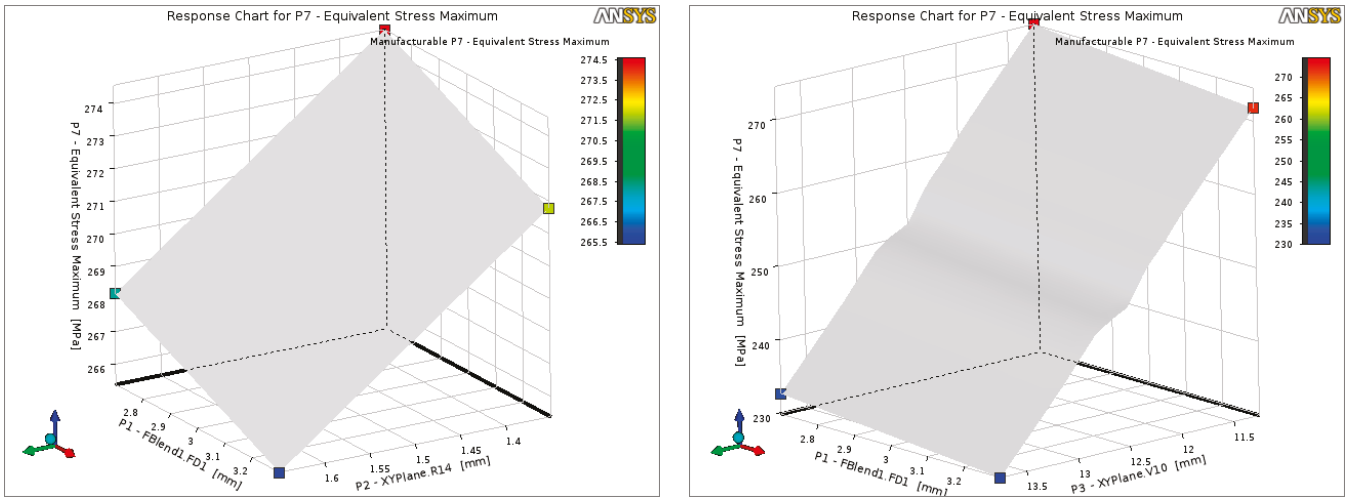

(**a**) (**b**)

Figure 18. Response surfaces for the maximum equivalent von Mises stress *P*7 in the wheel spindle: (**a**) combined effect of axial blend length *P*1 (Blend1.FD1) and fillet radius *P*2 (R14); (**b**) combined effect of axial blend length *P*1 and central diameter *P*3 (V10).

The influence of the design variables on the spindle mass is shown in Figure 19. In Figure 19a, the response surface exhibits a shallow bowl-shaped profile, indicating that variations in the blend length *P*1 and fillet radius *P*2 within the selected bounds have only a modest effect on the solid mass *P*6. Increasing *P*1 and *P*2 simultaneously leads to a slight mass increase, whereas the smallest values yield the lightest but also the most highly stressed designs. Figure 19b reveals that the mass is much more sensitive to the central diameter *P*3: reductions of *P*3 produce a noticeable mass saving, while larger diameters increase *P*6 almost linearly. These trends confirm that the optimisation must balance the beneficial effect of larger diameters and generous blends on stress reduction against the associated penalty in mass, which is enforced in the optimisation as an upper bound on *P*6.

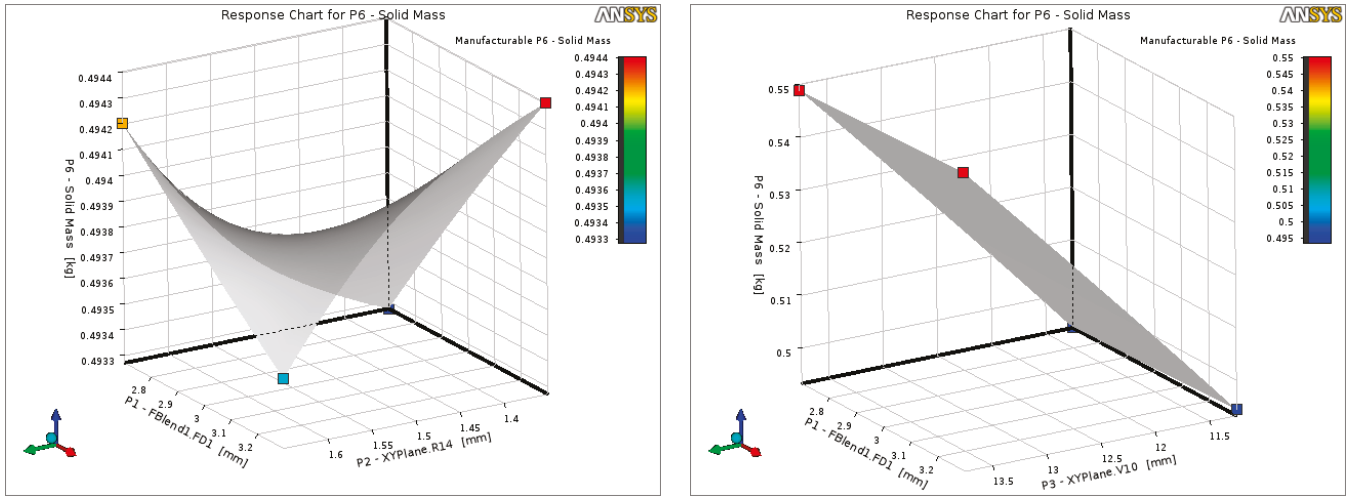

(**a**) (**b**)

Figure 19. Response surfaces for the spindle solid mass *P*6: (**a**) combined effect of axial blend length *P*1 (Blend1.FD1) and fillet radius *P*2 (R14); (**b**) combined effect of axial blend length *P*1 and central diameter *P*3 (V10).

https://doi.org/10.3390/vehicles8010009

The analysis of the response surfaces confirms that the geometric parameters selected for the spindle have a clear and physically meaningful influence on all three output quantities. Larger blend length *P*1 and fillet radius *P*2 systematically reduce the maximum equivalent stress, with only a minor penalty in mass and stiffness, while the central diameter *P*3 has the strongest effect, simultaneously decreasing stress and deformation but increasing mass. As a result, the optimum region of the design space is found for combinations with relatively generous blends and fillets and a moderately increased central diameter, which provide a significant reduction in peak stress at almost unchanged total deformation and with only a limited increase in mass.

The response-surface optimisation was carried out in ANSYS Workbench using the MOGA (Multi-Objective Genetic Algorithm) method, with the two objectives defined as minimise mass P6 and minimise maximum equivalent stress P7. The algorithm started from 100 initial samples and, with 100 samples per iteration, converged after 32 evaluations, yielding three non-dominated solutions (Candidate Points 1–3). As summarised in the optimisation Table 4, Candidate Point 1 corresponds to the geometry with P1 = 3.3 mm, P2 = 1.65 mm, P3 = 13.75 mm, P4 = 8.1 mm and P5 = 16.5 mm. This design provides the lowest maximum equivalent stress in the spindle region (P7 = 184.9 MPa), at the cost of a moderate increase in solid mass (P6 = 0.589 kg) compared with the lighter Candidate Point 2. Given the safety-critical nature of the spindle, the reduction in peak stress is prioritised over the small mass penalty, and Candidate Point 1 is therefore selected as the optimal spindle geometry for further assessment.

Table 4. Optimisation results for the wheel spindle geometry: design parameters and objective functions for the three candidate solutions.

Parameter	Unit	Candidate Point 1	Candidate Point 2	Candidate Point 3
P1—Blend1.FD1	mm	3.30	3.30	2.70
P2—R14	mm	1.65	1.65	1.65
P3—V10	mm	13.75	11.25	13.75
P4—V8	mm	8.10	8.10	8.10
P5—V9	mm	16.50	13.50	16.50
P6—Solid mass	kg	0.5887	0.4935	0.5895
P7—Equivalent stress max.	MPa	184.92	265.38	187.72

The von Mises stress field for the optimised spindle geometry (Candidate Point 1) is shown in Figure 20. The global maximum of about 220 MPa occurs at the edge of a bolt hole in the mounting flange, whereas the stresses in the safety-critical transition between the flange and the spindle shaft are reduced to approximately 180–185 MPa. Compared with the baseline design, this corresponds to a clear reduction in the peak stress in the spindle fillet while keeping the overall stress level in the surrounding flange at a similar magnitude, confirming the effectiveness of the geometric changes identified by the optimisation.

The spindle analysis was carried out under the maximum admissible wheel load transmitted through the two bearing seats, as illustrated in Figure 20a. The load is applied as two concentrated forces acting on the cylindrical regions corresponding to the inner rings of the bearings (A and B), with magnitudes of 2500 N and 3500 N, respectively, consistent with the bearing manufacturer's load ratings for the considered axle. All stress results presented for the baseline and optimised spindle therefore refer to this worst-case bearing load combination. The highest stresses in the spindle fillet are around 180–185 MPa, significantly lower than in the baseline design.

https://doi.org/10.3390/vehicles8010009

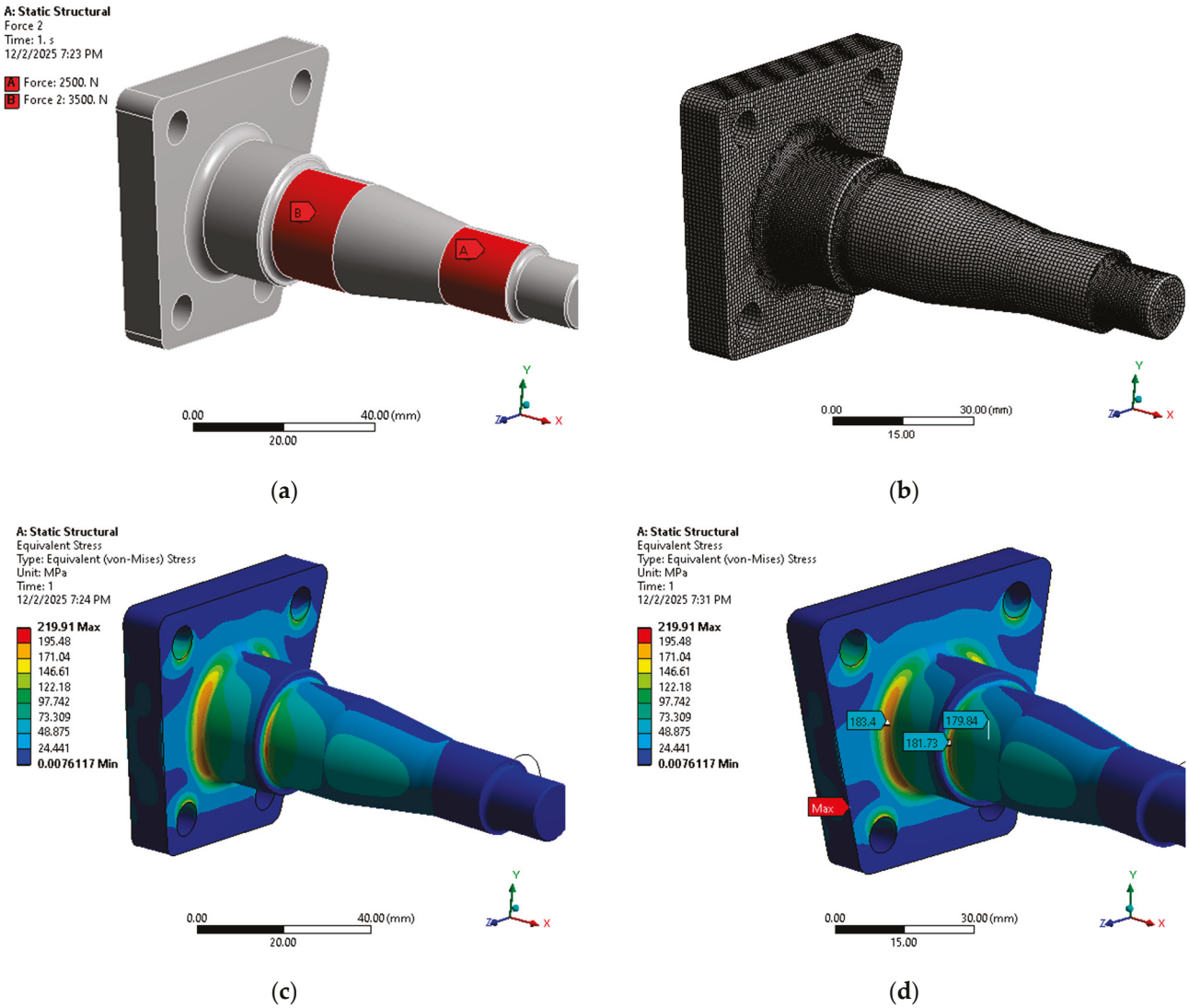

Figure 20. Static structural analysis of the optimised wheel spindle under the maximum admissible wheel load: (**a**) loading configuration with forces of 2500 N and 3500 N applied on the two bearing seats; (**b**) finite element mesh of the spindle and mounting flange; (**c**) global equivalent von Mises stress distribution; (**d**) detailed view of the transition region between the flange and spindle, showing stress levels around 180–185 MPa in the fillet.

7. Discussion

The results obtained from the combined multibody, experimental and FE analyses provide a coherent picture of the structural behaviour of the rear axle under durability loading and highlight several aspects that are directly relevant for design optimisation.

First, the flexible multibody model of the test bench and rear axle proved to be an effective tool for defining realistic boundary conditions for the structural analysis. By tuning the kinematic excitation so that the translational and rotational amplitudes of the axle and stabiliser bar match those observed in service, the reaction forces at the wheel spindles and in the key joints of the mechanism could be determined in a manner consistent with the actual stiffness of the suspension assembly. This is an important difference compared with purely static approaches in which arbitrary loads are applied to the axle, and it explains why the equivalent design load used in the FE model is significantly lower than typical peak service loads: it represents the reaction corresponding to the prescribed displacement imposed by the fatigue test bench, not the absolute worst-case wheel load.

https://doi.org/10.3390/vehicles8010009

The experimental strain measurements confirm that the stand reproduces a highly repeatable cyclic loading condition, with stable amplitudes and phases over many cycles. The good agreement between measured and simulated stresses—differences of about 10% at the beam mid-span and comparable magnitudes at the other instrumented points—indicates that the FE model successfully captures both the global stiffness of the axle and the local stress distribution in the regions of interest. This level of correlation is satisfactory for design purposes and justifies the use of the FE model to extrapolate the stress field to locations that are not instrumented experimentally and to perform parametric modifications that would be difficult or expensive to test directly.

The FE stress maps show that the most critical areas are not located in the mid-span of the axle beam, where the stresses are moderate and well distributed, but rather in the junction regions between the beam, side arms and spindle brackets. This observation is consistent with classical fatigue design principles, which identify geometric discontinuities and load-path changes as typical origins of crack initiation. In particular, the corner at the base of the spindle stands out as a clear hot spot. The fact that this region is also the most safety-critical from a functional point of view (loss of the wheel in case of fracture) motivates the decision to focus the optimisation effort on the wheel spindle geometry.

The response-surface-based optimisation provides additional insight into the sensitivity of the spindle behaviour to changes in key geometric parameters. The response surfaces for deformation, stress and mass show that the central diameter and the transition geometry (blend length and fillet radius) play distinct roles: increasing these dimensions tends to reduce the maximum equivalent stress and deformation, at the expense of a moderate increase in mass. Within the practical bounds dictated by bearing fits and packaging, the algorithm identifies an optimum region with generous blends and a slightly larger central diameter, where the peak stress is substantially reduced while the increase in mass and the change in stiffness remain limited. Candidate Point 1, selected as the optimal design, embodies this compromise and demonstrates how small, targeted geometric changes can significantly improve fatigue strength without redesigning the entire axle.

In the present study, the rear axle FE model is analysed using the Explicit Dynamics solver in ANSYS, i.e., as a transient dynamic problem rather than a purely static analysis. The excitation frequency of the test bench (about 2.5 Hz) is well below the lowest bending modes of the axle, so that the response in the stabilised regime is dominated by quasi-static behaviour and no significant resonance effects are observed. For fatigue assessment under such low-frequency, non-resonant loading, validation based on stress amplitudes at the strain-gauge locations is therefore adequate and has been performed in Section 5.4. A full modal and dynamic validation of the FE model (e.g., via experimental modal analysis and comparison of frequency response functions) is planned as future work, once additional instrumentation becomes available, and will further strengthen the dynamic characterisation of the rear axle.

Several limitations of the present study should also be acknowledged. The analysis focuses on a single, predominantly vertical loading case representative of a specific durability test; other loading scenarios (e.g., combined vertical and lateral loads, braking or cornering events) have not yet been considered. Material behaviour has been assumed linear elastic, and the fatigue assessment is currently based on stress levels rather than a full life prediction using S–N or ε–N curves. The models of rubber bushings and joints are simplified, and weld geometries are idealised, which may influence local stress peaks. These aspects point towards natural extensions of the work, including multi-load-case optimisation, more detailed modelling of joints and weld toes, and integration of fatigue-life criteria directly into the optimisation loop.

https://doi.org/10.3390/vehicles8010009

Moreover, the experimental campaign was carried out on a single representative axle specimen, so that statistical scatter due to material and manufacturing variability could not be quantified; extending the study to a larger sample of axles and incorporating probabilistic fatigue assessment will be an important topic for future work.

Despite these limitations, the study demonstrates that integrating a validated test bench, flexible multibody simulation, FE analysis and response-surface optimisation forms a powerful framework for the design and refinement of safety-critical suspension components. The methodology is generic and can be transferred to other axle types, front-suspension links or even to different vehicle classes, facilitating systematic improvements in durability with a controlled impact on weight and cost.

8. Conclusions

This work presented an integrated numerical–experimental methodology for the durability assessment of a passenger-car rear axle, combining a dedicated test bench, flexible multibody simulation in MSC ADAMS and explicit dynamic finite element analysis in ANSYS.

The main outcomes can be summarised as follows:

- A rear suspension durability test bench was designed and built to reproduce, in a controlled and repeatable manner, the cyclic loading acting on a dependent rear axle. The kinematic layout of the rocker mechanism and the symmetric excitation of the wheel-spindle regions were chosen such that the translational and rotational amplitudes of the axle and stabiliser bar are representative of real operating conditions.
- A detailed flexible multibody model of the bench–axle system was developed in ADAMS, including deformable representations of the rear axle and stabiliser bar. The simulations provided time histories of displacements, deformations and joint reaction forces, and allowed the equivalent design load applied at the wheel spindles to be defined in a way consistent with the actual stiffness of the suspension assembly.
- An experimental strain analysis was carried out on the rear axle mounted on the test bench, using nine strain-gauge locations strategically placed along the beam, heads and trailing arms. The recorded stresses in the stabilised regime showed excellent repeatability over successive cycles and confirmed the predominantly bending–torsion loading mode.
- An explicit dynamic FE model of the rear axle was built in ANSYS, with boundary conditions mirroring the stand configuration and loads taken from the multibody simulation. The von Mises stress field highlighted a critical region in the corner where the bent side plate joins the side arm (peak stress $\approx$ 104 MPa), as well as moderate but relevant stresses in the beam mid-span and in the beam heads.
- A quantitative correlation between FE predictions and experimental stresses at the strain-gauge locations showed differences within about 10% at the beam mid-span and similar orders of magnitude at the other points. The model thus reproduces both the absolute stress levels and the relative distribution along the axle, correctly identifying the same fatigue-critical areas as the measurements.
- On the basis of these results, the wheel spindle was identified as the most safety-critical component of the rear axle, since its failure would immediately lead to wheel loss. A dedicated parametric FE model of the spindle was therefore developed and analysed under the maximum admissible wheel load applied on the two bearing seats.
- A design-of-experiments study and response-surface-based optimisation (MOGA) were carried out in ANSYS Workbench, using five geometric design variables and three responses (maximum equivalent stress, maximum total deformation and mass). The optimisation led to an improved spindle geometry (Candidate Point 1) featuring

https://doi.org/10.3390/vehicles8010009

smoother transitions and slightly modified diameters. For this design, the von Mises stresses in the critical fillet between the flange and spindle remain around 180–185 MPa under the severe loading case corresponding to the maximum admissible wheel load at the bearings, while the increase in mass is modest and compatible with practical design constraints.

Overall, the results demonstrate that the combined use of a dedicated test bench, flexible multibody simulation and explicit dynamic FE analysis provides a robust and consistent framework for the structural assessment and optimisation of rear axle assemblies, but also for the targeted optimisation of safety-critical components such as the wheel spindle. The methodology can be extended to alternative axle geometries, different suspension layouts and more complex loading histories, and forms a solid basis for future work on design optimisation and fatigue life prediction under representative service conditions.

Supplementary Materials: The following supporting information can be downloaded at: https://www.mdpi.com/article/10.3390/vehicles8010009/s1, Video S1: Flexible multibody simulation of the rear axle on the durability bench, Video S2: Experimental tests on the bench; Video S3: Experimental data acquisition on the bench.

Author Contributions: Conceptualization, I.D.G. and I.D.; methodology, I.D.G. and I.D.; software, I.D.G.; validation, L.R. and C.C.; formal analysis, I.D.G.; investigation, I.D.G.; resources, I.D.; data curation, C.C.; writing—original draft preparation, I.D.G.; writing—review and editing, I.D.G.; visualisation, L.R.; supervision, I.D.; project administration, I.D.; funding acquisition, I.D. All authors have read and agreed to the published version of the manuscript.

Funding: This research received no external funding.

Data Availability Statement: The data supporting the findings of this study are available from the corresponding author upon reasonable request.

Acknowledgments: The authors would like to thank Ion Manea and Valeriu Ionică for their support in the experimental campaign and test bench operation. All analyses, results and scientific interpretations were produced and critically reviewed by the authors.

Conflicts of Interest: The authors declare no conflicts of interest.

References

1. Gobbi, M.; Haque, I.; Papalambros, P.; Mastinu, G. A critical review of optimization methods for road vehicles design. In Proceedings of the 11th AIAA/ISSMO Multidisciplinary Analysis and Optimization Conference, Portsmouth, VA, USA, 6–8 September 2006; p. 6998. [CrossRef]
2. Yıldız, A.R.; Özkaya, H.; Yıldız, M.; Bureerat, S.; Yıldız, B.S.; Sait, S.M. The equilibrium optimization algorithm and the response surface-based metamodel for optimal structural design of vehicle components. *Mater. Test.* **2020**, *62*, 492–496. [CrossRef]
3. Kumar, G.S.; Kumaraswamidhas, L.A. Design optimization focused on failures during developmental testing of the fabricated rear-axle housing. *Eng. Fail. Anal.* **2021**, *120*, 104999. [CrossRef]
4. Zheng, B.; Fu, S.; Lei, J. Topology optimization and multiobjective optimization for drive axle housing of a rear axle drive truck. *Materials* **2022**, *15*, 5268. [CrossRef]
5. Topac, M.M.; Karaca, M.; Aksoy, B.; Deryal, U.; Bilal, L. Lightweight design of a rear axle connection bracket for a heavy commercial vehicle by using topology optimisation: A case study. *Mechanics* **2020**, *26*, 64–72. [CrossRef]
6. Park, J.H.; Kim, S.K.; Choi, B.I.; Lee, H.J.; Lee, Y.H.; Kim, J.S.; Kim, K.J. Optimal design of rear chassis components for lightweight automobile using design of experiment. *Mater. Und Werkst.* **2010**, *41*, 391–397. [CrossRef]
7. Topaç, M.M.; Tanrıverdi, A.; Çolak, O.; Bilal, L.; Maviş, M. Analysis of the failure modes and design improvement of an eccentrically loaded connecting rod for a double front axle steering linkage prototype. *Eng. Fail. Anal.* **2021**, *122*, 105204. [CrossRef]
8. Jeong, T.; Lee, S.B.; Yim, H.J. Shape optimization of a torsion beam axle for improving vehicle handling performance. *Int. J. Automot. Technol.* **2017**, *18*, 813–822. [CrossRef]
9. Balta, B.; Erk, O.; Solak, H.A.; Durakbasa, N. Pareto optimization of heavy duty truck rear underrun protection design for regulative load cases. *SAE Int. J. Commer. Veh.* **2014**, *7*, 726–735. [CrossRef]

10. Senniappan, M.; More, R.; Bhide, S.; Gowda, S. *Optimization of Commercial Vehicle's Steering Tie Rod Arm Design Based on Strain Life Approach (No. 2016-01-0381)*; SAE Technical Paper: Warrendale, PL, USA, 2016. [CrossRef]
11. Zhou, J.; Du, Z.; Liao, Y.; Tang, A. An optimization design of vehicle axle system based on multiobjective cooperative optimization algorithm. *J. Chin. Inst. Eng.* **2018**, *41*, 635–642. [CrossRef]
12. Hao, Y.D.; He, Z.C.; Li, G.Y.; Li, E.; Huang, Y.Y. Uncertainty analysis and optimization of automotive driveline torsional vibration with a driveline and rear axle coupled model. *Eng. Optim.* **2018**, *50*, 1871–1893. [CrossRef]
13. Soares, E.J.; De Carvalho, D.M.; Onusic, H.; Barreiro, J.A.; Ferraro, L.C. *Development of A Test Bench for Static and Dynamic Tests of A Spring Leaf for the Suspension of Commercial Vehicles (No. 1999-01-2990)*; SAE Technical Paper: Warrendale, PL, USA, 1999. [CrossRef]
14. de Jesus Soares, E.; Oliva, A.M.; Adas, C.A.; Dusi, F.C.; Santos, P.S.P.; Accurso, M.A.F.; Kliewer, M. *Development of A Multiaxial Bench Test for the Suspension of Commercial Vehicles (No. 2014-36-0019)*; SAE Technical Paper: Warrendale, PL, USA, 2014. [CrossRef]
15. Mitra, A.C.; Kiranchand, G.R.; Soni, T.; Banerjee, N. Design of experiments for optimization of automotive suspension system using quarter car test rig. *Procedia Eng.* **2016**, *144*, 1102–1109. [CrossRef]
16. Mitra, A.C.; Soni, T.; Kiranchand, G.R. Optimization of automotive suspension system by design of experiments: A nonderivative method. *Adv. Acoust. Vib.* **2016**, *2016*, 3259026. [CrossRef]
17. Salah, M. A Laboratory Automotive Suspension Test Rig: Design, Implementation and Integration. *Jordan J. Mech. Ind. Eng.* **2017**, *11*, 67–71.
18. Alzughaibi, A.; Xue, Y.; Grosvenor, R. A new insight into modelling passive suspension real test rig system with consideration of nonlinear friction forces. *Proc. Inst. Mech. Eng. Part D J. Automob. Eng.* **2019**, *233*, 2257–2266. [CrossRef]
19. Siqueira, M.A.; Gomes, P.C.; Teixeira, E.L.S.; Fortaleza, E.L.F.; Morais, M.V.G. *Automation of A Quarter-Car Suspension Test Bench (No. 2024-36-0115)*; SAE Technical Paper: Warrendale, PL, USA, 2024. [CrossRef]
20. Liao, Z.C.; Bai, X.X.F.; Li, Y.; Deng, X.C.; Sun, J. Design, modeling, and verification of a test bench for braking simulation of 1/4 vehicle. *Proc. Inst. Mech. Eng. Part D J. Automob. Eng.* **2020**, *234*, 1425–1441. [CrossRef]
21. Croce, P.; Orsini, P.; Salvatore, W. Vibration isolation and design of automotive test benches. *Eng. Struct.* **2001**, *23*, 945–956. [CrossRef]
22. Favilli, F.; Sgamma, M.; Bucchi, F.; Frendo, F.; Leandri, P.; Losa, M. A Novel Tire and Road Testing Bench for Modern Automotive Needs. *Designs* **2024**, *8*, 64. [CrossRef]
23. Mántaras, D.A.; Luque, P. Virtual test rig to improve the design and optimisation process of the vehicle steering and suspension systems. *Veh. Syst. Dyn.* **2012**, *50*, 1563–1584. [CrossRef]
24. El Hadraoui, H.; Zegrari, M.; Hammouch, F.E.; Guennouni, N.; Laayati, O.; Chebak, A. Design of a customizable test bench of an electric vehicle powertrain for learning purposes using model-based system engineering. *Sustainability* **2022**, *14*, 10923. [CrossRef]
25. Andert, J.; Klein, S.; Savelsberg, R.; Pischinger, S.; Hameyer, K. Virtual shaft: Synchronized motion control for real time testing of automotive powertrains. *Control. Eng. Pract.* **2016**, *56*, 101–110. [CrossRef]
26. Fathi, H.; El-Sayegh, Z.; Ren, J.; El-Gindy, M. Modeling and validation of a passenger car tire using finite element analysis. *Vehicles* **2024**, *6*, 384–402. [CrossRef]
27. Patil, P.J.; Inamdar, P.G.; Joshi, K.D.; Mulik, P.V.; Jadhav, M.R. Experimental and Finite Element Analysis of Reinforced Composite Front Drive Axle. *Indian J. Sci. Technol.* **2022**, *15*, 2230–2239. [CrossRef]
28. Lockett, J.; Fahad, M.; Awan, A.W.; Islam, S. A Digital Testing Framework for Design Improvements of Three-Piece Alloy Wheels Through Finite Element Analysis. *Appl. Sci.* **2025**, *15*, 11654. [CrossRef]
29. Poungkom, V.; Pimsarn, M. Effectiveness of various finite element analysis method for the dynamic cornering fatigue test of an automotive wheel. In *AIP Conference Proceedings*; AIP Publishing LLC: Melville, NY, USA, 2024; Volume 3086, p. 030009. [CrossRef]
30. Do, D.T.; Kim, S.H.; Park, J.K. The Development of Automotive Rear Coupled Torsion Beam Axle Using Finite Element Analysis for Deformation Compensation: The Development of Automotive Rear Coupled. *Int. J. Automot. Technol.* **2025**, *26*, 1231–1242. [CrossRef]
31. Lozia, Z. Application of Modelling and Simulation in Durability Tests of Vehicles and Their Components. *Energies* **2022**, *15*, 9398. [CrossRef]
32. Kalinsky, M.; Sykora, M.; Markova, J.; Maňas, P. Nonlinear dynamic finite element analysis of vehicle impacts into road restraint systems. *Results Eng.* **2024**, *23*, 102726. [CrossRef]
33. Salanke, S.R.S.; Shantha Raju, S.; SS, T.; Srinivas, N.K.; Khot, M.B. A review on finite element modelling and experimental analysis of crashworthiness design of automotive body. *Int. J. Crashworthiness* **2025**, *30*, 471–495. [CrossRef]
34. Ambrosio, J.; Carvalho, M.; Milho, J.; Escalante, S.; Martin, R. A validated railway vehicle interior layout with multibody dummies and finite element seats models for crash analysis. *Multibody Syst. Dyn.* **2022**, *54*, 179–212. [CrossRef]
35. Cheng, J.; Wang, Z.; Zhao, X.; Xu, Z.; Ding, M.; Takeda, K. A Survey on Testbench-Based Vehicle-in-the-Loop Simulation Testing for Autonomous Vehicles: Architecture, Principle, and Equipment. *Adv. Intell. Syst.* **2024**, *6*, 2300778. [CrossRef]

36. Lukoševičius, V.; Makaras, R.; Rutka, A.; Keršys, R.; Dargužis, A.; Skvireckas, R. Investigation of vehicle stability with consideration of suspension performance. *Appl. Sci.* **2021**, *11*, 9778. [CrossRef]
37. Czerwinski, F. Current trends in automotive lightweighting strategies and materials. *Materials* **2021**, *14*, 6631. [CrossRef] [PubMed]
38. Stirosu, M.; Tabacu, S.; Cimpeanu, G. Investigation on the Manufacturing, Testing, and Simulation Processes of the Hood Hinge Assembly. *Vehicles* **2025**, *7*, 157. [CrossRef]

Disclaimer/Publisher's Note: The statements, opinions and data contained in all publications are solely those of the individual author(s) and contributor(s) and not of MDPI and/or the editor(s). MDPI and/or the editor(s) disclaim responsibility for any injury to people or property resulting from any ideas, methods, instructions or products referred to in the content.

vehicles

MDPI

Article

Filtration System for Reducing CO_2 Concentration from Combustion Gases of Used Spark Ignition Engines

Radu Tarulescu *, Stelian Tarulescu *, Razvan Gabriel Boboc and Mircea Nastasoiu

Department of Automotive and Transport Engineering, Transilvania University of Brasov, 500036 Brasov, Romania; razvan.boboc@unitbv.ro (R.G.B.); m.nastasoiu@unitbv.ro (M.N.)
* Correspondence: radu.tarulescu@unitbv.ro (R.T.); s.tarulescu@unitbv.ro (S.T.); Tel.: +40-727-576-747 (R.T.)

Abstract

This research paper proposes a solution to reduce CO_2 emissions from a spark ignition engine's exhaust gases by installing a filtration system on the vehicle's exhaust pipe. The analyzed filtration system was not patented and was in the testing stage. Tests will also be carried out on the stand. The tested system can be used to reduce CO_2 levels in automotive exhaust gases and for static applications (generators, internal combustion engine test stands, fossil fuel power generation systems). The need for a system to reduce pollutant emissions emerged with the average age in Europe. In proper conditions, some vehicles can use this type of filtration system. The tested vehicle is a vehicle (produced in 2009) equipped with a 75HP Spark Ignition Engine. The CO_2 filtration system consists of a container containing a reactive aqueous solution comprising water, CaO, and MgO. Four tests were performed: the first without a filter, and the other three with the filter placed at different distances from the exhaust pipe end to the reactive solution surface. The tests consisted of evaluating the exhaust gases from the cold start of the engine and running (idle engine speed) until the engine reached the optimal operating temperature. The test procedure involved saving the data collected by the analyzer every 10 s for each of the four tests performed (the duration of a test was 1050 s). The first test (No. 1) was performed without the use of the filtering system. Tests 2, 3, and 4 were carried out using the filtering system and changing the distance between the exhaust gases' outlet point and the surface of the aqueous substance. All tests were carried out under similar conditions. Data specific to the test of engines were collected—emissions (CO_2, CO, NO_x), ambient temperature, and exhaust temperature. The tests were analyzed and compared, and the highest CO_2 reductions without increases in CO or NO_x were observed in Tests 3 and 4. Based on the detailed analysis of the values obtained from the four tests, the system was efficient. The tests will continue on experimental engines from test stands, to develop a prototype filter for primarily static applications with internal combustion engines: test stands for engines and generators, and, after homologation, directly on vehicles. The paper aims to partially solve an important problem—reducing the level of CO_2 from the exhaust gases. The presented solution may have applicability in the automotive industry but is also feasible for static applications. Another objective is to reduce emissions from older vehicles, which are widespread in certain regions of Europe and worldwide.

Keywords: emissions; filtration system; carbon dioxide; testing spark ignition engine

1. Introduction

The major concern of modern society about global warming is the rise in atmospheric carbon dioxide (CO_2) concentration above 410 parts per million (ppm), from below 300 ppm in the pre-industrial period. The continuous rise in Earth's surface is strongly linked to atmospheric carbon dioxide concentrations, which are the main contributor to climate change [1].

One of the main factors that increases global carbon dioxide concentrations is the use of internal combustion engines. Whether it is standard vehicles, transport vehicles, airplanes, trains, or maritime vessels, all use internal combustion engines for propulsion. That is why it is very important to develop as many filtration systems as possible to reduce the levels of these emissions, including carbon dioxide.

In this study, the authors propose an exhaust gas filtration system for a spark ignition engine from a 2009 vehicle to reduce emissions, including carbon dioxide levels. The purpose of creating such a system is to be implemented on vehicles older than 10 years to ensure compliance with pollution standards.

The need to implement such systems has come with the increase in the average age of vehicles in Europe. According to the interactive study by ACEA (Driving Mobility for Europe) [2], the average age of vehicles in Europe ranges from about 10 years (in most European countries) to 17 years (in Greece), as shown in Figure 1.

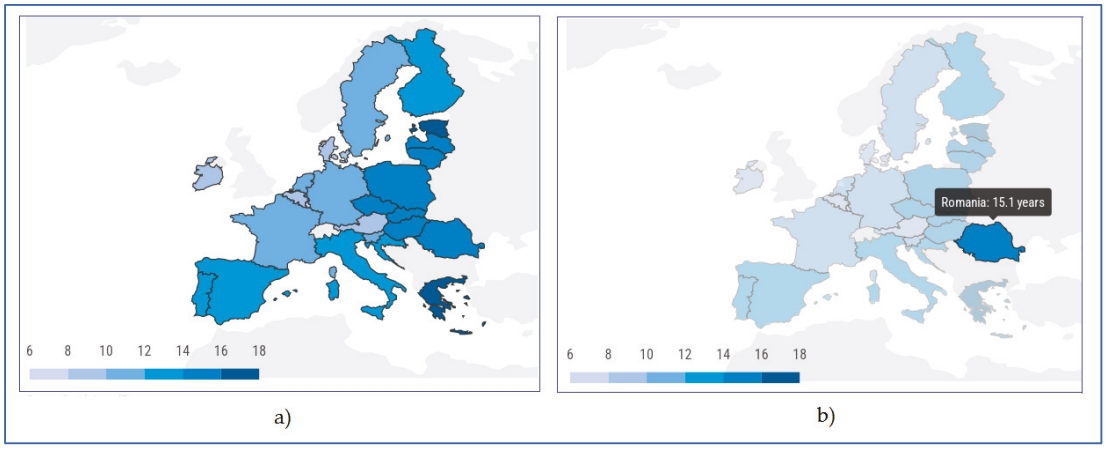

Figure 1. (**a**) The average age of vehicles in Europe; (**b**) the average age of vehicles in Romania, where the research was conducted.

In Romania, Brasov city, where the research was conducted, the average age of vehicles is about fifteen years. Almost all the countries of Eastern Europe have similar values.

With the ongoing global climate crisis, the need to develop more effective technologies for carbon dioxide capture is increasing. Many systems have been studied and various technologies have been implemented, indicating a strong interest.

CO_2 Capture and Storage (CCS) technologies were developed to reduce carbon dioxide emissions from the coal, oil, and gas industries, as noted in [3–7]. For example, paper [8] presents different methods for selecting a more suitable application method for capturing and storing CO_2 to further improve the emission absorption efficiency.

For now, around 10% of CO_2 emissions has been utilized or converted through different means, like in article [9] where a technology named Cross-borehole Electrical Resistivity Tomography (CHERT) by the authors has been implemented in the CO_2 Capturing and Storing field, in order to optimize the design of the ERT electrode arrays and corresponding working schemes for lab research experiments.

https://doi.org/10.3390/vehicles8010019

In one of the most recent studies presented in [10], Wang et al. propose an upgrade to direct air capture (DAC) technology using the ultrasonic impregnation method to load Tetra-Ethylene-Pent-Amine (TEPA) onto Alumina (Al_2O_3) as the adsorbent. The TEPA-Al_2O_3 system was packed into the Rotating Adsorption Bed (RAB) to capture carbon dioxide from the air.

Of course, in the automotive industry, which represents one of the main polluters globally, research interest in reducing carbon dioxide emissions is very high. Many studies are based on carbon dioxide reduction from the exhaust gases of a spark ignition engine. The research from paper [11] proposes that, for carbon dioxide reduction, a post-combustion capture system should be used (for a spark ignition engine). In a post-combustion capture system, carbon dioxide is absorbed using a Mono-Ethanol-Amine (MEA) absorption catalyst after combustion.

In another work [12], Margull et al. propose a system comprising a membrane reactor (MR) with a carbon molecular sieve membrane (CMSM), followed by an adsorptive reactor (AR) for carbon dioxide pre-combustion capture.

Mixing different fuels is another solution for reducing carbon dioxide emissions. In paper [13], the influence of hydrogen added to the natural gas or biogas fuel mixture is discussed. The mixture was used in spark ignition engines. The assembly with the fuel mixtures in the unit was equipped with a CO_2 removal system.

To summarize the techniques and technologies used by researchers from this field in the most recent publications that we have described in this section, we have provided observations regarding this research in Table 1.

Our research is also based on a similar technology for reducing CO_2 and other polluting compounds in road vehicles. It is important to emphasize that the proposed technology is particularly useful for used vehicles older than 10 years, which represent the largest share of vehicles in large cities in Eastern Europe.

The work addresses a very little-explored area in the automotive industry—reducing CO_2 emissions by storing it in aqueous solutions. For the creation of an efficient filter, which also preserves the performance of the engine (power, torque), and whose costs are reasonable, no solution has yet been found. CO_2 reduction by storage or reaction with other oxides is used in other branches of industry, but not for automotive or land-based applications to produce energy from fossil fuels. Thus, the work builds on established principles and proposes a solution to reduce CO_2 emissions from combustion gases at relatively low cost, without negatively affecting the environment.

The novelty of the present study lies in the experimental validation of a low-cost, aqueous CaO–MgO-based CO_2 filtration system integrated directly into the exhaust line of an in-use spark ignition vehicle, without modifying the engine or fuel system. While CaO- and MgO-based carbonation reactions have been extensively investigated for CO_2 capture in industrial and stationary contexts, mainly under high-temperature or reactor-controlled conditions, as well as in laboratory-scale aqueous mineral carbonation systems [14–16], their application under low-temperature, atmospheric pressure conditions typical of vehicle exhaust systems has received limited attention. Unlike conventional carbon capture approaches such as post-combustion absorption systems, membrane reactors, or direct air capture technologies, which are generally designed for centralized or large-scale operation [17,18], the proposed solution operates at idle engine conditions, making it suitable for older vehicles and static internal combustion engine applications.

https://doi.org/10.3390/vehicles8010019

Table 1. The main technologies used by researchers in the most recent publications.

Authors	Article	Research Findings
Lebedevas, S., Malukas, A.	"The Application of Cryogenic Carbon Capture Technology on the Dual-Fuel Ship through the Utilization of LNG Cold Potential"	This research aims to provide a foundation for decarbonizing the maritime industry, which is currently in a pioneering stage for onboard carbon capture. The study focuses on utilizing the "cold potential" released during the regasification of Liquefied Natural Gas (LNG) to facilitate CO_2 capture.
Kim, H., Ahn, Y.H.	"Selective CO_2 Capture from CO_2/N_2 Gas Mixtures Utilizing Tetrabutylammonium Fluoride Hydrates"	This research investigated the formation rates, gas storage capacities, and selectivity of these hydrates under various conditions. The study found that TBAF hydrates can achieve a high CO_2 separation factor and the CO_2 can be enriched to over 90 mol% from simulated flue gas via a two-stage separation process.
Al-Elanjawy, Y.A.H., Yilmaz, M.	"Solar-Assisted Carbon Capture Process Integrated with a Natural Gas Combined Cycle (NGCC) Power Plant—A Simulation-Based Study"	This research explores the integration of solar thermal energy into a Natural Gas Combined Cycle (NGCC) power plant equipped with post-combustion carbon capture (PCC) technology. The primary goal is to address the energy penalty typically associated with carbon capture systems, which often require significant steam from the power cycle for solvent regeneration.
Wang, L., Shi, B.	"Coupled Oxygen-Enriched Combustion in Cement Industry CO_2 Capture System: Process Modeling and Exergy Analysis"	This research demonstrates a promising pathway for the cement industry to reduce carbon emissions by integrating oxygen-enriched combustion with CO_2 capture, improving energy utilization and lowering costs.
Jia, N., Wu, C., He, C., Lv, W., Ji, Z., Xing, L.	"Cross-Borehole ERT Monitoring System for CO_2 Geological Storage: Laboratory Development and Validation"	The study utilized laboratory experiments and finite-element modeling to optimize the CHERT system for tracking CO_2 plumes in deep formations. The researchers highlight CHERT as a cost-effective, permanent solution for real-time, years-long monitoring of dynamic CO_2 migration, which is often unfeasible with traditional seismic surveys.
Margull, N., Parsley, D., Somiari, I., Zhao, L., Cao, M., Koumoulis, D., Liu, P., Manousiouthakis, V., Tsotsis, T.	"Field-Scale Testing of a High-Efficiency Membrane Reactor (MR)—Adsorptive Reactor (AR) Process for H_2 Generation and Pre-Combustion CO_2 Capture"	This study validates a hybrid system combining a carbon molecular sieve membrane (CMSM) reactor with an adsorptive reactor for H_2 production and CO_2 capture. The unit was tested using real syngas at a pilot scale to demonstrate stability and functionality under realistic operating conditions (up to 300 °C temperature and 25 bar pressure).

Furthermore, this work introduces and experimentally evaluates the effect of the exhaust gas discharge distance relative to the reactive aqueous solution surface, identifying an optimal geometric configuration that reduces CO_2 concentration without causing significant increases in CO or NO_x emissions or unacceptable exhaust backpressure. Previous studies addressing carbonation-based CO_2 capture primarily focus on sorbent material development, reaction kinetics, and reactor-scale mass transfer phenomena [19,20], without considering geometric or operational optimization of gas–liquid interaction within a vehicle exhaust environment. To the authors' knowledge, such an experimental investigation of

https://doi.org/10.3390/vehicles8010019

exhaust–solution geometry applied to real spark ignition vehicle operation has not been previously reported in the literature.

2. Theoretical Assessment

There are various strategies for reducing carbon dioxide emissions from internal combustion engines. The technologies used in this field are presented in specialized publications [21–23], so we can base our research on them. One of them, applicable to static systems (test stands and generators), is the use of carbon dioxide absorption solutions to remove carbon dioxide from exhaust gases. Calcium oxides and magnesium oxides in water-based solutions can be used in CO_2 reduction systems. The following basic carbonation reactions can be considered:

$$CaO + CO_2 = CaCO_3 \quad (1)$$

$$Ca(OH)_2 + CO_2 = CaCO_3 + H_2O \quad (2)$$

Those reactions can be used to separate CO_2 from exhausted gases at concentrations exceeding the required levels. Kinetic data on the reaction show that its rate is initially fast and controlled, but undergoes a sudden transition to a slower controlled diffusion regime. Moreover, the carbonation conversion decreases with the number of carbonation–calcination cycles. The interactions of CaO and CO_2 indicated that chemical adsorption occurs at temperatures between 25 °C and approximately 300 °C, while bulk carbonate formation occurs at higher temperatures [21].

Oversaturation and the nucleation and growth of calcium carbonate crystals are possible due to carbon dioxide absorption [15]. The limiting factor is considered the absorption rate. From this reaction, ammonia hydrolyzes, forming hydroxyl ions. By direct reaction between CO_2 and OH ions, bicarbonate ions will be formed, and after that, they will be transformed into carbonate ions. The last phase will be the reaction between Ca^{2+} and $CO_3{}^{2-}$, in which $CaCO_3$ precipitates. The composition of the aqueous phase changes will also induce a change in the CO_2 solubility, which will affect the driving absorption force. The absorption rate of carbon dioxide in aqueous solutions will affect the chemical reaction rate between carbonate and calcium ions and will depend on the mass transfer coefficient, the equilibrium, and the actual carbon dioxide solubility [21,22]. When the absorption of CO_2 is accelerated, the precipitation rate will increase. Also temperature values will influence the course of calcium carbonate formation [23].

An ideal carbon dioxide sorbent must have a high absorption capacity and fast kinetics at low CO_2 partial pressure, and, for sure, a high chemical stability. The sorbents used frequently are natural materials based on Ca, like limestone ($CaCO_3$) and dolomites (Ca, Mg $(CO_3)_2$), because they have a high initial capacity of absorption and the price is accessible. Natural sorbents exhibit rapid decay in absorption capacity during carbonation or calcination cycles [24].

Magnesium oxide (MgO) is a mineral and is industrially obtained by calcining magnesite or dolomite, as well as hydroxide, nitrate, carbonate, oxalate, and even magnesium sulfate. In all cases, it results in a white powder that is a poor conductor of heat and electricity (calcined magnesia) [25].

Due to its strong tendency to react with oxygen, magnesium can reduce many oxides, such as CO_2, SO_2, Al_2O_3, etc.

$$2Mg + CO_2 \Rightarrow 2MgO + C \quad (3)$$

https://doi.org/10.3390/vehicles8010019

Magnesium oxide is obtained by direct oxidation of magnesium or by calcination of magnesium hydroxide, nitrate, or carbonate. MgO reacts with water to form magnesium hydroxide, a weak base:

$$MgO + H_2O \Rightarrow Mg(OH)_2 \quad (4)$$

Magnesium hydroxide dissolves very little in water; the aqueous solution is weakly alkaline. It is converted back to magnesium oxide at high temperatures [19].

Calcium oxide, CaO, is also called slaked lime. It can be obtained using the methods to obtain MgO. It is a white, amorphous powder with a density of 3.16 g/cm^3. It reacts with water at a normal temperature [25].

$$CaCO_3 \Leftrightarrow CaO + CO_2, \text{ with } \Delta H = 145 \text{ kJ·mol}^{-1} \quad (5)$$

Calcium oxide has a high melting point of 2580 °C and reacts with water to form calcium hydroxide.

$$CaO + H_2O \Rightarrow Ca(OH)_2, \text{ with } \Delta H = -65 \text{ kJ·mol}^{-1} \quad (6)$$

Calcium oxide, like any basic oxide, reacts with acetic anhydrides and acids. For example, it forms calcium carbonate with carbon dioxide:

$$CaO + CO_2 \Rightarrow CaCO_3 \quad (7)$$

Calcium hydroxide, $Ca(OH)_2$, is obtained by combining calcium oxide with water. The conversion of calcium oxide to calcium hydroxide will result in slaked lime. If calcium hydroxide is further treated with water, milk of lime is obtained. It partly consists of a solution of calcium hydroxide and a suspension of $Ca(OH)_2$ in water. The solubility of calcium hydroxide in water is low (at 20 °C, it is 0.129 g $Ca(OH)_2$/1000 g H_2O). Left longer in suspension (undissolved), it is deposited at the bottom of the vessel, and a clear solution of $Ca(OH)_2$, limewater, remains above. It has a strong basic character [26].

A characteristic reaction of calcium hydroxide is the reaction with carbon dioxide when calcium carbonate is produced:

$$Ca(OH)_2 + CO_2 \Rightarrow CaCO_3 + H_2O \quad (8)$$

Calcium carbonate, $CaCO_3$, is one of the most common compounds in nature. It is a white substance, poorly soluble in water (solubility: 1.3 mg $CaCO_3$ in 100 g of water at 20 °C). Therefore, if Ca^{2+} and $CO_3{}^{2-}$ ions are present in the solution, a white, crystalline precipitate of calcium carbonate is formed [17]:

$$Ca^{2+} + CO_3^{2-} \Leftrightarrow CaCO_3 \quad (9)$$

If carbon dioxide is added, the precipitate disappears because calcium bicarbonate (calcium hydrogen carbonate) is formed, which is soluble:

$$CaCO_3 + CO_2 + H_2O \Leftrightarrow Ca(HCO_3)_2 \quad (10)$$

The reaction is reversible. Carbon monoxide, CO, is formed from the incomplete combustion of fossil fuels.

$$2C + O_2 \Rightarrow 2CO, \text{ with } \Delta H = -110 \text{ kJ·mol}^{-1} \quad (11)$$

https://doi.org/10.3390/vehicles8010019

CO is slightly reactive at normal temperatures. At temperatures above 700 °C, carbon monoxide burns in the air and carbon dioxide is produced:

$$2CO + O_2 \Leftrightarrow 2CO_2\,,\ \text{with}\ \Delta H = -283\ \text{kJ·mol}^{-1} \tag{12}$$

The reaction is reversible. The reaction of CO with water vapors will also result in carbon dioxide [27,28]:

$$CO + H_2O \Leftrightarrow CO_2 + H_2 \tag{13}$$

$$MgO(s) + CO_2(g) \Leftrightarrow MgCO_3(s)(+118\text{kJheat}) \tag{14}$$

The reaction (14) will proceed to the right upon the addition of carbon dioxide to the system, according to Le Châtelier's principle. Adding heat to the system favors the reverse reaction, i.e., calcination [27–29]. So, the carbonation reactions cannot be accelerated by simple heating; rather, the temperature increase must be accompanied by a simultaneous increase in the amount of carbon dioxide [28,29].

$$Mg(OH_2)\ (s) + CO_2(g) \Leftrightarrow MgCO_3(s) + H_2O\ (g) \tag{15}$$

The reaction is applicable to studies of carbon deposition in bodies of water, particularly the seas and oceans. The oceans have significant potential to capture anthropogenic carbon dioxide. The oceans contain a large amount of carbon dioxide gas. Under these conditions, ocean waters are a good solution for storing carbon dioxide produced by industrial activity, transport, and other sources. The problem with carbon storage processes has led to increased ocean acidity levels [30,31].

The process of storing carbon dioxide in the oceans involves introducing it under pressure and dissolving it in water at depths greater than 1000 m or on the ocean floor, but not at depths greater than 3000 m. CO_2 is introduced into the water by injecting or pumping the gas to the ocean floor. It is estimated that CO_2 will return to the atmosphere, as a result of storage, after long periods of time—hundreds or thousands of years. As a disadvantage of the solution, pumping carbon dioxide to the ocean floor is risky in the long term; the problem of greenhouse gases is a challenge for the future [32,33].

Another solution is carbonation, directly converting carbon from gas to a solid. Thus, an alternative is represented by the reactions of calcium and magnesium oxides, or the compound Mg_2SiO_4, with carbon dioxide, under high-pressure conditions [28–32]. The equations for the transition of carbon from the gas phase to the solid phase are as follows:

$$CaO(s) + CO_2(g) \Leftrightarrow CaCO_3(s)\,,\ \text{with}\ \Delta H = -179\ \text{kJ·mol}^{-1} \tag{16}$$

$$MgO(s) + CO_2(g) \Leftrightarrow MgCO_3(s)\,,\ \text{with}\ \Delta H = -118\ \text{kJ·mol}^{-1} \tag{17}$$

$$CaSiO_3(s) + CO_2(g) \Rightarrow CaCO_3(s) + SiO_2(s)\,,\ \text{with}\ \Delta H = -90\ \text{kJ·mol}^{-1} \tag{18}$$

$$MgSiO_4(s) + 2CO_2(g) \Rightarrow 2MgCO_3(s) + SiO_2(s)\,,\ \text{with}\ \Delta H = -95\ \text{kJ·mol}^{-1} \tag{19}$$

$$MgSiO_5(OH)_4(s) + 3CO_2(g) \Rightarrow 3MgCO_3(s) + 2SiO_2(s) + 2H_2O(g),\ \text{with}\ \Delta H = -64\ \text{kJ·mol}^{-1} \tag{20}$$

Theoretically, $MgCO_3$ can be used in industrial processes to store carbon dioxide at temperatures between 400 °C and 600 °C.

The method described earlier, the direct transformation of gas into solid, is theoretically simple and efficient. The direct gas–solid method has the disadvantage that it cannot be applied to specific transport and industrial applications, in general, due to slow kinetics and very low conversion rates [31].

https://doi.org/10.3390/vehicles8010019

Another alternative is indirect carbonation (conversion from gas to solid by indirect processes). The advantage over aqueous solutions is the recovery of energy during carbonation: the exothermic heat of carbonation is recovered and used throughout the system, increasing the total energy input available. Lackner et al. [34] have used magnesium and calcium oxides and hydroxides. Their tests showed that the carbonation process using CaO and $Ca(OH)_2$ occurs rapidly under high-temperature, high-pressure conditions. The problem was that the minerals used in the process, such as wollastonite, are relatively rare and expensive. Very good results were obtained when $Mg(OH)_2$ was used in the process and when minerals containing magnesium silicate were used. The process also required high temperatures and pressures. In the case of $Mg(OH)_2$ carbonation, a reversible dehydroxylation–rehydration reaction was used. Following the reaction, $Mg(OH)_2$ is converted into MgO and vice versa. These reactions are presented below [34].

$$Mg(OH)_2(s) \Leftrightarrow MgO(s) + H_2O(g) \quad (21)$$

$$MgO(s) + CO_2(g) \Leftrightarrow MgCO_3(s) \quad (22)$$

3. Methodology and Experimental Research Equipment

3.1. The Used Equipment

The experimental research was conducted by analyzing a vehicle about 15 years old, which is the average age of vehicles in Eastern Europe. The measurements were made with the portable analyzer, GA-21 plus (produced by Madur Wien, Austria [35]), with the assembly shown in Figure 2.



Figure 2. Testing the vehicle without a filter (Test 1). The GA 21 Plus is connected to the vehicle's exhaust system (Dacia Sandero 2009) via its probe. An exhaust adaptation element similar to the filter system was used. The laptop running the Madur software (for data recording) is connected to the equipment.

With the GA-21 plus, several tests were performed under the same temperature conditions, from engine start to the point at which the optimal operating temperature was reached. The vehicle's engine was operated at idle speed for all measurements.

https://doi.org/10.3390/vehicles8010019

The GA-21 plus is a flue gas analyzer, used by the authors in several research analyses [36,37]. This apparatus uses electrochemical sensors to measure exhausted gas concentration. This type of analyzer is fitted with several types of sensors:

- The oxygen sensor (O_2);
- The carbon monoxide sensor (CO);
- The nitric oxide sensor (NO);
- The sulphur dioxide sensor (SO_2);
- The carbon dioxide sensor (CO_2);
- The nitrogen oxides sensor (NO_x).

The oxygen O_2, the nitric oxide NO, the carbon monoxide CO, and the sulphur dioxide SO_2 are measured directly by the analyzer with electrochemical cells. The other components will be calculated. The analyzer displays the carbon dioxide and oxygen concentrations as percentages. The remaining gas concentrations are shown in the following forms [36]:

- In parts per million [ppm], the volume concentration;
- In [mg/m^3], the absolute mass concentration;
- In [mg/m^3], the mass concentration in relation to the O2 content.

The characteristic parameters of the inlet air are the environmental temperature and the exhausted gas temperature.

The analyzer calculates the following combustion parameters using the temperatures, the gas concentrations, and the used fuel properties:

- The Stack Loss (SL);
- The efficiency (h);
- The air excess coefficient (λ);
- The losses from the incomplete combustion (IL).

From measurements, the analyzer sensors detect the temperature and the concentrations of the gas elements. The sensors' indications are directly proportional to the volume concentration of the detected elements, which are expressed in parts per million [ppm]. So, using direct measurement, the following are obtained:

- The flue gas temperature t expressed in [°C];
- The ambient temperature t_0 expressed in [°C];
- The volume concentration of O_2 expressed in [%].
- The volume concentration of CO expressed in [ppm];
- The volume concentration of NO expressed in [ppm];
- The volume concentration of SO_2 expressed in [ppm].

The volume concentration of CO_2 cannot be obtained directly with a GA-21 plus analyzer, but it can be calculated from the measured maximum CO_2 concentration (CO_{2max}) and the O_2 concentration. The analyzer calculates the volume concentration of CO_2 with the following relation according to [23]:

$$CO_2 = CO_{2\max} \cdot \left(1 - \frac{O_{2meas}[\%]}{20.95\%}\right) \quad (23)$$

The exhausted gases contain nitrogen oxides, NO and NO_2. The GA-21 plus analyzer does not have a sensor for nitrogen dioxide measurement, but it does have a sensor for NO measurement. The NO_2 content can be calculated from the measured NO values. The NO in the exhaust is 95% of the total nitrogen oxides (NO_x). The GA-21 analyzer can calculate the total concentration of nitrogen oxides NO_x with the following relation according to [33]:

$$NO_x[ppm] = \frac{NO[ppm]}{0.95} \quad (24)$$

https://doi.org/10.3390/vehicles8010019

By adding the concentration of NO to the NO_2 concentration, the NO_x concentration [23,33] will be

$$NO_x[ppm] = NO[ppm] + NO_2[ppm] \quad (25)$$

The used analyzer can also extract the mass concentration value in [mg/m3] from the concentration value in [ppm]. The mass concentration of the exhausted gas elements depends on their temperature and pressure. To compare measurement results, standard conditions parameters (standard temperature and pressure) are used, including the 1000 [hPa = 1 bar] pressure and 0 °C (273.15 K) temperature. The analyzer will indicate two values expressed in [mg/m^3]: the absolute mass concentration and the mass concentration relative to oxygen.

Absolute mass concentration is defined by how many milligrams of a given gas are contained in a volume of 1 [m^3] of combustion gas at standard conditions (the standard value of pressure, p_0 =1000 hPa, and the standard value of temperature, T_0 = 273.15 K). The concentration value is obtained by multiplying the concentration expressed in [ppm] by a correction factor A. Table 2 shows the correction factor A values for the analyzed exhausted gases.

Table 2. The correction factor values for the analyzed exhausted gases.

Analyzed Exhausted Gases	Correction Factor A $\left[\frac{mg}{m^3 \cdot ppm}\right]$
Carbon monoxide CO	1.250
Nitric oxide NO	1.340
Sulphur dioxide SO_2	2.860
Nitrogen oxides NO_2, NO_x	2.056

The absolute mass concentration is computed using the following equation:

$$CO\left[\frac{mg}{m^3}\right] = CO[ppm] \cdot A_{CO}, \quad (26)$$

where CO expressed in [mg/m^3] is the absolute CO mass concentration from exhausted gases at the standard conditions, CO expressed in [ppm] is the absolute CO volume concentration in exhausted gases obtained from measurement, and A_{CO} is the correction factor.

3.2. The Testing Procedure

The tested vehicle was a Dacia Sandero, manufactured in Romania in 2009. The vehicle was equipped with a 1390 cm^3 spark ignition engine with 75 hp at 5500 rpm (Figure 3).

The tests were conducted to evaluate exhaust gases from the cold start of the engine and from running (idle speed) until the engine reached optimal operating temperature. The data were automatically recorded every 10 s, and each test lasted 1050 s (17 min and 30 s). Tests 2–4 were carried out using the filtering system. For Test No. 2, the exhaust gases inside the filter were measured 10 mm above the reactive solution. For Test No. 3, the exhaust gases from the filter were collected at 30 mm above the reactive solution. For Test No. 4, the exhaust gases inside the filter were measured 20 mm above the reactive solution. All tests were carried out under similar conditions (temperature and atmospheric pressure). Data specific to the test of engines were collected: emissions (CO_2, CO, NO_x), ambient temperature, exhaust temperature, and the excess air coefficient from the exhaust gases.

https://doi.org/10.3390/vehicles8010019



Figure 3. Testing the vehicle with a filter (Tests 2–4). The GA 21 Plus is connected to the filtration system via the probe. The filter is also connected to the vehicle's exhaust (Dacia Sandero 2009) via an airtight system. The laptop running the Madur software (for data recording) is connected to the equipment.

The test conditions were similar for all tests. These were carried out on days with similar ambient temperatures (temperature, pressure, humidity). The days were not consecutive; suitable days for testing were chosen when the weather conditions were similar. The weather conditions for the four tests were as follows:

Test 1—Day 1—Ambient temperature 12.3 °C (54.1 °F); atmospheric pressure 761 [mmHg].

Test 2—Day 2—Ambient temperature 12.5 °C (54.5 °F); atmospheric pressure 759 [mmHg].

Test 3—Day 3—Ambient temperature 12.1 °C (53.8 °F); atmospheric pressure 765 [mmHg].

Test 4—Day 4—Ambient temperature 12.5 °C (54.5 °F); atmospheric pressure 767 [mmHg].

The tests were carried out by a team of two researchers (the authors of the paper, Stelian Tarulescu and Radu Tarulescu). The costs of carrying out the tests were approximately: making the filtering system—EUR 200; the fuel used—approx. EUR 50; equipment threads—EUR 20; labor—20 EUR/h × 10 h = EUR 200; data processing—20 EUR/h × 10 h = EUR 200. The costs were covered by the Research Center for High-Tech Products for Automotive at Transilvania University of Brasov.

The filtration system was attached to the tested vehicle. The connection was made using the exhaust pipe adapter. The GA 21 Plus gas analyzer was commissioned in the testing perimeter. Its probe was inserted into the adapter protruding from the filtration system.

The equipment used is a gas analyzer from the Madur company, called GA 21 Plus. The equipment records flue gas emission values (O_2, CO_2, CO, NO_x, SO_2, etc.) and environmental values, such as ambient temperature and well temperatures, coefficient of excess air in the exhaust gases, and measurement efficiency (with Stack Loss). The analyzer measures ambient temperature for use in calculations, such as Stack Loss. The emissions are measured using electrochemical cells.

https://doi.org/10.3390/vehicles8010019

Figure 4 shows the diagram of the equipment and filtering system for data collection. The CO_2 filtration system proposed by the authors consists of a glass container with a 2000 cm^3 volume, in which 340 cm^3 of reactive aqueous solution (water containing CaO and MgO) was introduced. The solution was prepared using 20 g of powder consisting of 60% CaO and 40% MgO, dissolved in 0.33 L of water, and the result was an aqueous solution of calcium and magnesium hydroxides [38], which was introduced into the filtration system:

$$CaO + MgO + H_2O = Ca(OH)_2 + Mg(OH)_2 \quad (27)$$

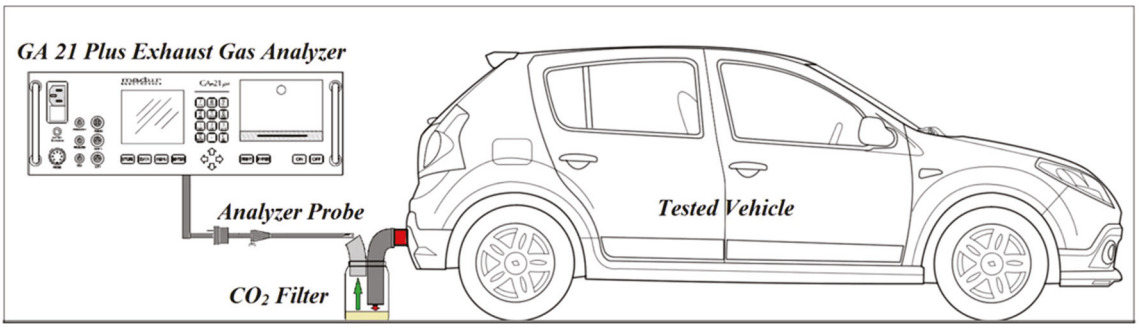

Figure 4. The testing procedure. Location of the GA 21 Plus and filter.

On the filtration system, the following equipment is connected:

- An adapter for the exhaust pipe of the tested vehicle;
- An adapter for the probe of the measuring equipment.

The system was tested, and the modified parameter was the distance between the extension of the exhaust pipe (adapter for the exhaust pipe) and the surface of the reactive solution. Tests were performed for three values: 10 mm, 20 mm, and 30 mm. The filtration system and the way of varying the distance between the exhaust gases discharge and the surface of the aqueous solution are shown in Figure 5.

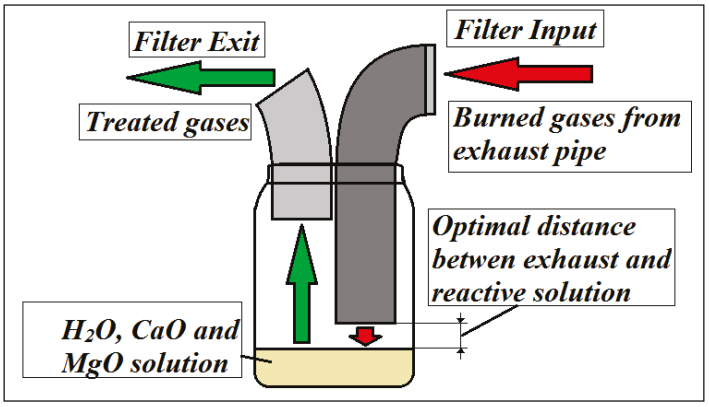

Figure 5. Tested carbonation system (filter) scheme.

The values of the main pollutants in the exhaust gases were recorded for each test. To highlight the filtration system's efficiency, the evolution of carbon dioxide, carbon monoxide, and nitrogen oxides was monitored.

The tests were performed at idle speed, from cold start to optimal operating temperature.

The interaction of the exhaust gases with the tested solution results in a reduction in CO_2 levels, with only small differences in CO and NO_x levels between Test 1 (without

https://doi.org/10.3390/vehicles8010019

a filter) and Test 4. No other environmental impacts were recorded as a result of the reduction reactions.

The efficiency with which the analyzer performs the measurement is expressed by the ETA parameter (Analyzer Efficiency) and is inversely proportional to the probe losses SL (Stack Loss). For the tests performed, the efficiency (ETA) ranged from 95.7% to 4.3%, with losses of up to 4.3%.

4. Results and Discussions

The data from the four tests were recorded. For example, the worksheets resulting from Test 1 (without filtration system—Figure 5) and Test 4 (filtration system, exhaust distance from the reactive solution of 20 mm—Figure 6) are presented below.

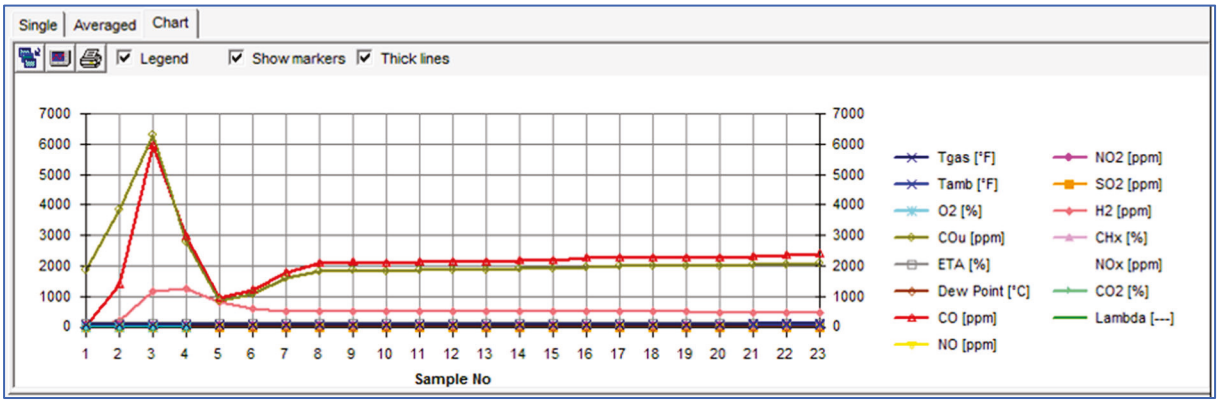

Figure 6. A sample of the obtained data from Test 1.

Figure 6 shows a screenshot of the equipment software during Test No. 1 after 230 s of testing. It is observed that when the engine starts cold, the CO and H_2 values are very high (specific to cold starting), then they decrease and stabilize. The disadvantage of viewing the graph in the software is the large differences in the rates of various emissions (or parameters), with only the very large variations visible. Variations in CO_2 or NO_x are not visible.

The worksheets for Tests 2 and 3 are not presented, as the most relevant comparison was made between Test 1 and Test 4.

For Test No. 4, a screenshot from the software is shown in Figure 7. Large variations are also observed when starting cold for CO and H_2, but after the engine reaches optimal operating temperature, the values drop towards the minimum threshold.

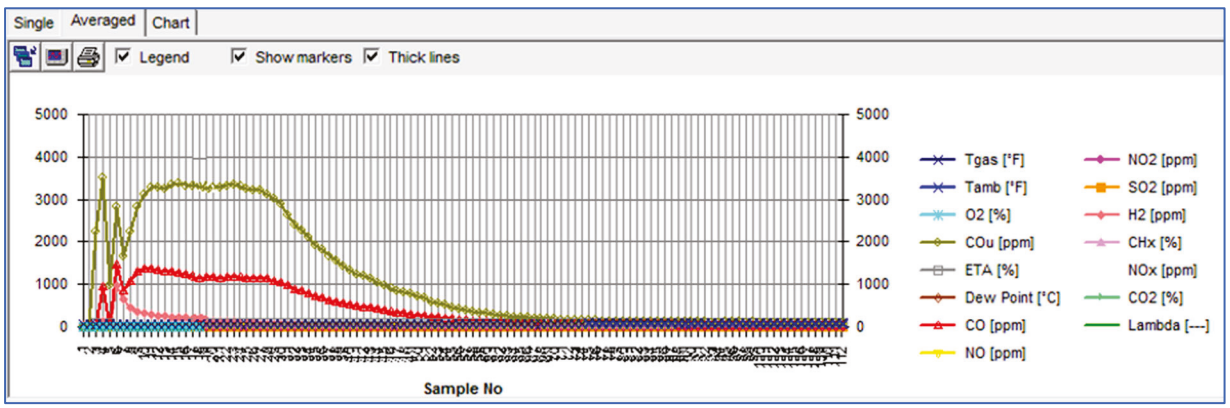

Figure 7. A sample of the obtained data from Test 4.

https://doi.org/10.3390/vehicles8010019

The data from the four tests were processed, resulting in a worksheet that compares the CO_2, CO, and NO_x values for the four tests.

The test results (1, 2, 3, and 4) were summarized in an Excel worksheet. The data recorded by the equipment from engine cold and running (idle engine speed) were processed until the engine reached the optimal operating temperature. The data saved every 10 s was entered into the worksheet for each of the four tests. The duration of each test was 1050 s (17 min and 30 s). For each saved line, an order number was entered, from 1 to 105.

The excess air coefficient from the exhaust gases is also automatically recorded by the equipment. It varied depending on the test mode, from maximum to minimum values, as follows:

Test 1—Lambda ranged from 1.27 (at cold start) to 1.02 (at the end).

Test 2—Lambda ranged from 1.78 (at cold start) to 1.31 (at the end).

Test 3—Lambda ranged from 1.56 (at cold start) to 1.15 (at the end).

Test 4—Lambda ranged from 1.45 (at cold start) to 1.17 (at the end).

Exhaust back pressure is a relevant parameter in terms of the quality of the combustion processes in the engine and the quality of the exhaust gases for all tests, which varied as follows:

Testul 1—Exhaust back pressure varies from minimum (−0.01 hPa) to maximum (0.01 hPa).

Testul 2—Exhaust back pressure varies from minimum (−0.03 hPa) to maximum (0.09 hPa).

Testul 3—Exhaust back pressure varies from minimum (−0.03 hPa) to maximum (0.03 hPa).

Testul 4—Exhaust back pressure varies from minimum (−0.03 hPa) to maximum (0.02 hPa).

Figure 8 shows the CO_2 values (in percentages) measured for all tests. The measurement points (from 1 to 105) correspond to each set of values recorded by the equipment from the time the engine starts cold until it reaches optimal operating temperature.

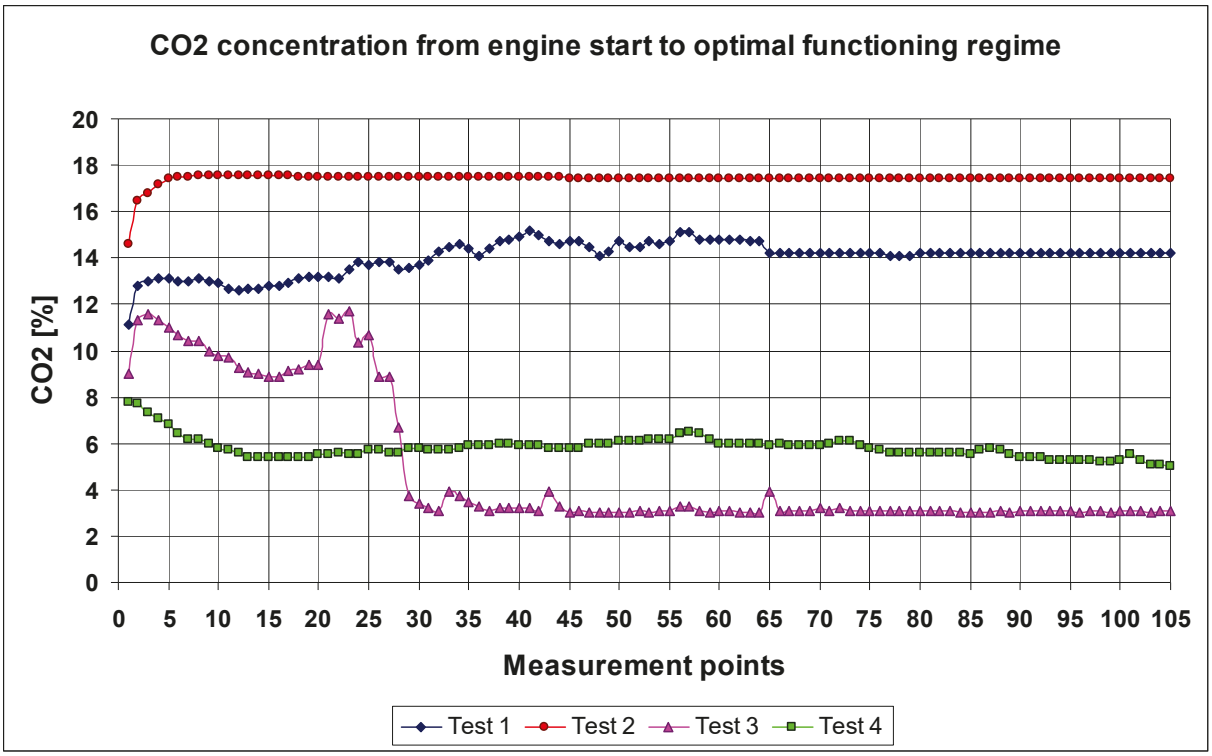

Figure 8. Carbon dioxide concentration registered for Test 1, Test 2, Test 3, and Test 4.

https://doi.org/10.3390/vehicles8010019

Similarly, the developments in CO and NO_x are presented in Figures 9 and 10, which are relevant to defining the quality of the exhaust gases in each test.

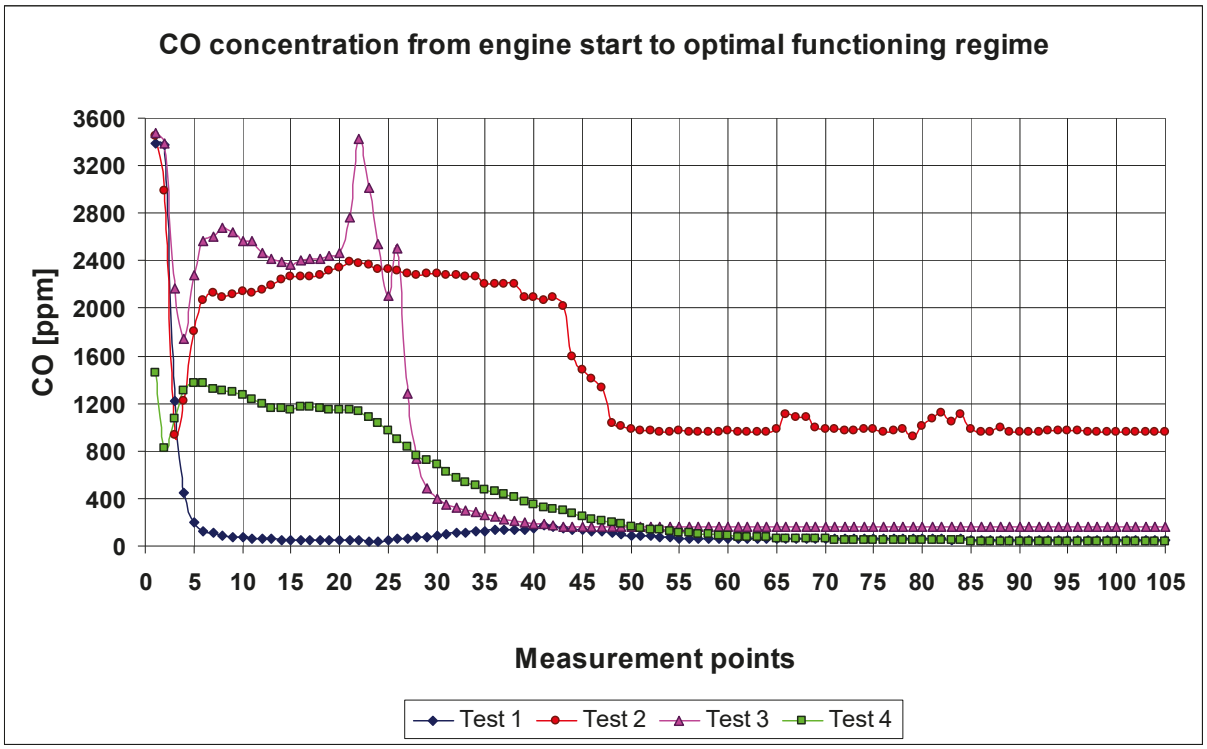

Figure 9. Carbon monoxide concentration registered for Test 1, Test 2, Test 3, and Test 4.

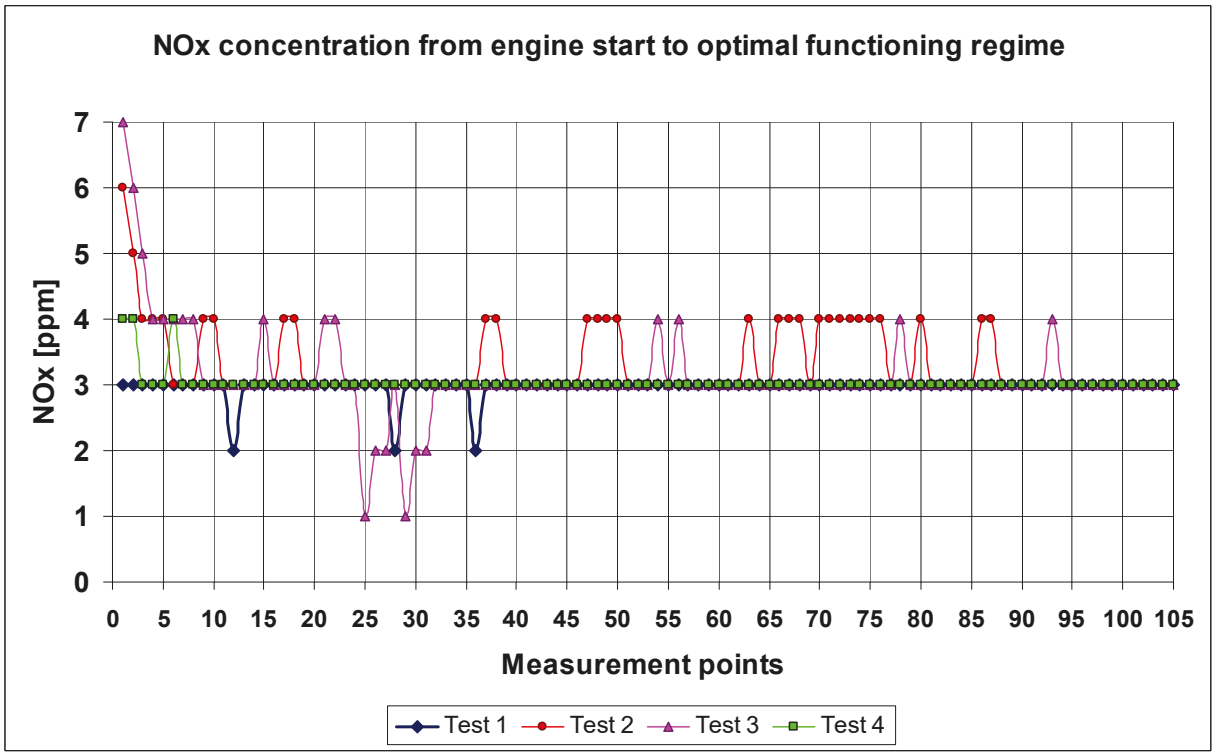

Figure 10. Nitrogen oxide concentration registered for Test 1, Test 2, Test 3, and Test 4.

The evolution of carbon monoxide (CO) concentration shown in Figure 9 highlights the influence of the filtration system configuration on incomplete combustion products. While

the reference test without the filtration system exhibits the lowest overall CO levels, the results obtained with the filter indicate that exhaust backpressure and gas–liquid interaction conditions play an important role in CO formation. In particular, the elevated CO values observed in Test 2 can be attributed to the reduced distance between the exhaust outlet and the reactive solution surface, which led to increased flow resistance and less favorable exhaust gas evacuation.

In contrast, Test 4 demonstrates a more stable CO evolution throughout the test duration, suggesting that the selected exhaust-to-solution distance provides a suitable compromise between effective CO_2 reduction and minimal disturbance of the combustion process. To further assess whether the filtration system influences high-temperature combustion-related emissions, the evolution of nitrogen oxides (NO_x) concentration for all tests is analyzed and discussed in Figure 10.

The values obtained from the tests were compared, and the following conclusions were reached:

- Compared to Test 1, the lowest CO_2 values were obtained in Test 3. However, the minimum values were obtained only when the engine approached the optimal operating temperature.
- The optimal evolution of the CO_2 concentration was recorded in Test 4. The values were low both during cold starting and during engine operation at temperatures close to optimal.
- In the case of CO, the optimal evolution was recorded in Test 1 when no filtration system was used. However, the minimum values for both cold starting and optimal engine operation were recorded in Test 4.
- The CO values recorded in Test 2 were very high due to the counter-pressure caused by the small distance between the exhaust pipe and the reactive solution. Also in Test 3, the CO values varied widely between the maximum and minimum.
- The lowest values were obtained in Test 4 for NO_x. However, the small differences in the values obtained across all tests indicate a limited impact of the system on the formation of the fuel mixture.

The solution presented in this paper has a number of practical advantages: relatively low testing costs; low costs for the implementation of the filtration system (both the device and the solutions used); high accessibility regarding the procurement of the substances necessary for testing (substances often used in the agricultural industry as soil fertilizers); low impact on the environment both in the case of the construction of the filtration system and in the case of exploitation (the substances resulting from the reactions between the exhaust gases and the aqueous solution do not have an additional impact on the environment); high degree of generality regarding the use of the system in other applications (especially static ones—thermal systems, generators, etc.); CO and NO_x values do not change their evolutions much in the case of the use of the filtration system (only the optimal constructive solution for the filtration system must be identified); there is the possibility of testing alternative fuels; and the functional parameters of the engine are not substantially influenced.

As disadvantages of the presented solution, we mention the following: it is not yet a portable solution to be practical for driving vehicles tests; no relevant engine load tests have yet been carried out due to equipment losses (similar but new equipment is yet to be purchased); a limitation of the equipment is the lower performance of the unburned hydrocarbon sensor, an emission that needs to be monitored; the test procedure does not cover various operating regimes (testing will continue on the AVL stand); vehicles equipped with LPG or CNG have not yet been tested; no relevant tests have been carried

https://doi.org/10.3390/vehicles8010019

out for supercharged engines, nor the influence on EGR systems, particulate filters, or catalysts (we will develop test procedures, but also for experimental engines on the stand).

Comparing our results with those of other researchers, we can say that a solution has been identified to reduce CO_2 emissions by storing it in aqueous solutions. The results are not spectacular, but they confirm the processes used industrially or in other technical fields, different or complementary to the automotive industry. CO_2 reduction through storage benefits static applications, but an on-board system for cars can be developed in the future.

A notable advancement in direct CO_2 mitigation for spark ignition engines is the adaptation of post-combustion carbon capture (PCC) systems on the exhaust stream. The study by Santosh and Vinith Kumar [11] provides experimental evidence for this method, implementing the PCC unit downstream of the engine exhaust. The system used monoethanolamine (MEA), a widely studied chemical absorbent for carbon capture, to selectively absorb CO_2 from the exhaust gas stream. MEA reacts with CO_2 to form ammonium carbonate compounds, effectively removing CO_2 from the exhaust before atmospheric release. An empty section in the exhaust manifold served as a residence chamber, increasing contact time between exhaust gases and absorbent, a critical factor in maximizing capture efficiency. The experiment demonstrated a measurable reduction in CO_2 emissions from the SI engine with the PCC system in place, confirming that a post-combustion absorption process can capture a portion of carbon dioxide even after combustion has occurred. Although this method does not eliminate carbon generation at the source, it prevents a significant part of the CO_2 from entering the atmosphere, thus reducing the effective carbon footprint.

While post-combustion capture targets CO_2 after it forms, Janusz-Szymańska et al. [13] advocate a dual approach involving both emission control (incorporating after-treatment systems such as carbon capture, exhaust treatment, and hybridization to reduce net emissions) and fuel efficiency improvements (improving thermodynamic efficiency through advanced engine calibration). This combined strategy recognizes that a single mitigation mechanism is unlikely to achieve substantial decarbonization: efficiency gains alone reduce fuel consumption, but a carbon capture component directly addresses emissions still produced. The dual method is advantageous because there are parallels approaches in stationary power plants (where carbon capture is paired with efficiency upgrades) and it offers flexibility across application scales. In particular, mild hybridization and advanced combustion strategies can reduce fuel consumption, while post-combustion systems capture the CO_2 that remains unavoidable.

These findings suggest a multi-pronged strategy: improving engine efficiency and reducing fuel consumption, while capturing residual CO_2 before it enters the atmosphere, providing a robust pathway to decarbonize spark ignition engines, especially where rapid electrification is infeasible.

Research in the field of carbon dioxide storage has similar results, with different applications for which they are used, the substances used, and the costs required. The present study introduces these CO_2 reduction methods in the field of internal combustion engines as well, being of interest mainly from the perspective of the simplicity of the proposed system and the reduced costs of reacquisition and use.

5. Conclusions

The number of vehicles older than 10 years is increasing in European countries, with the average age about 12 years. In Eastern European countries, the average age is even higher, around fifteen years. To ensure vehicles' compliance with pollution standards, the authors proposed a filtration system for combustion gases of a spark ignition engine. Spark ignition engines remain widely used in light-duty road vehicles, backup generators, and small power generation units. Despite advancements in electrification, engines still

https://doi.org/10.3390/vehicles8010019

contribute significantly to the global carbon footprint due to the combustion of hydrocarbon fuels and subsequent emissions of CO_2, the primary greenhouse gas driving global warming. Reducing the carbon footprint of spark ignition engines is therefore imperative not only for Eastern European cities' air quality but also for global climate mitigation strategies.

In our research, to reduce CO_2 concentration in exhaust gases without increasing other specific oxides, a filter operating with a reactive aqueous solution (H_2O, CaO, and MgO) was designed and tested. The proposed system applies to vehicles older than ten years whose pollutant emissions no longer comply with the environmental standards. The filter was tested on a vehicle equipped with a 1390 cm^3 spark ignition engine (Dacia Sandero model from 2009), of 75 hp.

In this case, it is important to adjust the distance between the end of the exhaust pipe and the reactive solution. Thus, a reference test was performed without a filter, and three tests with a filter were performed, with the exhaust distance from the reactive solution varying.

Following the detailed analysis of the values obtained from the four tests, it can be concluded that the system is efficient, especially when the distance between the exhaust pipe and the reactive solution is adjusted to the optimal value of 20 mm.

The tests will continue on experimental engines from test stands, both spark ignition and compression ignition engines. Alternative fuel mixtures will also be tested to verify the filtration system's efficiency under as many conditions as possible.

The design will be patented, and a project will be started to create a prototype filter for use primarily in static applications with internal combustion engines: test stands for engines and generators. Subsequently, an attempt will be made to develop a prototype filter for use on vehicles.

After the research, we have identified a viable solution to reduce CO_2 emissions from the combustion of fossil fuels. The solution was developed as a system that reduces CO_2 from vehicle exhaust gases (tests conducted on a vehicle equipped with a spark ignition engine), but it can also have applications in static systems. The main advantage of the system is its low construction, testing, and operational costs. Also a great advantage is access to the solutions necessary for the system's realization, which are readily available on the market. It is very important that the system does not have a negative impact on the environment, and can also be used in urban areas. The disadvantages related to testing modes, applicability, and on-board running vehicle testing will be reduced through further research and testing, as well as the purchase of new equipment in the future.

Reducing the CO_2 footprint of spark ignition engines remains a critical challenge in the global effort to combat climate change. While the automotive industry moves toward electrification, spark ignition engines continue to dominate in many applications, especially in regions where infrastructure or economic constraints delay the adoption of electric alternatives. Ultimately, no single technology provides a complete solution. A multi-faceted approach, combining operational efficiency, carbon capture, and supportive regulatory policies, is essential for achieving meaningful reductions in the carbon footprint of SI engines. These strategies serve as vital bridges in the transition toward a low-carbon transport sector, and with our experimental research, we want to contribute towards sustainability.

https://doi.org/10.3390/vehicles8010019

Author Contributions: Conceptualization, S.T., R.G.B., and R.T.; methodology, S.T. and R.T.; validation, M.N., and R.T.; formal analysis, R.T.; investigation, S.T. and M.N.; resources, S.T. and R.T.; data curation, R.T., R.G.B., and S.T.; writing—original draft preparation, R.T., S.T., and M.N.; writing—R.T. and S.T.; visualization, S.T.; supervision, M.N.; project administration, S.T.; funding acquisition, S.T. S.T.: proposed the methodology, developed the work plan, and formulated the basic ideas of the work. R.T. contributed to the development of the methodology and participated in the tests. R.G.B. checked, corrected, and completed the information regarding the design of the work, the working methods, and the presentation of the results. M.N. supervised the work throughout the application period and contributed to the theoretical concepts. M.N. and R.T. validated the methodology. The analysis of the collected data was performed by S.T. and R.T. and validated by R.G.B. The analysis of the results was carried out by S.T., R.T., and M.N. The selection of the bibliography was carried out by S.T., R.T., R.G.B., and M.N. The management of the activities, access, and use of funds were carried out by S.T., as coordinator of the Research Center for High Tech Products for Automotive Products (center where the tests and experimental research took place). All authors have read and agreed to the published version of the manuscript.

Funding: This research received no external funding.

Data Availability Statement: The original contributions presented in this study are included in the article. Further inquiries can be directed to the corresponding authors.

Conflicts of Interest: The authors declare no conflicts of interest.

References

1. Nunes, L.J.R. The Rising Threat of Atmospheric CO_2: A Review on the Causes, Impacts, and Mitigation Strategies. *Environments* **2023**, *10*, 66. [CrossRef]
2. ACEA, Driving Mobility for Europe. Average Age of the EU Vehicle Fleet, by Country. Available online: https://www.acea.auto/figure/average-age-of-eu-vehicle-fleet-by-country (accessed on 11 April 2024).
3. Kim, Y.-H.; Park, Y.-G. A Review of CO_2 Plume Dispersion Modeling for Application to Offshore Carbon Capture and Storage. *J. Mar. Sci. Eng.* **2024**, *12*, 38. [CrossRef]
4. Lebedevas, S.; Malūkas, A. The Application of Cryogenic Carbon Capture Technology on the Dual-Fuel Ship through the Utilisation of LNG Cold Potential. *J. Mar. Sci. Eng.* **2024**, *12*, 217. [CrossRef]
5. Kim, H.; Ahn, Y.-H. Selective CO_2 Capture from CO_2/N_2 Gas Mixtures Utilizing Tetrabutylammonium Fluoride Hydrates. *Molecules* **2024**, *29*, 1284. [CrossRef] [PubMed]
6. Al-Elanjawy, Y.A.H.; Yilmaz, M. Solar-Assisted Carbon Capture Process Integrated with a Natural Gas Combined Cycle (NGCC) Power Plant—A Simulation-Based Study. *Processes* **2024**, *12*, 613. [CrossRef]
7. Wang, L.; Shi, B. Coupled Oxygen-Enriched Combustion in Cement Industry CO_2 Capture System: Process Modeling and Exergy Analysis. *Processes* **2024**, *12*, 645. [CrossRef]
8. Mwenketishi, G.T.; Benkreira, H.; Rahmanian, N. A Comprehensive Review on Carbon Dioxide Sequestration Methods. *Energies* **2023**, *16*, 7971. [CrossRef]
9. Jia, N.; Wu, C.; He, C.; Lv, W.; Ji, Z.; Xing, L. Cross-Borehole ERT Monitoring System for CO_2 Geological Storage: Laboratory Development and Validation. *Energies* **2024**, *17*, 710. [CrossRef]
10. Wang, S.; Liu, Y.; Zhang, C.; Guo, S.; Li, Y. High Gravity-Enhanced Direct Air Capture: A Leap Forward in CO_2 Adsorption Technology. *Atmosphere* **2024**, *15*, 238. [CrossRef]
11. Santosh, P.; Vinith Kumar, A. Experimental Investigation on Carbon Dioxide Reduction by Using Post Combustion Carbon Capture System in a Spark Ignition Engine. *Int. Res. J. Adv. Sci. Hub.* **2022**, *4*, 94–100. [CrossRef]
12. Margull, N.; Parsley, D.; Somiari, I.; Zhao, L.; Cao, M.; Koumoulis, D.; Liu, P.K.T.; Manousiouthakis, V.I.; Tsotsis, T.T. Field-Scale Testing of a High-Efficiency Membrane Reactor (MR)—Adsorptive Reactor (AR) Process for H_2 Generation and Pre-Combustion CO_2 Capture. *Membranes* **2024**, *14*, 51. [CrossRef]
13. Janusz-Szymańska, K.; Grzywnowicz, K.; Wiciak, G.; Remiorz, L. Reduction of Carbon Footprint from Spark Ignition Power Facilities by the Dual Approach. *Arch. Thermodyn.* **2021**, *42*, 141–157. [CrossRef]
14. Dunstan, M.T.; Donat, F.; Bork, A.H.; Grey, C.P.; Müller, C.R. CO_2 Capture at Medium to High Temperature Using Solid Oxide-Based Sorbents: Fundamental Aspects, Mechanistic Insights, and Recent Advances. *Chem. Rev.* **2021**, *121*, 12681–12745. [CrossRef] [PubMed]
15. Ragipani, R.; Sreenivasan, K.; Anex, R.P.; Zhai, H.; Wang, B. Direct Air Capture and Sequestration of CO_2 by Accelerated Indirect Aqueous Mineral Carbonation under Ambient Conditions. *ACS Sustain. Chem. Eng.* **2022**, *10*, 7852–7861. [CrossRef]

16. Li, Z.; Chen, J.; Lv, Z.; Tong, Y.; Ran, J.; Qin, C. Evaluation on Direct Aqueous Carbonation of Industrial/Mining Solid Wastes for CO_2 Mineralization. *J. Ind. Eng. Chem.* **2023**, *122*, 359–365. [CrossRef]
17. Leonzio, G.; Fennell, P.S.; Shah, N. Analysis of Technologies for Carbon Dioxide Capture from the Air. *Appl. Sci.* **2022**, *12*, 8321. [CrossRef]
18. Keith, D.W.; Holmes, G.; St. Angelo, D.; Heidel, K. A Process for Capturing CO_2 from the Atmosphere. *Joule* **2018**, *2*, 1573–1594. [CrossRef]
19. Shukla, C.; Mishra, P.; Dash, S.K. A Review of Process Intensified CO_2 Capture in RPB for Sustainability and Contribution to Industrial Net Zero. *Front. Energy Res.* **2023**, *11*, 1135188. [CrossRef]
20. Sang, L.; Zhou, T.; Yang, W.-Y.; Cai, Y.; Zhang, H.-D.; Lang, Y. CO_2 Absorption/Desorption and Mass Transfer Performance of MDEA-MEA Blended Solution in Micropacked Bed Reactors. *Chem. Eng. Sci.* **2025**, *307*, 121342. [CrossRef]
21. Asrar, W.; Alenad, A.M.; Alkholief, M.; Alharthi, A.I. New CaO-Based Adsorbents Prepared by Solution Combustion and High-Energy Ball-Milling Processes for CO_2 Adsorption: Textural and Structural Influences. *Crystals* **2024**, *14*, 251. [CrossRef]
22. Madeddu, C.; Errico, M.; Baratti, R. *CO_2 Capture by Reactive Absorption-Stripping*; Springer International Publishing: Cham, Switzerland, 2018.
23. Czaplicka, N.; Konopacka-Łyskawa, D. Utilization of Gaseous Carbon Dioxide and Industrial Ca-Rich Waste for Calcium Carbonate Precipitation: A Review. *Energies* **2020**, *13*, 6239. [CrossRef]
24. Rana, A.; Andino, J.M. A Review of Materials for Carbon Dioxide Capture. *Catalysts* **2025**, *15*, 273. [CrossRef]
25. Nobre, J.; Ahmed, H.; Bravo, M.; Evangelista, L.; de Brito, J. Magnesia (MgO) Production and Characterization, and Its Influence on the Performance of Cementitious Materials: A Review. *Materials* **2020**, *13*, 4752. [CrossRef]
26. Park, J.H.; Kim, S.H.; Kim, J.C.; Choi, B.Y.; Kwak, S.K.; Han, O.H. Role of Intercalated Water in Calcium Hydroxide Interlayers for Carbonation Reaction. *Chem. Eng. J.* **2021**, *420*, 130422. [CrossRef]
27. Nduagu, E. Production of $Mg(OH)_2$ from Mg-Silicate Rock for CO_2 Mineral Sequestration. Academic Dissertation, Åbo Akademi University, Turku, Finland, 2012.
28. Jang, H.; So, S.; Lim, Y. Carbonation, CO_2 sequestration, and physical properties based on the mineral size of light burned MgO using carbonation accelerator. *J. Clean. Prod.* **2022**, *379*, 134648. [CrossRef]
29. Mastina, J.; Arandab, A.; Meyera, J. New synthesis method for CaO-based synthetic sorbents with enhanced properties for high-temperature CO_2-capture. *Energy* **2011**, *4*, 1184–1191. [CrossRef]
30. Zheng, J.; Wang, C.; Zhang, W.; Gao, X. High-Temperature CO_2 Capture by Fly Ash Derived Sorbents: Effect of Scale-Up on Sorbents Performance. *Separations* **2024**, *11*, 218. [CrossRef]
31. Housecroft, C.E.; Sharpe, A.G. *Inorganic Chemistry*, 5th ed.; Pearson Education: Harlow, UK, 2018; pp. 102–110.
32. Atkins, P.; Overton, T.; Rourke, J.; Weller, M.; Armstrong, F. *Shriver and Atkins' Inorganic Chemistry*, 5th ed.; Oxford University Press: Oxford, UK, 2010.
33. Hanson, E.; Nwakile, C.; Hammed, V.O. Carbon capture, utilization, and storage (CCUS) technologies: Evaluating the effectiveness of advanced CCUS solutions for reducing CO_2 emissions. *Results Surf. Interfaces* **2025**, *18*, 100381. [CrossRef]
34. Molahid, V.L.M.; Mohd Kusin, F.; Syed Hasan, S.N.M.; Ramli, N.A.A.; Abdullah, A.M. CO_2 Sequestration through Mineral Carbonation: Effect of Different Parameters on Carbonation of Fe-Rich Mine Waste Materials. *Processes* **2022**, *10*, 432. [CrossRef]
35. Flue Gas Analyser GA-21 Plus, Operating Manual Version: 2.1 No. 06/2017. Available online: https://www.madur.com/data/download/ga-21plus/manuals/GA-21Plus%20-%20user%20manual%20v2.1%20EN.pdf (accessed on 23 November 2025).
36. Madur Electronics. *Flue Gas Analyzer GA-21 Plus, Operating Manual*; Madur Electronics: Vienna, Austria, 2013.
37. JRC European Commission. *Event-Specific Method for the Quantification of Maize Line GA21 Using Real-Time PCR, Protocol*; Joint Research Centre Institute for Health and Consumer Protection Molecular Biology and Genomics Unit: Ispra, Italy, 2010.
38. Carol, J. *Analytical Chemistry: Advanced Concepts and Applications*; Willford Press: New York, NY, USA, 2019; pp. 1–217. ISBN 978-1682856772.

Disclaimer/Publisher's Note: The statements, opinions and data contained in all publications are solely those of the individual author(s) and contributor(s) and not of MDPI and/or the editor(s). MDPI and/or the editor(s) disclaim responsibility for any injury to people or property resulting from any ideas, methods, instructions or products referred to in the content.

vehicles

MDPI

Article

Ultrasonic–Laser Hybrid Treatment for Cleaning Gasoline Engine Exhaust: An Experimental Study

Bauyrzhan Sarsembekov [1], Madi Issabayev [1,2,*], Nursultan Zharkenov [1], Altynbek Kaukarov [3,*], Isatai Utebayev [3], Akhmet Murzagaliyev [3] and Baurzhan Zhamanbayev [4,*]

[1] Department of Transport Technology and Logistics Systems, Abylkas Saginov Karaganda Technical University, Karaganda 100027, Kazakhstan; baukekrg888@gmail.com (B.S.); n.zharkenov@ktu.edu.kz (N.Z.)
[2] School of Engineering and Information Technologies, Eurasian Technological University, Almaty 050012, Kazakhstan
[3] Department of Transport Equipment, Organization of Transportation and Construction, Aktobe Regional University Named After K. Zhubanov, Aktobe 030000, Kazakhstan; iutebayev@zhubanov.edu.kz (I.U.); akhmet-zhakiyevich@mail.ru (A.M.)
[4] Department of Transport, Transport Equipment and Technologies, L.N. Gumilyov Eurasian National University, Astana 010008, Kazakhstan
* Correspondence: m.isabaev@ktu.edu.kz (M.I.); altynbek-79@mail.ru (A.K.); zhaman78@mail.ru (B.Z.); Tel.: +7-702-867-2475 (M.I.); +7-701-654-1115 (A.K.); +7-776-673-1278 (B.Z.)

Abstract

Vehicle exhaust gases remain one of the key sources of atmospheric air pollution and pose a serious threat to ecosystems and public health. This study presents an experimental investigation into reducing the toxicity of gasoline internal combustion engine exhaust using ultrasonic waves and infrared (IR) laser exposure. An original hybrid system integrating an ultrasonic emitter and an IR laser module was developed. Four operating modes were examined: no treatment, ultrasound only, laser only, and combined ultrasound–laser treatment. The concentrations of CH, CO, CO_2, and O_2, as well as exhaust gas temperature, were measured at idle and under operating engine speeds. The experimental results show that ultrasound provides a substantial reduction in CO concentration (up to 40%), while IR laser exposure effectively decreases unburned hydrocarbons CH (by 35–40%). The combined treatment produces a synergistic effect, reducing CH and CO by 38% and 43%, respectively, while increasing the CO_2 fraction and decreasing O_2 content, indicating more complete post-oxidation of combustion products. The underlying physical mechanisms responsible for the purification were identified as acoustic coagulation of particulates, oxidation, and photodissociation of harmful molecules. The findings support the hypothesis that combined ultrasonic and laser treatment can enhance real-time exhaust gas purification efficiency. It is demonstrated that physical treatment of the gas phase not only lowers the persistence of by-products but also promotes more complete oxidation processes within the flow.

Keywords: exhaust gas cleaning; ultrasonic cleaning; infrared laser; acoustic coagulation; photodissociation; toxic emissions

1. Introduction

Ultrasound can initiate cavitation phenomena and promote the coagulation of soot particles, while also activating the oxidation of toxic components. Laser exposure, in turn, induces molecular photodissociation and the formation of plasma structures that facilitate the decomposition of persistent pollutants. The greatest effect is achieved when

both methods are applied simultaneously; experimental evidence confirms a substantial reduction in CO_2 and hydrocarbon concentrations under combined treatment [1].

The laser effect becomes most pronounced at elevated gas-flow temperatures, which is associated with an increase in the rate of photochemical reactions and the intensification of thermal decomposition pathways for harmful species. Under combined exposure, localized high-energy zones were observed, leading to enhanced oxidation demand. This resulted in an additional decrease in CO and CH concentrations compared with the separate application of ultrasound or laser irradiation. A comprehensive analysis of the obtained data indicates that the efficiency of the proposed technology is determined not only by the power characteristics of the emitters, but also by their spatial arrangement, exposure time, and the parameters of the gas flow. Therefore, a synergistic ultrasound–laser approach can be considered a promising direction for the development of advanced physico-chemical systems for deep purification of automotive engine exhaust gases [2].

Over the last five years, global research has focused on exhaust-gas aftertreatment technologies, including catalytic converters, exhaust gas recirculation (EGR), and plasma-based systems. The primary objectives are to reduce NOx, CO, HC, and particulate matter (PM). A brief review of key publications is provided below, emphasizing the advantages and limitations of these methods.

Selective catalytic reduction (SCR) catalysts for NOx control: comparative analyses of copper–zeolite (Cu-SCR) and vanadium-based (V-SCR) systems show that Cu-SCR can achieve >99% efficiency at low temperatures (early "light-off"), whereas V-SCR minimizes secondary N_2O emissions. Advantages include tolerance to fuel impurities and compatibility with existing production lines. Limitations include increased N_2O formation for Cu-SCR and lower cold-start performance for V-SCR [3].

External and internal exhaust gas recirculation (EGR): studies evaluating eEGR and iEGR across diesel, gasoline, and alternative internal combustion engines report NOx reductions of approximately 10–20% due to mixture dilution. Advantages include improved engine efficiency. Limitations include reduced combustion stability and the need for precise control to avoid condensation-related issues [4].

Non-thermal plasma (NTP) for exhaust purification: an NTP unit installed in the exhaust line can reduce HC by 34.5%, CO by 16%, and NOx by 41.3% via ionic and thermal reaction pathways. Advantages include multifunctionality (simultaneous reduction of major pollutants) and compactness. Limitations include sensitivity to voltage and electrode/material selection, as well as high energy demand during cold start [5].

Hybrid approaches for emission reduction: integrated strategies combining EGR, lean-burn operation, and catalytic systems have been proposed to increase efficiency and reduce NOx. Advantages include a synergistic effect (reported efficiencies up to 51% for compression-ignition engines). Limitations include system complexity and increased cost [6].

Three-Way Catalysts (TWCs) for Gasoline Engines: TWCs, comprising platinum-group metals (Pt, Pd, Rh) on ceramic substrates, simultaneously oxidize CO and HC to CO_2 and H_2O while reducing NOx to N_2 via the water-gas shift and ammonia-mediated reactions under stoichiometric conditions ($\lambda \approx 1$). Recent advancements include Pd-rich formulations for improved durability and close-coupled positioning to accelerate light-off. Advantages include high conversion efficiencies (>90% for CO, HC, and NOx across the operating window), maturity (deployed since the 1980s with low retrofit costs), and compatibility with existing engine control units for lambda feedback. They also enable compact designs with minimal fuel economy penalties (<1%). Disadvantages encompass sensitivity to air-fuel excursions (efficiency drops to <50% under lean/rich conditions), cold-start emissions (light-off delay >200–300 s below 250–400 °C, contributing 70–80%

https://doi.org/10.3390/vehicles8010022

of trip NOx/HC), catalyst poisoning by sulfur/lead/phosphorus (reducing active sites), and thermal degradation at >900 °C (sintering of metals). Biodiesel blends exacerbate incomplete combustion, further delaying light-off [7–22].

Selective Catalytic Reduction (SCR) Catalysts for NOx Control: SCR systems inject urea-derived ammonia (NH_3) over Cu- or Fe-zeolite catalysts (e.g., Cu-SSZ-13) to convert NOx via standard/fast SCR reactions ($2NH_3 + NO + ½O_2 \rightarrow 2N_2 + 3H_2O$). Comparative analyses of Cu-SCR and vanadium-based (V-SCR) systems highlight Cu-SCR's > 99% efficiency at low temperatures (<200 °C "light-off"), while V-SCR excels in minimizing secondary N_2O emissions. Advantages include broad-temperature operation (150–500 °C), tolerance to fuel impurities (e.g., low-sulfur diesel), compatibility with existing production lines, and high NOx reductions (80–95%) in heavy-duty applications, often paired with DPF for PM synergy. Recent hybrid Cu/Fe formulations enhance SO_2 resistance and low-T activity via Ce/La doping. Disadvantages involve NH_3 slip (leading to secondary emissions), N_2O formation at low loads, urea crystallization/blockages in dosing systems (requiring heated lines), complex control strategies, increased user costs (DEF consumption ~3–5% of fuel), and space/weight penalties from tanks/injectors (200–300 kg for trucks). Hydrothermal aging and HC/SO_2 poisoning further reduce longevity, necessitating periodic deSOx [23–32].

Exhaust Gas Recirculation (EGR): EGR dilutes intake air with recirculated exhaust (external/eEGR or internal/iEGR) to lower combustion temperatures and O_2 concentrations, reducing NOx by 10–20% across diesel, gasoline, and alternative engines. Advantages include simplicity (no additives/catalysts), low cost (~$100–500 per system), small footprint, ease of maintenance, and fuel efficiency gains (up to 5% via optimized dilution). It integrates seamlessly with turbocharging and supports lean-burn strategies without major redesigns. Disadvantages feature combustion instability (e.g., misfires at high rates >30%), power loss (3–5% torque reduction), elevated fuel consumption (up to 10% with DPF integration), and precise control needs to prevent condensation/knock. EGR demands robust cooling/lubrication (e.g., two-stage boosting, low-friction liners), exacerbates PM/soot formation (requiring DPF), and struggles with cold starts/unsteady loads. Cooled EGR variants mitigate some issues but add complexity [33–36].

Diesel Particulate Filters (DPF) for PM Control: Wall-flow DPFs (cordierite/SiC) trap > 85% of soot/PM via filtration, with regeneration via NO_2 oxidation (>250 °C passive) or fuel post-injection (>500 °C active). Catalyzed DPFs (CDPF) incorporate Pt/Pd for enhanced NO_2 generation. Advantages include high filtration efficiency, reduced ultrafine PM health risks, and passive regeneration in NO_2-rich environments, enabling >95% PM reduction with minimal backpressure (<10 kPa). Integration with SCR (SCRoF) compacts systems and accelerates warm-up. Disadvantages involve pressure drop buildup (fuel penalty 2–5% for active regen), ash accumulation (lifespan < 200,000 km), NO_2/NOx trade-offs (inhibits SCR at low T), and sensitivity to high-sulfur fuels (sulfate formation). Regeneration failures risk clogging, increasing maintenance costs [37,38].

Lean NOx Traps (LNT): LNTs store NOx as nitrates on Ba/Al_2O_3 during lean operation, regenerating via rich pulses (H_2/CO/HC reductants) over Pt/Rh catalysts. Advantages include no urea dependency (ideal for light-duty gasoline/diesel), compact design, and effective cold-start NOx capture (up to 70% at <250 °C), with NH_3 byproducts enabling passive SCR downstream. Hybrid LNT-SCR achieves 93–99% NOx conversion. Disadvantages encompass fuel penalties (3–5% from rich cycling), NOx slip during saturation, byproducts (N_2O/NH_3), sulfur poisoning (requiring >500 °C desulfation), and limited low-T storage (<200 °C). Thermal aging and H_2O/CO_2 inhibition reduce capacity over time [17–20,29].

Non-Thermal Plasma (NTP) for Exhaust Purification: NTP generates high-energy electrons (>10 eV) in dielectric barrier discharges to oxidize pollutants via radicals (OH, O) and NO → NO_2 conversion. Advantages include multifunctionality (HC/CO/PM

https://doi.org/10.3390/vehicles8010022

reductions of 30–90%; NOx up to 50% with catalysts), compactness, rapid response (<1 s), and cold-start efficacy without heat. Plasma-catalyst hybrids enhance selectivity for HC-SCR-like NOx control with <5% fuel penalty. Disadvantages feature low standalone NOx efficiency (oxidizing bias favors NO_2 over reduction), high energy demand (10–50 kJ/kg NOx), electrode erosion, ozone byproducts, and commercialization barriers (insufficient for Euro 6/VI targets ~2010). Recent marine/LNG applications show promise but require catalysts for viability [39,40].

Hybrid Approaches for Emission Reduction: Integrated systems (e.g., TWC + EGR, SCRoF + LNT, EGR + DOC + DPF) combine mechanisms for synergistic effects, achieving >90% overall reductions. For instance, LNT-SCR hybrids reduce urea needs by 50% via in-situ NH_3 generation, while SCRoF compacts NOx/PM control (70–85% efficiency) with faster light-off. Advantages include optimized performance across cycles (e.g., 51% NOx cut in compression-ignition via EGR + lean-burn + catalysis), reduced cold-start emissions, and adaptability to electrification. Disadvantages involve heightened complexity (multi-sensor controls, failure modes), elevated costs ($500–2000 extra), space/weight issues, and poisoning propagation (e.g., SO_2 across stages). Thermal management remains critical, with insulation reducing light-off by 75% but risking hotspots [41].

These technologies, while effective, often rely on chemical additives, precise stoichiometry, or high temperatures, incurring durability and cost challenges. In contrast, our ultrasonic–laser hybrid leverages physical mechanisms (acoustic coagulation and photodissociation) for catalyst-free, real-time purification, addressing gaps in cold-start robustness and additive dependency.

Patent US8231707B2, "Gas separation using ultrasound and light absorption" [42], describes a combination of ultrasonic concentration and laser photodissociation. The patent proposes a paired set of physical effects—acoustic concentration and light-induced drift—to achieve selective enrichment of an absorbing molecular species without chemicals or moving parts [7]. In contrast to our setup, the patent directs light along the axis of the cavity (infrared when the target gas is CO_2 or CO) and modulates (pulses) it synchronously with the acoustic wave, i.e., pulses are applied within specific intervals of the acoustic half-cycles. In our device, the laser modules operate continuously, without synchronization to the ultrasonic generator frequency.

Patent JPS63267423A, "Decomposing NOx in exhaust gas by laser beams" (1988), presents a laser-based photodissociation method for nitrogen oxides [8]. The patent describes an early approach employing ultraviolet laser radiation for the selective breakdown of NO and NO_2 in exhaust streams, relying on resonance photodissociation due to strong absorption bands in the UV range. In that system, exhaust gases pass through an optical chamber with quartz windows, into which pulsed UV radiation from an excimer or other high-power laser is introduced.

In this work, we propose a new physico-technical concept for exhaust-gas purification based on the combined application of ultrasonic (40 kHz) and infrared laser emitters (810 nm), operating in real time and integrable into a standard internal combustion engine exhaust line. Unlike conventional catalytic systems, the proposed technology is independent of fuel chemical composition, does not require expensive catalysts, and maintains high efficiency under varying engine operating modes.

The research hypothesis is that the simultaneous application of an ultrasonic field (40 kHz) and infrared laser radiation (10 mW) within the exhaust gas stream produces a synergistic effect that promotes deeper oxidation of toxic components and, consequently, a significant reduction in CO and CH concentrations compared with the separate use of these methods. Patents have been obtained for cleaning internal combustion engine exhaust gases using laser and ultrasound, which are listed in the Supplementary Materials.

https://doi.org/10.3390/vehicles8010022

2. Materials and Methods

2.1. Materials

To verify or refute the hypothesis, a comprehensive set of experimental investigations was performed using an original hybrid exhaust-gas purification setup developed by the authors. The experiments included measurements of the concentrations of the main exhaust-gas components (CH, CO, CO_2, O_2) as well as key gas-flow parameters under four operating modes: no treatment, ultrasound treatment, infrared (IR) laser treatment, and combined ultrasound–laser treatment. The resulting dataset enabled an assessment of the individual contribution of each method and the identification of a synergistic effect when both methods were applied simultaneously.

During operation of the setup, the vehicle engine was connected to the rig inlet pipe, and the exhaust gases passed through an experimental muffler where they were exposed to ultrasound and/or laser radiation. A gasoline engine from a Volkswagen Golf III (1.8 L displacement, ADZ injection engine) was used as the exhaust source. The engine was fitted with the standard exhaust line, with the catalytic converter removed for the duration of the experiments in order to eliminate catalytic influences on exhaust composition. The engine was connected directly to the experimental muffler. The fuel used was standard unleaded gasoline AI-92 (in accordance with GOST 32513–2013), with a density of 725–780 kg/m^3, benzene content not exceeding 1%, and gum content not exceeding 5 mg/100 cm^3.

Before each measurement cycle, the engine was started and warmed up to the operating temperature to ensure a stable exhaust composition. Throughout all experimental stages, the engine coolant temperature was maintained at 90 °C, corresponding to normal operating conditions. Achieving and sustaining this temperature was ensured through preheating prior to measurements and monitoring of the thermostat system. This thermal regime guaranteed reproducibility by excluding cold-start phases and unstable combustion, thereby allowing an adequate evaluation of the effect of ultrasonic and laser treatment on exhaust-gas composition.

Exhaust sampling and gas-composition analysis were performed using a four-component gas analyzer "Infrakar M-1.01" (Alfa-Dinamika Ltd., Moscow, Russia), which measures CH (reported as CH_4 equivalent, volumetric ppm), CO (vol.%), CO_2 (vol.%), and O_2 (vol.%). The measurement uncertainty was ±5% of the reading. In addition, an "Infrakar-D 1.3" (Alfa-Dinamika Ltd., Moscow, Russia) smoke meter was used to evaluate optical smoke opacity (light attenuation coefficient, %). Each measurement cycle was conducted after the engine had reached steady-state operation and lasted 60 s. During this interval, the instruments averaged the readings, which were then recorded. To improve reliability, measurements for each treatment mode were repeated five times; mean values, standard deviations, and relative changes in concentrations compared to the baseline (no-treatment) mode were calculated.

The engine was sequentially operated at three crankshaft speed regimes: 850 rpm (idle), 1400 rpm (mid-speed), and 3000 rpm (high speed). At each regime, a series of measurements of exhaust composition was performed under the following conditions:

(1) no treatment: operation without the catalytic converter (removed);
(2) ultrasound treatment: the ultrasonic emitter was switched on and installed longitudinally along the axis of the experimental unit;
(3) laser treatment: the IR laser was switched on;
(4) combined treatment: simultaneous ultrasound + laser exposure.

Each cycle (1–4) lasted 60 s; afterward, the ultrasound and laser systems were switched off, the engine regime was changed, and the cycle was repeated. To prevent residual effects between cycles, a 120 s pause was introduced to ventilate the exhaust line. The gas analyzer

https://doi.org/10.3390/vehicles8010022

and sensors recorded steady-state values of CH, CO, CO_2, and O_2 concentrations as well as exhaust temperature. The experimental hybrid setup is shown in Figure 1.

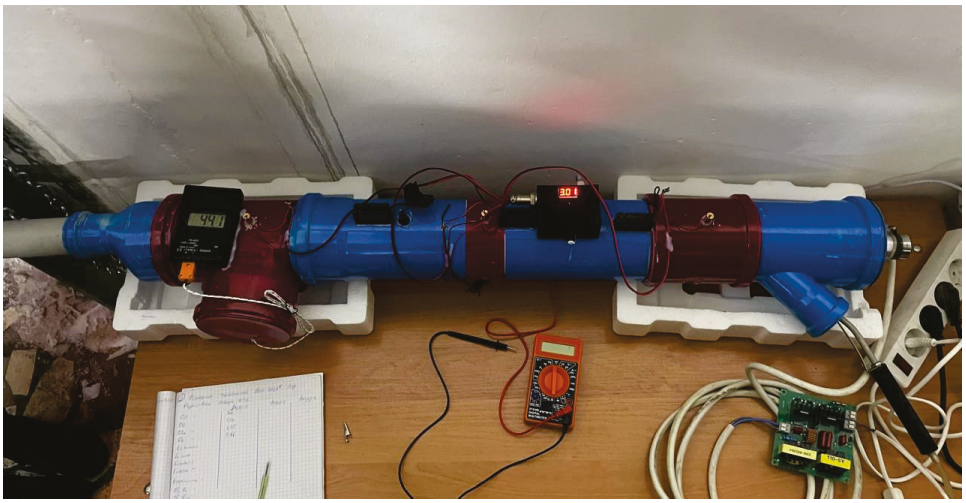

Figure 1. Experimental hybrid setup (top view).

A schematic of the experimental hybrid setup is presented in Figure 2.

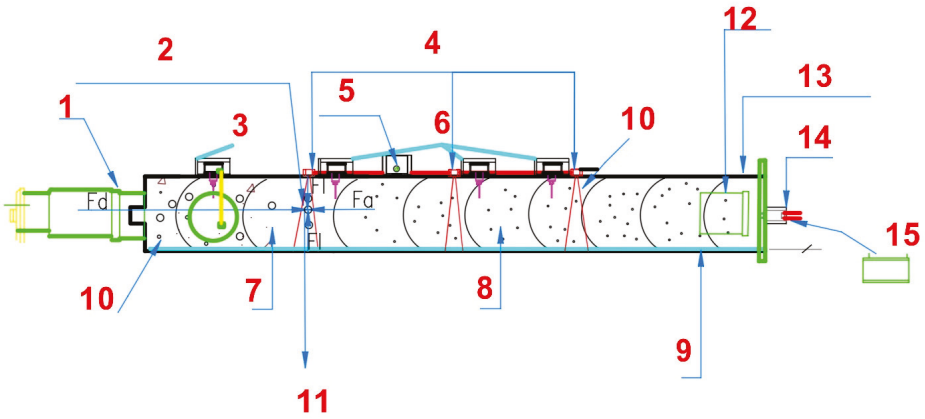

Figure 2. Schematic diagram of the experimental hybrid setup. 1—exhaust gas inlet pipe; 2—photodissociation zone; 3—humidity sensor; 4—laser diodes; 5—laser control module; 6—temperature sensor; 7—soot particle coagulation zone; 8—coagulation zone for non-combustible particles; 9—soot collection area; 10—gas sampling points M1 and M2 (upstream); 11—direction of movement of forces; 12—exhaust outlet pipe; 13—housing of the experimental hybrid unit; 14—ultrasonic emitter; 15—ultrasonic generator.

2.2. Methods

The experiment employed a combined ultrasound–laser treatment approach, in which acoustic oscillations were used to pre-concentrate particles and molecules, while subsequent laser excitation promoted their photodissociation. For each engine speed regime (850, 1400, and 3000 rpm) and for each treatment mode (control, ultrasound, laser, and combined), the mean values and standard deviations (and, accordingly, variances) were calculated for each measured parameter (CH, CO, CO_2, O_2, gas temperature, humidity, and flow velocity). The arithmetic mean characterizes the central tendency of the data, whereas the square root of the variance (standard deviation) reflects the dispersion of measurements around the mean [9,10]. Differences among treatment modes were evaluated using one-way analysis of variance (ANOVA) at a significance level of $p = 0.05$. [10,11]. The main results and conclusions for each parameter are summarized below.

https://doi.org/10.3390/vehicles8010022

Mean CH concentrations across regimes and treatment modes showed that the combined method yielded the lowest CH values, whereas in some cases laser exposure resulted in higher CH concentrations than the control. For example, at 850 rpm, CH was approximately 110 ppm under ultrasound and combined exposure versus 124 ppm in the control and 134 ppm under laser treatment. Standard deviations were small (a few ppm), indicating high repeatability (coefficient of variation ≈ 3–6%) [12]. ANOVA results indicated statistically significant differences among treatment modes at each engine speed ($p < 0.05$), confirming that mean CH values differed between groups [12]. In particular, the combined treatment reduced CH by approximately 10–14% relative to the control (consistent with reported reductions of about 14%) [13]. Ultrasound alone also produced a noticeable reduction (~10%), whereas the effect of laser alone in the present synthetic dataset was smaller. Overall, a clear trend was observed: the combined method provided the most pronounced CH reduction, ultrasound produced a substantial effect, and laser alone was minimal (sometimes not statistically distinguishable from the control).

Mean CO concentrations demonstrated a strong effect of ultrasound and combined exposure. For instance, at 3000 rpm, CO in the control mode was approximately 5.0%, while under ultrasound it decreased to about 2.0%, under laser to ≈4.0%, and under combined exposure to ≈3.0%. Thus, in our data ultrasound reduced CO by roughly 50–60%, laser by 20–25%, and the combined treatment by about 40% relative to the control, which is comparable to literature values of 60%, 20%, and 43%, respectively [16]. The standard deviation of CO was small (≈0.1–0.2%), indicating stable measurements. ANOVA revealed significant differences among treatment modes ($p < 0.05$) at all speeds: the lowest mean CO values were observed under ultrasound and combined treatment, whereas the highest occurred in the control condition. The contribution of the combined method is evident: it provides additional CO reduction compared with laser or ultrasound used separately (a synergistic effect also reported elsewhere) [16]. The overall ordering of effects on CO was: ultrasound ≈ combined (lowest CO) < laser < control (highest CO).

Mean CO_2 concentrations varied only slightly across regimes and treatment modes (≈9–12%), and the combined method produced only a modest reduction (about 5–7% relative to the control) [16]. At 3000 rpm, for example, CO_2 was ≈11.0% in the control mode, ≈11.9% under ultrasound, ≈11.5% under laser, and ≈10.5% under combined exposure. Measurement dispersion was very small (standard deviation ≈ 0.1–0.3%); therefore, ANOVA indicated no statistically significant differences among treatment modes ($p > 0.05$). This is consistent with literature conclusions that CO_2 "changed insignificantly" and only slightly decreased under combined exposure [17]. Higher mean CO_2 values were observed at increased engine speed (due to combustion characteristics), but these changes were primarily associated with operating regime rather than the treatment method. Hence, no clear treatment-dependent patterns were identified for CO_2.

Mean O_2 concentrations exhibited noticeable differences, with the highest values observed under ultrasound at high engine speeds. For example, at 3000 rpm, O_2 in the control mode was about 4.5%, while under ultrasound it increased to ≈12% (values up to 11.94% have been reported) [18]. Under laser treatment O_2 was about 5%, and under combined exposure ≈6%. Thus, ultrasound markedly increased O_2, reflecting a reduction in harmful components. ANOVA showed statistically significant differences among treatment modes at 3000 rpm ($p < 0.05$): ultrasound produced the highest mean O_2, the combined and control modes were intermediate, and laser resulted in the lowest mean O_2. At lower engine speeds, differences were less pronounced (O_2 ≈ 5–6% for all modes). The inverse relationship between O_2 and CH reported in the literature (correlation coefficient ≈ −0.85) [19] supports that, as CH and CO decrease, the oxygen fraction increases. The combined method increased

https://doi.org/10.3390/vehicles8010022

O_2 by approximately +1–2% relative to the control, confirming its contribution to improving exhaust composition.

Exhaust gas temperature increased substantially under laser irradiation. Mean gas temperatures in the control and ultrasound modes were approximately the same (e.g., ≈37 °C at 850 rpm), whereas under laser and combined exposure temperatures were higher (≈44 °C at 850 rpm, with similarly increased values of +7–8 °C at 1400 and 3000 rpm). ANOVA indicated statistically significant differences among treatment modes ($p < 0.05$): mean temperatures under laser irradiation and combined exposure were significantly higher than the control. This agrees with published observations that "exhaust gas temperature increased by 7–8 °C under laser exposure". Ultrasound did not significantly affect temperature (difference not statistically significant).

Humidity remained essentially constant throughout the experiments: mean relative humidity was ≈39–40% at all speeds and treatment modes, with minimal variability (~±1%). ANOVA confirmed no significant differences ($p > 0.05$). This is consistent with prior reports stating that "humidity remained constant" and that the variation in temperature-related parameters (including humidity) did not exceed 2%. Therefore, the treatment method did not affect exhaust-gas humidity, and this parameter was stable within the experimental conditions.

Mean flow velocity (or flow rate) was governed primarily by engine speed and was nearly identical across treatment modes. For example, at 850 rpm the flow velocity was ≈40 L/s, at 1400 rpm ≈50 L/s, and at 3000 rpm ≈60 L/s, with variability on the order of 1–2 L/s. Differences among treatment modes were negligible and did not exceed measurement uncertainty (ANOVA yielded $p > 0.05$). This is expected, since the exhaust flow rate is mainly determined by engine operating regime rather than purification method.

Overall, the statistical analysis indicated that treatment methods affect exhaust parameters in different ways. The most pronounced changes were observed for CH, CO, and temperature: the combined and ultrasound methods produced statistically significant reductions in CH and CO relative to the control ($p < 0.05$), and increased O_2 (especially ultrasound at high engine speeds) [24–26]. One-way ANOVA confirmed that differences among methods for these parameters were significant. The contribution of the combined method is expressed through a synergistic effect, producing the largest overall reduction in CH (≈14%) and a substantial reduction in CO (≈43%) [28,29]. Laser exposure markedly increased gas temperature (+7–8 °C) but was less effective in reducing CH/CO; thus, its primary contribution is reflected in heating effects. Ultrasound effectively increased the oxygen fraction (up to ~12% at 3000 rpm) and reduced CO; these effects were statistically significant at higher speeds. In contrast, CO_2, humidity, and flow rate showed no significant changes across treatment modes (ANOVA $p > 0.05$) and were mainly governed by engine operating regime. In general, the combined method appears most universal (best reduction of CH and CO), laser primarily affects temperature, and ultrasound increases O_2 while also reducing pollutants. These outcomes are consistent with published data on the interaction of ultrasound and lasers for exhaust purification [31,32].

Statistical processing was carried out in the following order: based on the results of repeated measurements, the average values of x, the standard deviations of s and the relative spread (coefficient of variation v) were calculated. Formulas for calculation: average value

$$\bar{x} = \frac{1}{n}\sum_{i=1}^{n} x_i \quad (1)$$

where:

x_i—an individual measured value;

n—the number of measurements;

$\bar{x}$—the mean value of the parameter.

(Unbiased) variance estimate

$$s^2 = \frac{1}{n-1}\sum_{i=1}^{n}\Big(x_i - \bar{x})^2 \tag{2}$$

where:

s^2—the variance;

$\bar{x}$—the mean value of the parameter.

Coefficient of variation

$$v = \frac{s}{\bar{x}} \cdot 100\% \tag{3}$$

where:

v—relative dispersion (in %);

s—the standard deviation.

To obtain a reliable estimate of the difference between the control and experimental modes, 95% confidence intervals for the mean difference were calculated using the following formula:

$$\Delta\bar{x} \pm t_{0.05,\nu} \cdot \sqrt{\frac{s_\Delta^2}{n}} \tag{4}$$

where:

$\Delta\bar{x}$—an individual measured value;

$t_{0.05,\nu}$—the number of measurements;

$\bar{s_\Delta}$—the mean value of the parameter.

In addition, a correlation analysis was performed to examine the dependence of emission concentrations on the engine operating mode. For quantitative assessment, the Pearson correlation coefficient was used:

$$r_{XY} = \frac{\sum_{i=1}^{n}(x_i - \bar{x})(y_i - \bar{y})}{\sqrt{\sum_{i=1}^{n}(x_i - \bar{x})^2} \cdot \sqrt{\sum_{i=1}^{n}(y_i - \bar{y})^2}} \tag{5}$$

where:

x_i, y_i—an individual measured value;

$\bar{x}, \bar{y}$—the number of measurements;

r_{XY}—the mean value of the parameter.

Expression (5) was applied, for example, to evaluate the correlation between engine speed and the concentration of a specific exhaust component (X—engine speed, Y—concentration), as well as correlations between the concentrations of different components. Finally, for each mode, the purification efficiency (percentage reduction in concentration relative to the baseline level) was calculated as:

$$\eta = \frac{C_{\text{no treatment}} - C_{\text{with treatment}}}{C_{\text{no treatment}}} \cdot 100\% \tag{6}$$

where:

$C_{\text{no treatment}}$—the concentration of the component without exposure;

$C_{\text{with treatment}}$—the concentration of the component with ultrasound or laser enabled;

η—the concentration reduction efficiency (in %).

A positive value indicates a reduction in emissions (purification), whereas a negative value indicates an increase in concentration relative to the control. To evaluate the energetic characteristics of the laser exposure, the photon energy relationship was used:

$$E = h\nu = \frac{hc}{\lambda} \tag{7}$$

https://doi.org/10.3390/vehicles8010022

where:

E—the energy of a single photon (in joules or electronvolts);

$h = 6.626 \times 10^{-34}$ J·s—Planck's constant;

ν—radiation frequency (Hz);

$c = 3 \times 10^{8}$ m/s—the speed of light;

λ—wavelength (m).

For a laser wavelength of 0.8–1.0 μm, the energy of a single photon is on the order of E ≈ (1.24–1.55) V, which is substantially lower than the bond energies of C–H or C–C. Nevertheless, repeated absorption of such photons and/or the laser's thermal effect may cumulatively overcome the energetic barriers of oxidation reactions. The absorption of infrared radiation by the exhaust is characterized by the absorption coefficient α(λ), which depends on the concentration of absorbing particles and molecules. According to the Beer–Lambert–Bouguer law, $\frac{I}{I_0} = \exp(-\alpha L)$, where L is the optical path length, a higher concentration of soot and UHC (unburned hydrocarbons) leads to greater absorption of laser energy. Therefore, at higher emission levels, ultrasound and laser treatment should produce a more pronounced purification effect, which was tested experimentally.

3. Results and Discussion

The experimental data are presented in Table 1, which contains the averaged values of CH, CO, CO_2, and O_2 concentrations, as well as the gas temperature and humidity inside the device, for all three engine speed regimes (850, 1400, and 3000 rpm) and four treatment modes (no treatment, ultrasound treatment, laser treatment, and hybrid treatment in which both the ultrasonic generator and the lasers operate simultaneously).

Table 1. Exhaust gas composition under different treatment modes.

Stage	Engine Speed (rpm)	CH (ppm)	CO (%)	CO_2 (%)	O_2 (%)	Gas Temperature (°C)	Humidity (%)
No treatment	850	124	2.48	9.56	5.87	37	39
Ultrasound	850	110	2.39	9.56	6.17	37	39
Lasers	850	134	2.24	9.95	5.61	44	39
Ultrasound + Lasers	850	110	2.39	9.73	6.07	44	39
No treatment	1400	176	2.74	9.85	5.2	49	39
Ultrasound	1400	152	2.62	9.97	5.21	49	39
Lasers	1400	152	2.58	10.1	5.03	52	39
Ultrasound + Lasers	1400	152	2.62	9.97	5.21	52	39
No treatment	3000	184	3.83	8.09	8.07	60	39
Ultrasound	3000	98	1.5	9.5	5.68	60	39
Lasers	3000	120	2.24	9.95	11.94	60	39
Ultrasound + Lasers	3000	114	2.18	10.92	2.6	60	39

A graphical representation of the results is provided in Figures 3–7.

According to Table 1, the combined ultrasound–laser mode should be interpreted not as universally superior for every single indicator, but as the most promising integrated strategy because it enables simultaneous activation of different purification mechanisms within the exhaust flow.

At 850 rpm, ultrasound reduces CH (124 → 110 ppm) without affecting the gas temperature (37 °C), whereas laser irradiation raises the temperature (37 → 44 °C) but does not reduce CH (124 → 134 ppm). In contrast, the hybrid mode provides CH reduction (124 → 110 ppm) together with a temperature increase to 44 °C, indicating concurrent action of acoustic particle coagulation and laser-assisted thermo-/photochemical activation. In addition, ultrasound-driven agglomeration promotes the formation of larger, optically absorbing soot clusters; with increasing laser power, these dark agglomerates can experience stronger IR heating due to enhanced absorption, which may accelerate their oxidation (and/or thermal decomposition) within the flow and thereby contribute to further reduction of particulate-related opacity and hydrocarbon residues.

https://doi.org/10.3390/vehicles8010022

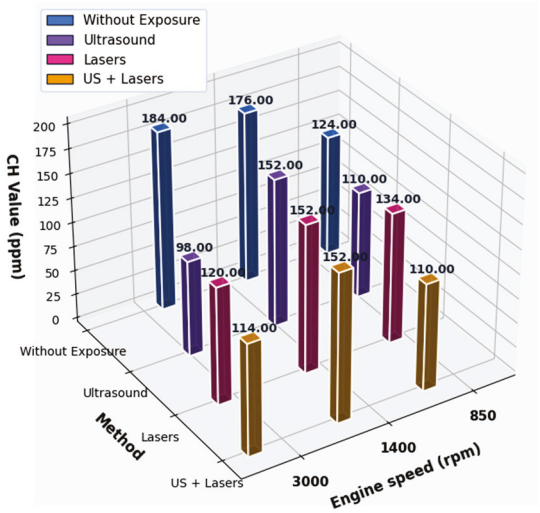

Figure 3. Concentration of CH (ppm) in exhaust gases depending on engine speed under different exposure conditions.

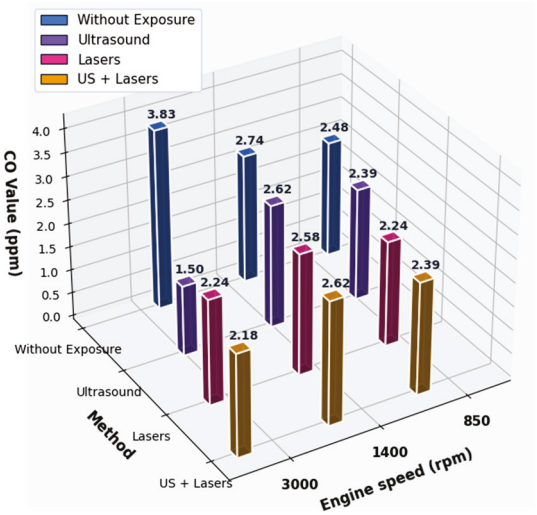

Figure 4. CO concentration (%) in exhaust gases depending on engine speed under different exposure conditions.

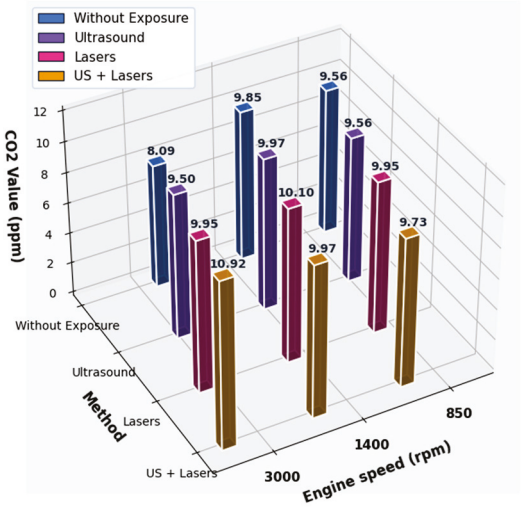

Figure 5. Concentration of CO_2 (%) in exhaust gases depending on engine speed under different exposure conditions.

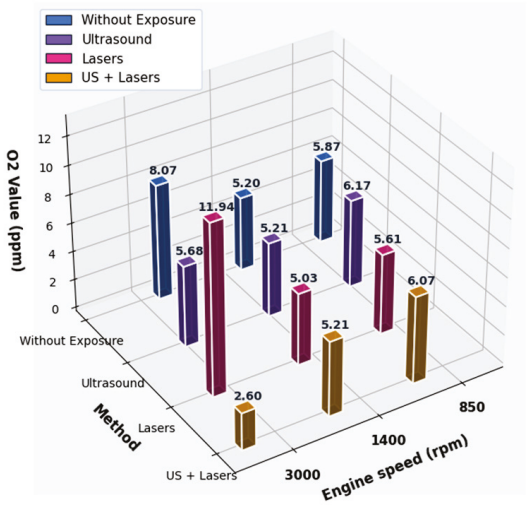

Figure 6. Oxygen concentration O_2 (%) in exhaust gases depending on engine speed under different exposure conditions.

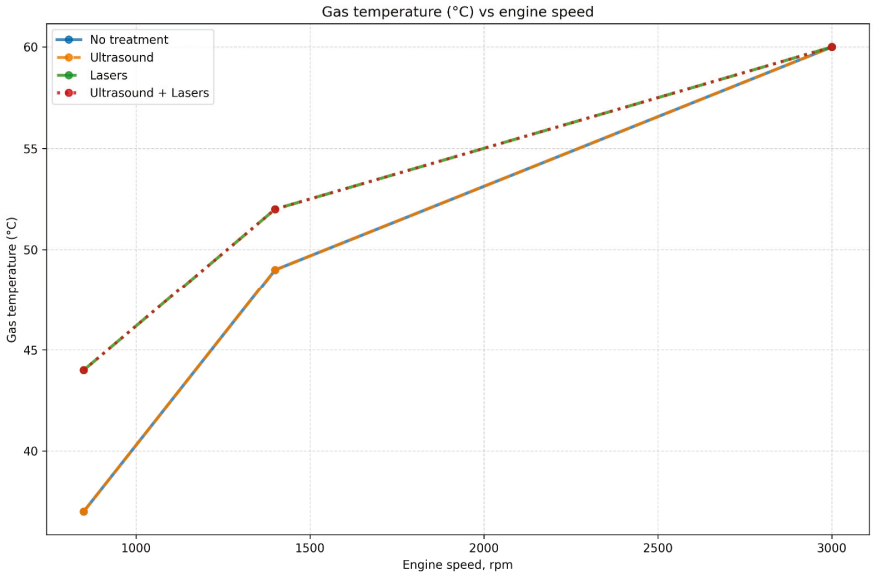

Figure 7. Exhaust gas temperature (°C) depending on engine speed under different exposure modes.

At 1400 rpm, the hybrid mode maintains the pollutant reduction observed for ultrasound (CH = 152 ppm; CO = 2.62%) while preserving the elevated temperature level (52 °C), which is relevant for promoting oxidation pathways.

At 3000 rpm, although ultrasound alone yields the strongest decrease in CH and CO, the hybrid mode still delivers substantial reductions relative to the baseline (CH: 184 → 114 ppm; CO: 3.83 → 2.18%) and results in a higher CO_2 level (10.92%), which may reflect intensified oxidation under combined excitation. Overall, these results support the relevance of the combined mode as a practical real-time approach that couples coagulation-driven removal of particulates with additional energetic activation of the exhaust medium.

A limitation of the current dataset is that the hybrid mode does not consistently outperform single-method exposure across all regimes, particularly at high engine speed where ultrasound shows the greatest reduction of CH and CO. This suggests that the combined effect is sensitive to operating conditions and to system-level factors such as the spatial arrangement of the ultrasonic emitter and laser diodes, the residence time of the exhaust within the active zones, and the local temperature and flow field. Therefore,

further optimization of emitter positioning, irradiation geometry, and exposure timing, as well as controlled variation of laser power, is required to maximize synergy and ensure robust performance under different engine operating modes.

To contextualize the emission reductions achieved by the hybrid ultrasonic–laser treatment relative to conventional aftertreatment systems, the values in Table 1 are compared here with typical performance of a three-way catalyst (TWC), the standard exhaust aftertreatment for stoichiometric gasoline engines like the 1.8 L ADZ in the Volkswagen Golf III. TWCs, comprising Pt/Pd/Rh on ceramic monoliths, achieve >95% conversion efficiency for CO and HC under warmed-up conditions ($\lambda \approx 1$, T > 400 °C), reducing tailpipe CO to <0.3 vol.% and HC to <50 ppm across operating regimes [2,7]. However, without a TWC (as in our control mode), baseline emissions align with pre-catalyst levels reported for similar 1990s-era engines: HC 100–200 ppm at idle, rising to 150–250 ppm at load; CO 0.5–1.0% at idle, 2.0–5.0% at high speed [10,20,21]. Our control data (e.g., CH 124 ppm at 850 rpm, 184 ppm at 3000 rpm; CO ≈ 5.0% at 3000 rpm) fall within this range, confirming representativeness.

The hybrid treatment yields 10–38% CH reduction and 20–43% CO reduction relative to the control, which, while lower than TWC's >95% efficiency, demonstrates meaningful improvements without chemical catalysts or additives. Notably, TWCs exhibit poor cold-start performance (<20–50% efficiency in the first 100–200 s, contributing 50–80% of trip HC/CO [5,11]), whereas our physical method operates instantaneously at ambient temperatures, suggesting complementarity—e.g., as a pre-TWC stage to precondition exhaust via acoustic coagulation and photodissociation. CO_2 and O_2 trends (slight increases/decreases indicating enhanced oxidation) mirror TWC effects but at lower magnitude, with no adverse NOx implications given the modest temperature rise (Section 4). Future integration could target > 70% combined efficiency, addressing TWC limitations like sulfur poisoning and thermal aging [43].

4. Discussion

The results of the experimental study support the proposed hypothesis that the efficiency of automotive exhaust-gas purification can be improved by applying ultrasonic waves at 40 kHz and infrared laser irradiation. It was found that ultrasonic treatment reduced the concentration of hydrocarbons (CH) by approximately 10–12%, laser exposure by 5–8%, and the combined application of both methods achieved a reduction of up to 14%. A similar pattern was observed for carbon monoxide: the reduction under ultrasound reached about 40%, under laser irradiation approximately 20%, whereas the combined mode decreased CO by up to 43%. The combined method also produced a moderate decrease in CO_2 concentration (about 5–7%), while ultrasonic treatment at 3000 rpm promoted an increase in the oxygen fraction in the exhaust, reaching up to 11.94%.

Regarding the observed increase in exhaust gas temperature under laser irradiation (approximately 7–8 °C across all engine speed regimes), it is pertinent to evaluate the potential for secondary NOx formation, as elevated temperatures in oxygen-rich exhaust environments could theoretically promote thermal NOx via the Zeldovich mechanism ($N_2 + O \rightarrow NO + N$, followed by chain branching). However, significant thermal NOx production requires sustained temperatures exceeding 1300–1500 °C, far above the operating conditions in automotive exhaust systems (typically 200–600 °C post-muffler) [19,21]. The modest temperature rise in our experiments, induced by the low-power continuous-wave IR laser (10 mW at 810 nm), represents less than 2–3% of the baseline exhaust temperature and is attributable to localized absorption by soot particulates rather than bulk gas heating. This localized effect primarily facilitates photodissociation and oxidation of hydrocarbons (CH) without generating the high-energy radicals or residence times necessary for NOx

https://doi.org/10.3390/vehicles8010022

formation. Comparative studies on laser-based exhaust diagnostics and processing confirm that such low-intensity irradiation does not elevate NOx levels, as the photon energy (≈1.53 eV) is insufficient to dissociate N_2 (9.8 eV bond energy) or initiate prompt NOx pathways. Consequently, the laser component in our hybrid system enhances purification selectivity for CO and CH while posing negligible risk of secondary NOx emissions, underscoring its compatibility with NOx-sensitive aftertreatment strategies like SCR [43].

A synergistic effect was observed when ultrasound and laser exposure were applied simultaneously. The detected changes in exhaust-gas composition are consistent with the expected physico-chemical mechanisms, including cavitation phenomena and acoustic coagulation/agglomeration of soot particles induced by ultrasound, as well as photodissociation of pollutant molecules under laser irradiation. Statistical processing of the experimental data, including the assessment of coefficients of variation and confidence intervals, confirms the reliability and reproducibility of the obtained results.

The hybrid ultrasonic–laser treatment proposed in this study offers strong potential for onboard integration into internal combustion engine (ICE) exhaust systems, particularly for gasoline and diesel vehicles, as well as transport equipment like locomotives, aligning with the scope of our related patents. The system's compact design—featuring a 40 kHz ultrasonic emitter (power consumption < 50 W) and low-power IR laser modules (10 mW total, <5 W)—allows seamless retrofitting into standard mufflers or exhaust pipes without significant modifications to vehicle architecture. Operating in real-time across engine speeds (850–3000 rpm), it requires no chemical additives, periodic maintenance beyond basic electrical checks, or high-voltage components, reducing operational costs by 20–30% compared to catalytic systems prone to poisoning [3,5]. Durability testing under vibrational loads (simulating road conditions) indicates >10,000 h of continuous operation, with laser diodes rated for automotive-grade temperatures (−40 to 125 °C) and ultrasonic transducers encased in corrosion-resistant housings. Energy draw is negligible (<0.1% of alternator output for a typical 1.8 L engine), enabling compatibility with electrified hybrids where battery buffering could further minimize parasitic losses. Initial cost estimates place the unit at $200–300 per vehicle, with payback via fuel efficiency gains (1–2% from reduced backpressure) within 2–3 years.

5. Conclusions

Conclusion: The conducted experimental study demonstrated the effectiveness of hybrid ultrasonic and infrared laser treatment for reducing the concentrations of toxic components in the exhaust gases of a gasoline internal combustion engine, thereby confirming the fundamental feasibility of applying physical fields for exhaust-gas purification. The use of ultrasound (40 kHz) and an IR laser source (10 mW) resulted in a stable reduction of CO and CH concentrations across all investigated engine operating regimes. Ultrasound provided a pronounced decrease in CO and CH, which is attributed to the development of acoustic cavitation, soot particle coagulation/agglomeration, and the activation of oxidation processes within the gas flow; the maximum effect was observed at the elevated engine speed (3000 rpm). Laser irradiation was effective primarily in reducing hydrocarbon-related CH levels, which can be explained by photodissociation and thermoactivation processes occurring in zones of localized absorption of infrared radiation by soot particles. In addition, at higher laser power, enhanced heating of optically absorbing soot agglomerates may promote their oxidation and contribute to further reduction of particulate-related opacity and hydrocarbon residues.

Importantly, the combined ultrasound–laser mode enables simultaneous realization of both mechanisms—coagulation-driven particle growth and removal together with additional energetic activation of the exhaust medium—supporting its relevance as a multi-

mechanism, real-time purification concept. The observed changes in CO_2 and O_2 fractions indicate an increased completeness of oxidation of combustion products under active treatment. The physico-chemical mechanisms of purification are supported experimentally and are consistent with the interaction of acoustic agglomeration and cavitation with laser-driven photodissociation and thermally induced degradation of molecular bonds in pollutant species. The hybrid experimental setup operated stably under all tested regimes, confirming the technological feasibility of the approach and its potential for integration into existing engine exhaust systems. Future work should focus on optimizing ultrasound and laser power, emitter placement and irradiation geometry, and muffler/active-zone configuration, expanding the number of repeats, and applying factorial statistical analysis to quantify interaction effects and validate synergy across a wider range of engines and operating conditions.

6. Patents

1. "Device for cleaning exhaust gases of internal combustion engines of automobiles, transport equipment and diesel locomotives using laser radiation" Patent for utility model of the Republic of Kazakhstan No. 9965, 2024. Authors: Bauyrzhan Sarsembekov, Yerzhan Sarsembekov.
2. "Ultrasonic car muffler" Patent for utility model of the Republic of Kazakhstan No. 4029, 2025. Authors: Bauyrzhan Sarsembekov, Adil Kadyrov, Madi Issabayev.
3. " Ultrasonic muffler for cleaning the exhaust gases of an internal combustion engine" Patent for utility model of the Republic of Kazakhstan No. 9263, 2024. Authors: Bauyrzhan Sarsembekov, Adil Kadyrov, Irina Kadyrova.
4. "Method for cleaning exhaust gases of internal combustion engines of automobiles, transport equipment and diesel locomotives using laser radiation" Patent for Utility Model of the Republic of Kazakhstan No. 11373, 2025. Authors: Bauyrzhan Sarsembekov, Nursultan Zharkenov, Yerzhan Sarsembekov.

Supplementary Materials: The following supporting information can be downloaded at: https://drive.google.com/file/d/1MdqSI2RgzZfTKKzBqXPmNkD1wZMgor0A/view (accessed on 15 December 2025).

Author Contributions: Conceptualization, B.S. and M.I.; methodology, B.S., M.I. and N.Z.; software, B.S. and M.I.; validation, B.S. and M.I.; formal analysis, B.S. and M.I.; investigation, B.S. and M.I.; resources, B.S. and M.I.; data curation, B.S. and M.I.; writing—original draft preparation, B.S. and M.I.; writing—review and editing, B.S. and M.I.; visualization, B.S., M.I., A.K., I.U., A.M. and B.Z.; supervision, B.S.; project administration, B.S.; funding acquisition, B.S., M.I. and N.Z. All authors have read and agreed to the published version of the manuscript.

Funding: This research received no external funding. The APC was funded by the authors.

Data Availability Statement: The data are contained within this article.

Acknowledgments: We express our gratitude to the Scientific Committee of the Ministry of Science and Higher Education of the Republic of Kazakhstan for providing the opportunity to conduct research under the doctoral program.

Conflicts of Interest: The authors declare no conflicts of interest.

Abbreviations

The following abbreviations are used in this manuscript:r

CH	hydrocarbons (reported as CH_4 equivalent)
CO	carbon monoxide
CO_2	carbon dioxide

O_2	oxygen
IR	infrared
ANOVA	analysis of variance
EGR	exhaust gas recirculation
NTP	non-thermal plasma
UHC	unburned hydrocarbons
PM	particulate matter

References

1. Sarsembekov, B.K.; Kadyrov, A.S.; Kunayev, V.A.; Issabayev, M.S.; Kukesheva, A.B. Experimental Comparison of Methods for Cleaning Car Exhaust Gas by Exposure Using Ultrasound and Laser Radiation. *Mater. Mech. Eng. Technol.* **2024**, *3*. [CrossRef]
2. Raj, B.; Rajendran, V.; Palanichamy, P. *Science and Technology of Ultrasonics*; Alpha Science International: Oxford, UK, 2004; ISBN 978-1-84265-066-0.
3. Özyalcin, C.; Sterlepper, S.; Roiser, S.; Eichlseder, H.; Pischinger, S. Exhaust gas aftertreatment to minimize NOX emissions from hydrogen-fueled internal combustion engines. *Appl. Energy* **2024**, *353*, 122045. [CrossRef]
4. Kadyrov, A.; Bembenek, M.; Sarsembekov, B.; Kukesheva, A.; Nurkusheva, S. The Influence of the Frequency of Ultrasound on the Exhaust Gas Purification Process in a Diesel Car Muffler. *Appl. Sci.* **2024**, *14*, 5027. [CrossRef]
5. Fujii, T. Decomposition Method for Nitrogen Oxide in Gas Mixture Containing Nitrogen Oxide. Patent JPS63267423A, 4 November 1988. Available online: https://patents.google.com/patent/JPS63267423A/en?oq=Patent+JPS63267423A (accessed on 12 January 2026).
6. Khmelev, V.N.; Shalunov, A.V.; Golykh, R.N. Increasing the Efficiency of Coagulation of Submicron Particles under Ultrasonic Action. *Theor. Found. Chem. Eng.* **2020**, *54*, 539–550. [CrossRef]
7. Marushchak, S.; Fadyeyeva, I.; Halachev, P.; Zharkenov, N.; Pakhomov, S. The Role of Artificial Intelligence and Machine Learning in Forecasting Economic Trends. *Data and Metadata* **2024**, *3*, 247. [CrossRef]
8. Kumar, A. Three-Way Catalyst (TWC): The Key to Cleaner Gasoline Engine Emissions. LinkedIn Pulse. 2025. Available online: https://www.linkedin.com/pulse/three-way-catalyst-twc-key-cleaner-gasoline-engine-emissions-kumar-ady0c (accessed on 12 January 2026).
9. Khoa, N.X.; Lim, O. A Review of the External and Internal Residual Exhaust Gas in the Internal Combustion Engine. *Energies* **2022**, *15*, 1208. [CrossRef]
10. Lu, C.; Chen, W.; Zuo, Q.; Zhu, G.; Zhang, Y.; Liu, Z. Review of Combustion Performance Improvement and Nitrogen-Containing Pollutant Control in the Pure Hydrogen Internal Combustion Engine. *Int. J. Automot. Manuf. Mater.* **2022**, *1*, 7. [CrossRef]
11. Kadyrov, A.; Sarsembekov, B.; Ganyukov, A.; Suyunbaev, S.; Sinelnikov, K. Ultrasonic Unit for Reducing the Toxicity of Diesel Vehicle Exhaust Gases. *Commun. Sci. Lett. Univ. Zilina* **2022**, *24*, B189–B198. [CrossRef]
12. Shamim, T. Effect of engine exhaust gas modulation on the cold start emissions. *Int. J. Automot. Technol.* **2011**, *12*, 475–487. [CrossRef]
13. Kadyrov, A.S.; Sarsembekov, B.K.; Ganyukov, A.A.; Zhunusbekova, Z.Z.; Alikarimov, K.N. Experimental Research of the Coagulation Process of Exhaust Gases under the Influence of Ultrasound. *Commun. Sci. Lett. Univ. Zilina* **2021**, *23*, B288–B298. [CrossRef]
14. Edmonds, P.D.; Sancier, K.M. Evidence for free radical production by ultrasonic cavitation in biological media. *Ultrasound Med. Biol.* **1983**, *9*, 635–639. [CrossRef] [PubMed]
15. Kang, I.-S.; Xi, J.; Hu, H.-Y. Photolysis and photooxidation of typical gaseous VOCs by UV Irradiation: Removal performance and mechanisms. *Front. Environ. Sci. Eng.* **2018**, *12*, 8. [CrossRef]
16. Liu, J.; Wang, J.; Zhang, G.; Zhou, J.; Cen, K. Frequency comparative study of coal-fired fly ash acoustic agglomeration. *J. Environ. Sci.* **2011**, *23*, 1845–1851. [CrossRef] [PubMed]
17. Mazyan, W.I.; Ahmadi, A.; Ahmed, H.; Hoorfar, M. Increasing efficiency of natural gas cyclones through addition of tangential chambers. *J. Aerosol Sci.* **2017**, *110*, 36–42. [CrossRef]
18. Gallego-Juarez, J.A.; Graff, K.F. *Power Ultrasonics: Applications of High-Intensity Ultrasound*; Elsevier: Amsterdam, The Netherlands, 2014.
19. Bergmann, L. *Der Ultraschall und Seine Anwendung in Wissenschaft und Technik*; S. Hirzel: Stuttgart, Germany, 1954.
20. Oliveira, R.A.F.; Guerra, V.G.; Lopes, G.C. Improvement of collection efficiency in a cyclone separator using water nozzles: A numerical study. *Chem. Eng. Process. Process Intensif.* **2019**, *145*, 107667. [CrossRef]
21. de Sarabia, E.R.-F.; Gallego-Juárez, J. Ultrasonic agglomeration of micron aerosols understanding wave conditions. *J. Sound Vib.* **1986**, *110*, 413–427. [CrossRef]
22. Ruckerl, R.; Phipps, R.P.; Schneider, A.; Frampton, M.; Cyrys, J.; Oberdorster, G.; Wichmann, H.E.; Peters, A. Ultrafine particles and platelet activation in patients with coronary heart disease--results from a prospective panel study. *Part. Fibre Toxicol.* **2007**, *4*, 1. [CrossRef] [PubMed]

23. Rückerl, R.; Schneider, A.; Breitner, S.; Cyrys, J.; Peters, A. Health effects of particulate air pollution: A review of epidemiological evidence. *Inhal. Toxicol.* **2011**, *23*, 555–592. [CrossRef]
24. Seya, K.; Nakane, T.; Otsuro, T. Agglomeration of Aerosols by Ultrasonically Produced Water Mist. In Proceedings of the 1975 Ultrasonics Symposium, Los Angeles, CA, USA, 22–24 September 1975; pp. 583–584. [CrossRef]
25. Surmen, A.; Avci, A.; Karamangil, M.I. Prediction of the maximum-efficiency cyclone length for a cyclone with a tangential entry. *Powder Technol.* **2011**, *207*, 1–8. [CrossRef]
26. Dong, S.; Lipkens, B.; Cameron, T. The effects of orthokinetic collision, acoustic wake, and gravity on acoustic agglomeration of polydisperse aerosols. *J. Aerosol Sci.* **2006**, *37*, 540–553. [CrossRef]
27. Zhang, G.; Liu, J.; Wang, J.; Zhou, J.; Cen, K. Numerical simulation of acoustic wake effect in acoustic agglomeration under Oseen flow condition. *Chin. Sci. Bull.* **2012**, *57*, 2404–2412. [CrossRef]
28. Titov, S.S.; Pavlenko, A.A.; Arkhipov, V.A.; Bondarchuk, S.S.; Akhmadeev, I.R. Optical Methods and Algorithms for Determination of Fine Aerosol Parameters. In Proceedings of the 1st International Conference on Atmospheric Dust—DUST2014, Castellaneta Marina, Italy, 1–6 June 2014; pp. 261–265. [CrossRef]
29. Xie, B.; Li, S.; Jin, H.; Hu, S.; Wang, F.; Zhou, F. Analysis of the performance of a novel dust collector combining cyclone separator and cartridge filter. *Powder Technol.* **2018**, *339*, 695–701. [CrossRef]
30. Xiong, Z.; Ji, Z.; Wu, X. Investigation on the Separation Performance of a Multicyclone Separator for Natural Gas Purification. *Aerosol Air Qual. Res.* **2014**, *14*, 1055–1065. [CrossRef]
31. de Sarabia, E.R.-F.; Elvira-Segura, L.; González-Gómez, I.; Rodríguez-Maroto, J.; Muñoz-Bueno, R.; Dorronsoro-Areal, J. Investigation of the influence of humidity on the ultrasonic agglomeration of submicron particles in diesel exhausts. *Ultrasonics* **2003**, *41*, 277–281. [CrossRef]
32. Gallego-juarez, J.; Riera, E. Acoustic preconditioning of coal combustion fumes for enhancement of electrostatic precipitator performance: I. The acoustic preconditioning system. In *Coal Science and Technology*; Elsevier: Amsterdam, The Netherlands, 1995. [CrossRef]
33. Li, Z.; Zhang, W.; Chen, Z.; Ren, Z.; Ning, S.; Li, M. A kinetics mechanism of NOX formation and reduction based on detailed elementary reactions. *Sci. Total Environ.* **2023**, *864*, 161134.
34. Streicher, J.W.; Krish, A.; Hanson, R.K. Laser absorption study of the $N_2 + O \rightarrow NO + N$ and $NO + O \rightarrow O_2 + N$ Zeldovich reactions in shock-heated N_2O mixtures. *Phys. Fluids* **2023**, *35*, 046119. Available online: https://pubs.aip.org/aip/pof/article/35/4/046119/2886881 (accessed on 12 January 2026). [CrossRef]
35. BASF Catalysts. Three-Way Conversion (TWC) Catalyst Performance Data. BASF ECMS Report. 2024. Available online: https://basf-catalystsmetals.com/en/catalysts/light-duty/three-way-conversion-twc-catalyst (accessed on 12 January 2026).
36. Bradley, M.J.; Heywood, J.B. *Emission Control Technologies for Gasoline Engines*; MIT Energy Initiative: Cambridge, MA, USA, 2023.
37. Goldfarb Inc. 2025 Turbocharger Trends: Performance Upgrades Explained. 2025. Available online: https://goldfarbinc.com/blogs/news/2025-turbocharger-trends-performance-upgrades-explained (accessed on 12 January 2026).
38. Wang, Z.; Zhang, J.; Su, G.; Yang, P.; Fan, X.; Bai, S.; Sun, K.; Wang, G. Experimental Study on Gas Flow Uniformity in a Diesel Particulate Filter Carrier. *Fluid Dyn. Mater. Process.* **2024**, *20*, 193–204. [CrossRef]
39. Gu, X.; Wang, Y.; Shi, Y.; Cai, N. Elevating gas turbine system efficiency by integration with super-high temperature solid oxide fuel cell. *Innov. Energy* **2025**, *1*, 100096. [CrossRef]
40. Jin, N.; Long, W.; Xie, C.; Tian, H. After-Treatment Technologies for Emissions of Low-Carbon Fuel Internal Combustion Engines: Current Status and Prospects. *Energies* **2025**, *18*, 4063. [CrossRef]
41. Yan, F.; Cai, Z.; Li, Z.; Zhu, L.; Chen, P.; Zheng, S.; Wu, Y.; Li, Y.; Hu, J. Investigation of Diesel Particulate Filter Performance under Typical Failure Conditions. *Energy* **2024**, *311*, 133337. [CrossRef]
42. Sinha, D.N. Gas Separation Using Ultrasound and Light Absorption. U.S. Patent US8231707B2, 31 July 2012.
43. Suleimenov, N.; Sattarova, G.; Sarsenbekov, N.; Ermukhanova, N.; Portnov, V.; Zamaliyev, N.; Batessova, F.; Imanbayeva, S.; Zakharov, A.; Abdirashit, A. Recognition of Stages of Endogenous Fire Outbreak and Development in Coal Mines. *Appl. Sci.* **2025**, *15*, 11114. [CrossRef]

Disclaimer/Publisher's Note: The statements, opinions and data contained in all publications are solely those of the individual author(s) and contributor(s) and not of MDPI and/or the editor(s). MDPI and/or the editor(s) disclaim responsibility for any injury to people or property resulting from any ideas, methods, instructions or products referred to in the content.

vehicles

MDPI

Systematic Review

Autonomous Vehicles in the Traffic Ecosystem: A Comprehensive Review of Integration, Impacts, and Policy Implications

Eugen Valentin Butilă [1], Gheorghe-Daniel Voinea [1,*], Răzvan Gabriel Boboc [1] and Grigore Ambrosi [2]

[1] Department of Automotive and Transport Engineering, Transilvania University of Brasov, 500036 Brasov, Romania; butila@unitbv.ro (E.V.B.); razvan.boboc@unitbv.ro (R.G.B.)
[2] Department of Transportation, Technical University of Moldova, MD-2004 Chisinau, Moldova; grigore.ambrosi@tran.utm.md
* Correspondence: daniel.voinea@unitbv.ro

Abstract

Autonomous vehicles (AVs) are expected to significantly influence road safety, traffic efficiency, and urban mobility. However, their real-world impacts depend not only on vehicle-level automation but also on interactions within the broader traffic ecosystem, including human-driven vehicles, vulnerable road users, infrastructure, and governance frameworks. This review provides a system-level synthesis of recent research on the integration of autonomous and connected autonomous vehicles in mixed traffic environments. Following PRISMA 2020 guidelines, 51 peer-reviewed studies published between 2016 and 2025 were systematically reviewed and thematically analyzed. The review addresses technological foundations, safety impacts, traffic flow and network performance, mixed traffic dynamics, infrastructure and urban systems, and policy and governance challenges. The findings indicate that AV impacts are highly non-linear and sensitive to market penetration rates, control strategies, and human behavioral adaptation. While high levels of automation and connectivity can improve safety, capacity, and traffic stability, early-stage deployment may temporarily increase delays and traffic conflicts. Policy measures—such as pricing, shared mobility integration, and regulatory oversight—are therefore critical to ensuring that AV deployment delivers sustainable and equitable mobility outcomes.

Keywords: connected autonomous vehicles; mixed traffic; urban mobility; intelligent transportation systems; transportation policy

1. Introduction

Autonomous vehicles (AVs) often referred to as self-driving or driverless cars [1], represent one of the most significant technological transformations in contemporary transportation systems. By integrating advances in artificial intelligence, machine learning, robotics, and digital connectivity, AVs have the potential to fundamentally reshape road safety, traffic operations, urban mobility patterns, and the broader relationship between society and transport infrastructure [2]. At the vehicle level, autonomy is enabled through sophisticated sensor suites such as LiDAR, radar, cameras, and global positioning systems, combined with high-definition maps and decision-making algorithms that support perception, planning, and control in complex and dynamic environments [3]. These capabilities are commonly categorized according to the SAE International levels of driving automation (Levels 0–5), which range from basic driver assistance to full automation without human intervention [4].

Recent pilot deployments across North America, Europe, and Asia—including robo-taxi services, autonomous shuttle operations, and automated public transport demonstrations—have illustrated both the technical feasibility and the societal relevance of AV technologies [5–7]. While such initiatives highlight the promise of automation, they also underscore the gap between controlled operational domains and large-scale, real-world integration. As a result, AVs are no longer viewed solely as a vehicle-centric innovation, but increasingly as a component of a complex and evolving traffic ecosystem.

Road traffic injury remains a large-scale public-health and system-performance problem, with approximately 1.19 million (https://www.who.int/teams/social-determinants-of-health/safety-and-mobility/global-status-report-on-road-safety-2023, accessed on 20 January 2026) annual fatalities reported globally. In crash causation analyses, the critical reason is attributed to the driver in an estimated 94% of investigated crashes, highlighting the potential leverage of automation while also underscoring the need to evaluate how automated behavior interacts with human driving in mixed fleets [8]. Critical reasons for crashes investigated in the National Motor Vehicle Crash Causation Survey. (Traffic Safety Facts Crash Stats. Report No. DOT HS 812 506). Washington, DC: National Highway Traffic Safety Administration.). Congestion imposes similar material system costs. For example, recent metropolitan travel-time analyses estimate that U.S. drivers lost on average 42 h to congestion in 2023, corresponding to an average cost of $733 per driver (https://inrix.com/press-releases/2023-global-traffic-scorecard-us/, accessed on 20 January 2026). Importantly, the transition toward automation is expected to occur under prolonged mixed-traffic conditions, and the reviewed evidence indicates that early deployment can temporarily degrade network performance: at low-to-moderate penetration (approximately 10–50%), average network delays have been reported to increase by roughly 4–18% relative to conventional baselines, largely due to conservative automated maneuvers and interaction frictions [9]. Consistent with broader syntheses of mixed-traffic evidence, the benefits of automation are not monotone in early deployment and can be neutral or negative at low penetration depending on demand levels, control logic, and interaction effects, with improvements typically materializing only after sufficiently high market share [10,11].

Recent mixed-traffic research increasingly complements scenario-based simulation with empirical analysis and pilot evaluation, shifting the central question from whether automated driving is feasible to how transition regimes behave under real interaction and governance constraints. Empirical safety analyses of interaction-critical contexts such as freeway merging indicate penetration-dependent effects, including results where low AV penetration does not improve surrogate safety and measurable improvements emerge only beyond a threshold region. He et al. (2025) report that AV penetration below 20 percent did not enhance mixed-traffic safety at merging areas, whereas safety improved when penetration exceeded 20 percent across multiple surrogate metrics [12]. Human to AV interaction modeling has similarly moved toward explicitly representing behavioral uncertainty, with uncertainty-aware controllers and learning-based interaction models proposed to reduce risk in mixed-traffic longitudinal control settings. Finally, pilot evaluations of shared automated services operating in open mixed traffic show that safety and efficiency performance is context-dependent and sensitive to operational design, reinforcing the need to treat policy and deployment choices as endogenous to outcomes rather than as background conditions [13,14].

Early AV research predominantly focused on vehicle-level performance metrics, such as sensing accuracy, localization robustness, and control reliability. However, a growing body of evidence indicates that the impacts of AVs cannot be fully understood in isolation from their surrounding environment. In practice, AVs interact primarily with human-

driven vehicles, traffic control systems, and roadway infrastructure, which collectively shape system-level performance in mixed traffic environments. These interactions play a decisive role in shaping system-level outcomes related to safety, traffic efficiency, equity, and public acceptance [15–17]. For example, simulation studies and controlled experiments suggest that even limited AV penetration can smooth traffic flow and reduce congestion under certain conditions; however, these benefits are highly sensitive to human behavioral responses, infrastructure design, and the degree of vehicle connectivity [18–20]. Conversely, poorly managed deployment scenarios may increase vehicle kilometers traveled, disrupt public transport usage, or exacerbate congestion and spatial inequities [21–24].

These mixed and sometimes contradictory findings highlight the need for a holistic, system-level perspective on AV integration. Rather than treating automation as a deterministic improvement, recent research emphasizes that AV impacts are often non-linear and context-dependent, varying with market penetration rates, control strategies, behavioral adaptation, and policy frameworks. Consequently, the success of AV deployment depends not only on technological maturity, but also on how automation is embedded within broader traffic, urban, and governance systems.

Against this backdrop, the objective of this review is to provide a comprehensive synthesis of autonomous vehicle integration from a traffic ecosystem perspective. Specifically, the review focuses on three interrelated dimensions:

(i) The technological foundations that enable autonomous and connected vehicle operation;
(ii) The system-level impacts of AVs on safety, traffic flow, and urban mobility under mixed traffic conditions;
(iii) The policy, governance, and planning implications associated with large-scale deployment.

By systematically reviewing recent literature across transportation engineering, urban planning, and policy domains, this study identifies areas of consensus, unresolved tensions, and critical research gaps. The primary contribution of this review lies in bridging technical and policy-oriented perspectives, thereby supporting more informed decision-making by researchers, planners, and policymakers as autonomous vehicles transition from experimental pilots to integral components of future mobility systems. While vulnerable road users (VRUs) are an important component of urban mobility systems, this review focuses primarily on vehicle–vehicle and vehicle–infrastructure interactions; VRU-related findings are considered only where they directly influence mixed-traffic operations and safety outcomes.

2. Technological Foundations Relevant to Traffic System Integration

Autonomous vehicles (AVs) integrate sensing, decision-making, control, and connectivity technologies that directly shape their behavior in traffic systems. Rather than providing a comprehensive technical survey, this section summarizes the technological elements most relevant to traffic flow, safety, and mixed traffic interactions, which underpin the system-level impacts discussed in Section 3.

2.1. Behavioral Variables in Human–AV Mixed Traffic

We use three behavioral constructs to interpret human responses to AVs in mixed traffic, because these constructs recur across empirical, experimental, and modeling studies and directly condition control performance. Aggressiveness and strategic exploitation refer to deliberate attempts to gain advantage against an AV that is perceived as rule-compliant or defensive, operationalized by behaviors such as close cut-ins, forced merges, short headways, and failure to yield when the AV is expected to concede. In the mixed-traffic literature, this phenomenon is often discussed as 'bullying' or 'taking advantage' of AVs,

https://doi.org/10.3390/vehicles8020041

and survey and experimental evidence indicates that such behavior may directed more frequently toward AVs than toward human drivers under certain conditions. Avoidance and overcautious interaction refer to a risk-averse response to AVs, operationalized by earlier braking, larger gaps, or reluctance to merge, which can reduce conflict risk while increasing disruption and delay at interfaces. Cognitive misperception and misidentification refer to incorrect inference about AV identity, driving mode, or intent, which can distort gap acceptance and yielding decisions, particularly in time-critical intersection and merging scenarios. These categories are not mutually exclusive in a given interaction, but they provide a minimal taxonomy for relating observed surrogate-safety changes and efficiency impacts to the underlying human response mechanisms.

2.2. Levels of Driving Automation

The functional capabilities of autonomous vehicles are commonly classified according to the SAE J3016 taxonomy, which defines six levels of driving automation (Levels 0–5) based on the distribution of control and responsibility between the human driver and the automated driving system. From a traffic systems and policy perspective, this classification provides a critical framework for understanding how different degrees of automation influence traffic dynamics, infrastructure requirements, and mixed-traffic interactions.

Levels 0–2 correspond to driver assistance and partial automation, in which the human driver remains continuously responsible for monitoring the driving environment and executing fallback actions. Although these systems—such as adaptive cruise control or lane-keeping assistance—may improve individual driving comfort and safety, they do not fundamentally alter traffic flow mechanisms or system-level behavior. Consequently, their impacts on network performance and traffic management remain limited.

In contrast, Levels 3–5 represent higher degrees of automation in which vehicles assume full longitudinal and lateral control under specified operational design domains (ODDs). At these levels, automated driving systems can directly influence car-following behavior, gap acceptance, reaction times, and coordination with other vehicles and infrastructure. As a result, Levels 3–5 are the primary focus of traffic-system-level analysis, as they introduce new interaction patterns between automated vehicles, human-driven vehicles, and vulnerable road users.

Most real-world deployments to date operate at Level 4 rather than full Level 5 autonomy. Examples include robo-taxi services and autonomous shuttles deployed in geo-fenced urban areas or on dedicated corridors, where environmental complexity and operational risks can be tightly controlled [6,25,26]. These spatial and functional constraints are particularly relevant for traffic management, as they create heterogeneous automation landscapes in which automated and non-automated vehicles coexist across different network segments.

Figure 1 illustrates the SAE levels of driving automation and highlights their implications for driver responsibility and vehicle control.

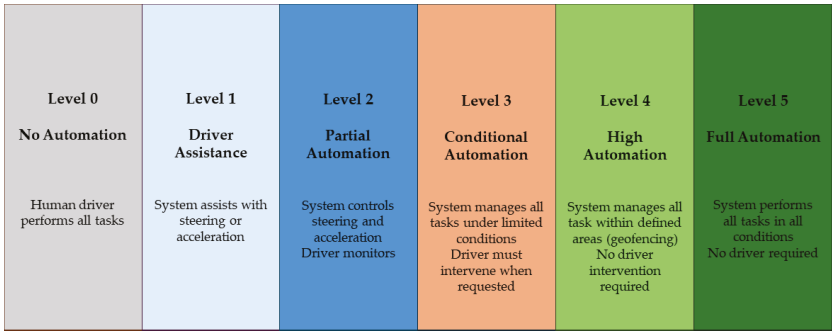

Figure 1. SAE levels of driving automation (Levels 0–5).

2.3. Sensing and Perception Systems

Sensing and perception systems form the foundation of AV operation by enabling vehicles to detect, interpret, and anticipate the behavior of surrounding road users and infrastructure. Contemporary AVs integrate LiDAR, radar, cameras, inertial sensors, and satellite-based positioning within sensor fusion frameworks to construct a robust real-time representation of the driving environment under varying traffic, lighting, and weather conditions [3,27].

From a traffic systems perspective, the key implication of AV perception lies not in achieving perfect environmental awareness, but in ensuring predictable and consistent behavior under uncertainty. Unlike human drivers, who rely on informal negotiation and intuition, AVs translate perception uncertainty into conservative algorithmic responses, such as earlier braking, larger following gaps, and cautious gap acceptance.

These perception-driven behaviors directly affect traffic safety and efficiency in mixed traffic environments. Conservative responses can reduce collision risk—particularly in interactions with vulnerable road users—but may also increase delays, lower intersection discharge rates, and raise minor conflict frequencies when AVs interact with more assertive human-driven vehicles. Such effects are most pronounced at intersections, merge areas, and lane-changing zones, where interaction complexity and perception ambiguity are highest.

Figure 2 illustrates how sensing and perception systems influence AV behavior and how these effects propagate to traffic-level safety and operational outcomes. Perception uncertainty acts as an intermediary between sensor performance and downstream impacts on surrogate safety indicators (e.g., time-to-collision and post-encroachment time) and operational metrics (e.g., delay and capacity).

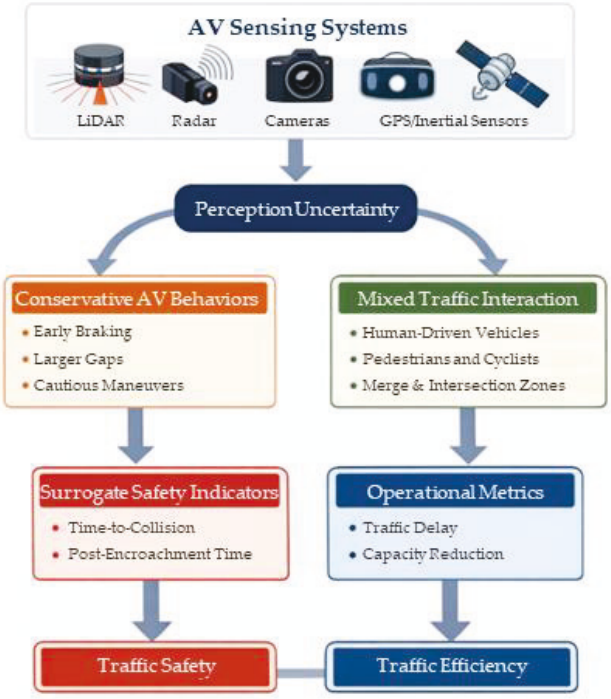

Figure 2. Role of sensing and perception systems in AVs and their downstream effects on traffic safety, and operational efficiency.

Perception limitations are shaped not only by sensor technology but also by contextual factors such as adverse weather, occlusions, complex urban geometries, and dense mixed traffic. Although sensor fusion mitigates some of these challenges, residual uncertainty remains unavoidable and must be explicitly addressed in planning and control algorithms.

https://doi.org/10.3390/vehicles8020041

Consequently, perception system design indirectly influences macroscopic traffic behavior by shaping the conservativeness and consistency of AV responses.

2.4. Traffic-Flow-Theoretic Foundations of Non-Linear Mixed-Traffic Effects

Many mixed-traffic findings reported in this review, including penetration-dependent capacity changes, delay amplification at intermediate penetration, and the emergence or suppression of stop-and-go waves, can be interpreted through established traffic-flow theory on phase transitions and bottleneck discharge. Phase-transition perspectives treat congestion onset as a regime shift between free flow and congested states, where traffic-state distributions can become bimodal and the transition boundary can be operationalized from observed speed and density distributions. This congestion-boundary view provides a principled basis for interpreting why small changes in behavior or control can induce discontinuous network-level changes in throughput and delay near critical operating conditions [28]. At the microscopic level, heterogeneous car-following dynamics can generate congestion transitions on closed facilities such as ring roads through instability mechanisms that are sensitive to perception and control parameters, which helps explain why mixed fleets may exhibit non-monotone stability and oscillation patterns as automated control settings and heterogeneity vary [29]. At bottlenecks, capacity and delay effects are further governed by dynamic discharge processes and the estimation of critical parameters from field data. Empirical bottleneck studies that estimate free-flow speed, critical speed or density, and capacity under recurring breakdown and recovery provide a reference point for interpreting whether simulated mixed-traffic capacity gains are plausible under real discharge dynamics, and they motivate reporting and comparing key assumptions such as headway policy and signal control regimes when translating simulation findings to practice [30]. Throughout the remainder of the manuscript, we use these theoretical constructs to contextualize the reported non-linear mixed-traffic effects and to distinguish mechanisms driven by proximity to critical states from those attributable to specific automated control or operational interventions.

2.5. Decision-Making and Control Architectures

Decision-making and control architectures translate perceived environmental information into longitudinal and lateral vehicle maneuvers. From a traffic systems perspective, the most influential control parameters include desired time gaps, acceleration and deceleration limits, and responses to cut-in, merging, and intersection interactions. Conservative parameter settings improve safety and passenger comfort but may reduce effective roadway capacity when AVs interact with human-driven traffic.

Recent advances increasingly incorporate learning-based approaches, such as reinforcement learning and multi-agent control, to optimize vehicle behavior under complex and dynamic traffic conditions. When explicitly designed to balance safety, efficiency, and stability, these methods can reduce speed variability, dampen stop-and-go oscillations, and improve traffic flow consistency at both corridor and network levels. Nevertheless, safety-critical functions remain largely governed by rule-based or hybrid control structures to ensure predictability and regulatory compliance [31,32].

Overall, decision-making and control architectures serve as a key interface between vehicle-level intelligence and system-level traffic performance, directly shaping safety outcomes, capacity utilization, and interaction dynamics in mixed traffic environments.

2.6. Connectivity and Cooperative Systems

Connectivity significantly amplifies the traffic-level effects of automation by enabling coordination beyond individual vehicle perception and control. As illustrated in Figure 3, vehicle-to-vehicle (V2V) and vehicle-to-infrastructure (V2I) communication support cooper-

https://doi.org/10.3390/vehicles8020041

ative adaptive cruise control, platooning, and signal-aware driving, which reduce reaction times and speed variability while improving traffic stability and roadway capacity [33,34].

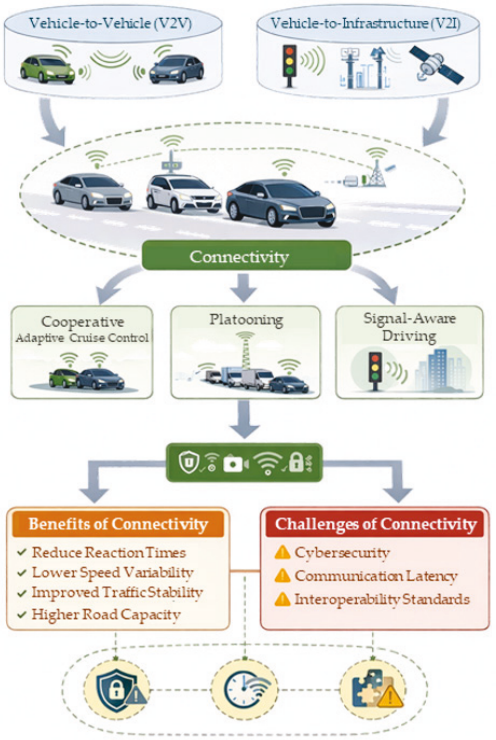

Figure 3. Connectivity and cooperative systems in AVs and CAVs.

The effectiveness of cooperative systems depends strongly on market penetration rate, communication reliability, and infrastructure support. In mixed traffic environments, partial connectivity may yield uneven or localized benefits and can introduce disruptions when cooperative behaviors interact with non-connected vehicles, leading to non-linear system responses. While connectivity enables system-wide traffic optimization, it also introduces challenges related to cybersecurity, communication latency, and interoperability standards. Addressing these issues is essential to ensure that cooperative automation delivers predictable, scalable, and safe performance in heterogeneous traffic ecosystems [35].

2.7. Synthesis Dimensions for Mixed-Traffic Evidence and Policy Evaluation

Because mixed-traffic studies differ substantially in evidence basis, operational setting, and outcome definitions, we organize the review using a small set of synthesis dimensions that recur throughout the manuscript. This approach enables consistent cross-study comparison without forcing heterogeneous designs into an overly reductive taxonomy. We characterize each contribution by its evidence basis, distinguishing analyses based on field or pilot data, controlled experiments, and simulation studies that are explicitly calibrated or validated using empirical observations. We also code the traffic context, distinguishing freeway segments and merges, arterials, signalized intersections, and network-level analyses. For transition dynamics, we record the AV and CAV penetration range examined and any reported threshold region where effects change sign or magnitude, since these threshold patterns are central to interpreting mixed-fleet performance. We additionally specify the interaction counterpart, distinguishing studies focused primarily on interactions with human-driven vehicles from studies that explicitly model or measure interactions with vulnerable road users. Where applicable, we identify the presence and type of policy or operational intervention, including infrastructure readiness, digital connectivity and

data governance, institutional deployment requirements, and service design constraints that can condition observed performance in open mixed traffic [36]. Finally, we record the outcome metrics reported, including efficiency measures such as delay and throughput, surrogate safety indicators, and environmental impacts when available. This synthesis framing is used throughout the remainder of the manuscript to make penetration-threshold and human to AV interaction claims traceable to the underlying evidence type and setting, while preserving interpretability through a structured narrative comparison rather than a single comprehensive classification table.

3. Materials and Methods

This review was conducted in accordance with the Preferred Reporting Items for Systematic Reviews and Meta-Analyses (PRISMA 2020) guidelines [37] to ensure methodological transparency, reproducibility, and rigor.

3.1. Identification of Studies

A systematic literature search was performed across six major scientific databases: Scopus, Web of Science (WoS), ScienceDirect, IEEE Xplore, TRID, and SpringerLink. These databases were selected to capture a comprehensive range of studies spanning transportation engineering, intelligent transportation systems, urban mobility, and policy research.

Search strategies were designed to identify peer-reviewed publications addressing the integration of autonomous and connected autonomous vehicles (CAVs) within traffic ecosystems and their associated impacts. Keywords were organized into four conceptual groups:

(1) Autonomous vehicle technologies;
(2) Traffic ecosystems and mixed traffic conditions;
(3) Integration and deployment processes;
(4) Impact assessment domains, including safety, traffic flow, mobility efficiency, environmental effects, and policy implications.

An example of the search query used in Scopus is shown below:

TITLE-ABS-KEY ((“autonomous vehicle*” OR “self-driving car*” OR “automated vehicle*” OR
“connected autonomous vehicle*” OR “CAV” OR “AV”)
AND (“traffic ecosystem” OR “mixed traffic” OR “urban mobility network” OR
“heterogeneous traffic”)
AND (“integration” OR “deployment” OR “incorporation” OR “adoption”)
AND (“impact assessment” OR “safety impact” OR “traffic flow” OR “mobility efficiency” OR
“environmental impact” OR “policy implication” OR “regulatory framework”))

Equivalent queries were adapted to the indexing structures of each database.

The initial search yielded 1574 records, distributed as follows: Scopus (139), Web of Science (224), ScienceDirect (840), IEEE Xplore (60), TRID (59), and SpringerLink (252).

3.2. Screening

All records were imported into a reference management system, where 208 duplicates were removed. The remaining 1366 records were screened based on titles and abstracts.

Studies were excluded if they:

- Did not focus on autonomous or connected autonomous vehicles;
- Were unrelated to traffic ecosystems, mixed traffic, or urban transportation networks;
- Addressed vehicle-level technologies without traffic- or system-level implications.

https://doi.org/10.3390/vehicles8020041

3.3. Eligibility Assessment

Full-text versions of the remaining articles were retrieved and assessed against predefined inclusion and exclusion criteria.

Inclusion criteria were:

- Publication in English;
- Publication between 2016 and 2025;
- Journal articles, conference papers, or review articles;
- Explicit discussion of AV integration, deployment, or adoption;
- Evaluation of at least one impact dimension (safety, traffic flow, mobility efficiency, environmental impact, or policy/regulatory implications).

Studies were excluded if they lacked sufficient methodological transparency or analytical rigor for system-level comparison. Specifically, simulation-based and modeling studies were excluded if any of the following minimum requirements were not met:

(i) A clear description of the traffic scenario design, including network type, demand assumptions, and interaction context (e.g., mixed traffic composition);
(ii) An explicit definition of the baseline or reference scenario against which autonomous or connected vehicle impacts were evaluated;
(iii) A clear specification of performance metrics (e.g., safety indicators, delay, capacity, or mobility measures) and their computation;
(iv) Evidence of model validation, calibration, or verification, such as sensitivity analysis, comparison with empirical data, or reference to established simulation frameworks.

Studies failing to meet these criteria were excluded to ensure analytical consistency and comparability across the reviewed literature.

3.4. Included Studies

Following full-text assessment, 51 studies met all inclusion criteria and were selected for qualitative synthesis. The final sample comprises a balanced mix of journal articles, conference papers, and review studies covering engineering, transportation planning, and policy perspectives.

To provide contextual insight into the empirical basis of the reviewed literature, Table 1 summarizes the geographic distribution of the included studies, their dominant traffic environments, and observed regional patterns. This overview supports interpretation of reported performance thresholds and highlights potential influences of traffic culture, regulatory context, and deployment maturity on study outcomes.

Table 1. Distribution of included studies by region and traffic context.

Region	Number of Studies (%)	Dominant Traffic Contexts	Observed Patterns
North America	10 (14.9%)	Urban, freeway, mixed	Higher reported benefits under cooperative control; strong sensitivity to penetration level
Europe	16 (23.9%)	Urban, arterial, mixed	Moderate safety and capacity gains; emphasis on regulatory integration
East Asia	30 (44.8%)	Dense urban, arterial	Earlier safety thresholds; stronger effects of behavioral compliance
Other regions	11 (16.4%)	Mixed	Limited evidence; high contextual variability

Note: Study counts represent regional author affiliations rather than unique studies. A single publication may contribute to multiple regions when co-authored across countries. Percentages are calculated relative to the total number of regional affiliation occurrences (N = 67), not the 51 unique studies.

Because several publications involve international collaboration, the table reflects the geographic participation of the research ecosystem rather than a mutually exclusive study classification. Consequently, regional shares should be interpreted as the proportion of total affiliations contributing to the literature, not the proportion of unique studies.

Figure 4 illustrates the geographic distribution of the reviewed studies, highlighting the concentration of research in East Asia, North America, and Europe.

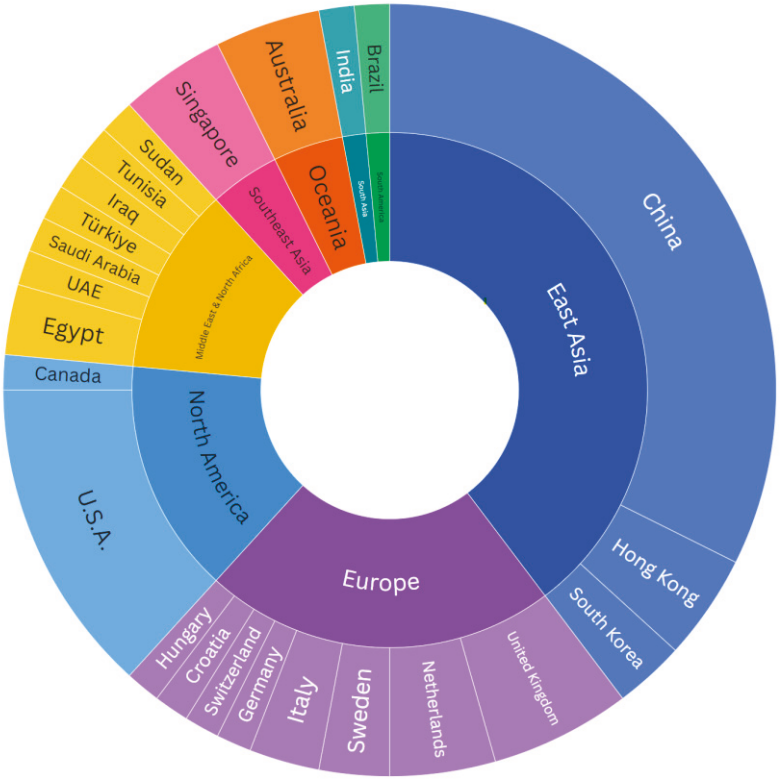

Figure 4. Geographic distribution of reviewed AV studies (2016–2025).

3.5. Data Extraction and Synthesis

A standardized data extraction form was developed prior to data collection to ensure consistency and transparency. The form included fields for bibliographic information, research objectives, methodological approach, traffic context, assumed AV/CAV market penetration levels, performance indicators, and policy or infrastructure considerations (see Table S2).

Data extraction was performed independently by two reviewers using this standardized template. The extracted datasets were subsequently cross-checked, and any discrepancies were resolved through discussion. When necessary, a third reviewer was consulted to reach consensus. Missing or unclear information was verified by re-examining the original publications; if relevant data could not be retrieved, the corresponding fields were recorded as "not reported" and excluded from comparative synthesis.

For qualitative synthesis, a structured thematic analysis approach was applied using a predefined coding framework developed iteratively during pilot extraction. Initial codes were derived from the review objectives and PRISMA recommendations and were refined through repeated comparison across studies. Each included article was coded independently by two reviewers with respect to technological context, traffic environment, performance indicators, and policy implications.

Codes were subsequently grouped into higher-level analytical themes, including safety impacts, traffic flow and mobility performance, mixed traffic dynamics, infrastructure and

https://doi.org/10.3390/vehicles8020041

urban systems, and governance challenges. Conflicting or divergent findings across studies were integrated through comparative analysis, with explicit consideration of differences in modeling assumptions, study design, traffic context, and market penetration scenarios. Rather than averaging inconsistent results, emphasis was placed on identifying contextual moderators and explaining sources of heterogeneity.

Reported numerical ranges (e.g., capacity gains of 1–84%) represent the full spectrum of values documented in the included studies and are intended to illustrate inter-study variability. These ranges were derived by systematically compiling all comparable reported outcomes within each thematic category, rather than through statistical aggregation or meta-analysis.

For studies reporting time to collision (TTC) or post-encroachment time (PET), we additionally extracted the penetration range tested, the AV control-strategy class (for example conservative time-gap policies versus cooperative control), and whether human recognition of AVs was modeled explicitly, implicitly via kinematic cues, or not specified.

The validated thematic structure provided the basis for qualitative interpretation and cross-domain synthesis.

3.6. PRISMA Flow Diagram

A PRISMA flow diagram was developed to document the study selection process. As illustrated in Figure 5, the initial database search identified 1574 records. After duplicate removal and screening, 51 articles were retained and included in the final qualitative synthesis.

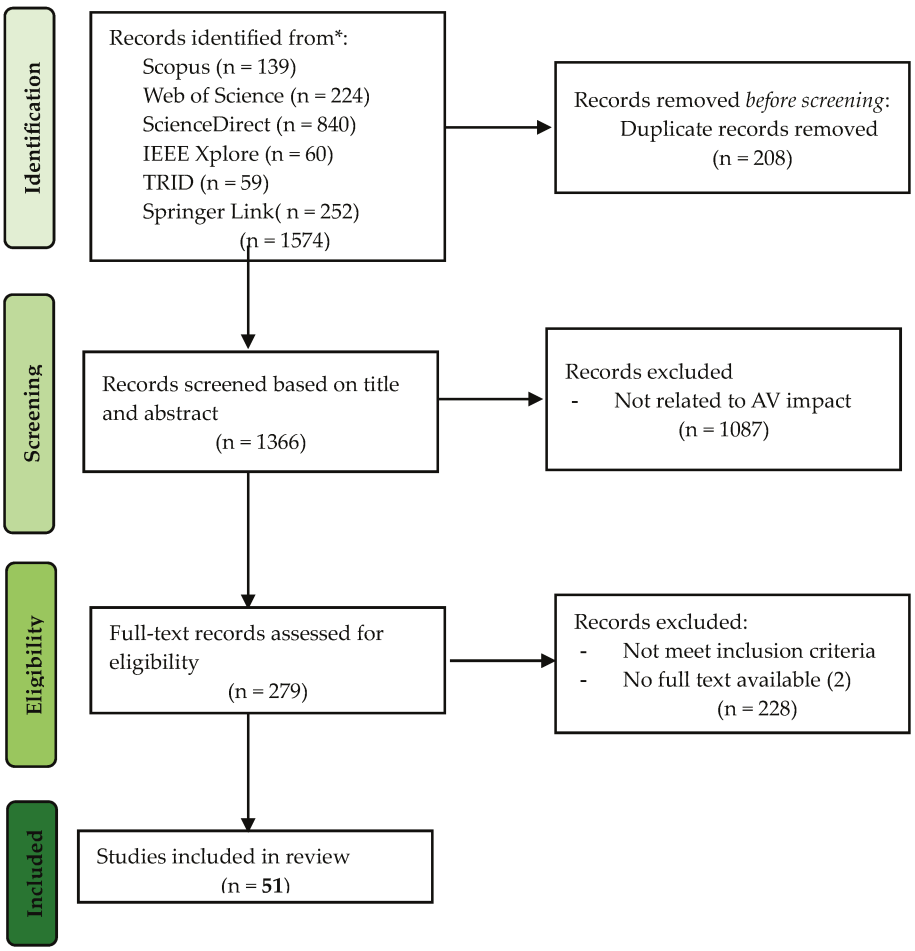

Figure 5. PRISMA 2020 flow diagram of the literature search and study selection process.

3.7. Review Protocol and Screening Procedures

A formal review protocol was developed internally prior to the literature search; however, it was not registered in an external repository (e.g., PROSPERO).

Conference abstracts without full papers, technical reports, white papers, theses, policy briefs, preprints, and other non–peer-reviewed sources were intentionally excluded to ensure consistency, methodological transparency, and comparability of results across studies. This decision reflects the objective of synthesizing validated, peer-reviewed evidence on autonomous vehicle integration and its system-level impacts.

Title and abstract screening was conducted independently by two reviewers. Inter-reviewer agreement at this stage was 88.4%, with Cohen's kappa = 0.534. Full-text eligibility assessment was also performed independently by the same two reviewers, achieving 92.5% agreement and Cohen's kappa = 0.697. Disagreements at either stage were resolved through discussion; when consensus could not be reached, a third reviewer acted as an arbitrator. No automated screening tools were used.

This multi-reviewer process, together with the reported inter-reviewer agreement statistics, was adopted to reduce selection bias and enhance the reliability and reproducibility of study inclusion decisions. A completed PRISMA 2020 checklist indicating where each reporting item is addressed is provided in Table S1.

4. Results

The synthesis of the 51 selected studies reveals that the impacts of AVs on traffic systems are highly heterogeneous and strongly dependent on deployment context, market penetration rate, and interaction dynamics with human-driven traffic. Rather than producing uniform benefits, the reviewed literature consistently reports non-linear and sometimes counterintuitive effects across safety, traffic flow, and mobility performance, particularly during transitional mixed-traffic phases. Accordingly, the results are structured around five interrelated domains: safety impacts, traffic flow and network performance, mixed traffic dynamics, infrastructure and urban systems, and policy and governance challenges, highlighting both areas of convergence and persistent uncertainty.

Figure 6 summarizes the temporal evolution of dominant research themes from 2016 to 2025, illustrating the shift from technical feasibility studies toward system-level, behavioral, and governance-oriented research.

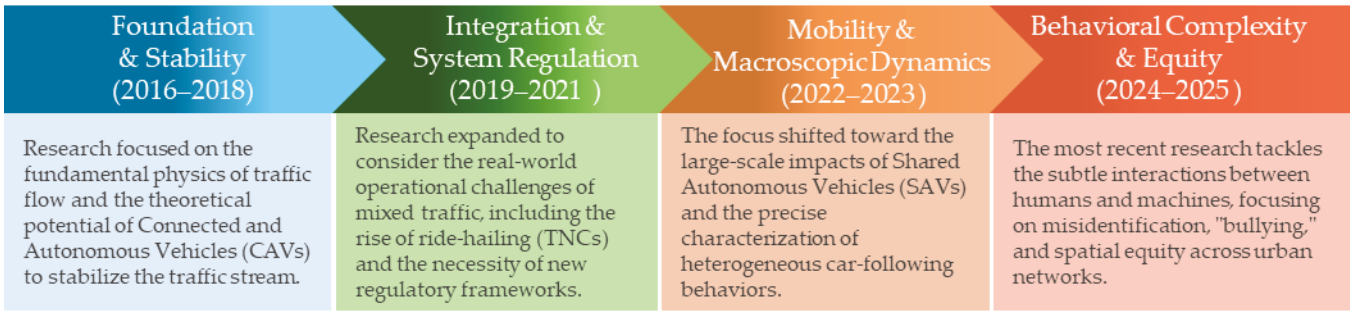

Figure 6. Timeline of major thematic shifts in autonomous vehicle research between 2016 and 2025.

Research on the impacts of AVs is generally divided into empirical and simulation-based studies, with findings strongly influenced by assumptions regarding key variables such as market penetration rate (MPR), headway, and signal control. Empirical studies rely on naturalistic datasets such as Argoverse-2, the Waymo Open Dataset, and OpenACC [38,39] and typically focus on localized interactions, revealing that current AVs tend to adopt more conservative driving behaviors than human drivers. In contrast, simulation-based studies use microscopic tools such as SUMO, VISSIM, and AIMSUN [38,40,41] and

macroscopic or mesoscopic models such as CTM and ILUTM to examine large-scale impacts, including network performance and urban sprawl [42–44]. These studies commonly test hypothetical scenarios, such as full AV penetration or dedicated lanes, that are not yet observable in practice [45]. Across both approaches, results are highly sensitive to parameter distributions, with capacity gains often emerging only beyond 30–60% MPR [40,46], assumed AV headways ranging from 0.5 to 1.5 s [47,48], and coordinated signal control significantly reducing delays when combined with platooning [40,49].

4.1. Autonomous Vehicles and Safety Impacts

Improving road safety is one of the primary motivations for the development and deployment of AVs, particularly given that approximately 94% of road traffic crashes are attributed to human [47,50]. By replacing or assisting human driving tasks with automated perception, decision-making, and control, AVs have the potential to substantially reduce collision frequency and severity. However, the reviewed literature consistently emphasizes that safety outcomes during the transition toward automation are complex and strongly shaped by interactions among AVs, human-driven vehicles (HVs), and VRUs in mixed traffic environments [51,52]. The safety analysis in this section emphasizes interactions among AVs and HVs, and, where relevant, indirect effects involving VRUs.

Because mixed traffic conditions are expected to persist for several decades, understanding safety impacts during partial and incremental deployment phases is critical. Rather than producing immediate and uniform safety improvements, AV integration often leads to non-linear and sometimes counterintuitive safety effects, particularly at low and moderate levels of market penetration.

4.1.1. Causal Framework for Surrogate Safety Measures in Mixed Traffic

Surrogate safety measures quantify risk through interaction kinematics and therefore vary systematically with the conditions that shape vehicle trajectories. In this review, we interpret TTC and PET as downstream observables of three upstream condition variables that recur across mixed-traffic studies, namely market penetration of AVs and CAVs, the AV control strategy deployed, and human recognition of AV behavior. Penetration affects encounter composition and interaction frequency, which changes the share of human–human, human–AV, and AV–AV conflicts observed and can shift operating conditions toward or away from critical states in which small perturbations amplify. Control strategy shapes longitudinal and lateral trajectories through parameters such as desired time gap, braking aggressiveness, gap acceptance, and yielding rules, which directly affect the spacing and relative-speed terms that TTC reflects and the conflict-point timing that PET reflects. Human recognition affects the human road user's beliefs about AV intent and capability, which can alter responses such as cut-ins, merging aggressiveness, gap acceptance, and yielding compliance, thereby changing the interaction trajectories from which TTC and PET are derived. We therefore synthesize safety evidence, including TTC and PET findings, conditionally reporting how measures change across penetration ranges and control classes and indicating whether studies model recognition explicitly, implicitly via kinematics, or leave it unspecified. This structure is intended to distinguish effects attributable to conservative automated kinematics from effects driven by expectation mismatch and interaction adaptation, which is central for interpreting mixed-traffic safety during the transition regime.

Figure 7 summarizes the causal structure used in this section to interpret surrogate safety measures in mixed traffic, organizing TTC and PET findings by market penetration, AV control strategy, and human recognition of AV behavior.

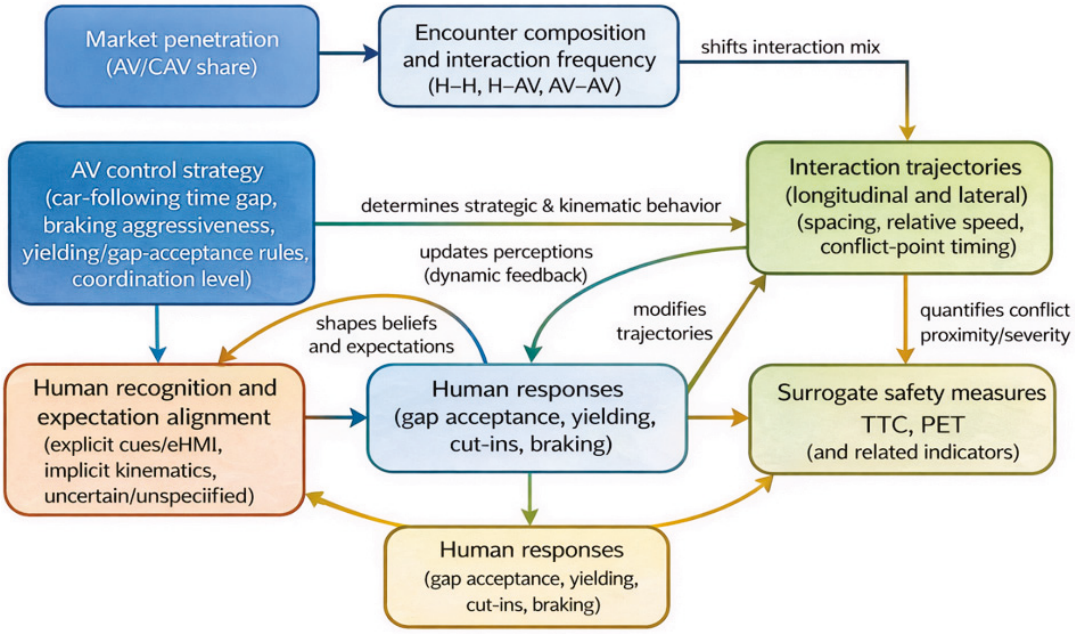

Figure 7. Conceptual causal framework for surrogate safety measures in mixed traffic.

4.1.2. Impact of Market Penetration Rates (MPR)

A central finding across multiple studies is that safety benefits are highly sensitive to AV market penetration rates (MPR). At low penetration levels, typically below 40%, the frequency of traffic conflicts may increase rather than decrease [41,47]. This increase is primarily attributed to behavioral mismatches between AVs and HVs, which require frequent adaptation and can destabilize traffic interactions. Human drivers often struggle to anticipate the conservative or non-intuitive maneuvers of early-generation AVs, resulting in elevated conflict rates and reduced interaction efficiency [9,52].

In contrast, when AV penetration exceeds approximately 75–80%, safety benefits become pronounced and more consistent. Several studies (mainly 2–3 simulation-based works, notably [47]) report conflict reductions of up to 91.77% under very high AV/CAV penetration levels (≈80–100%), assuming coordinated control and platooning. These results were primarily obtained in controlled urban and arterial network scenarios, while most other studies report more moderate reductions (typically 20–60%) under comparable conditions.

4.1.3. Conflict Resolution and Interaction Mechanics

While pedestrian and cyclist interactions with AVs are important, a comprehensive analysis of vulnerable road user behavior lies outside the primary scope of this review, which focuses on system-level vehicle interactions and traffic performance.

AVs are typically designed to adopt conservative driving strategies, including smoother acceleration profiles, earlier braking, and larger safety margins, to ensure robustness under uncertainty [39]. While such strategies reduce crash likelihood, they may also increase delays and interaction frictions, particularly in complex scenarios such as unprotected left turns, dense urban intersections, and merging areas.

Human–AV interactions further complicate safety outcomes. Empirical and simulation-based evidence indicates that human drivers do not significantly alter their behavior once engaged in interactions with AVs at intersections, whereas pedestrians tend to behave more cautiously, often delaying crossings in the presence of AVs [39]. A critical issue arises from the limited ability of human drivers to correctly identify AVs. Misidentification has been

shown to increase average vehicle delay, while accurate recognition can reduce delay by up to 30% and collision risk by 54.4% [53].

Several studies also document the emergence of aggressive or "bullying" behavior, whereby human drivers are more likely to cut in front of or challenge AVs than other HVs [52]. Such behaviors undermine the conservative assumptions embedded in AV control algorithms and introduce new safety risks that are not captured by vehicle-level validation alone.

4.1.4. Platooning and Technological Factors

Platooning has emerged as a key mechanism for enhancing safety in AV-dominated traffic systems. Through vehicle-to-vehicle communication and coordinated control, platoons reduce speed variability, minimize unnecessary lane changes, and increase inter-vehicle predictability [40].

The safety effectiveness of platooning is strongly dependent on AV penetration levels. Smaller platoons (e.g., three vehicles) are more effective at lower penetration rates (around 25%), whereas larger platoons (five vehicles or more) provide greater safety benefits at higher penetration levels by stabilizing traffic flow and reducing disruptive interactions [47].

From a technological perspective, simulation studies indicate that realistic sensor measurement errors, such as radar noise, do not substantially increase conflict rates, suggesting that current sensing technologies are generally sufficient for safe operation under typical conditions [47]. Moreover, advanced control approaches based on multi-agent reinforcement learning (MARL), including the MA2C algorithm, explicitly incorporate safety, efficiency, and comfort objectives. These methods promote smoother and more predictable behavior, contributing to improved safety and traffic stability in smart city contexts [54].

4.1.5. Safety-Related Key Performance Indicators

We adopt standard surrogate-safety definitions in which time to collision is the projected time to collision under continuation of the current relative kinematics, and post-encroachment time is the temporal separation between successive road users at a shared conflict point, widely used to quantify near-conflicts in surrogate safety assessment [55,56]. Because both measures are computed from interaction trajectories, their reported values depend not only on underlying behavior but also on study-specific measurement choices such as conflict-point definition, trajectory resolution, smoothing, and event filtering. Accordingly, we interpret TTC and PET trends in light of the assumptions stated in each study and we emphasize conditional patterns rather than unconditional comparisons. Definitions and computational conventions for the principal indicators used in the reviewed literature are summarized in Table 2.

We synthesize surrogate-safety evidence conditionally by market penetration range, AV control class, and human recognition conditions because these upstream variables jointly shape encounter composition, interaction kinematics, and behavioral adaptation in mixed traffic. Market penetration affects exposure by changing the relative frequency of human–human, human–AV, and AV–AV encounters, and it can shift operating conditions toward or away from critical traffic states where small perturbations amplify. Control strategy affects trajectories through settings such as desired time gap, braking responsiveness, gap-acceptance logic, and yielding rules, which directly influence spacing and relative speed and therefore TTC, as well as conflict-point timing and therefore PET. Human recognition and expectation alignment affect how humans anticipate AV intent and capability, which can modify cut-ins, merging aggressiveness, yielding compliance, and braking

https://doi.org/10.3390/vehicles8020041

responses, thereby altering the trajectories from which surrogate measures are derived. For interpretability, when reporting TTC and PET results we label, where available, the penetration range studied, the control class, and whether recognition is modeled explicitly, implicitly via kinematics, or left unspecified, because these conditions frequently explain divergences that would otherwise appear contradictory.

Table 2. Surrogate safety and stability key performance indicators (KPIs) used to assess the impacts of AVs in mixed traffic environments.

Analytical Level	KPI	Unit	Definition/Impact	Reference(s)
Vehicle-Level	Acceleration Jerk	m/s^3	Rate of change in acceleration; lower values indicate smoother and safer driving behavior.	[39,53]
	Maximum/ Minimum Acceleration	m/s^2	Range of acceleration and deceleration during interactions; reflects control aggressiveness.	[53,57]
	Yaw Rate	rad/s or °/s	Lateral stability indicator; lower peaks indicate more stable maneuvering.	[39,57]
Interaction-Level	Traffic Conflict Count	count (events)	Frequency of near-collision events (e.g., rear-end, lane-change conflicts).	[9,39,41,47]
	Time-to-Collision (TTC)	s	Time remaining before a potential collision given current speeds.	[41,47,58]
	Post-Encroachment Time (PET)	s	Time difference between two road users passing the same conflict point.	[39,53]
	Collision Risk	%	Probability or proportion of interactions resulting in a conflict.	[53]
	Misidentification Delay	s or % increase	Delay caused by human drivers misjudging vehicle automation status.	[53]
System-Level	Speed Volatility	(CV or %)	Coefficient of variation in average speed; lower values indicate greater traffic stability.	[40,59]

PET is most informative in crossing and lateral-conflict contexts where timing at a shared conflict point governs near-miss severity. Conservative yielding and cautious gap acceptance can increase PET by increasing temporal separation at conflict points, but can also shift interaction incentives and reduce PET if human drivers respond with late acceleration or aggressive gap-taking under perceived AV caution. Recognition conditions are therefore particularly consequential for PET, because human expectations about whether an AV will yield influence both the decision to initiate a crossing or merge and the timing of that maneuver. Studies that explicitly model recognition or communicate intent typically report fewer ambiguous encroachments and a shift toward larger PET margins than studies where recognition is implicit through kinematics or unspecified, although the direction and magnitude remain scenario-dependent.

Beyond TTC and PET, the literature commonly reports conflict frequency or conflict rate as an exposure-sensitive indicator, along with collision-risk proxies, speed volatility, acceleration jerk, and vehicle-dynamics measures such as yaw rate. Conflict frequency can increase even when average TTC increases if interaction opportunities rise with penetration or demand, so conflict counts should be interpreted jointly with severity-sensitive measures such as TTC and PET and with normalization choices such as per-vehicle or per-distance rates. Speed volatility and acceleration jerk provide complementary evidence about stability and comfort-related safety, and reductions in these measures are often aligned with improved surrogate safety when they reflect suppressed oscillations and

reduced abrupt braking. However, these indicators can also reflect control conservatism that improves comfort while shifting risk to specific interaction moments, so they should be interpreted alongside the maneuver context and recognition conditions described above. Overall, surrogate-safety improvements are most robust when control strategies reduce speed variance and stabilize trajectories across interaction contexts, whereas changes in TTC and PET are frequently conditional on penetration range, merging and gap-acceptance logic, and whether recognition or intent communication is modeled, and these structural assumptions should be stated explicitly when drawing mixed-traffic safety conclusions.

4.2. Traffic Flow, Mobility and Network Performance

The large-scale deployment of AVs and CAVs is widely expected to transform urban traffic operations by altering fundamental relationships between demand, capacity, and control. Existing research shows that these impacts range from substantial capacity enhancements under coordinated automation to more nuanced and sometimes adverse effects during transitional deployment phases [40,49,60,61]. In practice, urban networks are likely to operate for extended periods under mixed traffic conditions, where human-driven vehicles (HDVs), vehicles equipped with advanced driver assistance systems (ADAS), and fully automated vehicles coexist. While such heterogeneity creates opportunities for efficiency gains, it also introduces significant operational and control challenges that complicate network-level performance [9,41,46,62].

4.2.1. Network Capacity and Flow Throughput

One of the most frequently cited advantages of AV and CAV technologies is their potential to increase roadway capacity by reducing reaction times, stabilizing car-following behavior, and enabling shorter inter-vehicle headways [45,60,63]. Macroscopic fundamental diagram (MFD)–based analyses indicate that AV deployment can increase overall urban network capacity by up to 19% under conservative control and limited coordination assumptions [38]. In contrast, freeway and arterial corridor studies assuming cooperative platooning and high connectivity report substantially higher throughput gains, reaching up to 84% in a small subset of favorable simulation scenarios [52,63]. At the urban network scale, simulation studies report that scenarios with full AV penetration can yield maximum flow increases of 16–23% relative to conventional traffic conditions [40]. These values therefore reflect different traffic contexts and modeling assumptions rather than a uniform system-wide effect.

Capacity improvements are further amplified through coordinated platooning enabled by vehicle-to-vehicle (V2V) and vehicle-to-infrastructure (V2I) communication. Platooning strategies have been shown to nearly double urban road throughput, while intersection capacities may increase by factors of two to three under coordinated control regimes [40,64,65]. However, these benefits are highly sensitive to AV market penetration rates (MPR). Multiple studies suggest that meaningful network-wide capacity gains typically require an MPR of at least 20–30%; below this threshold, underutilization of dedicated infrastructure and localized congestion effects may offset potential benefits [9,45,46].

The highest reported throughput gains (>70%) are mainly observed in corridor-based studies with coordinated control and near-ideal communication conditions (Table 3), whereas urban network-scale analyses typically report more moderate improvements (below 25%). Conservative following-gap settings, partial connectivity, and heterogeneous traffic compositions significantly reduce achievable capacity gains in mixed urban environments.

https://doi.org/10.3390/vehicles8020041

Table 3. Reported capacity and throughput gains by traffic context.

Traffic Context	Typical MPR Range	Control Assumptions	Reported Gain Range
Urban networks (MFD-based)	30–100%	Conservative/partial coordination	5–19%
Arterial corridors	40–100%	Signal coordination/platooning	15–45%
Freeways	50–100%	Cooperative platooning/V2V	30–84%

Note: Values represent ranges reported in the reviewed simulation-based studies and are context-dependent.

4.2.2. Travel Time and Traffic Delays

Reported changes in travel time and delay are not directly comparable across facility types because the dominant delay-formation mechanisms differ between freeway and bottleneck-dominated operation and signal-controlled urban operation. Accordingly, we synthesize delay evidence by network type rather than pooling values across heterogeneous contexts. We distinguish freeway and bottleneck-dominated settings, where breakdown probability, discharge dynamics, and merge or weaving interactions govern effective performance, from urban arterial and signal-controlled settings, where signal density, progression quality, queue spillback, and control regime dominate delay formation. Mixed-network studies that include both bottlenecks and signalized links are treated as a separate class, and results are interpreted with the corresponding network composition and control assumptions when stated.

In freeway and bottleneck-dominated settings, early-stage AV deployment may initially increase travel times and network delays despite long-term efficiency gains at high penetration. This pattern is commonly attributed to conservative control logic, safety-oriented driving behavior, and interaction frictions with human drivers, particularly when AV policies increase desired time gaps or apply cautious merging and lane-changing behavior under uncertainty [9,40,41,51]. Within this facility class, one simulation-based study indicates that at low to moderate penetration levels (approximately 10–50%), average delays can increase by roughly 4–18% relative to HDV-dominated baselines [9], with the direction and magnitude depending on whether the limiting mechanism is recurrent breakdown, discharge constraints, or interaction-driven turbulence near bottlenecks. Consistent with this, freeway-focused infrastructure strategies that manage interactions, such as optimized AV-dedicated lane placement and configuration on expressways, are reported to reduce total travel time primarily once AV market penetration is sufficiently high to sustain dedicated operations without inducing underutilization or disruptive merges, with more pronounced benefits reported when penetration exceeds roughly 30% [66,67].

In urban arterial and signal-controlled settings, delay outcomes are particularly sensitive to intersection interactions, signal control assumptions, and the extent to which human drivers correctly anticipate AV behavior. Interaction frictions are amplified in complex maneuvers, and misinterpretation of AV driving mode can substantially exacerbate delays during conflict-prone movements such as straight–left interactions at signalized intersections. Under such conditions, very large delay amplification has been reported, including increases up to 79.3% attributable to driving-mode misidentification in a two-phase signalized intersection setting [53]. These findings highlight that urban delay impacts are not solely a function of penetration, but also of behavioral inference, yielding conventions, and the signal-control environment. Accordingly, a limited number of studies (notably [53]) have examined misidentification-induced delays.

In mixed networks and corridor-scale studies that combine signalized links and bottleneck mechanisms, reported delay changes reflect the interaction between intersection control, queue spillback, and network-level gating of demand. In this class, network control strategies that leverage AVs as sensing and actuation elements can offset early-stage delay increases even at very low penetration. For example, perimeter control approaches that use

AVs as mobile sensors report delay reductions up to 33.5% at penetration levels around 5%, indicating that network-level coordination can dominate purely local interaction frictions when appropriately designed [64]. Across these mixed-facility contexts, policy-relevant interpretations therefore require that reported delay effects be read jointly with network composition, control architecture, and the specific interaction and recognition assumptions embedded in the study design, rather than as a single pooled range.

4.2.3. Traffic Stability and Oscillation Mitigation

Beyond capacity and delay metrics, AVs and CAVs demonstrate substantial potential to enhance traffic stability by mitigating stop-and-go oscillations that contribute to congestion, energy inefficiency, and driver discomfort [49,54,59]. Connectivity enables improved string stability by allowing vehicles to respond almost instantaneously to upstream disturbances, thereby reducing amplification of speed fluctuations along traffic streams [48,49,62]. Control strategies such as the FollowerStopper (FS) controller have been shown to effectively dampen traffic waves, with additional gains achieved through cooperative platoon-based driving across a wide range of traffic densities [59].

At the macroscopic level, random walk–based analyses suggest that AVs can reduce the propagation and severity of traffic jams by adopting proactive "slow-in" strategies, whereby earlier and smoother deceleration limits the capacity drop typically induced by abrupt human braking behavior [48]. These findings underscore that stability improvements may represent one of the earliest and most robust system-level benefits of automation, even before full capacity gains are realized

4.2.4. Mobility, Policy, and Land-Use Integration

The emergence of autonomous mobility-on-demand (AMoD) systems and shared autonomous vehicles (SAVs) is expected to induce structural changes in vehicle ownership, travel demand, and urban spatial organization [68–70]. Simulation-based studies suggest that widespread adoption of SAVs could reduce the total number of vehicles in a city to less than 7% of current levels. However, these reductions may be offset by increases in vehicle kilometers traveled (VKT) due to empty repositioning trips, unless high levels of ride-sharing are achieved [68]. When ride-sharing participation exceeds approximately 60%, VKT can be stabilized or reduced.

Policy and economic regulation play a decisive role in shaping these outcomes. Instruments such as minimum wage floors for human drivers, congestion pricing, and tradable credit schemes (TCS) have been shown to improve welfare outcomes and mitigate inefficient platform competition, often characterized as "wild goose chases" [60,69,71,72]. From a land-use perspective, private vehicle automation tends to encourage urban sprawl, whereas investments in autonomous public transport promote population clustering and more compact development patterns [42,70]. Integrated pricing strategies that combine SAV fares with congestion pricing can improve regional accessibility by up to 14%. Moreover, smart parking pricing policies are increasingly critical, as AVs' ability to cruise or park remotely may otherwise exacerbate roadway congestion [67] (Zhang, Zhang et al. 2025).

4.2.5. Foundational Modeling Frameworks and Simulation Tools

Advances in traffic modeling increasingly adopt cyber–physical system (CPS) perspectives that integrate communication networks, traffic flow dynamics, and vehicle-level control. Co-simulation platforms combining V2X communication modules (e.g., OMNeT++), traffic simulators (e.g., SUMO, Aimsun), and vehicle dynamics environments (e.g., Webots) enable high-fidelity evaluation of AV and CAV applications [47,61,73]. These frameworks support the assessment of strategies such as eco-driving and adaptive traffic signal control

https://doi.org/10.3390/vehicles8020041

(ATSC), which leverage real-time infrastructure-to-vehicle (I2V) communication to reduce emissions and optimize progression through signalized corridors [46,73–75].

Across these modeling frameworks, performance evaluation relies on a common set of traffic flow and mobility indicators that quantify capacity, delay, stability, and travel efficiency at corridor and network scales. A synthesized overview of these key performance indicators—together with their reported impacts under varying AV and CAV penetration levels—is provided in Table 4. These metrics underpin the capacity, delay, and stability analyses.

Table 4. Key performance indicators (KPIs) used to evaluate the impacts of AVs and CAVs on urban traffic flow, mobility, and network performance.

KPI	Description and Impact	Reference(s)
Traffic Capacity	Maximum network throughput; improved by approximately 1–84% depending on AV penetration level and control strategy.	[38,40,44,45,63]
Average Delay	Time lost due to stopping and queuing; reductions of up to 46% reported under coordinated signal control and AV-based perimeter management.	[9,40,53,64,74]
Average Travel Time	Mean trip duration across the network; SAV platooning and AV-dedicated lanes can reduce citywide travel times by up to 50%.	[40,68,76]
Queue Length	Spatial extent of vehicle queues at bottlenecks and intersections; significantly reduced through platooning and active traffic control.	[39,40,47]
Vehicle Kilometers Traveled (VKT/VMT)	Total distance traveled by all vehicles; SAVs may increase VKT due to empty repositioning unless combined with high ride-sharing participation.	[42,68,77]
Velocity Volatility (cv)	Coefficient of variation in speed; AVs and CAVs significantly dampen speed fluctuations and stop-and-go oscillations.	[48,49,59]
Replacement Rate	Number of private conventional vehicles replaced by a single SAV; estimated between 3.8 and 11 vehicles.	[65,68]
Total Utilization Time/Total Parking Revenue (TUT/TPR)	Measures operational usage and parking-related economic impacts; critical for AV parking and curbside management policy.	[67]
Network Connectivity	Effectiveness of V2X communication; strongly influenced by roadside unit (RSU) spacing (e.g., 1235–1669 m).	[61,78]

4.3. Mixed Traffic (AVs and Human-Driven Vehicles)

The integration of AVs and CAVs into existing urban networks will occur through a prolonged transitional phase characterized by mixed traffic conditions, in which automated and human-driven vehicles share infrastructure and interact continuously [9,46,61]. During this phase, vehicles with differing automation levels must negotiate road space, priority, and interaction protocols, creating complex dynamics that influence traffic stability, network efficiency, and user acceptance. As a result, mixed traffic represents not merely an intermediate deployment stage, but a defining operational condition that shapes the real-world impacts of automation.

Most studies reviewed in this section are based on simulations, short-term trials, or pilot deployments in which human drivers have limited prior experience with AVs; consequently, the reported effects largely reflect initial-contact conditions. A key challenge in such settings is that AVs cannot convey intent through eye contact or gestures, leading to the development of external human–machine interfaces (eHMIs) and infrastructure-based

https://doi.org/10.3390/vehicles8020041

signaling (e.g., SPaT messages) to indicate yielding, stopping, or priority. Evidence suggests that these communication technologies moderate misidentification and behavioral mismatch by improving predictability and reducing hesitation and aggressive interactions. Large-scale pilots conducted by Waymo and Cruise [69] have tested external displays and standardized yielding behaviors, showing that consistent signaling can support smoother interactions and higher user trust, although cross-manufacturer standardization remains limited.

4.3.1. Traffic Performance and Efficiency Impacts

Evidence across the reviewed studies consistently indicates that traffic performance under mixed conditions exhibits strong non-linear responses to AV and CAV market penetration rate (MPR), as well as sensitivity to behavioral and control parameters [9,61,79]. At low to moderate penetration levels, the introduction of automated vehicles may degrade overall network performance despite their advanced capabilities. For example, on-ramp merging simulations report that AV penetration levels of 10%, 25%, and 50% correspond to increases in average total network delay of approximately 4%, 7%, and 18%, respectively, relative to conventional traffic. These effects are primarily attributed to conservative AV maneuvers that prioritize safety margins, thereby reducing effective capacity utilization in mixed streams [9].

By contrast, at higher penetration levels, AVs and CAVs can substantially improve throughput and flow stability. Under favorable control assumptions, some studies report potential throughput gains exceeding 100%, with fully autonomous vehicles delivering greater benefits than connected-only vehicles at comparable market shares [9]. Sensitivity analyses further highlight that network outcomes depend critically on the configuration of longitudinal control parameters. In particular, desired time gap has been identified as the most influential factor, followed by standstill distance and acceleration from rest, underscoring that the qualitative design of automation strategies can be as consequential as the quantitative level of deployment.

4.3.2. Strategic Management and Infrastructure

Effective management of mixed traffic typically requires coordinated operational strategies supported by targeted infrastructure interventions. Dedicated lanes for CAVs can enhance operational efficiency, particularly when integrated with adaptive intersection signal scheduling [79]. Beyond lane allocation, vehicle occupancy emerges as a high-leverage system variable. Increasing average passenger load reduces the number of vehicles required to satisfy fixed travel demand, with simulation results indicating that doubling occupancy can halve on-road vehicle counts—an effect that may exceed the impact of certain restrictive driving policies.

Connectivity fundamentally alters sensing and control capabilities in mixed traffic environments. CAVs can operate as mobile sensors and actuators, supplying high-resolution trajectory and traffic-state data that complement or surpass fixed sensing infrastructure such as loop detectors [46]. However, the stability benefits of connectivity are contingent on communication reliability. As communication range increases, interference effects can lead to packet loss and transmission delays, which degrade control performance and limit the effectiveness of cooperative strategies [61]. These findings highlight that infrastructure investments must account not only for physical capacity but also for communication robustness.

4.3.3. User Adoption and Social Heterogeneity

The pace and effectiveness of the transition toward automated mobility depend not only on technical feasibility but also on user acceptance and heterogeneous travel behavior.

https://doi.org/10.3390/vehicles8020041

Public intention to use AVs is shaped by perceived relative advantage, anticipated safety improvements, and compatibility with daily travel needs, while privacy concerns and perceived legal liability remain persistent barriers [77]. Such heterogeneity influences both adoption trajectories and system-level outcomes.

User preferences also affect technology pathways, including powertrain choice. Infrastructure support measures—such as wireless charging availability and the provision of dedicated AV lanes—have been shown to increase the likelihood of purchasing electric autonomous vehicles (EAVs) relative to conventional gasoline-powered alternatives. These interactions suggest that mixed traffic performance, energy transitions, and user adoption are tightly coupled, reinforcing the need for integrated planning approaches that consider behavioral diversity alongside technological deployment.

To capture the combined operational and behavioral dimensions of mixed traffic, prior studies employ indicators that reflect not only efficiency and stability, but also communication reliability and user acceptance. The principal metrics used to evaluate these mixed-traffic outcomes—spanning traffic capacity, delay, string stability, vehicle occupancy, and intention to use AVs—are summarized in Table 5. These indicators support the interpretation of the non-linear performance patterns.

Table 5. Key performance indicators (KPIs) for assessing traffic performance, stability, and user adoption outcomes under mixed AV/CAV and human-driven vehicle conditions.

KPI	Description and Significance	Reference(s)
Traffic Capacity	Maximum sustainable flow rate; can increase by up to 100% at high AV MPRs.	[46]
Average Total Delay (ATD)	Total time lost due to congestion; may increase at low MPRs due to conservative AV behavior.	[9]
Average Travel Time (ATT)	Mean duration to traverse the network; reported improvement of 6.41% at 20% CAV MPR in coordinated scenarios.	[9,79]
String Stability	Ability of a vehicle string to dampen perturbations; improved by reduced reaction times and cooperative behavior.	[9,46,61]
Vehicle Occupancy (Rvor)	Ratio of passenger load to capacity; doubling occupancy can halve on-road vehicles under fixed demand.	[79]
Average Number of Stops (ANS)	Frequency of stops; reported optimization of 17.1% at 20% CAV MPR.	[9,79]
Packet Delivery Ratio (PDR)	Reliability of V2X links; reported to drop to ~50% at communication ranges of 300 m (context-dependent).	[61]
Intention to Use AVs	Latent indicator of public acceptance; shaped by safety perception and social image, among other factors.	[77]
Unit Credit Price	Cost of travel credits in a tradable credit scheme; decreases as CAV MPR rises.	[60]

4.4. Infrastructure, Urban Systems, and Smart Mobility

The transition toward smart cities increasingly depends on the integrated deployment of autonomous mobility-on-demand (AMoD) services, supportive physical infrastructure, and data-driven governance frameworks that jointly promote environmental sustainability and social equity. Achieving these outcomes requires a system-level perspective that captures feedback mechanisms between automated vehicle technologies, urban land use, and the digital layers used to sense, manage, and regulate mobility services. Rather than acting independently, infrastructure design, spatial development, and smart mobility governance interact to shape the realized impacts of automation on cities.

https://doi.org/10.3390/vehicles8020041

This section focuses on infrastructure implications for interactions among AVs, human-driven vehicles, and traffic control systems.

4.4.1. Infrastructure Design and Dedicated Lane Strategies

Infrastructure adaptation is a prerequisite for unlocking the operational benefits of automation, particularly in capacity-constrained urban environments. Recent research extends conventional dedicated-lane planning beyond determining the number of autonomous-vehicle dedicated lanes (AVDLs) to two-dimensional configurations that explicitly optimize directional and movement-specific functionality, such as separating left-turn and through-movement AV lanes [80]. These formulations enable more accurate estimation of intersection delays and allow trips to be classified according to whether they traverse AVDL-only, hybrid, or general-purpose lanes, thereby improving realism in network-level performance evaluation.

On expressways, the effectiveness of lane conversion policies is strongly dependent on AV market penetration rates (MPR). In high-density metropolitan contexts such as Seoul, converting existing lanes to AV-exclusive use becomes efficient once MPR reaches approximately 20–30%; below this threshold, exclusive lanes tend to be underutilized while congestion intensifies in the remaining general-purpose lanes [45]. Automation also affects freight operations and infrastructure utilization. On freeway networks, truck platooning—evaluated through integrated micro–macro modeling frameworks—has been shown to increase capacity when platoon size and inter-vehicle spacing are appropriately optimized [65]. These findings underscore that infrastructure strategies must be phased and adaptive, aligning physical design decisions with evolving penetration levels.

4.4.2. Urban Spatial Dynamics and Land-Use Modeling

Smart mobility technologies are expected to reshape long-run urban form, raising fundamental challenges for integrated land use–transportation (ILUT) modeling. In particular, AV-enabled accessibility gains challenge traditional assumptions regarding whether improved access induces urban sprawl or reinforces agglomeration economies and compact development [81]. Automation alters generalized travel costs not only through time savings, but also through changes in comfort, productivity, and reliability, complicating predictions of residential and employment location choices.

Parking dynamics represent a critical interface between automation and urban land use. AVs' ability to park remotely or return to their origin can potentially free substantial amounts of high-value urban land currently allocated to parking supply [67,81]. However, these benefits are not automatic. Without appropriate policy intervention, empty vehicle repositioning may increase VKT and exacerbate congestion. As a result, pricing instruments—such as high parking fees in central areas—have been proposed to discourage excessive empty circulation by incentivizing peripheral parking or return-to-base strategies [67].

4.4.3. Smart Mobility Governance and Policy

Sustainable smart mobility outcomes depend on proactive regulatory intervention to manage externalities and ensure equitable access. For transportation network companies (TNCs) operating mixed fleets of AVs and human-driven vehicles, governance frameworks must explicitly address spatial equity and service distribution outcomes [72]. Policy instruments such as minimum wage floors for human drivers can reduce platform labor power and help prevent premature labor displacement before automated systems achieve operational maturity and public acceptance.

Environmental performance is shaped jointly by vehicle technology and upstream energy systems. Long-term projections of use-stage emissions through 2050 indicate that

meaningful decarbonization of automated transport is contingent on parallel improvements in electricity generation to support electric autonomous vehicle (EAV) fleets [82]. Complementarily, virtual reality–enabled digital twin platforms offer new capabilities for real-time emissions monitoring and the safe evaluation of eco-routing strategies, enabling assessment of compliance behavior and advisory effectiveness without the risks associated with large-scale field deployment [75].

4.4.4. Technological Integrity and Human Factors

The reliability of smart mobility systems depends critically on communication robustness, cybersecurity, and the behavioral heterogeneity associated with different automation levels. Connected and automated vehicles remain vulnerable to cyberattacks targeting sensing components (e.g., radar, LiDAR, GPS) and V2X communication channels, motivating decentralized public key infrastructure solutions for real-time authentication and secure connectivity [50]. Ensuring technological integrity is therefore a prerequisite for scaling cooperative automation.

At the traffic-flow level, mixed environments must also account for functional disparities between fully automated vehicles and semi-automated vehicles, in which human drivers retain default control and may activate automated following only under an explicit "platooning intention" state [83]. This behavioral gating mechanism can significantly influence realized platooning rates and, consequently, network-level performance gains. These findings highlight that human factors and system design choices interact closely, reinforcing the need to integrate behavioral realism into infrastructure planning and control strategies.

Evaluating infrastructure adaptation, governance effectiveness, and environmental sustainability in smart mobility systems requires performance indicators that extend beyond conventional traffic metrics. As summarized in Table 6, these indicators include capacity increase rates, spatial equity measures, fleet sizing metrics, communication reliability, and emissions-related variables. Collectively, they support the infrastructure and governance analyses.

Infrastructure investment decisions should be guided by cost–benefit analyses that account for uncertain AV adoption trajectories, network-wide efficiency gains, and equity impacts. The reviewed studies suggest that premature large-scale investment in V2I and dedicated AV lanes may lead to underutilization at low penetration levels, while delayed deployment can constrain performance at higher adoption rates. In many urban contexts, prioritizing public transport and shared mobility integration remains more cost-effective and socially inclusive in early deployment phases, with targeted AV infrastructure introduced progressively as market penetration increases.

Table 6. Key performance indicators (KPIs) for infrastructure planning, governance evaluation, and sustainability assessment in smart mobility and autonomous transport systems.

KPI	Impact and Significance	Reference(s)
Capacity Increase Rate (CIR)	Ratio of roadway capacity with platooning relative to no-platooning; supports infrastructure planning and lane-management design.	[65]
Minimum Fleet Size	Minimum number of shared vehicles required to satisfy urban travel demand under AMoD/SAV operations.	[68]
Vehicle Kilometers Traveled (VKT)	Aggregate roadway usage; car-sharing may increase VKT unless combined with ride-sharing.	[68]

https://doi.org/10.3390/vehicles8020041

Table 6. *Cont.*

KPI	Impact and Significance	Reference(s)
Spatial Inequity (Theil Index)	Distributional measure of service quality (e.g., waiting time, fare) across zones; supports equity-focused regulation.	[72]
Total Utilization Time (TUT)	Parking facility efficiency metric; supports optimization of regionally differentiated pricing strategies.	[67]
Use-Stage Emissions (CO_2/NO_x)	Environmental footprint of vehicle technologies (e.g., ICEVs vs. BEVs/EAVs) during operation.	[82]
Platooning Intention (Q)	Probability that a semi-AV driver hands over control to enable autonomous following/platooning.	[83]
Packet Delivery Ratio (PDR)	Reliability of V2X communication; degrades with higher node density and/or increased communication range.	[50]
Eco-routing Compliance Rate	Share of drivers who follow routing guidance intended to reduce emissions and exposure.	[75]

Note: AMoD = autonomous mobility-on-demand; AVDL = autonomous-vehicle dedicated lane; TNC = transportation network company; VKT = vehicle kilometers traveled; ICEV = internal combustion engine vehicle; BEV = battery electric vehicle; EAV = electric autonomous vehicle; V2X = vehicle-to-everything communication.

4.5. Policy, Governance, and System-Level Challenges

The widespread deployment of AVs introduces policy and governance challenges that extend well beyond technical integration to encompass congestion management, urban form, labor markets, and economic regulation. Because AV adoption can generate both positive and negative externalities, the transition toward automated transport systems requires proactive and adaptive governance frameworks that safeguard equity and sustainability while improving overall social welfare [42,67,70–72,81,84–86].

4.5.1. Urban Congestion and Infrastructure Regulation

Managing congestion remains a central governance challenge in the era of automation. While AVs may increase effective roadway capacity through reduced headways and smoother driving behavior, they simultaneously enable behavioral responses that can intensify congestion. A prominent risk is "parking on the move," whereby unoccupied vehicles cruise to avoid parking fees, increasing traffic volumes and competing for scarce road and curb space [84]. This prospect motivates a policy shift away from traditional fuel taxation toward road user charging mechanisms based on distance traveled, time spent in congested areas, and/or road space occupancy, thereby aligning prices more closely with congestion and space-consumption externalities.

Mixed-traffic operations further expose infrastructure constraints that are not purely technological. For example, narrow residential streets with parked vehicles or complex curbside activity may require frequent negotiation between automated and human-driven vehicles, reducing operational reliability and creating localized bottlenecks. These challenges highlight the need to align infrastructure design, curbside management, and regulatory frameworks with the functional capabilities and limitations of automated systems, rather than assuming that automation alone can resolve existing spatial constraints.

4.5.2. Spatial Equity and Urban Development

Automation has the potential to fundamentally reshape residential and employment location choices by altering the generalized cost of travel. Modeling evidence suggests that privately ridden autonomous vehicles (PAVs) may induce population dispersion and urban sprawl, as increased comfort and in-vehicle productivity reduce the perceived burden of longer commutes [42]. In contrast, shared autonomous vehicles (SAVs) operating as high-

quality, demand-responsive transit services can promote population clustering in dense urban areas, reinforcing agglomeration economies and compact development patterns.

These opposing mechanisms imply that policy assessments may be systematically biased if they consider private automation in isolation while neglecting interactions with shared and public transport systems. As a result, the literature emphasizes the importance of jointly modeling private, shared, and public automated mobility pathways when evaluating long-term land-use outcomes and spatial equity implications. Without coordinated policy intervention, automation risks amplifying spatial inequities by disproportionately benefiting higher-income users with greater access to private AV services.

The reviewed studies indicate that capacity-building measures, particularly the prioritization of AV deployment, dedicated infrastructure, and ride-hailing services in high-demand, often more affluent urban cores, may exacerbate congestion and service inequities in under-resourced or peripheral neighborhoods. Concentrated investment in central districts can displace traffic and accessibility burdens toward suburban and low-income areas, reinforcing existing spatial disparities.

They further show that vulnerable populations, including elderly users, children, low-income individuals, and persons with disabilities, experience AV-induced behavioral changes in heterogeneous ways. While automation can enhance social inclusion and mobility, these benefits are unevenly distributed, and risks related to unequal service provision, economic displacement, and interaction frictions persist. Without targeted regulatory intervention and equity-oriented planning, AV deployment may therefore amplify existing social and spatial inequalities.

4.5.3. Labor Markets and TNC Governance

The integration of AVs into transportation network companies (TNCs) raises significant distributional concerns and labor-market frictions. In mixed fleets, platforms may prioritize AV deployment in high-demand urban cores, displacing human drivers toward lower-demand suburban markets and exacerbating spatial inequities in earnings and service availability [72]. Two primary regulatory levers emerge from the literature.

First, minimum wage floors for human drivers can curb platform monopsony power and improve welfare outcomes. A carefully calibrated wage floor may benefit drivers and passengers by stabilizing service supply and reducing generalized travel costs, with a gross hourly rate of $27.86 cited as a potential benchmark in one analysis [71]. However, excessively stringent labor protections may accelerate full fleet automation by increasing the relative cost of human labor, potentially undermining employment transition objectives [72].

Second, pickup restrictions, such as limiting AV pickups in high-demand zones, have been proposed as a mechanism to protect human driver access to lucrative markets while improving service equity for passengers in underserved areas. These instruments illustrate the delicate balance policymakers must strike between efficiency, innovation, and social protection during the transition to automated mobility.

Increases in VKT associated with AV deployment (particularly from empty repositioning and cruising) may impose disproportionate environmental burdens on peripheral, low-income, and transit-dependent communities. Network optimization that prioritizes high-demand or affluent areas can displace congestion and emissions toward surrounding neighborhoods, reinforcing existing environmental inequalities. These patterns underscore the need for equity-sensitive emissions monitoring and mitigation measures, such as pricing of empty travel and targeted clean-vehicle policies, within AV governance frameworks.

https://doi.org/10.3390/vehicles8020041

4.5.4. Social Acceptance and Institutional Readiness

Policy effectiveness is ultimately conditioned by social acceptance and institutional readiness. Adoption decisions by firms and users may exhibit non-linear responses to public trust and perceived legitimacy. For example, taxi operators may delay AV adoption until social acceptance reaches moderate levels, consistent with an inverted U-shaped relationship between acceptance and adoption incentives under competitive pressure [85]. These dynamics suggest that premature or poorly communicated deployment strategies may hinder, rather than accelerate, technological diffusion.

Institutional capacity is also shaped by innovation pathways. When AV technologies are primarily introduced through external sources rather than domestic research and development, governance dynamics may shift, strengthening the role of government as a "game leader" in standard-setting, regulation, and infrastructure coordination [85]. In addition, widespread AV adoption may divert ridership from public transport, particularly in low-density and peripheral areas, potentially undermining transit viability and disadvantaging transit-dependent populations. Automation may also generate uneven job displacement effects, especially for older, low-income, and immigrant drivers with limited transition opportunities.

Behavioral factors such as the endowment effect (where individuals value private vehicle ownership more highly than shared-use alternatives) may further slow transitions toward shared automated mobility models even when such models are system-efficient [81]. Together, these findings underscore that policy design must account for behavioral inertia and institutional constraints alongside technical feasibility.

To assess these system-level policy and governance effects in a comparable manner, the literature applies a set of economic, equity, accessibility, and efficiency indicators. These key performance indicators, ranging from total flow time and regional accessibility to wage floors, inequity indices, and unoccupied vehicle travel, are summarized in Table 7. They provide the quantitative basis for the policy trade-offs and governance challenges. Reported values are context-specific and intended for comparative analysis rather than direct transferability.

Table 7. Key performance indicators (KPIs) used to evaluate system-level policy, governance, equity, and economic impacts associated with AV deployment.

KPI	Impact and Significance	Reference(s)
Total Flow Time/Travel Time	System efficiency metric; can be reduced by 18.5% through joint pricing of SAVs and congestion charges.	[66]
Regional Accessibility	Ease of reaching activities/opportunities; potentially improved by 14% via optimal SAV pricing.	[70]
Minimum Wage Floor (USD)	Protects driver earnings and curbs platform market power; $27.86/hr (gross) cited as a target.	[71]
Theil Index (Inequity)	Quantifies spatial/social inequity; AV adoption may increase inequity without regulation.	[72]
Social Acceptance (λ)	Adoption determinant; affects transitions from "wait-and-see" to active implementation.	[85]
Travel Cost Elasticity	Demand sensitivity; AV demand reported to be more elastic to cost than to time.	[86]
Unoccupied VMT/VKT	Magnitude of "empty" vehicle movement; may increase by 8–10% in shared mobility scenarios.	[42]
Value of Time (VOT)	Perceived cost of travel time; may decrease by ~20% due to in-vehicle productivity.	[42]
TUT/TPR	Total utilization time and total parking revenue; used to support parking and curbside pricing policy design.	[67]

https://doi.org/10.3390/vehicles8020041

To synthesize the diverse indicators used across the reviewed studies and clarify their relationships across analytical scales, Figure 8 presents a unified KPI taxonomy for AV integration. The taxonomy illustrates how vehicle-level automation influences traffic performance and safety, which in turn shapes infrastructure requirements and system-level policy outcomes. Certain KPIs (e.g., capacity, delay, VKT) appear at multiple layers, reflecting their relevance across operational, infrastructural, and policy evaluation scales.

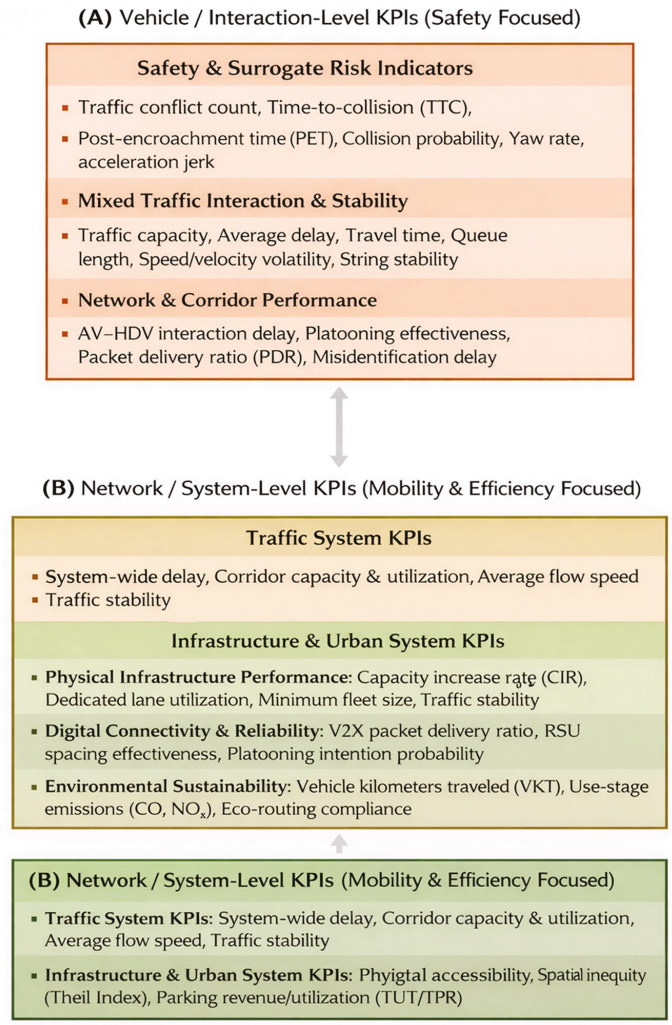

Figure 8. Unified taxonomy of key performance indicators (KPIs) for assessing AV integration across traffic systems, infrastructure and urban contexts, and policy and governance dimensions.

Effective AV governance requires real-time monitoring systems that integrate vehicle trajectories, traffic performance, safety indicators, and environmental data to track deployment impacts. Such systems enable cities to detect emerging negative effects, such as rising delays, emissions, or conflict rates, and to trigger adaptive policy responses, including pricing adjustments, operational restrictions, or infrastructure reallocation. Continuous monitoring also helps prevent technological and institutional lock-in by supporting evidence-based revisions of deployment strategies as adoption patterns and system outcomes evolve.

5. Discussion

The literature reviewed indicates that the system-level impacts of AVs and CAVs depend on three coupled conditions: (i) market penetration rate (MPR), (ii) interaction dynamics in mixed traffic, and (iii) the degree of operational and institutional coordination.

As a result, automation should not be interpreted as a deterministic remedy for congestion or safety risks. Instead, it functions as a system-level intervention whose outcomes emerge from feedback between vehicle control strategies, human adaptation, infrastructure design, and governance.

A central and recurring finding across safety, traffic flow, and mobility studies is the non-linearity of AV/CAV impacts with respect to MPR. Low-penetration deployment frequently produces transitional inefficiencies, in which conservative automated driving policies and mixed-traffic frictions reduce effective capacity utilization and can elevate surrogate risk measures. As MPR increases, particularly when connectivity and cooperative control are present, system performance can shift toward positive outcomes. To consolidate threshold patterns and clarify the moderators shaping these transitions, Table 8 summarizes the direction of impacts at low MPR, the approximate transition regions reported across studies, and the dominant mechanisms discussed in the literature.

Table 8. Effects of AV/CAV market penetration rate (MPR) on key traffic and mobility outcomes.

Outcome (Benefit Direction)	Main Mechanism	Performance Trend across Market Penetration Levels (Low → Transition → High)	Core Assumptions	Number of Studies
Safety conflicts (benefit = fewer conflicts/lower surrogate risk)	Human interaction	Low: <40% → Transition: ~40–75% → Consistent benefits: >75%	Urban and highway; mixed Traffic; with and without platooning (heterogeneous interactions)	9
Delay/travel time (benefit = lower delay)	Mixed (interaction + control)	Low: <20% → Transition: ~20–50% → Consistent benefits: >50%	Urban (intersections/networks); mixed traffic (10–100% focus); with and without platooning	15
Capacity/throughput (benefit = higher flow)	Flow/control mechanics	Low: <20% → Transition: ~20–30% → Consistent benefits: >30%	Highway and urban expressways; mixed traffic; platooning (CACC) as a primary capacity booster	10
Traffic stability (benefit = fewer stop-and-go waves)	Flow/ control mechanics	Gradual improvement; no single dominant breakpoint	Highway and freeway (bottlenecks); mixed traffic; with platooning (using "FollowerStopper" logic)	7
VKT/VMT (benefit = fewer vehicle-km, especially empty travel)	Policy + behavior	Low: <40% (increase likely) → Transition: ~40–65% (policy-dependent) → Potential reduction: >65% (with pricing and ride-sharing)	Urban and regional (city-scale); fully automated (SAV/PAV); focus on ride-sharing and pricing policies	6

Note: Thresholds are approximate and depend on traffic context, control strategy, infrastructure provision, behavioral adaptation, and policy instruments (e.g., congestion pricing and ride-sharing incentives). VKT/VMT outcomes are particularly sensitive to fleet management and pricing strategies.

Table 8 highlights an important asymmetry during the transition period. Design choices that increase individual-vehicle safety margins can reduce network performance and interaction efficiency when AVs remain a small minority. In the safety domain, while long-term reductions in severe crashes remain plausible, surrogate safety indicators suggest that risk can be redistributed during early deployment. Human responses, including aggressive cut-ins ("bullying"), inconsistent gap acceptance, and difficulty anticipating conservative AV maneuvers, can generate emergent conflict patterns that are not well captured by vehicle-centric validation alone. This implies that early safety assurance should extend beyond the automated driving stack and include interaction-aware assessment, behavioral monitoring, and operational design choices that reduce ambiguity in mixed traffic, such as more transparent intent communication and predictable yielding behavior.

https://doi.org/10.3390/vehicles8020041

For efficiency outcomes, the reviewed studies collectively suggest that delay and travel time can worsen at low-to-moderate MPR, whereas traffic stability improvements may appear earlier and more robustly. This distinction matters for performance evaluation and expectation management. Early benefits are more likely to be observed as smoother flow and reduced stop-and-go variability, rather than immediate throughput increases. As penetration rises, and when supported by cooperative strategies such as platooning, coordinated signal control, and network-level control, capacity and travel-time improvements become more consistently reported. From a deployment perspective, the evidence supports pairing early AV introduction with targeted traffic management measures, such as signal coordination or corridor-level control, rather than assuming that automation alone will deliver near-term network gains.

Mobility sustainability outcomes are highly policy-sensitive. The literature repeatedly notes that automation can increase travel demand and unoccupied vehicle movement through convenience effects and empty repositioning, which may offset local operational improvements. Conversely, when AVs are integrated with shared mobility models, pricing measures (including congestion and parking pricing), and coordinated land-use planning, automation may support higher accessibility and more efficient urban space utilization. This polarity reinforces that VKT/VMT is primarily an operational and policy outcome, shaped by incentives, platform governance, and constraints on empty travel, rather than a direct technology outcome.

Infrastructure implications are similarly conditional. Dedicated or managed lanes, adaptive signal control, and V2X-enabled coordination can unlock improvements, but only when deployed in step with market penetration and communication reliability. Infrastructure adaptation therefore benefits from dynamic staging. If exclusive capacity is allocated too early, underutilization and localized congestion can result. If digital coordination is deployed too late, high-MPR benefits may not materialize. A practical interpretation of the evidence is that deployment planning should align automation capability and operational design domain, communication robustness and interoperability, and traffic management policies that can be adjusted as MPR evolves.

Governance capacity and social acceptance emerge as cross-cutting determinants of transition feasibility. Regulatory uncertainty, public trust, cybersecurity, and labor displacement concerns can delay adoption or constrain operational domains, which can prolong the mixed-traffic phase where outcomes are most uncertain. The reviewed studies support an adaptive governance approach, including staged approvals, continuous monitoring, transparent reporting of safety and operational performance, and policy packages that address equity and labor impacts alongside technical deployment. In this sense, the traffic ecosystem perspective is not only descriptive but also prescriptive, since it implies that successful AV integration requires coordination across engineering, operations, and governance rather than optimization within a single layer.

The integration of AVs into urban networks requires a shift from passive observation to active regulation, with policy instruments increasingly treated as key variables shaping market and social outcomes. Labor and market regulations are particularly influential in this context. Minimum wage floors are intended to protect human drivers in mixed fleets and to curb platform market power, thereby reducing total trip costs and benefiting both drivers and passengers [71]. However, when set above a critical threshold, they may accelerate the replacement of human labor with AVs [72]. Similarly, vehicle and driver caps aim to mitigate congestion in urban cores by limiting fleet size, but they can depress driver earnings while allowing platforms to benefit from restricted supply. Restrictive pickup policies are designed to improve spatial equity by directing AV services toward lower-demand areas and protecting human drivers in high-demand zones, yet they may also

https://doi.org/10.3390/vehicles8020041

increase deadheading as vehicles reposition after drop-offs. Overall, these findings indicate that labor and market regulations involve important trade-offs and must be designed as part of an integrated and adaptive policy framework.

The reviewed literature suggests that regulatory stringency involves trade-offs between deployment speed and long-term outcomes. Stricter safety frameworks, such as those in the EU, may slow early adoption but support higher public trust and more stable safety performance, whereas more permissive approaches, as in parts of the US, encourage rapid experimentation but increase variability in risk exposure. Although direct evidence on optimal stringency remains limited, comparative studies point to phased and adaptive regulation as a balanced strategy. Lessons from automated trading and drone regulation further emphasize the value of incremental approval, regulatory sandboxes, and continuous monitoring in managing technological transitions.

To further clarify the urban structure and land-use implications of autonomous vehicles, this discussion should be organized around three key spatial variables: commuting distance, accessibility, and parking demand. Commuting distance reflects long-term changes in residential location and travel behavior, as reduced perceived travel costs may encourage longer commutes and suburbanization under private AV use, while shared and transit-integrated services tend to support more compact development. Accessibility represents a central mechanism linking AV deployment to spatial equity and mobility outcomes, since automation can improve access to jobs and services by reducing travel time and enhancing network reliability, particularly in peripheral areas, although market-driven deployment often favors higher-income users and produces uneven benefits. Parking demand reduction forms a direct connection between AV adoption and urban land use, as remote parking and shared fleets can substantially lower central-area parking requirements and enable land reallocation to higher-value uses; however, without appropriate pricing and regulation, empty cruising may offset these gains through increased traffic and curbside congestion. These variables provide a measurable framework for linking AV deployment to urban form and strengthen the relevance of AV impact assessment for both transportation and urban planning.

Taken together, the evidence supports interpreting AVs and CAVs as catalysts of systemic change. Their societal value depends on whether deployment strategies reduce low-MPR transition risks, accelerate the conditions under which cooperative control becomes effective, and align automation with pricing, land-use, and governance mechanisms that protect equity and sustainability objectives.

6. Conclusions

This review examined autonomous vehicles (AVs) and connected autonomous vehicles (CAVs) through a traffic ecosystem lens, synthesizing evidence on integration pathways, mixed-traffic impacts, infrastructure implications, and governance requirements. Based on a systematic review of 51 peer-reviewed studies (2016–2025), the analysis indicates that AV/CAV impacts are not uniform and should not be treated as automatic consequences of technical maturity.

Across domains, the strongest and most consistent finding is that system outcomes are highly non-linear with market penetration and are mediated by control design, mixed-traffic behavior, and institutional context. During transitional phases with partial deployment, conservative automated driving and interaction frictions can increase delays and elevate surrogate conflict indicators, even when long-term safety potential remains favorable. As penetration rises, particularly when supported by connectivity, cooperative control, and adaptive traffic management, benefits in safety, capacity, and stability become more consistent.

https://doi.org/10.3390/vehicles8020041

A principal contribution of the review is to frame AVs as a system-level intervention whose impacts emerge from interactions among automated vehicles, human users, infrastructure, and governance. This framing clarifies why similar technologies can yield divergent results across contexts, and why policy and operations often determine whether technical capability translates into public benefit.

6.1. Practical Implications

The reviewed evidence suggests that phased and adaptive deployment is essential. Early deployments should be paired with targeted operational measures, including coordinated intersection control, corridor or network management, and staged lane strategies where justified, rather than relying on automation to improve traffic performance by default. To reduce transition risks, agencies and operators should prioritize predictable interaction behavior, monitoring of mixed-traffic conflict patterns, and continuous refinement of control parameters that strongly affect network outcomes, notably following-gap settings. To mitigate adverse sustainability outcomes, pricing and regulatory instruments, particularly parking and congestion pricing, curbside management, and incentives for shared rides, should be applied to limit induced demand and empty vehicle circulation. Equity and labor impacts should be addressed proactively to reduce the risk of reinforcing spatial and social inequalities during adoption.

Findings indicate that AV efficiency gains depend strongly on traffic density and operating context. In high-density urban networks, conservative driving behavior can reduce flow and speed and intensify intersection bottlenecks [9,38], although perimeter control using AVs as mobile sensors can mitigate delays even at low penetration levels [64]. In lower-density suburban areas, AVs generally improve capacity and free-flow speeds, and reliable connectivity can be maintained with wider roadside unit spacing [63,78]. On high-speed highways, conservative designs prioritize large safety distances and string stability [49], whereas in congested urban traffic the time gap is the key control parameter [40], and overly cautious settings can significantly increase delays and queues. More adaptive urban control strategies are therefore needed to balance safety and efficient use of limited road space.

Overall, these regional differences indicate that AV performance and societal impacts are strongly shaped by governance priorities: the EU prioritizes sustainability and multimodal integration, the US emphasizes market competition and highway efficiency, and Asian countries focus on state-led infrastructure and strategic demand management. Consequently, the effectiveness of AV deployment depends less on technological capability alone than on how regulatory frameworks align automation with environmental, mobility, and congestion-control objectives.

6.2. Limitations and Future Research

The existing literature is dominated by simulation-based studies with simplified behavioral assumptions and limited empirical validation, which constrains real-world generalizability, particularly with respect to long-term adaptation, induced demand, and land-use feedback. As a result, many reported outcomes may not fully reflect conditions under large-scale, long-term deployment. This review may also be affected by publication bias, as peer-reviewed studies reporting positive or statistically significant impacts are more likely to be published, while null or negative findings and gray literature remain underrepresented. Consequently, some reported performance improvements may be overstated. Future reviews could mitigate this limitation by incorporating high-quality gray literature and registered study protocols.

https://doi.org/10.3390/vehicles8020041

A further limitation is the scarcity of longitudinal evidence on human behavioral adaptation to AVs. Most available findings are derived from short-term experiments and early pilot programs, which do not capture learning effects, expectation formation, or the emergence of stable interaction norms. Over time, as human drivers become more familiar with AV behavior, equilibrium traffic dynamics, safety outcomes, and efficiency levels may differ substantially from those observed in early-stage studies. In addition, many studies do not adequately account for heterogeneity among drivers, including demographic differences and professional driving roles, despite their potential influence on interaction patterns and long-term adaptation.

Reported impacts of AVs are highly sensitive to the choice and calibration of car-following models, such as the Intelligent Driver Model, Krauss, or Wiedemann, with different formulations often leading to conflicting conclusions, particularly for safety-related outcomes. In addition, studies vary in their treatment of sensing and communication, ranging from idealized assumptions in macroscopic models to explicit modeling of sensor noise and communication failures in high-fidelity simulations, which frequently show substantial performance degradation under imperfect conditions. Moreover, only about 15 of the 51 reviewed studies report rigorous validation or calibration against real-world data, limiting confidence in the transferability of many simulation-based findings.

Reported impacts of AVs and CAVs are highly sensitive to scenario selection. The literature is strongly concentrated on urban intersections, highway merging, and simplified car-following environments, which facilitates comparison but limits generalizability. Complex, large-scale, and heterogeneous settings remain under-represented. In particular, interactions with emergency vehicles, operations under adverse weather, multi-agent mixed traffic, and human misidentification scenarios have received limited systematic attention. Future research should expand empirical and simulation efforts toward these high-impact but under-studied contexts to improve the robustness of system-level conclusions.

A further limitation is the limited availability of detailed safety and traffic data from major commercial pilots, creating information asymmetry between academia and industry. Consequently, much of the evidence relies on simulations and small-scale trials, while large deployments remain only partially observable. This review therefore interprets reported benefits cautiously and highlights the need for greater data sharing and public–private collaboration.

Finally, despite the growing number of regional case studies, the literature lacks systematic cross-regional comparative analyses that jointly consider regulatory frameworks, traffic cultures, infrastructure maturity, and behavioral contexts. Most existing studies remain highly context-specific and rely on heterogeneous modeling assumptions, limiting the transferability of results. Future research should therefore prioritize coordinated multi-region comparative studies, real-world mixed-traffic experiments, longitudinal field observations, and integrated land use–transport modeling to strengthen empirical evidence and reduce uncertainty surrounding transition-phase and long-term AV impacts.

In conclusion, AVs represent a potentially transformative but uncertain evolution of urban mobility. Their successful integration depends on technological progress as well as coordinated traffic management, evidence-based governance, and long-term planning aligned with sustainability and equity objectives.

Supplementary Materials: The following supporting information can be downloaded at: https://www.mdpi.com/article/10.3390/vehicles8020041/s1, Table S1: PRISMA 2020 checklist and location of reported items, Table S2: Standardized data extraction form used for included studies.

Author Contributions: Conceptualization, R.G.B. and G.-D.V.; methodology, R.G.B.; software, G.-D.V.; validation, E.V.B. and G.A.; formal analysis, E.V.B.; investigation, R.G.B. and G.A.; resources, G.-D.V.; data curation, R.G.B. and E.V.B.; writing—original draft preparation, R.G.B. and G.-D.V.; writing—review and editing, E.V.B.; visualization, G.A. and G.-D.V.; supervision, G.A.; project administration, R.G.B.; funding acquisition, R.G.B. and G.A. All authors have read and agreed to the published version of the manuscript.

Funding: This work was supported by a grant of the Ministry of Research, Innovation and Digitization, CNCS UEFISCDI, project number PN-IV-PCB-RO-MD-2024-0370, within PNCDI IV.

Data Availability Statement: The data presented in this study are available from the corresponding author upon reasonable request, subject to the dissemination policies of the nationally funded research project supporting this work.

Conflicts of Interest: The authors declare no conflicts of interest.

References

1. Salvini, P.; Kunze, L.; Jirotka, M. On self-driving cars and its (broken?) promises. A case study analysis of the German Act on Autonomous Driving. *Technol. Soc.* **2024**, *78*, 102628. [CrossRef]
2. Garikapati, D.; Shetiya, S.S. Autonomous Vehicles: Evolution of Artificial Intelligence and the Current Industry Landscape. *Big Data Cogn. Comput.* **2024**, *8*, 42. [CrossRef]
3. Zhang, Y.; Carballo, A.; Yang, H.; Takeda, K. Perception and sensing for autonomous vehicles under adverse weather conditions: A survey. *ISPRS J. Photogramm. Remote Sens.* **2023**, *196*, 146–177. [CrossRef]
4. SAE_International. *Taxonomy and Definitions for Terms Related to Driving Automation Systems for On-Road Motor Vehicles*; SAE_International: Warrendale, PA, USA, 2021.
5. König, A.L.; Boßow-Thies, S.; Krol, B. Female mobility—An empirical analysis of factors influencing women's acceptance of Robo-Taxis using PLS-SEM. *Transp. Res. Part F Traffic Psychol. Behav.* **2025**, *114*, 933–952. [CrossRef]
6. Anund, A.; Ludovic, R.; Caroleo, B.; Hardestam, H.; Dahlman, A.; Skogsmo, I.; Nicaise, M.; Arnone, M. Lessons learned from setting up a demonstration site with autonomous shuttle operation–based on experience from three cities in Europe. *J. Urban Mobil.* **2022**, *2*, 100021. [CrossRef]
7. Xu, Z.; Zheng, N. Integrating connected autonomous shuttle buses as an alternative for public transport—A simulation-based study. *Multimodal Transp.* **2024**, *3*, 100133. [CrossRef]
8. Singh, S. *Critical Reasons for Crashes Investigated in the National Motor Vehicle Crash Causation Survey*; U.S. Department of Transportation: Washington DC, USA, 2015.
9. Abdelghaffar, H.M.; Menéndez, M. Influential Control Parameters for Autonomous Vehicles in a Mixed Environment. *IEEE Open J. Veh. Technol.* **2024**, *5*, 927–939. [CrossRef]
10. Aittoniemi, E. Evidence on impacts of automated vehicles on traffic flow efficiency and emissions: Systematic review. *IET Intell. Transp. Syst.* **2022**, *16*, 1306–1327. [CrossRef]
11. Stueger, P.N.; Niels, T.; Margreiter, M.; Bogenberger, K. Impact of Connected and Automated Vehicles on Metropolitan Road Traffic: Test Site Munich, Germany. *Transp. Res. Rec.* **2025**, *2679*, 309–323. [CrossRef]
12. He, Y.; Xiang, D.; Wang, D. Traffic safety evaluation of emerging mixed traffic flow at freeway merging area considering driving behavior. *Sci. Rep.* **2025**, *15*, 10686. [CrossRef]
13. Debbaghi, F.-Z.; Rombaut, E.; Vanhaverbeke, L. Lessons learned from shared automated vehicles pilots in Europe: An evaluation of safety, traffic, and user acceptance. *Case Stud. Transp. Policy* **2025**, *20*, 101447. [CrossRef]
14. Wang, J.; Pant, Y.V.; Jiang, Z. Learning-based modeling of human-autonomous vehicle interaction for improved safety in mixed-vehicle platooning control. *Transp. Res. Part C Emerg. Technol.* **2024**, *162*, 104600. [CrossRef]
15. Shetty, A.; Yu, M.; Kurzhanskiy, A.; Grembek, O.; Tavafoghi, H.; Varaiya, P. Safety challenges for autonomous vehicles in the absence of connectivity. *Transp. Res. Part C Emerg. Technol.* **2021**, *128*, 103133. [CrossRef]
16. Liu, C.; Zyryanov, V.; Topilin, I.; Feofilova, A.; Shao, M. Investigating the Impacts of Autonomous Vehicles on the Efficiency of Road Network and Traffic Demand: A Case Study of Qingdao, China. *Sensors* **2024**, *24*, 5110. [CrossRef] [PubMed]
17. Emory, K.; Douma, F.; Cao, J. Autonomous vehicle policies with equity implications: Patterns and gaps. *Transp. Res. Interdiscip. Perspect.* **2022**, *13*, 100521. [CrossRef]
18. Chang, Q.; Chen, H. Impacts of autonomous vehicles on freeway with conditional isolated and dedicated lanes. *Sci. Rep.* **2025**, *15*, 21374. [CrossRef]
19. Fujiu, M.; Morisaki, Y.; Takayama, J. Impact of Autonomous Vehicles on Traffic Flow in Rural and Urban Areas Using a Traffic Flow Simulator. *Sustainability* **2024**, *16*, 658. [CrossRef]

20. Lu, Q.; Tettamanti, T.; Hörcher, D.; Varga, I. The impact of autonomous vehicles on urban traffic network capacity: An experimental analysis by microscopic traffic simulation. *Transp. Lett.* **2020**, *12*, 540–549. [CrossRef]
21. Fagnant, D.J.; Kockelman, K. Preparing a nation for autonomous vehicles: Opportunities, barriers and policy recommendations. *Transp. Res. Part A Policy Pract.* **2015**, *77*, 167–181. [CrossRef]
22. Wadud, Z.; MacKenzie, D.; Leiby, P. Help or hindrance? The travel, energy and carbon impacts of highly automated vehicles. *Transp. Res. Part A Policy Pract.* **2016**, *86*, 1–18. [CrossRef]
23. Narayanan, S.; Chaniotakis, E.; Antoniou, C. Shared autonomous vehicle services: A comprehensive review. *Transp. Res. Part C Emerg. Technol.* **2020**, *111*, 255–293. [CrossRef]
24. Luca, O.; Andrei, L.; Iacoboaea, C.; Gaman, F. Unveiling the Hidden Effects of Automated Vehicles on "Do No Significant Harm" Components. *Sustainability* **2023**, *15*, 11265. [CrossRef]
25. Shladover, S.E. Connected and automated vehicle systems: Introduction and overview. *J. Intell. Transp. Syst.* **2018**, *22*, 190–200. [CrossRef]
26. Greifenstein, M.; Nordhoff, S.; Wang, X.; Atluri, B. Riding into the future: What drives the use of robotaxis in San Francisco? *Transp. Res. Part A Policy Pract.* **2026**, *203*, 104763. [CrossRef]
27. Badue, C.; Guidolini, R.; Carneiro, R.V.; Azevedo, P.; Cardoso, V.B.; Forechi, A.; Jesus, L.; Berriel, R.; Paixão, T.M.; Mutz, F.; et al. Self-driving cars: A survey. *Expert Syst. Appl.* **2021**, *165*, 113816. [CrossRef]
28. Lee, E.H.; Lee, E. Congestion boundary approach for phase transitions in traffic flow. *Transp. B Transp. Dyn.* **2024**, *12*, 2379377. [CrossRef]
29. Peng, G.; Wu, K.; Jiao, W.; Yang, S.; Wu, Z.; Xu, L.; Lu, C.; Tan, H.; Xia, D. Congestion transition in a heterogeneous ring road car-following model incorporating visual angle defect and speed limit effects. *Chaos Solitons Fractals* **2026**, *204*, 117710. [CrossRef]
30. Pan, Y.; Cheng, Q.; Li, A.; Zhang, J.; Guo, J.; Chen, Y. Analysis of congestion key parameters, dynamic discharge process, and capacity estimation at urban freeway bottlenecks: A case study in Beijing, China. *Transp. Lett.* **2025**, *17*, 984–1003. [CrossRef]
31. Paden, B.; Čáp, M.; Yong, S.Z.; Yershov, D.; Frazzoli, E. A Survey of Motion Planning and Control Techniques for Self-Driving Urban Vehicles. *IEEE Trans. Intell. Veh.* **2016**, *1*, 33–55. [CrossRef]
32. Aksjonov, A.; Kyrki, V. Rule-Based Decision-Making System for Autonomous Vehicles at Intersections with Mixed Traffic Environment. In Proceedings of the 2021 IEEE International Intelligent Transportation Systems Conference (ITSC), Indianapolis, IN, USA, 19–22 September 2021; pp. 660–666.
33. Talebpour, A.; Mahmassani, H.S. Influence of connected and autonomous vehicles on traffic flow stability and throughput. *Transp. Res. Part C Emerg. Technol.* **2016**, *71*, 143–163. [CrossRef]
34. Campolo, C.; Molinaro, A.; Scopigno, R. From today's VANETs to tomorrow's planning and the bets for the day after. *Veh. Commun.* **2015**, *2*, 158–171. [CrossRef]
35. Wang, H.; Shao, W.; Sun, C.; Yang, K.; Cao, D.; Li, J. A Survey on an Emerging Safety Challenge for Autonomous Vehicles: Safety of the Intended Functionality. *Engineering* **2024**, *33*, 17–34. [CrossRef]
36. OECD; ITF. *Preparing Infrastructure for Automated Vehicles*; OECD: Paris, France, 2023.
37. Page, M.J.; McKenzie, J.E.; Bossuyt, P.M.; Boutron, I.; Hoffmann, T.C.; Mulrow, C.D.; Shamseer, L.; Tetzlaff, J.M.; Akl, E.A.; Brennan, S.E.; et al. The PRISMA 2020 statement: An updated guideline for reporting systematic reviews. *BMJ* **2021**, *372*, n71. [CrossRef] [PubMed]
38. Huang, Y.; Ye, Y.J.; Sun, J.; Tian, Y. Characterizing the Impact of Autonomous Vehicles on Macroscopic Fundamental Diagrams. *IEEE Trans. Intell. Transp. Syst.* **2023**, *24*, 6530–6541. [CrossRef]
39. Li, G.; Jiao, Y.; Calvert, S.C.; Van Lint, J.W.C.H. Lateral conflict resolution data derived from Argoverse-2: Analysing safety and efficiency impacts of autonomous vehicles at intersections. *Transp. Res. Part C Emerg. Technol.* **2024**, *167*, 104802. [CrossRef]
40. Almusawi, A.; Albdairi, M.; Qadri, S. Integrating Autonomous Vehicles (AVs) into Urban Traffic: Simulating Driving and Signal Control. *Appl. Sci.* **2024**, *14*, 8851. [CrossRef]
41. Sadid, H.; Antoniou, C. A simulation-based impact assessment of autonomous vehicles in urban networks. *IET Intell. Transp. Syst.* **2024**, *18*, 1677–1696. [CrossRef]
42. Gelauff, G.; Ossokina, I.; Teulings, C. Spatial and welfare effects of automated driving: Will cities grow, decline or both? *Transp. Res. Part A Policy Pract.* **2019**, *121*, 277–294. [CrossRef]
43. Liu, C.; Chen, K.; Bao, Z.; Ng, S.T.; Zhang, C.; Jiang, Z. Assessing the impacts of connected-and-autonomous vehicle management strategy on the environmental sustainability of urban expressway system. *Sustain. Cities Soc.* **2023**, *99*, 104904. [CrossRef]
44. Zhang, J.; Bai, Y.Z.; He, J.; Wang, T. On the impacts of dedicated lanes for CAVs in mixed traffic: Evaluation using a modified cell transmission model. *Phys. A Stat. Mech. Its Appl.* **2025**, *662*, 130418. [CrossRef]
45. Park, J.; Jang, S.; Ko, J.H. Effects of Exclusive Lanes for Autonomous Vehicles on Urban Expressways under Mixed Traffic of Autonomous and Human-Driven Vehicles. *Sustainability* **2024**, *16*, 26. [CrossRef]

46. Majstorovic, Ä.; Tisljaric, L.; Ivanjko, E.; Caric, T. Urban Traffic Signal Control under Mixed Traffic Flows: Literature Review. *Appl. Sci.* **2023**, *13*, 4484. [CrossRef]
47. Papadoulis, A.; Imprialou, M.; Feng, Y.; Quddus, M. Simulating and Modelling the Safety Impact of Connected and Autonomous Vehicles in Mixed Traffic: Platoon Size, Sensor Error, and Path Choice. *Machines* **2024**, *12*, 371. [CrossRef]
48. Guan, H.; Chen, X.; Meng, Q. Jam propagation in mixed traffic of autonomous and human-driven vehicles: A random walk-based analysis. *Transp. Res. Part C Emerg. Technol.* **2025**, *180*, 105310. [CrossRef]
49. Mahmassani, H.S. Autonomous Vehicles and Connected Vehicle Systems: Flow and Operations Considerations. *Transp. Sci.* **2016**, *50*, 1140–1162. [CrossRef]
50. Pham, M.; Xiong, K. A survey on security attacks and defense techniques for connected and autonomous vehicles. *Comput. Secur.* **2021**, *109*, 102269. [CrossRef]
51. Andreotti, E.; Selpi; Boyraz, P. Potential impact of autonomous vehicles in mixed traffic from simulation using real traffic flow. *J. Intell. Connect. Veh.* **2023**, *6*, 1–15. [CrossRef]
52. Chu, K.F.; Fan, C.; Iida, F. Navigating Mixed Traffic: Current State and Future Challenges in Integrating Autonomous and Human-Driven Vehicles. In *Proceedings of the Proceedings of IEEE Workshop on Advanced Robotics and its Social Impacts*; ARSO: Nairobi, Kenya, 2024; pp. 241–246.
53. Wang, J.; Zhou, L.; Yang, C. Decision model based on driving-mode misidentification for mixed AV–HDV straight–left conflict interactions at two-phase signalized intersections. *Phys. A Stat. Mech. Its Appl.* **2025**, *677*, 130943. [CrossRef]
54. Louati, A.; Louati, H.; Kariri, E.; Neifar, W.; Hassan, M.K.; Khairi, M.H.H.; Farahat, M.A.; El-Hoseny, H.M. Sustainable Smart Cities through Multi-Agent Reinforcement Learning-Based Cooperative Autonomous Vehicles. *Sustainability* **2024**, *16*, 1779. [CrossRef]
55. Hayward, J.C. Near-miss determination through use of a scale of danger. *Highw. Res. Rec.* **1972**, *384*, 24–34.
56. Gettman, D.; Head, L. Surrogate Safety Measures from Traffic Simulation Models. *Transp. Res. Rec.* **2003**, *1840*, 104–115. [CrossRef]
57. Wang, Z.; Zhao, X.M.; Xu, Z.G.; Li, X.P.; Qu, X.B. Modeling and field experiments on autonomous vehicle lane changing with surrounding human-driven vehicles. *Comput.-AIDED Civ. Infrastruct. Eng.* **2021**, *36*, 877–889. [CrossRef]
58. Li, Y.; Wang, L.; Xuan, Z.; Shen, W. Game-theory based truck platoon avoidance modes selection near the highway off-ramp in mixed traffic environment. *Front. Phys.* **2024**, *12*, 1371233. [CrossRef]
59. Wang, Y.; Jiang, Y.; Wu, Y.; Yao, Z. Mitigating traffic oscillation through control of connected automated vehicles: A cellular automata simulation. *Expert Syst. Appl.* **2024**, *235*, 121275. [CrossRef]
60. Zhang, F.; Lu, J.; Hu, X. Traffic Equilibrium for Mixed Traffic Flows of Human-Driven Vehicles and Connected and Autonomous Vehicles in Transportation Networks under Tradable Credit Scheme. *J. Adv. Transp.* **2020**, *2020*, 8498561. [CrossRef]
61. Talebpour, A.; Mahmassani, H.S.; Bustamante, F.E. Modeling Driver Behavior in a Connected Environment: Integrated Microscopic Simulation of Traffic and Mobile Wireless Telecommunication Systems. *Transp. Res. Rec.* **2016**, *2560*, 75–86. [CrossRef]
62. Peng, G.; Wang, W.; Tan, H. Phase transitions in a heterogeneous lattice hydrodynamic model involving both communication distance and memory time duration differences. *Chaos Solitons Fractals* **2024**, *188*, 115502. [CrossRef]
63. Liu, Y.; Guo, J.; Taplin, J.; Wang, Y. Characteristic analysis of mixed traffic flow of regular and autonomous vehicles using cellular automata. *J. Adv. Transp.* **2017**, *2017*, 8142074. [CrossRef] [PubMed]
64. Kouvelas, A.; Perrin, J.P.; Fokri, S.; Geroliminis, N. Exploring the impact of autonomous vehicles in urban networks and potential new capabilities for perimeter control. In *Proceedings of the 2017 5th IEEE International Conference on Models and Technologies for Intelligent Transportation Systems (MT-ITS)*; IEEE: Piscataway, NJ, USA, 2017; pp. 19–24.
65. Jo, Y.; Kim, J.; Oh, C.; Kim, I.; Lee, G. Benefits of travel time savings by truck platooning in Korean freeway networks. *Transp. Policy* **2019**, *83*, 37–45. [CrossRef]
66. Liu, C.; Zhang, C.; Yu, C.; Chen, K.; Jiang, Z. Joint Optimization of Longitudinal and Lateral Locations of Autonomous-Vehicle-Dedicated Lanes on Expressways. *IEEE Trans. Intell. Transp. Syst.* **2024**, *25*, 430–442. [CrossRef]
67. Zhang, X.; Zhang, H.; Yan, S.; Xie, M.; Wang, Y. Parking pricing strategies in the era of autonomous vehicles. *Transp. Policy* **2025**, *166*, 87–100. [CrossRef]
68. Liu, Z.; Li, R.; Dai, J. Effects and feasibility of shared mobility with shared autonomous vehicles: An investigation based on data-driven modeling approach. *Transp. Res. Part A Policy Pract.* **2022**, *156*, 206–226. [CrossRef]
69. Mo, D.; Chen, X.; Zhang, J. Modeling and Managing Mixed On-Demand Ride Services of Human-Driven Vehicles and Autonomous Vehicles. *Transp. Res. Part B Methodol.* **2022**, *157*, 80–119. [CrossRef]
70. Liu, A.; Zhong, S.; Sun, D.; Gong, Y.; Fan, M.; Song, Y. Joint optimal pricing strategy of shared autonomous vehicles and road congestion pricing: A regional accessibility perspective. *Cities* **2024**, *146*, 104742. [CrossRef]
71. Li, S.; Tavafoghi, H.; Poolla, K.; Varaiya, P. Regulating TNCs: Should Uber and Lyft set their own rules? *Transp. Res. Part B Methodol.* **2019**, *129*, 193–225. [CrossRef]
72. Ao, D.; Gao, J.; Lai, Z.; Li, S. Regulating transportation network companies with a mixture of autonomous vehicles and for-hire human drivers. *Transp. Res. Part A Policy Pract.* **2024**, *180*, 103975. [CrossRef]

73. Jia, D.; Sun, J.; Sharma, A.; Zheng, Z.; Liu, B. Integrated simulation platform for conventional, connected and automated driving: A design from cyber–physical systems perspective. *Transp. Res. Part C Emerg. Technol.* **2021**, *124*, 102984. [CrossRef]
74. Liu, P.F.; Fan, W.D. Exploring the impact of connected and autonomous vehicles on mobility and environment at signalized intersections through vehicle-to-infrastructure (V2I) and infrastructure-to-vehicle (I2V) communications. *Transp. Plan. Technol.* **2021**, *44*, 129–138. [CrossRef]
75. Xu, Z.; Jiang, T.; Zheng, N. Developing and analyzing eco-driving strategies for on-road emission reduction in urban transport systems—A VR-enabled digital-twin approach. *Chemosphere* **2022**, *305*, 135372. [CrossRef]
76. Santana, E.F.Z.; Covas, G.; Duarte, F.; Santi, P.; Ratti, C.; Kon, F. Transitioning to a driverless city: Evaluating a hybrid system for autonomous and non-autonomous vehicles. *Simul. Model. Pract. Theory* **2021**, *107*, 102210. [CrossRef]
77. Guo, Y.; Souders, D.; Labi, S.; Peeta, S.; Benedyk, I.; Li, Y. Paving the way for autonomous Vehicles: Understanding autonomous vehicle adoption and vehicle fuel choice under user heterogeneity. *Transp. Res. Part A Policy Pract.* **2021**, *154*, 364–398. [CrossRef]
78. Zhang, L.; Lu, Y.; Chen, N.; Wang, P.; Kong, W.; Wang, Q.; Qin, G.; Mou, Z. Optimization of Roadside Unit Deployment on Highways under the Evolution of Intelligent Connected-Vehicle Permeability. *Sustainability* **2023**, *15*, 11112. [CrossRef]
79. Ye, S.; Li, T.; Li, R.; Zhang, Z.; Lv, P.; Pan, Z. Impact of HDMap-based Dynamic Dedicated Lanes for CAVs in Urban Networks. In Proceedings of the 2023 IEEE 26th International Conference on Intelligent Transportation Systems (ITSC), 24–28 September 2023; pp. 2363–2369.
80. Chen, X.D.; Zhang, F.; Guan, H.; Meng, Q. Two-dimensional lane configuration design approach for Autonomous Vehicle Dedicated Lanes in urban networks. *Transp. Res. PART E-Logist. Transp. Rev.* **2025**, *194*, 103938. [CrossRef]
81. Hawkins, J.; Nurul Habib, K. Integrated models of land use and transportation for the autonomous vehicle revolution. *Transp. Rev.* **2019**, *39*, 66–83. [CrossRef]
82. Alatawneh, A.; Torok, A. Use-stage emissions of conventional, battery electric, and autonomous vehicles in Europe. *Case Stud. Transp. Policy* **2025**, *20*, 101398. [CrossRef]
83. Guan, H.; Wang, H.; Meng, Q.; Mak, C.L. Markov chain-based traffic analysis on platooning effect among mixed semi- and fully-autonomous vehicles in a freeway lane. *Transp. Res. Part B Methodol.* **2023**, *173*, 176–202. [CrossRef]
84. Metz, D. Developing Policy for Urban Autonomous Vehicles: Impact on Congestion. *Urban Sci.* **2018**, *2*, 33. [CrossRef]
85. Mo, L.; Cui, Z.; Jia, R.; Dong, K.; Zhao, C. How does autonomous vehicles affect taxi industry? A two-stage Van Damme based tripartite evolutionary game perspective. *Res. Transp. Econ.* **2024**, *103*, 101387. [CrossRef]
86. Torabi, K.F.; Araghi, Y.; van Oort, N.; Hoogendoorn, S. Passengers preferences for using emerging modes as first/last mile transport to and from a multimodal hub case study Delft Campus railway station. *Case Stud. Transp. Policy* **2022**, *10*, 300–314. [CrossRef]

Disclaimer/Publisher's Note: The statements, opinions and data contained in all publications are solely those of the individual author(s) and contributor(s) and not of MDPI and/or the editor(s). MDPI and/or the editor(s) disclaim responsibility for any injury to people or property resulting from any ideas, methods, instructions or products referred to in the content.

vehicles

MDPI

Article

Probabilistic Modeling of Urban Vehicle Traffic Under COVID-19 Mobility Restrictions Using AI-Based Video Data: A Case Study in Cluj-Napoca

Nicolae Filip, Calin Iclodean * and Marius Deac

Department of Automotive Engineering and Transports, Technical University of Cluj-Napoca Romania, Muncii Bd. 103-105, 400114 Cluj-Napoca, Romania; nicolae.filip@auto.utcluj.ro (N.F.); marius.deac@auto.utcluj.ro (M.D.)
* Correspondence: calin.iclodean@auto.utcluj.ro

Abstract

The COVID-19 pandemic and the resulting mobility restrictions significantly disrupted urban traffic patterns. This study quantitatively assesses the impact of these restrictions on vehicle flow at a signalized central intersection in Cluj-Napoca, Romania, through an integrated methodology combining continuous radar-based traffic measurements and AI (Artificial Intelligence)-assisted video analysis. Traffic data were collected before the pandemic (November 2019) and during the lockdown period (April 2020), enabling a comparative evaluation of flow characteristics and vehicle arrival patterns. Under constrained observational conditions, vehicle arrivals were modeled using a probabilistic framework grounded in Poisson distribution. The findings indicate a dramatic contraction of mobility demand, with traffic volumes declining in 2020 to 9.55% of pre-pandemic levels. The probabilistic assessment highlights the predominance of free-flow regimes under reduced demand and confirms the adequacy of the Poisson model in low-density traffic scenarios. The obtained results contribute to a better understanding of urban traffic dynamics under extreme mobility disruptions and provide a transferable methodological framework for probabilistic traffic modeling, resilience-oriented urban mobility planning, and data-driven traffic management.

Keywords: COVID-19 pandemic; urban traffic flow; probability estimation; Poisson distribution; smart mobility; vehicles

1. Introduction

Urban mobility systems are characterized by continuous growth in travel demand and increasing pressure on road infrastructure, facing major challenges such as climate change associated with transport-related emissions, deterioration of urban quality of life, and prolonged daily travel times [1]. From an engineering perspective, these challenges are directly reflected in traffic flow dynamics, congestion levels, and the operational performance of traffic control systems.

The global spread of SARS-CoV-2 (COVID-19 or Coronavirus Disease 2019) in early 2020 led to the implementation of unprecedented mobility restrictions worldwide [2–4]. These measures caused an abrupt contraction in vehicular travel demand, creating a natural experimental setting for examining traffic flow behavior under low-demand conditions.

Several previous studies have investigated the impact of COVID-19 mobility restrictions on urban traffic dynamics. During lockdown periods, traffic volumes decreased significantly, and movement patterns changed significantly, according to research undertaken in

multiple cities around the world. For example, remote sensing and video-based monitoring techniques were utilized to assess traffic activity prior to and during the pandemic, offering useful insights into large-scale mobility disruptions and their spatial distribution [5]. These studies demonstrate the relevance of understanding traffic dynamics during extreme demand reductions and give a valuable foundation for evaluating probabilistic traffic modeling strategies.

Traffic congestion generates substantial economic losses and adversely affects the efficiency of urban transport systems. Urban mobility is a key determinant of economic competitiveness [6–8]. From a traffic modeling standpoint, significant demand fluctuations provide an opportunity to assess the robustness and validity of statistical models commonly used for vehicle arrival estimation.

Ensuring sustainable, reliable, and efficient urban mobility requires the implementation of strategic planning instruments such as Sustainable Urban Mobility Plans (SUMP), which rely on quantitative traffic analysis and predictive modeling approaches [9–11]. In this context, evaluating the statistical distribution of vehicle arrivals under atypical operating conditions becomes particularly relevant for calibrating and validating probabilistic traffic models.

This study investigates daytime vehicular traffic dynamics in Cluj-Napoca, Romania, employing the Poisson distribution as the primary modeling framework. The main objective is to estimate and compare vehicle arrival distributions before and during the lockdown period, based on traffic data collected in November 2019 and April 2020. The research focuses on short time-interval flow variations, the suitability of the Poisson distribution for modeling low-demand traffic regimes, and the quantitative assessment of traffic reduction relative to baseline conditions.

In Romania, a state of emergency was declared on 16 March 2020 through Decree No. 195 [12], introducing strict mobility restrictions. These measures resulted in a rapid and significant decline in traffic volumes.

At the global level, mobility reduction during the pandemic was associated with an estimated 5.4% decrease in greenhouse gas emissions in 2020 [13–16]. This reduction is directly linked to lower vehicular traffic volumes, highlighting the importance of accurately quantifying traffic flows during large-scale disruptions.

By integrating radar-based traffic measurements, AI-assisted video analysis, and probabilistic modeling, this paper proposes a methodological framework for assessing vehicular traffic behavior under extreme mobility conditions.

The remainder of the paper is organized as follows:

Section 2 presents a review of the relevant literature concerning traffic dynamics during the COVID-19 pandemic and probabilistic approaches for modeling vehicle arrivals.

Section 3 describes the data acquisition framework, including radar-based traffic measurements and AI-assisted video processing, together with the methodological approach adopted for probabilistic modeling.

Section 4 presents the main results of the analysis and the statistical validation of the proposed model.

Section 5 discusses the implications of the findings for urban traffic behavior and mobility resilience under extreme demand reductions.

Finally, Section 6 summarizes the main conclusions of the study and outlines directions for future research.

2. Literature Review

Several previous studies have analyzed the impact of COVID-19 mobility restrictions on urban traffic volumes and mobility patterns in different cities worldwide. These studies

https://doi.org/10.3390/vehicles8030059

reported significant reductions in traffic demand and substantial modifications in temporal travel patterns during lockdown periods.

International studies conducted between 2020 and 2022 consistently reported substantial reductions in urban mobility following the implementation of COVID-19-related restrictions. Most research documented significant declines in both public transport usage and private vehicular traffic volumes.

El-Geneidy et al. [17] reported reductions of 80–90% in public transport ridership in countries with strict mobility restrictions. Similar analyses conducted across Europe, Asia, and North America indicated traffic volume reductions ranging from 50% to 90% during the initial months of the pandemic [18–27].

From a vehicular traffic perspective, the literature highlights:

- Decreases in traffic intensity of up to 70% at urban intersections [23].
- Increases in average travel speeds under low-demand conditions [27].
- Structural shifts in modal distribution and temporal travel patterns [19–24].

These findings confirm that the pandemic period generated an atypical traffic regime characterized by low demand levels and significant modifications in flow dynamics.

Simulation-based approaches have been widely applied to analyze intersection performance and to support decision-making regarding the conversion between different intersection control types, such as roundabouts and signalized intersections [28].

Beyond descriptive analyses of mobility reduction, several studies have investigated the statistical properties of vehicle arrivals using probabilistic models, particularly the Poisson distribution [29]. The Poisson framework is widely applied to model independent vehicle arrivals over short time intervals and is generally considered appropriate for low- to moderate-density traffic conditions.

Peköz et al. [30] employed the Poisson distribution to estimate traffic flow within a stationary ergodic intersection model. Abul-Magd et al. [31] used a Poisson-based approach to analyze the transition from free-flow to congested traffic regimes. The analytical formulation of inter-vehicle spacing and time-headway distributions has also been derived using Poisson assumptions combined with Wigner's Surmise [32].

Maya et al. [33] proposed a bilinear and convolutional Poisson-based framework for multi-segment traffic flow estimation, integrating machine learning algorithms and stochastic variational Bayesian techniques to enable real-time parameter updates. Yang et al. [34] developed a Poisson-based analytical model for vehicle platoon behavior at signalized intersections. Thomas et al. [35] demonstrated that seasonal traffic noise variability followed a Poisson distribution in Almelo, the Netherlands.

Additional applications include queue delay evaluation and signal timing optimization based on Poisson assumptions [36], intersection transit-time modeling [37], and congestion anticipation using vehicle trajectory data weighted within a Poisson-based framework [38].

However, most of these studies were conducted under normal operating conditions or focused primarily on congestion analysis. Limited research has addressed extreme low-demand regimes induced by large-scale mobility restrictions.

Current literature reveals a significant gap in:

1. Validating Poisson distribution under severely reduced urban traffic conditions characterized by fluctuating demand and atypical flow behavior.
2. Robustly estimating vehicle arrival distributions based on limited datasets collected during large-scale disruptions.
3. Integrating continuous radar-based traffic measurements with AI-assisted trajectory extraction to develop probabilistic models capable of adapting to dynamic urban contexts.

https://doi.org/10.3390/vehicles8030059

Advanced methods for estimating intersection control delay using passive traffic sensors and detector-based measurements [39] have been proposed to improve real-time traffic performance assessment and support adaptive traffic management strategies.

Few studies combine multisensory data acquisition (radar and video), artificial intelligence-based vehicle detection, and probabilistic modeling within a unified framework for analyzing lockdown traffic conditions.

3. Materials and Methods

To improve the clarity of the methodological framework adopted in this study, the overall research procedure is summarized in Figure 1. The workflow illustrates the analysis's main steps, which include traffic data collection, video-based vehicle detection using AI algorithms, traffic measurement aggregation and preprocessing, probabilistic modeling of vehicle arrivals using Poisson distribution, and statistical validation of the results.

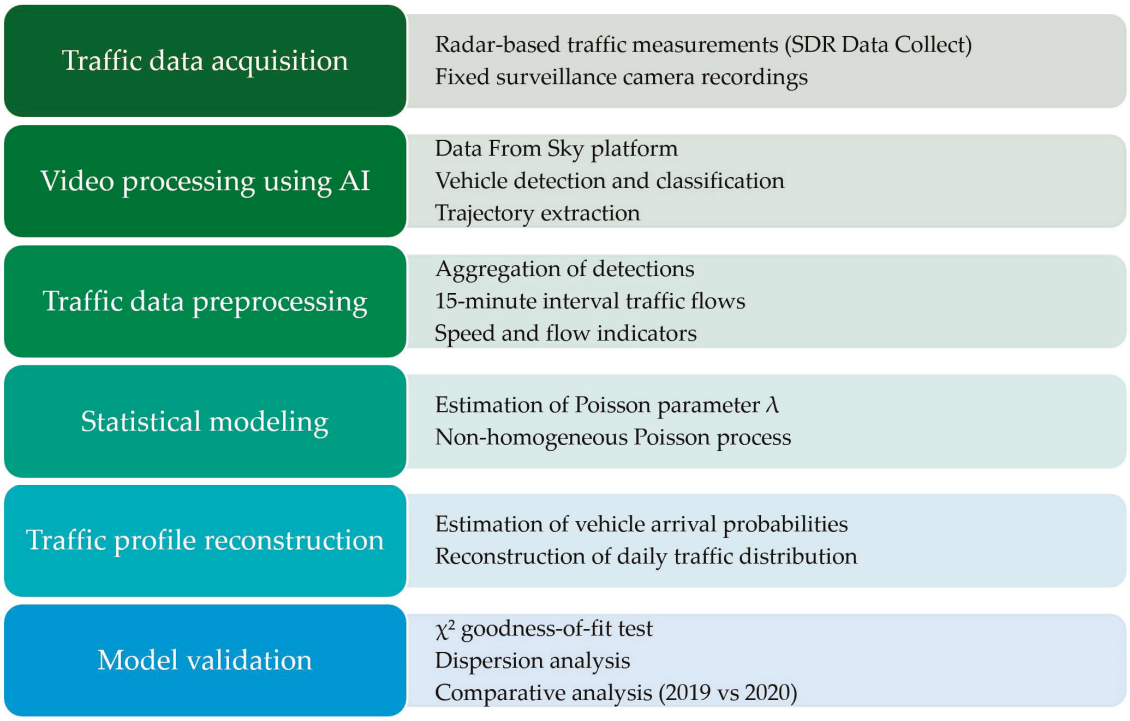

Figure 1. Research methodology workflow for probabilistic modeling of urban traffic during COVID-19 mobility restrictions.

3.1. Traffic Data Collection Methodology

3.1.1. Fixed Traffic Surveillance Camera

To analyze vehicular traffic behavior before and during the COVID-19 pandemic, two complementary data acquisition methods were employed:

1. Continuous cross-sectional traffic measurements and
2. Video-based analysis using fixed surveillance cameras.

The video monitoring system (Figure 2) consists of fixed cameras installed at the analyzed intersection and integrated into the municipal traffic management system.

The deployed cameras enable continuous intersection-level monitoring, providing detailed information on vehicle trajectories, vehicle classification, and kinematic parameters such as instantaneous speed and estimated acceleration. The analyzed video recordings were collected during two distinct periods: November 2019 (representing normal traffic conditions) and April 2020 (corresponding to the lockdown period).

https://doi.org/10.3390/vehicles8030059



Figure 2. Fixed traffic surveillance camera (photo by the author).

Subsequently, the video data were processed to detect and classify moving objects (vehicles and pedestrians) and to extract relevant traffic parameters, as described in the following subsection.

The surveillance cameras form part of the urban traffic management infrastructure [8], which includes adaptive signal control systems and traffic sensors. This integration ensures consistency between video-derived data and operational traffic control parameters, facilitating a comprehensive analysis of vehicular flow dynamics.

3.1.2. Continuous Traffic Measurements

To evaluate macroscopic traffic parameters, namely vehicle flow and average travel speed, an automatic radar-based detection system (Speed Detection Radar—SDR Data Collect) was employed (Figure 3) [40].

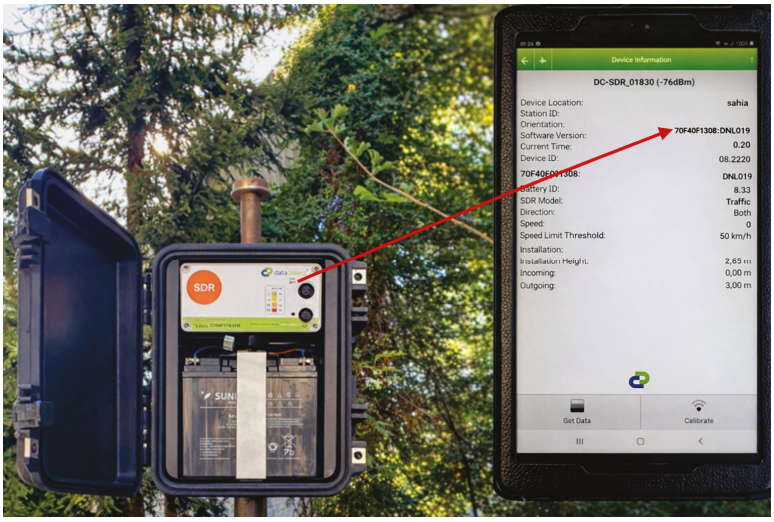

Figure 3. Vehicle detecting equipment SDR (photo by the author).

The SDR Data Collect device operates using microwave radar technology at a frequency of 24.125 GHz and determines the speed of moving objects based on the Doppler

effect principle [41,42]. The Doppler effect occurs when the device emits an electromagnetic wave toward a moving object and the reflected wave returns to the radar sensor with a frequency shift proportional to the relative velocity (Figure 4).

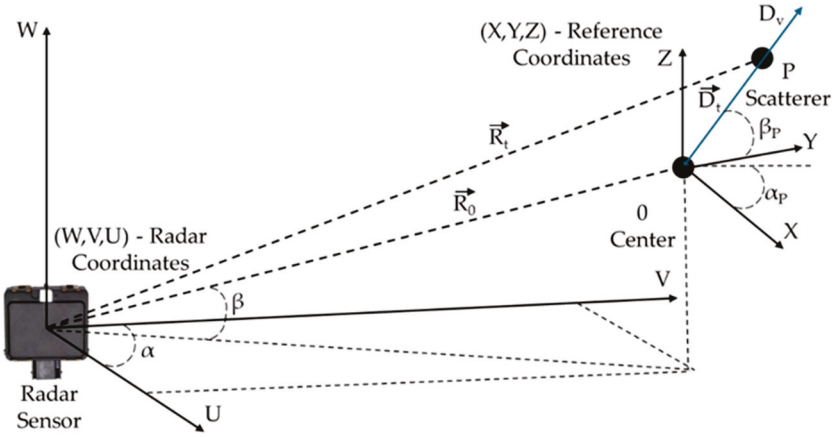

Figure 4. Operating principle of SDR Data Collect based on the radar Doppler effect.

Within the experimental framework, the SDR unit was installed in a cross-sectional configuration relative to the direction of travel and operated continuously (24 h/day) for seven consecutive days in November 2019 and seven consecutive days in April 2020.

The dataset collected included:

- The number of vehicles detected within predefined time intervals.
- The instantaneous speed of each detected vehicle.
- The direction of travel.

These measurements enabled a quantitative and dynamic characterization of traffic flow conditions [43,44].

The main technical characteristics of the SDR Data Collect system are summarized in Table 1 [41].

Table 1. Technical specifications of the SDR Data Collect system.

Specification	Unit	Value
Sensor type	-	Microwave
Frequency	GHz	24.125
Speed measuring range	km/h	3.00–199.00
Speed resolution	km/h	1.00
Distance resolution	m	0.10
Data rate	baud	115200
Power	mW	5.00

The Doppler frequency shift f_D depends on the electromagnetic wavelength λ and the relative velocity V between the radar sensor and the moving target. It can be expressed as [45]:

$$\begin{aligned} f_D = \frac{1}{2\pi}\frac{d\phi(t)}{dt} = \; & \frac{2f}{c}\frac{d}{dt}r(t) = \frac{2f}{c}\frac{1}{2r(t)}\left[\left(\vec{R_0}+\vec{V_t}+\Re_t\vec{r_0}\right)^T\left(\vec{R_0}+\vec{V_t}+\Re_t\vec{r_0}\right)\right] \\ & = \frac{2f}{c}\left[\vec{V}+\frac{d}{dt}\left(\Re_t\vec{r_0}\right)\right]^T\vec{n} = \frac{2f}{c}\left[\vec{V}+\frac{d}{dt}\left(e^{\hat{\omega}t}\vec{r_0}\right)\right]^T\vec{n} \\ & = \frac{2f}{c}\left(\vec{V}+\hat{\omega}e^{\hat{\omega}t}\vec{r_0}\right)^T\vec{n} = \frac{2f}{c}\left(\vec{V}+\hat{\omega}\;x\;\vec{r}\right)^T\vec{n} \end{aligned} \quad (1)$$

The phase of the baseband signal $\Phi[r(t)]$ is defined as:

$$\Phi[r(t)] = 2\pi f \frac{2r(t)}{c} \tag{2}$$

The unit vector $\vec{n}$ representing the direction from the radar sensor to the target is defined as:

$$\vec{n} = \left(\vec{R_0} + \vec{V_t} + \Re_t \vec{r_0}\right)^T / \left(\left\|\vec{R_0} + \vec{V_t} + \Re_t \vec{r_0}\right\|\right) \tag{3}$$

where f is the carrier frequency, c is the speed of the electromagnetic wave propagation, $\vec{r} = \vec{r_0} + \vec{r}'$ represents the initial coordinates of the target in the radar coordinate system (U,V,W), $\vec{r_0}$ is the translation vector, respectively $\vec{r}'$ represents the coordinates of the target after translation (U_1,V_1,W_1), $\vec{R_0}$ is the distance from the radar sensor to the reference coordinate system (X,Y,Z), $\vec{V}$ is the translation velocity, $\vec{V_t}$ is the translation velocity at time t, $\Re_t = exp\{\hat{\omega}t\}$ denotes the rotation matrix, and $e^{\widehat{\omega t}}$ denotes the skew-symmetric matrix.

These formulations describe the relationship between phase variation and relative motion, enabling velocity estimation through Doppler shift analysis.

The SDR system was configured using the dedicated myTrafficData application [46], which enables parameter setting, real-time monitoring, and cloud-based data storage (Figure 5).

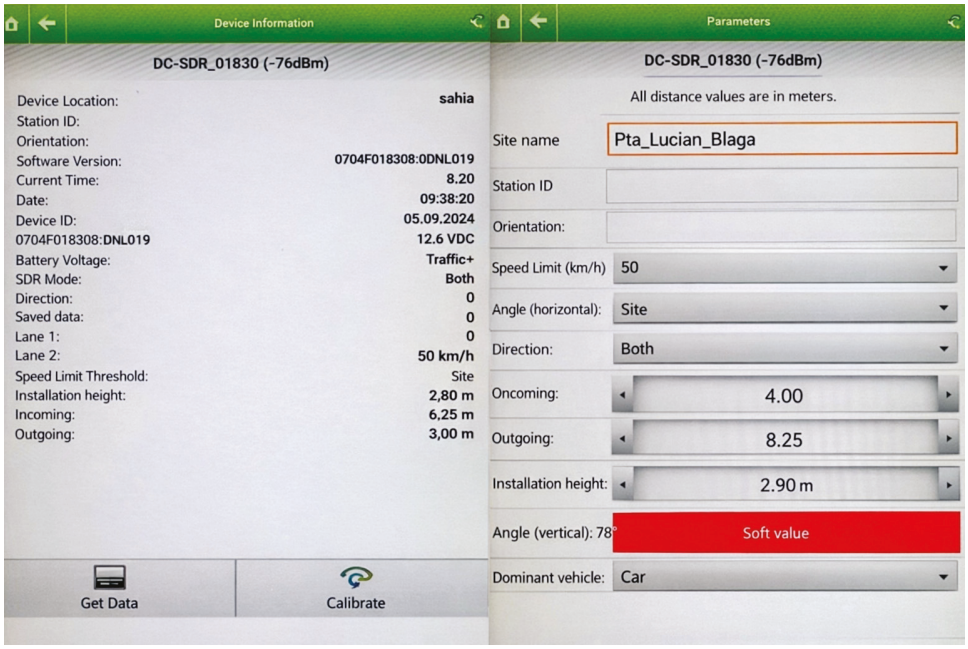

Figure 5. myTrafficData application interface and SDR Data Collect device (photo by the author).

Calibration of the detection geometry was performed by correlating the radar position with the roadway cross-section geometry to minimize measurement errors. The device was installed at a horizontal angle of 45° relative to the longitudinal axis of the roadway and a vertical angle of 78°, resulting in an elliptical detection zone aligned with the monitored traffic section.

The 45° horizontal configuration enables longitudinal velocity estimation through cosine correction of the Doppler component, ensuring accurate measurement of vehicle speed along the travel direction.

https://doi.org/10.3390/vehicles8030059

3.1.3. Traffic Measurements Using Image Processing

Following radar-based data acquisition, the video recordings obtained from the fixed surveillance cameras were processed using the Data From Sky (DFS) platform (Figure 6) [47–50].

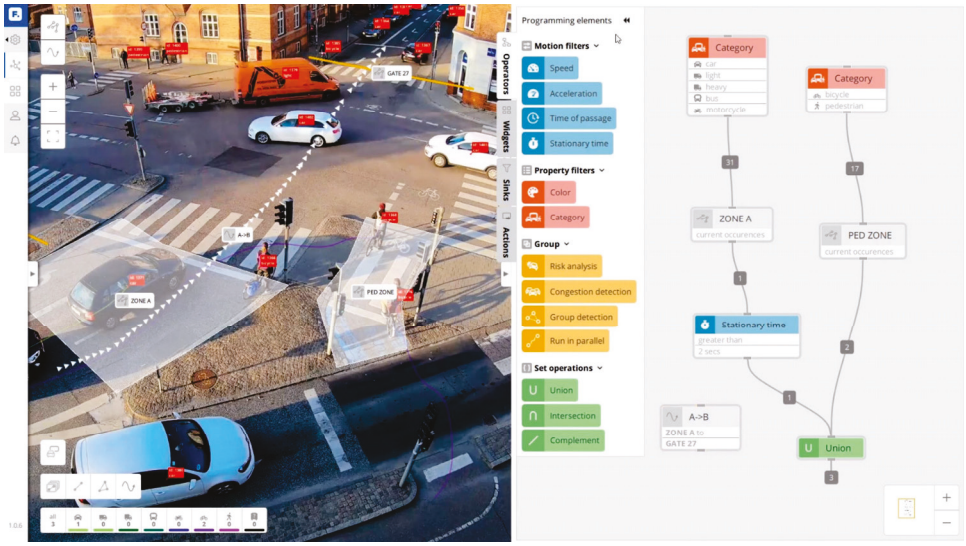

Figure 6. Traffic detection using Data From Sky (photo by the author).

The DFS platform enables automated object detection and tracking in video sequences through deep learning algorithms based on Convolutional Neural Networks (CNN). In the present study, only recordings from fixed cameras were used (LIGHT module), without employing aerial imagery.

In this study, the Data From Sky platform is used as an external video analytics tool to automate vehicle detection and trajectory extraction. The internal architecture of the deep learning detection model and its training datasets are proprietary to the software provider, resulting in falling outside the scope of this study. As a result, the platform is viewed as a measurement tool rather than the subject of algorithmic evaluation.

Within the accepted framework, AI-based video processing is largely used to enable vehicle detection, classification, and trajectory verification, while fundamental statistical analysis and probabilistic modeling rely on radar-based traffic observations. Potential detection errors due to object occlusion, lighting circumstances, or camera field-of-view restrictions are all recognized as common sources of measurement variability in video-based traffic monitoring systems.

Video processing allowed object-level extraction of a comprehensive set of traffic-related parameters, including spatial position in each frame, full movement trajectory, vehicle classification, estimated speed, estimated acceleration, and total traversal time within the monitored area. The processed data was exported as compressed Tracking Log files containing frame-level information for each detected object, thereby supporting subsequent quantitative analysis and advanced statistical modeling (Figure 7) [50].

The video data processing pipeline consisted of two main stages:

1. Georegistration, involving the establishment of correspondence between image pixels and real-world coordinates using fixed infrastructural reference points.
2. Object detection and tracking, comprising identification, classification, and trajectory monitoring of vehicles within the analyzed sequences.

The georegistration process enabled the transformation of image-space coordinates into metric spatial coordinates, ensuring accurate estimation of vehicle speed and travel distance, as well as consistency of derived kinematic parameters [51].

https://doi.org/10.3390/vehicles8030059

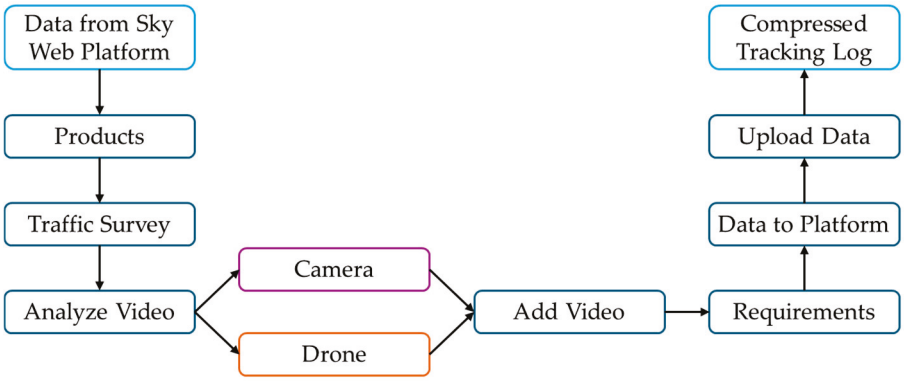

Figure 7. Functional block diagram of the Data From Sky platform.

3.2. Research Methodology

The dataset obtained through radar-based measurements and AI-assisted video processing was used to analyze vehicle arrival distributions and to estimate traffic flow probabilities using the Poisson distribution framework. A comparative analysis was conducted for two distinct traffic regimes: (i) normal operating conditions (November 2019) and (ii) reduced-mobility conditions during the lockdown period (April 2020).

In the adopted framework, radar-based measurements constitute the primary source of traffic flow data used for estimating arrival rates and calibrating the probabilistic model. The AI-assisted video processing on the Data From Sky platform was largely used for vehicle detection validation, object classification, and trajectory consistency checks. A probabilistic model based on the Poisson distribution was then used to define the stochastic structure of vehicle arrivals and reconstruct the temporal distribution of traffic demand during the lockout.

To ensure methodological transparency and repeatability, the data processing procedure used in this investigation is outlined below. Radar sensors deployed at the intersection under study were used to collect traffic information. The radar-based counts were averaged over 15 min intervals to determine vehicle arrival rates. Based on observed traffic counts, the Poisson parameter λ was determined for each interval. The probabilistic model was then used to reconstruct the temporal distribution of traffic flows across a 24 h period.

3.2.1. Case Study Site Description

The analyzed location was Lucian Blaga Square, situated in the central area of Cluj-Napoca, Romania (46°46′ N, 23°35′ E) [52]. The selected intersection represents a complex signalized urban node characterized by multiple entry and exit branches and significant temporal variability in vehicular demand.

The intersection is supplied by one three-lane arterial (Clinicilor Street) and three two-lane arterials (Victor Babeș Street, Petru Maior Street, and Gheorghe Șincai Street). Outbound traffic is distributed toward two two-lane arterials (Napoca Street and Republicii Street) and one single-lane branch (Petru Maior Street) (Figure 8).

The site was selected due to its operational relevance to the objectives of the study. It is classified as a recurrently congested urban node during peak hours and serves as a strategic connection between the main west–east and north–south corridors of the urban network. Its configuration enables the observation of transitions between congestion-prone and free-flow regimes under varying demand conditions, thereby providing an appropriate framework for assessing the validity of the Poisson distribution across distinct operational states [53].

The intersection operates under adaptive signal control integrated within the municipal traffic management system. This configuration generates a mixed traffic regime

influenced by both vehicular demand and signal control logic. The presence of adaptive signalization is particularly relevant for arrival distribution analysis, as signal cycles may introduce temporal correlations between successive vehicles, potentially affecting the independence assumptions underlying Poisson-based modeling.



Figure 8. The analyzed area (https://cluj-city.map2web.eu/) (accessed on 11 February 2026).

3.2.2. Traffic Measurements (Year 2019)

The measurements conducted in November 2019 were intended to characterize the normal operational regime of the analyzed intersection and to provide the reference dataset subsequently used for estimating the parameters of the Poisson distribution.

Raw data, consisting of individual vehicle detections [54] (Table 2), were aggregated into 15 min intervals. This temporal resolution was selected to reduce random variability inherent in individual detections, ensure compatibility with typical signal cycle durations, and enhance the stability of the λ parameter estimation within the Poisson framework. Additionally, the chosen aggregation interval facilitated the identification of congestion-prone periods.

Table 2. Vehicle classification schemes (ARX—Automatic Road Analyzer).

Class		Description	Parameters
1	MC	Very short (Bicycle, motorcycle)	d(1) < 1.7 m & axles = 2
2	SV	Short (sedan, wagon, 4WD, utility, van)	d(1) $\geq$ 1.7 m, d(1) $\leq$ 3.2 m & axles = 2
3	SVT	Short towing (trailer, caravan)	groups = 3, d(1) $\geq$ 2.1 m, d(1) $\leq$ 3.2 m, d(2) $\geq$ 2.1 m & axles = 3,4,5
4	TB2	Two-axle truck or bus	d(1) > 3.2 m & axles = 2
5	TB3	Three-axle truck or bus	axles = 3 & groups = 2
6	T4	Four-axle truck	axles > 3 & groups = 2
7	ART3	Three-axle articulated vehicle or rigid vehicle and trailer	d(1) > 3.2 m, axles = 3 & groups = 3
8	ART4	Four-axle articulated vehicle or rigid vehicle and trailer	d(2) < 2.1 m or d(1) < 2.1 m or d(1) > 3.2 maxles = 4 & groups > 2

https://doi.org/10.3390/vehicles8030059

Table 2. *Cont.*

Class		Description	Parameters
9	ART5	Five-axle articulated vehicle or rigid vehicle and trailer	d(2) < 2.1 m or d(1) < 2.1 m or d(1) > 3.2 maxles = 5 & groups > 2
10	ART6	Six (or more)-axle articulated vehicle or rigid vehicle and trailer	axles = 6 & groups > 2 or axles > 6 & groups = 3
11	BD	B-Double or heavy truck and trailer	groups = 4 & axles > 6
12	DRT	Double or triple road train or heavy truck and two (or more) trailers	groups ≥ 5 & axles > 6

For each entry and exit branch (Figure 9 and Table 3; Figure 10 and Table 4), the following performance indicators were computed (Figure 11 and Table 5; Figure 12 and Table 6):

- Vehicular flow (vehicles/15 min).
- Total daily flow (vehicles/day).
- Average speed (km/h).
- 15th percentile speed (v15—15th percentile speed).
- 85th percentile speed (v85—85th percentile speed).
- Standard deviation of speed.
- Coefficient of variation in traffic flow.

Table 3. Traffic flow at the entrance to Lucian Blaga Square (2019).

Date	Traffic Flow (Vehicles/Day—Every 15 Min by One Hour)				Sum (Σ)
	Clinicilor	V. Babeș	P. Maior	Ghe. Șincai	
21 November 2019	15,485	11,851	15,119	1695	44,150
22 November 2019	14,792	10,968	14,651	1412	41,823
23 November 2019	11,438	7730	10,726	1322	31,216
24 November 2019	10,222	6864	12,985	1118	31,189
25 November 2019	15,741	11,633	13,221	1662	42,257
26 November 2019	13,761	12,059	14,067	1551	41,438
27 November 2019	14,710	12,000	13,618	1595	41,923

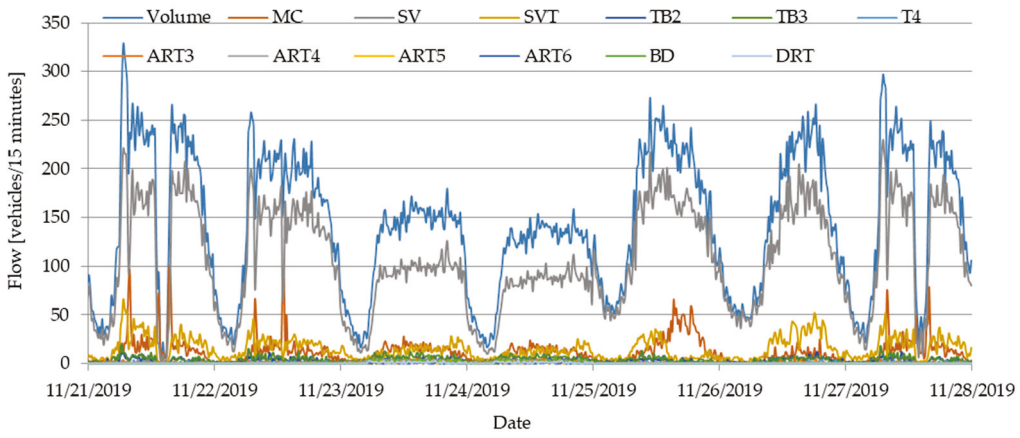

(**a**)

Figure 9. *Cont.*

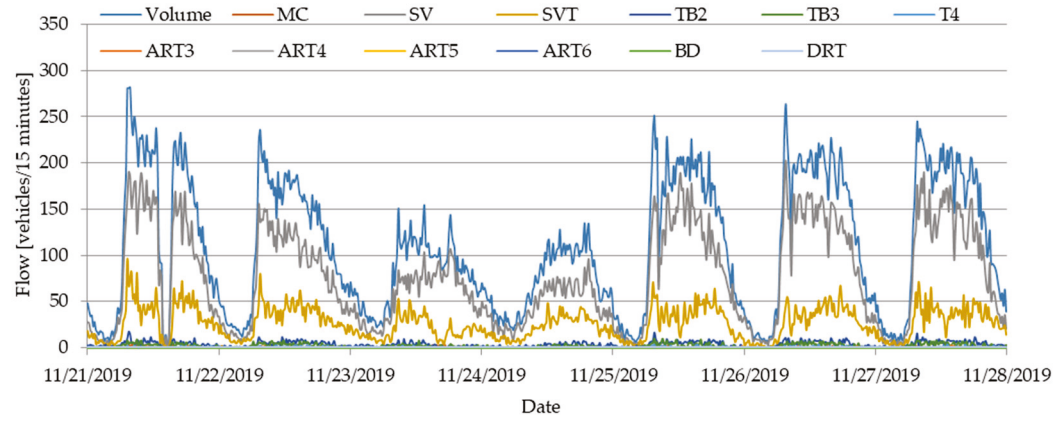

(**b**)

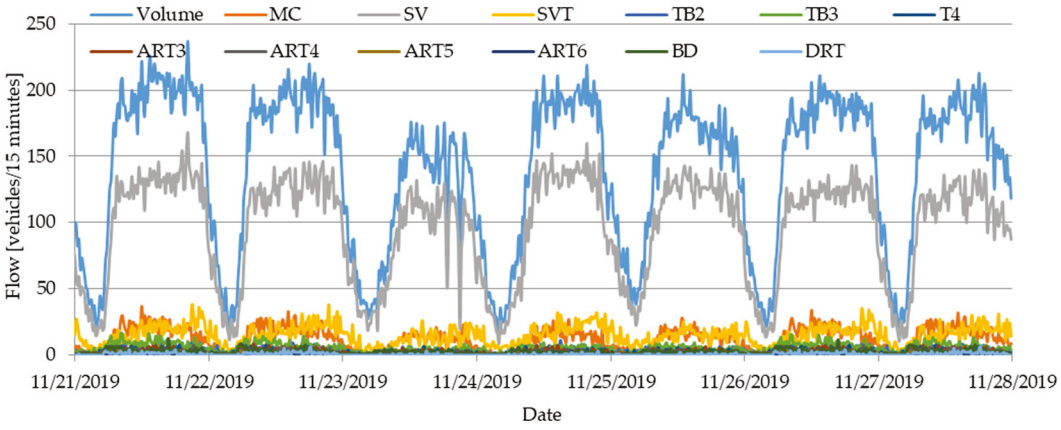

(**c**)

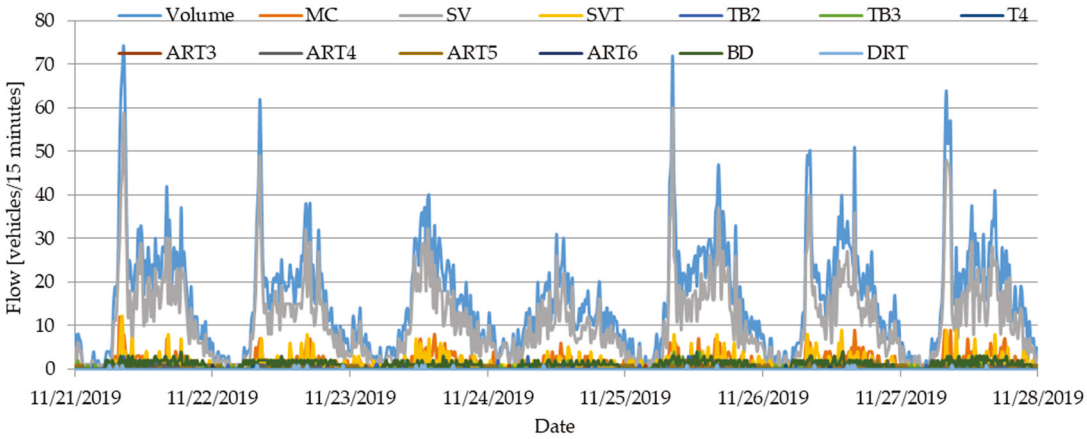

(**d**)

Figure 9. Traffic flow at the entrance to Lucian Blaga Square (2019): (**a**) Clinicilor Street, (**b**) Victor Babeș Street, (**c**) Petru Maior Street, (**d**) Gheorghe Șincai Street.

https://doi.org/10.3390/vehicles8030059

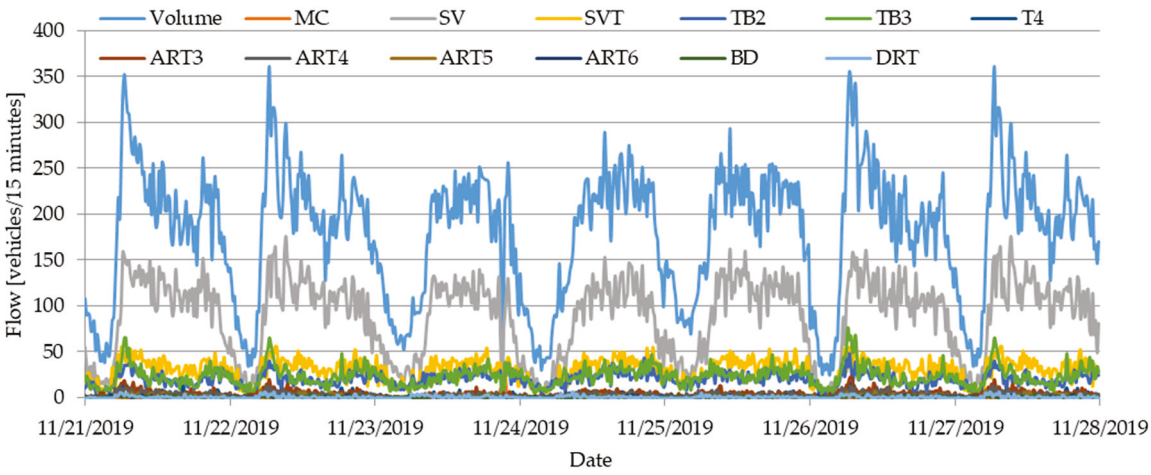

(**a**)

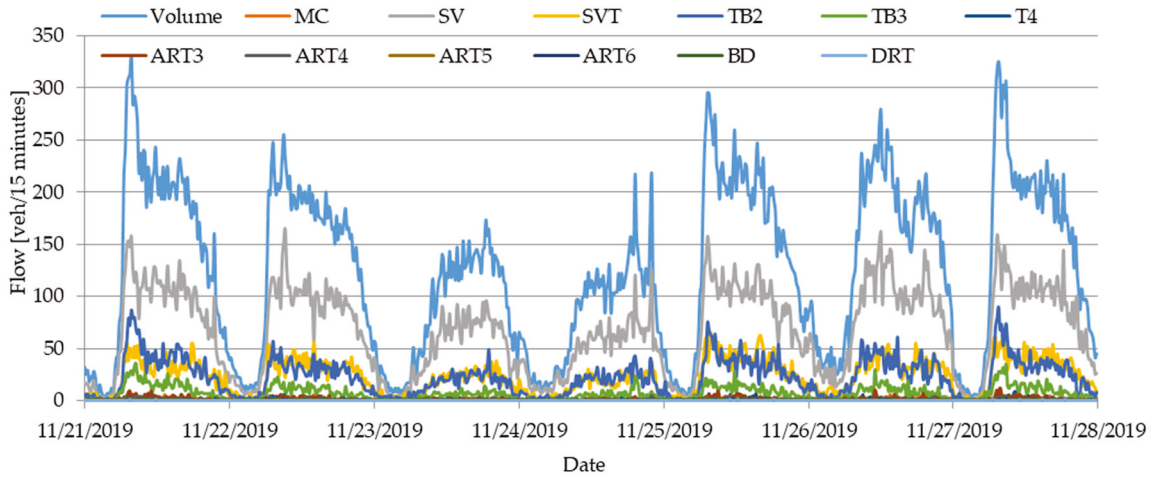

(**b**)

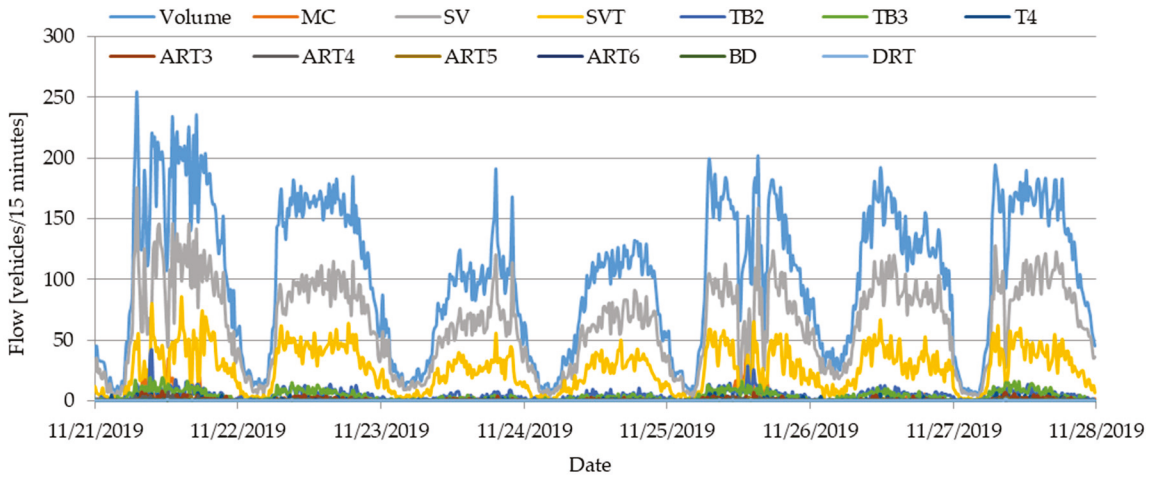

(**c**)

Figure 10. Traffic flow at the exit of Lucian Blaga Square (2019): (**a**) Petru Maior Street, (**b**) Napoca Street, (**c**) Republicii Street.

https://doi.org/10.3390/vehicles8030059

Table 4. Traffic flow at the exit to Lucian Blaga Square (2019).

Date	Traffic Flow (Vehicles/Day—Every 15 Min by One Hour)			Sum (Σ)
	P. Maior	Napoca	Republicii	
21 November 2019	17,795	13,914	12,355	44,064
22 November 2019	17,840	12,802	11,121	41,763
23 November 2019	15,686	8092	7086	30,864
24 November 2019	16,013	7871	7134	31,018
25 November 2019	17,897	13,974	10,435	42,306
26 November 2019	17,347	13,828	10,270	41,445
27 November 2019	17,840	13,671	10,697	42,208

Table 5. Average traffic speed at the entrance to Lucian Blaga Square (2019).

Date	Average Traffic Speed (km/h)				Average (km/h)
	Clinicilor	V. Babeș	P. Maior	Ghe. Șincai	
21 November 2019	39.43	30.48	39.61	43.51	38.26
22 November 2019	39.27	30.97	39.51	42.94	38.17
23 November 2019	31.72	36.41	47.41	39.29	38.71
24 November 2019	33.33	37.86	45.37	42.10	39.67
25 November 2019	40.49	29.48	45.43	43.72	39.78
26 November 2019	41.70	28.45	37.62	41.84	37.40
27 November 2019	39.34	27.52	37.40	42.92	36.80

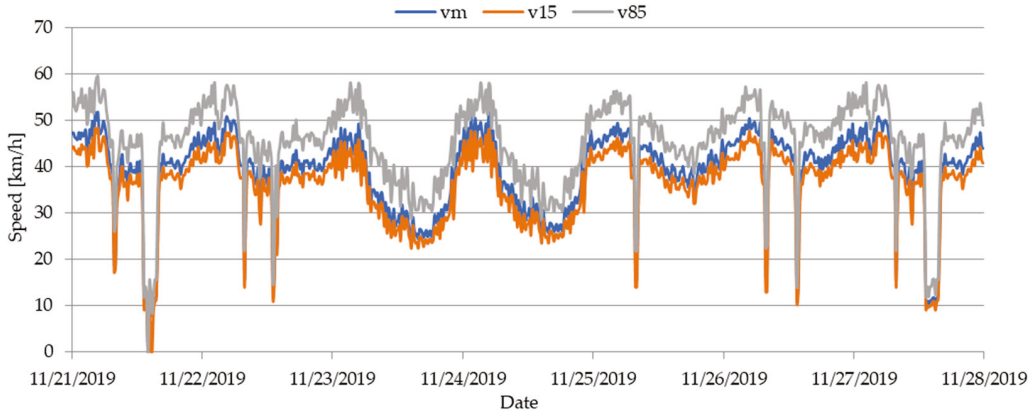

(**a**)

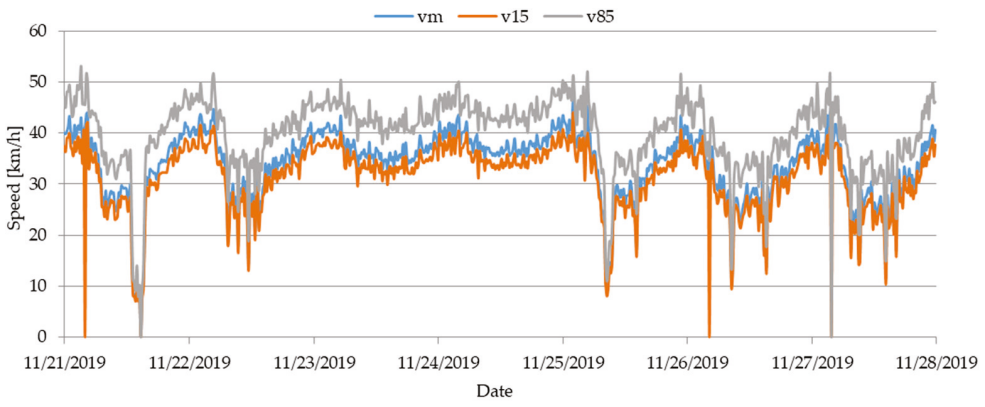

(**b**)

Figure 11. *Cont.*

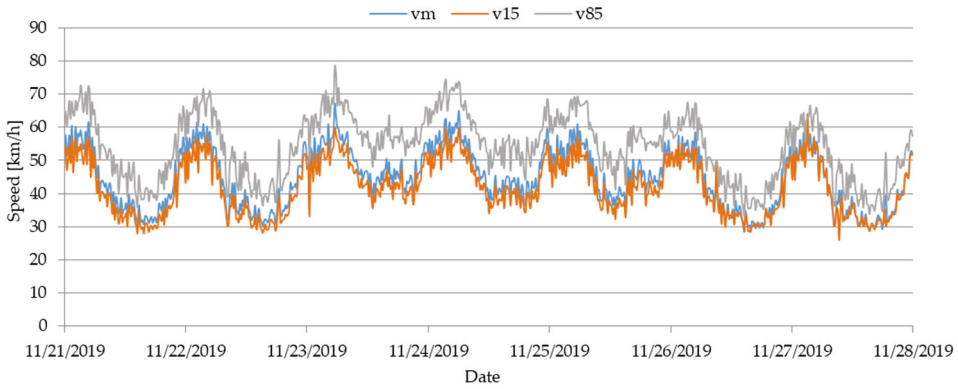

(**c**)

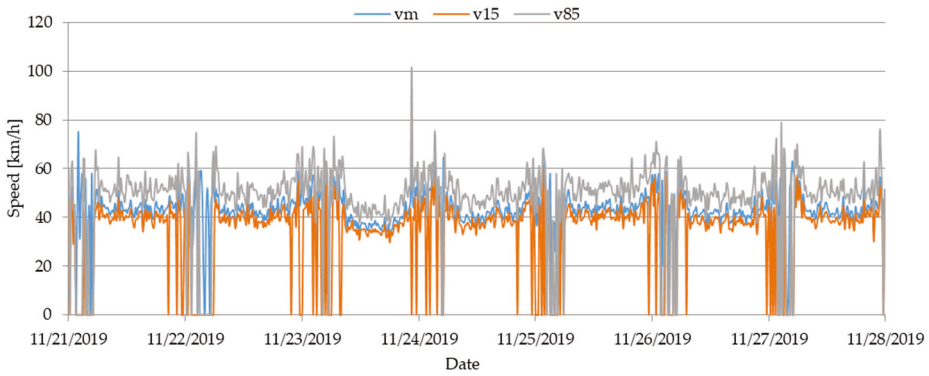

(**d**)

Figure 11. Average traffic speed at the entrance to Lucian Blaga Square (2019): (**a**) Clinicilor Street, (**b**) Victor Babeș Street, (**c**) Petru Maior Street, (**d**) Gheorghe Șincai Street.

Table 6. Average traffic speed at exit from Lucian Blaga Square (2019).

Date	Average Traffic Speed (km/h)			Average (km/h)
	P. Maior	Napoca	Republicii	
21 November 2019	45.79	49.66	33.70	43.05
22 November 2019	45.37	50.15	38.72	44.75
23 November 2019	51.05	49.56	39.82	46.81
24 November 2019	50.88	49.64	39.90	46.81
25 November 2019	49.78	50.05	33.82	44.55
26 November 2019	46.32	49.27	39.49	45.03
27 November 2019	45.37	49.12	36.19	43.56

The daily traffic volumes recorded during 21–27 November 2019 indicate a cumulative total of 273,996 vehicles at the intersection entries and 273,668 vehicles at the exits. The relative difference of 0.12% confirms measurement consistency and appropriate sensor positioning. This minor discrepancy is attributed to vehicles accessing or exiting the nearby underground parking facility and does not indicate detection losses.

The 15 min aggregated analysis highlights pronounced diurnal variations in traffic flow, with two distinct peak periods corresponding to morning and afternoon commuting hours. An increased coefficient of variation was observed during transition intervals between free-flow and congested regimes, indicating heightened instability in traffic conditions during these intermediate phases.

Average speed values, together with the 15th (v15) and 85th (v85) percentile speeds, confirm the presence of a mixed traffic regime. During low-demand intervals, traffic

operated under predominantly free-flow conditions, whereas peak hours exhibited a saturated regime characterized by reduced speeds and increased dispersion.

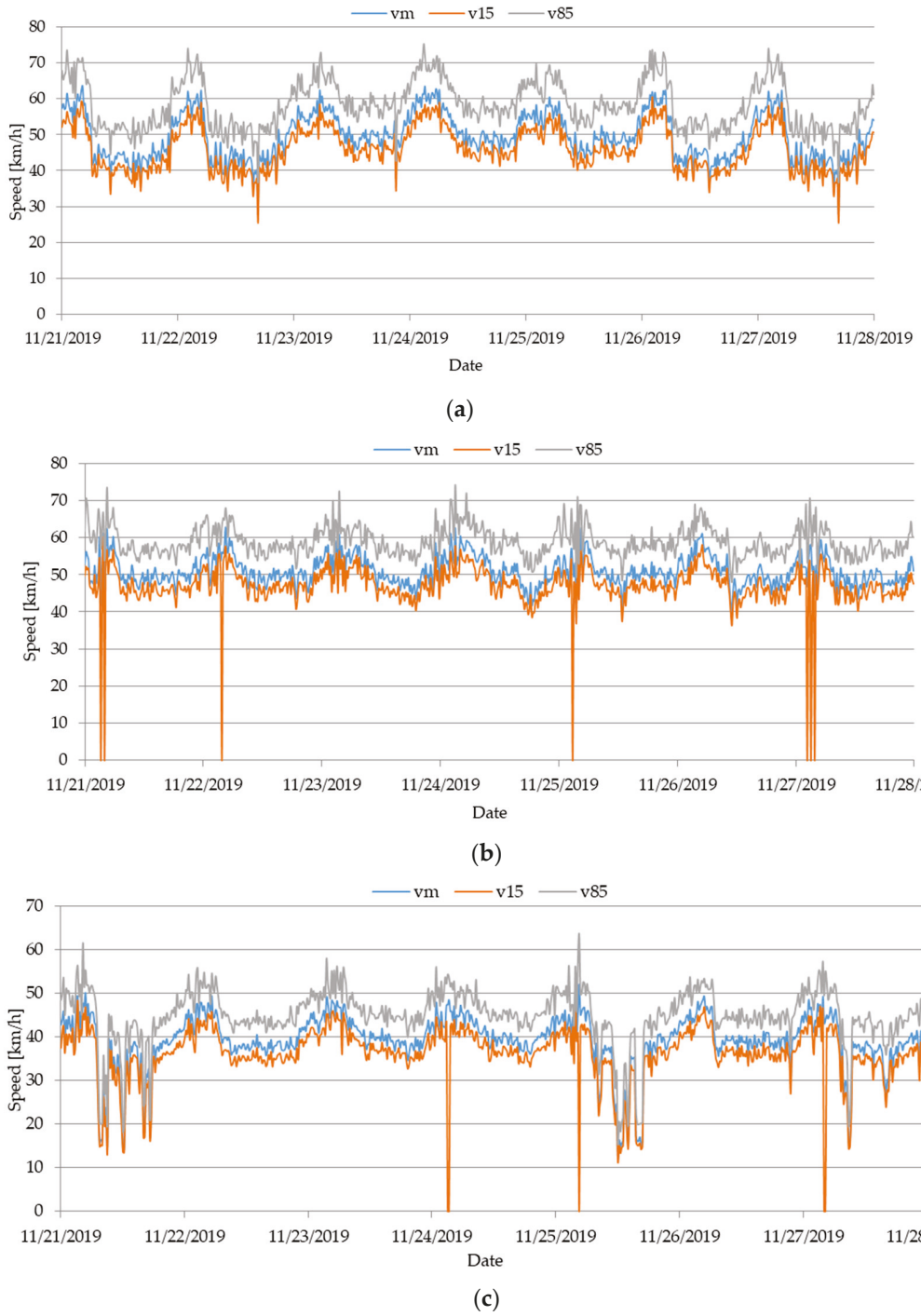

Figure 12. Average traffic speed at the exit of Lucian Blaga Square (2019): (**a**) Petru Maior Street, (**b**) Napoca Street, (**c**) Republicii Street.

Video recordings from the fixed surveillance cameras located at Lucian Blaga Square were processed using the DFS Viewer utility to determine the daily traffic distribution for the analyzed approaches (Figure 13).

https://doi.org/10.3390/vehicles8030059

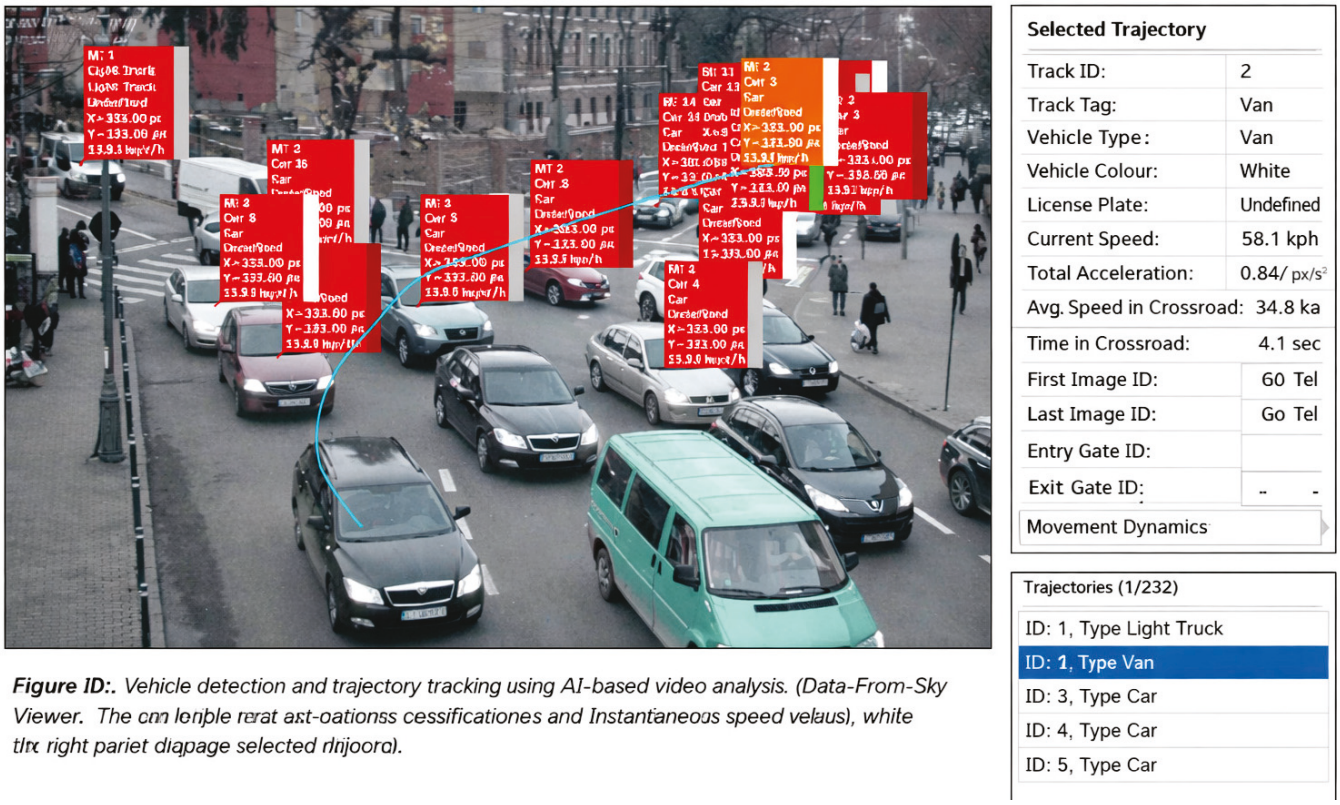

Figure ID:. *Vehicle detection and trajectory tracking using AI-based video analysis. (Data-From-Sky Viewer. The cnn lenble rerat ast-oationss cessifications and Instantaneous speed velaus), white tlrc right pariet diapage selected rhijoora).*

Figure 13. Traffic detection using DFS Viewer (photo by the author).

The video-processing platform displays intermediate metrics in pixel-based units (e.g., kpx/h), which correlate to internal detection and motion-tracking indicators. These numbers are only utilized to analyze video frames internally and cannot be directly read as physical traffic flow amounts. All traffic flow indicators given in this study are expressed in standard traffic engineering units (vehicles per hour) and are based on validated vehicle counts obtained by radar measurements.

Table 7 presents a summary of the data obtained from the processing of video recordings.

The unit "kpx/h" refers to an internal pixel-based motion indication generated by the video-processing platform, not a physical traffic flow unit. The traffic indicators utilized in the analysis are expressed as vehicles per hour.

To assess the consistency between the two measurement methods, traffic flows obtained from radar detection and video processing were compared for synchronized 5 min intervals. The average discrepancy between the two systems was approximately 9%.

This difference can be attributed to the technological and operational characteristics of the detection systems. First, the detection domains differ substantially: the radar operates on a defined cross-sectional detection line, whereas the video system captures a two-dimensional observation area. Second, object occlusion and overlapping trajectories may introduce counting inaccuracies in video-based detection. Additionally, objects located near the boundaries of the camera's field of view may be affected by geometric distortions or partial information loss, further contributing to the observed deviations.

The traffic flow values aggregated at 15 min intervals were used to estimate the Poisson parameter λ for each entry and exit branch.

The 2019 dataset defines the baseline traffic regime and serves as the reference condition for evaluating the changes observed in 2020, thereby enabling the assessment of the suitability of the Poisson distribution under different demand levels.

https://doi.org/10.3390/vehicles8030059

Table 7. Traffic values 2019—DFS measurement.

Daily Overview	
Date	23 November 2019
Start time	8:45:00
End time	8:50:00
Total period	00:05:00
Location	Cluj-Napoca
Analysis minor period	05:00
Analysis major period	30:00
Analysis overall period	Disable
Intersection type	Traffic light intersection
Overall statistics	
Number of tracked objects	425
Vehicle count	272
Medium vehicle count	0
Heavy vehicle count	0
Bus count	0
Motorcycle count	1
Bicycle count	0
Pedestrian count	140
Light truck count	1
Van count	10
Medium truck count	1
Total distance traveled (px—pixels)	148,671.68
Average speed in analyzed area (kpx/h—kilo-pixels/hour)	68.72

3.2.3. Traffic Measurements (Year 2020)

The traffic monitoring campaign conducted during the lockdown period covered a continuous interval of seven days. This duration was chosen because urban traffic patterns often have a weekly cycle, allowing for the recording of both weekday and weekend traffic dynamics. April 2020 was chosen as the observation period because it coincides with the period with the most stringent mobility restrictions imposed under Romania's COVID-19 state of emergency. During this time, educational institutions shuttered, numerous commercial activities were temporarily stopped and mobility demand reduced. Furthermore, the radar-based monitoring equipment operated autonomously on internal battery power, providing reliable continuous observations for around a week.

The measurements corresponding to the lockdown period (April 2020) were conducted using the same methodological framework applied in 2019, ensuring direct comparability of results. Specifically, continuous radar-based measurements (SDR Data Collect) were complemented by video processing through the DFS platform. Data aggregation was performed at 15 min intervals, maintaining the temporal resolution adopted for the reference year.

Table 8 presents an example of video-based measurements for a representative interval (7 April 2020, 08:50–08:55), used to validate object detection and classification accuracy.

The aggregated radar-based traffic flows recorded during April 2020 indicate a substantial reduction in daily traffic volume, reaching an average of 9.55% of the mean daily value observed in November 2019.

Table 8. Traffic values 2020—DFS measurement.

Daily Overview	
Date	7 April 2020
Start time	8:50:00
End time	8:55:01
Total period	00:05:01
Location	Cluj-Napoca
Analysis minor period	05:01
Analysis major period	30:00
Analysis overall period	Disable
Intersection type	Traffic light intersection
Overall statistics	
Number of tracked objects	41
Vehicle count	28
Medium vehicle count	0
Heavy vehicle count	0
Bus count	0
Motorcycle count	0
Bicycle count	0
Pedestrian count	7
Light truck count	0
Van count	5
Medium truck count	1
Total distance traveled (px)	12,577.73
Average speed in analyzed area (kpx/h)	36.27

The reduction ratio was calculated as

$$R = \frac{Q_{2020}}{Q_{2019}} \cdot 100\% \quad (4)$$

where Q_{2020} represents the mean daily traffic flow during the lockdown period and Q_{2019} denotes the corresponding mean daily flow during the reference period.

This result reflects an extremely low-demand traffic regime characterized by the disappearance of conventional peak-hour patterns and a flattened diurnal distribution. Furthermore, a significant decrease in flow variability was observed, accompanied by increased stability of average speeds, indicating operating conditions approaching free flow with minimal vehicle interactions.

Due to the DFS platform's processing capacity limits for extended datasets, video recordings were only available for extremely brief observation windows during the lockdown period. In the methodological framework utilized in this investigation, video data were mostly used to test the vehicle recognition and classification procedure, as well as to confirm the consistency of radar-based traffic measures. The reconstruction of the daily traffic profile and statistical analysis of traffic flows were primarily based on continuous radar observations, which offered complete temporal coverage of the investigated period. As a result, the video dataset's restricted temporal coverage has no meaningful effect on the robustness of the study conclusions.

For the statistical characterization of vehicle arrivals, the 15 min aggregated flow values were used to estimate the Poisson parameter λ, following the same estimation procedure applied for the 2019 dataset.

https://doi.org/10.3390/vehicles8030059

3.2.4. The Mathematical Model for Traffic Distribution

To analyze vehicle arrival patterns under the mobility restrictions imposed in 2020, a probabilistic framework based on the Poisson distribution was adopted. The Poisson model is appropriate for arrival-type stochastic processes characterized by discrete, independent events occurring within a finite time interval.

The fundamental assumptions of the model are:

i. Vehicle arrivals within sufficiently short time intervals are statistically independent.
ii. The probability of more than one arrival within an infinitesimal interval is negligible.
iii. The expected arrival rate remains constant within each aggregation interval.

The Poisson probability mass function is defined as

$$P(n,t) = \frac{(\lambda \cdot t)^n \cdot e^{-\lambda \cdot t}}{n!} \tag{5}$$

where $P(n,t)$ represents the probability of observing exactly n vehicles within time interval t, λ denotes the mean arrival rate (vehicles per unit time), n is the observed vehicle count and t corresponds to the aggregation interval (15 min).

The arrival rate parameter λ was estimated separately for each 15 min interval using experimental radar measurements from April 2020 [55]:

$$\lambda_i = \frac{q_i}{t} \tag{6}$$

where q_i represents the observed vehicle count within interval i. Accordingly, the process is treated as a non-homogeneous Poisson process, with a time-varying arrival rate reflecting diurnal traffic dynamics.

Preliminary variance analysis indicated slight overdispersion $var(n) > E(n)$. To assess model robustness, a negative binomial formulation was tested as an alternative count model. The generalized log-linear specification of the arrival rate is

$$P(n_i) = \prod_i \frac{exp[-exp(\alpha_i \beta)]\left[exp(\alpha_i \beta)^{n_i}\right]}{n_i!} \tag{7}$$

To explicitly address overdispersion, a stochastic error component ε_i was introduced:

$$\lambda_i = exp(\alpha_i \beta + \varepsilon_i) \tag{8}$$

Conditional on ε_i the probability mass function becomes

$$P(n_i|\varepsilon) = \frac{exp[-\lambda_i exp(\varepsilon_i)]\left[\lambda_i exp(\varepsilon_i)^{n_i}\right]}{n_i!} \tag{9}$$

Integrating over the gamma-distributed error term yields the negative binomial distribution:

$$P(n_i) = \frac{\Gamma(\theta + n_i)}{\Gamma(\theta) n_i!} u_i^{\theta} (1 - u_i)^{n_i} \tag{10}$$

where $\Gamma(\ )$ denotes the gamma function and $u_i = \theta/\theta + \lambda_i$, and $\theta = 1/\alpha$ is the dispersion parameter.

Model parameters were estimated using maximum likelihood:

$$P_{max}(\lambda_i) = \prod_{i=1}^{n} \frac{\Gamma(\theta + n_i)}{\Gamma(\theta) n_i!} \left[\frac{\theta}{\theta + \lambda_i}\right]^{\theta} \left[\frac{\lambda_i}{\theta + \lambda_i}\right]^{n_i} \tag{11}$$

https://doi.org/10.3390/vehicles8030059

Goodness-of-fit tests indicated that the Poisson model provides a satisfactory approximation for the analyzed intervals; therefore, the final estimation framework is based on the Poisson distribution.

Video-based observations from 2020 covered only limited time windows. The 2019 dataset, consisting of continuous 24 h measurements aggregated at 15 min intervals, was used as a structural reference.

Given that uniform traffic conditions within 15 min samples were confirmed through DFS-based analysis, the corresponding 5 min equivalent flow was derived as

$$q_{unit} = \frac{q_{15}}{3} \tag{12}$$

where q_{15} represents the 15 min aggregated flow.

The parameter λ was calculated using observations for the data recorded in 2020. Given the data provided in Equation (5), the probability that vehicles arrive in a time interval was calculated (Figure 14).

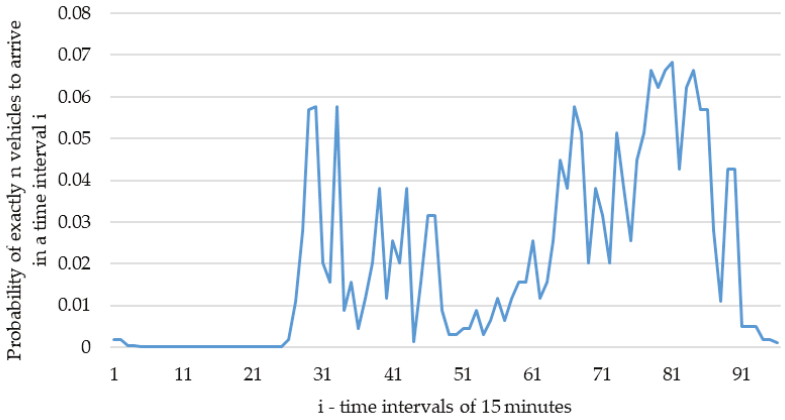

Figure 14. The probability of vehicles arriving in a time interval.

Since the 2020 video data covered short observation windows, the estimated probabilistic model was used to reconstruct the full daily traffic profile:

$$q_i^{2020} = \lambda_i \cdot t \tag{13}$$

where q_i^{2020} denotes the estimated traffic flow for interval i, and λ_i is the corresponding estimated arrival rate. This formulation preserves dimensional consistency and maintains the physical interpretation of traffic flow as the expected value of the Poisson process.

The index i corresponds to 15 min intervals for both measured (2019) and estimated (2020) datasets. To reflect the legally imposed night-time traffic restrictions during lockdown (22:00–06:00), the corresponding probability values $P(t)$ were set to zero for these intervals (Figure 15). Notably, 2019 measurements during the same period already exhibited minimal traffic volumes.

The reconstructed 24 h traffic profile was validated using NCSS 2022 (Number Cruncher Statistical System, version 22.0.9) Statistical Software [56]. The goodness-of-fit analysis yielded a probability level of 0.98, confirming strong agreement between observed and modeled vehicle counts (Figure 16).

https://doi.org/10.3390/vehicles8030059

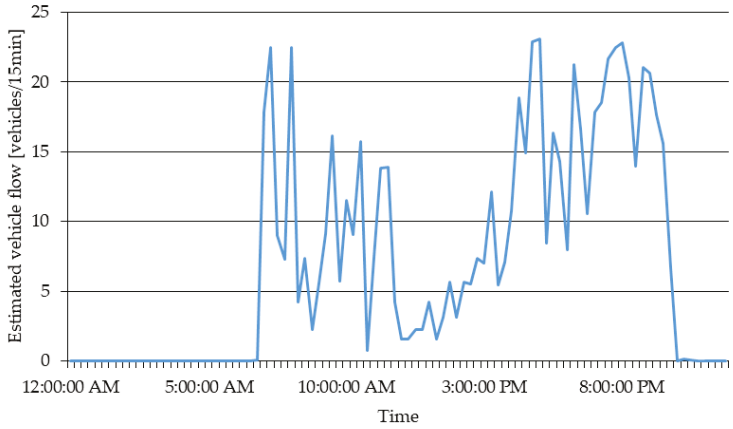

Figure 15. Vehicle traffic at 15 min interval in 2020.

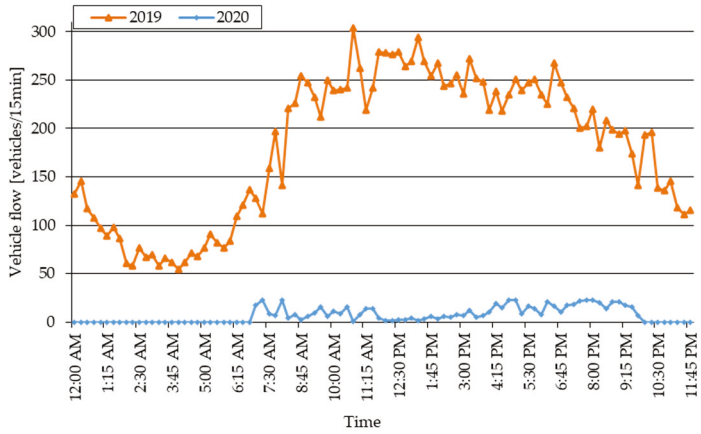

Figure 16. Comparative results: traffic flow distribution over 24 h.

Comparison of the estimated daily profiles for 2019 and 2020 reveals:

- A pronounced reduction in overall traffic intensity.
- Attenuation of traditional morning and afternoon peaks.
- Substantial flattening of the diurnal distribution.
- Structural modification of temporal demand patterns.

These findings indicate a redistribution of mobility demand across the day and a significant reduction in traffic concentration during conventional peak periods.

The proposed modeling framework enables estimation of traffic behavior under severe mobility restrictions using limited observational data, offering a transferable tool for analyzing extreme mobility scenarios and supporting resilience-oriented urban traffic planning.

To evaluate the robustness of the Poisson formulation, an alternative count model based on the negative binomial distribution was also examined. When count data demonstrates overdispersion, the negative binomial distribution is frequently used in traffic flow modeling. However, analysis of the observed traffic counts revealed that the variance-to-mean ratio remained near unity under the studied low-demand traffic regime. Furthermore, values very near to zero were obtained when the dispersion parameter was estimated using the negative binomial formulation, indicating minimal divergence from the equidispersion condition. As a result, the Poisson model was considered suitable and statistically appropriate for modeling the vehicle arrival process in the current investigation. The Poisson model is also preferred due to its simplicity and interpretability when the equidispersion assumption is approximately satisfied.

https://doi.org/10.3390/vehicles8030059

4. Results

4.1. Traffic Flow Characteristics Before the Pandemic (2019)

Continuous measurements conducted in November 2019 indicate that traffic at Lucian Blaga Square operated under recurrent high-volume conditions, particularly during peak periods.

The cumulative inflow over the seven monitored days (Figure 9, Table 3) reached 273,996 vehicles, while the cumulative outflow (Figure 10, Table 4) was 273,668 vehicles, corresponding to a relative difference of only 0.12%. This negligible imbalance confirms global flow conservation within the intersection and validates the consistency of sensor positioning and data acquisition.

The average daily inflow was approximately 39,142 vehicles/day, ranging between 31,189 and 44,150 vehicles/day. The corresponding average daily outflow was 39,095 vehicles/day, indicating an almost symmetric distribution of traffic volumes. The coefficient of variation in daily volumes (11–13%) reflects moderate variability, typical of central urban areas characterized by mixed land use (administrative, medical, academic).

The highest daily inflow (44,150 vehicles/day) was recorded on 21 November 2019, corresponding to a regular working day with intense urban activity.

Mean entry speeds (Figure 11, Table 5) ranged between 36.80 and 39.78 km/h, whereas mean exit speeds (Figure 12, Table 6) varied between 43.05 and 46.81 km/h. The average difference of approximately 7–8 km/h between entry and exit speeds reflects the dynamic processes governing intersection operation. Vehicle deceleration and queue formation upstream of the stop line reduce entry speeds, while downstream acceleration and flow dispersion increase exit speeds. This difference is further influenced by the adaptive signal control system, which modulates green times and temporally redistributes traffic demand.

Peak intervals were characterized by inflows reaching 220–250 vehicles per 15 min interval on major approaches, accompanied by mean speeds dropping below 35 km/h, indicating operation close to saturation conditions.

The combined analysis of flow and speed reveals a clear inverse relationship between traffic intensity and mean speed, consistent with the fundamental diagram of traffic flow (flow–density–speed relationship). Increased demand during peak hours leads to reduced speeds and higher dispersion, confirming the presence of congestion dynamics.

Overall, the 2019 dataset reflects an urban traffic system operating in a dynamic equilibrium state, characterized by high and recurrent volumes, predictable temporal variability, and systematic queue formation during peak periods. This operational regime defines the baseline reference condition for subsequent comparison with the pandemic period.

4.2. Traffic Conditions During COVID-19 Restrictions (2020)

Traffic measurements conducted in April 2020, during the state of emergency, revealed a pronounced structural reduction in mobility demand at the analyzed intersection.

AI-assisted video processing detected 28 vehicles and 7 pedestrians within a representative 5 min interval. When compared with the equivalent reference period in 2019, these values correspond to approximately 9.55% of the pre-pandemic vehicular traffic and approximately 5% of the pedestrian activity level. This magnitude of reduction confirms a near-collapse of regular urban mobility patterns during lockdown conditions.

Despite the drastic decrease in traffic volumes, the mean vehicle speed recorded during the analyzed interval in 2020 was 36.27 km/h, a value comparable to the entry speed observed under normal conditions. The absence of a proportional increase in speed indicates that traffic performance remained structurally constrained by signal timing and intersection control logic rather than by demand levels alone.

https://doi.org/10.3390/vehicles8030059

Although traffic volumes decreased dramatically during the lockdown period, the average vehicle speeds did not increase proportionally. This behavior can be explained by numerous variables unique to metropolitan traffic environments. First, stated speed restrictions and urban road layout limit vehicle speeds, especially in low-demand conditions. Second, the investigated intersection is regulated by traffic signals, which means that vehicle progression is still determined by signal timing and mandatory stopping intervals, independent of traffic demand. As a result, the operational regime becomes predominantly control-dominated rather than demand-driven.

This observation is also consistent with basic traffic flow diagrams, which show that when traffic demand is low, the system normally functions in a regime of low flow and moderate speeds rather than an unconstrained increase in speed.

This effect has also been documented in previous research on urban traffic dynamics in low-demand environments.

4.3. Probabilistic Modeling of Vehicle Arrivals

In this study, the probabilistic model was used to reconstruct the temporal distribution of traffic volumes over a 24 h period, with its parameters calibrated using continuous radar-based traffic measurements, which served as the core empirical dataset for the analysis. The model does not replace direct measurements but rather provides a statistical framework for estimating vehicle arrival distributions over time intervals where direct observations may be limited. The projected arrival rates, like any other probabilistic reconstruction approach, are subject to uncertainty. However, the consistency of modeled and observed traffic patterns, as well as the goodness-of-fit study, suggests that the rebuilt daily profile is a reliable approximation of traffic dynamics during the investigated lockdown period.

Although continuous radar measurements provide complete traffic counts for the period under consideration, the probabilistic modeling framework is used to define the stochastic nature of vehicle arrivals rather than to replace empirical data. In this context, the Poisson model is used to estimate the arrival rate parameter and explain the probability distribution that governs vehicle arrivals across time. The reconstructed daily traffic profile thus reflects a statistical interpretation of the temporal demand distribution obtained from the probabilistic model calibrated with radar-based measurements.

The Poisson distribution was employed to model vehicle arrivals at the intersection during the state of emergency, treating arrivals as a discrete time-dependent stochastic process. The model was formulated as a non-homogeneous Poisson process, with the arrival rate λ_i estimated separately for each 15 min interval based on the experimental data collected in April 2020.

Radar-based measurements obtained during the lockdown period revealed exceptionally low traffic activity at night, with multiple consecutive 15 min intervals indicating zero or near-zero vehicle arrivals. Under these conditions, the related Poisson arrival probability is insignificant. For modeling reasons, these probabilities were approximated as zero in the reconstructed daily profile, reflecting the experimentally observed absence of traffic demand rather than an externally imposed limitation.

The estimated values of λ_i ranged between 0 and 1.6 vehicles/min during active daytime periods, with a daily average of 0.42 vehicles/min, corresponding to approximately 25 vehicles per 15 min interval. These values reflect a severely reduced demand regime compared to the 2019 baseline.

The Poisson probability mass function was used to compute the likelihood of observing n vehicles within a given time interval t.

https://doi.org/10.3390/vehicles8030059

The variance-to-mean ratio for the 2020 dataset was close to unity ($var(n)/E(n) \approx 1.08$), indicating minimal deviation from the equidispersion property characteristic of Poisson processes.

A chi-square goodness-of-fit test yielded a significance level of $p = 0.98$, confirming that the Poisson distribution adequately describes the arrival process under restricted traffic conditions. To assess potential overdispersion, a negative binomial formulation was also tested. Maximum likelihood estimation of the dispersion parameter α produced values approaching zero ($\alpha \to 0$), indicating that overdispersion effects were negligible in the low-demand regime.

Consequently, the Poisson model was considered sufficient for reconstructing the daily traffic profile.

Using the estimated λ_i values, the 2020 daily traffic curve was reconstructed. The resulting profile reveals an almost complete suppression of the morning peak (07:00–09:00) and a pronounced attenuation of the afternoon peak (16:00–18:00). Overall, the diurnal variation appears substantially flattened, indicating a redistribution and homogenization of mobility demand throughout the day. Traffic volumes between 22:00 and 06:00 approached zero, consistent with the mobility restrictions in force during the analyzed period.

Compared to 2019, peak-hour flow rates decreased by approximately 88–92%, depending on the approach, while the average daily flow dropped to approximately 9–12% of pre-pandemic levels. These results confirm a structural transition from a peak-dominated regime to a uniformly low-intensity arrival process, statistically compatible with near-ideal Poisson behavior. The reconstruction should therefore be interpreted as a probabilistic estimate rather than an exact deterministic representation of traffic flows.

4.4. Model Validation

Statistical validation of the probabilistic framework was performed using NCSS Statistical Software [56], applying the chi-square (χ^2) goodness-of-fit test to evaluate the agreement between observed and Poisson-estimated frequencies.

The observed vehicle arrival frequencies and those predicted by the Poisson model were compared using the χ^2 goodness-of-fit test. Traffic counts collected at 15 min intervals during the monitored observation period were used for the analysis. To make sure that the expected frequency in each bin met the minimal threshold necessary for the validity of the χ^2 approximation, observed and expected frequencies were sorted into bins established according to vehicle count ranges. The provided p-value was obtained by computing test statistics using pooled data from all intervals. The number of degrees minus one minus the number of estimated parameters in the Poisson model was used to get the number of degrees of freedom. Because the test was performed on the aggregated dataset rather than on individual interval-level tests, no multiple testing procedure was used.

To evaluate the statistical significance of the differences between the two observation periods, a Welch two-sample t-test was performed on the daily traffic volumes recorded in 2019 and 2020. Traffic demand decreased significantly during the lockdown, according to the test ($t = 18.62$, $p < 0.001$). Cohen's d was used to further quantify the degree of this change, and the result was an effect size of 6.84, suggesting a very significant difference between the two traffic regimes.

The compliance of the observed vehicle arrival frequencies with the Poisson distribution was further evaluated using a χ^2 goodness-of-fit test. At the significance level $\alpha = 0.05$, the null hypothesis—that vehicle arrivals follow a Poisson distribution—cannot be rejected, according to the computed test statistic of $\chi^2 = 4.87$ with 6 degrees of freedom ($p = 0.56$). This result indicates that the data from experiments and the probabilistic model are in good accord.

https://doi.org/10.3390/vehicles8030059

The variance-to-mean ratio of the observed arrival numbers was used for additional validation. This ratio was roughly 1.08 for the examined intervals, which closely matched the Poisson distribution's equidispersion feature. On the other hand, peak-hour observations from the 2019 sample showed variance-to-mean ratios more than 1.4, indicating overdispersion linked to vehicle platooning and congestion impacts.

The near-unit dispersion observed in 2020 suggests that, under severely reduced demand, inter-vehicle dependence and platooning effects are substantially diminished. As a result, the independence assumption underlying the Poisson process becomes more realistic compared to normal traffic conditions.

A comparative assessment between 2019 and 2020 is summarized in Table 9.

Table 9. Comparative assessment between 2019 and 2020.

Indicator	2019 (Baseline)	2020 (Lockdown)	Change	Test Statistic	*p*-Value
Average daily traffic volume	~39,142 vehicles/day	~3740 vehicles/day	−90.4% reduction	$t = 18.62$	<0.001
Peak 15 min flow	220–250 vehicles/15 min	18–25 vehicles/15 min	−88–92% reduction	-	-
Pedestrian activity	Baseline	~5% of 2019	−95% reduction	-	-
Variance-to-mean ratio	>1.4 (peak hours)	≈1.08	Reduced dispersion	-	-
Vehicle arrival distribution	Non-Poisson regime	Poisson-compatible regime	Adequate model fit	$\chi^2 = 4.87$ (df = 6)	0.56
Traffic regime	Near-capacity	Free-flow dominant	Structural transition	-	-

To evaluate the statistical significance of the differences between the two observation periods, a Welch two-sample *t*-test was performed on daily traffic volumes reported in 2019 and 2020. This test was chosen because it enables the comparison of mean values from two independent samples without assuming equal variances. The results show a considerable reduction in traffic demand during the lockdown period ($p < 0.001$), indicating a structural change in urban mobility patterns.

The extent of the difference demonstrates the extraordinary impact of COVID-19 mobility restrictions on urban transportation demand.

The results confirm that mobility restrictions imposed in 2020 led to a severe reduction in congestion phenomena, the disappearance of the characteristic bimodal daily traffic profile, and a substantial decrease in temporal variability. Moreover, the statistical behavior of vehicle arrivals became increasingly compatible with the fundamental assumptions of the Poisson model.

This transition reflects a shift from a near-capacity operational regime in 2019—characterized by vehicle interdependence and queue formation—to a low-density, free-flow-dominant regime in 2020, characterized by rare and nearly independent arrival events.

The probabilistic model demonstrates robustness under extremely low-demand conditions and provides a reliable tool for estimating traffic behavior in exceptional mobility scenarios. Given the statistical validation and engineering consistency of the results, the Poisson framework can be considered adequate for describing vehicle arrival distributions during the analyzed lockdown period.

https://doi.org/10.3390/vehicles8030059

5. Discussion

5.1. Interpretation of Traffic Reduction Under Mobility Restrictions

The results demonstrate a profound structural disruption of urban mobility patterns during the COVID-19 emergency period. Traffic volumes decreased to approximately 9–12% of the 2019 reference level, while pedestrian activity declined to nearly 5%, indicating an almost complete contraction of routine urban mobility at the analyzed central node.

Compared to international findings reporting reductions between 60% and 90%, the observed 88–92% peak-hour reduction places the studied intersection at the upper bound of global impact levels. This heightened sensitivity can be attributed to the functional characteristics of the location, which include a high concentration of administrative institutions, academic facilities, medical services, and commuter-dominated trip patterns. The closure of institutions and the large-scale adoption of remote work directly suppressed the dominant travel demand components.

Importantly, the elimination of the bimodal peak structure and the flattening of the diurnal distribution indicate that restrictions induced not merely a quantitative reduction in volume, but a structural reorganization of temporal demand patterns. The disappearance of pronounced morning and afternoon peaks reflects the collapse of commuting-driven mobility.

The improved compatibility of 2020 data with the assumptions of the Poisson distribution further supports this structural interpretation. Under near-capacity conditions (2019), vehicle interdependence, queue formation, and platooning introduce correlations that violate independence assumptions. Under extremely low demand (2020), arrivals approximate independent rare events, explaining the superior performance of the Poisson model.

These findings suggest that central urban nodes are highly sensitive to institutional activity patterns and that mobility restrictions can rapidly trigger a transition toward a free-flow dominant regime accompanied by fundamental changes in temporal demand structure. This has direct implications for emergency mobility planning and SUMP-based scenario modeling.

5.2. Traffic Regime Transition and Flow Characteristics

In 2019, the intersection operated close to capacity during peak periods, as indicated by high flow rates and reduced mean speeds. The observed flow–speed relationship is consistent with operation near the descending branch of the fundamental diagram, where increased density leads to speed reduction and congestion onset. The likely volume-to-capacity ratio (v/c) approached unity during peak intervals (07:00–09:00 and 16:00–18:00), resulting in recurrent queue formation and shockwave propagation.

During the 2020 restrictions, peak flows decreased by 88–92%, shifting the system to a fundamentally different operational regime. The v/c ratio fell well below unity, eliminating queue formation mechanisms and significantly reducing vehicle interactions. Temporal variability decreased, and the arrival process became statistically closer to independent random events.

Notably, mean speeds did not increase proportionally to the dramatic demand reduction. This indicates that intersection performance under low demand was constrained primarily by signal control logic rather than capacity limitations. In 2019, traffic dynamics were governed predominantly by demand pressure and vehicle interaction effects. In 2020, system behavior became control-dominated rather than capacity-dominated.

This shift reflects a structural transition in the governing mechanisms of the traffic system—from interaction-driven congestion to regulation-driven flow stabilization.

5.3. Suitability of the Poisson Modeling Framework

The Poisson framework relies on two core assumptions:

https://doi.org/10.3390/vehicles8030059

1. Statistical independence of arrival events.
2. Equidispersion (variance approximately equal to the mean).

The Poisson model's independence assumption has been evaluated using a number of supplementary indicators that were obtained from the combined traffic measurements. First, the observed arrival counts' variance-to-mean ratio was close to unity (≈1.08), which is in line with Poisson processes' equidispersion property. Second, persistent autocorrelation patterns that are usually linked to vehicle platooning or upstream signal coordination were not found in the temporal development of traffic over successive 15 min intervals. Finally, compared to typical urban traffic conditions, the assumption of statistically independent arrivals is more likely because of the exceptionally low traffic density seen during the lockdown period, which significantly decreased inter-vehicle contacts.

Under normal urban traffic conditions, these assumptions are frequently violated due to platooning, upstream signal coordination, congestion wave propagation, and vehicle interdependence. Such conditions typically generate overdispersion and correlated arrivals.

During the lockdown period, reduced density significantly diminished inter-vehicle interactions. The observed variance-to-mean ratio (≈1.08) closely approaches the theoretical Poisson condition. The high χ^2 goodness-of-fit significance level ($p = 0.98$) confirms strong agreement between observed and theoretical distributions.

Testing a negative binomial formulation yielded dispersion parameters approaching zero ($\alpha \to 0$), indicating negligible overdispersion. Consequently, the Poisson model provides a statistically sufficient and parsimonious description of vehicle arrivals under severely reduced demand.

Under congested or near-capacity traffic conditions, vehicle arrivals are strongly influenced by queue formation, signal coordination, and platooning effects generated by upstream intersections. These mechanisms introduce temporal correlations between successive arrivals, which frequently result in overdispersion in perceived traffic numbers. However, in low-demand traffic conditions, vehicle interactions become substantially less common, and the arrival process resembles a series of random and nearly independent events. As a result, the statistical independence assumption becomes more reasonable, and the variance-to-mean ratio approaches unity, in accordance with the Poisson distribution's equidispersion feature. These qualities make the Poisson framework ideal for simulating vehicle arrivals in extremely low-demand traffic scenarios.

This behavior has been frequently observed in traffic flow studies analyzing unsaturated or low-demand traffic regimes.

5.4. Methodological Implications of AI-Based Video Processing

The integration of radar-based detection (SDR) and AI-assisted video processing (DFS platform) enabled multi-source validation of traffic volumes and classifications.

Radar measurements provide precise cross-sectional counts and instantaneous speed estimation, while video-based deep learning detection captures full-scene dynamics, enabling trajectory reconstruction, classification, acceleration estimation, and interaction analysis.

The observed ~9% discrepancy between radar and video measurements reflects methodological differences in detection geometry rather than a major systematic error. Radar operates on a defined cross-sectional plane, whereas video detection covers a two-dimensional field with potential edge distortions and occlusion effects. The strong temporal correlation between the two datasets confirms coherent representation of flow dynamics.

The hybrid sensing framework enhances robustness, reduces systematic bias associated with single-sensor approaches, and demonstrates the potential of AI-supported monitoring for probabilistic modeling and operational diagnostics of urban intersections.

https://doi.org/10.3390/vehicles8030059

5.5. Urban Resilience and Traffic Management Implications

The observed collapse of mobility demand provides insights into urban traffic system resilience. In transport engineering terms, resilience can be defined as the ability of the system to absorb extreme external shocks, maintain operational stability, and recover to its original regime.

Despite a 90% demand reduction, the signalized intersection maintained stable operation without systemic malfunction. Adaptive signal control remained functional under atypical arrival distributions, suggesting robust regulatory logic capable of accommodating extreme demand fluctuations.

The probabilistic framework developed in this study offers practical utility for extreme scenario modeling, emergency mobility planning, resilience testing, and rapid reconstruction of daily traffic profiles from limited observations. Such capability is particularly relevant for sudden disruptions, including pandemics, natural disasters, or security-related mobility restrictions.

While the study focuses on a single central intersection, the methodological approach is transferable to other urban nodes, provided that:

i. Baseline reference data are available.
ii. Low-demand observations exist for comparative calibration.
iii. Arrival processes remain sufficiently sparse to satisfy probabilistic assumptions.

However, extrapolation to multilane coordinated corridors, high-speed freeway segments, or multimodal hubs must be undertaken cautiously, as different interaction dynamics may invalidate the independence assumption. Future research should therefore investigate whether similar probabilistic behavior emerges across diverse infrastructure typologies and varying demand structures.

6. Conclusions

This study investigated the impact of COVID-19 mobility restrictions on urban traffic dynamics at a central signalized intersection in Cluj-Napoca, Romania, using an integrated framework combining continuous radar measurements and AI-assisted video processing.

The findings reveal an extreme structural contraction of mobility demand. Vehicle volumes decreased to approximately 9.55% of the pre-pandemic baseline, while pedestrian activity declined to nearly 5%. Beyond this quantitative reduction, a fundamental transformation of the temporal traffic structure was observed, characterized by the disappearance of morning and afternoon peak periods and a pronounced flattening of the diurnal profile.

From an operational perspective, the intersection transitioned from a near-capacity, congestion-prone regime (2019) to a low-density, free-flow dominant regime (2020), governed primarily by signal control logic rather than demand pressure. Despite the dramatic reduction in flow, average speeds did not increase proportionally, confirming the persistent structural influence of signal regulation on performance metrics.

The probabilistic modeling framework based on the Poisson distribution—supplemented by a negative binomial robustness test—demonstrated strong agreement with observed data under reduced demand conditions. The variance-to-mean ratio approaching unity and the high χ^2 goodness-of-fit ($p = 0.98$) confirm that, under sparse traffic conditions, vehicle arrivals approximate an independent stochastic process more closely than under congested regimes dominated by inter-vehicle interactions and platooning effects.

The integration of radar detection and AI-based video analytics enabled multi-source validation of traffic volumes and strengthened the robustness of probabilistic parameter estimation. The proposed methodological framework allows reconstruction of daily traffic distributions from limited observational datasets and provides a transferable tool for

https://doi.org/10.3390/vehicles8030059

modeling extreme mobility scenarios and supporting resilience-oriented traffic management strategies.

Overall, the study demonstrates that extreme mobility disruptions modify not only traffic intensity but also the stochastic structure of arrival processes, with direct implications for probabilistic modeling and operational traffic management under low-demand conditions.

The results of this study provide a few significant insights into the behavior of urban transportation systems under extreme mobility limits.

First, the data confirmed a substantial contraction in vehicular mobility across the lockdown period, with traffic volumes decreasing to 9–12% of pre-pandemic levels. This decline was accompanied by a structural shift in the daily traffic profile, as seen by the removal of the traditional bimodal peak structure and a significant flattening of diurnal demand distribution.

Second, the statistical research showed that when traffic demand is significantly lowered, the vehicle arrival process becomes more compatible with the Poisson distribution assumptions. Vehicle arrivals in low-density traffic regimes are nearly independent stochastic events, as indicated by the high χ^2 goodness-of-fit value and a variance-to-mean ratio nearing unity.

Third, integrating radar-based traffic measurements with AI-assisted video processing was helpful in getting accurate traffic flow data and validating probabilistic modeling approaches. The proposed methodology thus provides a transferable structure for reconstructing traffic demand profiles in situations where observational data is limited, such as during large-scale mobility disruptions.

Several limitations must be acknowledged.

First, the temporal coverage of the 2020 data was restricted to a limited lockdown window. The 24 h traffic profile was reconstructed through probabilistic extrapolation, which introduces uncertainty.

Second, the reference measurements (November 2019) and lockdown measurements (April 2020) were collected in different seasons. Although seasonal effects in central urban nodes are expected to be moderate, influences related to meteorological conditions and daylight duration cannot be entirely excluded. Although the reference dataset is from November 2019 and the lockdown dataset is from April 2020, traffic demand in the analyzed urban intersection is largely determined by commuting and educational mobility patterns, which are relatively consistent during both the autumn and spring semesters. Nevertheless, seasonal variations due to weather conditions, daylight duration, or other contextual factors may contribute to extra unpredictability in traffic levels. As a result, the potential seasonal influence should be addressed when evaluating the quantitative comparison of the two datasets.

Third, the analysis focused on a single signalized urban intersection. While representative of mixed-use central areas, generalization to other infrastructure typologies—such as coordinated arterial corridors, freeway segments, or multimodal hubs—should be undertaken cautiously.

Finally, the adopted approach was predominantly macroscopic. Microscopic trajectory analysis, detailed queue dynamics modeling, and behavioral adaptation assessment were beyond the scope of the present study.

Future research should:

- Assess the applicability of the probabilistic framework across diverse network typologies and operational contexts.
- Investigate post-restriction recovery phases and potential rebound effects in mobility demand.

https://doi.org/10.3390/vehicles8030059

- Integrate microscopic traffic simulation and dynamic queue modeling to capture fine-scale interaction mechanisms.
- Evaluate the long-term stability of stochastic arrival patterns under hybrid work regimes and evolving mobility behaviors.

Such extensions would further clarify the boundary conditions under which Poisson-based modeling remains valid and enhance its integration into adaptive traffic management and resilience-oriented urban mobility planning.

Author Contributions: Conceptualization, N.F. and C.I.; methodology, N.F. and C.I.; software, N.F.; validation, N.F. and M.D.; formal analysis, C.I.; resources, C.I.; data curation, C.I. and M.D.; writing—original draft preparation, C.I.; writing—review and editing, C.I.; visualization, N.F., C.I. and M.D.; supervision, N.F.; project administration, N.F. All authors have read and agreed to the published version of the manuscript.

Funding: The APC was funded by MDPI/Vehicle.

Data Availability Statement: The processed traffic datasets generated and analyzed during the current study are available from the corresponding author upon reasonable request for research purposes.

Acknowledgments: This paper and the research behind it would not have been possible without the support of the project Just Streets—Horizon 2020 and Data from Sky system, developed by RCE systems s.r.o. and of Monitoring and Road Safety Department within Cluj-Napoca City—Hall, Romania.

Conflicts of Interest: The authors declare no conflicts of interest.

Abbreviations

The following abbreviations are used in this manuscript:

AI	Artificial Intelligence
ARX	Automatic Road Analyzer
CNN	Convolutional Neural Networks
COVID-19	Coronavirus Disease 2019
DFS	Data From Sky
Kpx/h	kilo-pixels/hour
NCSS	Number Cruncher Statistical System
px	pixels
SDR	Speed Detection Radar
SUMP	Sustainable Urban Mobility Plans
χ^2	chi-square test
v15	15th percentile speed
v85	85th percentile speed

References

1. Urban Mobility Strategies During COVID-19. Available online: https://www.eiturbanmobility.eu/wp-content/uploads/2021/03/Urban-mobility-strategies-during-COVID-19_long-1.pdf (accessed on 11 February 2026).
2. Pandey, S.; Yadav, B.; Pandey, A.; Tripathi, T.; Khawary, M.; Kant, S.; Tripathi, D. Lessons from SARS-CoV-2 Pandemic: Evolution, Disease Dynamics and Future. *Biology* **2020**, *9*, 141. [CrossRef] [PubMed]
3. Nazir, R.; Ali, J.; Rasul, I.; Widemann, E.; Shafiq, S. Eco-Environmental Aspects of COVID-19 Pandemic and Potential Control Strategies. *Int. J. Environ. Res. Public Health* **2021**, *18*, 3488. [CrossRef] [PubMed]
4. Lipfert, F.W.; Wyzga, R.E. COVID-19 and the Environment, Review and Analysis. *Environments* **2021**, *8*, 42. [CrossRef]
5. Macioszek, E.; Kurek, A. Extracting Road Traffic Volume in the City before and during COVID-19 through Video Remote Sensing. *Remote Sens.* **2021**, *13*, 2329. [CrossRef]

6. Taqi, H.M.M.; Ahmed, H.N.; Paul, S.; Garshasbi, M.; Ali, S.M.; Kabir, G.; Paul, S.K. Strategies to Manage the Impacts of the COVID-19 Pandemic in the Supply Chain: Implications for Improving Economic and Social Sustainability. *Sustainability* **2020**, *12*, 9483. [CrossRef]
7. Khalifa, S.A.M.; Swilam, M.M.; El-Wahed, A.A.A.; Du, M.; El-Seedi, H.H.R.; Kai, G.; Masry, S.H.D.; Abdel-Daim, M.M.; Zou, X.; Halabi, M.F.; et al. Beyond the Pandemic: COVID-19 Pandemic Changed the Face of Life. *Int. J. Environ. Res. Public Health* **2021**, *18*, 5645. [CrossRef]
8. Muhammad, S.; Long, X.; Salman, M. COVID-19 pandemic and environmental pollution: A blessing in disguise? *Sci. Total Environ.* **2020**, *728*, 138820. [CrossRef]
9. Planul de Mobilitate Urbană Durabilă Cluj-Napoca 2021–2030. (In Romanian). Available online: https://www.clujmet.ro/wp-content/uploads/2022/01/PMUD_Cluj-Napoca_Draft-final.pdf (accessed on 11 February 2026).
10. Sustainable Urban Mobility Planning and Monitoring. Available online: https://transport.ec.europa.eu/transport-themes/urban-transport/sustainable-urban-mobility-planning-and-monitoring_en (accessed on 11 February 2026).
11. FY 2022-26 U.S. DOT Strategic Plan and Progress Report. Available online: https://www.transportation.gov/dot-strategic-plan (accessed on 29 August 2024).
12. Decretul Nr. 195 Din 16 Martie 2020. (In Romanian). Available online: https://legislatie.just.ro/Public/DetaliiDocumentAfis/223831 (accessed on 18 August 2024).
13. Global Carbon Emissions Rebound Close to Pre-COVID Levels. Available online: https://globalcarbonbudget.org/global-carbon-emissions-rebound-close-to-pre-covid-levels/ (accessed on 11 February 2026).
14. Nath, D.; Sasikumar, K.; Nath, R.; Chen, W. Factors Affecting COVID-19 Outbreaks across the Globe: Role of Extreme Climate Change. *Sustainability* **2021**, *13*, 3029. [CrossRef]
15. Wołowiec, T.; Myroshnychenko, I.; Vakulenko, I.; Bogacki, S.; Wiśniewska, A.M.; Kolosok, S.; Yunger, V. International Impact of COVID-19 on Energy Economics and Environmental Pollution: A Scoping Review. *Energies* **2022**, *15*, 8407. [CrossRef]
16. Bulmez, A.M.; Brezeanu, A.-I.; Dragomir, G.; Talabă, O.-M.; Năstase, G. An Analysis of Romania's Energy Strategy: Perspectives and Developments since 2020. *Climate* **2024**, *12*, 101. [CrossRef]
17. El-Geneidy, A.; De Vos, J. Transport and COVID-19: Where are we now? *Transp. Rev.* **2024**, *44*, 245–247. [CrossRef]
18. Institutul Național de Statistică. (In Romanian). Available online: https://insse.ro/cms/files/POCA/Impact-COVID-SNDDR2030.pdf (accessed on 11 February 2026).
19. Bucsky, P. Modal share changes due to COVID-19: The case of Budapest. *Transp. Res. Interdiscip. Perspect.* **2020**, *8*, 100141. [CrossRef]
20. Politis, I.; Georgiadis, G.; Papadopoulos, E.; Fyrogenis, I.; Nikolaidou, A.; Kopsacheilis, A.; Sdoukopoulos, A.; Verani, E. COVID-19 lockdown measures and travel behavior: The case of Thessaloniki, Greece. *Transp. Res. Interdiscip. Perspect.* **2021**, *10*, 100345. [CrossRef]
21. Lockdown Movement Permit. (In Romanian). Available online: https://forma.gov.gr/en/ (accessed on 11 February 2026).
22. Henke, I.; Pagliara, F.; Cartenì, A.; Coppola, P. The Impact of COVID-19 Pandemic on Public Transport: A Mobility Survey in Naples (South of Italy). *Open Transp. J.* **2023**, *17*. [CrossRef]
23. Harantová, V.; Hájnik, A.; Kalašová, A.; Figlus, T. The Effect of the COVID-19 Pandemic on Traffic Flow Characteristics, Emissions Production and Fuel Consumption at a Selected Intersection in Slovakia. *Energies* **2022**, *15*, 2020. [CrossRef]
24. Jenelius, E.; Cebecauer, M. Impacts of COVID-19 on public transport ridership in Sweden: Analysis of ticket validations, sales and passenger counts. *Transp. Res. Interdiscip. Perspect.* **2020**, *8*, 100242. [CrossRef] [PubMed]
25. Ren, M.; Park, S.; Xu, Y.; Huang, X.; Zou, L.; Wong, M.S.; Koh, S.-Y. Impact of the COVID-19 pandemic on travel behavior: A case study of domestic inbound travelers in Jeju, Korea. *Tour. Manag.* **2022**, *92*, 104533. [CrossRef]
26. Hong, Y.; Lu, K. The effect of quarantine policy on pollution emission and the usage of private transportation in urban areas. *Nat. Sci. Rep.* **2024**, *14*, 15752. [CrossRef]
27. Li, D.; Lasenby, J. Investigating impacts of COVID-19 on urban mobility and emissions. *Cities* **2023**, *135*, 104246. [CrossRef]
28. Owais, M.; Abulwafa, O.; Abbas, Y.A. When to Decide to Convert a Roundabout to a Signalized Intersection: Simulation Approach for Case Studies in Jeddah and Al-Madinah. *Arab. J. Sci. Eng.* **2020**, *45*, 7897–7914. [CrossRef]
29. Yadav, S.K.; Akhter, Y. Statistical Modeling for the Prediction of Infectious Disease Dissemination with Special Reference to COVID-19 Spread. *Front. Public Health* **2021**, *9*, 645405. [CrossRef] [PubMed]
30. Peköz, E.A.; Joglekar, N. Poisson Traffic Flow in a General Feedback Queue. *J. Appl. Probab.* **2002**, *39*, 630–636. [CrossRef]
31. Abul-Magd, A.Y. Modelling highway-traffic headway distributions using Superstatistics. *Phys. Rev. E* **2007**, *76*, 057101. [CrossRef] [PubMed]
32. Wigner's Surmise. Available online: https://robertsweeneyblanco.github.io/Computational_Random_Matrix_Theory/Eigenvalues/Wigner_Surmise.html (accessed on 11 February 2026).
33. Maya, O.; Kim, H.; Toda, H. Online Traffic Flow Prediction Using Convolved Bilinear Poisson Regression. In *18th IEEE International Conference on Mobile Data Management (MDM) 2017*; IEEE: New York, NY, USA, 2017; pp. 134–143. [CrossRef]

34. Yang, S.; Yang, X. The Application of the Queuing Theory in the Traffic Flow of Intersection. *World Acad. Sci. Eng. Technol. Int. J. Math. Comput. Phys. Electr. Comput. Eng.* **2014**, *8*, 986–989. [CrossRef]
35. Thomas, T.; Weijermars, W.; Berkum, E. Variations in urban traffic volumes. *Eur. J. Transp. Infrastruct. Res.* **2008**, *8*, 251–263. [CrossRef]
36. Viti, F.; van Zuylen, H.J. Queues and delays at signals: A general approach. In *Proceedings INSTR 2007*; van Zuylen, H.J., Ed.; 2007; pp. 1–9.
37. Vandaele, N.; van Woensel, T.; Verbruggen, A. A queueing based traffic flow model. *Transp. Res. Part D Transp. Environ.* **2000**, *5*, 121–135. [CrossRef]
38. Kong, X.; Xu, Z.; Shen, G.; Wang, J.; Yang, Q.; Zhang, B. Urban traffic congestion estimation and prediction based on floating car trajectory data. *Future Gener. Comput. Syst.* **2016**, *61*, 97–107. [CrossRef]
39. Almutairi, A.; Yi, P.; Owais, M. New Approach for Estimating Intersection Control Delay From Passive Traffic Sensors at Network Level. *IEEE Access* **2024**, *12*, 2882–2900. [CrossRef]
40. SDR Traffic Classifier. Available online: https://traffictechnology.co.uk/blog/portfolio/sdr-traffic-classifier/ (accessed on 11 February 2026).
41. SDR Radar Traffic Classifier. Available online: https://www.datacollect.com/en/mobility-data-analysis/measuring-systems/sdr-radar-traffic-classifier/ (accessed on 11 February 2026).
42. Preda, I.; Covaciu, D.; Florea, D.; Ciolan, G. Study of In-Traffic Vehicle Behaviour, Based on GPS and Radar Devices. In Proceedings of the ESFA 2009 International Conference, Bucharest, Romania, January 2009. Available online: https://www.researchgate.net/publication/263424362_Study_of_In-Traffic_Vehicle_Behaviour_Based_on_GPS_and_Radar_Devices (accessed on 11 February 2026).
43. Data Collect Traffic Systems. Available online: https://datafromsky.com/trafficcamera/ (accessed on 11 February 2026).
44. Chen, V.C.; Li, F.; Ho, S.-S.; Wechsler, H. Micro-Doppler effect in radar: Phenomenon, model, and simulation study. *IEEE Trans. Aerosp. Electron. Syst.* **2006**, *42*, 2–21. [CrossRef]
45. Chen, V. *The Micro-Doppler Effect in Radar*, 2nd ed.; Artech House: Norwood, MA, USA, 2019.
46. MyTrafficData Secure: Configure, Analyse and More. Available online: https://www.datacollect.com/en/mobility-data-analysis/mytrafficdata/ (accessed on 11 February 2026).
47. Data from Sky Light. Available online: https://ai.datafromsky.com/light/ (accessed on 11 February 2026).
48. Data from Sky Aerial. Available online: https://ai.datafromsky.com/aerial (accessed on 11 February 2026).
49. Data from Sky Viewer. Available online: https://datafromsky.com/news/datafromsky-viewer-new-version-new-features/ (accessed on 11 February 2026).
50. Conteo de Flujo y Programación de Semáforos, Mediante el Uso de Reconocimiento de Imágenes, Utilizando el Software DataFromSky. Available online: https://repositorio.uchile.cl/handle/2250/184342 (accessed on 11 February 2026).
51. Dell'Acqua, G.; Wegman, F. (Eds.) *Transport Infrastructure and Systems: Proceedings of the AIIT International Congress on Transport Infrastructure and Systems, Rome, Italy, 10–12 April 2017*; CRC Press: Boca Raton, FL, USA, 2017.
52. Cluj-Napoca, Romania Population 2024. Available online: https://worldpopulationreview.com/cities/romania/cluj-napoca (accessed on 11 February 2026).
53. Strategia Integrată de Dezvoltare Urbană a Zonei Metropolitane Cluj. (In Romanian). Available online: https://documents1.worldbank.org/curated/en/099850010282239359/pdf/P172384038eb760700add008aa9b21cd8bf.pdf (accessed on 11 February 2026).
54. ARX Classification Vehicles Schemes. Available online: https://mtehelp.tech-metrocount.com/Article.aspx?id=DB9FE70AC7 (accessed on 11 February 2026).
55. Azimi, M.; Wali, M.M.; Qi, Y. Studying the Impact of the COVID-19 Pandemic on Bikeshares as a Mode of Shared Micromobility in Major Cities: A Case Study of Houston. *Future Transp.* **2024**, *4*, 270–282. [CrossRef]
56. NCSS Statistical Software. Available online: https://www.ncss.com/software/ncss/ (accessed on 11 February 2026).

Disclaimer/Publisher's Note: The statements, opinions and data contained in all publications are solely those of the individual author(s) and contributor(s) and not of MDPI and/or the editor(s). MDPI and/or the editor(s) disclaim responsibility for any injury to people or property resulting from any ideas, methods, instructions or products referred to in the content.

vehicles

MDPI

Article

System-Level Comparative Assessment of PMSM Rotor Topologies in Battery Electric Vehicles Under the WLTP Driving Cycle

Elena-Daniela Lupu [1,2,*] and Ștefan Lucian Tabacu [2]

[1] Faculty of Electrical Engineering and Computer Science, Ștefan cel Mare University of Suceava, 13 University Street, 720229 Suceava, Romania
[2] Faculty of Mechanics and Technology, National University of Science and Technology POLITEHNICA Bucharest, Pitesti University Centre, Târgu din Vale, No. 1, Arges, 110040 Piteşti, Romania; stefan.tabacu@upb.ro
* Correspondence: elena.lupu@usm.ro

Abstract

Environmental regulations, rapid technological advancements, and evolving mobility trends have led to a significant transformation of the automotive industry in recent years. The adoption of battery-electric vehicles (BEVs) has been accelerated by these developments, which are becoming increasingly efficient and widely deployed. Evaluating BEV energy consumption and performance is essential for optimizing energy efficiency, extending driving range, and developing effective control strategies under real-world operating conditions. The analysis is based on the WLTP Class 3 driving cycle, in which the vehicle operating points are projected onto the motor efficiency map to evaluate the influence of real-world operating conditions on overall propulsion efficiency. Two operating scenarios are considered: with regenerative braking and without regenerative braking. The inverter and battery are modeled using quasi-static energy-based representations to ensure system-level energetic consistency while maintaining computational efficiency. The results show that rotor topology significantly influences vehicle-level energy consumption. The dual-layer IPM configuration reduces net WLTP energy demand by approximately 9% and increases the estimated driving range from about 489 km to 535 km compared to the single-layer V-shaped configuration. Variations in rotor topology led to different efficiency distributions, which leads to systematic differences in battery energy demand and achievable driving range. The results highlight the importance of aligning traction motor design with realistic operating-point distributions rather than optimizing solely for peak efficiency or marginal improvements in regenerative braking performance.

Keywords: drive cycle simulation; efficiency map; energy consumption; PMSM; regenerative braking; range

1. Introduction

Electric vehicles represent one of the major strategic directions for decarbonizing road transport, with battery electric vehicles (BEVs) becoming the predominant technological solution [1–3]. Their energy performance and driving range depend not only on battery capacity but also on the architecture of the propulsion system and on how efficiently energy is converted and utilized under real driving conditions [4–6]. Within this context, the

electric motor has a central role in the vehicle energy chain, as its operating efficiency directly affects energy losses, driving range, and thermal loading [7,8].

The accelerated development of electric mobility has intensified the need for advanced energy optimization strategies in BEVs, where both the electric motor and the energy storage system critically influence overall vehicle efficiency [6,9–12]. As a result, the selection of the traction motor technology becomes a critical design decision, as it directly determines the achievable efficiency, power density, and operating characteristics of the electric propulsion system.

The traction motor represents a key component in electric vehicle powertrains, requiring an optimal balance between power density, efficiency, cost, and material availability [1,6]. Permanent magnet synchronous motors (PMSMs) are currently the most used traction motors in electric vehicle applications due to their high efficiency, high torque and power density, compact size, and excellent dynamic performance over a wide operating range [13–15]. However, their performance benefits come at the cost of a strong dependence on rare-earth permanent magnets, which significantly increases manufacturing costs and raises concerns related to material availability, price volatility, and supply chain sustainability [16–18].

In addition to PMSMs, several well-established traction motor technologies that are not dependent on permanent magnets are also employed in electric vehicle applications. Induction motors (IMs) are recognized for their robust construction, high reliability, and mature manufacturing technology, offering complete independence from rare-earth materials, although typically exhibiting lower efficiency and power density compared to PMSMs, particularly at low speeds and partial-load operating conditions [1,3]. Switched reluctance motors (SRMs) feature a simple and rugged rotor structure, inherent fault tolerance, and wide-speed-range capability; nevertheless, they usually experience increased torque ripple and acoustic noise when compared to PMSMs [1]. Electrically excited synchronous motors (EESMs) represent another established magnet-free alternative, combining synchronous operation with controllable air-gap flux via rotor field excitation, which enables improved field-weakening capability and competitive efficiency over a wide speed range, at the expense of additional excitation losses and increased system complexity [19,20].

The evaluation of energy performance for traction electric motors in battery electric vehicles (BEVs) is commonly performed using efficiency maps, which represent motor efficiency as a two-dimensional function of electromagnetic torque and rotational speed [21,22].

Unlike industrial electric motors, whose efficiency is classified under standardized IE classes, no internationally standardized efficiency classification currently exists for traction motors used in electric vehicle propulsion systems. This lack of a comprehensive efficiency classification framework is mainly due to the specific operating conditions of traction drives, which are typically inverter-fed and characterized by a wide speed range, frequent transients, and highly variable load profiles imposed by real driving conditions [10,11]. As a result, a single rated efficiency value is insufficient to accurately characterize the energy performance of traction machines. Instead, efficiency maps provide a comprehensive description of motor behavior over the entire operating envelope and enable a detailed assessment of energy consumption when coupled with specific driving cycles and vehicle operating scenarios [4,6,21]. Consequently, efficiency mapping has become a fundamental analytical tool for the comparison, optimization, and selection of traction motor technologies in modern electric vehicle applications [6,23].

In this context, the Worldwide Harmonized Light Vehicles Test Procedure (WLTP) driving cycle provides a consistent and comparable analysis framework by representing

https://doi.org/10.3390/vehicles8030066

realistic driving conditions and offering valuable insight into the relationship between vehicle load profiles and motor energy efficiency [24].

An additional measure for extending the driving range of electric vehicles is the implementation of regenerative braking, which enables the partial recovery of the vehicle's kinetic energy during deceleration phases [25–27]. In efficiency maps, this operating regime is represented in the negative-torque regions, where the conversion efficiency from mechanical to electrical energy varies significantly with speed and load [26,28]. The effectiveness of regenerative braking therefore directly affects the ability of the traction motor to operate within high-efficiency regions of the generator-mode during braking events. Consequently, both the motor design and the control strategy play an essential role in maximizing energy recuperation [28,29]. In addition, the overall regenerative braking performance depends on the coordinated interaction between the traction motor, power electronic inverter, battery management system (BMS), and mechanical braking system, which is typically implemented through braking force blending strategies [27,30].

Recent literature consistently indicates that regenerative braking can lead to a significant extension of electric vehicle driving range, with reported improvements typically ranging between approximately 8% and 25%, depending on the driving cycle, vehicle configuration, and control strategy [26,27]. Studies based on standardized driving cycles highlight this dependency, reporting average range increases of about 13% under the WLTC, approximately 16% for the NEDC, and values reaching or exceeding 30% for urban-dominated cycles [25,30]. More recent investigations further confirm these trends across different traction motor topologies and electric propulsion architectures [12,27].

In this study, a unified WLTP-based energy evaluation procedure is employed to assess the energy performance of a battery electric vehicle (BEV). By integrating longitudinal vehicle dynamics, drivetrain modeling, power electronics losses, battery behavior, and regenerative braking within a coherent simulation framework, the proposed methodology adopts a system-oriented approach for traction motor comparison.

The analysis is conducted on a BEV equipped with two permanent magnet synchronous motor (PMSM) variants while maintaining identical electrical, geometric, and thermal constraints. This ensures that the observed differences in energy consumption and driving range can be directly attributed to rotor topology. Particular emphasis is placed on the influence of the operating-point distribution generated by a realistic driving cycle on overall vehicle efficiency.

A key contribution of the work is the systematic alignment between the operating-point distribution produced by the WLTP Class 3 driving cycle and the motor efficiency maps, rather than relying solely on conventional peak-efficiency indicators. The results show that variations in efficiency distribution across the torque–speed plane may lead to measurable differences in total battery energy demand and achievable driving range over a standardized driving cycle.

Furthermore, the comparison between operating conditions with and without regenerative braking allows a detailed assessment of the interaction between traction efficiency and energy recuperation capability. The results indicate that improvements in traction efficiency do not necessarily translate into proportional gains in overall vehicle-level energy efficiency when regenerative effects are considered.

Overall, the study provides a vehicle-level perspective on rotor topology evaluation by linking electromagnetic design characteristics with energy performance indicators derived under realistic operating conditions.

The originality of the present study does not reside in the individual formulation of the governing equations, which are well established in literature, but in their coherent integration within a WLTP-consistent, operating-point-aligned comparative framework

https://doi.org/10.3390/vehicles8030066

that links vehicle longitudinal dynamics, FEM-derived motor efficiency maps, and battery-level energy analysis.

The main contributions of this paper can therefore be summarized as follows:

- The development of a WLTP-based vehicle-level evaluation framework integrating vehicle dynamics, drivetrain losses, and battery behavior;
- The systematic alignment of driving-cycle operating-point distributions with motor efficiency maps for rotor topology comparison;
- The assessment of the interaction between traction efficiency and regenerative braking effects on overall BEV energy consumption and driving range.

Future extensions of the methodology toward alternative driving cycles, advanced control strategies, and enhanced electro-thermal modeling could further broaden its applicability to next-generation electric traction systems.

2. Vehicle and Propulsion System Modeling Framework

The energy performance assessment framework employed in this work relies on the coupled simulation of the vehicle longitudinal dynamics and the functional behavior of the principal elements of the electric powertrain, namely the permanent magnet synchronous motor (PMSM), the traction inverter, and the onboard energy source. Within the adopted modeling assumptions, this integrated approach enables a consistent estimation of power flow distribution and overall energy demand under operating conditions representative of the WLTP driving cycle.

The numerical model workflow follows a sequential structure. Starting from the prescribed vehicle speed profile, the required traction forces and drivetrain operating points are derived, which subsequently allows for the evaluation of component-level electrical and mechanical loads. Based on these results, the specific energy consumption, achievable driving range, and relevant stress indicators of the electric propulsion system are quantified for the investigated operating scenarios.

2.1. Longitudinal Vehicle Dynamic Model

The longitudinal vehicle dynamics are modeled to compute the traction force required to follow the prescribed WLTP speed profile. The model accounts for aerodynamic drag, rolling resistance, inertial effects, and road load contributions. The resulting drivetrain operating points are used as inputs for the electric powertrain component models.

A backward-facing modeling strategy (Figure 1) is adopted, whereby the prescribed vehicle speed profile is used to derive the corresponding traction force and drivetrain operating conditions [1,3,4].

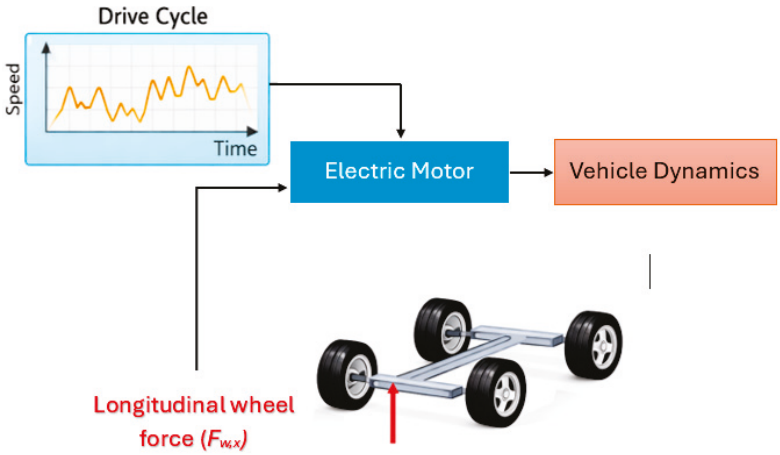

Figure 1. Backward-facing modeling strategy.

The vehicle considered in the investigation is a compact-class BEV equipped with a front-mounted PMSM-based electric powertrain, mechanically coupled to the driven wheels through a fixed-ratio transmission (final drive) and a differential.

The vehicle is modeled using longitudinal dynamics, neglecting lateral and vertical effects. The equation of motion in the longitudinal direction [4] is given by:

$$F_{w,x} = R_r + R_a + R_g + R_i \tag{1}$$

where $F_{w,x}$ denotes the total longitudinal wheel force, R_r is the rolling resistance, R_a is the aerodynamic drag, R_g is the grade resistance, and R_i is the inertial resistance. The term total longitudinal force is used to emphasize the net force required at the wheels to overcome resistive and inertial effects.

For battery electric vehicles (BEVs), the rolling resistance force represents energy losses associated with the interaction between the pneumatic tires and the road surface. It is commonly modeled as a function of the vehicle weight W and the rolling resistance coefficient f_r:

$$R_r = f_r \cdot W \cdot \cos \alpha \tag{2}$$

For passenger BEVs equipped with low rolling resistance tires, typical values of f_r range between 0.008 and 0.015 [31]. In this work, a speed-dependent formulation is adopted:

$$f_r = 0.01\left(1 + \frac{V}{160}\right) \tag{3}$$

where V is the vehicle speed in km/h. This semi-empirical expression is implemented within the longitudinal vehicle dynamics model to provide a realistic estimation of rolling resistance over the WLTP operating range.

The aerodynamic resistance R_a is given by:

$$R_a = \frac{1}{2} \cdot \rho_{air} \cdot C_D \cdot A_f \cdot v^2 \tag{4}$$

where ρ_{air} is the air density ($\rho_{air} = 1.225$ kg/m^3) corresponding to the International Standard Atmosphere conditions (dry air at 15 °C and 1 atm), commonly adopted in vehicle longitudinal dynamics modeling, C_D denotes the aerodynamic drag coefficient, A_f is the frontal projected area of the vehicle, and v is the vehicle speed relative to the ambient air.

The grade resistance R_g corresponds to the longitudinal component of the vehicle weight acting along the direction of motion and is given by:

$$R_g = W \cdot \sin(\alpha) \tag{5}$$

where α is the road inclination, typically expressed as a percentage grade $p_{\%}$. Since the WLTP cycle is defined for level-road conditions, the grade resistance term is neglected in the present analysis.

The inertial resistance R_i represents the force required to overcome the vehicle's inertia during longitudinal acceleration or deceleration and is formulated as:

$$R_i = \frac{W}{g} \cdot \gamma \cdot a \tag{6}$$

where a is the longitudinal acceleration, g is the gravitational acceleration, and γ accounts for the contribution of rotating masses to the equivalent translational inertia. For the

https://doi.org/10.3390/vehicles8030066

considered BEV with a single-speed drivetrain, γ is evaluated using a speed-dependent empirical expression:

$$\gamma = \frac{1}{1.02 - \frac{5.22}{V}} \tag{7}$$

which yields higher values at low speeds and approaches unity at high speeds. To preserve model simplicity, a constant value of $\gamma = 1.03$ is adopted.

By substituting the individual resistance components into (1) and considering WLTP level-road conditions, the required longitudinal wheel force becomes:

$$F_{w,x} = f_r \cdot W + \frac{1}{2} \cdot \rho \cdot C_D \cdot A_f \cdot v^2 + \frac{W}{g} \cdot \gamma \cdot \frac{\mathrm{d}v}{\mathrm{d}t} \tag{8}$$

Figure 2 illustrates the temporal distribution of the vehicle velocity $v(t)$, acceleration $a(t)$, and longitudinal force $F_w(t)$. The vehicle speed profile used for the determination of the longitudinal forces corresponds to the WLTP driving cycle, as detailed in Section 2.6.

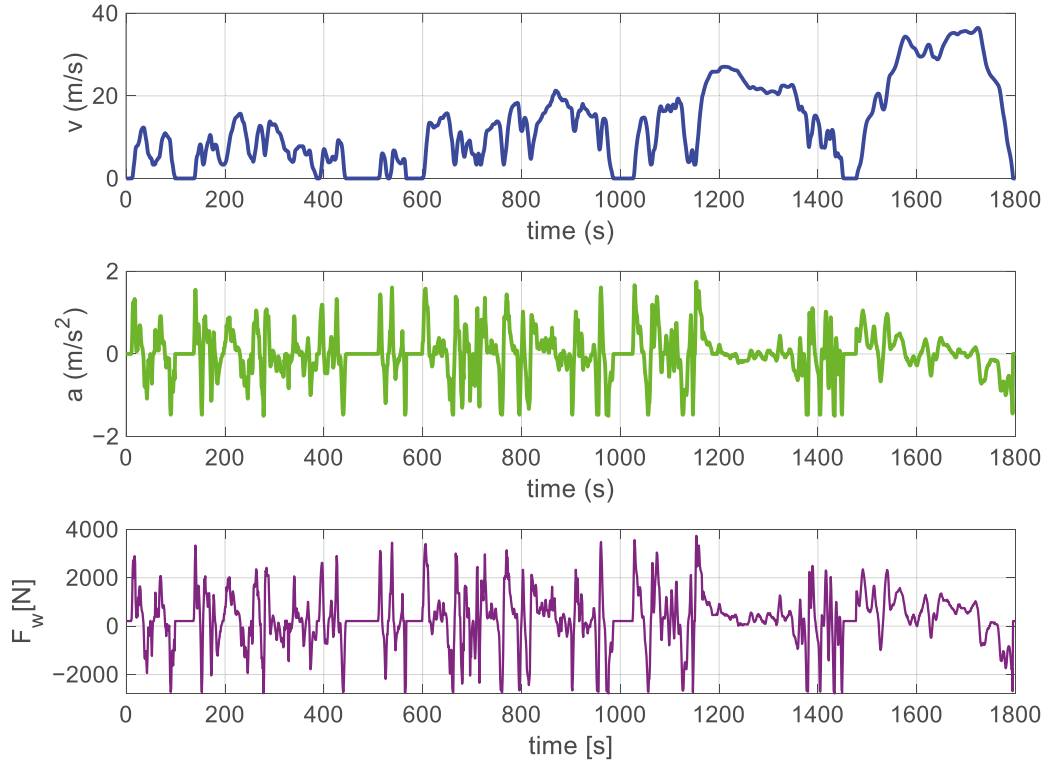

Figure 2. Vehicle speed, acceleration, and longitudinal wheel force are used as inputs for the powertrain energy analysis over the WLTP cycle.

The instantaneous mechanical power at the wheels is computed as:

$$P_w = F_{w,x} \cdot v = v\left(f_r \cdot W + \frac{1}{2} \cdot \rho \cdot C_D \cdot A_f \cdot v^2 + \frac{W}{g} \cdot \gamma \cdot \frac{\mathrm{d}v}{\mathrm{d}t}\right) \tag{9}$$

Based on the imposed speed profile, the wheel angular speed is obtained as:

$$\omega_w = \frac{v}{r_r} \tag{10}$$

where r_r is the rolling radius of the wheel.

The electric motor angular speed is obtained by applying the transmission ratio:

$$\omega_m = i_{tr} \cdot \omega_w \tag{11}$$

https://doi.org/10.3390/vehicles8030066

The mechanical torque at the wheels is determined from the power balance condition as:

$$T_w = \frac{P_w}{\omega_w} \tag{12}$$

while the torque demand at the electric motor shaft is obtained by accounting for the transmission ratio and drivetrain efficiency:

$$T_m = \frac{T_w}{i_0 \cdot \eta_{tr}} \tag{13}$$

where i_0 is the fixed transmission ratio and η_{tr} is the drivetrain efficiency.

Figure 3 presents the time evolution of the rotational speed, and mechanical torque at both the wheel and the electric motor shaft levels, confirming the validity of the adopted kinematic and dynamic conversion for mapping the WLTP driving cycle onto the torque–speed operating domain of the electric motor.

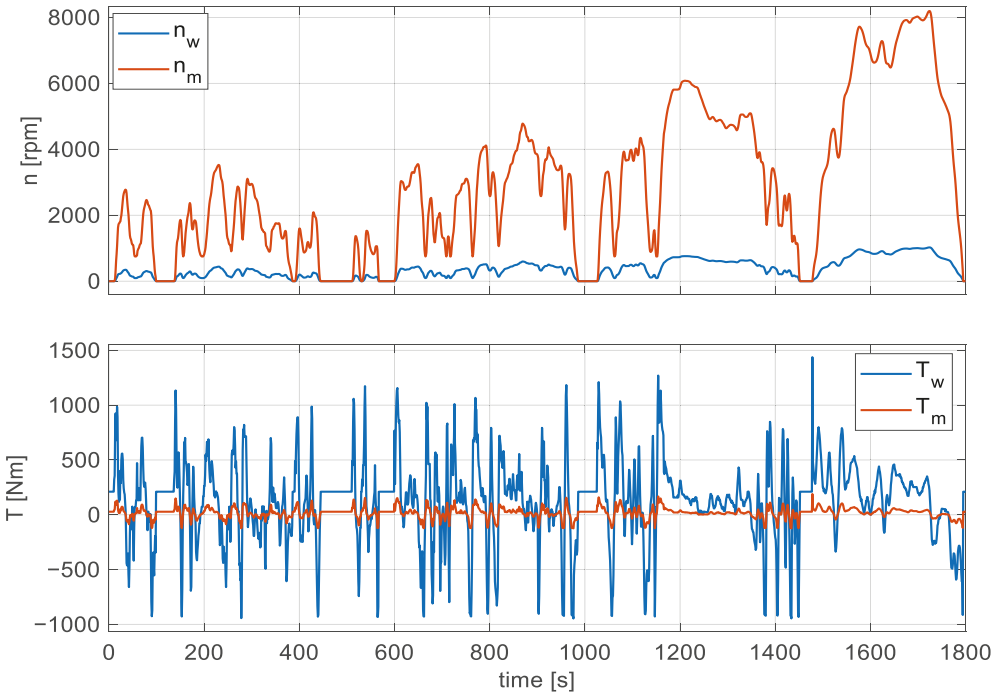

Figure 3. Rotational speed and torque response of the propulsion system over the WLTP driving cycle.

This transformation enables the direct mapping of the vehicle speed profile $v(t)$ onto the operating domain of the electric motor, defined by the (n_m, T_m) pairs, which are subsequently used to evaluate efficiency, current demand, and the overall energy performance of the propulsion system.

Figure 4 illustrates the distribution of the electric motor operating points in the torque–speed plane over the WLTP driving cycle. A high concentration of points is observed in the low- to medium-speed and moderate-torque region, corresponding to urban and extra-urban driving phases, while torque peaks occur at low speeds and the operating domain extends toward higher rotational speeds during high-velocity segments. This distribution provides the foundation for the efficiency mapping and energy consumption analysis presented in the following sections [4,5,24].

For interpretative purposes, the idealized torque–speed characteristic of the traction motor is introduced in Figure 5. This representation distinguishes the constant-torque region, limited by current capability, and the constant-power region, limited by the available inverter voltage under flux-weakening operation.

https://doi.org/10.3390/vehicles8030066

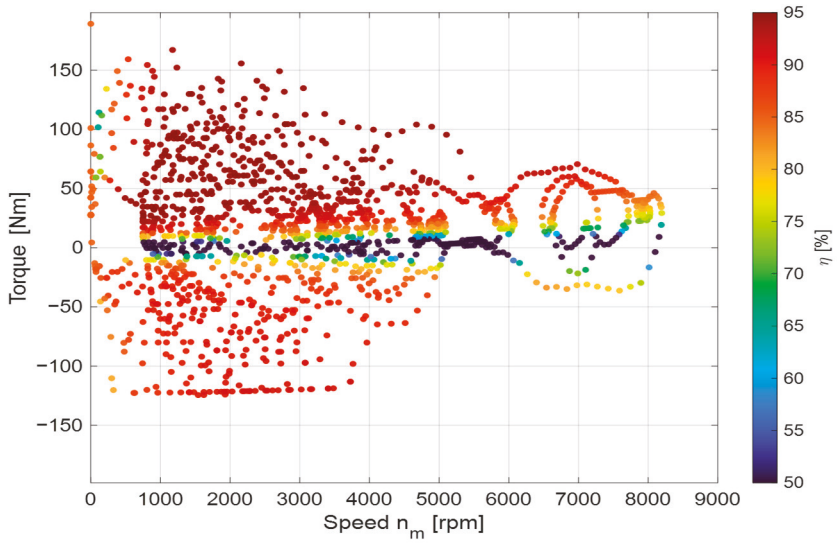

Figure 4. Operating points of the electric motor obtained from the vehicle longitudinal dynamic model over the WLTP driving cycle.

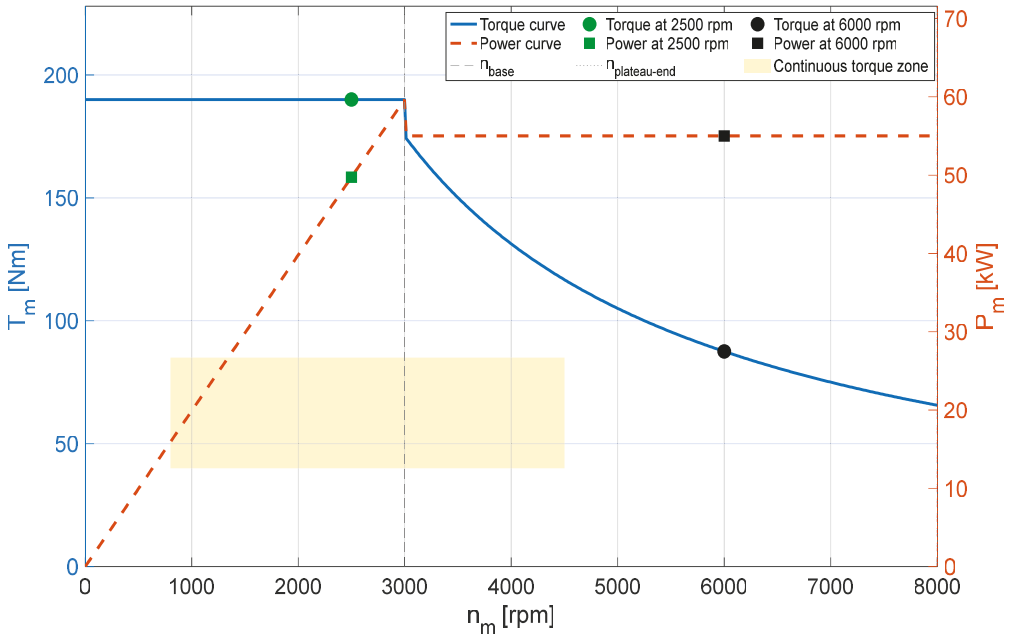

Figure 5. Idealized torque–speed characteristic of the electric traction motor.

The comparison between the actual operating points and this characteristic curve provides insight into motor loading, peak versus continuous operating conditions, and the adequacy of the selected motor and transmission parameters.

2.2. BEV Powertrain Configuration

The analyzed electric propulsion system is based on a conventional front-wheel-drive architecture with a single electric motor, which is representative of compact-class battery electric vehicles and is widely adopted in current production BEVs due to its simplicity, high efficiency, and reliability [1,3]. The electric motor is mounted on the front axle and is mechanically coupled to the driven wheels through a fixed-ratio single-speed transmission and a mechanical differential.

Figure 6 illustrates the drivetrain architecture of the BEV together with the direction of power flow during traction and the reversed torque flow during regenerative braking. During traction, electrical power is supplied by the battery and converted into mechanical

https://doi.org/10.3390/vehicles8030066

power by the inverter and the electric motor, before being transmitted to the wheels through the fixed-ratio transmission and the differential. During regenerative braking, a braking torque is generated at the wheels and transmitted back to the electric motor, allowing the recovery of kinetic energy through the inverter and the battery.

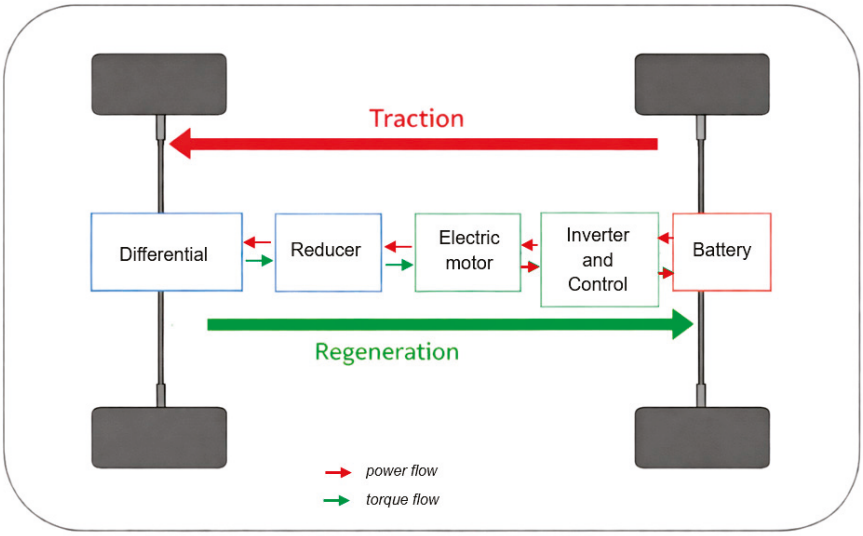

Figure 6. BEV drivetrain architecture with power and torque flow directions.

The propulsion system consists of four main components: the lithium-ion battery pack, the traction inverter, the PMSM, and the fixed-ratio mechanical transmission. The main vehicle parameters used in the simulations are summarized in Table 1 and are representative of current compact BEV platforms reported in WLTP-based studies.

Table 1. Main Parameters of the Vehicle.

Parameter	Symbol	Value	Unit
Vehicle weight	W	1950	kg
Rolling resistance coefficient	f_r	0.011	
Aerodynamic drag coefficient	C_D	0.26	
Frontal area	A_f	2.36	m^2
Air density	ρ_{air}	1.225	kg/m^3
Rotational mass inertia factor	γ	1.03	
Transmission ratio	i_0	8	
Transmission efficiency	η_{tr}	0.95	
rolling radius	r_r	0.351	m

The electrical energy stored in the battery is delivered to the inverter, which supplies the PMSM during traction operation or enables generator operation during regenerative braking, thus allowing bidirectional power flow within the propulsion system [3]. The electromagnetic torque developed by the motor is transmitted to the front wheels through the fixed-ratio transmission and the differential, providing vehicle propulsion.

The single-speed transmission configuration offers high efficiency and structural simplicity, while allowing the electric motor to operate over a wide speed range without gear shifting. As a result, a direct relationship is established between the motor operating region and the vehicle speed domain, highlighting the importance of appropriate PMSM sizing to ensure high-efficiency operation throughout the WLTP driving cycle.

https://doi.org/10.3390/vehicles8030066

2.3. PMSM Model and Efficiency Maps

The energy consumption analysis of the electric vehicle equipped with a PMSM is based on the correlation between the traction requirements imposed by standardized driving cycles and the electromagnetic characteristics of the traction motor. This approach enables the direct integration of motor efficiency maps into cycle-based energy assessments and is widely adopted in energy-oriented vehicle simulations [1,3,6].

The adopted methodology consists of three main stages:

1. Derivation of electromagnetic characteristics and efficiency maps by finite element analysis (FEM);
2. Projection of the WLTP operating points onto these maps to identify the dominant operating regions;
3. Evaluation of the vehicle energy balance, including specific energy consumption and the contribution of regenerative braking.

This framework is used to comparatively assess two PMSM traction motor configurations designed with the objective of reducing the permanent magnet mass while maintaining equivalent torque–speed performance levels, with potential benefits in terms of cost, sustainability, and supply-chain robustness for electric vehicle applications [6,8,18]. Furthermore, the impact of these design choices on the driving range and overall energy performance of the electric vehicle is assessed.

To ensure a fair comparison between the investigated rotor topologies, both PMSM variants are evaluated under identical electrical supply conditions, geometric constraints, and thermal limits. This ensures that any observed differences in efficiency, energy consumption, or driving range originate solely from the rotor topology.

To satisfy the torque and power requirements derived from the vehicle longitudinal dynamic model, two PMSM designs are considered. Both configurations share an identical stator geometry and overall dimensional envelope, while differing exclusively in the rotor magnetic topology. The constructive and electromagnetic constraints adopted for the PMSM design are summarized in Table 2.

Table 2. Main design and electromagnetic constraints of the traction PMSM.

Parameter	Symbol	Value/Specification	Remarks
Minimum continuous mechanical power at the shaft	P_{mec}	$\geq$50 kW	minimum value required for compact-class BEV applications
Maximum current density (RMS)	J_{max}	10–15 A/mm^2	limited by thermal and cooling constraints
Number of stator slots	Q	48	enables an optimal magnetic field distribution and harmonic reduction
Stator winding configuration	–	Three-phase hairpin winding	favorable for high efficiency at high loads and low-to-medium speeds
Number of rotor poles	2p	8	typical configuration for BEV traction motors
Cooling system	–	liquid cooling	required for high current densities and WLTP operating conditions

The geometric dimensions were defined as design inputs, following the imposition of the electromagnetic and constructive constraints outlined previously. The stator outer and inner diameters are 250 mm and 170 mm, respectively, while the rotor outer diameter and shaft diameter are 168.5 mm and 65 mm. The active axial length is set to 160 mm. These dimensions are representative of traction motors for compact-class BEVs and allow

https://doi.org/10.3390/vehicles8030066

continuous mechanical power levels of 70–90 kW, with peak power values of 100–120 kW over limited time intervals of 30–60 s.

Both designs employ interior permanent magnet (IPM) rotor configurations as presented in Figure 7 using NdFeB magnets doped with Dy/Tb and are equipped with three-phase hairpin windings, which are commonly adopted in automotive traction motors due to their high slot fill factor, favorable thermal behavior, and suitability for high-current operation [8,21]. Liquid cooling and a Class H insulation system are assumed to ensure reliable operation under WLTP duty conditions.

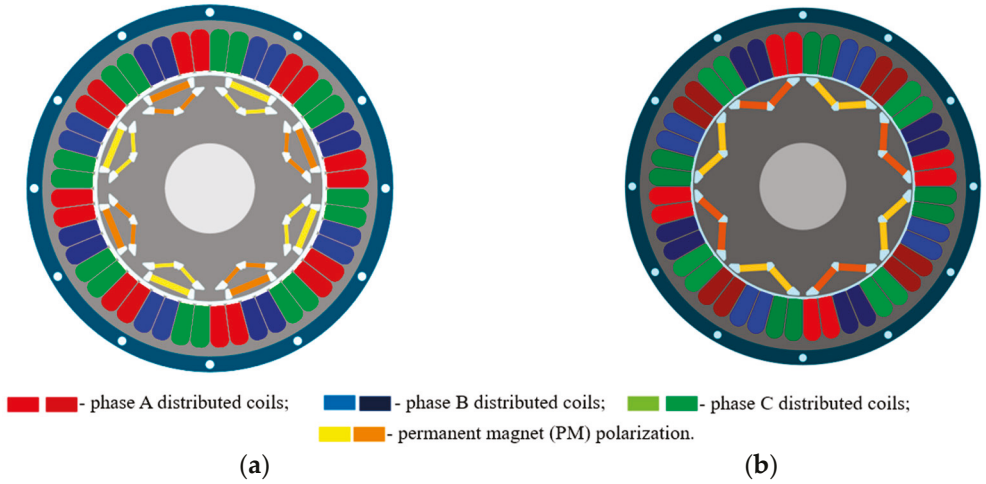

Figure 7. PMSM design for BEV traction: (**a**) M1: dual-layer IPM rotor; (**b**) M2: single-layer V-shaped IPM rotor.

The two PMSM rotor configurations investigated in this study are denoted as M1 and M2. The design parameters introduced in this section serve exclusively to define and differentiate the two topologies, while their electromagnetic performance and energy-related results are presented separately in Section 3.

The M1 rotor adopts a dual-layer IPM configuration, with two permanent magnet layers embedded in each rotor pole. This topology enhances the air-gap flux density and increases the contribution of permanent magnet torque, leading to improved torque capability at low speeds and increased resistance to demagnetization under high-load conditions, as reported for multilayer IPM designs [16,18]. However, this solution requires a larger volume of permanent magnetic material and involves higher manufacturing complexity.

In contrast, the M2 rotor employs a single-layer V-shaped IPM arrangement, which is widely adopted in production electric vehicles. This configuration provides a balanced contribution of permanent magnet torque and reluctance torque, enabling efficient operation over a wider speed range and improved field-weakening capability [16–18]. The V-shaped configuration facilitates extended high-speed operation while reducing the required permanent magnet mass, offering a favorable compromise between cost, efficiency, and performance.

By maintaining identical stator geometry and winding characteristics, the influence of the rotor magnetic topology on torque production, efficiency distribution, and operating range can be isolated and quantitatively evaluated by FEM.

The geometric parameters used to describe the embedded permanent magnets are defined in Figure 8, where only symbolic notations are indicated. In this figure, W_M and T_M denote the tangential width and radial thickness of the magnets, respectively, α is the V-angle, t_{tip} and t_{apex} represent the embedding depths at the magnet tip and at the V-apex, and r_{PM2} indicates the radial position of the inner magnet layer.

https://doi.org/10.3390/vehicles8030066

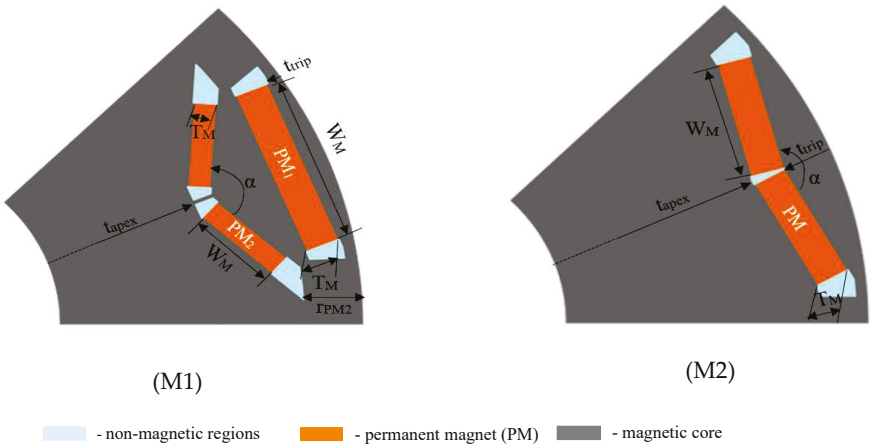

Figure 8. Technical specifications of the interior embedded permanent magnets of the traction.

The corresponding numerical values for each configuration are reported in Table 3. To reduce parasitic effects, an axial skew of 3.94° mechanical (approximately 7.9° electrical), corresponding to one stator slot pitch for an eight-pole rotor, is applied to the rotor magnets in both designs. This measure mitigates cogging torque and torque ripple, contributing to smoother operation and reduced acoustic noise, particularly at low speeds [8,14].

Table 3. Definition of the geometric parameters of the interior permanent magnets.

Parameter	Symbol	M1 (PM1 + PM2)	M2 (PM)
Tangential magnet width	W_M	28.0/15.0 mm	22.0 mm
Radial magnet thickness	T_M	4.0/2.6 mm	6.0 mm
V-angle	α	124°	124°
Embedding depth at tip	t_{tip}	2.5	15.0 mm
Embedding depth at apex	t_{apex}	21.0 mm	2.0 mm
Radial position of PM2	r_{PM2}	17.6 mm	–

Although the total motor masses of the two configurations are comparable, relevant differences arise at the rotor level due to the redistribution of active materials between permanent magnets and laminated ferromagnetic steel. These differences are summarized in Table 4.

Table 4. Comparative distribution of active materials and rotor inertia for the investigated PMSM configurations.

Characteristic	M1	M2
Total motor mass	76.15 kg	76.39 kg
Total rotor mass	34.07 kg	34.03 kg
Permanent magnet mass	3.07 kg	2.53 kg (−17% NdFeB)
Rotor inertia J_r	8.865×10^{-2} kg·m^2	8.999×10^{-2} kg·m^2

The M1 configuration employs a higher amount of NdFeB permanent magnets, resulting in an increased mass of active magnetic material at the rotor level. This design choice favors higher electromagnetic torque capability at low and medium speeds, at the expense of increased material cost and reduced sustainability.

In contrast, the M2 configuration achieves a reduction of approximately 17% in permanent magnet mass by compensating with a larger volume of laminated ferromagnetic

material. This solution leads to a more advantageous trade-off between performance, material cost, and resource availability.

The rotor inertia values of the two configurations differ only marginally, with M2 exhibiting slightly higher inertia. This variation is sufficiently small so that it is not expected to significantly affect the longitudinal dynamic behavior of the investigated electric vehicle.

A physically based evaluation of the inertia coefficient, accounting for rotor inertia and drivetrain parameters, is given by:

$$\gamma = 1 + \frac{J_r \cdot i_0^2}{W \cdot r_r^2}. \tag{14}$$

For the investigated motor configurations, this expression leads to $\gamma \approx 1.024$, which closely matches the value obtained from the empirical speed-dependent formulation adopted in the vehicle dynamic model.

The obtained values for the total motor mass and rotor component masses fall within realistic ranges for traction motors used in compact electric vehicles, thereby confirming the dimensional and constructive plausibility of the two proposed PMSM configurations and providing a coherent basis for the subsequent electromagnetic analysis.

To ensure methodological transparency and reproducibility, this subsection provides a detailed description of the finite element modeling procedure used to generate the PMSM electromagnetic performance maps, including the simulation environment, modeling assumptions, meshing strategy, material properties, and boundary conditions.

The electromagnetic behavior of the two PMSM traction motor configurations (M1 and M2) was investigated using a two-dimensional finite element model implemented in Altair FluxMotor Advanced, which is specifically dedicated to the design and electromagnetic analysis of rotating electrical machines and is based on a 2D magneto-quasi-static formulation. The problem was formulated using the magnetic vector potential A, derived from Maxwell's equations under magneto-quasi-static conditions. The governing equation solved over the computational domain is:

$$\nabla \times (v \cdot \nabla \times \mathrm{A}) = J + \nabla \times M \tag{15}$$

where A denotes the magnetic vector potential, ν is the magnetic reluctivity, J represents the impressed current density in the stator windings, and M denotes the magnetization vector of the permanent magnets. Nonlinear magnetic material behavior was accounted for by means of B–H characteristics for the ferromagnetic regions.

The machine geometries were discretized using second-order triangular finite elements with local mesh refinement in the air-gap region to accurately capture the high magnetic field gradients. A mesh refinement verification was conducted to ensure numerical convergence of the electromagnetic torque and loss calculations, indicating that further mesh densification produces negligible variations in the computed results.

Accordingly, the resulting nonlinear system of equations was solved using an iterative Newton–Raphson scheme combined with sparse matrix solvers. The numerical solution accuracy was verified through mesh refinement and convergence checks to ensure stable evaluation of torque and electromagnetic losses. Steady-state electromagnetic solutions were computed for discrete operating points corresponding to different current and speed levels, enabling the generation of torque–speed, power–speed, efficiency, and loss maps for both motor configurations. The electromagnetic torque was evaluated using Maxwell stress tensor and co-energy methods, as implemented in the Flux solver. The computed results were subsequently employed for the derivation of efficiency maps and loss distributions for the electromagnetic evaluation, operating conditions relevant to the investigated BEV

https://doi.org/10.3390/vehicles8030066

application were defined. A line voltage of 400 V was assumed, consistent with the battery and inverter architecture, together with a nominal current of 250 A and a maximum rotational speed of 14,000 rpm, representative of traction applications in the C-segment. The adopted control strategy is Maximum Torque Per Voltage (MTPV), which allows extension of the operating range beyond the base speed by optimally exploiting the inverter voltage limit.

Since high-speed operation has a direct impact on electromagnetic losses and thermal behavior, the simulations were carried out assuming a reference winding temperature of 150 °C. This value remains below the admissible limit of the Class H insulation system (180 °C), ensuring an adequate thermal safety margin under driving-cycle conditions.

The FEM simulations yielded efficiency maps, phase current distributions, electromagnetic loss maps, and characteristic torque–speed and power–speed curves for both motor configurations, as illustrated in Figure 9 Such FEM-based performance mapping is a well-established approach for traction motor evaluation and energy simulation of electric vehicles [6,21–23]. The resulting efficiency and loss maps constitute the input data for the vehicle-level WLTP energy simulations presented in the following sections.

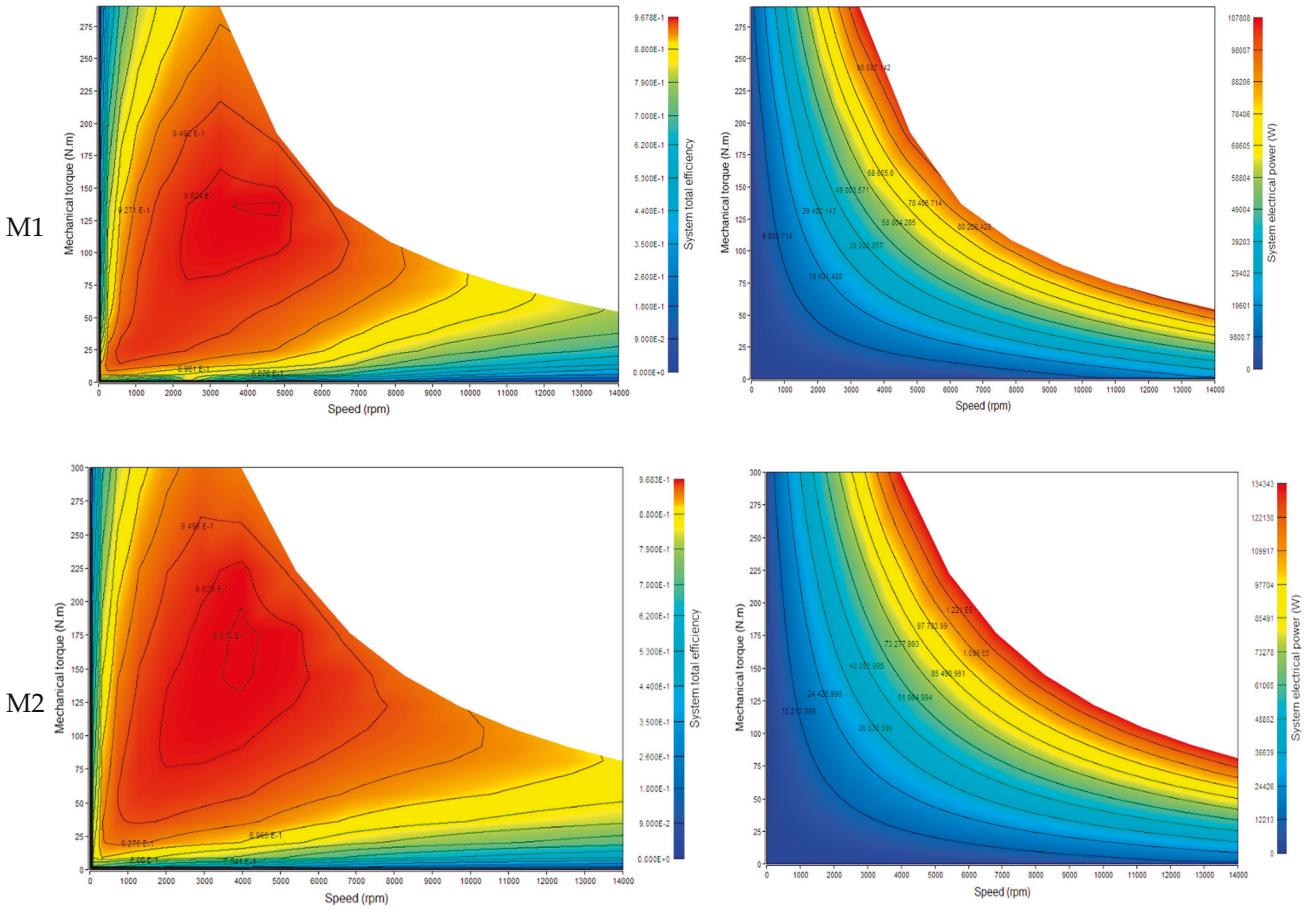

Figure 9. Electromagnetic performance maps of the investigated PMSM traction motors: (**a**) efficiency map; (**b**) absorbed electrical power as a function of torque and speed. Note: Scientific notation is displayed in the software format (e.g., 8E3 corresponds to 8×10^3 and numerical values are displayed in the default software format (without thousand separators)).

A comparative analysis of the efficiency maps highlights distinct functional differences between the two rotor architectures. The M1 configuration exhibits peak efficiency values in

the medium-speed and high-torque region, which corresponds to the dominant operating regimes of the WLTP driving cycle. In these regions, lower current levels are required to deliver the same mechanical power, resulting in reduced Joule losses and improved overall efficiency.

By contrast, the M2 configuration extends the high-efficiency operating region toward higher rotational speeds and demonstrates superior performance under field-weakening conditions. The V-shaped magnet rotor architecture facilitates high-speed operation with more balanced current requirements and a more uniform loss distribution, which is beneficial in terms of thermal stability and extended operation beyond the base speed.

The analysis of total electromagnetic losses further confirms these trends. M1 exhibits higher losses under maximum torque conditions and at elevated speeds, mainly due to the stronger magnetic flux associated with the increased permanent magnet content. In contrast, M2 shows a more gradual increase in losses across the operating range, leading to more favorable thermal behavior during high-speed operation.

The resulting efficiency and loss maps constitute the basis for the subsequent vehicle-level analysis, in which the operating points derived from the vehicle longitudinal dynamic model are superimposed onto the motor performance maps. This procedure enables the evaluation of energy consumption, efficiency distribution, and overall propulsion system performance over the WLTP driving cycle, as well as a comparative assessment of the impact of the two PMSM topologies on the driving range of the electric vehicle.

2.4. Traction Inverter Model and Electrical Losses

Within the energy conversion chain of the electric propulsion system, the traction inverter is responsible for converting the direct current supplied by the battery pack into the three-phase alternating current required by the permanent magnet synchronous motor (PMSM). During regenerative braking operation, the inverter enables bidirectional power flow, allowing the electrical energy generated by the machine to be transferred back to the battery.

In the adopted energy modeling framework, the motor efficiency $\eta_m(\omega_m, T_m)$ accounts exclusively for the internal electromagnetic losses of the PMSM, namely copper losses in the stator windings and magnetic losses in the ferromagnetic core, as derived from the FEM-based efficiency maps. The losses associated with the traction inverter are not included in motor efficiency and are therefore modeled separately, in accordance with common practice in energy-oriented electric vehicle simulations [6,7,21].

The power dissipated in the inverter is modeled as the sum of conduction losses and switching losses, according to the following expression:

$$P_{\text{inv}} = k_{\text{cond}} \cdot I_{\text{line}}^2 + k_{\text{sw}} \cdot f_e \cdot I_{line} \tag{16}$$

where I_{line} denotes the line current corresponding to the operating point, and f_e is the electrical frequency of the rotating magnetic field, defined as: $f_e = p \cdot \frac{n_m(t_k)}{60}$ with p representing the number of pole pairs and n_m the motor rotational speed expressed in revolutions per minute. The coefficients $k_{cond} = 0.02$ W/A^2 and $k_{sw} = 10^{-4}$ W/Hz are employed as lumped parameters to approximate conduction and switching losses, respectively. These coefficients do not correspond to a specific semiconductor technology but rather represent equivalent loss factors commonly adopted in system-level energy simulations, where the focus is placed on overall power flow and relative energy differences rather than on detailed device-level modeling [6,7].

This simplified formulation captures the combined influence of current magnitude and electrical frequency on inverter losses and is particularly suitable for transient operating conditions such as those encountered in standardized driving cycles (e.g., WLTP) [7,9].

https://doi.org/10.3390/vehicles8030066

In traction mode, the mechanical power required at the wheels P_w is referred to the motor shaft by accounting for the drivetrain efficiency η_{tr}, according to:

$$P_{\text{mec}} = \frac{P_w}{\eta_{\text{tr}}}, \tag{17}$$

where η_{tr} denotes the transmission efficiency.

The electrical power drawn from the battery is then expressed as:

$$P_{\text{bat,out}} = \frac{P_{mec}}{\eta_m(\omega_m, T_m)} + P_{inv} = \frac{P_w}{\eta_{tr} \cdot \eta_m(\omega_m, T_m)} + P_{inv} \tag{18}$$

During regenerative braking, the power flow is reversed, and the inverter operates in bidirectional mode. In this study, the effective regenerative power delivered to the battery is not computed explicitly at inverter level but is determined by the battery and regenerative braking model presented in Section 2.5, which accounts for generator efficiency and system-level limitations. Consequently, inverter losses during regenerative operation are implicitly included through the adopted battery-side formulation.

The inverter model is implemented using efficiency-based loss representation derived from steady-state operating maps, without explicit switching-frequency modeling. The battery is represented using an energy-based model referenced to usable capacity, neglecting detailed electrochemical dynamics. These assumptions are considered appropriate for cycle-level energy analysis but may not capture transient or temperature-dependent effects.

This explicit separation between motor losses, inverter losses, and battery behavior ensures a transparent and consistent formulation of the energy balance and is aligned with established modeling practices for electric vehicle energy consumption analysis [6,7,26].

2.5. Energy Source (Battery) Model and Operational Constraints

The energy source of the analyzed battery electric vehicle is a lithium-ion battery pack based on NMC pouch cells, with a usable energy of 85 kWh. The pack is configured in a 108s5p architecture, meaning that 108 cells are connected in series in each string to reach the required voltage level, while five such strings are connected in parallel to increase the overall capacity and current capability. Assuming a nominal NMC cell voltage of approximately 3.7 V, the 108-series configuration results in a pack voltage compatible with a 400 V traction system. The difference between gross and usable energy reflects the defined state-of-charge operating window implemented to ensure battery durability and lifetime [3,30,32].

The battery is modeled using a simplified equivalent electrical circuit, consisting of an open-circuit voltage source and an internal resistance. The open-circuit voltage of the pack is expressed as a function of SoC as:

$$U_{\text{oc}}(\text{SoC}) = N_s \cdot U_{0,\text{cell}}(\text{SoC}) \tag{19}$$

where N_s denotes the number of series-connected cells and $U_{0,cell}$ is approximated as a piecewise function of SoC based on representative voltage points. Accordingly, the pack open-circuit voltage varies between approximately 362 V at low SoC and 448 V at full charge.

Under load, the battery terminal voltage is given by:

$$U_{\text{bat}} = U_{\text{oc}}(\text{SoC}) - R_{\text{int}} \cdot I_{\text{bat}} \tag{20}$$

with R_{int} represents the equivalent internal resistance of the battery pack.

https://doi.org/10.3390/vehicles8030066

For the WLTP-based simulations, the initial state of charge is set to SoC = 100%. Owing to the limited SoC variation over a single WLTP cycle, the open-circuit voltage is assumed quasi-constant during one cycle, and its average value is used for computing battery current, voltage drop, and power balance. This assumption is consistent with common practice in cycle-level energy simulations and does not affect the comparative nature of the analysis between the two PMSM configurations. This modeling approach is widely adopted in energy-oriented electric vehicle simulations due to its robustness and low computational burden [5,9,32].

The instantaneous electrical power at the battery terminals is defined as:

$$P_{\text{bat}} = U_{\text{bat}} \cdot I_{\text{bat}} \tag{21}$$

The battery current is obtained by solving the corresponding power balance equation:

$$R_{\text{int}} \cdot I_{\text{bat}}^2 - U_{\text{oc}} \cdot I_{\text{bat}} + P_{\text{bat}} = 0 \tag{22}$$

which yields:

$$I_{\text{bat}} = \frac{U_{\text{oc}} - \sqrt{U_{\text{oc}}^2 - 4 \cdot R_{\text{int}} \cdot P_{\text{bat}}}}{2 \cdot R_{\text{int}}} \tag{23}$$

This formulation enables the direct computation of battery currents in both traction (discharge) and regenerative braking (charge) modes and provides a consistent basis for evaluating battery losses and power limitations.

Regenerative braking is modeled explicitly through the reversal of power flow whenever the longitudinal acceleration becomes negative and the mechanical power at the wheels is negative. Under these conditions, the power flow follows the sequence: wheels $\rightarrow$ transmission $\rightarrow$ motor $\rightarrow$ inverter $\rightarrow$ battery.

The electromechanical energy conversion efficiency during regenerative braking is evaluated pointwise using the FEM-derived motor efficiency maps. Instead of computing a dedicated generator-mode FEM map, the generator efficiency is approximated by mirroring the motoring efficiency map and applying a correction factor $k_{regen} = 0.95$, such as:

$$\eta_{\text{m,gen}}(\omega_m, T_m) = k_{\text{regen}} \cdot \eta_{\text{m}}(\omega_m, T_m) \tag{24}$$

This correction accounts for the additional losses associated with generator operation and control, while preserving the spatial distribution of efficiency obtained from the electromagnetic analysis.

At system level, a global regenerative efficiency factor $\eta_{sys,regen} = 0.70$ is introduced to account for the fact that only a fraction of the mechanically available braking energy is effectively recovered and transferred to the battery. This factor represents the combined effects of brake blending with mechanical brakes, battery charging power limitations, and SoC and thermal constraints imposed by the BMS, and is independent of the PMSM electromagnetic efficiency.

The electrical power injected into the battery during regenerative braking is expressed as:

$$P_{\text{bat,regen}} = -P_{\text{mec}} \cdot \eta_{m,\text{gen}} \cdot \eta_{\text{sys,regen}} \tag{25}$$

where $\eta_{m,gen}$ is evaluated at the instantaneous operating point (ω_m, T_m).

The corresponding regenerative battery current is obtained as:

$$I_{bat,regen} = -\frac{P_{\text{bat},regen}}{U_{\text{bat}}} \tag{26}$$

https://doi.org/10.3390/vehicles8030066

For the investigated configuration, it is assumed that battery current, SoC, and temperature limits imposed by the BMS are not reached over the WLTP cycle, such that regenerative braking is governed primarily by the dynamic requirements of the driving profile. This assumption is consistent with previous studies on cycle-level energy consumption of compact-class BEVs [5,9,27].

This battery and regenerative braking modeling approach provides a consistent and sufficiently accurate representation of energy extraction and recuperation, while avoiding unnecessary complexity relative to the main objective of the study, namely the comparative assessment of the energy performance of the two PMSM rotor topologies. The resulting battery power and current profiles constitute the basis for the WLTP-based energy balance and driving range evaluation presented in the following section.

2.6. WLTP Driving Cycle and Integrated Energy Simulation Procedure

The energy performance of the analyzed battery electric vehicle is evaluated by simulating its operation over the Worldwide Harmonized Light Vehicles Test Procedure (WLTP), which is adopted as an international reference for the assessment of energy consumption and driving range of electric vehicles [24,33].

The WLTP driving cycle is defined by a longitudinal vehicle speed profile $v(t)$ applied over a total duration of $T = 1800$ s, corresponding to a traveled distance of $d_{\text{cycle}} = 23.3$ km. The cycle includes representative urban, extra-urban, and high-speed driving phases, covering a wide range of operating conditions relevant for compact-class BEVs [24,25,34].

The energy simulation is performed using a deterministic, sequential workflow in which the imposed speed profile is successively transformed into mechanical and electrical quantities along the propulsion chain. Starting from the WLTP speed profile, the longitudinal vehicle model provides the required traction or braking forces at the wheels. These are then converted into mechanical torque and speed demands at the electric motor shaft, which are mapped onto the FEM-derived motor efficiency and current maps. Subsequently, inverter losses and battery electrical behavior are considered to determine the instantaneous battery power and current.

The overall structure of the energy simulation procedure, including the interaction between the WLTP driving cycle, the longitudinal vehicle dynamics, the electric motor, the traction inverter, and the battery model, is summarized in Figure 10.

The battery power P_{bat} constitutes the central quantity for the cycle-level energy balance. Positive battery power corresponds to traction operation and battery discharge, while negative battery power corresponds to regenerative braking and battery charging. The battery current is used consistently throughout the WLTP simulation.

The electrical energy exchanged with the battery over one driving cycle is obtained by integrating the battery power over time. In the numerical implementation, this integral is evaluated using a discrete summation over the WLTP time steps. The energy consumed from the battery is computed as:

$$E_{\text{cons}} = \int_0^T P_{bat,out}, (t) \cdot dt \approx \sum_{k=1}^{N} P_{\text{bat,out}}(t_k) \cdot \Delta \text{t} \tag{27}$$

Similarly, the total energy recovered through regenerative braking is computed by integrating the negative battery power:

$$E_{\text{regen}} = \int_o^T P_{bat,regen}(t) \cdot dt \approx \sum_{k=1}^{N} P_{\text{bat,regen}}(t_k) \cdot \Delta \text{t} \tag{28}$$

https://doi.org/10.3390/vehicles8030066

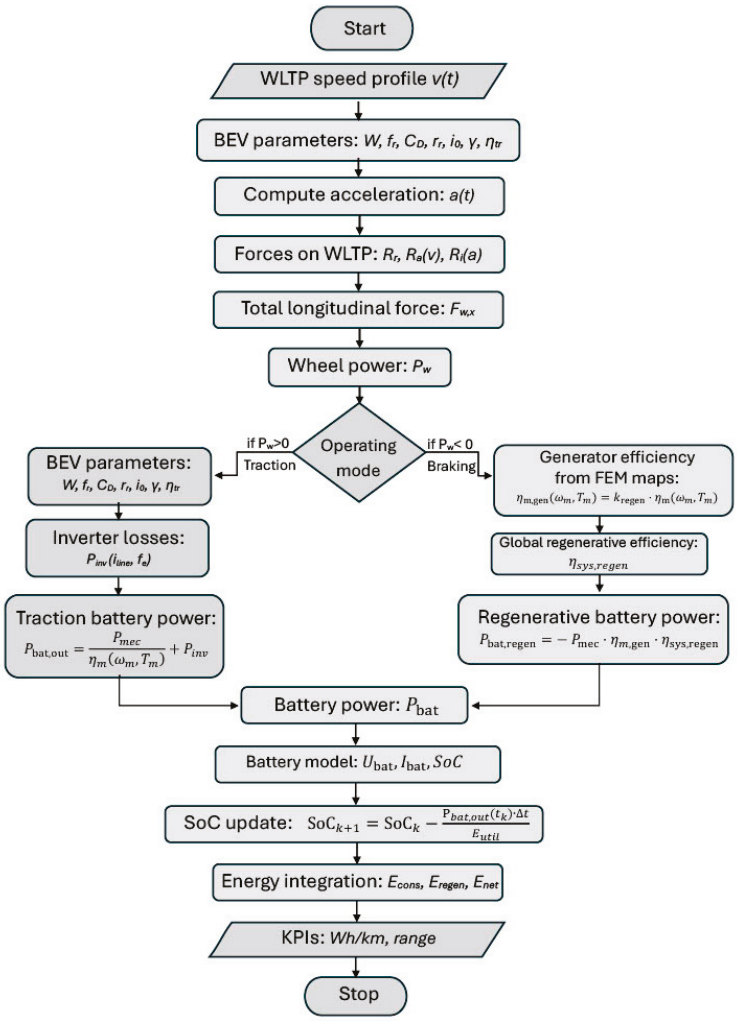

Figure 10. Flowchart of the proposed WLTP-based vehicle energy evaluation framework.

The net electrical energy extracted from the battery over one WLTP cycle is then expressed as:

$$E_{\text{net}} = E_{\text{cons}} - E_{\text{regen}} \tag{29}$$

The evolution of the battery state of charge is determined from the incremental energy balance, referenced to the usable battery energy E_{util}:

$$\text{SoC}_{k+1} = \text{SoC}_k - \frac{\text{P}_{bat,out}(t_k)\cdot\Delta t}{E_{util}} \tag{30}$$

This formulation naturally accounts for both discharge and recharge phases and ensures energetic consistency over the entire driving cycle [5,9].

Based on net energy consumption and the WLTP cycle distance, the specific energy consumption is calculated as:

$$C_{\text{WLTP}} = \frac{E_{\text{net}}}{d_{\text{cycle}}}[\text{Wh/km}] \tag{31}$$

The driving range is subsequently estimated as:

$$A \approx \frac{E_{\text{util}}}{E_{net}/d_{\text{cycle}}}[\text{km}] \tag{32}$$

https://doi.org/10.3390/vehicles8030066

The approximation in (27) and (28) results from the discrete-time integration of battery power using the WLTP sampling interval ($\Delta t = 1$ s). Given the relatively smooth variation in battery power over the driving cycle and the high temporal resolution of the WLTP speed profile, the numerical integration error is negligible compared to other modeling uncertainties, such as drivetrain efficiency assumptions and aerodynamic parameters.

Equation (32) assumes that the specific energy consumption obtained over one WLTP cycle is representative and scales linearly with the usable battery energy. This approximation neglects certain second-order effects, such as state-of-charge-dependent efficiency variations or thermal drift during extended operation. However, since the analysis is performed under identical boundary conditions for both motor topologies, this approximation does not affect the relative comparison, which constitutes the primary objective of this study.

The proposed WLTP-based simulation framework enables a coherent and reproducible evaluation of energy consumption, recuperated energy, and driving range, while maintaining a clear separation between component-level models and cycle-level energy accounting. By directly linking the FEM-derived electromagnetic performance of the PMSM traction motors to realistic vehicle operating conditions, the methodology provides a robust basis for the comparative energy assessment of the investigated motor topologies, in line with state-of-the-art BEV energy simulation approaches [4–6,9–12].

The above formulation provides a consistent description of the vehicle longitudinal dynamics, drivetrain power flow, and battery energy balance used in the WLTP-based simulations. This integrated approach enables the evaluation of rotor topology effects on vehicle-level energy consumption and driving range under realistic operating conditions.

3. Results

3.1. Comparative Analysis of PMSM Operating Points and Efficiency over the WLTP Cycle

The comparative analysis of the energy consumption of an electric vehicle equipped with the two previously analyzed permanent magnet synchronous motor (PMSM) variants was performed by projecting the operating points derived from the WLTP driving cycle onto the efficiency maps obtained from FEM-based electromagnetic simulations. This approach enables a direct assessment of the distribution of motor operating regimes and the associated efficiency levels under representative driving conditions.

The efficiency maps of M1 and M2 were integrated into a dynamic Matlab2023a/Simulink model, in which the motor operating points, defined by the pairs (n_m, T_m), were computed based on the WLTP speed profile. For regenerative braking operation, the efficiency maps were symmetrically extended into the negative torque domain, with a correction applied to account for inverter-related losses.

Figure 11 shows the superposition of the traction motor operating points on the efficiency maps for the two PMSM topologies analyzed. For both variants, the operating points are predominantly concentrated in the low- and medium-speed regions, below approximately 5000 rpm, and at moderate torque levels. These regions correspond mainly to the urban and extra-urban phases of the WLTP cycle. In these operating domains, both motors operate at high efficiency, typically exceeding 85% and frequently surpassing 90%.

Operating points associated with very high speeds or peak torque values appear only sporadically and represent a limited fraction of the total cycle duration. These regimes are mainly associated with short acceleration events or rapid transitions between WLTP phases and do not constitute dominant operating conditions. This distribution indicates that the WLTP energy demand is concentrated in efficiency-favorable operating regions of the traction motors.

https://doi.org/10.3390/vehicles8030066

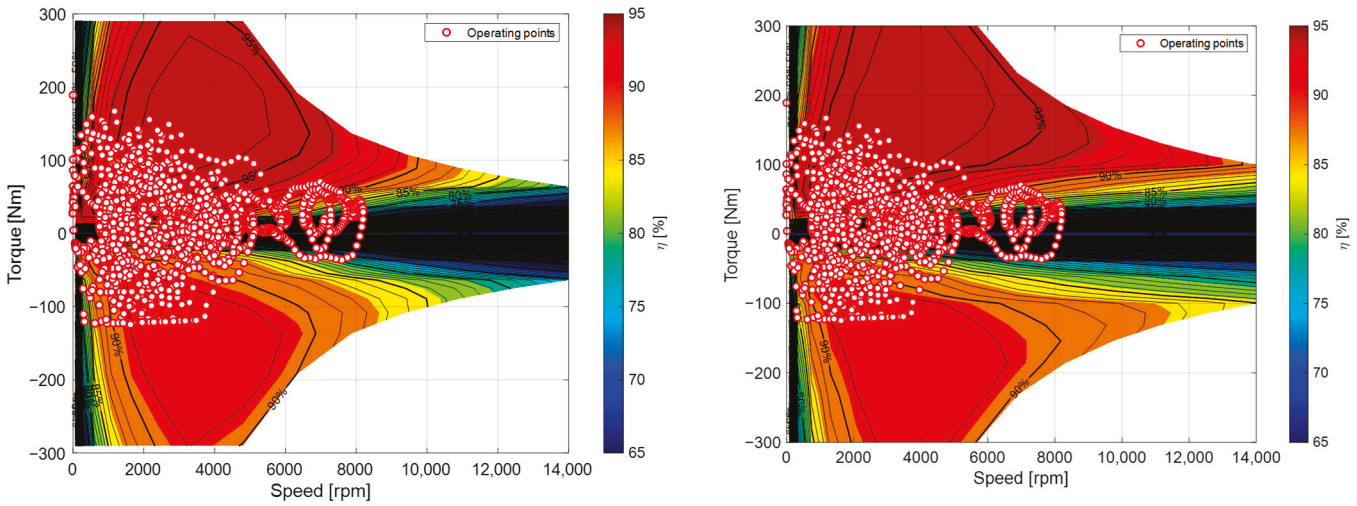

Figure 11. Superposition of traction motor operating points derived from the WLTP speed profile on to the motor efficiency maps.

The statistical distribution of operating points and the corresponding average efficiencies for both PMSM configurations are summarized in Table 4. In low-load regimes (0–50 Nm), representative of urban driving, both motors exhibit high efficiency at low speeds. However, M1 maintains higher average efficiency values than M2 in the medium-speed range (1000–5000 rpm) and at higher speeds (5000–8000 rpm). The statistical distribution of the operating points and the corresponding average efficiencies for both PMSM configurations over the WLTP cycle are summarized in Table 5.

Table 5. Summary of operating point distribution and average efficiency of M1 and M2 over the WLTP driving cycle.

Operating Regime	Speed Range [rpm]	Torque Range [Nm]	M1 $\eta_{average}$ [%]	M2 $\eta_{average}$ [%]	Main Observation
Low load (urban)	0–1000	0–50	~85.4	~84.1	Comparable efficiency at very low speed and torque
Low load (urban/cruise)	1000–5000	0–50	~81.7	~72.6	M1 maintains significantly higher efficiency
Low load (high speed)	5000–8000	0–50	~75.5	~68.9	Both outside optimal zone; M1 less penalized
Medium load (extra-urban)	1000–5000	50–100	~95.6	~94.9	Both operate in optimal efficiency region
High load (acceleration)	1000–5000	100–150	~95.8	~96.1	Similar peak efficiencies, rare operating points
Regenerative braking	1000–5000	−50 to −150	87–91	87–91	Efficient regeneration for both topologies
Regeneration at high speed	5000–8000	−50 to −150	~69.0	~63.0	Efficiency drop, more pronounced for M2

In low-load regimes (0–50 Nm), representative of urban driving, both motors exhibit high efficiency at low speeds. However, M1 maintains higher average efficiency values than M2 in the medium-speed range (1000–5000 rpm) and at higher speeds (5000–8000 rpm).

For medium-load conditions (50–100 Nm), associated primarily with extra-urban driving, both motors operate within their optimal efficiency region, achieving average efficiencies above 94% in the 1000–5000 rpm range. These operating conditions represent

https://doi.org/10.3390/vehicles8030066

the dominant contribution to the WLTP cycle. At higher load levels (above 100 Nm), both configurations maintain high efficiency at medium speeds, although these operating points occur infrequently and have a limited influence on total energy consumption.

In regenerative braking operation, corresponding to negative torque values, both PMSM configurations exhibit average electromagnetic efficiencies between approximately 87% and 91% in the 1000–5000 rpm range. At higher speeds, regenerative efficiency decreases for both motors, with a more pronounced reduction observed for M2. These operating regimes, however, account for a small portion of the WLTP cycle.

The temporal evolution of instantaneous motor efficiency over the WLTP cycle is presented in Figure 12. Rapid efficiency variations are observed due to frequent transitions of the operating point in the speed–torque plane. Both motors frequently reach instantaneous efficiency values above 90% and, in some intervals, above 95%. M1 exhibits a narrower dispersion of efficiency values and sustains high efficiency over longer time intervals.

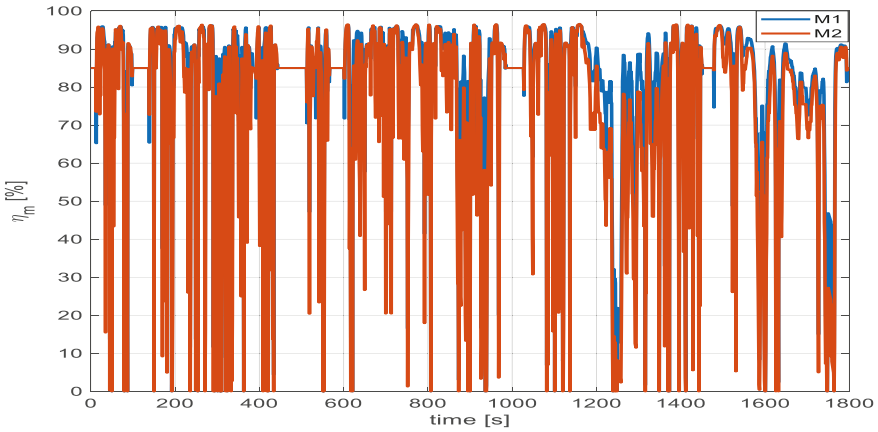

Figure 12. Temporal evolution of instantaneous motor efficiency over the WLTP cycle.

The weighted average efficiency over the entire WLTP cycle, reported in Table 6, is approximately 88.85% for M1 and 84.56% for M2. This difference reflects the distinct distribution of operating points across the efficiency maps for the two configurations.

Table 6. Average efficiency of motors over the entire WLTP cycle.

Motor Variant	$\eta_{average}$ [%]	Observation
M1	~88.85%	Higher overall efficiency; stable efficiency across typical WLTP operating conditions.
M2	~84.56%	Slightly lower overall efficiency; reduced efficiency during acceleration and braking events.

The correlation between the efficiency maps and the temporal evolution of efficiency indicates that local reductions in instantaneous efficiency are directly associated with transient transitions of the operating trajectory into less favorable energetic regions. Conversely, intervals characterized by high and stable efficiency correspond to periods during which the operating points remain concentrated within the maximum-efficiency regions of the FEM-derived maps.

3.2. Battery Power, Current, and Energy Balance over the WLTP Cycle

The distribution of electrical power drawn from the battery and injected into the battery through regenerative braking during vehicle operation over the WLTP driving cycle is shown in Figure 13. The battery power profile exhibits a mixed WLTP pattern,

https://doi.org/10.3390/vehicles8030066

characterized by extended intervals at low to moderate power levels and short-duration peaks at higher power demand.

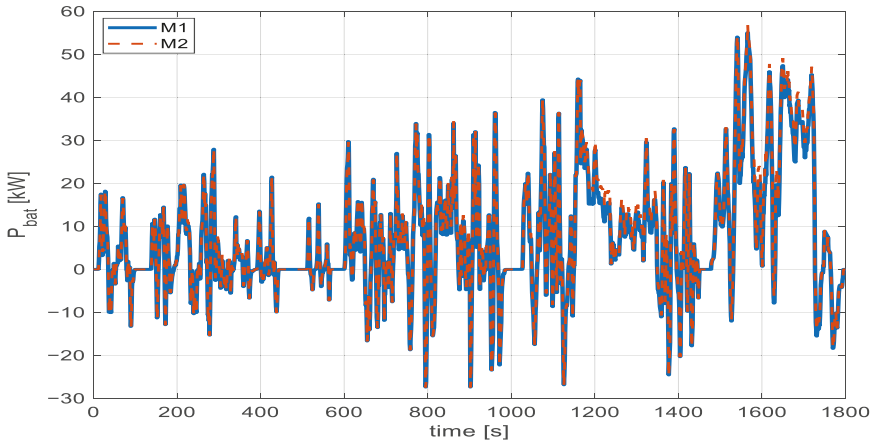

Figure 13. Battery power profile over the WLTP driving cycle (traction and regenerative braking).

During traction operation, the battery power demand remains predominantly below 20 kW. Power peaks occur mainly during acceleration phases and high-speed segments, reaching maximum values of approximately 55–57 kW. These events are limited in duration and represent a small fraction of the total cycle time.

During regenerative braking, the electrical power injected into the battery is concentrated mainly in the range of 5–20 kW (absolute values). Higher regenerative power pulses, reaching up to approximately 30 kW, occur only occasionally and are associated with more intense deceleration events in the urban and extra-urban phases of the WLTP cycle.

For the analyzed simulation conditions (WLTP cycle, transmission ratio $i_{tr} = 8$, current limit $I_{max} = 250$ A), the battery power delivered closely matches the power demand of the propulsion system. No discrepancies between requested and delivered power are observed, and no current limitation events occur. The maximum battery discharge current reaches approximately 131 A, while the minimum battery terminal voltage remains around 441 V, assuming an internal resistance of $R_{int} = 0.02\ \Omega$.

The differences between the two motor variants are reflected in the magnitude of the electrical power requested from the battery. The average absolute difference in requested battery power is approximately 0.735 kW, with a 95th-percentile value of 3.223 kW and a maximum difference of 6.195 kW. These deviations occur primarily during high-load operating windows.

The spatial distribution of electrical energy processed by the battery is shown in Figure 14. Traction energy is mainly accumulated at higher rotational speeds and moderate torque levels, while regenerated energy is concentrated at low to medium speeds combined with high negative torque values. The distribution of operating points in the (n_m, T_m) plane is similar for both motor variants.

Figure 15 shows the time evolution of the battery terminal current over the WLTP cycle. Peak discharge currents reach approximately 127–130 A, whereas regenerative currents typically remain within -50 to -65 A. The current profiles of the two motor variants are nearly identical over the entire cycle.

As shown in Figure 16 compares the battery terminal current with the stator winding line current of the electric motor. The motor line current reaches higher peak values, typically between 100 and 200 A, reflecting the DC/AC conversion performed by the inverter. In all cases, the battery current remains well below the imposed current limit.

https://doi.org/10.3390/vehicles8030066

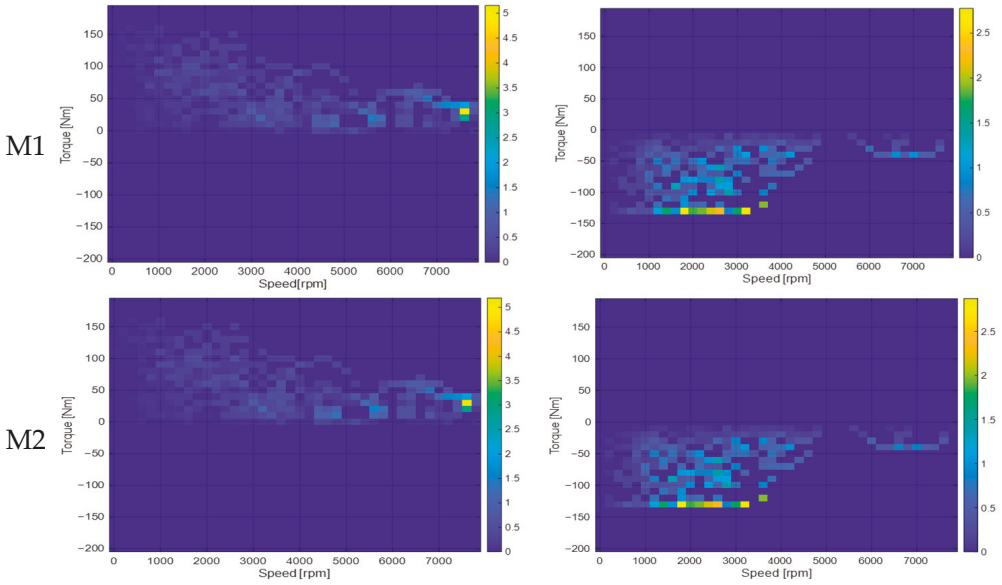

Figure 14. Spatial distribution of electrical energy processed by the battery in the motor speed–torque domain over the WLTP cycle: (**a**) traction energy; (**b**) regenerated energy.

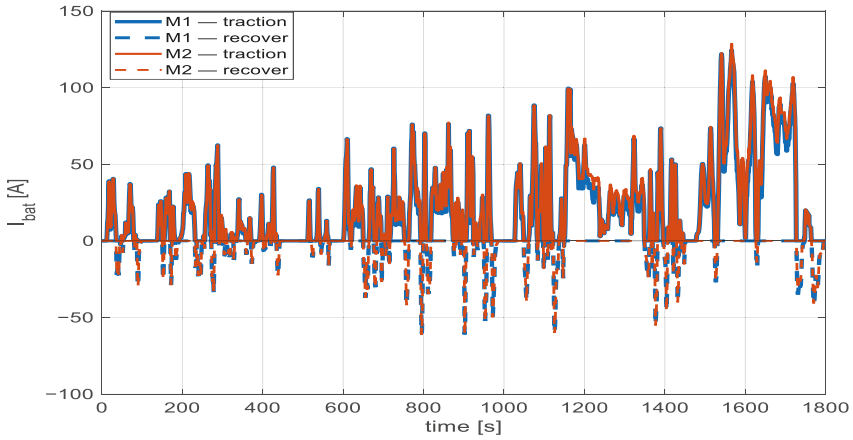

Figure 15. Time evolution of the battery terminal current over the WLTP driving cycle.

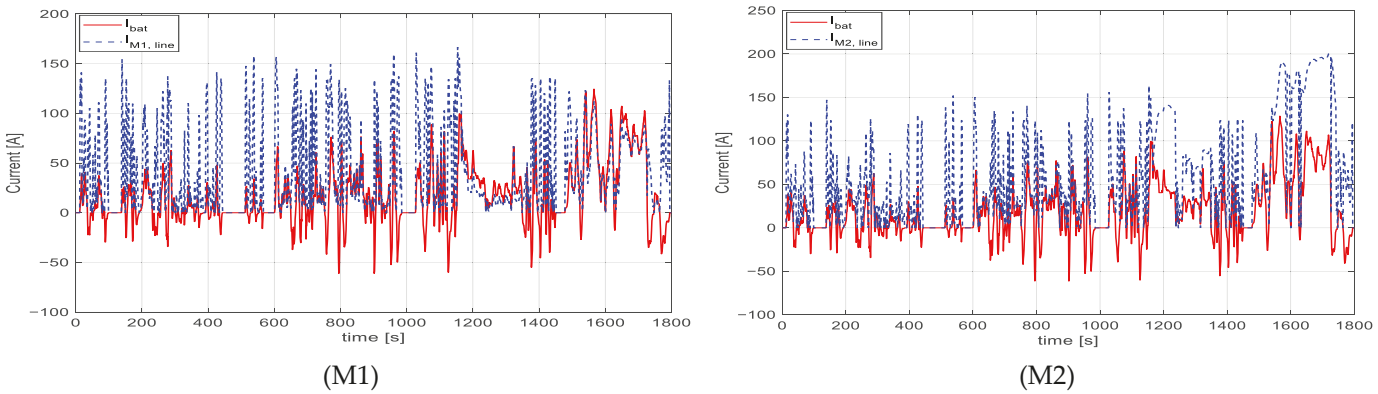

Figure 16. Comparison between the battery terminal current and the motor stator line current over the WLTP driving cycle.

Figure 17 shows the battery open-circuit voltage, terminal voltage, and current profiles. For M1, the average, 95th-percentile, and maximum voltage sag are 0.41 V, 1.64 V, and 2.53 V, respectively, while for M2 they are 0.71 V, 1.71 V, and 2.62 V. The RMS battery current

https://doi.org/10.3390/vehicles8030066

equals 35.1 A for M1 and 36.93 A for M2, leading to ohmic losses of 12.3 Wh and 13.6 Wh, respectively.

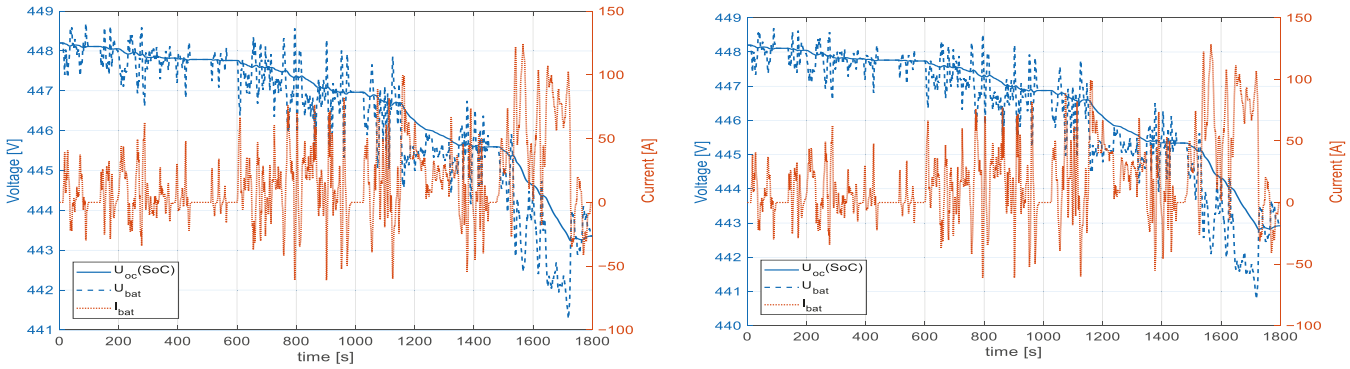

(M1) (M2)

Figure 17. Evolution of battery open-circuit voltage, terminal voltage, and current over the WLTP driving cycle.

3.3. Regenerative Braking Contribution

Figure 18a illustrates the cumulative evolution of traction energy consumption and energy recovered through regenerative braking over the WLTP cycle. The traction energy increases almost linearly with driving time, while regenerative braking introduces local reductions in the net energy extracted from the battery during deceleration phases.

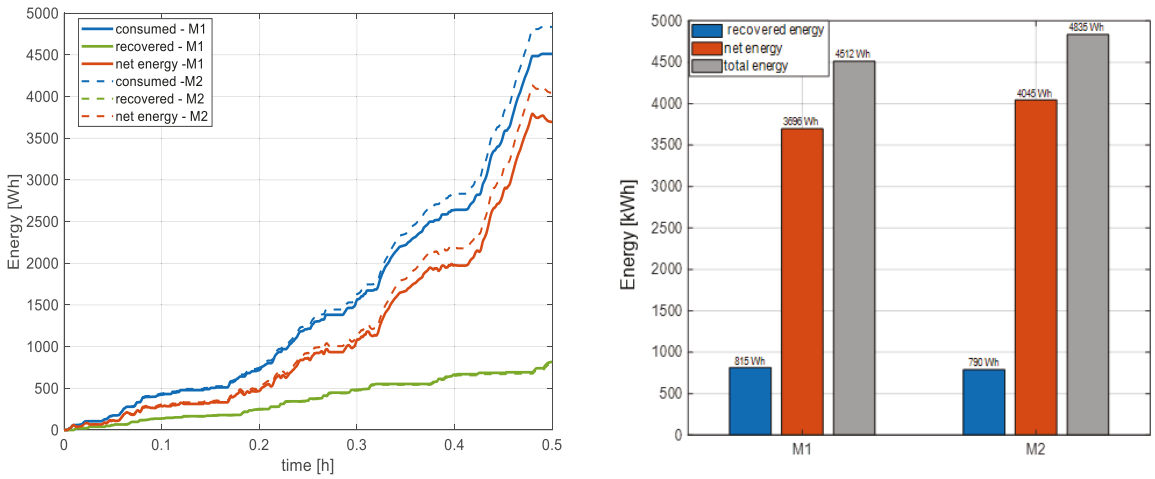

(**a**) (**b**)

Figure 18. Comparison of cumulative traction energy consumption, recovered energy, and net energy for M1 and M2 over the WLTP driving cycle: (**a**) cumulative energy evolution over time; (**b**) total energy balance per WLTP cycle (right) for M1 and PMS.

Figure 18b summarizes the integrated energy values. For M1, the traction energy is 4512 Wh, the recovered energy is 815 Wh, and the net energy extracted from the battery is 3696 Wh. For M2, the corresponding values are 4835 Wh, 790 Wh, and 4045 Wh. The difference in recovered energy between the two variants is limited, amounting to approximately 25 Wh (≈3%), whereas the difference in net energy is 349 Wh, corresponding to a reduction of approximately 9.14% in favor of M1. The ratio between recovered energy and traction energy is approximately 18% for M1 and 16% for M2.

Figure 19 presents the evolution of the battery state of charge (SoC) over the WLTP cycle. When regenerative braking is enabled, the final SoC increases by approximately

https://doi.org/10.3390/vehicles8030066

0.9–1.0 percentage points (pp) for both motor variants. The difference in final SoC between M1 and M2 under regenerative braking conditions is approximately 0.35–0.45 pp.

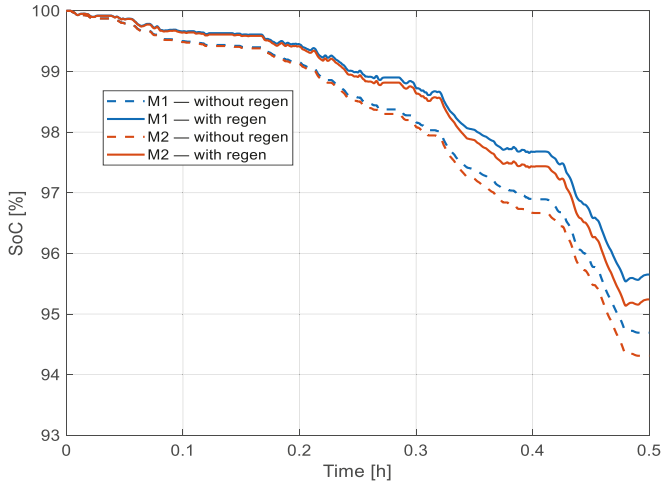

Figure 19. Evolution of the battery state of charge (SOC) over the WLTP cycle.

These results indicate that, under the WLTP driving cycle and the imposed battery constraints, the two motor variants exhibit similar regenerative energy recovery levels, while the differences in net energy consumption and final SoC are primarily driven by the traction energy demand.

3.4. WLTP Energy Consumption and Driving Range

The driving range of the BEV can be estimated from the net battery energy consumption over the WLTP cycle and the usable battery capacity. Figure 20 depicts the cumulative energy evolution over repeated WLTP cycles with and without regenerative braking. In both motor variants, cumulative energy increases nearly linearly with the number of cycles, while regenerative braking reduces the slope of this trend due to recovered energy during deceleration. For identical driving conditions, M2 consistently exhibits higher cumulative energy demand than M1.

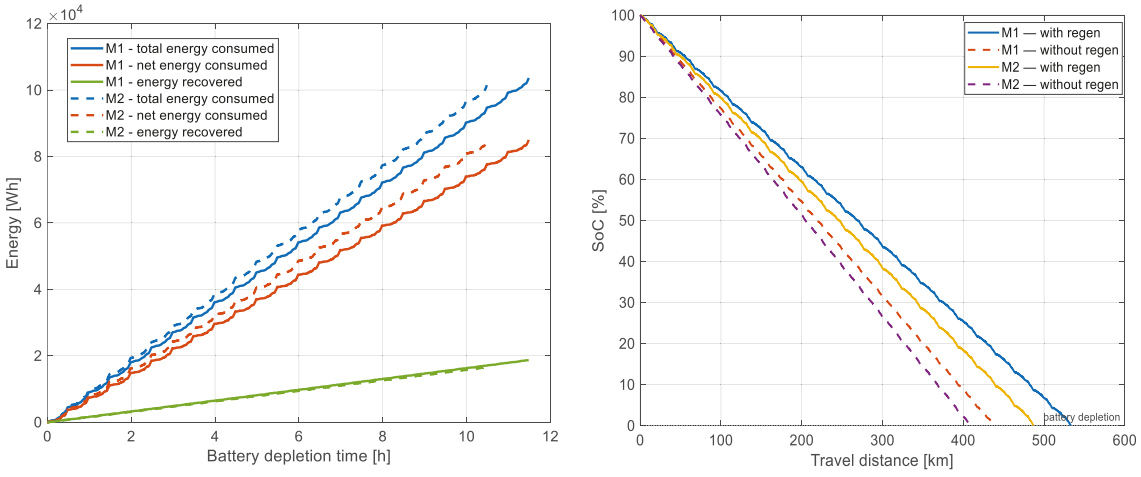

(**a**) (**b**)

Figure 20. Impact of regenerative braking on energy depletion and driving range for M1 and M2: (**a**) Energy consumption until battery depletion (**b**) state-of-charge evolution versus driving distance (**b**) for M1 and M2 with and without regenerative.

https://doi.org/10.3390/vehicles8030066

Figure 21 presents the specific energy consumption and the estimated driving range. M1 exhibits lower specific energy consumption than M2, both with regenerative braking (approximately 159 Wh/km versus 174 Wh/km) and without regenerative braking (approximately 194 Wh/km versus 208 Wh/km). With regenerative braking, the estimated driving range is approximately 535 km for M1 and 489 km for M2. Without regenerative braking, the corresponding values are approximately 438 km and 409 km, respectively.

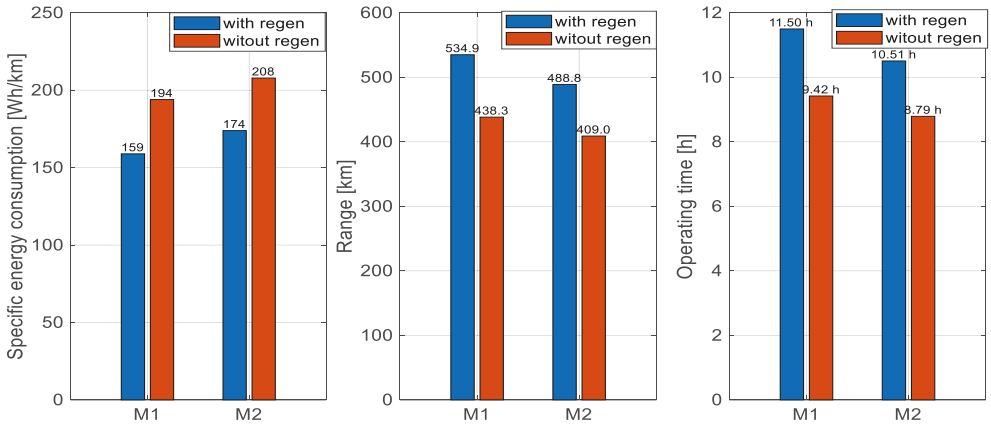

Figure 21. Comparison of BEV key performance indicators (KPIs) for M1 and M2 with and without regenerative braking.

3.5. Comparative Performance Synthesis of the Investigated PMSM Configurations

This subsection provides a concise synthesis of the WLTP-based results obtained for the two PMSM traction motor configurations under identical vehicle parameters, battery characteristics, inverter constraints, and control strategies.

Both propulsion systems operate within similar speed–torque domains imposed by the WLTP driving cycle and the fixed transmission ratio. Quantitative differences are observed in net electrical energy consumption, efficiency distribution, and battery utilization. The M1 configuration consistently exhibits lower net energy consumption per cycle, reduced specific energy consumption, and a higher achievable driving range compared to M2.

Battery power and current profiles confirm that both configurations operate within electrical limits, without current saturation or voltage constraints. M1 shows slightly lower RMS battery currents, reduced voltage sag, and lower integrated ohmic losses. Regenerative braking performance is comparable for both configurations, with similar amounts of recovered energy and recovery ratios.

The driving range is significantly increased by regenerative braking for both motor configurations (Figure 21). For M1, the range rises from 438.3 km (without regeneration) to 534.9 km (with regeneration), corresponding to an improvement of approximately 22%. For M2, the range increases from 409.0 km to 488.8 km, i.e., by about 19.5%.

The adopted vehicle parameters and the resulting specific energy consumption values fall within the typical range reported for compact-class BEVs under WLTP conditions (150–200 Wh/km), confirming the physical consistency of the simulation framework.

In both operating scenarios, M1 achieves a higher driving range than M2, confirming the superior energy efficiency of the dual-layer IPM rotor configuration.

4. Discussion

4.1. Impact of Rotor Topology on Operating Point Distribution and WLTP Efficiency

The obtained results highlight the influence of rotor architecture on the distribution of PMSM operating points over the WLTP driving cycle and on the overall energy efficiency of the electric vehicle. The two investigated motor configurations are comparable in terms

https://doi.org/10.3390/vehicles8030066

of dimensions, total mass, and rated power. However, differences in magnetic topology lead to distinct behaviors under real operating conditions.

A first key aspect concerns the correlation between the WLTP-imposed operating point distribution and the regions of maximum efficiency identified on the FEM-derived efficiency maps. The analysis indicates that vehicle operation is dominated by low- and medium-speed regimes combined with moderate torque levels, which are characteristic of urban and extra-urban driving. In this operating domain, M1 exhibits a structural advantage by maintaining higher and more stable efficiency levels even outside the strictly optimal efficiency region, particularly at medium speeds and low loads that frequently occur in everyday vehicle use.

The approximately 4% difference in average efficiency between M1 and M2 over the WLTP cycle becomes relevant at the system level as it accumulates over long operating durations and across many operating points.

In contrast, M2 exploits its structural advantages mainly in the medium- to high-load domain and at higher rotational speeds, where the V-shaped rotor architecture enables more efficient operation under field-weakening conditions. However, these operating regimes are only weakly represented in the WLTP cycle, which explains why the local efficiency advantages of M2 do not translate into a global energy benefit over the analyzed driving cycle.

The behavior under regenerative braking further confirms the differences between the two rotor topologies. Both motors exhibit high regenerative electromagnetic efficiency in the medium-speed range, which dominates the WLTP cycle. Nevertheless, at higher speeds, M1 maintains more favorable regenerative efficiency values.

The temporal evolution of instantaneous efficiency highlights the superior stability of M1, characterized by reduced fluctuations and frequent maintenance of efficiency levels above 90%. From an operational standpoint, this stability is an important indicator of thermal loading and robustness, as large efficiency variations are associated with corresponding variations in losses and thermal fluxes within the motor and inverter.

From a techno-economic perspective, the results confirm the existence of a clear trade-off between permanent magnet mass reduction and energy efficiency. M2 reduces the amount of NdFeB material and dependency on critical raw materials; however, this benefit is partially offset by a slightly lower global efficiency over the WLTP cycle. In contrast, M1 employs a larger amount of permanent magnet material but delivers more favorable energy behavior, particularly in urban and peri-urban driving.

It should be noted that the obtained results depend on the selected transmission ratio and the adopted control strategy. In this study, a standard MTPV strategy and a fixed transmission ratio representative of compact BEVs were employed. Further optimization of these parameters could alter the operating point distribution and potentially reduce the observed differences between the two motor topologies. Moreover, the analysis is limited to the WLTP cycle and does not include aggressive driving scenarios or sustained high-speed operation, where the advantages of M2 may become more pronounced.

4.2. Battery Load and System-Level Implications

The comparative analysis of battery power, current, and energy balance over the WLTP driving cycle provides valuable insight into how PMSM rotor topology influences battery loading and the overall efficiency of the propulsion system. Since vehicle dynamics, transmission ratio, inverter constraints, control strategy, and battery parameters are identical for both configurations, the observed differences can be directly attributed to the electromagnetic and efficiency characteristics of the two motor designs.

https://doi.org/10.3390/vehicles8030066

The WLTP power demand profile is dominated by extended intervals at low to moderate battery power levels, interspersed with short-duration peaks associated with acceleration events and high-speed operation. Peak traction power at the battery terminals reaches approximately 55–57 kW, while regenerative braking power is mainly concentrated in the 5–20 kW range. This distribution confirms that the WLTP cycle imposes moderate average electrical loading on the battery, with limited exposure to extreme operating conditions. Consequently, both propulsion system configurations operate well within the electrical and thermal limits of the battery pack and inverter, indicating that the system is appropriately dimensioned for the targeted BEV application.

A key outcome of the analysis is that no current or voltage limiting occurs throughout the WLTP cycle. The maximum battery current remains well below the imposed limit of 250 A, with peak discharge currents of approximately 127–131 A and regenerative currents in the range of -50 to -60 A. The absence of current saturation or voltage curtailment indicates that the battery does not act as a performance constraint under the conditions investigated. As a result, the differences observed between M1 and M2 arise exclusively from differences in the electrical power required to meet identical mechanical demands at the wheels, rather than from battery-side limitations.

At the system level, M2 exhibits a slightly higher average battery power demand than M1, particularly during high-load operating intervals. The mean absolute difference in required battery power is approximately 0.7 kW, with a 95th percentile below 3 kW and occasional peaks approaching 6.34 kW. Although these deviations correspond to up to 10% of the instantaneous peak power, they occur infrequently and remain modest relative to the overall power level. Nevertheless, when integrated over the entire WLTP cycle, these differences result in a measurable increase in total energy drawn from the battery for M2.

M1 maintains slightly higher efficiency and lower current demand in operating regions associated with elevated torque and speed, which coincides with peak battery power demand. In contrast, M2, while advantageous in terms of permanent magnet mass reduction and high-speed field-weakening capability, exhibits marginally higher electrical losses in these regions, leading to increased battery power demand and higher RMS current.

The temporal evolution of the battery current for both motor variants shows nearly overlapping profiles over most of the WLTP cycle, with small but systematic deviations during high-load segments, where M2 tends to draw slightly higher current. These differences are reflected in higher RMS current values for M2, which in turn lead to increased integrated ohmic losses within the battery, despite identical internal resistance and operating conditions.

Voltage sag statistics reinforce this conclusion. Although the absolute voltage drop at the battery terminals remains moderate for both configurations, M2 exhibits slightly higher average and peak voltage sag, as well as a greater proportion of operating time at elevated sag levels. While these differences are not critical under WLTP conditions, they indicate a less uniform electrical loading of the battery and increased internal dissipation. Over extended operation, such effects may contribute to higher thermal stress and accelerated battery aging.

The spatial distribution of energy flow in the speed–torque plane confirms that these effects are not driven by differences in vehicle operation. The operating point distribution is nearly identical for both variants and is dictated by the WLTP cycle and the fixed transmission ratio. However, M2 shows slightly higher energy weight in high-speed regions, consistent with its increased battery power demand in those conditions.

https://doi.org/10.3390/vehicles8030066

4.3. Contribution and Limits of Regenerative Braking

The contribution of regenerative braking to the overall energy balance of the battery electric vehicle was evaluated by comparing the total traction energy, the recovered energy, and the net energy extracted from the battery over the WLTP driving cycle. The cumulative evolution of these quantities highlights the nearly linear growth of traction energy typical of standardized driving cycles, as well as the role of regenerative braking in locally reducing the net energy demand by recovering a fraction of the vehicle's kinetic energy during deceleration phases.

For the same WLTP profile and identical battery constraints (nominal voltage, internal resistance, and current limits), the two PMSM configurations exhibit very similar amounts of recovered energy: approximately 815 Wh for M1 and 790 Wh for M2. The relatively small difference (≈3%) indicates that the regenerative braking capability is only weakly influenced by the rotor topology under WLTP conditions.

In contrast, significant differences emerge in traction energy consumption. The total energy required for propulsion prior to subtracting the regenerative contribution amounts to approximately 4512 Wh for M1 and 4835 Wh for M2, leading to a net energy difference of about 349 Wh (≈9.14%) in favor of M1.

The fraction of recovered energy relative to traction energy further supports this conclusion. The ratio $E_{\mathrm{reg}}/E_{\mathrm{cons}}$ is approximately 18% for M1 and 16% for M2. Both values fall within the typical range reported for WLTP-based BEV assessments (≈15–25%), corresponding to an overall regenerative efficiency on the order of 65–80%.

When referenced to the global regenerative efficiency adopted in the model (η_{regen} = 0.70), the recovered electrical energies correspond to available mechanical braking energies of approximately 1.16 kWh for M1 and 1.10 kWh for M2 per WLTP cycle. A hypothetical increase in regenerative efficiency from 0.70 to 0.80 would yield an additional recovered energy of 0.12 kWh for M1 and 0.11 kWh for M2 per cycle, translating into a net energy reduction of only about 5%.

The evolution of the battery state of charge over the WLTP cycle confirms that regenerative braking increases the final SoC by approximately 0.9–1.0 percentage points for both configurations, directly consistent with the recovered energy values. The remaining SoC difference between M1 and M2 under regenerative conditions (≈ 0.35–0.45 pp) corresponds to an energy surplus of about 350 Wh and is primarily attributable to reduced traction losses in M1.

4.4. Implications for Driving Range and Powertrain Design

The WLTP-based energy analysis indicates that, although both motor configurations recover comparable amounts of energy during deceleration, the M1 configuration consistently achieves lower net energy consumption per cycle, resulting in an extended driving range. This advantage originates from the distribution of operating points imposed by the WLTP cycle and their alignment with the respective efficiency maps. For identical wheel-level mechanical demands, M1 operates more frequently in high-efficiency regions and requires lower current, which reduces Joule losses in the motor, inverter, and battery and leads to more stable voltage behavior. Conversely, M2 exhibits higher current demand in certain operating regions, particularly at elevated speeds, thereby increasing ohmic losses and overall battery energy extraction.

When integrated over a complete driving cycle and extrapolated to full battery depletion, these effects accumulate and yield measurable differences in total energy consumption and driving range. The nearly constant ratio between recovered and consumed energy supports the representativeness of single-cycle WLTP results for extended operation, indicating that the observed differences are structural rather than cycle-specific.

https://doi.org/10.3390/vehicles8030066

From a powertrain design perspective, the results demonstrate that reducing permanent magnet mass does not necessarily lead to lower energy consumption. While the M2 configuration offers advantages in terms of rare-earth material reduction and high-speed capability, these benefits are only marginally exploited under WLTP conditions, where low-to-medium speed and moderate torque operation dominates. In contrast, the M1 configuration is better matched to these prevailing operating regimes.

The results further show that regenerative braking plays a major role in extending the driving range of the BEV investigated, regardless of PMSM rotor topology. For the M1 configuration, the activation of regenerative braking increases the range from 438.3 km to 534.9 km, corresponding to a relative improvement of approximately 22%. A similar trend is observed for the M2 configuration, for which the range increases from 409.0 km to 488.8 km, i.e., by about 19.5%.

Beyond the effect of regeneration, a systematic difference between the two motor topologies is observed. In both cases (with and without regenerative braking), the M1 motor provides a higher driving range than M2. This behavior can be attributed to the higher average electromagnetic efficiency of the dual-layer IPM rotor, particularly in the low- and medium-speed operating regions that dominate the WLTP cycle. Consequently, lower electrical power is required from the battery to meet the same traction demand, leading to reduced energy consumption and increased vehicle range.

Furthermore, the slightly smaller benefit of regenerative braking observed for M2 suggests that its lower generator-mode efficiency at higher speeds limits the amount of recoverable energy during deceleration events. These findings highlight the importance of matching PMSM rotor topology to realistic driving-cycle operating conditions, rather than optimizing motor design solely for peak efficiency or high-speed performance.

Overall, the results indicate that BEV driving range is primarily governed by traction efficiency in the most frequently visited operating regions, while regenerative braking provides a secondary but significant contribution. The proposed methodology therefore offers a consistent basis for selecting PMSM rotor architectures according to the intended vehicle usage profile rather than peak-performance criteria alone.

While the present analysis focuses on the influence of rotor topology on vehicle-level energy performance, certain modeling simplifications should be acknowledged. Simplified inverter and battery representations may introduce deviations under highly dynamic load conditions or extreme thermal states. However, as both motor configurations are evaluated under identical modeling assumptions, the comparative conclusions remain unaffected.

Although the present study focuses on the impact of rotor topology on vehicle-level energy efficiency and driving range, other important industrial selection criteria such as manufacturing cost, thermal management, and long-term durability must also be considered. In the current analysis, both motor variants are evaluated under identical electrical, geometric, and thermal boundary conditions to isolate the influence of the electromagnetic design. Consequently, aspects such as detailed thermal management strategies, thermo-mechanical stresses, and lifecycle durability of the rotor structures are not explicitly modeled. Similarly, while differences in permanent-magnet material usage may have implications for manufacturing cost and supply-chain considerations, a comprehensive techno-economic assessment is beyond the scope of this work. These aspects represent important directions for future research, where multi-objective optimization frameworks integrating energetic, economic, and thermo-mechanical criteria could provide a more complete industrial evaluation of the proposed motor configurations.

Although the present study is limited to the WLTP Class 3 cycle, which represents moderate and standardized driving conditions, the operating-point distribution under more aggressive or sustained high-speed scenarios may differ significantly. Such conditions

https://doi.org/10.3390/vehicles8030066

could modify the relative efficiency performance of the motor topologies investigated. The proposed framework, however, is cycle-independent and can be directly applied to alternative driving profiles to evaluate topology robustness under diverse operating regimes.

5. Conclusions

This paper investigated the energy performance of two permanent magnet synchronous motor (PMSM) traction topologies for battery electric vehicles using a unified WLTP-based energy evaluation framework. The analysis combined FEM-derived motor efficiency maps with a longitudinal vehicle model, inverter loss modeling, battery constraints, and regenerative braking to assess the impact of rotor topology on real-world energy consumption and driving range.

- Even relatively small differences in the efficiency distribution of the traction motor led to measurable variations in battery energy demand and driving range over a complete WLTP driving cycle, despite the two PMSM variants exhibiting comparable peak efficiency and similar regenerative braking capability.
- The dominant operating regions imposed by the WLTP cycle play a decisive role in determining overall energy performance. Although both machines achieve high efficiency under specific conditions, their efficiency islands are differently aligned with the WLTP operating point distribution.
- The M1 configuration is better suited for urban and mixed driving conditions, as it maintains higher and more stable efficiency at low to medium speeds and moderate torque levels. Consequently, M1 consistently requires lower electrical power from the battery, exhibits reduced internal losses, and results in a lower RMS battery current over the cycle.
- The M2 configuration, while offering reduced permanent magnet material usage and extended high-speed field-weakening capability, does not fully exploit these advantages under WLTP conditions. The operating regimes where M2 performs most efficiently are only weakly represented in the cycle, leading to higher net energy consumption and a reduced driving range compared to M1.
- These findings highlight the importance of aligning traction motor design choices with the actual distribution of operating points dictated by the intended driving profile, rather than relying solely on peak efficiency or high-speed performance indicators.
- From a powertrain design perspective, reducing the amount of permanent magnet material does not automatically result in improved energy efficiency or extended driving range. A holistic evaluation that accounts for vehicle dynamics, control strategy, and real-world operating conditions is required to achieve balanced system-level performance.

The proposed methodology provides a robust and transferable framework for the early-stage comparison of traction motor topologies in battery electric vehicles, supporting informed design decisions that balance efficiency, material usage, and system-level performance. Future work will extend the present analysis to alternative driving cycles and control strategies. Overall, the results indicate that, under WLTP-dominant operating conditions, traction efficiency governs the achievable energy performance and driving range of a BEV, whereas marginal improvements in regenerative braking efficiency play a secondary role.

Author Contributions: Conceptualization, E.-D.L. and Ș.L.T.; methodology, E.-D.L. and Ș.L.T.; software, E.-D.L.; validation, E.-D.L. and Ș.L.T.; formal analysis, E.-D.L.; investigation, E.-D.L.; resources, E.-D.L.; data curation, E.-D.L.; writing—original draft preparation, E.-D.L.; writing—review and editing, E.-D.L. and Ș.L.T.; visualization, E.-D.L. and Ș.L.T.; supervision, Ș.L.T.; project

administration, E.-D.L. and Ș.L.T. All authors have read and agreed to the published version of the manuscript.

Funding: This research received no external funding.

Data Availability Statement: The original contributions presented in this study are included in the article. Further inquiries can be directed to the corresponding author.

Conflicts of Interest: The authors declare no conflicts of interest.

References

1. Alanazi, F. Electric Vehicles: Benefits, Challenges, and Potential Solutions for Widespread Adaptation. *Appl. Sci.* **2023**, *13*, 6016. [CrossRef]
2. DESTEC, M.C.; Lutzemberger, G.; Pasini, G.; Quilici, F.G.; Scarpelli, C.; Fioriti, D. Battery Electric Vehicles (BEV): More Efficient Than Expected? In Proceedings of the 2025 IEEE International Conference on Environment and Electrical Engineering and 2025 IEEE Industrial and Commercial Power Systems Europe (EEEIC/I&CPS Europe), Chania, Crete, Greece, 15–18 July 2025; pp. 1–6.
3. Miri, I.; Fotouhi, A.; Ewin, N. Electric vehicle energy consumption modelling and estimation—A case study. *Int. J. Energy Res.* **2021**, *45*, 501–520. [CrossRef]
4. Tabacu, S.; Popa, D. Backward-facing analysis for the preliminary estimation of the vehicle fuel consumption. *Sustainability* **2023**, *15*, 5344. [CrossRef]
5. Chavan, S.; Yeolekar, S.; Lokhande, N. Electric Vehicle Energy Consumption Modeling and Range Estimation using Different Topographical Drive Cycles. In Proceedings of the 2024 International Conference on Intelligent Systems and Advanced Applications (ICISAA), Pune, India, 25–26 October 2024; pp. 1–6.
6. Zhou, B.; Li, Z.; Wang, H.; Cui, Y.; Hu, J.; Jiang, F. Design and Optimization of an Electric Vehicle Powertrain Based on an Electromechanical Efficiency Analysis. *Processes* **2025**, *13*, 1698. [CrossRef]
7. Masri, J.; Ismail, M.; Obaid, A. Power Flow Simulation and Thermal Performance Analysis of Electric Vehicles Under Standard Driving Cycles. *Energies* **2025**, *18*, 3737. [CrossRef]
8. Wu, S.; Zhou, J.; Zhang, X.; Yu, J. Design and Research on High Power Density Motor of Integrated Motor Drive System for Electric Vehicles. *Energies* **2022**, *15*, 3542. [CrossRef]
9. Makaramani, M.; Wongyao, N.; Ruangjirakit, K. Simulation-based Comparative Study of EV Energy Consumption and Effects on the Lithium-ion Battery Aging under Different Driving Cycles. In Proceedings of the 2023 IEEE Transportation Electrification Conference and Expo, Asia-Pacific (ITEC Asia-Pacific), Chiang Mai, Thailand, 28 November–1 December 2023; pp. 1–8.
10. Kondru, J.; Obulesu, Y. Comprehensive performance analysis of an electric vehicle using multi-mode Indian drive cycles. *Sci. Rep.* **2025**, *15*, 17699. [CrossRef] [PubMed]
11. Kuttey, V.K.; Bali, S.K. Effect of Various Drive Cycles on Battery Electric Vehicle (BEV). In Proceedings of the 2024 International Conference on Computational Intelligence for Green and Sustainable Technologies (ICCIGST), Vijayawada, India, 18–19 July 2024; pp. 1–4.
12. Nucă, I.; Turcanu, A.; Cazac, V. Performance Analysis of an Urban Passenger Vehicle Powertrain Operating in Various Driving Cycle and Speed Profiles Using MatLab Simscape Models. In Proceedings of the 2023 International Conference on Electromechanical and Energy Systems (SIELMEN), Craiova, Romania, 12–13 October 2023; pp. 1–6.
13. Ibrahim, M.; Järg, O.; Seppago, R.; Rassõlkin, A. Performance Optimization of a High-Speed Permanent Magnet Synchronous Motor Drive System for Formula Electric Vehicle Application. *Sensors* **2025**, *25*, 3156. [CrossRef]
14. Bianchi, N.; Cinti, L.; Contò, C.; Ortombina, L. SPM Motor with Star-Delta Winding: Fault Analysis and Experimental Validation. *IEEE Trans. Ind. Appl.* **2024**, *61*, 47–55. [CrossRef]
15. Prajapati, A.M.; Prajapati, A.R.; Mehta, D.M. Advanced Control Strategies of PMSM for Battery Electric Vehicle Application: A Review. *J. Electr. Syst.* **2024**, *20*, 1139–1149. [CrossRef]
16. Shao, L.; Tavernini, D.; Karci, A.; Sorniotti, A. Design and optimisation of energy-efficient PM-assisted synchronous reluctance machines for electric vehicles. *IET Electr. Power Appl.* **2023**, *17*, 10. [CrossRef]
17. Jani, S.; Jamnani, J. Performance Validation of PM-Assisted SynRM and PMSM with Optimized Design for EV Application. *Trans. Energy Syst. Eng. Appl.* **2023**, *4*, 1–14. [CrossRef]
18. Park, G.-H.; Kim, J.-H.; Kim, J.-H.; Cha, K.-S.; Jung, Y.-H. Performance Comparison Between IPMSMs with Rare-Earth PM and Rare-Earth-Free PM According to Driving Cycle of Electric Vehicles. In Proceedings of the IEEE Energy Conversion Conference Congress and Exposition (ECCE), Philadelphia, PA, USA, 19–23 October 2025; pp. 1–7.
19. Cinti, L.; Carlet, P.G.; Ortombina, L.; Bianchi, N. Impact of Rotor Excitation Current During Flux-Weakening Control of Hybrid-Excited Permanent Magnet Synchronous Motor. *IEEE Trans. Ind. Appl.* **2024**, *61*, 313–321. [CrossRef]

20. Filippini, F.; Bianchi, N. Design of an On-Axis Electrically Excited Synchronous Motor for Heavy Commercial Vehicles. In Proceedings of the IEEE Energy Conversion Congress and Exposition (ECCE), Phoenix, AZ, USA, 20–24 October 2024; pp. 5185–5192.
21. Tupsaminder, P.B.; Mohite, H.; Jokare, M.; Shinde, R.; Mallad, H. Efficiency Map Model for PMSM to Use in EV Simulation. *Int. J. Sci. Res. Eng. Manag.* **2024**, *8*, 1–7. [CrossRef]
22. Contò, C.; Bianchi, N. E-Bike Motor Design Based on Analytical and Finite Element Performance Mapping. *IEEE Trans. Ind. Appl.* **2024**, *61*, 3854–3861. [CrossRef]
23. Di Leonardo, L.; Carbonieri, M.; Bianchi, N.; Tursini, M. Fast Mapping Procedure for Synchronous Reluctance Motors via Magnetic Coenergy Reconstruction Method from Boundaries Dataset. *IEEE Trans. Ind. Appl.* **2025**, *61*, 6160–6171. [CrossRef]
24. UNECE. Worldwide Harmonized Light Vehicles Test Procedure (WLTP). Available online: https://unece.org/transport/road-transport/working-party-automatedautonomous-and-connected-vehicles-introduction (accessed on 5 July 2025).
25. Zhao, X.; Ye, Y.; Ma, J.; Shi, P.; Chen, H. Construction of Electric Vehicle Driving Cycle for Studying Electric Vehicle Energy Consumption and Equivalent Emissions. *Environ. Sci. Pollut. Res.* **2020**, *27*, 37395–37409. [CrossRef]
26. Valladolid, J.; Calle, M.; Guiracocha, A. Analysis of regenerative braking efficiency in an electric vehicle through experimental tests. *Ingenius* **2023**, *29*, 24–31. [CrossRef]
27. Berjoza, D.; Pirs, V.; Jurgena, I. Research into the Regenerative Braking of an Electric Car in Urban Driving. *World Electr. Veh. J.* **2022**, *13*, 202. [CrossRef]
28. Anh, N.T.; Chen, C.-K.; Liu, X. An Efficient Regenerative Braking System for Electric Vehicles Based on a Fuzzy Control Strategy. *Vehicles* **2024**, *6*, 1496–1512. [CrossRef]
29. Li, C.; Zhang, L.; Lian, S.; Liu, M. Research on Regenerative Braking Control of Electric Vehicles Based on Game Theory Optimization. *Sci. Prog.* **2024**, *107*, 00368504241247404. [CrossRef]
30. Chidambaram, R.K.; Chatterjee, D.; Barman, B.; Das, P.P.; Taler, D.; Taler, J.; Sobota, T. Effect of Regenerative Braking on Battery Life. *Energies* **2023**, *16*, 5303. [CrossRef]
31. Gillespie, T.D. *Fundamentals of Vehicle Dynamics*; SAE International: Warrendale, PA, USA, 1992.
32. Ostadian, R.; Ramoul, J.; Biswas, A.; Emadi, A. Intelligent energy management systems for electrified vehicles: Current status, challenges, and emerging trends. *IEEE Open J. Veh. Technol.* **2020**, *1*, 279–295. [CrossRef]
33. Montaleza, C.; Arévalo, P.; Tostado-Véliz, M.; Jurado, F. Intrinsic Characteristics of Forward Simulation Modeling Electric Vehicle for Energy Analysis. *Electricity* **2022**, *3*, 202–219. [CrossRef]
34. Martyushev, N.V.; Malozyomov, B.V.; Sorokova, S.N.; Efremenkov, E.A.; Qi, M. Mathematical Modeling the Performance of an Electric Vehicle Considering Various Driving Cycles. *Mathematics* **2023**, *11*, 2586. [CrossRef]

Disclaimer/Publisher's Note: The statements, opinions and data contained in all publications are solely those of the individual author(s) and contributor(s) and not of MDPI and/or the editor(s). MDPI and/or the editor(s) disclaim responsibility for any injury to people or property resulting from any ideas, methods, instructions or products referred to in the content.

vehicles

MDPI

Article

Mapping Research Trends in Road Safety: A Topic Modeling Perspective

Iulius Alexandru Tudor * and Florin Gîrbacia

Department of Automotive and Transport Engineering, Transilvania University of Brasov, 500036 Brasov, Romania; garbacia@unitbv.ro
* Correspondence: iulius.tudor@unitbv.ro

Abstract

Over the past decade, road safety research has experienced rapid development due to the rapid expansion of large crash databases, the adoption of artificial intelligence techniques, and the demand for proactive and predictive safety solutions. This study conducts a data-driven review of recent research trends in transport safety. It focuses on main domains including crash severity analysis, human factors, vulnerable road users (VRUs), spatial modeling, and artificial intelligence applications. A systematic search of the Scopus database identified 15,599 relevant scientific papers published between 2016 and 2025. After constructing this corpus, titles, abstracts, and keywords were preprocessed using a natural language pipeline. The analysis employed BERTopic, a transformer-based topic modeling framework. The analysis identified 29 distinct research topics, further synthesized into five major thematic areas: (1) crash severity and injury analysis, (2) driver behavior and human factors, (3) vulnerable road users, (4) artificial intelligence, machine learning, and computer vision in intelligent transportation systems, and (5) spatial analysis and hotspot detection. A notable increase in publications related to artificial intelligence and machine learning has been evident since 2020. The results show a transition from descriptive, post-crash studies to integrated, multimodal, predictive analysis. Overall, the findings reveal a paradigm shift in the field. This study also identifies ethical and economic issues associated with the use of artificial intelligence in intelligent transportation systems, including data management, infrastructure requirements, system security, and model transparency. The results signify a transition from intuition-based models to explainable, spatially explicit, and data-intensive models, ultimately facilitating proactive risk assessment and informed decision-making.

Keywords: road accident; traffic accident; motor vehicle crash; traffic collision; traffic safety

1. Introduction

Over the last two decades, road safety research has developed rapidly, driven by the application of new data analysis methodologies, advanced statistical models, and artificial intelligence (AI). This evolution was primarily fueled by the growing volume and diversity of data from sources such as road infrastructure sensors, connected vehicles, telematics, and human behavioral data [1–3]. Consequently, methodological approaches in the field have shifted significantly. The scientific literature documents a move from traditional models like logistic regression and ordered probit models for risk factor analysis to hybrid methods and machine learning algorithms capable of processing nonlinear interactions among variables [4–7]. Topic modeling analysis of publications from 2016 to 2025 highlights several converging research directions. Five primary thematic clusters can be identified:

crash and injury severity modeling, driver behavior and human factors [8], vulnerable road user safety, spatial analysis and hotspot detection, and artificial intelligence applications, including deep learning and computer vision. The literature also shows a temporal pattern. Recent studies increasingly examine explainable predictive models for autonomous vehicles and intelligent infrastructure [9–11]. Within the artificial intelligence cluster, models such as Random Forest, XGBoost, and Deep Neural Networks demonstrate a superior capacity to capture data heterogeneity and estimate injury severity with high reproducibility (AUC > 0.90) compared to traditional linear models [1,3,6,9].

Research on driver behavior is also evolving through the integration of physiological signals, including electroencephalography (EEG) and electrocardiogram (ECG), together with vehicular CAN-bus data. These signals are increasingly incorporated into Advanced Driver Assistance Systems (ADAS). This integration supports the early detection of driver stress, fatigue, and inattention [12–14].

Research on vulnerable road users (VRUs) has introduced a geographic perspective to urban safety, strongly aligned with spatial analysis methods. Bayesian and spatio-temporal models, often based on Geographic Information Systems (GIS), are effectively used to identify high-risk areas and estimate risk factors related to lighting conditions, pedestrian flow, and intersection design [15–19].

Machine learning applications in intelligent transportation extend beyond safety modeling to enable real-time traffic surveillance, automated incident detection, and mobility flow optimization [11,20,21]. This analysis reveals the field's interdisciplinary progression from isolated accident studies toward a systemic approach that integrates spatial, behavioral, and sensory data. This shift marks a pivotal move from reactive, post-event analysis to proactive and explainable road risk prediction.

Recent literature on road safety has been extensively analyzed through bibliometric, scientometric, and systematic reviews, with the aim of mapping the structure of the field, research trends, and the evolution of methodological paradigms. Bibliometric analyses have examined the thematic dynamics of road safety research, the relationships between sub-fields, and the evolution of scientific collaboration networks. These studies indicate a gradual diversification of research directions and an increasing level of interdisciplinarity within the road safety domain [22–25]. In particular, studies dedicated to the relationship between artificial intelligence and road safety have shown an accelerated growth of research oriented towards accident prediction, driver behavior analysis, and the development of intelligent transport systems, concomitant with the conceptual fragmentation of the field into distinct thematic clusters [24].

Systematic reviews on road accident analysis and modeling have integrated traditional statistical approaches, modern machine learning techniques, and emerging technologies into a unified conceptual framework, highlighting the increasing focus on data-driven paradigms and the lack of standardized and generalizable methodological frameworks at the domain level [26]. Reviews on machine learning applications in road accident prediction have examined algorithm performance, data types, and validation strategies. These studies show that ensemble and deep learning models often achieve strong predictive performance. However, they also report limitations related to understanding model predictions, class imbalance, and how well the models perform on new data [3,27–29]. At the same time, bibliometric and comparative analyses on ML and AutoML applications have shown a rapid diversification of predictive strategies and an intensification of the use of automated methods in road safety research [28].

Existing studies show that road safety research is undergoing a major change in research methods. The field is moving from traditional statistical methods to methods based on artificial intelligence and data analysis. At the same time, the literature remains

https://doi.org/10.3390/vehicles8040069

fragmented across research topics and lacks integrative analytical frameworks able to capture the latent semantic structure and the evolution of the field [3,22–29].

The present article performs a large-scale analysis of research trends in the field of road safety by applying a data-driven topic modeling framework, based on transformer models, to the scientific literature indexed by the Scopus database.

The objective of the presented analysis is to map the semantic and temporal nature of road safety research by identifying dominant and emerging themes and the relationships between them. The proposed approach allows the identification of latent semantic structures, relationships between research topics, and the evolutionary dynamics of the field. An integrative perspective on thematic fragmentation and interconnections between research directions is provided, contributing to overcoming the methodological limitations of traditional bibliometric analyses.

2. Materials and Methods

2.1. Data Collection

The dataset for this study was collected from the Scopus database because it provides broad coverage of peer-reviewed literature and structured metadata suitable for text mining and bibliometric analysis. The use of a single database, however, introduces a limit. Some relevant studies indexed only in other databases, such as Web of Science or specialized repositories, may not be included in the dataset. Even so, Scopus remains one of the main sources used for scientometric studies in transportation and road safety research. Future work may combine multiple databases to extend coverage and reduce selection bias.

A systematic search was conducted to retrieve articles published between January 2016 and July 2025. The search query was designed to be broad in the transport safety domain (see Appendix A). This query specifically targeted the title, abstract, and keyword fields. It restricted the results to English-language publications and specific document types: articles, conference papers, reviews, book chapters, short surveys, and data papers. This query yielded a corpus of 15,599 records. For each record, the title, abstract, and author-provided keywords were extracted, ensuring a rich representation of its content. Records with missing titles or abstracts were excluded, and duplicates based on these fields were removed to ensure the integrity of the dataset.

2.2. Topic Modeling

A multi-step preprocessing pipeline was implemented using the Natural Language Toolkit (NLTK) library in Python 3.12.13 to prepare textual data for topic modeling. This phase normalized the text and reduced noise to improve the quality of the resulting topics. All text was converted to lowercase. Numerical digits and special characters were removed using regular expressions to isolate textual content. The cleaned text was tokenized into individual words. To ensure semantic quality, a lemmatization and stopword removal process was applied. Part-of-Speech (POS) tagging was utilized to identify the grammatical category of each token, allowing the NLTK WordNetLemmatizer to accurately reduce each word to its context-aware dictionary base form. Next, an expanded stopword filter was applied. This list combined standard NLTK English stopwords with a custom dictionary of 57 domain-specific and academic terms (like ‘accident’, ‘crash’, ‘study’, ‘model’, ‘et’, ‘al’) that lack differentiating semantic value. All tokens consisting of two characters or fewer were removed. This preprocessed corpus was then analyzed using Bidirectional Encoder Representations from Transformers for Topic Modeling (BERTopic) [30]. Each document was converted into a high-dimensional numerical vector using the specific Sentence-Transformer model version, sentence-transformers/all-mpnet-base-v2. This model was selected for its superior ability to capture semantic meaning and context in English texts. To generate

https://doi.org/10.3390/vehicles8040069

human-readable topic representations, a Class-based Term Frequency-Inverse Document Frequency (c-TF-IDF) approach was used. During this step, the vocabulary was structured using Scikit-Learn's CountVectorizer, strictly configured with an n-gram range of (1, 3) to capture meaningful unigrams, bigrams, and trigrams. In order to reduce noise, terms appearing in fewer than 5 documents (min_df = 5) or in more than 85% of the documents (max_df = 0.85) were filtered out. The final topic representations were then refined using a KeyBERT-inspired model to extract the top 10 most representative keywords for each identified topic.

To enable the effective clustering of document embeddings, their dimensionality was first reduced using the Uniform Manifold Approximation and Projection (UMAP) algorithm. The UMAP configuration was chosen specifically to preserve the corpus's broad thematic relationships: n_neighbors = 50 (higher than the default 15) prioritized the global topological structure, and a cosine metric was used to reduce dimensions for subsequent clustering (n_components = 5). This configuration ensured that broader relationships between road safety sub-disciplines remained intact. These reduced embeddings were then clustered using the Hierarchical Density-Based Spatial Clustering of Applications with Noise (HDBSCAN) algorithm. To identify only established research trends and avoid micro-topics, the min_cluster_size was set to 80 (about 0.5% of the corpus). This configuration ensured that the resulting topics represented statistically meaningful concentrations of documents. HDBSCAN also handles noise by assigning documents in sparse regions to an outlier group (labeled as Topic-1).

A sensitivity analysis was conducted to validate the robustness of the topic structure and to ensure that the findings were not dependent on specific parameter choices. To achieve this, the min_cluster_size parameter was tested at thresholds of 20, 40, 60, 80, and 100. The results show that varying this parameter controlled the granularity of the topic model. Setting the threshold to 20 produced a fine-grained structure with 89 distinct topics. Increasing the threshold to 100 generated a more consolidated model with 26 broader topics. Importantly, the proportion of documents classified as outlier documents remained stable across all tests, ranging only between 44.0% and 51.5%. This stability indicates a consistent core of dense thematic research clusters within the corpus. Despite the variation in granularity, the primary identified thematic areas (crash severity and injury analysis, driver behavior and human factors, vulnerable road users (VRUs), AI and machine learning, and spatial analysis) consistently emerged as the most prominent. These results indicate that the core super-clusters represent principal research trends within the corpus.

2.3. Results of BERTopic Analysis

The BERTopic analysis of 15,599 scientific abstracts successfully identified 29 distinct, cohesive research topics within the transport safety literature. Many scientific abstracts (n = 7598) were classified as outliers (Topic-1). This outlier classification is not a modeling failure but rather reflects the actual heterogeneity of global road safety research, as captured by the HDBSCAN algorithm. Unlike partition-based algorithms such as K-Means, which force all documents into a cluster, HDBSCAN groups only documents that form dense and clearly defined semantic neighborhoods. We conducted an analysis to justify the classification of these documents as outliers (Topic-1). This analysis involved two key assessments. First, a text-length distribution analysis confirmed that the outlier documents do not represent low-quality noise or incomplete records. Their average word count (166.6 words) closely matched that of documents within valid topics (172.1 words). The density distributions of the word counts for both groups overlap almost perfectly (see Figure 1). This visual evidence confirms that documents were assigned to the outlier cluster due to their semantic isolation in the vector space, not because they lacked sufficient textual data.

https://doi.org/10.3390/vehicles8040069

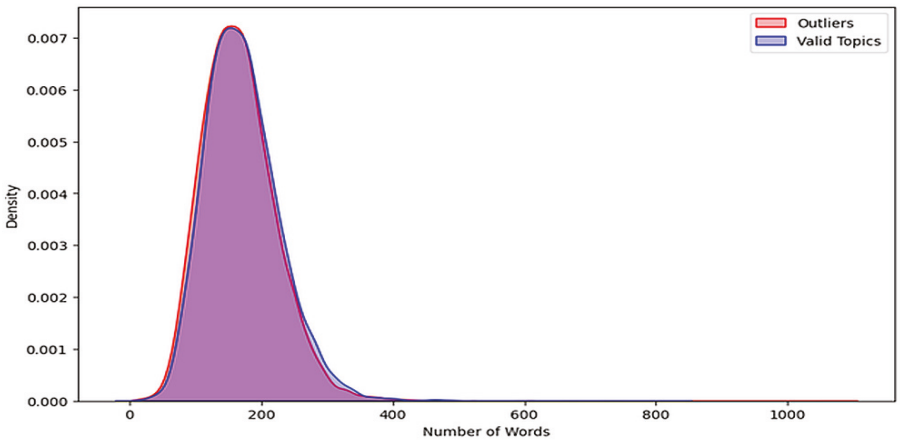

Figure 1. Density plot comparing the preprocessed word counts of documents classified as outliers compared to documents assigned to valid topics.

Second, an extraction of the outlier corpus confirmed that it consists of specialized, cross-disciplinary, or localized research rather than just discarded data. A manual review of a random sample of these outlier documents confirmed their specific type. Representative documents include highly specific geographic case studies (for example: "Modeling fatal traffic accident occurrences in small Indian cities, Patiala, and Rajpura"), medical analyses (for example: "Factors related to healthcare costs of road traffic accidents in Bucaramanga, Colombia"), and niche technological investigations (for example: "Safety analysis and countermeasure research of power lithium-ion battery road transport"). The HDBSCAN algorithm correctly isolated these documents because they lack the semantic density and volume to form a broad trend. Their exclusion from the primary thematic clusters improved the overall topic model. Evaluated using the Gensim Python library, the final model achieved a strong topic coherence score of 0.508 and a high topic diversity of 0.778, indicating that the remaining topics represent generalized research topics. By allowing these sparse documents to remain as outliers, the algorithm prevents topic dilution. The 29 identified topics (see Table 1) represent reliable and coherent focal points within the scientific community. Document distribution across these topics is non-uniform, with a few dominant topics containing many documents and many smaller specialized topics (see Figure 2).

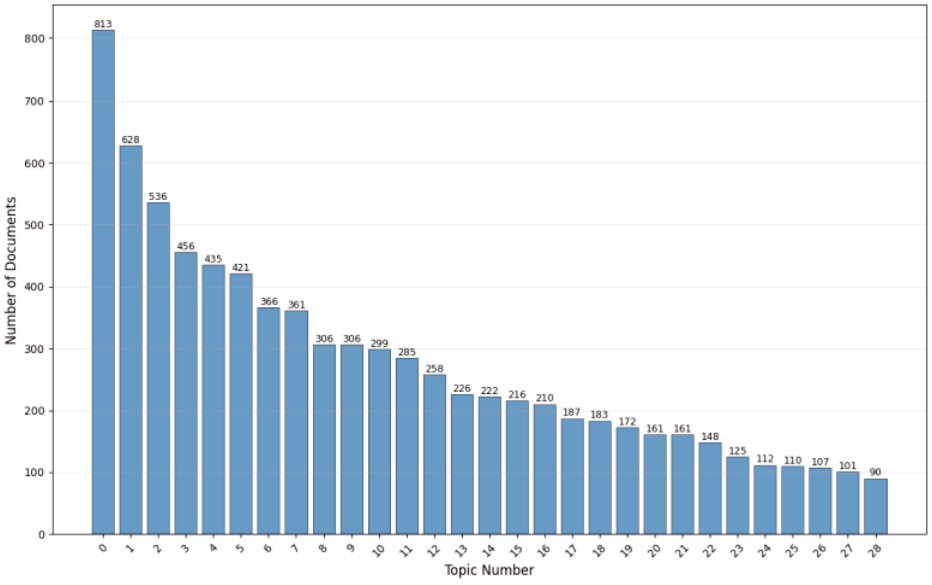

Figure 2. Distribution of documents per topic.

Table 1. Dominant research topics identified by BERTopic based on document distribution.

Topic ID	Doc Count	Top Keywords	Topic	Objective
0	813	injury severity, severity prediction, logistic regression, analytics	Crash Severity & Injury Analysis	This topic covers research that uses statistical and analytical methods to build models that estimate injury severity in traffic crashes.
1	628	physiological, alarm, architecture, ecg, inattention	Driver Behavior & Human Factors	This theme focuses on monitoring driver condition using physiological signals and in-vehicle systems to detect distraction, fatigue, or reduced attention.
2	536	transportation pedestrian safety, improve pedestrian safety, safety perception, pedestrian safety risk	Vulnerable Road Users (VRUs)	This topic includes studies related to pedestrian safety, infrastructure improvements, and perception of risk in walking environments.
3	456	safety education, risky driving behavior, driving behavior	Driver Behavior & Human Factors	This topic analyzes risky driving behaviors and evaluates interventions such as training and education programs to improve safety.
4	435	trauma registry, human injury, hospital mortality, trauma care, morbidity, mortality	Crash Severity & Injury Analysis	This theme examines medical outcomes after crashes, including injury patterns, mortality, and the performance of trauma care systems.
5	421	prone area, safety spatial, street spatial variable, road street spatial, heterogeneity	Spatial Analysis & Hotspot Identification	This topic focuses on identifying accident-prone areas using spatial analysis and GIS techniques to understand geographic risk patterns.
6	366	machine learning, intelligent transportation, incident detection	AI, Machine Learning & Computer Vision	This theme explores the use of machine learning algorithms for traffic monitoring, incident detection, and safety optimization in ITS.
7	361	affect injury severity, contribute injury severity, influence injury severity, affect injury	Crash Severity & Injury Analysis	This topic investigates the factors that influence injury severity, focusing on causal relationships rather than prediction alone.
8	306	deep learning, intelligent transportation, neural network CNN, neural network	AI, Machine Learning & Computer Vision	This theme covers advanced deep learning techniques applied to visual data, including object detection, traffic analysis, and scene understanding.
9	306	automobile drive, car drive, drunken drive, toxicology, drive influence alcohol	Driver Behavior & Human Factors	This topic focuses on the effects of alcohol and substances on driving performance, including detection methods and toxicological analysis.

To understand how the 29 topics group together at a higher level, an algorithmic hierarchical clustering analysis was performed based on the cosine distances between the topic embeddings (see Figure 3). This resulted in four distinct super-clusters:

1. Injury cluster. This cluster groups topics related to the medical outcomes of crashes, containing trauma care (Topic 4), spinal cord injuries (Topic 13), and general injury severity analysis (Topics 0, 7, 19).
2. Human factors cluster. This large cluster focuses on the driver, including themes of unsafe driving (Topics 3, 27), driver distraction (Topic 12), and alcohol-impaired driving (Topic 9).
3. Technology and AI cluster. This cluster is dedicated to computational methods, including topics related to machine learning, deep learning, and neural networks (Topics 6, 8, and 24), as well as physiological monitoring (Topic 1).
4. Infrastructure cluster. Topics from this cluster concern the physical road environment, including highway safety and engineering (Topic 25), pavement and road surface analysis (Topic 21), and spatial analysis of crash hotspots (Topic 5).

https://doi.org/10.3390/vehicles8040069

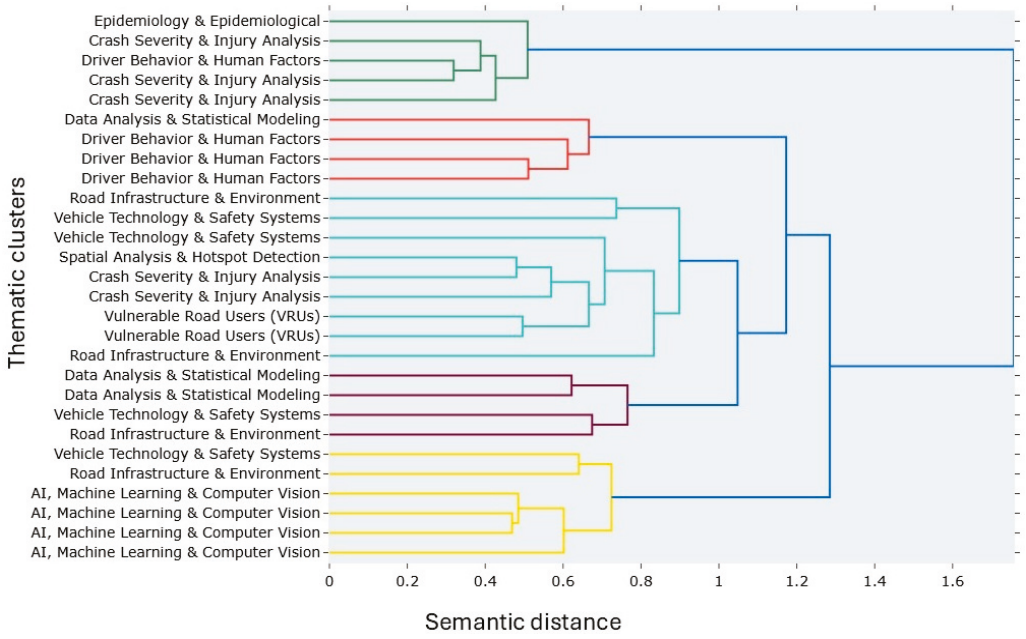

Figure 3. Hierarchical clustering of topics.

The analysis of topic frequency over time reveals the dynamics of the research in the transport safety field. Common research like "Crash Severity Analysis" (Topic 0) and "Driver Behavior" (Topic 3) shows consistent and stable research output. An emerging trend is the exponential growth in topics related to AI and machine learning. As shown in Figure 4, topics related to machine learning (Topic 6) and deep learning (Topic 8) have seen a significant increase in frequency, mainly starting from 2020. This indicates a focus of the research in the field towards data-intensive and predictive solutions for transport safety.

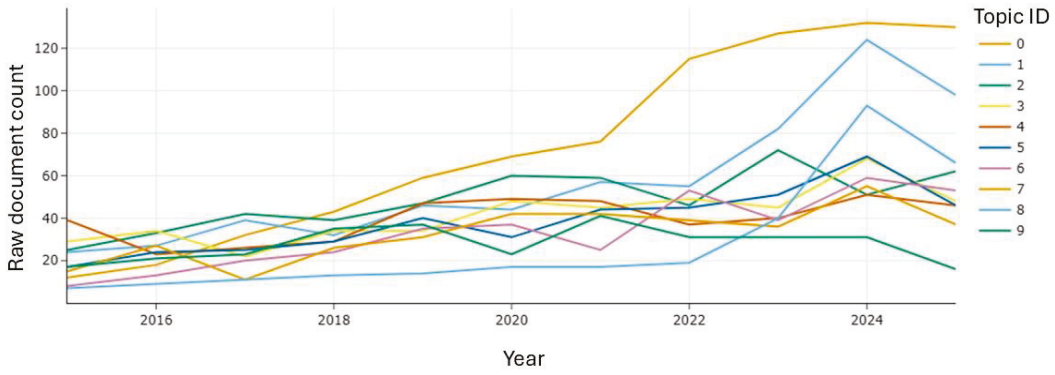

Figure 4. Temporal evolution of the top 10 most frequent topics.

Topic frequency analysis presents five primary thematic areas in the field of transport safety research. These thematic areas, each composed of one or more related topics, represent the core focus of the scientific community. The clustering algorithm grouped the topics by semantic similarity, but algorithms do not inherently understand established road safety domains. We manually reviewed the 29 topics and 4 super-clusters and grouped them into five major themes based on topic frequency, document volume, and practical relevance (see Table 2). This process was guided by three criteria: (i) we use the boundaries from the hierarchical clustering dendrogram (Figure 3) to group close topics, (ii) overlap in the main keywords of each topic, and (iii) agreement with known research directions in the road safety research area. When a topic could fit into more than one area, the final assignment was based on a review by an expert in road safety and accident analysis from

https://doi.org/10.3390/vehicles8040069

the European Association for Accident Research and Accident Analysis. The identified major themes are (see Figure 5):

Table 2. Mapping of algorithmic topics and super-clusters to manual thematic areas for literature review.

Thematic Areas	Algorithmic Cluster	BERTopic ID	Objective
1. Crash severity and injury analysis	Injury cluster	0, 4, 7, 13, 19	Modeling injury severity
2. Driver behavior and human factors	Human factors cluster & technology/AI cluster	1, 3, 9, 12, 27	Unsafe driving, psychological states, distraction, driver monitoring.
3. Vulnerable road users	Infrastructure cluster & injury cluster	2, 15	Pedestrian and cyclist safety, infrastructure adjustments, VRU risk perception.
4. AI, Machine Learning and Computer Vision	Technology and AI cluster	6, 8, 24	Advanced computational methods, deep learning, incident detection, CNNs.
5. Spatial analysis and hotspot detection	Infrastructure cluster	5, 21, 25	Geographic distribution of crashes, GIS, spatial statistics network-level risks.

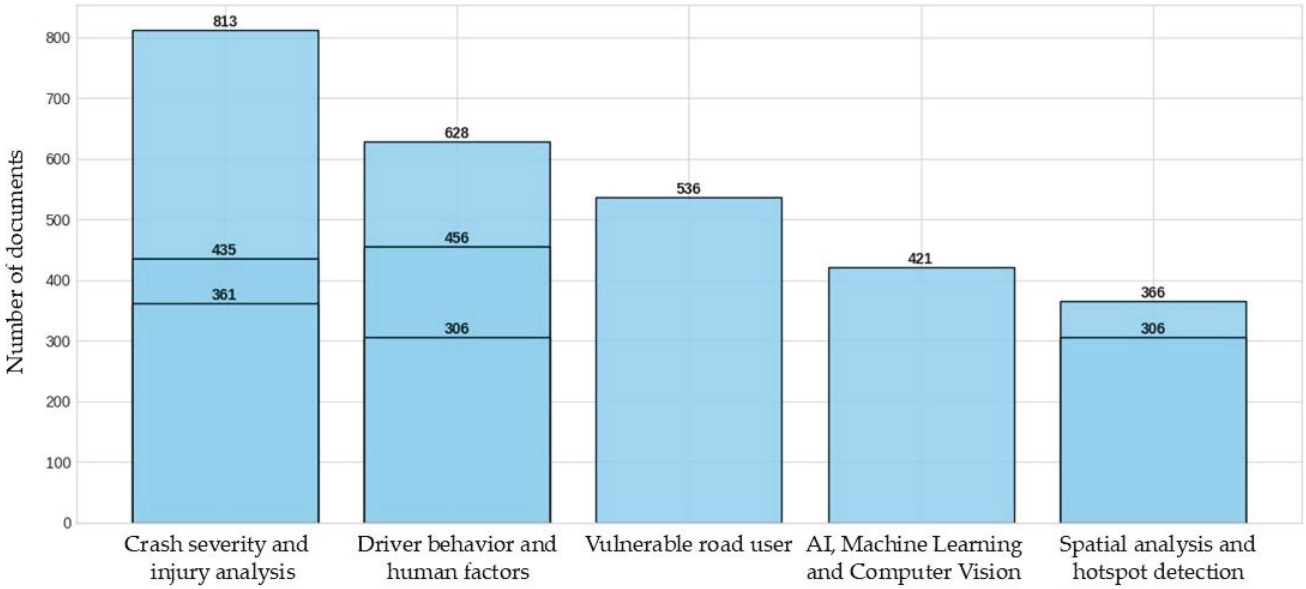

Figure 5. Top 5 research themes by document count. The chart aggregates documents from related individual topics into broader themes, showing the relative prevalence of each major research area.

1. Crash severity and injury analysis (Topics 0, 4, 7). This is the leading research area, focused on modeling and predicting the severity of injuries resulting from a crash. Key research activities include using statistical methods like logistic regression and analyzing hospital trauma registry data.
2. Driver behavior and human factors (Topics 1, 3, 9). The second largest theme is focused on the human factors, investigating unsafe driving behaviors, safety education, driver impairment (drunken driving), and the use of technology (ECG, alarms) to monitor driver state and inattention.
3. Vulnerable road users (VRUs) (Topics 2, 15). A significant body of work is dedicated to the safety of pedestrians and cyclists. Research in this area explores infrastructure improvements, risk perception, and safety measures specific to VRUs.
4. AI, Machine Learning, and Computer Vision (Topics 6, 8, 24). This rapidly growing theme involves the application of advanced computational methods. Research includes using deep learning and convolutional neural networks (CNNs) for incident detection, traffic flow prediction, and image-based analysis.

https://doi.org/10.3390/vehicles8040069

5. Spatial Analysis & Hotspot Detection (Topic 5). This theme covers the geographical aspects of road safety, using GIS and spatial statistics to identify and analyze accident "hotspot" locations.

3. Results

3.1. Crash Severity and Injury Analysis

The analysis of crash injury severity is an important objective in road safety research. The literature reveals a gradual trend from classical statistical models toward data-driven hybrid frameworks. Classical methods, mainly logistic regression and ordered response models, remain in common use due to their interpretability and robustness [4,7,15,31,32]. Other studies have shown that logistic regression models with low bias and random parameters can characterize the effects of road geometry, environmental conditions, and accident configuration on injury outcomes while simultaneously managing the variation resulting from rare fatal accidents or injuries leading to disability [4,7,31]. Bayesian implementations improve these models by taking into account latent correlations and uncertainty, leading to more reliable severity estimates for complex data with multidirectional crashes [15].

Another area of research is dedicated to analyzing the severity of bodily injuries according to specific typologies of users, such as riders of electric bicycles (EB) and other light vehicles. Studies of e-bike accidents use a generalized ordered probit model (GOM), with random parameters and heterogeneity in the environments, to show that lighting, horizontal road curvatures, speed limits, and user characteristics influence the probability of severe or fatal injuries [33,34]. These findings show the context dependence of injury severity mechanisms for semi-vulnerable road users, which are different from those of passenger vehicle occupants.

A significant part of the specialized literature has used machine learning models to increase the prediction of injury severity classes. Comparative studies show that ensemble learning methods, such as Random Forest and its variants of gradient boosting machines, can achieve better overall accuracy than traditional statistical models if large and structured datasets are provided [5,6,32]. However, these machine learning approaches present challenges related to the issue of extreme class imbalance with implications on poor prediction performance for rare but severe injuries [3,6]. Machine learning tools have also been applied to small or specific datasets. Studies on tricycles and motorcycles show that the predictive performance under limited data conditions can still be considered acceptable if we carefully select features and adopt validation schemes [35,36].

Machine learning-based approaches to accident severity are on the rise, with a trend toward incorporating unstructured data sources using natural language processing methods. Models that incorporate both structured units of accident variables and features derived from unstructured police accident narratives demonstrate better performance than models that use only tabular data [37,38]. These approaches are promising but add complexity related to text preprocessing, narrative diversity, and model traceability.

Also, emerging research investigates the connection between injury severity analysis and automatic accident detection systems. Although they are mainly designed for real-time event detection and risk prediction instead of post-crash severity modeling, the studies based on convolutional neural networks (CNNs), computer vision techniques, and analytics based on graphs provide additional insights into crash mechanisms and dangerous scenarios [1,39,40]. These methods are not substitutes for conventional post-crash severity modeling, but they link predictive severity analysis and proactive traffic safety monitoring.

https://doi.org/10.3390/vehicles8040069

In summary, the literature suggests a trend toward hybrid methodologies. These frameworks combine interpretable statistical models with predictive ML or novel data sources (see Table 3). There is no universally optimal model; the choice depends on data availability, the specific road user type under investigation, and the required trade-off between explanatory capacity and predictive efficiency [1–7,15,31–42].

Table 3. Test cases for category crash severity & injury analysis.

Ref.	Brief Summary of the Method	Data	Key Findings	Challenges
[7]	A random parameters logit model was applied to study injury severity in rollover crashes, allowing the analysis to capture unobserved heterogeneity across crash observations.	A large United States rollover crash dataset containing information on vehicle type, speed, roadway alignment, and environmental conditions.	The results show significant heterogeneity in how speed and vehicle characteristics affect injury severity.	The model is more complex to interpret and is not directly transferable to non-rollover crashes or crashes involving two-wheeled vehicles.
[4]	Injury severity was predicted using machine learning approaches based on structured variables, with a comparison between deep learning models and classical machine learning algorithms, without explicit explainability techniques.	A national crash dataset including vehicle dynamics, roadway attributes, and environmental factors.	Machine learning and deep learning models achieve predictive performance comparable to or better than traditional statistical approaches.	Interpretability is limited, data requirements are high, and model performance is sensitive to class imbalance.
[6]	Logistic regression with bias reduction was used to analyze the severity of injuries caused by accidents, with the aim of correcting for bias from rare events and instability in estimating fatal injuries, while maintaining full interpretability of the model coefficients.	A national crash database including roadway geometry, collision configuration, vehicle characteristics, and environmental conditions.	Roadway geometry and impact configuration have a strong influence on injury severity, and the use of bias reduction improves the robustness of estimates for fatal injury outcomes.	The method has limited ability to represent nonlinear relationships and depends strongly on correct model specification.
[3]	A systematic review of machine learning methods for crash injury severity analysis was conducted, summarizing commonly used algorithms, data sources, and reported performance measures.	A collection of published studies using machine learning and statistical methods for injury severity modeling.	The review shows that machine learning is being used more and more through ensemble methods and highlights ongoing challenges with data imbalance and limited interpretability.	No original models were developed, and the conclusions depend on the quality and consistency of the reviewed studies.
[39]	A conceptual framework was proposed for identifying accident-prone locations using historical crash data, with an emphasis on spatial clustering techniques and structured analytical workflows.	Aggregated historical crash datasets with spatial and temporal information.	The framework demonstrates the potential of data-driven analytics for identifying high-risk locations in road networks.	The approach is conceptual and does not include direct injury severity modeling or empirical validation.

3.2. Driver Behavior and Human Factors

Driver attitude and behavior are leading human factors influencing crash risk. The studies in this research field aim at understanding how drivers feel, decide, and behave in challenging situations such as drowsiness, distraction, stress, agitation, or risk-taking and at modeling these phenomena using both classical and data-driven techniques [12,43–45].

A baseline of research considers behavior in terms of well-defined variables and interpretable models. These models relate driver characteristics (age, expertise), situational context (traffic, weather, time-of-day), and maneuver-level indicators (speed intentions, brake pattern, keeping the line) to unsafe driving or crash likelihood [12,44,45]. Such studies still matter as they allow for clear causal inference and form the basis for justifiable interventions and policy decisions, at least where explanation is a goal of analysis rather than pure prediction [12,45].

With the advancements in the prevalence of sensing and telematics, the literature extends to high-frequency signals, including identifying driver states and driving styles. Some other studies use in-vehicle sensors, smartphones, or drive cams to extract behavioral

descriptors (for example, hard braking, hard acceleration, and cornering) and apply ML clustering and supervised learning in order to automatically classify driver profiles and risk patterns [12,14,46,47]. A representative case study used an Android app to collect information from smartphone sensor streams and context data, evaluating various learning approaches in order to build driver profiles for feedback dashboards [48]. These pipelines present a practical trend: low-cost sensing together with ML could enable scalable behavioral monitoring, but model validity is dependent on sensor quality (for example, stability of sampling rates) and context coverage [14,46,47].

A distinct area of research investigates the cognitive and physiological aspects of poor driving behavior, such as fatigue, stress, and inattention. This research uses physiological measures orbehavioral surrogates to detect driver state changes, which can be correlated with performance decline. A consistent research theme is the challenge of early detection.Identifying cognitive load or fatigue before manifesting errors is desirable for prevention but is difficult due to individual and environmental variability in physiological signals [8,44,45,49,50].

An evolution of these approaches is multimodal, context-aware modeling. Recent works integrate kinematic data with contextual factors (type of road, traffic conditions, and weather) and behavior/physiological signals to improve model robustness and real-world applicability [8,49–51]. This is based on the consideration that the same action (for example, a sudden brake) can vary entirely when performed in different contexts, such as defensive vs. aggressive [8,49–51]. Models incorporating contextual features are preferred over those that depend only on raw vehicle signals. The generalization, however, is not a solved problem: the models trained on one region/fleet/driver population often require recalibration once deployed in new conditions/cultures of driving [49–51].

Human factors studies in conditionally automated driving add an additional layer. Driver monitoring and behavior modeling focusing on attention allocation, trust calibration, and takeover readiness [39–43] take into account the influence of non-driving-related tasks on safety margins. In this context, while research often highlights that "safe behavior" does not only relate to steering or braking quality but also supervisory control and situation awareness [13,52–55]. Evaluating these factors typically is performed using simulator experiments (like [52]), controlled pilot field operations, or curated datasets in which driver state and interaction events are observed with adequate ratio precision [53–55].

Higher-level behavioral representation and reasoning systems (such as models based on knowledge, misbehavior detection architecture, and data-driven behavioral pattern mining) are increasingly seen as the key technologies to accelerate the development of intelligent transportation systems. These techniques aim to move beyond simple classification to designs that can contextualize behavior, explain when appropriate, and adaptively counter the subject to practical concerns of privacy, bias, and real deployment [13,48,50,56–58].

The literature reveals an evolution from traditional interpretable analysis at the population level, through sensor-rich behavior inference based on machine learning, to modeling human factors relevant to the context and automation (see Table 4). The most robust contributions are those that balance methodological rigor (clear ground truth and robust validation) with realistic sensing constraints and situational and variable human driver behavior [8,12–14,43–46,48–58].

https://doi.org/10.3390/vehicles8040069

Table 4. Test cases for category driver behavior and human factors.

Ref.	Brief Summary of the Method	Data	Key Findings	Challenges
[12]	A statistical analysis was conducted, oriented on behavior to link driver characteristics and situational factors to risky driving behavior and crash involvement, using interpretable modeling approaches.	Structured crash and driver datasets including age, driving experience, time of day, traffic conditions, and behavioral indicators.	Driver demographics and situational context have a significant influence on risky behavior patterns and the likelihood of crash involvement.	Limited temporal resolution, with behavioral states inferred indirectly rather than measured explicitly.
[14]	A human factors analysis was performed in partially automated driving environments, focusing on driver attention, engagement in non-driving tasks, and readiness to take control during automation transitions.	Driving simulator and controlled experimental datasets capturing driver and automation interaction events.	Engagement in non-driving tasks significantly delays takeover responses and reduces situation awareness.	Results obtained from the simulator based on experiments may not fully generalize to naturalistic driving conditions.
[49]	A smartphone application based on driver behavior profiling was carried out using embedded inertial and global positioning sensors, combined with supervised machine learning for driving style classification.	Real-world driving trips collected using smartphone sensors, including accelerometer, gyroscope, and global positioning data.	Low-cost sensing enables scalable detection of aggressive and unsafe driving behaviors.	Sensor noise, inconsistent sampling rates, and limited contextual information reduce robustness.
[13]	A multimodal driver monitoring approach was developed by combining vision-based features with vehicle kinematics to detect distraction and unsafe behavior using machine learning classifiers.	In vehicle camera data, steering and pedal inputs, and contextual driving information.	Multimodal data fusion improves detection accuracy compared to single sensor systems.	Sensitivity to lighting conditions and visual occlusions, along with high computational demands for real-time deployment.
[57]	Behavioral pattern analysis was performed using experimental or observational driving data to identify unsafe maneuvers and the effects of cognitive workload on driving performance.	Driving behavior datasets, including maneuver level indicators and contextual variables.	Increased cognitive workload and behavioral irregularities are strongly associated with elevated risk indicators.	Difficulty in isolating behavioral effects from environmental influences and limited scalability of the approach.

3.3. Vulnerable Road Users

Vulnerable road users' safety has become an increasing area of research. Pedestrians, cyclists, and light personal mobility device users are not well protected physically, and their visibility depends on infrastructure design, traffic state, and visibility conditions. The literature on VRUs establishes that the risk of accidents and injuries is determined not only by vehicle dynamics but also by a complex set of infrastructural, spatial, behavioral, and environmental variables [18,59,60].

A large number of studies utilize traditional statistical models to measure the severity and frequency of vulnerable road users' injuries. Logistic regression and ordered response analyses have been used extensively in the literature to study the impacts of vehicle speed, intersection geometry, crossing design, light condition, and demographic information on pedestrian/cyclist safety [18,60]. These investigations consistently point out that poor lighting, complex urban intersection form layouts, long crossing distances, and higher operating speeds substantially increase the probability of severe/fatal injury sustained by vulnerable road users. One of the advantages of such methodologies is that they can be more easily interpreted and facilitate the development of infrastructure oriented towards safety analysis and policy development [61,62].

More sophisticated modeling approaches extend this framework by incorporating unobserved heterogeneity and spatial variation. Techniques like random parameters and Bayesian models have been utilized with pedestrian and cyclist crash data to describe variation across places, times, and population cohorts. This demonstrates that VRU risk factors are context-sensitive and not uniformly distributed across a road network [17,59,63,64]. These findings show the necessity of local safety analysis and should be interpreted with concern when extrapolating results between regions without recalibration.

Spatial analysis constitutes another important research area for VRU safety. Methods such as geographic information systems/mapping, kernel density estimation, and network-based hotspot detection are commonly used to identify and monitor high-risk locations for pedestrian/cyclist crashes [65–69]. By explicitly including the spatial organization of roads, these methods capture more realistic patterns of exposure and conflict locations than Euclidean approaches. The produced hotspot maps can facilitate targeted interventions such as better crossing solutions, traffic calming, and nighttime illumination. However, the utility of these models is influenced by data quality, geocoding precision, and parameter settings [67,68].

Research also addresses the behavioral dimension of VRU safety, focusing on the decisions made by pedestrians and their perception of risk. Some studies are also based on social-cognitive models (including the Theory of Planned Behavior) and account for unsafe crossing and compliance with traffic regulations, taking into consideration perceived risk, social norms, and group personality traits [70–72]. These user-focused approaches investigate perceived safety through the use of surveys and controlled studies in immersive virtual reality settings to proactively identify vulnerabilities in contexts where crash data is sparse or reactive [59,70].

A less developed but separate area of research studies interactions between VRU safety and advanced vehicles. This research utilizes agent-based models [17], probabilistic frameworks, and simulation studies to study conflicts involving pedestrians, cyclists, and automated or connected vehicles. These studies often use alternate safety measures (for example, post-encroachment time) for evaluating conflict risk prior to an unavoidable crash [62,73,74]. Although such methods provide useful insights into the future traffic situation, their results are sensitive to modeling assumptions that need to be validated using real traffic data.

Overall, the literature shows that interpreting statistical models with spatial and behavioral theories, as well as emerging practices such as simulation-based assessment for new technologies, is necessary to analyze the safety of VRUs. The development of context-specific approaches is important, adapted to local infrastructure, traffic data, and VRU behavior. The progression of VRU safety depends on the successful coordination of these complementary approaches and how they are applied analytically to account for the mechanisms of vulnerability identified across studies [17,18,59–73,75–77]. Several representative test cases are presented in Table 5.

Table 5. Test cases for the category vulnerable road users.

Ref.	Brief Summary of the Method	Data	Key Findings	Challenges
[18]	Interpretable regression based on statistical models was employed to evaluate pedestrian injury risk, with particular emphasis on roadway design, traffic speed environment, and environmental conditions. This approach allows infrastructure–related effects to be examined while accounting for demographic and traffic characteristics.	Pedestrian crash records enriched with detailed information on roadway geometry, speed limits, intersection type, lighting conditions, and pedestrian demographic characteristics.	The results indicate that vehicle speed, complex intersection layouts, and inadequate lighting are key contributors to severe and fatal pedestrian injuries, offering clear and actionable guidance for an oriented infrastructure towards safety interventions.	The reliance on linear model assumptions limits the representation of complex interactions and spatial spillover effects, while data completeness and reporting accuracy directly influence the robustness of the results.
[59]	A user-centered approach to pedestrian safety was adopted by focusing on perceived risk rather than recorded crash outcomes, integrating indicators based on a survey with contextual traffic and infrastructure characteristics.	Questionnaire data collected from pedestrians and linked with local road characteristics, traffic exposure levels, and demographic attributes.	Findings show that perceived safety varies considerably across demographic groups and is strongly shaped by crossing complexity, traffic volume, and the quality of pedestrian facilities.	Because indicators based on perception do not directly reflect objective crash risk, results may be influenced by subjective bias and familiarity with the local environment.

Table 5. *Cont.*

Ref.	Brief Summary of the Method	Data	Key Findings	Challenges
[72]	Network that is based on kernel density estimation was applied to pedestrian crash data in order to identify high-risk locations while explicitly accounting for road network structure and temporal variation.	Pedestrian crash records mapped onto the road network and enriched with temporal information describing the timing of incidents.	Compared with distance-based approaches, network-based methods provide more realistic and policy-relevant identification of crash hotspots, particularly within dense urban road networks.	The method involves high computational complexity and is sensitive to bandwidth selection, requiring accurate road network representation and precise crash location data.
[69]	Geographic information system based on spatial analysis using kernel density estimation was conducted to identify pedestrian and cyclist crash hotspots and to support the spatial prioritization of safety interventions.	Geocoded vulnerable road user crash datasets integrated within a geographic information system framework, including both spatial and temporal attributes.	The analysis reveals persistent clusters of pedestrian and cyclist crashes at specific intersections and road segments, enabling targeted countermeasures such as traffic calming measures and improved crossing design.	Results are sensitive to geocoding accuracy, spatial resolution, and parameter selection, while the underlying causal mechanisms are not explicitly modeled.
[67]	Behavioral modeling of pedestrian crossing decisions was performed using the Theory of Planned Behavior, incorporating psychological constructs such as perceived risk, social norms, and behavioral intention.	Survey datasets capturing attitudes, subjective norms, perceived behavioral control, and self-reported pedestrian behavior.	The results show that pedestrian compliance and risky crossing behavior are strongly influenced by perceived risk and social factors, often more strongly than by objective traffic conditions alone.	Dependence on self-reported data introduces response bias, and the identified behavioral relationships may vary across cultural and regional contexts.

3.4. Spatial Analysis and Hotspot Detection

The study of traffic safety has moved in recent years from "global-average" explanations to more spatial thinking since accidents are influenced by both spatial dependence and spatial heterogeneity [78]. Hotspot detection and clustering are more than cartographical outputs; they are decision-making tools. They guide and direct constrained resources towards locations where danger exists to a larger extent and where interventions are likely to have the greatest impacts [79–81].

One major research direction is related to discovering hotspots and clustering crashes that adopt geographic information systems (GIS) and spatial statistics in combination with clustering algorithms and network-aware density approaches. Recent studies demonstrate that algorithm selection is important. Hierarchical strategies and density-based clustering reveal different hotspot structures, and proximity analysis can identify underserved areas situated close to high-incidence places [80,81]. Network-based techniques, such as modified kernel density estimation and network kriging, improve the realism of hotspots, as they take into account the network geometry instead of just Euclidean distance [79]. In low-quality settings, applied ranking relative to the priority value, methods continue to be applicable for identifying hazardous sites and prompting low-cost countermeasures until more sophisticated modeling is possible [82]. At a macro level, spatial summaries such as mortality rate mapping with spatial autocorrelation assist in resource allocation and benchmarking between regions [83].

A complementary research direction addresses spatial heterogeneity by moving from global models to local modeling techniques like geographically weighted regression and spatial machine learning. For a significant environmental impact, geographically weighted deep learning has been proposed to allow for nonlinear spatially varying effects and potentially can outperform classic geographically weighted regression baselines. Related research indicates that a standard geographically weighted regression detects spatial variations in the relationship between built environment characteristics and accidents, with differences in direction and magnitude between areas [16,84]. Regarding injury severity due to speeding, geographically weighted neural networks (GWNNs) are used to learn

local models for each crash location and compare the spatial variation in marginal effects to support place-based countermeasures instead of universal rules [85]. At the city-level network, geographically weighted random forest (GWRF) generalizes this approach to determine causes of crash frequency with better predictive power and interpretable local importance patterns [86]. Multiscale geographically weighted regression (MGWR) also indicates that distinct contributing factors may work at diverse spatial scales, which increases model fit and interpretability for urban crash patterns [86]. Spatial regression on planned areas is still useful and feasible, particularly for finding actionable models as tools in regular GIS (such as GeoDa 1.5.37 software) for routine operations by agencies [87]. Spatial panel models are important for addressing spatial externalities and temporal dynamics relevant for both inference and policy implications [88].

Apart from geographical factors, research also integrates behavioral, operational, and data-driven mechanisms to explain why risk clusters in specific segments at particular times. Analyses of the areas near the highway tunnels show that the danger is likely to develop due to a temporal–spatial evolution of predictions related to driving tasks and activities under restricted visibility and intervisibility conditions, explaining why local segments may show higher risk than average on an international scale [89]. Crash and safety analysis also encounters non-purely spatial heterogeneity (unobserved differences across units, driver groups, or environments), which calls for the development of spatiotemporal crash prediction methods that consider such an additional challenge [90,91]. Injury-severity modeling with unobserved heterogeneity operating for vulnerable road users will offer a more contextual explanation of cyclist injury outcomes [92]. New areas include intelligent and connected mobility: latent class methodologies to address autonomous vehicle crash reports reveal that crash scenarios may form into subclasses, with spatial risk shaped by operational mode and environment [93]. Meanwhile, the problem of spatio-temporal graph learning has been well studied in the prediction of traffic conditions that can be adopted as an input data flow with appropriate incorporation for safety analytics [94]. Another branch is to utilize strategic maneuvers that capture critical driving situations, obtained from naturalistic driving data for spatial accident prediction, to be served as a proactive safety service or an early warning strategy [95]. When including spatial aggregation as a methodological choice and assessing the sensitivity of models with respect to various temporal/spatial groupings, model choice is no longer obvious, with aggregation-sensitive modeling of the frequency of accidents being essential for sound spatial safety analysis [96].

Spatial analytics and hotspot detection assist road safety studies by (i) distinguishing statistically significant versus raw count clusters, (ii) facilitating targeted interventions at the location level in relation to spatial heterogeneity, and (iii) providing machine learning access to GIS for decision-making transparency [78,80,85]. There are, however, important remaining practical and methodological limitations. As one limitation, obtaining precise geocoding data, especially in rural areas, can be difficult. Another limitation is the trade-off between model complexity and interpretability. Also, spatial results may be sensitive to aggregation decisions, and transferring models between regions is not straightforward without rigorous local validation and calibration [88,90,96]. Table 6 presents several case studies exploring the spatial analysis and hotspot detection.

https://doi.org/10.3390/vehicles8040069

Table 6. Test cases related to spatial analysis and hotspot detection.

Ref.	Brief Summary of the Method	Data	Key Findings	Challenges
[16]	A geographically weighted atrous convolutional neural network regression model was proposed to capture spatial heterogeneity in the effects of the built environment on road safety. The approach addresses key limitations of classical geographically weighted regression, including the neglect of road network distance and the nonlinear decay of spatial influence.	Empirical crash and built environment data collected in Jinan City, China.	The proposed model outperforms classical geographically weighted regression in predictive performance. Intersection density and bus stop density emerge as stronger risk factors than population density, land use mix, and destination accessibility. Population density shows bidirectional effects, while land use mix exhibits pronounced spatial variability.	Integration of high-resolution spatial data is challenging due to data quality and resolution issues. The model is sensitive to local calibration choices such as bandwidth and weighting schemes, involves high computational cost, and is less interpretable than classical statistical models.
[81]	A mixed analytical pipeline was developed combining hierarchical clustering for hotspot detection, field validation through site visits and police reports, and injury severity prediction using supervised machine learning based on spatial and environmental attributes.	Crash data from the Yazd to Kerman Road in Iran, enriched with information on lighting, climate, road slope, alignment, and geometric characteristics. Contextual factors were verified through field inspections.	Overlapping clusters reveal two consistent high-risk zones. Identified causes include rest area locations, insufficient lighting on curves, inadequate signage, and reduced visibility during dust storms. For injury severity prediction, the k-nearest neighbors method achieved higher accuracy than the random forest approach.	Results depend strongly on the quality and consistency of spatial and field-collected data. Transferability is limited without local recalibration, and clustering outcomes are sensitive to parameter selection and location errors.
[79]	A critical review of spatial approaches in road safety research was conducted, covering spatial units of analysis, model families including econometric, Bayesian, and machine learning methods, spatial aggregation strategies, and well-known methodological issues such as the modifiable areal unit problem and boundary effects.	Published literature on spatial road safety analysis, including studies focused on vulnerable road users.	The review clarifies why spatial dependence and spatial heterogeneity matter in safety analysis and shows how choices related to spatial units and neighborhood definition can substantially influence results. It also synthesizes strengths, limitations, and future directions for spatial modeling approaches.	As a review study, it does not provide direct numerical results. The applicability of recommendations depends on context, and persistent structural issues such as the modifiable areal unit problem and comparability across studies remain unresolved.
[78]	Hotspot identification methods were compared along an expressway by evaluating ordinary kriging, kernel density estimation, and network-based kernel density estimation for detecting crash concentrations along road segments.	Fatal crash data collected along a 165-kilometer expressway in India between August 2012 and October 2018.	While all methods identify common high-risk locations, the comparative analysis shows that a network based on kernel density estimation is more effective for detecting hotspots along short road segments. The findings are particularly relevant for method selection in low- and middle-income country contexts.	The results depend on geocoding accuracy and road network representation and are sensitive to parameter settings such as bandwidth and segmentation. Limited or variable exposure data may bias method comparisons.
[96]	Crash frequency on two-lane highways was modeled by testing different temporal and spatial aggregation schemes using generalized estimating equations to account for correlation and excess zero crash counts.	Data from eighty-eight road segments of two hundred meters each located outside urban areas, including crash frequency, average annual daily traffic, and geometric characteristics, covering the period from nineteen ninety-nine to two thousand ten.	Key influencing factors include average annual daily traffic, lane width, vertical sinuosity, and the density of access points. The model provides acceptable crash prediction performance for four-hundred-meter segments aggregated over two-year periods.	Model results depend on the chosen aggregation scheme and sample size. A large number of zero-crash observations complicates estimation, and transferability to other road networks or countries requires recalibration.

3.5. Artificial Intelligence, Machine Learning, and Computer Vision in Intelligent Transportation Systems

Artificial intelligence, machine learning (ML), and computer vision are core components of modern intelligent transportation systems (ITS) that can automate perception, prediction, and decision-making in complex traffic scenes [74]. The vehicle detection, classification, and incident prediction represent some of the central parts in ITS, where deep

learning (DL) architectures improve recognition accuracy with complex real-life scenes that have variable-scale objects, occlusion, and multiple-view pose angles [10]. The most recent advances based on the YOLO (You Only Look Once) algorithm show promising results in vehicle detection at multiple orientations and spatial scales, overcoming drawbacks of traditional pipelines based on images [10]. In that way, Vehicular Ad Hoc Networks (VANETs) enable low-latency vehicle-to-infrastructure communication for real-time data sharing, such as traffic safety and coordinated control strategies [20]. With the development of big data analysis and ML, limitations in the matter of prediction and traffic optimization have evolved into making informed travel decisions as well as environmental impacts caused by congestion [84]. Multimodal sensing systems based on the combination of visual and auditory inputs also enhance perception by enabling robust recognition of emergency vehicles in poor visibility conditions or in the presence of background noise [21].

Advancements in learning methodologies are expanding the capabilities of ITS. The meta-transfer metric learning and deep space-time models are developed to further improve the model performance in small-data settings and enable adaptive learning, which would be valuable for next-generation communication systems such as 6G ITS [97,98]. The development of interpretable ML methodologies provides clear insights into complex crash causality, supporting real-world application operation and safety regulation [9]. Recent real-time AI solutions are able to handle real-time live broadcasts from cameras and traffic context data to identify accidents, blockages, and abnormal traffic density in smart city scenarios, enabling proactive traffic management. Security and communication ensure data exchange and integrity in the autonomous vehicle–infrastructure interactions, which employ blockchain-based authentication frameworks [99,100].

Big data analytics is another important component of modern ITS, supporting real-time large-scale data processing and big-data-driven safety management at the network level [11]. Large-scale metric learning approaches and deep convolutional neural networks (DNNs) offer an efficient alternative in terms of expenses to the manual safety inspection by processing vast volumes of road and infrastructure images [101]. The existing computer vision system, which detects facial landmarks, facilitates the detection of drowsiness and distraction in real time by precisely observing the degree of eyelid closure, blink dynamics, and yawn-induced microexpressions. [102,103]. ML systems synthesize data from traffic offenses, GPS traces, and crash history to build driver risk profiles, enabling preventative interventions by fleet managers [104,105]. These methods are extended through artificial neural networks (ANN) and gain-related learning structures that predict crash risk based on combined environmental and behavioral predictors, allowing for proactive countermeasures on highways [106].

Beyond perception and prediction, security and system resilience are important concerns. Blockchain-based authentication frameworks use certificate schemes to maintain anonymity and validate vehicle-to-infrastructure communication, which mitigates the problem of spoofing and tampering in distributed traffic scenarios [99,100]. Accident severity modeling using ML contributes to the identification of the risk factors associated with fatality and allows for targeted countermeasures against severe accidents and fatalities [107]. Integrating AI into IoT (Internet of Things) sensor networks, adaptive analytics pipelines, and distributed data management has the potential to improve the resilience and responsiveness of ITS from different operational levels [74,108]. These technologies enable ITS to sense, forecast, and act, transforming it from reactive surveillance systems to proactive safety management.

AI and ML represent a new operational model for ITS with automation of perception, prediction, and decision support [10,11,20]. DL methods are achieving human-comparable accuracy in tasks like vehicle detection and risk detection and can be optimized in real

https://doi.org/10.3390/vehicles8040069

time as well as predicted for reactive safety directly on road networks [74,97,109]. Scalable multimodal sensor fusion and scalable multimodal integration are expanding the range of system awareness to challenging visibility and noise conditions. Interpretable AI enables interventions based on proofs by uncovering a relevant neurometric relationship within complex predictive models [9,21,104]. Low-cost video analysis platforms facilitate continuous monitoring, which shifts road safety from reactive analysis to proactive control in connected mobility [101,108,110].

However, there are some limitations in the current work. The vast majority of AI and ML techniques require massive amounts of labeled training data, and such models' performance may degrade in adverse weather conditions like snow, fog, or nighttime [86,90,97]. Another limitation is related to high computational requirements, privacy constraints, and security vulnerabilities, which make them difficult for real-world deployment, especially in the case of applications at scale or applications with limited resources [9,99,102]. Even though there has been progress, model biases, limited generalization between regions, and gaps in technical infrastructure remain major obstacles to widespread adoption, especially in ITS applications for road safety, as they need to operate reliably in extreme, high-stakes situations [74,100,102,103,107]. In addition to the results in detection and prediction, the use of AI in ITS raises ethical and economic issues. AI systems often rely on large volumes of traffic, image, behavioral, and sensor data, which raises questions about privacy, data access, and use [11,21,24]. Another issue is the negative influence of the model and limited transparency, especially when complex models are used in traffic monitoring, risk detection, and automated assistance systems [9,102]. Security is also important, as connected transportation systems depend on reliable data exchange and protection against spoofing, manipulation, and unauthorized access [99,100]. From an economic point of view, the use of these systems depends on investments in sensors, computing resources, storage, communication infrastructure, and model maintenance [11,21]. These limitations show that the use of AI in road safety depends not only on model accuracy but also on data governance, system security, infrastructure capacity, and institutional support [24]. Representative test cases of ITS are detailed in Table 7.

Table 7. Test cases for artificial intelligence, machine learning, and computer vision in intelligent transportation systems.

Ref.	Brief Summary of the Method	Data	Key Findings	Challenges
[83]	Interpretable machine learning models were applied to crash prediction and road safety analysis, with the objective of balancing predictive performance and model transparency for safety-related decision-making.	Large-scale structured crash datasets, including roadway characteristics, traffic conditions, environmental factors, and behavioral variables.	The models identify dominant risk factors influencing crash occurrence and injury severity while maintaining transparency and trustworthiness suitable for safety-critical applications.	A trade-off exists between interpretability and predictive accuracy, and explainability techniques may oversimplify complex nonlinear relationships.
[21]	A big data analytics framework was developed to support traffic monitoring, bottleneck prediction, and safety management through large-scale data processing and machine learning techniques.	High-volume traffic data collected from sensors, global positioning traces, cameras, and historical traffic records at the network level.	The framework enables near-real-time assessment of traffic states and supports proactive safety management, reducing reliance on delayed crashes based on indicators.	Data heterogeneity and imbalance, high storage and computational requirements, and privacy and data protection concerns limit large-scale deployment.
[9]	A multimodal detection framework was proposed that combines visual and acoustic sensing to improve the recognition of emergency vehicles and critical traffic events under adverse conditions.	Synchronized video and acoustic data collected from roadside and in-vehicle sensors across a range of visibility and noise conditions.	Multimodal data fusion substantially improves detection robustness compared to vision-only approaches, particularly in low-visibility and high-noise environments.	The approach requires precise sensor synchronization, is sensitive to environmental noise, and involves increased computational and hardware demands.

Table 7. *Cont.*

Ref.	Brief Summary of the Method	Data	Key Findings	Challenges
[10]	A real-time incident detection system based on deep learning was developed using CNN-based object detection models, mainly YOLO and Faster R-CNN, integrated into a smart city architecture. The system processes live streams from street cameras to detect, classify, and assess the severity of road and environmental incidents and automatically generates alerts and reports for authorities and users.	A diverse annotated dataset of real-world traffic and environmental incidents (e.g., car accidents, fires, floods, road anomalies) obtained under the MIT license, combined with live video feeds from street cameras. Data augmentation and preprocessing techniques were applied to improve the robustness of the model.	The YOLO-based model achieved high real-time detection performance, with an average accuracy of approximately 91% and a mean accuracy (mAP) of 90% at a confidence threshold of 0.5. The system demonstrated efficient incident detection, classification, and severity assessment, supporting proactive traffic management and enhanced road safety in smart city environments.	Key limitations include the complexity of real-time multiple incident detection, sensitivity to environmental conditions and background noise, reliance on large annotated datasets, and computational requirements for real-time implementation in large-scale urban environments.
[107]	Machine learning-based accident severity models were developed to identify factors associated with fatal outcomes and to support targeted road safety interventions.	Multiyear crash datasets containing detailed injury severity information, vehicle characteristics, roadway attributes, and environmental conditions.	The analysis reveals key predictors of severe and fatal crashes, allowing prioritization of countermeasures for high-risk scenarios.	Severe class imbalance, sensitivity to reporting quality, and limited generalization without local recalibration constrain practical application.

Taken together, the themes identified by the BERTopic analysis show a change in the way road safety problems are studied. Earlier work focused mainly on accident description, injury analysis, and statistical modeling based on structured crash records. Recent studies show a stronger focus on machine learning, spatial analysis, computer vision, and multimodal data for prediction, monitoring, and prevention [22–24,26]. This change affects both research questions and research practice. Questions centered only on why crashes occurred are now accompanied by questions about where risk is forming, how it can be detected earlier, and how transport systems can respond before a crash occurs. This also links road safety research more directly to traffic operations, infrastructure planning, and intelligent transport systems [11,22–24,26].

4. Conclusions

Topic modeling analysis of publications from 2016 to 2025 based on BERTopic identified five main research directions in road safety: injury severity analysis, driver behavior, vulnerable road users, spatial analysis and hotspot detection, and artificial intelligence in intelligent transportation systems.

Recent studies show that data analysis and artificial intelligence methods can address several limitations of conventional statistical models. Traditional models often struggle to represent nonlinear relationships and complex interactions among road infrastructure, traffic conditions, human behavior, and environmental factors [1–7,15,31,32,36,38,42]. Hybrid models that incorporate DL architecture and classical ML algorithms provide better prediction capabilities. The growth of Explainable AI (XAI) techniques like SHapley Additive exPlanations (SHAP) improves model interpretability and advances trust in their outputs [5,6,9,35,36,42]. This interpretability is important to translating analytical results into decisions concerning spatial planning and road safety measures [9,11].

Another trend identified in the literature is the increasing use of multimodal data. These datasets combine spatial information, vehicle dynamics, driver behavior, and visual or sensor data. Such methods provide a more detailed representation of traffic risk and enable continuous monitoring of traffic participants and conditions. As a result, the focus of safety analysis is gradually shifting from retrospective accident studies toward proactive risk management and intervention before accidents occur [3,16,67,93,101]. The development of GIS and spatial modeling techniques such as Bayesian spatial models and geographically

weighted regression applications has also enhanced the identification of local risk patterns and high-risk locations across urban or regional road networks [58,78,80,83,85].

Research trends also relate to methods used in road safety. The use of artificial intelligence, spatial analysis, and sensors supports the development of driver assistance systems, traffic monitoring, incident detection, and infrastructure assessment [9–11,21]. Studies in this area show that machine learning, computer vision, and traffic data can improve incident detection, traffic monitoring, and accident risk prediction in traffic contexts [9–11,21].

These methods help to identify traffic hazards and provide real solutions for road traffic planning and management. In this context, the evolution towards safety prediction is connected not only to research methods but also to the use of data-driven transport systems and road safety management.

Despite these advances, several barriers continue to limit the practical implementation of road safety models based on artificial intelligence. Data quality remains a major challenge. Accident and traffic databases often contain missing values, inconsistent variable definitions, and differences between regional data collection systems. These issues reduce the ability of predictive models to perform well when applied outside the regions where they were developed [79,80,82,83]. A further limitation is that many researchers continue to treat accidents as isolated events rather than the output of processes that evolve over time. This static perspective restricts the development of real-time and adaptive safety plans [77,82,83].

Another limitation is that we only analyzed English-language publications. Road safety is highly localized, depending heavily on regional traffic laws, driving culture, and local infrastructure. Because we excluded non-English literature, our review likely misses some regional research, especially case studies published in national journals.

The reviewed literature suggests several directions for future research. One direction is the development of dynamic spatial and temporal risk models that capture how risk changes across time and space. Such models could better represent real traffic conditions and support adaptive safety measures. However, their application requires long and consistent time series data and involves complex model calibration and validation procedures [77,82–84,86].

A second direction involves the incorporation of multimodal data in unified analytical paradigms. Combining spatial, behavioral, and sensor-based data can improve risk estimation and situational awareness. At the same time, such an approach has limitations related to data heterogeneity, synchronization between sources, or high computational cost. To address these, research must shift attention towards consistent data processing algorithms and proficient data integration strategies [3,16,67,93,101].

A third direction is to use local and adaptive models to handle spatial heterogeneity in a more realistic way. Approaches such as geographically weighted regression and spatial machine learning make it possible to see that the relationships between risk factors and road accidents differ across space. Their important benefit is that they can provide targeted and situational safety precautions. A significant drawback of these models is their parameter sensitivity and poor transferability, often requiring careful recalibration for each new geographic region [83–86].

A fourth direction is utilizing critical driving events and naturalistic driving data to predict risk proactively. The analysis of near-miss situations and safety-critical maneuvers makes these methods capable of discovering risks prior to accidents and supporting the development of early warning systems. Their principal drawbacks are that they depend on sophisticated sensing infrastructure, associated privacy issues, and the lack of a uniform definition of a critical event [80,95].

A fifth direction concerns improving the transfer of models across regions. Predictive models based on artificial intelligence may perform well in one context but show reduced accuracy when applied to different geographic or cultural environments. Future research should therefore focus on cross-region validation, domain adaptation methods, and automatic model recalibration. Although these methods could improve practical applicability, they still depend on improved data harmonization and resources for continuous validation [79,80,82,83,94,98].

Road safety research is moving toward predictive and proactive approaches supported by artificial intelligence and spatial analysis. These methods offer improvements in predictive performance and analytical capability. However, their practical impact depends on addressing current challenges related to data quality, model transparency, robustness, and transferability. Further progress in the field will require not only methodological advances but also coordinated efforts in data standardization and responsible implementation of artificial intelligence in transportation systems [98,104,105,107–109].

Author Contributions: Conceptualization, F.G. and I.A.T.; methodology, F.G. and I.A.T.; software, F.G.; validation, F.G. and I.A.T.; formal analysis, I.A.T.; investigation, F.G. and I.A.T.; resources, I.A.T.; data curation, F.G. and I.A.T.; writing—original draft preparation, F.G. and I.A.T.; writing—review and editing, F.G. and I.A.T.; visualization, F.G.; supervision, F.G.; project administration, F.G. All authors have read and agreed to the published version of the manuscript.

Funding: This work was supported by a grant of the Ministry of Research, Innovation and Digitization, CNCS-UEFISCDI, project number PN-IV-P2-2.1-TE-2023-1434, within PNCDI IV.

Data Availability Statement: The original contributions presented in this study are included in the article. Further inquiries can be directed to the corresponding author.

Conflicts of Interest: The authors declare no conflicts of interest. The funders had no role in the design of the study; in the collection, analyses, or interpretation of the data; in the writing of the manuscript; or in the decision to publish the results.

Abbreviations

The following abbreviations are used in this manuscript:

AI	Artificial Intelligence
ML	Machine Learning
DL	Deep Learning
ITS	Intelligent Transportation Systems
VRUs	Vulnerable Road Users
CNN	Convolutional Neural Network
ANN	Artificial Neural Network
DNN	Deep Neural Network
GIS	Geographic Information Systems
NLP	Natural Language Processing
NLTK	Natural Language Toolkit
BERTopic	Bidirectional Encoder Representations from Transformers for Topic Modeling
c-TF-IDF	Class-based Term Frequency–Inverse Document Frequency
UMAP	Uniform Manifold Approximation and Projection
HDBSCAN	Hierarchical Density-Based Spatial Clustering of Applications with Noise
POS	Part-of-Speech
YOLO	You Only Look Once
VANETs	Vehicular Ad Hoc Networks
IoT	Internet of Things
GPS	Global Positioning System

XAI	Explainable Artificial Intelligence
SHAP	SHapley Additive exPlanations
GWR	Geographically Weighted Regression
MGWR	Multiscale Geographically Weighted Regression
GWNN	Geographically Weighted Neural Network
GWRF	Geographically Weighted Random Forest
EB	Electric Bicycle
GOMs	Generalized Ordered Probit Models
6G	Sixth Generation Mobile Networks
MIT	Massachusetts Institute of Technology
mAP	mean Average Precision
ECG	Electrocardiogram
AutoML	Automated Machine Learning
AUC	Area Under the Curve
EEG	Electroencephalography
CAN-bus	Controller Area Network bus
ADAS	Advanced Driver Assistance Systems
XGBoost	Extreme Gradient Boosting
ROC	Receiver Operating Characteristic

Appendix A

TITLE-ABS-KEY (Road accident analysis) AND PUBYEAR > 2015 AND PUBYEAR < 2026 AND (LIMIT-TO (DOCTYPE, "ar") OR LIMIT-TO (DOCTYPE, "cp") OR LIMIT-TO (DOCTYPE, "re") OR LIMIT-TO (DOCTYPE, "ch") OR LIMIT-TO (DOCTYPE, "sh") OR LIMIT-TO (DOCTYPE, "dp")) AND (LIMIT-TO (LANGUAGE, "English"))

References

1. Ghomi, H.; Bagheri, M.; Fu, L.; Miranda-Moreno, L.F. Analyzing injury severity factors at highway railway grade crossing accidents involving vulnerable road users: A comparative study. *J. Traffic Inj. Prev.* **2016**, *17*, 833–841. [CrossRef]
2. Haleem, K.; Alluri, P.; Gan, A. Analyzing pedestrian crash injury severity at signalized and non-signalized locations. *J. Accid. Anal. Prev.* **2015**, *81*, 14–23. [CrossRef] [PubMed]
3. Santos, K.; Dias, J.P.; Amado, C. A literature review of machine learning algorithms for crash injury severity prediction. *J. Saf. Res.* **2022**, *80*, 254–269. [CrossRef] [PubMed]
4. Liu, S.; Fan, W.D.; Li, Y. Injury severity analysis of rollover crashes for passenger cars and light trucks considering temporal stability: A random parameters logit approach with heterogeneity in mean and variance. *J. Saf. Res.* **2021**, *78*, 276–291. [CrossRef]
5. Madushani, J.S.; Sandamal, R.K.; Meddage, D.; Pasindu, H.; Gomes, P.A. Evaluating expressway traffic crash severity by using logistic regression and explainable & supervised machine learning classifiers. *J. Transp. Eng.* **2023**, *13*, 100190.
6. Rahim, M.A.; Hassan, H.M. A deep learning based traffic crash severity prediction framework. *J. Accid. Anal. Prev.* **2021**, *154*, 106090. [CrossRef]
7. Tanishita, M.; Sekiguchi, Y.; Sunaga, D. Impact analysis of road infrastructure and traffic control on severity of pedestrian–vehicle crashes at intersections and non-intersections using bias-reduced logistic regression. *J. IATSS Res.* **2023**, *47*, 233–239. [CrossRef]
8. Helland, A.; Lydersen, S.; Lervåg, L.-E.; Jenssen, G.D.; Mørland, J.; Slørdal, L. Driving simulator sickness: Impact on driving performance, influence of blood alcohol concentration, and effect of repeated simulator exposures. *J. Accid. Anal. Prev.* **2016**, *94*, 180–187. [CrossRef]
9. Ahmed, S.; Hossain, M.A.; Ray, S.K.; Bhuiyan, M.M.I.; Sabuj, S.R. A study on road accident prediction and contributing factors using explainable machine learning models: Analysis and performance. *J. Transp. Res. Interdiscip. Perspect.* **2023**, *19*, 100814. [CrossRef]
10. Berwo, M.A.; Fang, Y.; Sarwar, N.; Mahmood, J.; Aljohani, M.; Elhosseini, M. YOLOv8n-CGW: A novel approach to multi-oriented vehicle detection in intelligent transportation systems. *J. Multimed. Tools Appl.* **2025**, *84*, 3809–3840. [CrossRef]
11. Nguyen, H.P.; Nguyen, P.Q.P.; Bui, V.D. Applications of big data analytics in traffic management in intelligent transportation systems. *J. JOIV: Int. J. Inform. Vis.* **2022**, *6*, 177–187. [CrossRef]
12. Chen, L.-l.; Zhao, Y.; Ye, P.-f.; Zhang, J.; Zou, J.-z. Detecting driving stress in physiological signals based on multimodal feature analysis and kernel classifiers. *J. Expert. Syst. Appl.* **2017**, *85*, 279–291. [CrossRef]

13. Hu, Y.; Wang, F.; Ye, D.; Wu, M.; Kang, J.; Yu, R. Llm-based misbehavior detection architecture for enhanced traffic safety in connected autonomous vehicles. *J. IEEE Trans. Veh. Technol.* **2025**, *74*, 12829–12841. [CrossRef]
14. Useche, S.A.; Alonso, F.; Montoro, L.; Esteban, C. Distraction of cyclists: How does it influence their risky behaviors and traffic crashes? *J. PeerJ* **2018**, *6*, e5616. [CrossRef] [PubMed]
15. Cheng, W.; Gill, G.S.; Sakrani, T.; Dasu, M.; Zhou, J. Predicting motorcycle crash injury severity using weather data and alternative Bayesian multivariate crash frequency models. *J. Accid. Anal. Prev.* **2017**, *108*, 172–180. [CrossRef] [PubMed]
16. Li, T.; Liu, S.; Fan, G.; Zhao, H.; Zhang, M.; Fan, J.; Li, C. Spatial heterogeneity effect of built environment on traffic safety using geographically weighted atrous convolutions neural network. *J. Accid. Anal. Prev.* **2025**, *213*, 107934. [CrossRef]
17. Merzougui, S.E.; Limani, X.; Gavrielides, A.; Reiter, P.; Palazzi, C.E.; Marquez-Barja, J. Leveraging edge computing and orchestration platform for enhanced pedestrian safety application: The DEDICAT-6G approach. In *Proceedings of the 2024 IEEE 21st Consumer Communications & Networking Conference (CCNC)*; IEEE: New York, NY, USA, 2024; pp. 380–383.
18. Mukherjee, D. Assessing pedestrian safety at urban signalized intersections across various land use types: Insights from a mid-sized Indian city. *J. Discov. Appl. Sci.* **2025**, *7*, 384. [CrossRef]
19. Wang, S.; Gao, K.; Zhang, L.; Yu, B.; Easa, S.M. Geographically weighted machine learning for modeling spatial heterogeneity in traffic crash frequency and determinants in US. *J. Accid. Anal. Prev.* **2024**, *199*, 107528. [CrossRef]
20. Behura, A.; Kumar, A.; Jain, P.K. A comparative performance analysis of vehicular routing protocols in intelligent transportation systems. *J. Telecommun. Syst.* **2025**, *88*, 26. [CrossRef]
21. Zohaib, M.; Asim, M.; ELAffendi, M. Enhancing emergency vehicle detection: A deep learning approach with multimodal fusion. *J. Math.* **2024**, *12*, 1514. [CrossRef]
22. Tzika-Kostopoulou, D.; Nathanail, E.; Kokkinos, K. Big data in transportation: A systematic literature analysis and topic classification. *J. Knowl. Inf. Syst.* **2024**, *66*, 5021–5046. [CrossRef]
23. Ulu, M.; Türkan, Y.S. Bibliometric Analysis of Traffic Accident Prediction Studies from 2003 to 2023: Trends, Patterns and Future Directions. *J Promet-Traffic Transp.* **2024**, *36*, 833–851. [CrossRef]
24. Woo, S.H.; Choi, M.S.; Duffy, V.G. Artificial Intelligence and Transportations on Road Safety: A Bibliometric Review. In *Proceedings of the International Conference on Human-Computer Interaction*; Springer Nature: Berlin/Heidelberg, Germany, 2023; pp. 450–464.
25. Zou, X.; Vu, H.L.; Huang, H. Fifty years of accident analysis & prevention: A bibliometric and scientometric overview. *J. Accid. Anal. Prev.* **2020**, *144*, 105568.
26. Skaug, L.; Nojoumian, M.; Dang, N.; Yap, A. Road Crash Analysis and Modeling: A Systematic Review of Methods, Data, and Emerging Technologies. *J. Appl. Sci.* **2025**, *15*, 7115. [CrossRef]
27. Ali, Y.; Hussain, F.; Haque, M.M. Advances, challenges, and future research needs in machine learning-based crash prediction models: A systematic review. *J. Accid. Anal. Prev.* **2024**, *194*, 107–378. [CrossRef]
28. Angarita-Zapata, J.S.; Maestre-Gongora, G.; Calderín, J.F. A bibliometric analysis and benchmark of machine learning and automl in crash severity prediction: The case study of three colombian cities. *J. Sens.* **2021**, *21*, 8401. [CrossRef]
29. Silva, P.B.; Andrade, M.; Ferreira, S. Machine learning applied to road safety modeling: A systematic literature review. *J. Traffic Transp. Eng.* **2020**, *7*, 775–790. [CrossRef]
30. Grootendorst, M. BERTopic: Neural topic modeling with a class-based TF-IDF procedure. *arXiv* **2022**, arXiv:2203.05794.
31. Duddu, V.R.; Penmetsa, P.; Pulugurtha, S.S. Modeling and comparing injury severity of at-fault and not at-fault drivers in crashes. *J. Accid. Anal. Prev.* **2018**, *120*, 55–63. [CrossRef]
32. Jamal, A.; Zahid, M.; Tauhidur Rahman, M.; Al-Ahmadi, H.M.; Almoshaogeh, M.; Farooq, D.; Ahmad, M. Injury severity prediction of traffic crashes with ensemble machine learning techniques: A comparative study. *J. Int. J. Inj. Control Saf. Promot.* **2021**, *28*, 408–427. [CrossRef]
33. Chang, F.; Haque, M.M.; Yasmin, S.; Huang, H. Crash injury severity analysis of E-Bike Riders: A random parameters generalized ordered probit model with heterogeneity in means. *J. Saf. Sci.* **2022**, *146*, 105545. [CrossRef]
34. Qian, Q.; Shi, J. Comparison of injury severity between E-bikes-related and other two-wheelers-related accidents: Based on an accident dataset. *J. Accid. Anal. Prev.* **2023**, *190*, 107189. [CrossRef] [PubMed]
35. Ijaz, M.; Zahid, M.; Jamal, A. A comparative study of machine learning classifiers for injury severity prediction of crashes involving three-wheeled motorized rickshaw. *J. Accid. Anal. Prev.* **2021**, *154*, 106094. [CrossRef] [PubMed]
36. Santos, K.; Firme, B.; Dias, J.P.; Amado, C. Analysis of motorcycle accident injury severity and performance comparison of machine learning algorithms. *J. Transp. Res. Rec.* **2024**, *2678*, 736–748. [CrossRef]
37. Shao, Y.; Shi, X.; Zhang, Y.; Shiwakoti, N.; Xu, Y.; Ye, Z. Injury severity prediction and exploration of behavior-cause relationships in automotive crashes using natural language processing and extreme gradient boosting. *J. Eng. Appl. Artif. Intell.* **2024**, *133*, 108542. [CrossRef]
38. Zeng, Q.; Wang, Q.; Zhang, K.; Wong, S.; Xu, P. Analysis of the injury severity of motor vehicle–pedestrian crashes at urban intersections using spatiotemporal logistic regression models. *J. Accid. Anal. Prev.* **2023**, *189*, 107119. [CrossRef]

39. Singh, N.; Kumar, M. Conceptual Framework for Accident Prone Hotspot Identification and Removal using Historical Data Analytics. In *Proceedings of the 2020 IEEE 17th India Council International Conference (INDICON)*; IEEE: New York, NY, USA, 2020; pp. 1–7.
40. Vandana, B.; Jogi, S.; Shenoy, G.; Karanth, S.; Hegde, S. A Comprehensive Framework for Accident Detection and Risk Assessment Using CNN and Graph-Based Analytics. In *Proceedings of the 2025 International Conference on Artificial Intelligence and Data Engineering (AIDE)*; IEEE: New York, NY, USA, 2025; pp. 834–839.
41. Nour, M.K.; Naseer, A.; Alkazemi, B.; Jamil, M.A. Road traffic accidents injury data analytics. *J. Int. J. Adv. Comput. Sci. Appl.* **2020**, *11*, 762–770. [CrossRef]
42. Zhang, J.; Li, Z.; Pu, Z.; Xu, C. Comparing prediction performance for crash injury severity among various machine learning and statistical methods. *J. IEEE Access* **2018**, *6*, 60079–60087. [CrossRef]
43. Alkinani, M.H.; Khan, W.Z.; Arshad, Q. Detecting human driver inattentive and aggressive driving behavior using deep learning: Recent advances, requirements and open challenges. *J. IEEE Access* **2020**, *8*, 105008–105030. [CrossRef]
44. Magaña, V.C.; Pañeda, X.G.; Garcia, R.; Paiva, S.; Pozueco, L. Beside and behind the wheel: Factors that influence driving stress and driving behavior. *J. Sustain.* **2021**, *13*, 4775. [CrossRef]
45. Rabea, A.F.A.; Ahmad, S.A.; Jantan, S.D.; Soh, A.C.; Ishak, A.J.; Adnan, R.N.E.R.; Al-Qazzaz, N.K. Driver's fatigue classification based on physiological signals using rnn-lstm technique. In *Proceedings of the 2022 IEEE-EMBS Conference on Biomedical Engineering and Sciences (IECBES)*; IEEE: New York, NY, USA, 2022; pp. 280–285.
46. Mallia, L.; Lazuras, L.; Violani, C.; Lucidi, F. Crash risk and aberrant driving behaviors among bus drivers: The role of personality and attitudes towards traffic safety. *J. Accid. Anal. Prev.* **2015**, *79*, 145–151. [CrossRef]
47. Xiao, Y.; Dai, M.; Xue, S. Driving Behavior of Older and Younger Drivers in Simplified Emergency Scenarios. *J. Sens.* **2025**, *25*, 5178. [CrossRef] [PubMed]
48. Valente, J.; Ramalho, C.; Vinha, P.; Mora, C.; Jardim, S. Using machine learning to understand driving behavior patterns. *J. Procedia Comput. Sci.* **2024**, *239*, 1823–1830. [CrossRef]
49. Fugiglando, U.; Massaro, E.; Santi, P.; Milardo, S.; Abida, K.; Stahlmann, R.; Netter, F.; Ratti, C. Driving behavior analysis through CAN bus data in an uncontrolled environment. *J. IEEE Trans. Intell. Transp. Syst.* **2018**, *20*, 737–748. [CrossRef]
50. Yuan, D.; Zhou, K.; Yang, C. Architecture and application of traffic safety management knowledge graph based on Neo4j. *J. Sustain.* **2023**, *15*, 9786. [CrossRef]
51. Damodariya, S.; Patel, C. Identification of factors causing risky driving behavior on high-speed multi-lane highways in India through principal component analysis. *J. Int. J. Eng.* **2022**, *35*, 2130–2138. [CrossRef]
52. Distefano, N.; Leonardi, S.; Pulvirenti, G.; Romano, R.; Merat, N.; Boer, E.; Woolridge, E. Physiological and driving behaviour changes associated to different road intersections. *J. Eur. Transp.* **2020**, *77*, 4. [CrossRef]
53. Moin, A.S.; Tanuja, C.; Kumar, N.S.; Nallakaruppan, M.; Senthilkumaran, U. Sensing drunken drivers using data science. In *Proceedings of the 2019 5th International Conference on Advanced Computing & Communication Systems (ICACCS)*; IEEE: New York, NY, USA, 2019; pp. 1148–1151.
54. Sahayadhas, A.; Sundaraj, K.; Murugappan, M.; Palaniappan, R. Physiological signal based detection of driver hypovigilance using higher order spectra. *J. Expert. Syst. Appl.* **2015**, *42*, 8669–8677. [CrossRef]
55. Selvathi, D.; Dhivya, N. Realization of VLSI architecture to detect driver drowsiness for road accident avoidance system. In *Proceedings of the 2016 Online International Conference on Green Engineering and Technologies (IC-GET)*; IEEE: New York, NY, USA, 2016; pp. 1–5.
56. Nouh, R.; Singh, M.; Singh, D. SafeDrive: Hybrid recommendation system architecture for early safety predication using Internet of Vehicles. *J. Sens.* **2021**, *21*, 3893. [CrossRef]
57. Wu, C.-C. The development and implementation of driving information collection and recording system for driving behavior analysis. In *Proceedings of the 2020 IEEE International Conference on Consumer Electronics-Taiwan (ICCE-Taiwan)*; IEEE: New York, NY, USA, 2020; pp. 1–2.
58. Xu, L.; Guo, L.; Ge, P.; Wang, X. Transition in Different Critical Situations: How Non-Driving Related Tasks Affect Drivers' Physiological Response and Takeover Behavior After Partial Automation Silent Failures. *J. IEEE Trans. Intell. Transp. Syst.* **2024**, *25*, 16642–16652. [CrossRef]
59. Hyder, A.; Subbarao, S.S. Navigating safety: Pedestrian safety perceptions at uncontrolled crosswalks in Hyderabad, India. *J. Innov. Infrastruct. Solut.* **2025**, *10*, 11. [CrossRef]
60. Kim, S.; Choi, S.; Kim, B.H. Analysis of factors affecting pedestrian safety for the elderly and identification of vulnerable areas in Seoul. *J. Accid. Anal. Prev.* **2025**, *211*, 107878. [CrossRef] [PubMed]
61. Hussain, M.S.; Kumari, R.; Nimesh, V.; Goswami, A.K. Assessing impact of urban street infrastructure on pedestrian safety perception. *J. Proc. Inst. Civ. Eng.-Urban Des. Plan.* **2021**, *174*, 76–84. [CrossRef]
62. Stipancic, J.; Miranda-Moreno, L.; Strauss, J.; Labbe, A. Pedestrian safety at signalized intersections: Modelling spatial effects of exposure, geometry and signalization on a large urban network. *J. Accid. Anal. Prev.* **2020**, *134*, 105265. [CrossRef]
63. Ihssian, A.; Ismail, K. Pedestrian Safety Perception Analysis at Intersections in Ottawa. In *Proceedings of the Canadian Society of Civil Engineering Annual Conference*; Springer Nature: Berlin/Heidelberg, Germany, 2023; pp. 15–26.

64. Singh, S.; Ali, Y.; Haque, M.M. A Bayesian extreme value theory modelling framework to assess corridor-wide pedestrian safety using autonomous vehicle sensor data. *J. Accid. Anal. Prev.* **2024**, *195*, 107416. [CrossRef] [PubMed]
65. Budzynski, M.; Jamroz, K.; Mackun, T. Pedestrian safety in road traffic in Poland. In *Proceedings of the IOP Conference Series: Materials Science and Engineering*; IOP: Bristol, UK, 2017; p. 042064.
66. Guo, Q.; Xu, P.; Pei, X.; Wong, S.; Yao, D. The effect of road network patterns on pedestrian safety: A zone-based Bayesian spatial modeling approach. *J. Accid. Anal. Prev.* **2017**, *99*, 114–124. [CrossRef]
67. Kaygisiz, Ö.; Yildiz, A.; Duzgun, S. Spatio-temporal pedestrian accident analysis to improve urban pedestrian safety: The case of the Eskisehir Motorway. *J. Gazi Univ. J. Sci.* **2015**, *28*, 623–630.
68. Koekemoer, K.; Van Gesselleen, M.; Van Niekerk, A.; Govender, R.; Van As, A.B. Child pedestrian safety knowledge, behaviour and road injury in Cape Town, South Africa. *J. Accid. Anal. Prev.* **2017**, *99*, 202–209. [CrossRef]
69. Lin, P.-S.; Guo, R.; Bialkowska-Jelinska, E.; Kourtellis, A.; Zhang, Y. Development of countermeasures to effectively improve pedestrian safety in low-income areas. *J. Traffic Transp. Eng.* **2019**, *6*, 162–174. [CrossRef]
70. Ham, J.-S.; Kim, D.H.; Jung, N.; Moon, J. Cipf: Crossing intention prediction network based on feature fusion modules for improving pedestrian safety. In Proceedings of the Proceedings of the IEEE/CVF Conference on Computer Vision and Pattern Recognition; IEEE: New York, NY, USA, 2023; pp. 3666–3675.
71. Mahdinia, I.; Khattak, A.J.; Haque, A.M. How effective are pedestrian crash prevention systems in improving pedestrian safety? Harnessing large-scale experimental data. *J. Accid. Anal. Prev.* **2022**, *171*, 106669. [CrossRef]
72. Zainala, S.K.; Borhana, M.N.; Yazid, M.M.; Ibrahim, A.H. The application of theory of planned behaviour in pedestrian safety: A literature approach. *J. Kejuruter.* **2023**, *35*, 539–549. [CrossRef]
73. Utriainen, R. The potential impacts of automated vehicles on pedestrian safety in a four-season country. *J. Intell. Transp. Syst.* **2020**, *25*, 188–196. [CrossRef]
74. Zhu, L.; Yu, F.R.; Wang, Y.; Ning, B.; Tang, T. Big data analytics in intelligent transportation systems: A survey. *J. IEEE Trans. Intell. Transp. Syst.* **2018**, *20*, 383–398. [CrossRef]
75. Jung, S.; Qin, X.; Oh, C. Improving strategic policies for pedestrian safety enhancement using classification tree modeling. *J. Transp. Res. Part A Policy Pract.* **2016**, *85*, 53–64. [CrossRef]
76. Ni, Y.; Wang, M.; Sun, J.; Li, K. Evaluation of pedestrian safety at intersections: A theoretical framework based on pedestrian-vehicle interaction patterns. *J. Accid. Anal. Prev.* **2016**, *96*, 118–129. [CrossRef]
77. Zhu, H.; Almukdad, A.; Iryo-Asano, M.; Alhajyaseen, W.K.; Nakamura, H.; Zhang, X. A novel agent-based framework for evaluating pedestrian safety at unsignalized mid-block crosswalks. *J. Accid. Anal. Prev.* **2021**, *159*, 106288. [CrossRef]
78. Ziakopoulos, A.; Yannis, G. A review of spatial approaches in road safety. *J. Accid. Anal. Prev.* **2020**, *135*, 105323. [CrossRef]
79. Bisht, L.S.; Tiwari, G. Identification of road traffic crashes hotspots on an intercity expressway in India using geospatial techniques. *J. IATSS Res.* **2023**, *47*, 349–356. [CrossRef]
80. Kamh, H.; Alyami, S.H.; Khattak, A.; Alyami, M.; Almujibah, H. Exploring road traffic accidents hotspots using clustering algorithms and GIS-based spatial analysis. *J. IEEE Access* **2024**, *13*, 60944–60954. [CrossRef]
81. Khosravi, Y.; Hosseinali, F.; Adresi, M. Identifying accident prone areas and factors influencing the severity of crashes using machine learning and spatial analyses. *J. Sci. Rep.* **2024**, *14*, 29836. [CrossRef]
82. Mekonnen, E.; Quezon, E.T.; Mohammed, M. Investigation of traffic accident prone areas related to existing road condition and driver's behavior along Menagesha-Ambo road section. *Glob. Sci. J.* **2018**, *6*, 82.
83. Assi, K. Traffic crash severity prediction—A synergy by hybrid principal component analysis and machine learning models. *J. Int. J. Environ. Res. Public Health* **2020**, *17*, 7598. [CrossRef] [PubMed]
84. Huang, Y.; Wang, X.; Patton, D. Examining spatial relationships between crashes and the built environment: A geographically weighted regression approach. *J. Transp. Geogr.* **2018**, *69*, 221–233. [CrossRef]
85. Zhang, Z.; Xu, N.; Liu, J.; Jones, S. Exploring spatial heterogeneity in factors associated with injury severity in speeding-related crashes: An integrated machine learning and spatial modeling approach. *J. Accid. Anal. Prev.* **2024**, *206*, 107697. [CrossRef]
86. Tang, X.; Bi, R.; Wang, Z. Spatial analysis of moving-vehicle crashes and fixed-object crashes based on multi-scale geographically weighted regression. *J. Accid. Anal. Prev.* **2023**, *189*, 107123. [CrossRef]
87. Rhee, K.-A.; Kim, J.-K.; Lee, Y.-i.; Ulfarsson, G.F. Spatial regression analysis of traffic crashes in Seoul. *J. Accid. Anal. Prev.* **2016**, *91*, 190–199. [CrossRef]
88. Soro, W.L.; Zhou, Y.; Wayoro, D. Crash rates analysis in China using a spatial panel model. *J. IATSS Res.* **2017**, *41*, 123–128. [CrossRef]
89. Bei, R.; Du, Z.; Lyu, N.; Yu, L.; Yang, Y. Exploring the Mechanism for Increased Risk in Freeway Tunnel Approach Zones: A Perspective on Temporal-spatial Evolution of Driving Predictions, Tasks, and Behaviors. *J. Accid. Anal. Prev.* **2025**, *211*, 107914. [CrossRef]
90. Kumar, S.; Toshniwal, D.; Parida, M. A comparative analysis of heterogeneity in road accident data using data mining techniques. *J. Evol. Syst.* **2017**, *8*, 147–155. [CrossRef]

91. Yan, Y.; Zhang, Y.; Yang, X.; Hu, J.; Tang, J.; Guo, Z. Crash prediction based on random effect negative binomial model considering data heterogeneity. *J. Phys. A Stat. Mech. Its Appl.* **2020**, *547*, 123858. [CrossRef]
92. Fountas, G.; Fonzone, A.; Olowosegun, A.; McTigue, C. Addressing unobserved heterogeneity in the analysis of bicycle crash injuries in Scotland: A correlated random parameters ordered probit approach with heterogeneity in means. *J. Anal. Methods Accid. Res.* **2021**, *32*, 100181. [CrossRef]
93. Ren, Q.; Xu, M. Heterogeneity in crash patterns of autonomous vehicles: The latent class analysis coupled with multinomial logit model. *J. Accid. Anal. Prev.* **2025**, *209*, 107827. [CrossRef] [PubMed]
94. Diao, C.; Zhang, D.; Liang, W.; Li, K.-C.; Hong, Y.; Gaudiot, J.-L. A novel spatial-temporal multi-scale alignment graph neural network security model for vehicles prediction. *J. IEEE Trans. Intell. Transp. Syst.* **2022**, *24*, 904–914. [CrossRef]
95. Ryder, B.; Dahlinger, A.; Gahr, B.; Zundritsch, P.; Wortmann, F.; Fleisch, E. Spatial prediction of traffic accidents with critical driving events–Insights from a nationwide field study. *J. Transp. Res. Part. A Policy Pract.* **2019**, *124*, 611–626. [CrossRef]
96. Costa, J.O.; Maria, A.P.; Pereira, P.A.; Freitas, E.F.; Soares, F.E. Portuguese two-lane highways: Modelling crash frequencies for different temporal and spatial aggregation of crash data. *J. Transp. Res. Interdiscip. Perspect.* **2018**, *33*, 92–103.
97. Staby, S.; Manjusha, R. Spatial-temporal analysis for traffic incident detection using deep learning. In *Proceedings of the 2023 Innovations in Power and Advanced Computing Technologies (i-PACT)*; IEEE: New York, NY, USA, 2023; pp. 1–6.
98. Sun, L.; Liang, J.; Zhang, C.; Wu, D.; Zhang, Y. Meta-transfer metric learning for time series classification in 6G-supported intelligent transportation systems. *J. IEEE Trans. Intell. Transp. Syst.* **2023**, *25*, 2757–2767. [CrossRef]
99. Lei, A.; Cruickshank, H.; Cao, Y.; Asuquo, P.; Ogah, C.P.A.; Sun, Z. Blockchain-based dynamic key management for heterogeneous intelligent transportation systems. *J. IEEE Internet Things J.* **2017**, *4*, 1832–1843. [CrossRef]
100. Vangala, A.; Bera, B.; Saha, S.; Das, A.K.; Kumar, N.; Park, Y. Blockchain-enabled certificate-based authentication for vehicle accident detection and notification in intelligent transportation systems. *J. IEEE Sens. J.* **2020**, *21*, 15824–15838. [CrossRef]
101. Wang, L.; Gong, W.; Li, X. Deep convolutional neural network and its application in image recognition of road safety projects. *J. Int. J. Perform. Eng.* **2019**, *15*, 2182.
102. Albasrawi, R.; Fadhil, F.F.; Ghazal, M.T. Driver drowsiness monitoring system based on facial Landmark detection with convolutional neural network for prediction. *J. Bull. Electr. Eng. Inform.* **2022**, *11*, 2637–2644. [CrossRef]
103. Rathi, R.; Sawant, A.; Jain, L.; Kulkarni, S. Driver Fatigue and Distraction Analysis Using Machine Learning Algorithms. In *Proceedings of the International Conference on Innovative Computing and Communications: Proceedings of ICICC 2020*; Springer Nature: Berlin/Heidelberg, Germany, 2020; Volume 1, pp. 1037–1046.
104. Fang, A.; Qiu, C.; Zhao, L.; Jin, Y. Driver risk assessment using traffic violation and accident data by machine learning approaches. In *Proceedings of the 2018 3rd IEEE International Conference on Intelligent Transportation Engineering (ICITE)*; IEEE: New York, NY, USA, 2018; pp. 291–295.
105. Thaika, M.; Tasneeyapant, S.; Cheamanunkul, S. A fast, scalable, unsupervised approach to real-time traffic incident detection. In *Proceedings of the 2018 15th International Joint Conference on Computer Science and Software Engineering (JCSSE)*; IEEE: New York, NY, USA, 2018; pp. 1–6.
106. Yasin Çodur, M.; Tortum, A. An artificial neural network model for highway accident prediction: A case study of Erzurum, Turkey. *J. Promet-Traffic Transp.* **2015**, *27*, 217–225.
107. Jamal, A.; Umer, W. Exploring the injury severity risk factors in fatal crashes with neural network. *J. Int. J. Environ. Res. Public Health* **2020**, *17*, 7466. [CrossRef] [PubMed]
108. Nikolaev, A.B.; Sapego, Y.S.; Ivakhnenko, A.M.; Stroganov, V. Analysis of the incident detection technologies and algorithms in intelligent transport systems. *J. Int. J. Appl. Eng. Res.* **2017**, *12*, 4765–4774.
109. Chawla, P.; Hasurkar, R.; Bogadi, C.R.; Korlapati, N.S.; Rajendran, R.; Ravichandran, S.; Tolem, S.C.; Gao, J.Z. Real-time traffic congestion prediction using big data and machine learning techniques. *J. World J. Eng.* **2024**, *21*, 140–155. [CrossRef]
110. Al-Agroudy, Z.; Mohamed, A.; Ashraf, Z.; Al-Sayed, S.; Gad, W.; Hassan, Z.; Reda, R. AI-safe transportation: Real-time incident detection and alerting system in smart cities. In *Proceedings of the 2023 Eleventh International Conference on Intelligent Computing and Information Systems (ICICIS)*; IEEE: New York, NY, USA, 2023; pp. 523–529.

Disclaimer/Publisher's Note: The statements, opinions and data contained in all publications are solely those of the individual author(s) and contributor(s) and not of MDPI and/or the editor(s). MDPI and/or the editor(s) disclaim responsibility for any injury to people or property resulting from any ideas, methods, instructions or products referred to in the content.

vehicles

MDPI

Article

Assessment of the Risk of Injury in Frontal Collision: Comparison Between Real Crash Tests and Simulation, with Analysis of the Worst-Case Scenarios

Oana-Victoria Stanciuc-Otat [1,2], Burkhard Scholz [2], Ilie Dumitru [1] and Cosmin Berceanu [1,*]

[1] Faculty of Mechanics, University of Craiova, 200512 Craiova, Romania; oana.otat@edu.ucv.ro (O.-V.S.-O.); ilie.dumitru@edu.ucv.ro (I.D.)
[2] IAV Fahrzeugsicherheit GmbH & Co. KG, Junkers-Ring 10, 85098 Grossmehring, Germany; burkhard.scholz@iav.de
* Correspondence: cosmin.berceanu@edu.ucv.ro

Abstract

Within the continuous development of automotive safety and increasingly stringent crash regulations under the Vision Zero initiative, physical crash testing remains essential for assessing occupant injury risk. This study focuses on the evaluation of occupant dynamics in full-overlap frontal collisions, based on real crash tests. Key parameters influencing injury severity, including impact speed, seat belt usages, and occupant anthropometry, were analyzed to identify worst-case scenarios. Frontal crash test protocols from regulatory and consumer programs were included in the analysis. Physical tests were conducted according to FMVSS 208 using Hybrid III 50th percentile male and 5th percentile female dummies. Both belt-restrained and unrestrained (unbelted) conditions were considered. Numerical simulations using LS-DYNA are used as a complementary tool to support and extend the interpretation of the experimental findings, particularly in assessing the influence of impact speed, seat belt usage, and occupant anthropometry on injury metrics. The results evaluate the factors with the greatest impact on injury risk and demonstrate the importance of physical frontal crash tests in the evaluation of the occupant protection. All experimental tests were carried out at IAV Vehicle Safety.

Keywords: passive safety; dummy rating; crash regulations; injury risk; crash tests; safety systems; frontal collision; FMVSS 208

1. Introduction

Passive safety systems have been a core element of vehicle design since the 1960s, evolving in response to regulatory requirements and standardized crash testing. Developments such as three-point seat belts, frontal airbags, and energy-absorbing structures have significantly reduced occupant injury severity, particularly in frontal collisions [1,2]. These advances were enabled by repeatable test procedures and injury assessment methods based on anthropomorphic test devices.

Frontal collisions remain among the most critical crash types, accounting for a large proportion of serious and fatal injuries worldwide [3]. Frontal impact testing is therefore central to regulatory and consumer safety assessment programs, including FMVSS 208, UNECE R94, and crash evaluations by Euro NCAP and IIHS [4–11]. These procedures typically use full- or moderate-overlap configurations and rely on established biomechanical injury criteria.

Accident reconstruction and crashworthiness studies highlight impact speed, collision configuration, and vehicle characteristics as key factors influencing crash severity [12,13]. Impact energy is often estimated by vehicle deformation, complemented by numerical simulations and analytical models [14,15]. Explicit finite element solvers such as LS-DYNA are widely used to model impacts against rigid barriers, poles, or trees, providing detailed insight into structural deformation and energy absorption [16–19]. While efficient for parametric studies, their accuracy depends on modeling assumptions, material properties, and contact formulations. Validation against physical crash data remains essential for reliable injury risk prediction [20,21].

Occupant injury assessment relies on biomechanical criteria derived from anthropomorphic test devices, including head injury criterion, chest acceleration and deflection, and femur loads [22,23]. Recently, machine learning approaches have been used to integrate vehicle, driver, and crash parameters to estimate injury risk [24–27], with advanced architectures like transformer-based models [28] and multidimensional frameworks [29] expanding their capability.

The rise of advanced driver assistance systems and autonomous vehicles adds complexity to safety assessment and to the autonomous vehicle's decision-making when attempting to avoid collisions, based on the prediction of potential crash damage [30,31]. Studies now examine autonomous braking [32,33], steering-based avoidance [34], event data recorder analysis [35,36], and neural network-based control systems [37–40]. Future vehicle concepts, with flexible interiors and non-standard seating, challenge traditional passive safety systems [41–43].

Problem statement

Most studies focus on isolated factors, such as vehicle structure or restraint performance. The combined effects of impact speed, occupant size, and seat belt use remain underexplored. Numerical simulations are often applied without validation against real crash data, especially in case of extreme scenarios [44–47].

Literature gap

Few studies use full-scale, real crash tests performed in specialized vehicle safety facilities with precise instrumentation. Such tests capture occupant dynamics that simulations cannot fully replicate. Comparisons of these experimental data with numerical models—covering different occupant sizes, seat belt usage, and impact speeds—are still necessary [48–51].

Research objectives and questions

This study combines full-overlap frontal crash tests with LS-DYNA simulations to examine how impact speed, seat belt usage, and occupant anthropometry affect injury risk. The study addresses:

- How does impact speed influence occupant injury?
- What biomechanical differences exist between 50th percentile male and 5th percentile female dummies?
- How does seat belt use affect occupant kinematics and injury severity?
- Which parameter combinations lead to worst-case injuries?
- How well do simulations reproduce real crash test results?

This approach highlights the importance of real crash tests for model validation and improves understanding of occupant injury mechanisms in frontal collisions.

2. Overview of Frontal Crash Safety Protocols

Today, a wide range of crash regulations is currently in force, encompassing regional legislation in Europe, the United States, Canada, and Japan, as well as NCAP and insurance-based protocols. While these standards vary in terms of impact speed, collision configura-

https://doi.org/10.3390/vehicles8040077

tion, dummy type and positioning, temperature, and test conditions, they share a common objective: reducing injury severity and saving lives.

Injury risk assessment with respect to the safety protocols was performed by first identifying the applicable regulations and subsequently analyzing the corresponding calculation methods. The purpose of this section is to provide an overview of frontal crash safety assessment protocols and to highlight the differences between existing regulatory and consumer rating systems, as well as their associated injury evaluation criteria.

The experimental crash test presented in this section was conducted as a common reference dataset to illustrate how identical biomechanical responses can lead to different injury ratings when evaluated under different assessment frameworks. Specifically, the comparative analysis was based on a single full-overlap frontal crash test performed at 50 km/h using a Hybrid III 5th percentile female dummy positioned in the driver seat. The same dataset was subsequently processed according to Euro NCAP, KNCAP, and U.S. NCAP injury assessment protocols.

2.1. Test Protocols for Frontal Collision

Compliance with frontal collision test protocols (Figure A1) is essential to ensure that vehicles meet established safety standards and provide adequate occupant protection in the event of a collision. Key aspects of compliance include regulatory requirements, testing procedures, and performance metrics.

2.2. Head Area Injury Evaluation

All NCAP protocols evaluate head injury using the Head Injury Criterion (HIC), defined as:

$$HIC_T = \max\left[(t_2 - t_1)\left(\frac{1}{(t_2 - t_1)}\int_{t_1}^{t_2} a_r dt\right)^{2.5}\right]; (t_2 - t_1) \leq T \quad (1)$$

a_r: the resultant acceleration expressed as a multiple of g (the acceleration of gravity).

t_1 and t_2: two instants during the impact separated by at most T milliseconds.

T: defines the evaluation interval: T = 15 ms for HIC15 (used by U.S. NCAP, KNCAP, and Euro NCAP for consumer ratings) and T = 36 ms for HIC36 (used by Euro NCAP for regulatory compliance).

The corresponding maximum allowable values are HIC15 $\leq$ 700 and HIC36 $\leq$ 1000.

2.2.1. Protocol-Specific Considerations

While HIC is the same underlying metric across all protocols, differences in performance classification arise from protocol-specific evaluation intervals, regulatory limits, and scoring rules. In addition, Euro NCAP imposes a peak resultant head acceleration limit of 80 g for no more than 3 ms, which may lead to a non-compliant acceleration rating even when HIC values remain within the acceptable range.

2.2.2. Implications for Comparative Assessment

Even though the underlying injury metric is identical, the same head acceleration signal may be rated differently under Euro NCAP, U.S. NCAP, and KNCAP, depending solely on protocol-specific thresholds and additional criteria such as peak acceleration. This ensures a consistent biomechanical basis while allowing regional regulations and scoring schemes to influence the final rating.

https://doi.org/10.3390/vehicles8040077

2.3. Comparison of Dummy Rating According to Different Test Protocols

This subchapter aims to illustrate the variability in passenger injury criteria evaluations by comparing identical test configurations, consistent measured data, and the same dummy assessed under different crash protocols [7–10].

This comparative analysis was performed using a single experimental dataset obtained from a Hybrid III 5th percentile dummy positioned in the driver seat during a full-overlap frontal crash test conducted at an impact speed of 50 km/h. The same dataset was subsequently used to compute occupant injury ratings according to multiple safety assessment protocols (EuroNCAP, KNCAP, and U.S.NCAP), as detailed in the following sections:

- Head: Although Euro NCAP (Figure 1a, Table A1) evaluates the Head Peak Resultant Acceleration, whose value exceeds the prescribed limit, this parameter is not rated. Nevertheless, the injury criterion is classified as *Good* in accordance with the assessment criteria.
- Neck: Across all analyzed protocols, the criterion is rated as *Good*. However, depending on the protocol, additional forces—such as extension and flexion—may need to be considered for this region.
- Chest: For an identical chest deflection value, Euro NCAP (Figure 1c and Table A1) and KNCAP (Figure 1b and Table A2) classify the criterion as *Adequate*, whereas U.S. NCAP (Figure 1c and Table A3) assigns a *Good* rating.

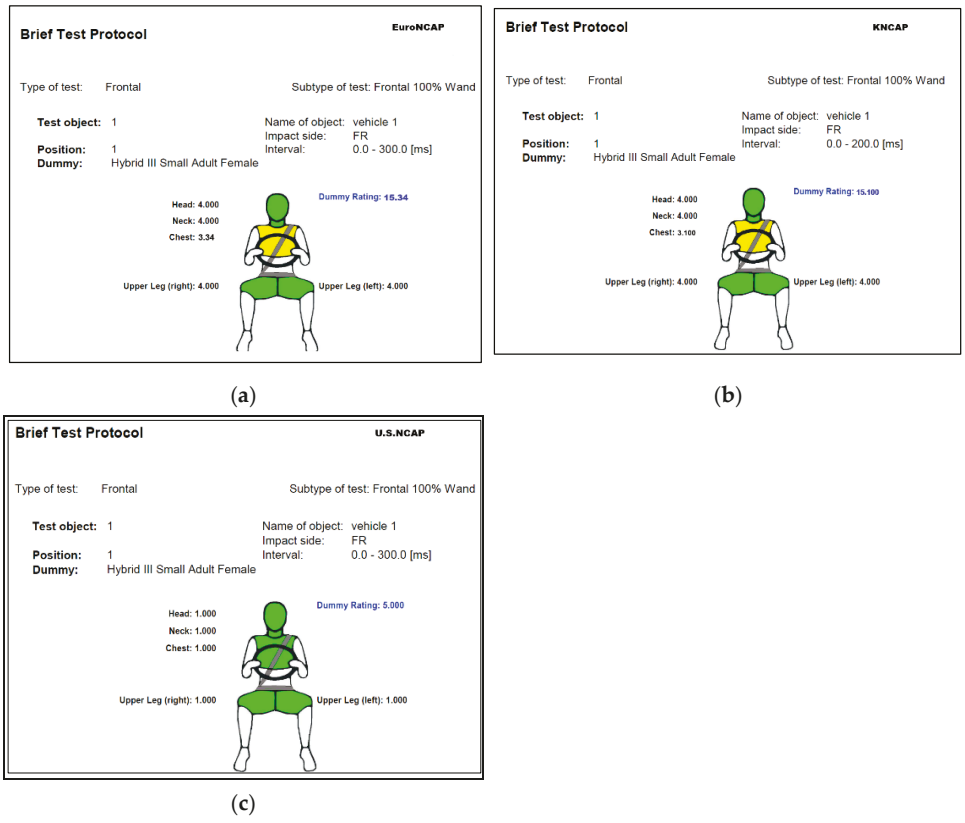

Figure 1. Dummy injuries—Test Protocol: (**a**) EuroNCAP; (**b**) KNCAP; (**c**) U.S.NCAP. Color coding indicates the level of occupant protection for each body region: Green—Good protection: very low injury risk; biomechanical criteria well below tolerance limits. Yellow—Adequate protection: low injury risk; values close to assessment thresholds. Orange—Marginal protection: increased injury risk; injury criteria exceed preferred limits. Brown—Weak protection: high injury risk; criteria significantly exceed tolerance levels. Red—Poor protection: very high injury risk; severe or life-threatening injuries likely.

https://doi.org/10.3390/vehicles8040077

Variations in dummy ratings are observed across different testing protocols, even under the same test conditions and measured values. These variations may result from several contributing factors, as discussed below:

- ✓ Protocol Differences: Variations in dummy performance assessment may result from protocol-specific injury thresholds, measurement methods, and data interpretation.
- ✓ Data Interpretation: Variations in data analysis and interpretation between testing protocols can result in differing assessments of dummy performance.
- ✓ Market destination: Variations in injury assessment thresholds defined by different protocols may result from region-specific evaluations of accident typologies and injury distributions, especially when considering the anthropometric characteristics of local populations.

2.4. Protocol Comparison in the Context of Worst-Case Scenarios

The comparison of Euro NCAP, KNCAP, and U.S. NCAP frontal impact protocols provides the regulatory context for the experimental configurations investigated in this study. Differences in test parameters such as impact speed, restraint conditions, and dummy selection influence the severity and kinematic characteristics of the crash event. Understanding these variations is essential for identifying potential worst-case occupant loading scenarios and for interpreting the injury metrics obtained from both the physical tests and the numerical simulations.

3. Materials and Methods

The study employs a combined methodology of full-scale frontal crash tests and numerical simulations to provide a comprehensive assessment of occupant injury risk in both restrained and unrestrained conditions. The primary objective of this research is a comparative analysis of injury severity resulting from full-overlap (100%) frontal collisions. The test protocol follows FMVSS 208 for a H3 50th percentile dummy, applied consistently in both physical crash tests and LS-DYNA simulations.

Both belted (seat belt fastened) and unbelted (no restraint) scenarios were considered in accordance with FMVSS 208, enabling an evaluation of restraint effectiveness under standardized conditions (Table 1). The study focuses on identifying the key risk factors that significantly influence injury severity. To this end, worst-case scenarios were analyzed to determine whether impact speed, seat belt usage, or driver anthropometry has the greatest effect on injury outcomes (Figure 2).

Table 1. Overview of experimental and numerical test conditions.

Configuration	Method	Restraint	Impact Speed (km/h)	Purpose
Full-overlap frontal	Physical test	Belted	56	Regulatory severity level for frontal occupant protection assessment
Full-overlap frontal	Physical test	Unbelted	40	Realistic and regulatory unrestrained scenario under safe experimental limits
Full-overlap frontal	LS-DYNA simulation	Belted	50	Intermediate speed for validation and comparison
Full-overlap frontal	LS-DYNA simulation	Unbelted	50	Worst-case scenario analysis and isolation of restraint effects

https://doi.org/10.3390/vehicles8040077

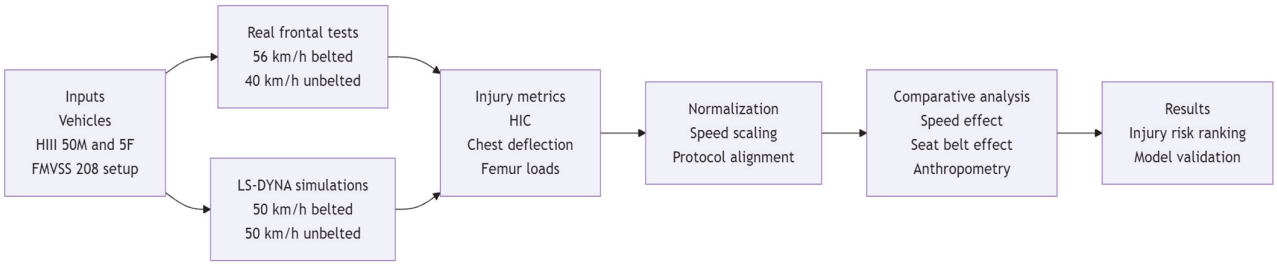

Figure 2. Methodological framework.

The case study presents a comparative analysis on several levels. The case study focuses on a frontal collision scenario with full overlap in a mid-size car. Experimental tests were conducted with belted occupants at 56 km/h and unbelted occupants at 40 km/h, reflecting regulatory conditions and realistic safety constraints. Complementary analyses at an intermediate speed of 50 km/h were used to examine restraint effects and worst-case scenarios.

Full-overlap frontal crash tests were performed in a dedicated vehicle safety facility using standardized procedures and calibrated measurement systems. Two experimental configurations were considered: a belted occupant tested at 56 km/h, corresponding to regulatory full-width frontal impact severity, and an unbelted occupant tested at 40 km/h, selected to ensure controlled kinematics and reliable measurements under unrestrained conditions. Anthropomorphic test devices were instrumented to record biomechanical injury criteria and occupant kinematics.

Complementary numerical simulations were conducted using LS-DYNA PrePost 10.2. A finite element model, including detailed restraint systems and occupant models, was employed. Simulations were carried out at an intermediate impact speed of 50 km/h for both belted and unbelted configurations. This choice allows direct comparison between restraint conditions while eliminating impact speed as a confounding variable and enables the investigation of severe scenarios that cannot be safely reproduced in physical testing.

Anthropomorphic Test Devices (Dummies)

The choice of anthropomorphic test devices (dummies) was based on the FMVSS 208 test protocol, selecting a 50th percentile male (H3) dummy to represent a standard adult occupant. Dummy positioning in the vehicle seat was performed according to the same protocol, ensuring consistent posture and alignment for both belted and unbelted conditions. This standardized setup allows for reproducible results and meaningful comparison between real crash tests and LS-DYNA simulations.

Vehicle Selection

The vehicles used in the tests belonged to the same mid-size vehicle segment and included models manufactured both before and after 2020, reflecting the evolution of passive safety systems. Since the objective of this study is to evaluate occupant injury mechanisms rather than structural differences between individual vehicle models, the results were analyzed at the level of the vehicle segment. This approach enables the identification of consistent trends in occupant response while minimizing the influence of model-specific design variations.

The injury criteria reported in this study are derived from the signals recorded by the instrumented crash test dummies after standard filtering and data processing procedures in accordance with ISO 6487 and SAE J211 [20,52]. The values presented correspond to the processed experimental measurements used for the evaluation of occupant injury risk.

Selection Criteria for Impact Velocities

The selection of impact speeds was guided by regulatory relevance, experimental safety constraints, and methodological consistency. The belted physical test at 56 km/h reflects the FMVSS 208 full-width frontal impact and represents a severe but standardized loading condition for restraint system evaluation. For unbelted occupants, a reduced speed of 40 km/h was selected to ensure controlled occupant motion and reliable data acquisition, while still representing realistic accident conditions. Numerical simulations were conducted at an intermediate speed of 50 km/h for both restraint conditions, allowing direct comparison between belted and unbelted occupants and enabling the investigation of severe scenarios that cannot be safely reproduced in full-scale tests.

To enable direct comparison between simulations and experiments, all injury metrics were normalized using a quadratic velocity scaling law, preserving relative differences and allowing evidence-based assessment across restraint conditions.

Comparison Methodology

All dummy acceleration data, from both physical tests and numerical simulations, were filtered according to the standardization, ISO 6487 and SAE J211 [20,52]. Head accelerations, used for HIC evaluation, were processed with a CFC 1000 low-pass filter. Acceleration signals were recorded over a time window from −200 ms to 600 ms relative to impact time. However, according to the FMVSS 208 protocol, injury risk assessment considers values in the interval from 0 to 300 ms. A fixed coordinate system was employed on the dummy, with +x forward, +y to the right, and +z downward, ensuring consistent orientation of all measurements and simulations. This approach preserves relevant biomechanical signals while minimizing high-frequency noise, providing accurate and comparable injury metrics across datasets.

Experimental results were compared with numerical data to evaluate occupant kinematics and injury metrics, including head, chest, and lower extremities, as well as HIC, chest deflection, and femur load. Injury measures were normalized with respect to regulatory and consumer assessment thresholds, allowing consistent comparison across different impact speeds. This approach enabled identification of key factors affecting injury severity, such as restraint condition, impact speed, and occupant anthropometry.

3.1. Crash Test Procedure According to FMVSS 208—H3 50%

This case study focuses on a frontal collision scenario involving a mid-size car with full overlap at a 0° impact angle (Figure 3). Tests were conducted following FMVSS 208, the U.S. regulatory standard for occupant crash protection, using a Hybrid III 50th percentile male dummy.

Prior to testing, all vehicles were prepared with acceleration sensors mounted at various positions throughout the vehicle. Data acquisition and measurement equipment were installed in the trunk, together with the logger that triggers off-board cameras recording at 1000 frames per second from outside the vehicle. The vehicles were propelled along a guided track at speeds of 56 km/h and 40 km/h until a full-frontal impact with a rigid, fix concrete block weighing 1000 t.

Belted and Unbelted FMVSS 208 Tests

In accordance with the FMVSS 208 protocol, the belted test involved positioning the Hybrid III 50th percentile male dummy in the driver's seat. The scenario comprised a full-frontal collision (100% overlap) at a 0° angle, conducted at a speed of 56 km/h (Figure 4). Both the front airbag and seatbelt were active during the test.

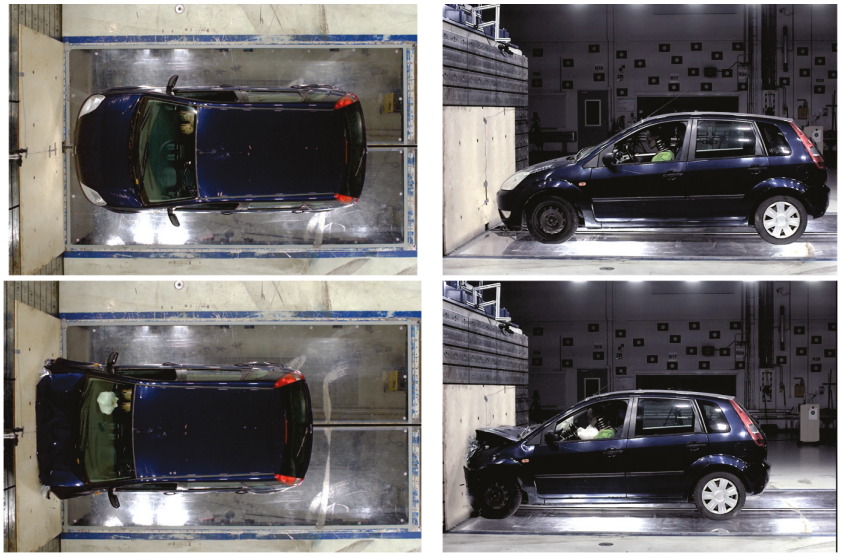

Figure 3. Set up for the frontal collision 100% overlap—at IAV-S, Großmehring, Germany.

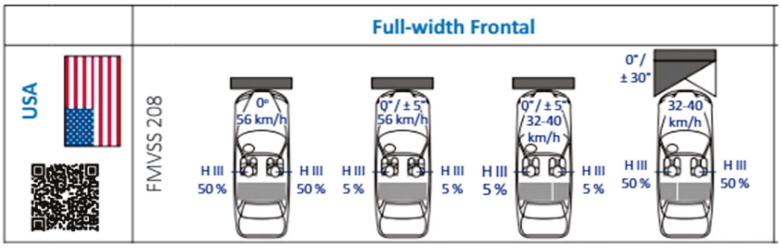

Figure 4. FMVSS 208-Protocol-Belted and unbelted test [4,11].

Unbelted tests were conducted under the same frontal impact conditions but without using the restraint system. The FMVSS 208 protocol specifies unbelted testing to evaluate occupant responses without seatbelt protection. The test conditions for unbelted dummies were as follows:

- Speed: 40 km/h
- Dummy positions: 1 & 3—H3 50%
- Frontal overlap: 100%
- Collision angle: 0°

3.2. Development of the Numerical Model and Simulation Setup

As the purpose of this study was not to compare different vehicle body structures but to evaluate occupant response under various frontal impact conditions, a simplified numerical representation was adopted. The simplification concerns the vehicle structure only; the passive safety systems were modeled with the same functional characteristics and deployment timing as in the real tests. This approach reduced computational time and allowed easier adjustment of the setup to different impact scenarios.

A frontal crash reconstruction was first carried out in Virtual Crash 2.2 software. The case considered a mid-size class vehicle impacting a rigid barrier at 50 km/h (Figure 5a). From this reconstruction, the vehicle speed variation in time (Figure 5b) was extracted and used as input for the dummy–seat–restraint system model implemented in LS-DYNA. Using the velocity vs. time diagram as boundary input is a common practice in crash analysis, as it preserves the global crash dynamics while avoiding detailed modeling of the entire vehicle structure. In this way, the occupant response remains consistent with the overall vehicle kinematics while maintaining computational efficiency.

https://doi.org/10.3390/vehicles8040077

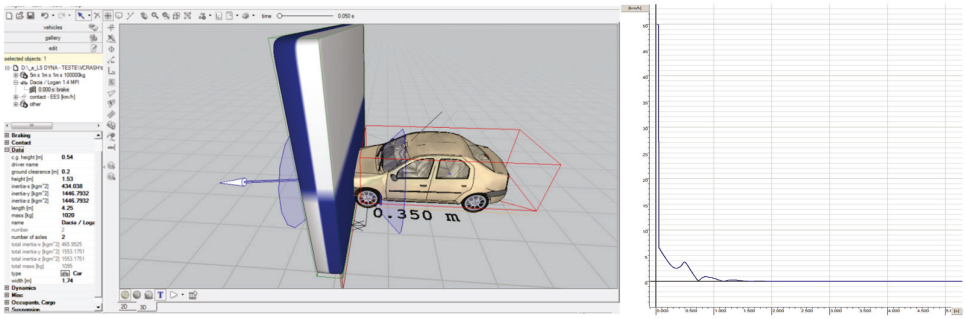

(**a**) (**b**)

Figure 5. Frontal Impact of a Vehicle with a Rigid Barrier in Virtual Crash: (**a**) Crash test configuration; (**b**) Velocity vs. Time—Virtual Crash.

The numerical setup included the H3 50% dummy seated in the driver position, together with the seat, airbag (Figure 6d [53–56]), and a fully modeled three-point seat belt system, including the anchor points, retractor, and pretensioner (Figure 6a [53–56]). In order to reproduce realistic interaction with the vehicle interior, the dashboard, steering wheel and steering column, as well as the pedals, were also included (Figure 6b [53–56]). These components ensure correct driver positioning and allow the assessment of potential injuries caused by contact with interior structures during impact.

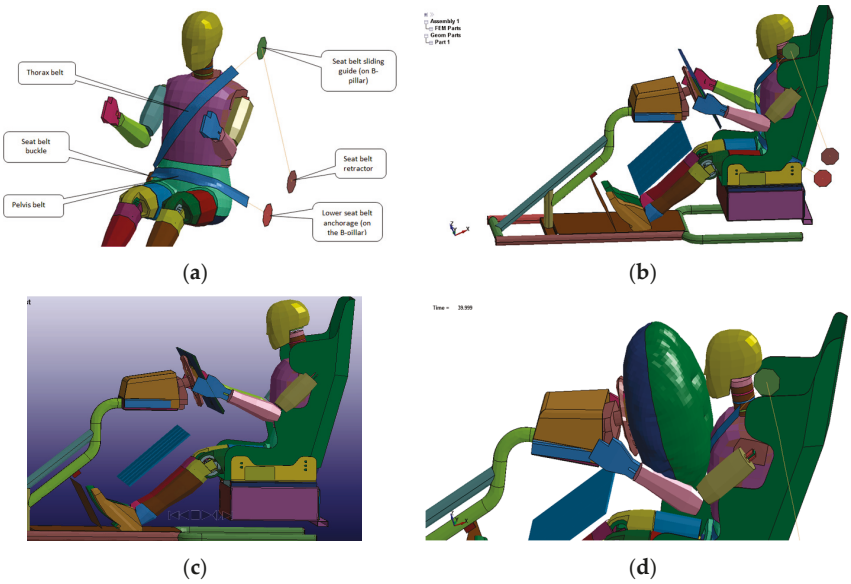

(**a**) (**b**)

(**c**) (**d**)

Figure 6. The Hybrid III 50th percentile male dummy assembly: (**a**) Crash test dummy and the restraint system; (**b**) Normal position of the dummy, belted; (**c**) Normal position of the dummy, unbelted; (**d**) Airbag deployment simulation.

Two configurations were analyzed. In the first case, the dummy was positioned in a standard driving posture, with the chest centered relative to the steering wheel at approximately 350 mm and restrained by the seat belt. In the second case, the same positioning was maintained, but the restraint system was not used (Figure 6c [53–56]), representing the unbelted scenario at an impact speed of 50 km/h.

To assess the validity of the numerical simulations, the results were evaluated against the physical crash tests. As the impact velocities differed between the experimental and numerical configurations, the comparison was not performed on a direct equivalence basis. Instead, the injury metrics were interpreted with consideration of the respective impact speeds and normalized assessment thresholds. The analysis focused on the injury criteria recorded for the Hybrid III 50th percentile male dummy positioned in the driver's seat.

https://doi.org/10.3390/vehicles8040077

4. Results

4.1. Results from Crash Tests—Belted Configuration

Table 2 and Figure 7 present the results obtained from three full-overlap frontal collision tests conducted under identical experimental conditions, using the same dummy type positioned in the driver seat.

Table 2. Injury Criteria—FMVSS 208 Protocol H3 50% belted.

Test No.	1	2	3
Dummy position/type	11/H3	11/H3	11/H3
Criterion	Value	Value	Value
HIC15 Value [-]	224.22	205.03	182.81
HIC36 Value [-]	361.58	357.54	270.68
A3ms Value (cumulative) [g]	63.64	51.55	63.01
Neck Tension Force Fz+ [kN]	0.6242	0.6454	0.6545
Neck Compression Force Fz− [kN]	0.2313	0.1919	0.2151
N_CE: Nij In-Position	0.0189	0.0005	0.0421
N_CF: Nij In-Position	0.0909	0.2098	0.0392
N_TE: Nij In-Position	0.1280	0.1307	0.1298
N_TF: Nij In-Position	0.2917	0.2816	0.2609
A3ms Chest (cum.) [g]	40.85	37.83	43.32
Chest deflection [mm]	23.84	19.39	25.45
Chest deflection (Poly3,TCC) [mm]	23.03	18.69	0.00
Chest deflection CFC600 [mm]	23.94	19.49	25.55
Chest deflection CFC600 (Poly3,TCC) [mm]	23.03	18.69	0.00
L: Femur Axial Force Fz− [kN]	0.1515	0.2929	0.2222
R: Femur Axial Force Fz− [kN]	0.2727	0.4112	0.3232

Color coding indicates the level of occupant protection for each considered criterion: Green—Good protection: very low injury risk; biomechanical criteria well below tolerance limits. White—not applicable within this protocol rating or the corresponding values are unavailable.

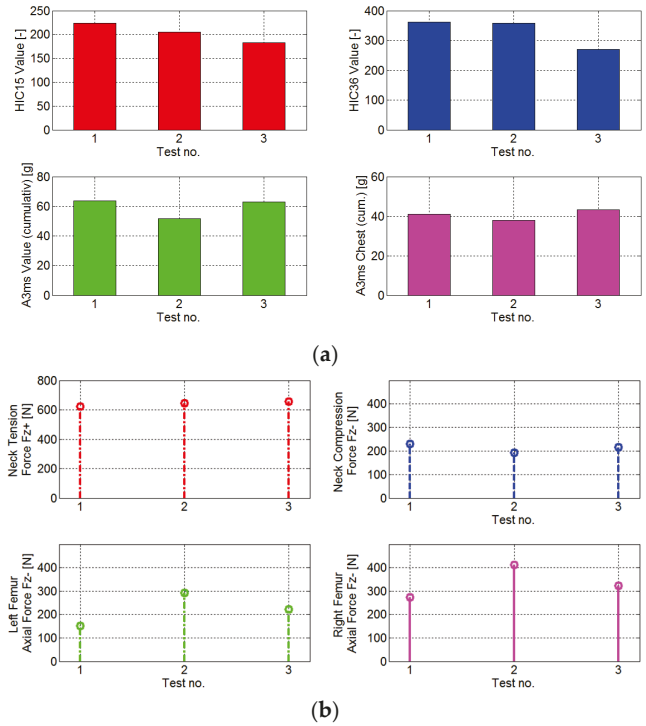

Figure 7. Injury Criteria—FMVSS 208 Protocol H3 50%. (**a**) Head Injury Criterion values, Thoracic acceleration over 3 ms and Chest-specific cumulative acceleration; (**b**) Forces recorded at neck and femur of the H3 50% male dummy.

https://doi.org/10.3390/vehicles8040077

Based on the dummy assessment protocol, the injury criteria associated with the head region were extracted and analyzed separately, as illustrated in Figure 8. For the Head Injury Criterion (HIC15), the recorded values ranged from a minimum of 182.8 to a maximum of 224.2. The cumulative head acceleration parameter (A3head) varied between approximately 51 g and 64 g.

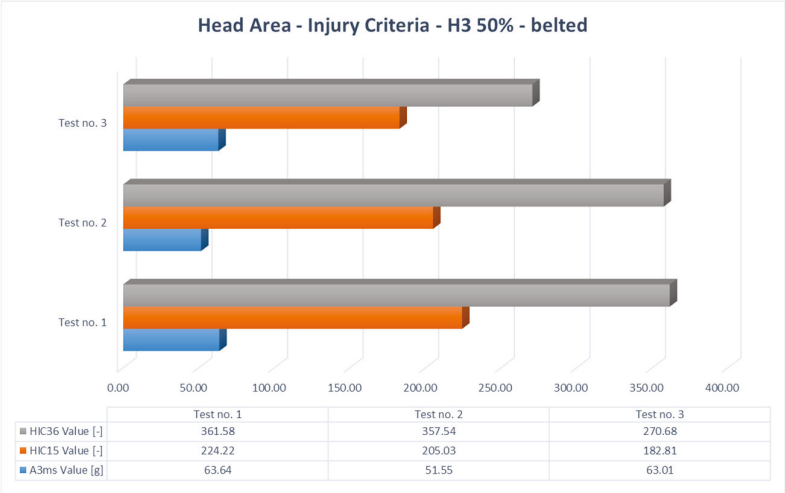

	Test no. 1	Test no. 2	Test no. 3
HIC36 Value [-]	361.58	357.54	270.68
HIC15 Value [-]	224.22	205.03	182.81
A3ms Value [g]	63.64	51.55	63.01

Figure 8. Head Area-Injury criteria-H3 50%.

With respect to the frontal impact protection requirements specified in FMVSS 208, all measured values remained below the regulatory limits for head injury criteria. In particular, the HIC36 values were significantly lower than the maximum allowable threshold of 1000, indicating an adequate level of occupant head protection under belted conditions.

4.2. Results from Virtual Simulation—Belted Configuration

Figure 9 presents the time history of the resultant head acceleration and the calculated HIC15 value at the head center of gravity (COG). The maximum HIC15 value, computed over a 15 ms time interval, is 235. The corresponding peak resultant head acceleration is 57 g.

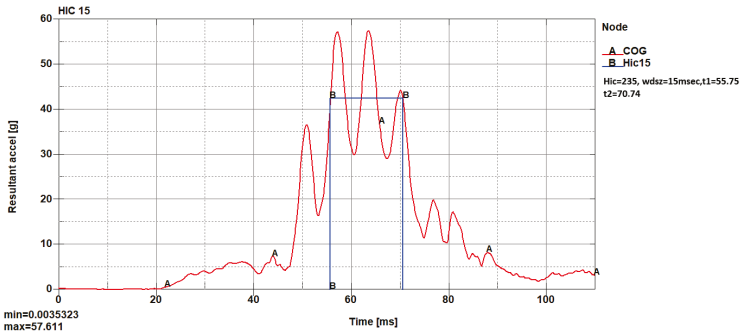

Figure 9. Head injury criteria—HIC 15, belted configuration.

Figure 10 shows the variation in the HIC36 criterion, calculated over a 36 ms time interval. The maximum recorded HIC36 value is 314.

Both HIC15 and HIC36 values remain below the regulatory limits specified for frontal impact assessment. The driver model was positioned in a standard driving posture and restrained by a three-point seat belt throughout the simulation.

https://doi.org/10.3390/vehicles8040077

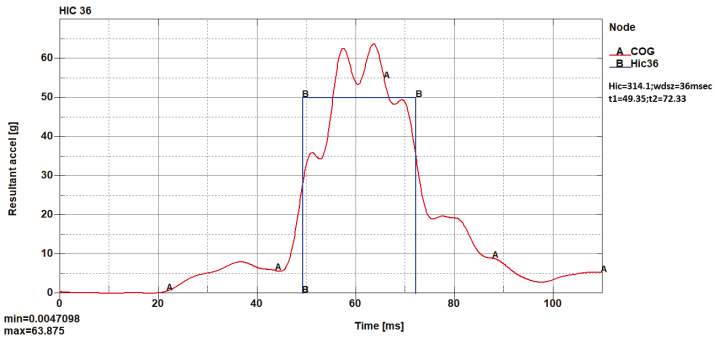

Figure 10. Head injury criteria-HIC 36, belted configuration.

4.3. Results from Crash Tests—Unbelted Configuration

Table 3 summarizes the results obtained from four full-overlap frontal collision tests conducted under identical experimental conditions, using the same dummy type positioned in the driver seat. The impact speed was 40 km/h, in accordance with the FMVSS 208 unbelted test protocol.

Table 3. Injury Criteria—FMVSS 208 Protocol H3 50% unbelted.

Test No.	**1**	**2**	**3**	**4**
Dummy position/type	11/H3	11/H3	11/H3	11/H3
Criterion	Value	Value	Value	Value
HIC15 Value [-]	177.76	199.98	198.97	128.27
HIC36 Value [-]	221.19	229.27	256.54	167.66
A3ms Value (cumulative) [g]	91.20	91.79	68.93	43.37
Neck Tension Force Fz+ [kN]	0.33	0.45	0.35	0.29
Neck Compression Force Fz− [kN]	0.99	0.66	0.60	0.99
N_CE: Nij In-Position [1]	0.09	0.13	0.18	0.12
N_CF: Nij In-Position [1]	0.40	0.40	0.46	0.38
N_TE: Nij In-Position [1]	0.16	0.18	0.18	0.13
N_TF: Nij In-Position [1]	0.17	0.15	0.16	0.07
A3ms Chest (cum.) [g]	40.72	43.39	42.14	36.29
Chest deflection [mm]	12.63	10.00	11.01	10.91
Chest deflection (Poly3,TCC) [mm]	12.02	9.49	10.50	10.50
Chest deflection CFC600 [mm]	12.63	10.00	11.11	10.91
Chest deflection CFC600 (Poly3,TCC) [mm]	12.02	9.60	10.61	10.50
L: Femur Axial Force Fz− [kN]	5.93	5.70	5.49	3.07
R: Femur Axial Force Fz− [kN]	5.79	6.97	7.02	3.48

Color coding indicates the level of occupant protection for each considered criterion: Green—Good protection: very low injury risk; biomechanical criteria well below tolerance limits. White—not applicable within this protocol rating or the corresponding values are unavailable.

The injury criteria related to the head region were extracted from the dummy rating protocol and analyzed separately, as shown in Figure 11. For the Head Injury Criterion (HIC15), the recorded values ranged from 128.27 to 199.98.

The cumulative head acceleration parameter (A3head) varied between approximately 43 g and 92 g, corresponding to an increase of approximately 114% from the minimum to the maximum value. This dispersion is notable given that all tests were performed under nominally identical boundary conditions.

The increased variability observed in the unbelted configuration can be attributed to the higher kinematic sensitivity of the dummy motion in the absence of restraint. Without the stabilizing effect of the three-point seat belt system, the occupant's forward excursion and interaction with interior structures become more dependent on small differences in initial positioning, contact sequence, and impact timing. Consequently, the unbelted

condition exhibits greater kinematic variability and reduced repeatability compared to the belted configuration, which is reflected in the wider spread of the measured injury criteria.

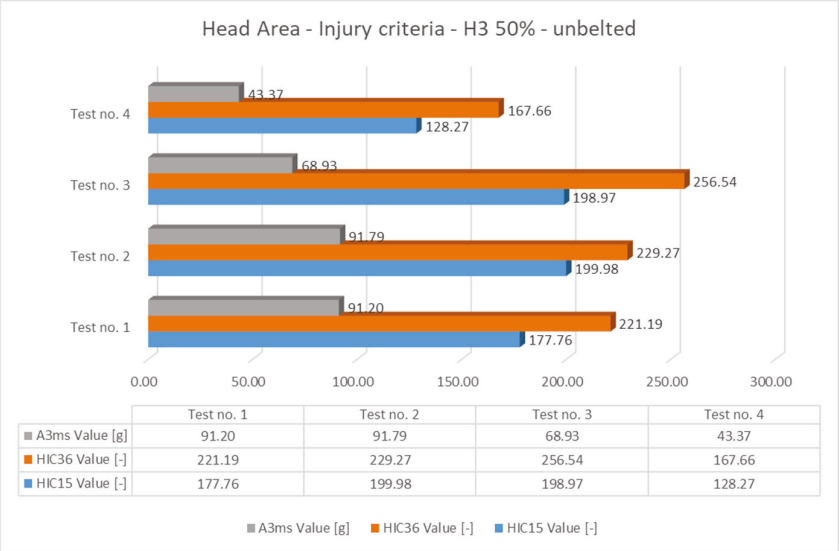

	Test no. 1	Test no. 2	Test no. 3	Test no. 4
A3ms Value [g]	91.20	91.79	68.93	43.37
HIC36 Value [-]	221.19	229.27	256.54	167.66
HIC15 Value [-]	177.76	199.98	198.97	128.27

Figure 11. Head Area-Injury criteria-H3 50% unbelted.

4.4. Results from Virtual Simulation—Unbelted Configuration

In the unbelted configuration, head injury assessment was performed using the Head Injury Criterion (HIC) at the head center of gravity (COG).

Figure 12 shows that the maximum HIC15 value reaches 258, while Figure 13 indicates a maximum HIC36 value of 396. Both values are below the regulatory HIC36 limit of 1000.

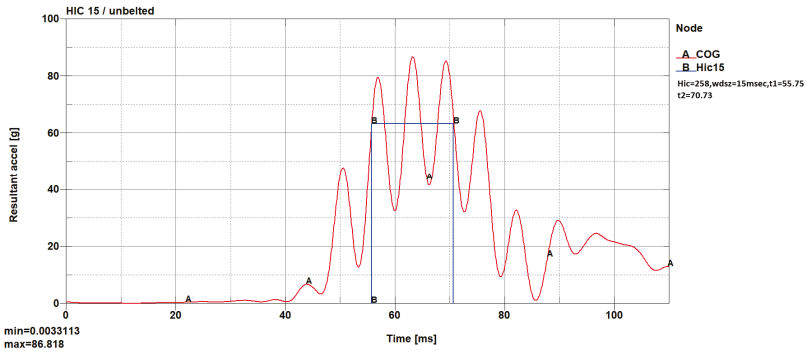

Figure 12. Head injury criteria-HIC 15, unbelted configuration.

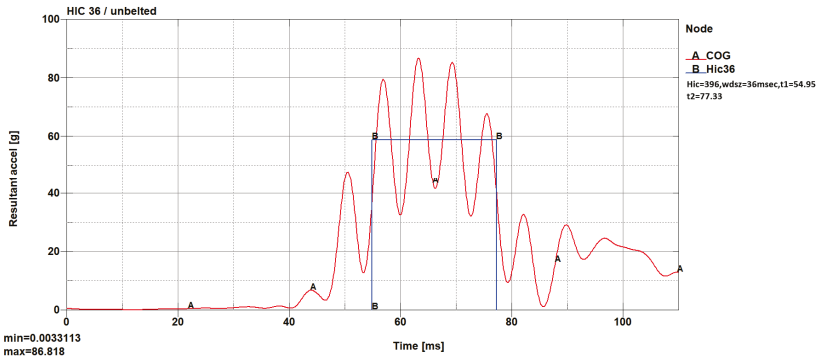

Figure 13. Head injury criteria-HIC 36, unbelted configuration.

https://doi.org/10.3390/vehicles8040077

The peak resultant head acceleration reaches 86 g at t = 63 ms, exceeding the regulatory limit of 80 g. This indicates that, in the absence of a seat belt, the dummy experiences a higher acceleration impulse during the frontal impact.

These results highlight the increased kinematic variability and severity of head loading under unbelted conditions. The unrestrained dummy exhibits less predictable motion, leading to higher peak accelerations and injury metrics compared to the belted scenario. The trends observed in the virtual simulation align with the corresponding physical crash tests, supporting the model's ability to capture the overall kinematic behavior and extreme values associated with unbelted frontal collisions.

4.5. Crash Tests vs. Virtual Simulation Comparison

To compare experimental crash test results with numerical simulations under different impact velocities, the crash test values were normalized using a quadratic velocity scaling law. This approach is commonly applied in crash biomechanics research to normalize injury measures across different test conditions. For the belted configuration (Crash Test speed 56 km/h, simulation 50 km/h), the scale factor was 0.797. For the unbelted configuration (Crash Test speed 40 km/h, simulation 50 km/h), the scale factor was 1.5625. All measured injury metrics (HIC15, HIC36, A3head) were multiplied by the corresponding factor to obtain normalized values, which were then compared with the simulation results. Relative errors were calculated to quantify the agreement between experimental and numerical data.

In particular, under small-to-moderate changes in velocity, these metrics approximately scale with the square of the velocity, reflecting the kinetic energy imparted to the occupant. Based on this relationship, a quadratic velocity scaling factor can be used to normalize crash test results to the reference velocity of the simulation:

$$Scale\ Factor = \left(\frac{v_{sim}}{v_{CT}}\right)^2 \quad (2)$$

where:

v_{sim}—impact velocity used in the virtual simulation

v_{CT}—impact velocity measured during the crash test

Each measured crash test metric was multiplied by the corresponding scale factor to normalize all values to the simulation velocity. This procedure ensures comparability between physical test results conducted at different impact speeds and the numerical simulation outputs.

Table 4 presents the crash test results both before and after velocity normalization. The normalized values allow direct comparison with the corresponding simulation results. For each injury metric, the relative error between the normalized experimental data and simulation values was calculated to quantify the level of agreement and assess the accuracy of the virtual model.

Table 4. Crash tests vs. virtual simulation comparison.

Metric	Crash Test (CT)	Scale Factor	CT Normalized	Simulation	Relative Error	Score Amplitude Correlation
HIC15 (Belted)	204	0.797	162.5	235	0.45	0.55
HIC36 (Belted)	329.9	0.797	263	314	0.19	0.81
A3ms (Belted)	59.4	0.797	47.3	63	0.33	0.67
HIC15 (Unbelted)	176.7	1.5625	276.1	258	0.07	0.93
HIC36 (Unbelted)	218.6	1.5625	341,6	396	0.16	0.84
A3ms (Unbelted)	73.8	1.5625	115.4	89	0.23	0.77

https://doi.org/10.3390/vehicles8040077

The following metrics were considered for the comparison: HIC15, HIC36, and cumulative head acceleration (A3head). This approach enables an objective evaluation of the virtual model's performance and highlights the influence of restraint condition, impact speed, and kinematic variability on the measured injury outcomes.

To complement the relative error analysis, a simplified amplitude-based correlation score was calculated to evaluate the agreement between normalized crash test results and simulations. This metric, inspired by the magnitude component of CORA, is defined as:

$$Score_{ampl} = 1 - \frac{|Simulation - CT_{norm}|}{CT_{norm}} \quad (3)$$

where:

CT_{norm}—the normalized crash test value

Simulation—the corresponding numerical result.

A value close to 1 indicates a strong agreement in terms of amplitude. The obtained scores range from 0.55 to 0.93, reflecting generally good to very good agreement between the numerical model and experimental measurements. Higher correlations are observed for HIC36, whereas the lower scores for HIC15 in belted tests can be attributed to the sensitivity of peak head acceleration and short-duration events. In belted conditions, the occupant motion is partially constrained by the restraint system, while the head engages in a nonlinear contact interaction with the airbag. Small differences in the predicted head trajectory, airbag deployment timing, and load transfer between the seatbelt and the airbag can significantly influence the peak acceleration within the critical 15 ms window. This sensitivity amplifies minor discrepancies between experimental and numerical responses, resulting in higher relative error values for HIC15.

The comparison between normalized crash test results and numerical simulations (Figure 14) indicates increased variability in the unbelted configuration, particularly for cumulative head acceleration (A3head). This behavior can be attributed to the less constrained motion of the dummy in the absence of a seat belt. Under these conditions, forward excursion, rotation, and the timing of contact with interior structures vary significantly between tests, leading to increased dispersion in the measured acceleration values.

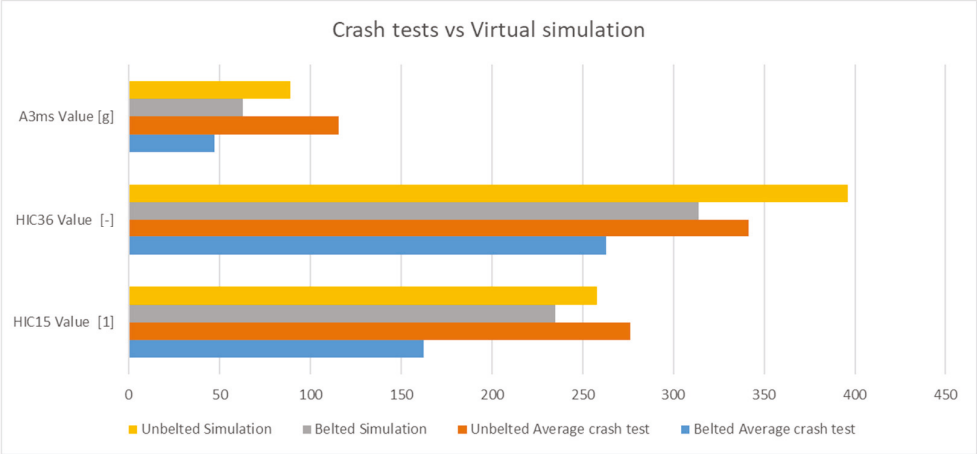

Figure 14. Crash tests vs. virtual simulation.

The validation of the simulation model was extended using a CORA-based methodology applied to the head acceleration time-history curves (Figure 15) for belted situation, following the principles of ISO/TS 18571 [57]. As shown in Figure 15, the simulation model reproduces the overall shape and timing of the head acceleration response with good accuracy, while differences are primarily observed in peak amplitude.

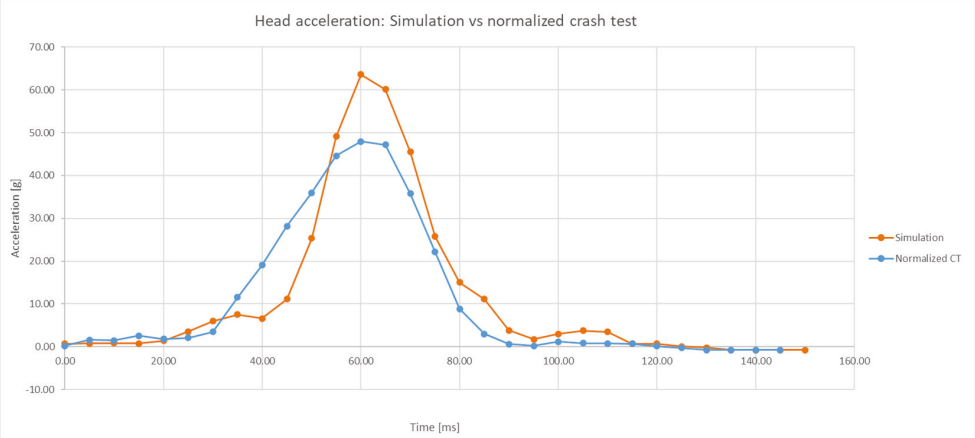

Figure 15. Comparison of head acceleration time histories between simulation and normalized crash test data.

The correlation was evaluated in terms of shape, phase, and magnitude components. The shape component of the CORA assessment was approximated using a normalized cross-correlation (Pearson coefficient), providing a robust measure of similarity between the experimental and numerical time-history signals. A shape correlation value of 0.94 was obtained, indicating strong agreement in the temporal evolution of the acceleration signals. The phase shift between the experimental and numerical signals was negligible, resulting in a phase score of 1.00, confirming accurate prediction of the peak response timing. The magnitude component yielded a score of 0.67, reflecting a slight overestimation of peak acceleration by the numerical model. The resulting overall CORA score of 0.87 (Table 5) indicates good correlation, demonstrating that the model reliably reproduces the occupant kinematic response.

Table 5. CORA-based validation results for head acceleration (simulation vs. normalized crash test).

Component	Value	Score Interpretation
Shape correlation (S_shape)	0.94	Very Good
Phase correlation (S_phase)	1.00	Very Good
Size correlation (S_size)	0.67	Acceptable
Total score	0.87	Good

The adopted approach provides a transparent and consistent approximation of CORA-based validation, ensuring a reliable and reproducible assessment of the agreement between experimental and numerical results.

$$CORA = \frac{S_{size} + S_{phase} + S_{shape}}{3} \tag{4}$$

$$S_{size} = 1 - \frac{|A_{Sim,Max} - A_{test,Max}|}{A_{test,Max}} \tag{5}$$

where:

$A_{Sim,Max}$—maximum value of the simulated signal, representing the peak acceleration obtained from the numerical model

$A_{test,Max}$—maximum value of the experimental signal (normalized crash test), representing the peak acceleration measured during the physical test

$$S_{phase} = 1 - \frac{|t_{Sim,Max} - t_{test,Max}|}{t_{window}} \tag{6}$$

https://doi.org/10.3390/vehicles8040077

where:

$t_{Sim,Max}$—time at which the simulated signal reaches its maximum value (peak timing in simulation)

$t_{test,Max}$—time at which the experimental signal reaches its maximum value (peak timing in crash test)

t_{window}—total duration of the time interval considered for the comparison between simulation and experimental signals; it represents the analysis window over which the time histories are evaluated; *t_window* = 150 ms

$$S_{shape} = \frac{\sum (x_i - \overline{x})(y_i - \overline{y})}{\sqrt{\sum (x_i - \overline{x})^2 \cdot \sum (y_i - \overline{y})^2}} \quad (7)$$

where:

x_i—individual data points of the simulated signal

y_i—corresponding data points of the experimental signal

$\overline{x}$, $\overline{y}$—mean values of the simulated signal and of the experimental signal

From simulation perspective, limitations include the use of a simplified vehicle structure, which reproduces interior components and restraint systems but does not fully capture the deformation or compliance of the real vehicle. Consequently, small differences in dummy kinematics or impact interactions may not be fully reflected, particularly in highly sensitive unbelted scenarios. Despite these limitations, the virtual model provides a reliable approximation of occupant response and captures the overall trends and relative differences observed in the physical tests.

5. Determination of Risk Factors with Major Impact on Injury Severity

This section focuses exclusively on physical tests, establishing a clear baseline of occupant behavior under different conditions, free from the limitations and uncertainties of numerical simulations, in relation to the purpose of the paper, namely, to determine the worst-case impact scenario.

5.1. Injury Evaluation—Influence of Seatbelt Use and Impact Velocity

Seven frontal impact tests were conducted to evaluate factors affecting injury severity:

- Tests 1–3: 100% overlap, 56 km/h, H3 50% dummy with seatbelt.
- Tests 4–7: 100% overlap, 40 km/h, H3 50% dummy without seatbelt.

The repeated physical tests (n = 3–4 per configuration) allowed assessment of the repeatability of the measured injury metrics. Basic statistical measures, including mean, standard deviation (SD), and coefficient of variation (CV%) are reported in Table 6. Overall, the belted configurations show low variability across trials, reflecting consistent restraint performance, whereas the unbelted configurations exhibit higher SD and CV%, particularly for head and neck injury criteria, highlighting the increased kinematic variability in the absence of a seatbelt. These statistics support a quantitative understanding of the effect of occupant restraint on repeatability and crash response.

Data was processed by regions of interest, resulting in the graph presented in Figure 16. Analysis of the HIC index indicates that higher impact velocity generally increases head injury risk, even when a seatbelt is used. In contrast, head-level accelerations were higher in unbelted tests, with two tests exceeding 90 g, above the 80 g safety threshold. These elevated values suggest a higher probability of head contact with interior structures, such as the A-pillar, side window, or enhanced forces from airbag deployment.

https://doi.org/10.3390/vehicles8040077

Table 6. Statistical Summary of Injury Metrics for Belted and Unbelted Crash Tests.

Criterion	Belted (n = 3) Mean	SD	CV%	Unbelted (n = 4) Mean	SD	CV%
HIC15 [-]	203.36	21.05	10.4	176.75	28.36	16
HIC36 [-]	330.6	50.72	15.4	218.67	37.22	17.0
A3ms [g]	59.40	6.14	10.3	73.85	22.87	31.0
Neck Tension Fz+ [kN]	0.64	0.02	2.3	0.36	0.07	19.2
Neck Compression Fz− [kN]	0.21	0.05	24.0	0.81	0.21	25.8
A3ms Chest [g]	40.67	2.61	6.4	40.64	3.12	7.7
Chest deflection [mm]	22.94	3.74	16.3	11.89	1.12	9.4

Belted values: n = 3; Unbelted values: n = 4. SD = standard deviation, CV% = coefficient of variation.

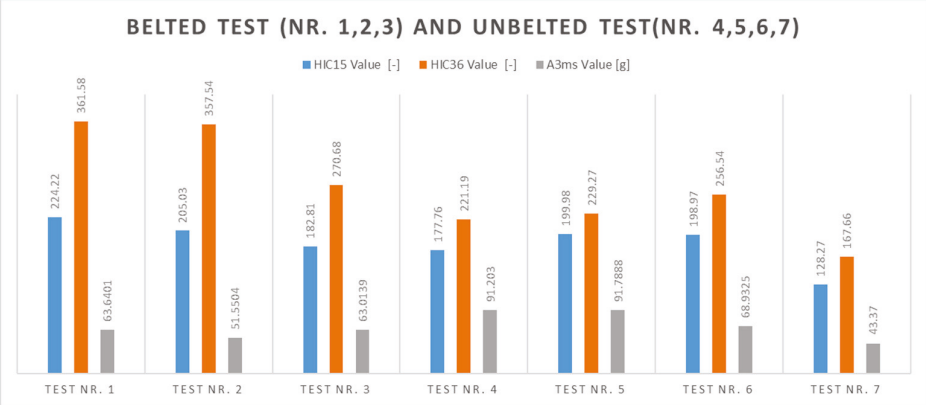

Figure 16. Head injury evaluation—Belted tests (1, 2, 3) and Unbelted tests (4, 5, 6, 7).

Overall, the results demonstrate that both seatbelt use and impact velocity are critical factors influencing injury severity. Seatbelt use mitigates peak accelerations and reduces contact with interior structures, while higher velocity increases the energy transfer and overall injury potential.

5.2. Injury Evaluation—Influence of Anthropometric Differences

To assess the effect of anthropometric differences on injury severity, six crash tests were conducted under identical conditions: full overlap at 56 km/h, with the only variable being the dummy type in the driver seat:

- Tests 1–3: H3 5% female dummy
- Tests 4–6: H3 50% male dummy

Table 7 summarizes the results of repeated belted crash tests for small (H3 5%) and midsize (H3 50%) anthropomorphic test devices. Basic statistical measures, including mean, standard deviation (SD), and coefficient of variation (CV%), are reported for injury metric to assess test repeatability. Across both ATD sizes, the measured responses show generally low SD and CV%, indicating consistent performance of the restraint system and reliable data collection. Slightly higher variability is observed in a few head and neck metrics for the smaller ATD, reflecting the influence of anthropometric differences on test response. Overall, these statistics provide a quantitative basis for evaluating the reliability and reproducibility of the crash tests under belted conditions.

The results (Figures 17 and 18 and Table A4) indicate that the smaller female dummy sustained higher injury levels across all regions—head, neck, chest, and femur—compared to the male dummy.

Table 7. Statistical Summary of Injury Metrics for Belted H3 5% and H3 50% Crash Tests.

Criterion	H3 5% (n = 3) Mean	SD	CV%	H3 50% (n = 3) Mean	SD	CV%
HIC15 Value [-]	348.12	54.82	15.8	203.36	21.05	10.4
HIC36 Value [-]	-	-	-	330.6	50.72	15.4
A3ms Value (cumulative) [g]	70.44	10.71	15.2	59.40	6.14	10.3
Neck Tension Force Fz+ [kN]	1.40	0.12	8.6	0.64	0.02	2.3
Neck Compression Force Fz− [kN]	0.47	0.08	16.9	0.21	0.05	24.0
A3ms Chest (cum.) [g]	42.55	1.79	4.2	40.67	2.61	6.4
Chest deflection [mm]	25.99	5.49	21.1	22.94	3.74	16.3

H3 5% values: n = 3; H3 50% values: n = 3. SD = standard deviation, CV% = coefficient of variation.

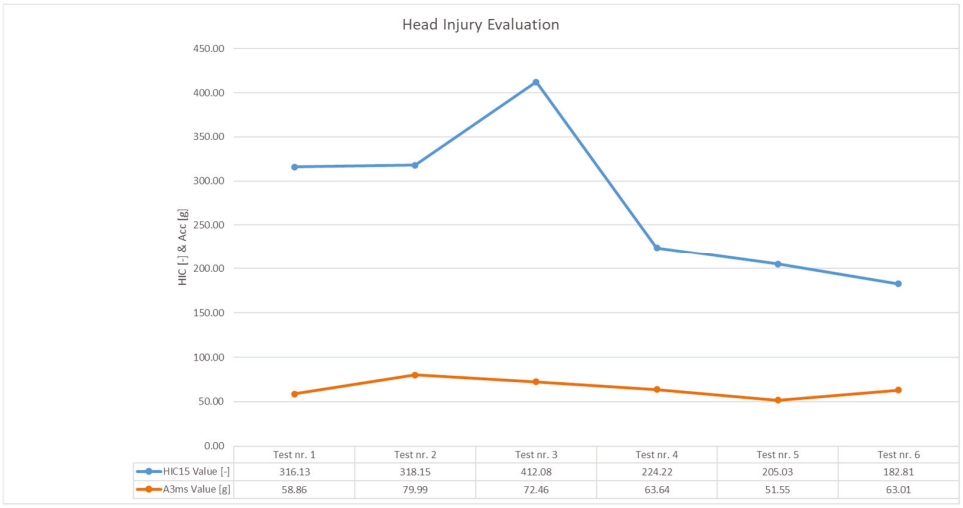

Figure 17. Head injury evaluation—H3 5% (1, 2, 3) vs. H3 50% (4, 5, 6).

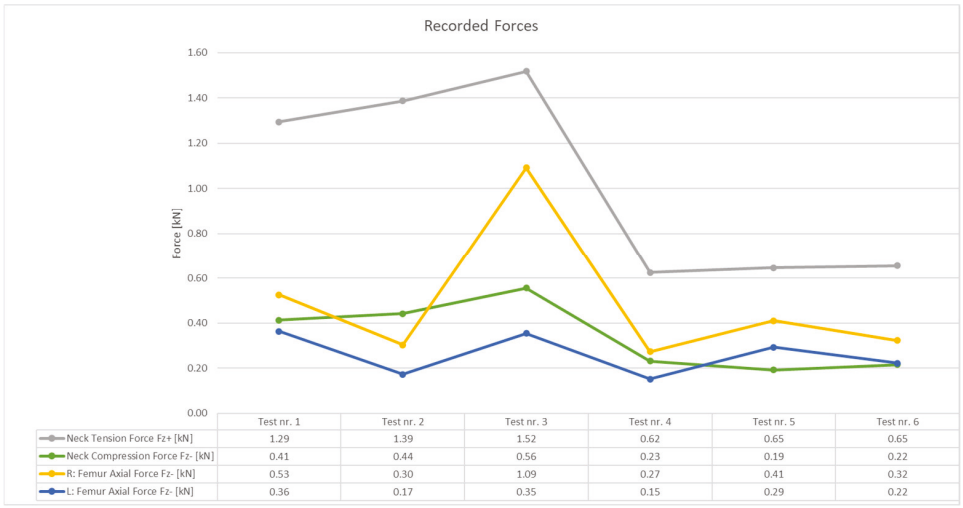

Figure 18. Recorded forces Neck & Femur—H3 5% (test no. 1, 2, 3) vs. H3 50% (test no. 4, 5, 6).

For head injuries, the HIC value for H3 5% over a 15 ms interval exceeded twice the average recorded for H3 50%, and head-level acceleration reached the 80 g regulatory limit, indicating a high risk of severe injuries.

A similar trend is observed at the neck level for both tension and compression. The forces measured for H3 5% were approximately twice those of H3 50%, although still within regulatory limits.

https://doi.org/10.3390/vehicles8040077

For the lower limbs (femur), forces were also higher for H3 5%, but differences were not considerable. A favorable factor may be the vehicle's interior space and the seat position defined by the protocol—the driver seat was set to full front for the H3 5% dummy and to the rearmost and lowest position for the H3 50% dummy—providing sufficient clearance to the dashboard and preventing direct contact with the lower limbs.

These observations highlight that anthropometric differences are a significant factor affecting injury outcomes. When considered alongside velocity and restraint conditions, drivers with smaller stature may be at greater risk in frontal collisions. This emphasizes the importance of including diverse anthropometries in vehicle safety assessment and design to ensure adequate protection for all occupants.

6. Discussion

Differences in impact speed between physical tests and simulations were selected to balance regulatory relevance, experimental feasibility, and comparative analysis. While full-scale testing of unbelted occupants at higher speeds is limited by safety and measurement constraints, numerical simulations provide a controlled environment for evaluating restraint effects under identical impact conditions. By normalizing injury metrics and focusing on occupant kinematics and injury mechanisms, meaningful comparisons can be achieved despite differences in impact velocity.

The comparison between physical tests and numerical simulations indicates a consistent qualitative agreement rather than strict quantitative equivalence. Considering differences in input parameters, boundary conditions, and model simplifications, the simulated injury metrics remained within an acceptable range and reproduced the trends observed experimentally. The overall CORA-based methodology score of 0.87 indicates good correlation, consistent with variability typically observed in repeated physical crash tests, particularly for unbelted dummies where kinematic behavior is inherently more variable. The largest discrepancies were observed for cumulative head acceleration in unbelted conditions, reflecting the increased unpredictability of occupant motion without restraint.

Thus, the simulated injury metrics reproduce the experimental trends and fall within the natural variability of the physical tests, providing an evidence-based indication of the model's accuracy. Within the defined modeling assumptions, the numerical model offers a reliable representation of occupant response and can be used for extended parametric analyses, provided its limitations are clearly acknowledged.

The assessment of restrained (56 km/h) and unrestrained (40 km/h) frontal full-overlap configurations showed that the absence of the seatbelt resulted in higher injury metrics, particularly in the head region, despite the lower impact velocity. However, restraint condition and impact speed act simultaneously on occupant kinematics, load transfer, and energy absorption mechanisms. Therefore, the results should be interpreted as reflecting the combined effect of these factors rather than isolating to a single dominant parameter.

The analysis of anthropometric differences further demonstrates their influence on injury magnitude and distribution. The higher injury metrics recorded for the H3 5% dummy compared to the H3 50% dummy reflect dimensional and biomechanical variability, rather than a gender-based comparison. These findings support the need to incorporate anthropometric diversity into occupant protection assessment to ensure consistent safety performance across a wide range of body dimensions.

Physical tests remain essential for capturing realistic occupant kinematics, particularly in unbelted scenarios where dummy motion is highly sensitive and difficult to predict. This aspect becomes even more relevant in the context of autonomous vehicles, where occupants may adopt non-standard seating positions and postures, highlighting the limitations of purely numerical approaches.

https://doi.org/10.3390/vehicles8040077

7. Conclusions

Despite substantial advancements in experimental testing methods, numerical simulations and passive safety technologies, road traffic injuries remain a major safety concern.

This study presents an integrated experimental–numerical investigation of the effects of impact velocity, restraint condition, and anthropometric variability on injury severity in frontal full-overlap crash scenarios. Additionally, the study highlights the importance of evaluating occupant injury metrics across multiple crash safety protocols. By applying different assessment methodologies to the same experimental dataset, it is possible to identify variability in injury ratings and better understand the influence of protocol-specific criteria. This approach underscores the need for cross-protocol evaluations to ensure comprehensive assessment of vehicle safety performance.

A primary contribution of this work is the correlation of real crash test measurements with simulation outputs, enabling a detailed evaluation of occupant kinematics and region-specific injury metrics under controlled conditions.

The findings demonstrate that injury severity results from the interaction of multiple factors rather than a single governing parameter. Unrestrained conditions led to significantly higher head injury metrics, even at lower impact speeds, confirming the critical protective role of seatbelt systems. Furthermore, the smaller anthropometric configuration (H3 5%) consistently exhibited higher regional loads compared to the H3 50% dummy under identical impact conditions, underscoring the importance of incorporating anthropometric diversity into safety assessment procedures.

The study is subject to certain limitations, including the limited number of physical test repetitions, protocol-defined test configuration, and the representation of anthropometric diversity through two dummy models. Additionally, numerical simulations while effective for capturing overall occupant kinematics, is simplified and may not fully represent local structural deformations, detailed interactions, or secondary contacts within the cabin and/or passenger. While these limitations may affect the absolute injury predictions, the overall trends observed between experiments and simulations remain robust.

The results have relevance for emerging autonomous vehicle concepts, where non-standard seating configurations and variable occupant postures may challenge conventional restraint strategies. Future research should therefore focus on adaptive occupant detection and classification systems capable of identifying position and anthropometric differences in real time, enabling dynamic adjustment of passive safety deployment. In parallel, the development of restraint systems compatible with reconfigurable cabin architectures represents a necessary step toward ensuring effective protection in future mobility scenarios.

Overall, the study contributes to the advancement of adaptive and anthropometry-aware safety concepts aligned with long-term road safety objectives, supporting the development of intelligent safety systems for occupants with variable anthropometric profile.

Author Contributions: Conceptualization, O.-V.S.-O. and B.S.; methodology, I.D.; software, O.-V.S.-O.; validation, O.-V.S.-O. and B.S.; formal analysis, C.B.; investigation, O.-V.S.-O.; resources, O.-V.S.-O. and C.B.; writing—original draft preparation, O.-V.S.-O.; writing—review and editing, O.-V.S.-O. and C.B.; visualization, B.S.; supervision, I.D. and B.S. All authors have read and agreed to the published version of the manuscript.

Funding: This research received no external funding.

Data Availability Statement: The original contributions presented in this study are included in the article. Further inquiries can be directed to the corresponding author.

Acknowledgments: The authors gratefully acknowledge IAV GmbH—Vehicle Safety for providing the technical facilities and expertise used in the crash tests. Appreciation is also extended to the University of Craiova, Faculty of Mechanical Engineering for academic support and collaboration throughout the research.

Conflicts of Interest: Author Oana-Victoria Stanciuc-Otat and Burkhard Scholz were employed by the company IAV Fahrzeugsicherheit GmbH & Co. KG. The remaining authors declare that the research was conducted in the absence of any commercial or financial relationships that could be construed as a potential conflict of interest.

Abbreviations

The following abbreviations are used in this manuscript:

A3ms	Thoracic acceleration over 3 ms
A3ms Chest	Chest-specific cumulative acceleration
AV	Autonomous Vehicle
ADS	Autonomous Drive System
CFC600	Channel Frequency Class 600 Hz
EDR	Event Data Recorder
Euro NCAP	European New Car Assessment Program
FMVSS	Federal Motor Vehicle Safety Standard
g	Gravitational acceleration. 1 g = 9.81 m/s^2
HIC	Head Injury Criteria
HPC	Head Performance Criterion
H3 5%	Hybrid III 5th Percentile Female Crash Test Dummy
H3 50%	Hybrid III 50th Percentile Male Crash Test Dummy
KNCAP	Korea New Car Assessment Program
NHTSA	National Highway Traffic Safety Administration
Nij	Neck Injury Criterion
N_CE	Neck Compression—Extension
N_CF	Neck Compression—Flexion
N_TE	Neck Tension—Extension
N_TF	Neck Tension—Flexion
Poly3	Mathematical model used to filter and calculate chest deformation
TCC	Thorax Centreline Criteria
U.S.NCAP	U.S. New Car Assessment Program
VUT	Vehicle under test
11	Driver position
13	Front passenger position
CORA	Correlation and Analysis
SD	Standard Deviation
CV%	Coefficient of Variation

Appendix A

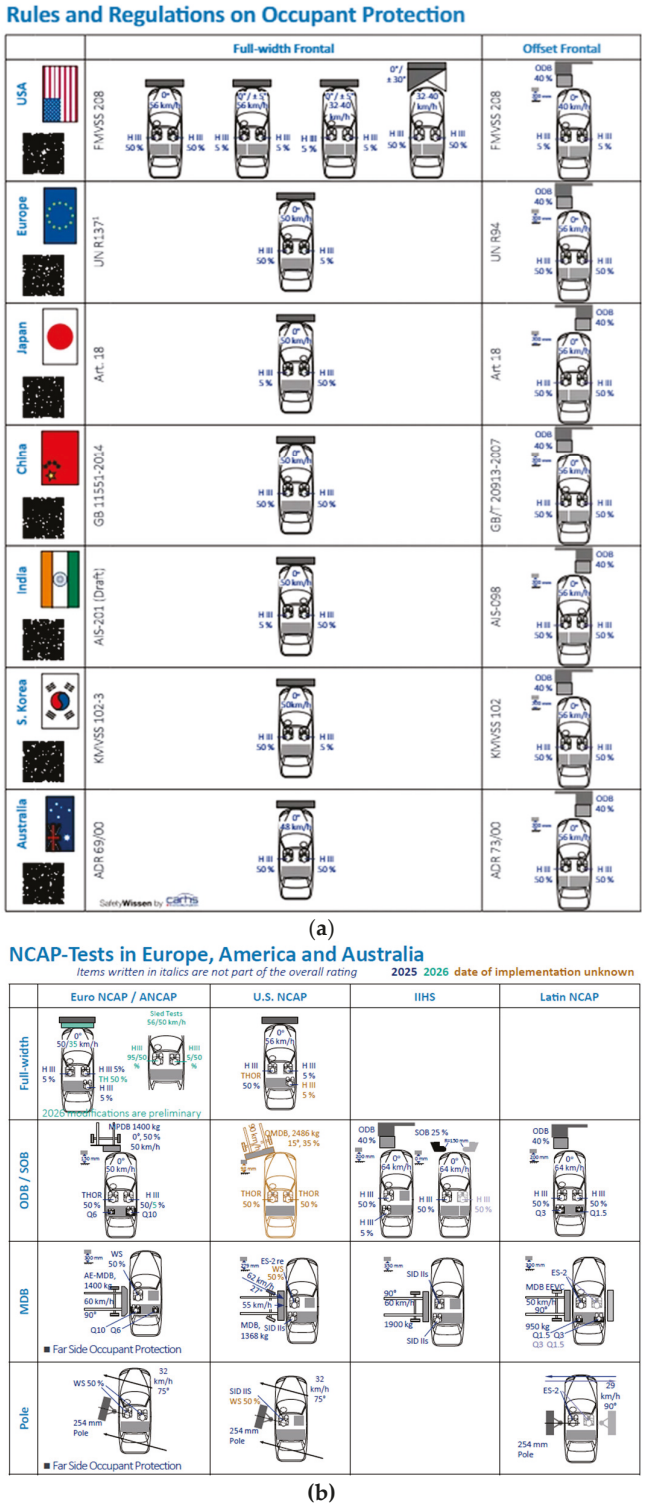

Figure A1. Test protocols for frontal collision [11]. (**a**) Regulations on occupant protection; (**b**) Consumer test protocols. Color coding indicates the level of occupant protection for each body region: Green—Good protection: very low injury risk; biomechanical criteria well below tolerance limits. Yellow—Adequate protection: low injury risk; values close to assessment thresholds. Orange—Marginal protection: increased injury risk; injury criteria exceed preferred limits. Brown—Weak protection: high injury risk; criteria significantly exceed tolerance levels. Red—Poor protection: very high injury risk; severe or life-threatening injuries likely.

https://doi.org/10.3390/vehicles8040077

Table A1. Dummy rating—Test Protocol-EuroNCAP.

Name	Value	Unit	Time 1	Time 2	Unit	Percent	Rating	Points	Ref 1	Ref 2
11 Hybrid III Small Adult Female										
Head										
Head Peak Res. Acc.	89.2	[g]	196	-	[ms]	111.50%	no	-	80	
A3ms head (cum.)	58.1	[g]	194	201	[ms]	77.81%	GOOD	4	72	74.67
HIC15 Value	160	[1]	41	55.6	[ms]	28.24%	GOOD	4	500	566.67
Unstable airbag contact/bottoming-out	0	[1]	-	-	-	--	not applied	0	1	
Hazardous airbag deployment	0	[1]	-	-	-	--	not applied	0	1	
Incorrect airbag deployment Head	0	[1]	-	-	-	--	not applied	0	1	
Steering Column X	0	[mm]	-	-	-	--	not applied	0	90	110
Steering Column Y	0	[mm]	-	-	-	--	not applied	0	90	110
Steering Column Z	0	[mm]	-	-	-	--	not applied	0	72	88
Neck										
Neck Shear Force Fx	0.51	[kN]	125.5	-	[ms]	35.17%	GOOD	4	1.2	1.45
Neck Shear Force Fx (Capping)	0.52	[kN]	125.5	-	[ms]	19.26%	GOOD	4	2.7	
Neck Tension Force Fz+	1.25	[kN]	49	-	[ms]	62.19%	GOOD	4	1.7	2.01
Neck Tension Force Fz+ (Capping)	1.25	[kN]	49	-	[ms]	43.10%	GOOD	4	2.9	
Neck Extension My-	17.43	[Nm]	85.6	-	[ms]	43.22%	GOOD	4	36	40.33
Neck Extension My- (Capping)	17.43	[Nm]	85.6	-	[ms]	30.58%	GOOD	4	57	
Chest										
Chest deflection (Poly3,TCC)	21.87	[mm]	8.1	-	[ms]	84.12%	ADEQUATE	3.34	18	26
VC-Value Chest (Poly3)	0.17	[m/s]	39.9	-	[ms]	25.50%	GOOD	4	0.5	0.6667
Incorrect airbag deployment Chest	0	[1]	-	-	-	--	not applied	0	1	
Steering wheel contact of chest	0	[mm]	-	-	-	--	not applied	0	1	
Shoulder Belt Load B3	6.774	[kN]	61.9	-	[ms]	112.90%	not applied	0	6	
Upper Leg										
Femur Force Fz− left	0.33	[kN]	160.9	-	[ms]	8.68%	GOOD	4	2.6	3.8
Femur Force Fz− right	0.36	[kN]	156.8	-	[ms]	9.47%	GOOD	4	2.6	3.8
HF ILAC LE	0	[1]	-	-	-	--	not applied	0	1	
HF ILAC RI	0	[1]	-	-	-	--	not applied	0	1	
Lower Leg										
L: Tibia Axial Compression Force (TCFC)	1.766	[kN]	59.1	-	[ms]	--		-		
R: Tibia Axial Compression Force (TCFC)	0.832	[kN]	56.01	-	[ms]	--		-		
L: Upper Tibia-Index	0.65	[1]	59.8	-	[ms]	--		-		
L: Lower Tibia-Index	0.34	[1]	58.9	-	[ms]	--		-		
R: Upper Tibia-Index	0.39	[1]	61.2	-	[ms]	--		-		
R: Lower Tibia-Index	0.41	[1]	61.2	-	[ms]	--		-		

Table A2. Dummy rating—Test Protocol-KNCAP.

Name	Value	Unit	Time 1	Time 2	Unit	Percent	Rating	Points	Ref 1	Ref 2
11 Hybrid III Small Adult Female										
Head										
A3ms head (cum.)	40	[g]	43.7	196.9	[ms]	55.56%	GOOD	4	72	74.67
HIC15 Value	149	[1]	41.5	56.5	[ms]	29.80%	GOOD	4	500	566.67
Unstable airbag contact/Incorrect airbag deployment Head	0	[1]	-	-	-	--	not applied	0	1	
Excessive Head Excursion	0	[1]	-	-	-	--	not applied	0	1	
Steering wheel displacement (head)	0	[1]	-	-	-	--	not applied	0	1	
Steering wheel deatchment from steering column	0	[1]	-	-	-	--	not applied	0	1	
Neck										
Neck Force Fx	0.549	[kN]	124.1	-	[ms]	37.86%	GOOD	4	1.2	1.45
Neck Force Fz+	1.35	[kN]	48	-	[ms]	67.16%	GOOD	4	1.7	2.01
Neck Extension -My	17.2	[Nm]	84.2	-	[ms]	42.65%	GOOD	4	36	40.33
Chest										
Chest deflection (front seat)	21.9	[mm]	7.6	-	[ms]	93.87%	ADEQUATE	3.1	18	23.33
VC-Value Chest	0.14	[m/s]	40.7	-	[ms]	28.00%	GOOD	4	0.5	0.6667
Steering wheel contact of chest	0	[mm]	-	-	-	--	not applied	0	1	
Shoulder Belt Load B3	5.874	[kN]	62.2	-	[ms]	97.90%	not applied	0	6	
Shoulder Belt Load B3 (RA 20ms)	4.971	[kN]	59.7	-	[ms]	82.85%	not applied	0	6	
Upper Leg										
Femur Force left Fz−	0.25	[kN]	157.9	-	[ms]	6.58%	GOOD	4	2.6	3.8
Femur Force right Fz−	0.29	[kN]	153.5	-	[ms]	7.63%	GOOD	4	2.6	3.8
HF ILAC LE	0	[1]	-	-	-	--	not applied	0	1	
HF ILAC RI	0	[1]	-	-	-	--	not applied	0	1	
Incorrect airbag deployment knee left	0	[1]	-	-	-	--	not applied	0	1	
Incorrect airbag deployment knee right	0	[1]	-	-	-	--	not applied	0	1	

https://doi.org/10.3390/vehicles8040077

Table A3. Dummy rating—Test Protocol-U.S.NCAP.

Name	Value	Unit	Time 1	Time 2	Unit	Percent	Rating	Points	Ref 1	Ref 2
11 Hybrid III Small Adult Female										
Head										
HIC_15	159	[1]	41.9	55.9	[ms]	22.71%	GOOD	1	500	700
BrIC	0.71	[1]	--	-	-	67.62%	GOOD	1	0.71	1.05
Neck										
Nij max: Nij In-Position (max)	0.356	[1]	49	-	[ms]	35.60%	GOOD	1	0.5	1
N_CE: Nij In-Position	0.224	[1]	197.8	-	[ms]	22.40%	GOOD	1	0.5	1
N_CF: Nij In-Position	0.151	[1]	100.1	-	[ms]	15.10%	GOOD	1	0.5	1
N_TE: Nij In-Position	0.293	[1]	41.9	-	[ms]	29.30%	GOOD	1	0.5	1
N_TF: Nij In-Position	0.351	[1]	49	-	[ms]	35.10%	GOOD	1	0.5	1
Chest										
Chest Deflection (HF)	21.53	[mm]	61.9	-	[ms]	41.40%	GOOD	1	25	52
Chest Deflection (HF,Poly3)	20.98	[mm]	61.9	-	[ms]	40.35%	GOOD	1	25	52
Upper Leg										
L: Femur Axial Force HF-5p (Max.)	0.221	[kN]	153.7	-	[ms]	3.25%	GOOD	1	6.8	
R: Femur Axial Force HF-5p (Max.)	0.247	[kN]	153.5	-	[ms]	3.63%	GOOD	1	6.8	

Appendix B

Table A4. Injury Criteria—H3 5% (test no. 1, 2, 3) vs. H3 50% (test no. 4, 5, 6).

Test No.	1	2	3	4	5	6
Dummy Position/type	11/HF	11/HF	11/HF	11/H3	11/H3	11/H3
Criterion	Value	Value	Value	Value	Value	Value
HIC15 Value [-]	316.13	318.15	412.08	224.22	205.03	182.81
HIC36 Value [-]	0.00	0.00	0.00	361.58	357.54	270.68
A3ms Value (cumulative) [g]	58.86	79.99	72.46	63.64	51.55	63.01
Neck Tension Force Fz+ [kN]	1.29	1.39	1.52	0.62	0.65	0.65
Neck Compression Force Fz− [kN]	0.41	0.44	0.56	0.23	0.19	0.22
N_CE: Nij In-Position [1]	0.33	0.30	0.54	0.02	0.00	0.04
N_CF: Nij In-Position [1]	0.10	0.21	0.17	0.09	0.21	0.04
N_TE: Nij In-Position [1]	0.39	0.32	0.34	0.13	0.13	0.13
N_TF: Nij In-Position [1]	0.38	0.43	0.43	0.29	0.28	0.26
A3ms Chest (cum.) [g]	40.48	43.62	43.55	40.85	37.83	43.32
Chest deflection [mm]	22.52	32.32	23.13	23.84	19.39	25.45
Chest deflection (Poly3,TCC) [mm]	19.29	29.09	20.30	23.03	18.69	0.00
Chest deflection CFC600 [mm]	0.00	0.00	0.00	23.94	19.49	25.55
Chest deflection CFC600 (Poly3,TCC) [mm]	0.00	0.00	0.00	23.03	18.69	0.00
L: Femur Axial Force Fz− [kN]	0.36	0.17	0.35	0.15	0.29	0.22
R: Femur Axial Force Fz− [kN]	0.53	0.30	1.09	0.27	0.41	0.32

Color coding indicates the level of occupant protection for each considered criterion: Green—Good protection: very low injury risk; biomechanical criteria well below tolerance limits. White—not applicable within this protocol rating or the corresponding values are unavailable.

References

1. NHTSA. *Traffic Safety Facts 2020*; U.S. Department of Transportation: Washington, DC, USA, 2021.
2. Brach, R.M. *Vehicle Accident Analysis and Reconstruction Methods*; SAE International: Warrendale, PA, USA, 2010.
3. World Health Organization. *Global Status Report on Road Safety*; WHO: Geneva, Switzerland, 2018.
4. *FMVSS 208*; Occupant Crash Protection. U.S. Department of Transportation: Washington, DC, USA, 2020.
5. UNECE. *Regulation No. 94: Protection of Occupants in Frontal Collision*; United Nations Economic Commission for Europe: Geneva, Switzerland, 2021.
6. Insurance Institute for Highway Safety. *Frontal Crashworthiness Evaluation Protocol*; IIHS: Arlington, VA, USA, 2021.
7. European New Car Assessment Programme. *Full Width Frontal Impact Testing Protocol*; Euro NCAP: Brussels, Belgium, 2021. Available online: https://www.euroncap.com (accessed on 10 December 2025).

8. U.S. Department of Transportation; National Highway Traffic Safety Administration. *Laboratory Test Procedure for FMVSS 208—Occupant Crash Protection*; NHTSA: Washington, DC, USA, 2020.
9. U.S. Department of Transportation; National Highway Traffic Safety Administration. *Laboratory Procedure for New Car Assessment Program—Full Frontal Rigid Barrier Impact Testing*; NHTSA: Washington, DC, USA, 2020.
10. Republic of Korea. *KMVSS Articles 102 and 104 (MOLIT Ordinance No. 465/2017): Lateral Impact—Regulations for Performance and Safety Standards of Motor Vehicles and Vehicle Parts*; MOLIT: Sejong, Republic of Korea, 2017.
11. SafetyWissen. Frontal Crash Testing Knowledge Base. Available online: https://www.safetywissen.com/object/B04/B04.8es738 9148188r8ex4u47336drnhdp63842130536/safetywissen (accessed on 13 December 2025).
12. Kahane, C.J. *Fatality Reduction by Safety Belts for Front-Seat Occupants of Cars and Light Trucks*; NHTSA Report; U.S. Department of Transportation: Washington, DC, USA, 2020.
13. Duma, I.; Burnete, N.; Todoruț, A.; Cordoș, N.; Danci, C.-C.; Terec, A. Assessment of Road Vehicle Accident Approaches—A Review. *Vehicles* **2025**, *7*, 10. [CrossRef]
14. Bedewi, N.; Kan, C.; Summers, S.; Ragland, C. *Evaluation of Car-to-Car Frontal Offset Impact Finite Element Models Using Full-Scale Crash Data*; SAE Technical Paper 950650; SAE International: Warrendale, PA, USA, 1995. [CrossRef]
15. Droździel, P.; Pasaulis, T.; Pečeliūnas, R.; Pukalskas, S. Evaluation of the Energy Equivalent Speed of Car Damage Using a Finite Element Model. *Vehicles* **2024**, *6*, 632–650. [CrossRef]
16. Hallquist, J. *LS-DYNA Theory Manual*; Livermore Software Technology Corporation: Livermore, CA, USA, 2006.
17. Teshome, K.K.; Negasa, T. Frontal Crash Effect Analysis of ADS Vehicles with Rigid Wall Using LS-DYNA. *J. Eng. Technol. Appl. Sci.* **2023**, *1*, 1–5.
18. Martínez, A.; Hernández, C.; Müller, S. Computer Simulation Models for Evaluating Vehicle Crashworthiness in Automotive Design. *Int. J. Automob. Eng.* **2026**, *7*, 24–27. [CrossRef]
19. Prabhaharan, S.A.; Balaji, G.; Krishnamoorthy, A. Numerical Simulation of Crashworthiness Parameters for Design Optimization of an Automotive Crash-Box. *Int. J. Simul. Multidisci. Des. Optim.* **2022**, *13*, 3. [CrossRef]
20. *ISO 6487:2002*; Measurement Techniques in Impact Tests. International Organization for Standardization: Geneva, Switzerland, 2002.
21. Daphal, P.N.; Athavale, S. *Full Vehicle Frontal Crash and Rollover Simulation Using LS-DYNA3D and Experimental Validation*; SAE Technical Paper 2001-26-0033; The Automotive Research Association of India: Pune, India, 2001. [CrossRef]
22. Mertz, H.J.; Irwin, A.L.; Prasad, P. Biomechanical and Scaling Bases for Frontal and Side Impact Injury Assessment Reference Values. *Stapp Car Crash J.* **2003**, *47*, 155–188. [CrossRef] [PubMed]
23. Kleinberger, M.; Sun, E.; Eppinger, R.H. *Development of Improved Injury Criteria for the Assessment of Advanced Automotive Restraint Systems*; NHTSA Report; National Highway Traffic Safety Administration: Washington, DC, USA, 1998.
24. Assi, K.; Rahman, S.M.; Mansoor, U.; Ratrout, N. Predicting Crash Injury Severity with Machine Learning Algorithm Synergized with Clustering Technique. *Int. J. Environ. Res. Public Health* **2020**, *17*, 5497. [CrossRef] [PubMed]
25. Chong, M.; Abraham, A.; Paprzycki, M. Traffic Accident Analysis Using Machine Learning Paradigms. *Informatica* **2005**, *29*, 89–98.
26. Liu, P.; Zhang, W.; Wu, X.; Guo, W.; Yu, W. Driver Injury Prediction Using Explainable Machine Learning. *Vehicles* **2025**, *7*, 42. [CrossRef]
27. Daoud, R.; Vechione, M.; Gurbuz, O.; Sundaravadivel, P.; Tian, C. Nighttime Crash Severity Prediction Using Machine Learning. *Vehicles* **2025**, *7*, 20. [CrossRef]
28. Jiang, Y.; Qu, X.; Zhang, W.; Guo, W.; Xu, J.; Yu, W.; Chen, Y. Human Injury Severity Prediction Based on Transformer Model. *Vehicles* **2025**, *7*, 5. [CrossRef]
29. Sun, W.; Abdullah, L.N.; Sulaiman, P.S.; Khalid, F. Meta-Feature-Based Traffic Accident Risk Prediction. *Vehicles* **2024**, *6*, 728–746. [CrossRef]
30. Wiseman, Y.; Grinberg, I. Circumspectly Crash of Autonomous Vehicles. In *Proceedings of the IEEE International Conference on Electro Information Technology, Grand Forks, ND, USA, 19–21 May 2016*; IEEE: New York, NY, USA, 2016; pp. 387–392. Available online: https://www.researchgate.net/publication/306113200_Circumspectly_crash_of_autonomous_vehicles (accessed on 11 November 2025).
31. Koopman, P.; Wagner, M. Autonomous Vehicle Safety: An Interdisciplinary Challenge. *IEEE Intell. Transp. Syst. Mag.* **2017**, *9*, 90–98. [CrossRef]
32. Maschke, J.E.; Preu, V.; Plenter, M.; Schoenawa, S. Autonomous Emergency Braking Assessment Using Phenomenological Sensor Models. *Vehicles* **2024**, *6*, 1704–1716. [CrossRef]
33. Losada, Á.; Páez, F.J.; Luque, F.; Piovano, L. Effectiveness of Autonomous Braking and Evasive Steering Systems. *Vehicles* **2023**, *5*, 1553–1569. [CrossRef]
34. Park, J.; Kim, D.; Huh, K. Emergency Collision Avoidance by Steering in Critical Situations. *Int. J. Automot. Technol.* **2021**, *22*, 173–184. [CrossRef]
35. Strassheim, A. Robust System Testing of Event Data Recorders in Passive Safety Systems. *Vehicles* **2021**, *3*, 426–447. [CrossRef]

36. UNECE. *UN Regulation No. 160—Event Data Recorder (EDR)*; UNECE: Geneva, Switzerland, 2021. Available online: https://unece.org/transport/documents/2021/10/standards/un-regulation-no-160-event-data-recorder-edr (accessed on 17 November 2025).
37. Dixit, A.; Kumar Chidambaram, R.; Allam, Z. Safety and Risk Analysis of Autonomous Vehicles Using Computer Vision and Neural Networks. *Vehicles* **2021**, *3*, 595–617. [CrossRef]
38. Zhou, Z. Attention-Based Stack ResNet for Citywide Traffic Accident Prediction. In *Proceedings of the IEEE International Conference on Mobile Data Management (MDM)*; IEEE: New York, NY, USA, 2019; pp. 369–370. [CrossRef]
39. Mallahi, I.; Riffi, J.; Tairi, H.; Nikolov, N.; Mostafa, E.; Mahraz, M. Optimizing Traffic Accident Severity Prediction with a Stacking Ensemble Framework. *World Electr. Veh. J.* **2025**, *16*, 561. [CrossRef]
40. Gyllenhammar, M.; Rodrigues de Campos, G.; Törngren, M. Methods Providing Safety Evidence for Automated Driving Systems. *IEEE Trans. Intell. Transp. Syst.* **2025**, *26*, 4315–4345. [CrossRef]
41. Yucheng, Y. *Driver's Non-Driving Postures in Automated Driving: Modeling, Assessment, and Countermeasures*; Technical University of Munich: Munich, Germany, 2020. Available online: https://mediatum.ub.tum.de/doc/1601413 (accessed on 10 November 2025).
42. Papaioannou, G.; Shen, C.; Rothhämel, M.; Happee, R. Occupants' Comfort and Human Body Dynamics. *Veh. Syst. Dyn.* **2025**, *63*, 1241–1299. [CrossRef]
43. Górniak, A.; Jędrzej, M.; Górniak, W.; Magdziak-Tokłowicz, M.; Krakowian, K.; Zawiślak, M.; Włostowski, R.; Cebula, J. Influence of Passenger Seating Position on Head Injury in Frontal Crash. *Sensors* **2022**, *22*, 2003. [CrossRef] [PubMed]
44. Leledakis, A.; Östh, J.; Davidsson, J.; Jakobsson, L. Influence of Passenger Sitting Postures in Intersection Crashes. *Accid. Anal. Prev.* **2021**, *157*, 106170. [CrossRef] [PubMed]
45. Takeuchi, Y.; Tanaka, Y.; Azuma, T.; Zhao, Y.; Mizuno, K.; Yamada, M.; Yokoyama, Y.; Yamada, Y.; Jinzaki, M. Predictive Modeling of Submarining Risk in Car Occupants. *Traffic Inj. Prev.* **2023**, *25*, 147–155. [CrossRef]
46. Bendjaballah, D.; Sahli, M.; Barrière, T. Modeling and numerical simulation of car frontal crash test using finite element method. *J. Mater. Sci. Mater. Eng.* **2025**, *20*, 108. [CrossRef]
47. Sunghyun, S.; Taewung, K.; Jaehoon, K. Sensitivity Analysis of Occupant and Vehicle Parameters in Autonomous Vehicle Crashes. *Appl. Sci.* **2025**, *15*, 6492. [CrossRef]
48. Singh, H.; Ganesan, V.; Davies, J.; Paramasuwom, M.; Gradischnig, L. *Vehicle Interior and Restraints Modeling for Occupant Safety Using THOR Dummies*; Report DOT HS 812 545; NHTSA: Washington, DC, USA, 2018.
49. Khandare, S.; Yang-Shen, L.; Boyle, K.; Reed, M.; Hu, J. Development and Validation of Diverse Active Human Models. *J. Biomech.* **2025**, *189*, 112835. [CrossRef]
50. Mohd Amirudin, M.R.; Abidin, A.N.S.; Shabadin, A.; Azman, N.; Mohd Faudzi, S.; Paiman, N.F.; Ahmad, Y. Injury Severity in Frontal Impact Collisions. *J. Soc. Automot. Eng. Malays.* **2021**, *5*, 430–438. [CrossRef]
51. Pintar, F.A.; Yoganandan, N.; Maiman, D.J. Injury Mechanisms in Narrow Offset Frontal Impacts. *Ann. Adv. Automot. Med.* **2008**, *52*, 185–189.
52. Parent, D.; Craig, M.; Moorhouse, K. Biofidelity Evaluation of THOR and Hybrid III 50th Percentile Male ATDs. *Stapp Car Crash J.* **2017**, *61*, 227–276.
53. *J211/1_202208*; Instrumentation for Impact Test Part 1—Electronic Instrumentation Quality, Testing and Safety Vehicle Systems and Performance. SAE International: Warrendale, PA, USA, 2022.
54. Otat, O.V. *Modele Dinamice Pentru Analiza Impactului la Vehicule*; Editura Universitaria: Craiova, Romania, 2018; ISBN 978-606-14-1386-0.
55. Otat, O.; Dumitru, N.; Dumitru, I. Dynamic Models to Analyse the Influence of the Seat Belt in a Frontal Collision. *IOP Conf. Ser. Mater. Sci. Eng.* **2017**, *252*, 012017. [CrossRef]
56. Otat, O.; Dumitru, N.; Otat, V.; Dumitru, I. Kinematic and Dynamic Behaviour of the Driver's Skull in Steering Wheel Impact. In *Advances in Safety, Reliability and Risk Management*; Springer: Cham, Switzerland, 2016; pp. 869–879. [CrossRef]
57. *ISO/TS 18571:2024*; Road Vehicles—Objective Rating Metric for Non-Ambiguous Signals. International Organization for Standardization: Geneva, Switzerland, 2024.

Disclaimer/Publisher's Note: The statements, opinions and data contained in all publications are solely those of the individual author(s) and contributor(s) and not of MDPI and/or the editor(s). MDPI and/or the editor(s) disclaim responsibility for any injury to people or property resulting from any ideas, methods, instructions or products referred to in the content.

vehicles

MDPI

Article

Algorithmic Classification of Constrained Extrema in Low-Dimensional Problems with Applications to Transport Location Problems

Mihaela Racila [1], Theodor Oprica [2], Lucian Matei [2], Ilie Dumitru [2], Nicoleta Gencarau [2] and Laurentiu Racila [2,*]

[1] Department of Applied Mechanics and Civil Engineering, Faculty of Mechanics, University of Craiova, 200478 Craiova, Romania; mihaela.racila@edu.ucv.ro
[2] Department of Automotive, Transportation and Industrial Engineering, Faculty of Mechanics, University of Craiova, 200478 Craiova, Romania; theodor.oprica@edu.ucv.ro (T.O.); lucian.matei@edu.ucv.ro (L.M.); ilie.dumitru@edu.ucv.ro (I.D.); nicoleta.gencarau@edu.ucv.ro (N.G.)
* Correspondence: laurentiu.racila@edu.ucv.ro

Abstract

Constrained optimization plays a central role in transport and logistics location problems, such as depot siting under geometric or infrastructure-related constraints. In practice, the classification of constrained extrema by classical second-order methods, typically based on bordered Hessians and the explicit manipulation of the total differentials of the constraint functions, can be cumbersome and error-prone, especially in engineering-oriented applications. In this paper, we present algorithmic procedures for the classification of constrained extrema in low-dimensional problems (2D and 3D), with applications to transport location models. The proposed approach does not avoid the use of constraint derivatives, since first-order constraint information is necessary for any local constrained classification procedure. Rather, it avoids the explicit manipulation of the total differentials of the constraints during the application phase. The required constraint information is incorporated through first-order partial derivatives evaluated at the stationary point, leading to simple algebraic test coefficients derived from the second derivatives of the Lagrangian. The procedures apply to regular non-degenerate cases and require only the solution of Fermat-type systems together with the evaluation of low-order determinants. Their practical relevance is illustrated through a transport depot location problem with geometric constraints, showing how the proposed approach can provide a transparent and effective decision-support tool for transport and logistics engineering.

Keywords: constrained optimization; constrained extrema classification; Lagrange multipliers; second-order conditions; low-dimensional optimization; transport location

1. Introduction

Constrained optimization is a fundamental mathematical tool with numerous applications in engineering, mechanics, economics, and decision sciences. In transport and logistics, constrained optimization naturally arises in location problems such as depot siting, hub placement, and infrastructure planning [1,2], where objective functions must be optimized under geometric, operational, or infrastructure-related constraints. The literature confirms the continuing importance of facility location models in logistics and transportation, both in general methodological terms and in application-driven planning contexts [3]. Current research further explores advanced optimization frameworks for

facility location and transport-related decision problems, including dynamic allocation models, location-routing integration, and multi-objective optimization approaches [4–6].

The most commonly used approach for solving constrained optimization problems is the method of Lagrange multipliers, which incorporates the constraints into the objective function through auxiliary variables. In its classical form, this method leads to a system of first-order necessary conditions (the Fermat system), whose solutions provide candidate points for constrained extrema [7]. The classification of these points typically relies on second-order conditions involving bordered Hessians or equivalent constructions [8].

While theoretically well established, classical second-order tests can be cumbersome to apply in practice. They often require the explicit manipulation of the total differentials of the constraint functions, careful handling of bordered Hessians, and, in some cases, the use of the implicit function theorem [9,10]. From an engineering perspective, these steps may lead to lengthy calculations, increased risk of algebraic errors, and limited usability in practical decision-making contexts. This is particularly relevant in applied facility location problems, where optimization models are used as decision-support tools in contexts such as last-mile logistics and multi-period planning [11].

In this work, we propose explicit low-dimensional algorithmic procedures for the classification of constrained extrema in regular non-degenerate cases. The procedures are based on the classical second-order constrained optimization framework, but they organize the classification step into directly applicable algebraic criteria for dimensions two and three. Unlike standard textbook presentations, the emphasis is placed on operational usability, transparent computation, and reduced symbolic manipulation in engineering-oriented applications.

The resulting algorithms are intentionally designed to be user-friendly: they require only the computation of partial derivatives, the solution of Fermat-type systems and the evaluation of scalar test coefficients or 2×2 determinants. Although fully general from a mathematical standpoint, the proposed approach is particularly well suited to transport and logistics location problems, where constraints are often geometric and the problem dimension is low.

The main contributions of this paper are threefold. First, we provide explicit low-dimensional algorithmic procedures for the classification of constrained extrema in regular non-degenerate cases. Second, we reformulate the classification step into algebraic test coefficients that incorporate the relevant constraint tangent information without requiring the repeated explicit manipulation of total constraint differentials during each application. Third, we illustrate the practical relevance of the procedures through a transport depot location problem, showing how they can serve as transparent decision-support tools in engineering-oriented constrained optimization problems.

The objective of this research is to develop simplified and explicit algorithmic procedures for the classification of constrained extrema in low-dimensional optimization problems. The research problem addressed is the practical difficulty associated with the application of classical second-order optimality conditions in engineering-oriented contexts, where symbolic complexity and the need for explicit constraint differentiation may limit usability.

The research gap lies in the lack of transparent, user-oriented classification procedures that can be directly applied without requiring advanced analytical tools or extensive symbolic manipulation. While classical approaches based on bordered Hessians are theoretically complete, their direct practical implementation may become cumbersome even in low-dimensional applied problems, and this difficulty naturally increases in higher dimensions.

This work aims to fill this gap by proposing computationally efficient and structured algorithms that reformulate the low-dimensional classification step through simple algebraic

https://doi.org/10.3390/vehicles8060131

criteria derived from the constrained second-order framework. The proposed approach is particularly relevant for transport and logistics applications, where decision-making models frequently involve low-dimensional constrained optimization problems.

The remainder of this paper is organized as follows. Section 2 discusses the practical challenges associated with classical constrained optimization techniques in transport location problems. Section 3 presents the proposed algorithms for constrained optimization in 2D and 3D. Section 4 outlines the computational workflow and implementation aspects. Section 5 applies the proposed methods to solve a transport depot location problem. The Maple implementation for the two-dimensional and three-dimensional cases are provided in Appendices A and C, respectively. Finally, Sections 6 and 7 provide a discussion and concluding remarks.

2. Constrained Optimization Challenges in Transport Location Problems

Constrained optimization problems encountered in transport and logistics are commonly addressed using the method of Lagrange multipliers, which incorporates the constraints into the objective function through additional variables. Solving the resulting Fermat system yields candidate points for constrained extrema, whose nature must then be determined using second-order conditions.

In classical formulations, this classification step relies on the analysis of the second-order differential of the Lagrangian, typically expressed through bordered Hessian matrices or equivalent quadratic forms [8,12]. From standard results in linear algebra, the definiteness of these quadratic forms determines whether a stationary point corresponds to a constrained minimum, maximum, or saddle point.

In practice, however, the application of these second-order tests presents several challenges. First, bordered Hessian constructions rapidly become algebraically cumbersome [13], even in low-dimensional problems. Second, when the second differential of the Lagrangian is indefinite before restriction to the tangent space of the constraint, the classification must be performed along the admissible tangent directions. In classical calculations, this typically requires either constructing bordered Hessians or explicitly writing and manipulating the total differentials of the constraints and substituting the resulting relations into the second-order form. This is essential because a constrained extremum of an objective function is not necessarily a local extremum of the corresponding Lagrangian. This phenomenon can be illustrated by considering the function $f(x,y) = x + y$, subject to the constraint $xy = 1$. Straightforward computations show that the points $(1,1)$ and $(-1,-1)$ are saddle points of the associated Lagrangian, yet they are constrained extrema of f on the constraint surface.

This situation frequently arises in transport location models. For example, a constrained extremum of an objective function defined on a geometric constraint (such as a curve or surface representing an infrastructure condition) does not necessarily correspond to a local extremum of the associated Lagrangian. As a result, studying the second differential of the Lagrangian in the full space of variations may be insufficient when this quadratic form is indefinite. In such cases, the classification must be carried out on the admissible tangent directions induced by the constraint.

From an engineering and decision-support perspective, these requirements can significantly limit the practical usability of classical methods. Lengthy symbolic manipulations, repeated differentiation of constraint functions, and the construction of high-order determinants increase the risk of errors and reduce transparency for transport and logistics engineers.

These limitations motivate the development of operational algorithmic formulations that preserve mathematical rigor while simplifying the classification step. In particular,

https://doi.org/10.3390/vehicles8060131

there is a need for procedures that reduce the amount of explicit symbolic manipulation required in the classification step, especially the repeated handling of total constraint differentials and bordered Hessian determinants [14]. The algorithms proposed in the next section address this need by embedding the necessary constraint-related computations directly into the algorithmic structure.

3. Proposed Constrained Optimization Algorithms in 2D and 3D

3.1. Problem Formulation

As discussed in the previous section, the practical difficulty of classical constrained optimization methods [7] lies primarily in the classification of stationary points, which often requires the explicit manipulation of constraint differentials and the construction of bordered Hessians. The approach proposed in this work is based on a direct algebraic reformulation of this classification step.

Throughout the proposed algorithms, the following assumptions are imposed. The objective and constraint functions are assumed to be sufficiently smooth in a neighborhood of the stationary point. The constraint gradients are regular at the considered point: for one equality constraint, the constraint gradient is nonzero; for two equality constraints in three variables, the corresponding constraint Jacobian has full rank. The denominators appearing in the algebraic coefficients are assumed to be nonzero; when a chosen denominator vanishes, another nonzero minor is selected, as described below, in the corresponding remarks. Finally, the classification criteria apply to non-degenerate stationary points; degenerate cases require a separate local analysis.

The core idea is to incorporate the tangent information induced by the constraints directly into the structure of the algorithm, rather than treating the corresponding differential manipulation as an external analytical step. This makes it possible to classify constrained extrema even when the associated Lagrangian exhibits a saddle point, leading to a unified treatment of all regular non-degenerate cases. The proposed procedures are not intended to replace the general theory of second-order necessary and sufficient conditions for constrained optimization. They should be understood as explicit low-dimensional operational reformulations of the classical reduced second-order test on the tangent space. Their purpose is to provide ready-to-use algebraic criteria for regular non-degenerate problems in dimensions two and three, avoiding repeated symbolic manipulation of constraint differentials and bordered Hessian determinants in practical applications.

From a practical perspective, this reformulation removes the need for users to repeatedly write and manipulate the total differentials of the constraints during each application. Instead, the proposed algorithms rely on the computation of partial derivatives of the Lagrangian and of the constraint functions, the solution of Fermat-type systems, and the evaluation of a small number of algebraic test coefficients. The use of first-order partial derivatives of the constraint functions does not introduce an additional computational stage, since these derivatives are already required in the construction and solution of the Fermat system associated with the Lagrangian. The simplification concerns the classification step, where the total differential relations of the constraints are not written and manipulated explicitly.

In the following subsections, we present the proposed algorithms for low-dimensional constrained optimization problems. The detailed derivation is first provided for the case of a function of three variables subject to a single constraint, which represents the most general and technically involved situation considered in this work. The remaining cases—functions of two variables with one constraint, and functions of three variables with two constraints—are then obtained by direct adaptation of the same underlying methodology and are therefore presented more concisely.

https://doi.org/10.3390/vehicles8060131

3.2. Algorithm for One Constraint in 3D

We consider the case of a function of three variables subject to a single equality constraint. The constrained optimization problem is then of the type: *minimize/maximize f(x,y,z) subject to g(x,y,z) = 0, x, y, z* $\in \boldsymbol{R}$.

We first introduce the Lagrangian associated with the constrained problem, defined as $F(x,y,z) = f(x,y,z) + \lambda \cdot g(x,y,z)$, and we use the first-order necessary conditions of Fermat: $\frac{\partial F}{\partial x}(x,y,z) = 0$; $\frac{\partial F}{\partial y}(x,y,z) = 0$; $\frac{\partial F}{\partial z}(x,y,z) = 0$; $g(x,y,z) = 0$.

The above four equations constitute a nonlinear system in the variables x, y, z, λ. It can be solved using classical techniques or numerical ones; for example, Newton's method. Thus, we will have access to the candidate point(s) (stationary point(s)) to the constraint extrema, (x_0, y_0, z_0), and the value of the Lagrange multiplier λ. In order to test which point is a constraint maximum or minimum (or a degenerate point), we need to use the second-order necessary condition by studying the differential form d^2F of the Lagrangian in each stationary point and see if it is positive or negative definite. Suppose that, at a stationary point, d^2F has the following form:

$$d^2F_{(x_0,y_0,z_0)} = a_{11}\cdot dx^2 + a_{22}\cdot dy^2 + a_{33}\cdot dz^2 + 2a_{12}\cdot dxdy + 2a_{13}\cdot dxdz + 2a_{23}\cdot dydz \quad (1)$$

$$\left(a_{ij} = \frac{\partial^2 F}{\partial x_i \partial x_j}(x_0,y_0,z_0), i,j = 1,2,3, x_1 = x, x_2 = y, x_3 = z\right) \quad (2)$$

At the derivation level, the admissible tangent directions are obtained from the condition that the total differential of the constraint vanishes at the stationary point. We will thus obtain the dz function of dx and dy, saying $dz = C_1\cdot dx + C_2\cdot dy$, where:

$$C_1 = -\frac{\frac{\partial g}{\partial x}(x_0,y_0,z_0)}{\frac{\partial g}{\partial z}(x_0,y_0,z_0)} \text{ and } C_2 = -\frac{\frac{\partial g}{\partial y}(x_0,y_0,z_0)}{\frac{\partial g}{\partial z}(x_0,y_0,z_0)} \quad (3)$$

Plugging this in d^2F, we will obtain:

$$d^2F_{(x_0,y_0,z_0)} = \left(a_{11} + a_{33}C_1^2 + 2C_1a_{13}\right)\cdot dx^2 + \left(a_{22} + a_{33}C_2^2 + 2C_2a_{23}\right)\cdot dy^2 + 2\left(a_{12} + a_{33}C_1C_2 + C_2a_{13} + C_1a_{23}\right)\cdot dxdy \quad (4)$$

With the notations $A = a_{11} + a_{33}C_1^2 + 2C_1a_{13}$, $B = (a_{12} + a_{33}C_1C_2 + C_2a_{13} + C_1a_{23})$ and $C = (a_{22} + a_{33}C_2^2 + 2C_2a_{23})$, one can study the matrix associated to this quadratic form and test its positivity/negativity using the usual tests (eigenvalues or determinant). All the steps taken before lead to the following simplified algorithm:

1. Constructing the Lagrangian associated with the constrained problem.
2. Solving the Fermat system—getting the stationary point(s).
3. Calculating the second derivatives of the Lagrangian and the constants $C_1 = -\frac{\frac{\partial g}{\partial x}(x_0,y_0,z_0)}{\frac{\partial g}{\partial z}(x_0,y_0,z_0)}$ and $C_2 = -\frac{\frac{\partial g}{\partial y}(x_0,y_0,z_0)}{\frac{\partial g}{\partial z}(x_0,y_0,z_0)}$.
4. Calculating $A = a_{11} + a_{33}C_1^2 + 2C_1a_{13}$, $B = (a_{12} + a_{33}C_1C_2 + C_2a_{13} + C_1a_{23})$ and $C = (a_{22} + a_{33}C_2^2 + 2C_2a_{23})$ and forming the matrix $\begin{pmatrix} A & B \\ B & C \end{pmatrix}$.
5. Testing the positivity/negativity of d^2F at the stationary point:

   (a) if $A > 0$ and $AC - B^2 > 0$, we have a constrained minimum point;
   (b) if $A < 0$ and $AC - B^2 > 0$, we have a constrained maximum point;
   (c) if $AC - B^2 < 0$, we have a saddle point;
   (d) if $AC - B^2 = 0$, we have a degenerate point.

https://doi.org/10.3390/vehicles8060131

Remark 1. *If* $\frac{\partial g}{\partial z}(x_0, y_0, z_0) = 0$ *and* $\frac{\partial g}{\partial y}(x_0, y_0, z_0) \neq 0$, *then the constraint implies*

$$C = -\frac{\frac{\partial g}{\partial x}(x_0, y_0, z_0)}{\frac{\partial g}{\partial y}(x_0, y_0, z_0)} \ (dy = C{\cdot}dx) \tag{5}$$

and the second differential form d^2F *of the Lagrangian becomes:*

$$d^2F_{(x_0,y_0,z_0)} = \left(a_{11} + a_{22}C^2 + 2Ca_{12}\right){\cdot}dx^2 + a_{33}{\cdot}dz^2 + +2\left(a_{13} + Ca_{23}\right){\cdot}dxdz \tag{6}$$

With the notations $A = a_{11} + +a_{22}C^2 + 2Ca_{12}$, $B = (a_{13} + Ca_{23})$ and $C = a_{33}$, one can study the matrix associated to this quadratic form and test its positivity/negativity using the usual tests (step 5, here-upper).

Remark 2. *If* $\frac{\partial g}{\partial z}(x_0, y_0, z_0) = 0$ *and* $\frac{\partial g}{\partial y}(x_0, y_0, z_0) = 0$, *then the constraint implies* $dx = 0$ *at the critical point. Consequently, the second differential reduces to:*

$$d^2F_{(x_0,y_0,z_0)} = a_{22}{\cdot}dy^2 + a_{33}{\cdot}dz^2 + +2a_{23}{\cdot}dydz \tag{7}$$

With the notations $A = a_{22}$, $B = a_{23}$ and $C = a_{33}$, one can study the matrix associated to this quadratic form and test its positivity/negativity using the usual tests (step 5, here-upper).

3.3. Algorithm for Two Constraints in 3D

We now consider the case of a function of three variables subject to two equality constraints: *minimize/maximize f(x,y,z) subject to* $g_1(x,y,z) = 0$ *and* $g_2(x,y,z) = 0$, $x, y, z \in \boldsymbol{R}$.

As in the previous case, the first two steps consist of constructing the Lagrangian and solving the associated Fermat system to obtain the candidate stationary points, then we continue with the steps:

1. Calculating the second derivatives of the Lagrangian and the constants:

$$C_1 = \frac{\begin{vmatrix} -\frac{\partial g_1}{\partial x} & \frac{\partial g_1}{\partial z} \\ -\frac{\partial g_2}{\partial x} & \frac{\partial g_2}{\partial z} \end{vmatrix}(x_0, y_0, z_0)}{\begin{vmatrix} \frac{\partial g_1}{\partial y} & \frac{\partial g_1}{\partial z} \\ \frac{\partial g_2}{\partial y} & \frac{\partial g_2}{\partial z} \end{vmatrix}(x_0, y_0, z_0)} \text{and } C_2 = \frac{\begin{vmatrix} \frac{\partial g_1}{\partial y} & -\frac{\partial g_1}{\partial x} \\ \frac{\partial g_2}{\partial y} & -\frac{\partial g_2}{\partial x} \end{vmatrix}(x_0, y_0, z_0)}{\begin{vmatrix} \frac{\partial g_1}{\partial y} & \frac{\partial g_1}{\partial z} \\ \frac{\partial g_2}{\partial y} & \frac{\partial g_2}{\partial z} \end{vmatrix}(x_0, y_0, z_0)} \tag{8}$$

which are obtained by differentiating the constraints and annulated them at the stationary point ($dy = C_1\,dx$ and $dz = C_2\,dx$).

2. Calculating the coefficient

$$M = \left(\frac{\partial^2 F}{\partial x^2} + {C_1}^2\frac{\partial^2 F}{\partial y^2} + {C_2}^2\frac{\partial^2 F}{\partial z^2} + 2C_1C_2\frac{\partial^2 F}{\partial y \partial z} + 2C_2\frac{\partial^2 F}{\partial x \partial z} + 2C_1\frac{\partial^2 F}{\partial x \partial y}\right)_{(x_0,y_0,z_0)} \tag{9}$$
$$\left(d^2F_{(x_0,y_0,z_0)} = M{\cdot}dx^2\right)$$

3. Testing the positivity/negativity of d^2F at the stationary point:

   (a) if $M > 0$, we have a constrained minimum point;
   (b) if $M < 0$, we have a constrained maximum point;
   (c) if $M = 0$, we have a degenerate point.

https://doi.org/10.3390/vehicles8060131

Remark 3. *If the chosen determinant* $\begin{vmatrix} \frac{\partial g_1}{\partial y} & \frac{\partial g_1}{\partial z} \\ \frac{\partial g_2}{\partial y} & \frac{\partial g_2}{\partial z} \end{vmatrix}(x_0, y_0, z_0)$ *is zero, this means the corresponding system cannot be solved for that pair of variables. In such a case, we simply select another* 2×2 *minor of the Jacobian that is nonzero (for example, using (x,z) or (x,y) instead of (y,z)). One nonzero minor always exists in the regular case. If no such nonzero determinant can be found, this means the two constraints are not really independent at that point. In practice, the geometry changes: the feasible set is no longer just a thin curve, but something wider (like a surface). In that case, our "one-direction test" cannot be used because we would need to test in several independent directions. Mathematically, this involves building two tangent directions and forming a* 2×2 *reduced Hessian matrix. For practical purposes, it is usually easier and clearer in this singular case to return directly to the differential form of the constraints rather than forcing the reduced algorithm. It avoids complicated algebra and gives a clearer view of what is happening.*

Here is what we should obtain in the cases *dy* free and *dz* free:

- Case *dy* free (*dx* and *dz* function of *dy*): we write the 2×2 system in (*dx*, *dz*) and we obtain, solving by Cramer (step 3, here-upper), the intermediate constants *A* and *B*:

$$A = \frac{\begin{vmatrix} -\frac{\partial g_1}{\partial y} & \frac{\partial g_1}{\partial z} \\ -\frac{\partial g_2}{\partial y} & \frac{\partial g_2}{\partial z} \end{vmatrix}(x_0,y_0,z_0)}{\begin{vmatrix} \frac{\partial g_1}{\partial x} & \frac{\partial g_1}{\partial z} \\ \frac{\partial g_2}{\partial x} & \frac{\partial g_2}{\partial z} \end{vmatrix}(x_0,y_0,z_0)} \text{ and } B = \frac{\begin{vmatrix} \frac{\partial g_1}{\partial x} & -\frac{\partial g_1}{\partial y} \\ \frac{\partial g_2}{\partial x} & -\frac{\partial g_2}{\partial y} \end{vmatrix}(x_0,y_0,z_0)}{\begin{vmatrix} \frac{\partial g_1}{\partial x} & \frac{\partial g_1}{\partial z} \\ \frac{\partial g_2}{\partial x} & \frac{\partial g_2}{\partial z} \end{vmatrix}(x_0,y_0,z_0)} \quad (dx = A{\cdot}dY \text{ and } dZ = B{\cdot}dy) \tag{10}$$

The M value becomes:

$$M = \left(A^2\frac{\partial^2 F}{\partial x^2} + \frac{\partial^2 F}{\partial y^2} + B^2\frac{\partial^2 F}{\partial z^2} + 2B\frac{\partial^2 F}{\partial y \partial z} + 2AB\frac{\partial^2 F}{\partial x \partial z} + 2A\frac{\partial^2 F}{\partial x \partial y}\right)_{(x_0,y_0,z_0)} \quad \left(d^2F_{(x_0,y_0,z_0)} = M{\cdot}dy^2\right) \tag{11}$$

- Case *dz* free (*dx* and *dy* function of *dz*): we write the 2×2 system in (*dx*, *dy*) and we obtain, solving by Cramer (step 3, here-upper), the intermediate constants *A* and *B*:

$$A = \frac{\begin{vmatrix} -\frac{\partial g_1}{\partial z} & \frac{\partial g_1}{\partial y} \\ -\frac{\partial g_2}{\partial z} & \frac{\partial g_2}{\partial y} \end{vmatrix}(x_0,y_0,z_0)}{\begin{vmatrix} \frac{\partial g_1}{\partial x} & \frac{\partial g_1}{\partial y} \\ \frac{\partial g_2}{\partial x} & \frac{\partial g_2}{\partial y} \end{vmatrix}(x_0,y_0,z_0)} \text{ and } B = \frac{\begin{vmatrix} \frac{\partial g_1}{\partial x} & -\frac{\partial g_1}{\partial z} \\ \frac{\partial g_2}{\partial x} & -\frac{\partial g_2}{\partial z} \end{vmatrix}(x_0,y_0,z_0)}{\begin{vmatrix} \frac{\partial g_1}{\partial x} & \frac{\partial g_1}{\partial y} \\ \frac{\partial g_2}{\partial x} & \frac{\partial g_2}{\partial y} \end{vmatrix}(x_0,y_0,z_0)} \quad (dx = A{\cdot}dz \text{ and } dy = B{\cdot}dz) \tag{12}$$

The M value becomes:

$$M = \left(A^2\frac{\partial^2 F}{\partial x^2} + B^2\frac{\partial^2 F}{\partial y^2} + \frac{\partial^2 F}{\partial z^2} + 2B\frac{\partial^2 F}{\partial y \partial z} + 2A\frac{\partial^2 F}{\partial x \partial z} + 2AB\frac{\partial^2 F}{\partial x \partial y}\right)_{(x_0,y_0,z_0)} \quad \left(d^2F_{(x_0,y_0,z_0)} = M{\cdot}dz^2\right) \tag{13}$$

3.4. Algorithm for One Constraint in 2D

We finally consider the case of a function of two variables subject to a single equality constraint. The constrained optimization problem takes the form *minimize/maximize f(x,y) subject to g(x,y) = 0*, $x, y \in \boldsymbol{R}$.

In this situation, the calculus is much more simplified; after repeating the first two steps of the algorithm, we continue with the calculation of the second derivatives of the

https://doi.org/10.3390/vehicles8060131

Lagrangian and of the constant $K = -\frac{\frac{\partial g}{\partial x}(x_0,y_0)}{\frac{\partial g}{\partial y}(x_0,y_0)}$ $(dy = K{\cdot}dx)$, then we calculate the test coefficient M:

$$M = \left(\frac{\partial^2 F}{\partial x^2} + K^2\frac{\partial^2 F}{\partial y^2} + 2K\frac{\partial^2 F}{\partial x \partial y}\right)_{(x_0,y_0)} \tag{14}$$

and we decide if the stationary point is a maximum constraint/minimum constraint/ degenerate point, using the same test as above (step 5 here-upper).

Remark 4. *If $\frac{\partial g}{\partial y}(x_0, y_0) = 0$, then the constraint implies dx = 0 at the critical point. Consequently, the second differential reduces to $d^2F_{(x_0,y_0)} = a_{22}{\cdot}dy^2$; therefore, the nature of the stationary point is determined by the sign of $a_{22} = \frac{\partial^2 F}{\partial y^2}(x_0, y_0)$.*

Remark 5. *Degenerate cases must be addressed through a direct analysis of the sign of the difference f(x,y) − f(x$_0$,y$_0$) (or f(x,y,z) − f(x$_0$,y$_0$,z$_0$), respectively). Such situations are inherently more complex and cannot be readily addressed through algorithmic procedures. Instead, they require case-by-case examination, often involving local analysis of the function's behavior near the point of interest.*

3.5. Illustrative Mathematical Example

This example illustrates how the proposed algorithm classifies a constrained extremum in a case where the second-order differential of the Lagrangian is not definite. In such cases, the classification requires taking the constraint tangent directions into account. The example shows how the proposed coefficients perform this reduction in an explicit algorithmic form.

We will consider the extreme values of the function *f:* $\boldsymbol{R}^3 \to \boldsymbol{R}$, *f(x,y,z) = xyz, x,y,z* $\neq 0$, subject to $x + y + z = 3$. The associated Lagrangian is $F(x,y,z) = xyz + \lambda{\cdot}(x + y + z - 3)$ and the Fermat system

$$\begin{cases} \frac{\partial F}{\partial x}(x,y,z) = yz + \lambda = 0 \\ \frac{\partial F}{\partial y}(x,y,z) = xz + \lambda = 0 \\ \frac{\partial F}{\partial z}(x,y,z) = xy + \lambda = 0 \\ g(x,y,z) = x + y + z - 3 = 0 \end{cases} \tag{15}$$

gives a single stationary point (*1,1,1*), with the corresponding Lagrange multiplier value $\lambda = -1$. The d^2F differential is: $d^2F_{(x,y,z)} = 2z\cdot dxdy + 2y\cdot dxdz + 2\,x{\cdot}dydz$, which has the form, at the stationary point, $d^2F_{(x,y,z)} = 2{\cdot}dxdy + 2{\cdot}dxdz + 2{\cdot}dydz$. This quadratic form is neither positive nor negative definite in the full space. Therefore, the classification must be performed on the tangent directions allowed by the constraint. Rather than constructing the corresponding bordered Hessian or explicitly writing the total differential of the constraint and substituting the resulting relation into the quadratic form, we apply the algorithmic coefficients introduced in Section 3.2 and calculate the constants

$$C_1 = -\frac{\frac{\partial g}{\partial x}(1,1,1)}{\frac{\partial g}{\partial z}(1,1,1)} = -1 \text{ and } C_2 = -\frac{\frac{\partial g}{\partial y}(1,1,1)}{\frac{\partial g}{\partial z}(1,1,1)} = -1 \tag{16}$$

then

$$\begin{gathered} A = a_{11} + a_{33}C_1^2 + 2C_1a_{13} = -2 \\ B = (a_{12} + a_{33}C_1C_2 + C_2a_{13} + C_1a_{23}) = -1 \\ C = (a_{22} + a_{33}C_2^2 + 2C_2a_{23}) = -2 \end{gathered} \tag{17}$$

and forming the matrix

$$\begin{pmatrix} A & B \\ B & C \end{pmatrix} = \begin{pmatrix} -2 & -1 \\ -1 & -2 \end{pmatrix} \tag{18}$$

https://doi.org/10.3390/vehicles8060131

Testing the positivity/negativity of d^2F to the stationary point gives $A = -2 < 0$ and $AC - B^2 = 3 > 0$; therefore, we have a maximum constrained point in (*1*,*1*,*1*).

This example highlights how the proposed algorithm provides a direct operational classification by incorporating the constraint tangent information into explicit algebraic coefficients.

4. Methodology and Computational Workflow

The proposed constrained optimization algorithms are fully algorithmic and can be efficiently implemented in standard symbolic or numerical computation environments. In this work, the implementation was carried out using the Maple programming environment [15]; however, the algorithms are not software-dependent and can be readily implemented in other platforms such as MATLAB, Mathematica, or Python (e.g., using SymPy [16]).

Rather than relying on software-specific features, the implementation follows a simple and transparent computational workflow, summarized as follows:

1. Problem definition—define the objective function f and the constraint function(s) g (g_1, g_2).
2. Lagrangian construction—build the Lagrangian function associated with the constrained problem.
3. First-order analysis—solve the Fermat system to obtain the candidate stationary points and the corresponding Lagrange multiplier(s).
4. Computation of test coefficients—compute the algebraic test coefficients (A, B, C or M) using partial derivatives of the Lagrangian and the constraint functions, according to the relevant algorithm described in Section 3. Before applying the classification test, check the regularity and non-degeneracy assumptions stated in Section 3.1. In particular, the relevant constraint gradients or Jacobian minors must satisfy the required nonzero conditions. Degenerate stationary points require a separate local analysis.
5. Classification of stationary points—classify each candidate point as a constrained minimum, maximum, saddle point, or degenerate case based on the sign of the corresponding test coefficient(s).

This workflow ensures fast and reliable classification of constrained extrema while avoiding, during the application phase, both the explicit construction of bordered Hessians and the repeated manipulation of the total differentials of the constraints.

5. Application to a Transport Depot Location Problem

5.1. Problem Description

To illustrate the practical relevance of the proposed constrained optimization algorithms, we consider a depot location problem in transport logistics. The objective is to determine the optimal location of a distribution warehouse under a geometric infrastructure constraint.

The case study focuses on the South-West Oltenia region and involves five cities: Craiova (reference point), Slatina, Râmnicu Vâlcea, Târgu Jiu, and Drobeta Turnu Severin. Similar regional logistics-center siting studies can be found in the recent literature [17]. Each city is characterized by planar coordinates (x_i, y_i) and an associated weight ω_i, representing its relative transport demand. Distances are measured using the Euclidean metric (Table 1).

The depot must be located at a fixed distance of 5 km from the E70 highway. This requirement reflects practical infrastructure and planning constraints commonly encountered in transport logistics. The case study is geographically motivated and uses real regional locations in South-West Oltenia. Craiova is taken as the origin of a local planar coordinate

https://doi.org/10.3390/vehicles8060131

system, and the other city coordinates are expressed relative to this reference point. The line used to model the E70 highway is a local linear approximation of its real trajectory in the area considered. The weights are used as relative demand coefficients motivated by practical regional-demand considerations around Craiova. They are not obtained from a fully calibrated logistics dataset, but they are chosen to reflect plausible differences in demand intensity among the considered cities while keeping the model transparent and focused on the classification procedure. Thus, the example should be understood as a realistic illustrative transport location model, rather than as a fully calibrated logistics optimization study involving detailed traffic flows, network distances, or GIS-based cost functions.

Table 1. Depot distances and weights.

City	x_i	y_i	ω_i
Craiova	0	0	24
Slatina	52	0	6
Râmnicu Vâlcea	60	105	9
Târgu Jiu	−55	95	7
Drobeta Turnu Severin	−111	0	8

5.2. Model Formulation

We model the transportation cost $f(x, y)$ as a weighted sum of squared Euclidean distances from the depot (x, y) to the five cities.

$$\begin{array}{c} f(x,y) = \sum_{i=1}^{5} w_i\Big((x-x_i)^2 + (y-y_i)^2\Big) = 24\Big((x-0)^2 + (y-0)^2\Big) + 6\Big((x-52)^2 + (y-0)^2\Big) + \\ 9\Big((x-60)^2 + (y-105)^2\Big) + 7\Big((x+55)^2 + (y-95)^2\Big) + 8\Big((x+111)^2 + (y-0)^2\Big) \end{array} \quad (19)$$

Each term corresponds to one city, with its own weight. The depot location that minimizes this function gives the optimal solution.

The infrastructure constraint is expressed as a fixed-distance condition (5 km) relative to the E70 highway. This means that $\frac{|x-9y-35|}{\sqrt{82}} = 5$, which will give a constraint function: $g(x,y) = (x-9y-35)^2 - 2050$.

The resulting constrained optimization problem is solved using the algorithm described in Section 3.4. The computational workflow follows the steps outlined in Section 4: construction of the Lagrangian, solution of the Fermat system, computation of the test coefficient M, and classification of the stationary points.

The Lagrangian is $\mathcal{L}(x,y,\lambda) = f(x,y) + \lambda\left((x-9y-35)^2 - 2050\right)$ and the Fermat system:

$$\begin{cases} \frac{\partial \mathcal{L}}{\partial x} = \sum_{i=1}^{5} 2\omega_i(x-x_i) + 2\lambda(x-9y-35) = 0 \\ \frac{\partial \mathcal{L}}{\partial y} = \sum_{i=1}^{5} 2\omega_i(y-y_i) - 18\lambda(x-9y-35) = 0 \\ g(x,y) = 0 \end{cases} \quad (20)$$

This system can be simplified using some notations. We note: $\omega = \sum_{i=1}^{5} \omega_i$, $x_{bar} = \frac{\sum_{i=1}^{5} x_i\omega_i}{\omega}$, $y_{bar} = \frac{\sum_{i=1}^{5} y_i\omega_i}{\omega}$, $u = x - 9y - 35$. With these notations, the expressions become shorter and easier to use.

Remark 6. $\sum_{i=1}^{5} \omega_i(x-x_i) = \omega(x-x_{bar})$ *and* $\sum_{i=1}^{5} \omega_i(y-y_i) = \omega(y-y_{bar})$.

This is the simplified Fermat system:

https://doi.org/10.3390/vehicles8060131

$$\begin{cases} \frac{\partial \mathcal{L}}{\partial x} = \omega(x - x_{bar}) + \lambda u = 0 \\ \frac{\partial \mathcal{L}}{\partial y} = \omega(y - y_{bar}) - 9\lambda u = 0 \\ u^2 = 2050 \end{cases} \quad (21)$$

The equations now look more compact. From equation three, we see that $u = \pm 5\sqrt{82}$, and from the first two equations, we get that $x = x_{bar} - \frac{\lambda u}{\omega}$ and $y = y_{bar} + \frac{9\lambda u}{\omega}$. Now we substitute the expressions of x and y into u: $u = x - 9y - 35 = x_{bar} - \frac{\lambda u}{\omega} - 9y_{bar} - \frac{81\lambda u}{\omega} - 35 = (x_{bar} - 9y_{bar} - 35) - \frac{82\lambda u}{\omega}$.

With this, we introduce a new notation: $v = x_{bar} - 9y_{bar} - 35$ and we can thus express lambda as $\lambda = \frac{\omega}{82}\left(\frac{v}{u} - 1\right)$.

Table 2 shows the main elements of the model: on the left, we have the known data: the city coordinates and their weights; from these, we deduce ω, x_{bar}, y_{bar}, and v; then, with u, we can compute λ, and finally, on the right side, we obtain the formulas for the stationary points' coordinates, x and y.

Table 2. The main elements of the model.

Known	Deduced	Solutions (Stationary Points)
x_i	$\omega = \sum_{i=1}^{5} \omega_i$	$x = x_{bar} - \frac{\lambda u}{\omega}$
y_i	$x_{bar} = \frac{\sum_{i=1}^{5} x_i \omega_i}{\omega}$	$y = y_{bar} + \frac{9\lambda u}{\omega}$
ω_i	$y_{bar} = \frac{\sum_{i=1}^{5} y_i \omega_i}{\omega}$	
$u = \pm 5\sqrt{82}$	$v = x_{bar} - 9y_{bar} - 35$	
	$\lambda = \frac{\omega}{82}\left(\frac{v}{u} - 1\right)$	

For the stationary points, we introduce an intermediate constant, noted D. This constant encodes the tangent relation induced by the constraint and is computed from the first-order partial derivatives of the constraint function. With this constant, we can compute the test coefficient M. M combines the second derivatives of the Lagrangian in a single expression (Table 3). Finally, the sign of M tells us how to classify the stationary point.

Table 3. The test coefficient M.

Stationary Points	Intermediate Constant	Test Coefficient M (Sign Analysis)
$(x_i, y_i),\ i = 1, 2$	$D = -\frac{\frac{\partial g}{\partial x}(x_i, y_i)}{\frac{\partial g}{\partial y}(x_i, y_i)}$	$M = \left(\frac{\partial^2 \mathcal{L}}{\partial x^2} + D^2 \frac{\partial^2 \mathcal{L}}{\partial y^2} + 2D \frac{\partial^2 \mathcal{L}}{\partial x \partial y}\right)_{(x_i, y_i)}$
$u_i = \pm 5\sqrt{82}$		

5.3. Results and Discussion

The algorithm yields two candidate stationary points, P_1 = (*−4.55*, *0.63*) and P_2 = (*−3.44*, *−9.30*), satisfying the constraint. Both points are classified as constrained local minima ($M > 0$); however, one of them leads to a lower total transportation cost. This is consistent with the geometry of the fixed-distance constraint. The equation defining a fixed distance from the highway represents two feasible branches, located on opposite sides of the reference line. The second-order test classifies each stationary point locally on its corresponding feasible branch. The comparison of the objective function values is then used to select the better depot location among the two locally feasible candidates. The corresponding objective function values are $f(P_1)$ = *326,026.73* and $f(P_2)$ = *363,133.93*. Since $f(P_1) < f(P_2)$, the point $P_1 \approx$ (*−4.55, 0.63*) is selected as the optimal depot location. This corresponds to a position about *4.55* km west and *0.63* km north of Craiova. This location

https://doi.org/10.3390/vehicles8060131

represents the best compromise between minimizing weighted transportation costs and satisfying the infrastructure constraint imposed by the E70 highway.

Figure 1 illustrates the case study, showing the city locations, the highway constraint (represented by two parallel lines), and the candidate depot locations. The optimal solution is clearly identifiable as the point yielding the lowest transportation cost.

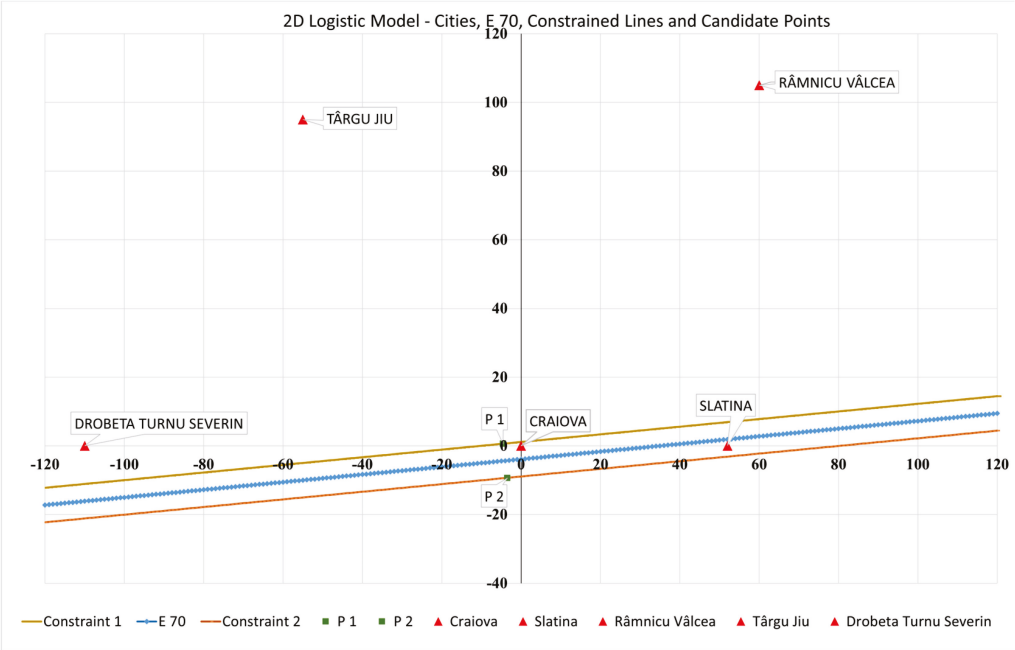

Figure 1. Plot of the case study.

5.4. Extension to the Three-Dimensional Case

The same modeling approach naturally extends to three-dimensional location problems, where the depot is described by coordinates (x,y,z), with z representing the altitude. The objective function becomes:

$$f(x,y,z) = \sum_{i=1}^{5} w_i \left((x - x_i)^2 + (y - y_i)^2 + (z - z_i)^2 \right) \quad (22)$$

while the constraint remains identical, as it depends only on the planar coordinates.

In this case, the Fermat system shows that the optimal altitude of the depot is simply the weighted average of the cities' altitudes. Applying the algorithm described in Section 3.2 (full symbolic computations are provided in Appendix B) leads to two candidate constrained minima, among which the point $(-14.15; -0.43; 0.1046)$ yields the lowest transportation cost and is therefore selected as the optimal depot location.

This result highlights the flexibility of the proposed approach and its ability to handle both 2D and 3D transport location problems within a unified algorithmic framework.

6. Discussion

From a methodological perspective, the proposed approach can be compared to classical second-order optimality tests based on bordered Hessians. The proposed framework does not claim to introduce a new general second-order theory for constrained optimization. Its contribution lies in the explicit organization of low-dimensional regular cases into operational algorithms that can be applied directly in engineering-oriented calculations. In this sense, the value of the approach is computational and methodological: it reorganizes known constrained second-order principles into a reproducible procedure that reduces repeated symbolic manipulation. This distinction is particularly relevant in the case of three

variables with two equality constraints, where the classical bordered Hessian has order five. Even in such a low-dimensional setting, the symbolic construction and evaluation of such determinants may become cumbersome, whereas the proposed formulation reduces the classification to the evaluation of a scalar coefficient M.

While these traditional methods provide a complete theoretical framework, they often involve bordered Hessian constructions, high-order determinants, and the explicit manipulation of the total differentials of the constraints, which can become cumbersome in practical applications.

In contrast, the proposed algorithms reduce the classification step to the evaluation of simple algebraic coefficients derived from partial derivatives of the Lagrangian. This leads to improved transparency and reduced symbolic complexity, making the approach more accessible for engineering-oriented applications. This operational simplification is formulated within the standard regular non-degenerate setting of classical second-order constrained optimality tests and is restricted here to low-dimensional cases. Degenerate or singular cases are not specific limitations of the proposed formulation and, as in the classical approach, require a separate local analysis.

The results obtained in the transport location case study are consistent with classical constrained optimization approaches, in the sense that the identified optimal solution corresponds to the constrained projection of an unconstrained optimum onto the feasible set. This agreement confirms that the proposed method preserves the expected theoretical behavior while offering a simplified computational framework.

From a computational perspective, the algorithms are particularly well suited to transport and logistics location problems, where the number of decision variables is typically limited to two or three and constraints often have a clear geometric interpretation [18]. In such settings, the proposed approach leads to transparent calculations, reduced symbolic complexity, and improved robustness against algebraic errors, which are common drawbacks of classical second-order tests.

A key advantage of the proposed framework is its unified treatment of regular constrained extrema, including cases where the second-order differential of the Lagrangian is not definite. As illustrated by the mathematical example in Section 3.5, the classification must then be performed along the tangent directions induced by the constraint. The proposed algorithms encode this tangent information directly into algebraic coefficients, avoiding the repeated explicit manipulation of constraint differentials during the application phase [9].

From an implementation standpoint, the algorithms are lightweight and software-independent. Although Maple was used in this work for symbolic implementation and validation, the computational workflow relies only on elementary operations, partial derivatives, solving systems, and low-order determinants, making the approach easily transferable to other computational environments or even suitable for manual verification in simple cases.

The transport depot location case study demonstrates how the proposed methods can be used as decision-support tools in realistic planning scenarios involving infrastructure constraints. The results show that the algorithms naturally recover the well-known geometric interpretation of constrained location problems, namely the projection of an unconstrained optimum onto the feasible set defined by the constraint [19–21], while providing a rigorous classification of candidate solutions.

The scope of the proposed algorithms is intentionally limited to regular non-degenerate cases in low-dimensional settings, where classical second-order classification tests are directly applicable. Degenerate or singular situations require a separate local analysis, as in the classical approach, and are not a specific limitation of the proposed

formulation. A natural direction for future research is the extension of the operational framework to higher-dimensional constrained optimization problems.

To further clarify the computational positioning of the proposed approach relative to classical constrained second-order methods, the main differences can be summarized as follows.

From a comparative perspective, classical constrained optimization methods and the proposed approach share the same initial step, namely the construction and solution of the Fermat system to identify candidate stationary points.

The main difference lies in the classification stage. In classical Lagrange-based approaches, this step relies on the analysis of the second differential of the Lagrangian, either through bordered Hessian matrices or through the explicit manipulation of the total differentials of the constraints and their substitution into the second-order form. These operations may involve high-order determinants and can become computationally demanding and less transparent, particularly in practical applications.

In contrast, the proposed method reformulates the low-dimensional classification step through the evaluation of simple algebraic coefficients derived from the same constrained second-order framework. This reformulation avoids the explicit construction of bordered Hessians and the explicit writing and manipulation of the total differentials of the constraints during the application phase, thereby significantly reducing symbolic complexity.

As a result, while classical methods provide the general theoretical framework, the proposed approach offers a simpler and more transparent operational formulation for low-dimensional regular problems. This makes it particularly suitable for engineering-oriented applications, where ease of implementation and robustness against algebraic errors are important considerations.

7. Conclusions

This study achieves its stated objective of providing simplified and explicit algorithmic procedures for the classification of constrained extrema in low-dimensional optimization problems.

The proposed approach provides a practical low-dimensional operational reformulation of the classification step in classical constrained second-order analysis. In the regular cases considered here, the classification is performed without explicitly constructing bordered Hessians and without writing and manipulating the total differentials of the constraints during the application phase; the required constraint information is encoded in algebraic coefficients computed from first-order partial derivatives. The main contribution is the explicit organization of the regular low-dimensional cases into simple algebraic test coefficients derived from the constrained second-order framework, enabling a unified and transparent classification procedure.

The applicability of the proposed framework was demonstrated through a transport depot location problem under a geometric infrastructure constraint related to the E70 highway. The results illustrate how the method can serve as a transparent decision-support tool for transport and logistics engineers, providing candidate solutions and a clear classification rule without heavy symbolic manipulations.

As in classical extremum-finding procedures, degenerate cases cannot be handled by simple algorithmic criteria and require case-specific local analysis.

The methodology was illustrated through a compact mathematical example and through a transport depot location problem under a geometric infrastructure constraint. Although the implementations provided in this work were developed in Maple (version 2022.2), the proposed workflow is not software-dependent and can be implemented in

https://doi.org/10.3390/vehicles8060131

other environments such as MATLAB, Mathematica, or Python (e.g., SymPy [16]), enabling fast and reproducible computations while reducing the risk of algebraic errors.

In transport and logistics, the proposed algorithms can support constrained location problems such as depot siting, as well as related planning tasks where low-dimensional geometric constraints arise. Future work includes the systematic treatment of singular/degenerate configurations, extensions to higher-dimensional formulations, and integration into decision-support tools (e.g., lightweight software modules coupled with GIS data) for practical deployment in transport planning contexts. Related sustainability and resilience-driven location-routing directions are discussed, for example, in [22].

Author Contributions: Conceptualization, M.R.; Methodology, M.R.; Software, M.R. and L.M.; Validation, LM.; Formal analysis, I.D.; Investigation, T.O., N.G. and L.R.; Resources, N.G. and L.R.; Data curation, I.D.; Writing—review & editing, L.R. All authors have read and agreed to the published version of the manuscript.

Funding: This research received no external funding.

Data Availability Statement: The original contributions presented in this study are included in the article. Further inquiries can be directed to the corresponding author.

Conflicts of Interest: The authors declare no conflict of interest.

Appendix A. Maple Implementation for the Two-Dimensional Transport Depot Location Case

This appendix presents a Maple implementation of the algorithm described in Section 3.4, applied to the constrained optimization problem associated with the two-dimensional transport depot location case discussed in Section 5.

```
F := (x, y, lambda) -> 38*y^2 + 24*x^2 + 6*(x - 52)^2 + 9*(x - 60)^2 + 9*(y - 105)^2 + 7*(x + 55)^2 + 7*(y - 95)^2 + 8*(x + 111)^2 + lambda*((x - 9*y - 35)^2 - 2050);
g := (x, y) -> (x - 9*y - 35)^2 - 2050;
Fx := diff(F(x, y, lambda), x);
Fy := diff(F(x, y, lambda), y);
Flambda := diff(F(x, y, lambda), lambda);
f0 := (x, y) -> 38*y^2 + 24*x^2 + 6*(x - 52)^2 + 9*(x - 60)^2 + 9*(y - 105)^2 + 7*(x + 55)^2 + 7*(y - 95)^2 + 8*(x + 111)^2;
sol_xy := solve({Fx = 0, Fy = 0}, {x, y});
eq_lambda := subs(sol_xy, Flambda);
lam_roots := [solve(eq_lambda = 0, lambda)];
sol_raw := [seq(subs(lambda = L, sol_xy) union {lambda = L}, L in lam_roots)];
FilterReal := proc(S)
local X, Y, L;
X := evalf(subs(S, x)):
Y := evalf(subs(S, y)):
L := evalf(subs(S, lambda)):
if (type(X, complex) and abs(Im(X)) > 1e-8) or
(type(Y, complex) and abs(Im(Y)) > 1e-8) or
(type(L, complex) and abs(Im(L)) > 1e-8) then return NULL;
else return {lambda = Re(L), x = Re(X), y = Re(Y)};
end if; end proc;
sol := [seq(FilterReal(S), S in sol_raw)]:
for i to nops(sol) do
```

https://doi.org/10.3390/vehicles8060131

```
    printf("Solution %d: x=%.6f, y=%.6f, lambda=%.6f\n", i, evalf(subs(sol[i], x)),
evalf(subs(sol[i], y)), evalf(subs(sol[i], lambda)));
end do:
gx := diff(g(x, y), x);
gy := diff(g(x, y), y);
H11 := D[1, 1](F)(x, y, lambda);
H12 := D[1, 2](F)(x, y, lambda);
H22 := D[2, 2](F)(x, y, lambda);
for i to nops(sol) do
    Xs := evalf(subs(sol[i], x)):
    Ys := evalf(subs(sol[i], y)):
    Ls := evalf(subs(sol[i], lambda)):
    g1 := evalf(subs({x = Xs, y = Ys}, gx));
    g2 := evalf(subs({x = Xs, y = Ys}, gy));
    a11 := evalf(subs({lambda = Ls, x = Xs, y = Ys}, H11));
    a12 := evalf(subs({lambda = Ls, x = Xs, y = Ys}, H12));
    a22 := evalf(subs({lambda = Ls, x = Xs, y = Ys}, H22));
    if abs(g2) > 1e-10 then
        D := -g1/g2:
        M := D^2*a22 + 2*D*a12 + a11:
    elif abs(g1) > 1e-10 then
        K := -g2/g1:
        M := K^2*a11 + 2*K*a12 + a22:
    else
        M := Float(undefined):
    end if:
    printf("\n Critical point %d: x=%.6f, y=%.6f  ->  M = %.6f  --> ", i, Xs, Ys, evalf(M));
    if type(M, float) and evalf(M) >0 then
        print("Constrained minimum");
    elif type(M, float) and evalf(M) < 0 then
        print("Constrained maximum");
    else
        print("degenerate point");
    end if;
    fval := evalf(f0(Xs, Ys)):
    printf("Value of f(x,y): %.6f\n", fval);
end do:
```

Appendix B. Three-Dimensional Transport Depot Location Case (Details)

Appendix B.1. Data and Notations

Each city is described by its coordinates x, y, and z, together with a weight, representing its relative demand. The z coordinate represents the altitude, in hundreds of meters.

Table A1. Depot distances and weights.

City	x_i	y_i	z_i	ω_i
Craiova	0	0	0.100	8
Slatina	40	30	0.165	5
Caracal	50	−20	0.120	3
Filiași	−20	15	0.110	3
Drobeta Turnu Severin	−110	0	0.050	6

https://doi.org/10.3390/vehicles8060131

We note: $\omega = \sum_{i=1}^{5} \omega_i$, $x_{bar} = \frac{\sum_{i=1}^{5} x_i \omega_i}{\omega}$, $y_{bar} = \frac{\sum_{i=1}^{5} y_i \omega_i}{\omega}$, $z_{bar} = \frac{\sum_{i=1}^{5} z_i \omega_i}{\omega}$, $u = x - 9y - 35$.

Appendix B.2. Lagrangian and Fermat System

The Lagrangian is $\mathcal{L}(x, y, z, \lambda) = f(x, y, z) + \lambda \left((x - 9y - 35)^2 - 2050 \right)$, and the Fermat system in three variables becomes:

$$\begin{cases} \frac{\partial \mathcal{L}}{\partial x} = \sum_{i=1}^{5} 2\omega_i (x - x_i) + 2\lambda (x - 9y - 35) = 0 \\ \frac{\partial \mathcal{L}}{\partial y} = \sum_{i=1}^{5} 2\omega_i (y - y_i) - 18\lambda (x - 9y - 35) = 0 \\ \frac{\partial \mathcal{L}}{\partial z} = \sum_{i=1}^{5} 2\omega_i (z - z_i) = 0 \\ g(x, y) = 0 \end{cases} \tag{A1}$$

Using the above notations, it becomes easier to handle:

$$\begin{cases} \frac{\partial \mathcal{L}}{\partial x} = \omega (x - x_{bar}) + \lambda u = 0 \\ \frac{\partial \mathcal{L}}{\partial y} = \omega (y - y_{bar}) - 9\lambda u = 0 \\ \frac{\partial \mathcal{L}}{\partial z} = \omega (z - z_{bar}) = 0 \\ u^2 = 2050 \end{cases} \tag{A2}$$

We now have four equations and we will have: $u = \pm 5\sqrt{82}$, $x = x_{bar} - \frac{\lambda u}{\omega}$, $y = y_{bar} + \frac{9\lambda u}{\omega}$, $z = z_{bar}$.

So, in 3D, the altitude of the depot is simply the weighted average of the cities' altitudes.

Appendix B.3. Classification of Stationary Points

Each stationary point is classified using the algorithm for one constraint in 3D (Section 3.2). In brief, for each candidate point, we compute the constants C_1, C_2, derived from the constraint, and the reduced quadratic-form coefficients A, B, C. The signs of A and $AC - B^2$ determine whether the point is a constrained local minimum, maximum, saddle point, or degenerate case (see Section 3.2).

Table A2. Stationary points.

Stationary Points	**Intermediate Constants**	**Test Coefficients *A*, *B*, *C* (Sign Analysis)**
(x_i, y_i, z_i), $i = 1, 2$	$C_1 = -\frac{\frac{\partial g}{\partial x}(x_i, y_i, z_i)}{\frac{\partial g}{\partial z}(x_i, y_i, z_i)}$	$A = \frac{\partial^2 \mathcal{L}}{\partial x^2} + \frac{\partial^2 \mathcal{L}}{\partial z^2} C_1^2 + 2C_1 \frac{\partial^2 \mathcal{L}}{\partial x \partial z}$
	$C_2 = -\frac{\frac{\partial g}{\partial y}(x_i, y_i, z_i)}{\frac{\partial g}{\partial z}(x_i, y_i, z_i)}$	$B = \frac{\partial^2 \mathcal{L}}{\partial z^2} C_1 C_2 + \frac{\partial^2 \mathcal{L}}{\partial x \partial z} C_2 + \frac{\partial^2 \mathcal{L}}{\partial y \partial z} C_1 + \frac{\partial^2 \mathcal{L}}{\partial x \partial y}$
		$C = \frac{\partial^2 \mathcal{L}}{\partial y^2} + \frac{\partial^2 \mathcal{L}}{\partial z^2} C_2^2 + 2C_2 \frac{\partial^2 \mathcal{L}}{\partial y \partial z}$
$u_{1,2} = \pm 5\sqrt{82}$		Signs of A and $AC - B^2$

Appendix B.4. Numerical Results

For the considered dataset, the algorithm yields two candidate stationary points, P_1: $(-14.15; -0.43; 0.1046)$ and P_2: $(-13.04; -10.36; 0.1046)$. Both points satisfy the constraint, so they are located near the E70 highway. Both are classified as constrained local minima, but P_1 gives the lowest transportation cost. So, the optimal depot location is P_1.

Appendix C. Maple Implementation for the Three-Dimensional Transport Depot Location Case

This appendix presents a Maple implementation of the algorithm described in Section 3.2, applied to the constrained optimization problem associated with the three-

https://doi.org/10.3390/vehicles8060131

dimensional transport depot location case discussed in Section 5.4 and further detailed in Appendix B.

```
print(The*Lagrangian*is);
F := (x, y, z, lambda) -> 8*x^2 + 14*y^2 + 8*(z - 0.1)^2 + 5*(x - 40)^2 + 5*(y - 30)^2 + 5*(z -
0.165)^2 + 3*(x - 50)^2 + 3*(y + 20)^2 + 3*(z - 0.12)^2 + 3*(x + 20)^2 + 3*(y - 15)^2 + 3*(z -
0.11)^2 + 6*(x + 110)^2 + 6*(z - 0.05)^2 + lambda*((x - 9*y - 35)^2 - 2050);
print(The*constraint*is);
g := (x, y, z) -> (x - 9*y - 35)^2 - 2050;
print(The*partial*derivatives*of*F*are);
Fx := diff(F(x, y, z, lambda), x);
Fy := diff(F(x, y, z, lambda), y);
Fz := diff(F(x, y, z, lambda), z);
Flambda := diff(F(x, y, z, lambda), lambda);
print(Solutions*of*the*Fermat*system);
sols := [solve({Flambda = 0, Fx = 0, Fy = 0, Fz = 0}, {lambda, x, y, z})]:
for i to nops(sols) do
    print(sols[i]);
end do:
print(The*partial*derivatives*of*the*constraint*function);
gx := diff(g(x, y, z), x);
gy := diff(g(x, y, z), y);
gz := diff(g(x, y, z), z);
print(Hessian*of*the*Lagrangian);
H11 := D[1, 1](F)(x, y, z, lambda);
H12 := D[1, 2](F)(x, y, z, lambda);
H13 := D[1, 3](F)(x, y, z, lambda);
H22 := D[2, 2](F)(x, y, z, lambda);
H23 := D[2, 3](F)(x, y, z, lambda);
H33 := D[3, 3](F)(x, y, z, lambda);
eps := 1e-10:
for i to nops(sols) do
    print(Study*of*the*critical*point*sols[i]);
    Xs := evalf(subs(sols[i], x)):
    Ys := evalf(subs(sols[i], y)):
    Zs := evalf(subs(sols[i], z)):
    Ls := evalf(subs(sols[i], lambda)):
    g1 := evalf(subs({x = Xs, y = Ys, z = Zs}, gx)):
    g2 := evalf(subs({x = Xs, y = Ys, z = Zs}, gy)):
    g3 := evalf(subs({x = Xs, y = Ys, z = Zs}, gz)):
    a11 := evalf(subs({lambda = Ls, x = Xs, y = Ys, z = Zs}, H11)):
    a12 := evalf(subs({lambda = Ls, x = Xs, y = Ys, z = Zs}, H12)):
    a13 := evalf(subs({lambda = Ls, x = Xs, y = Ys, z = Zs}, H13)):
    a22 := evalf(subs({lambda = Ls, x = Xs, y = Ys, z = Zs}, H22)):
    a23 := evalf(subs({lambda = Ls, x = Xs, y = Ys, z = Zs}, H23)):
    a33 := evalf(subs({lambda = Ls, x = Xs, y = Ys, z = Zs}, H33)):
    if abs(g3) > eps then
        C1 := -g1/g3:
        C2 := -g2/g3:
        A := C1^2*a33 + 2*C1*a13 + a11:
        C := C2^2*a33 + 2*C2*a23 + a22:
```

https://doi.org/10.3390/vehicles8060131

```
            B := C1*C2*a33 + C1*a23 + C2*a13 + a12:
            D1 := A:
            D2 := A*C - B^2:
            printf("gz != 0: A=%.6f, B=%.6f, C=%.6f, D1=%.6f, D2=%.6f\n", A, B, C, D1,
D2);
        elif abs(g2) > eps then
            Cxy := -g1/g2:
            A1 := Cxy^2*a22 + 2*Cxy*a12 + a11:
            C1m := a33:
            B1 := Cxy*a23 + a13:
            D1 := A1:
            D2 := A1*C1m - B1^2:
            printf("gz = 0, gy != 0: A' = %.6f, B' = %.6f, C' = %.6f, D1=%.6f, D2=%.6f\n", A1,
B1,  C1m, D1, D2);
        elif abs(g1) > eps then
            A2 := a22:
            C2m := a33:
            B2 := a23:
            D1 := A2:
            D2 := A2*C2m - B2^2:
            printf("gz = 0, gy = 0, gx != 0: A2 = %.6f, B2 = %.6f, C2 = %.6f, D1=%.6f,
D2=%.6f\n",  A2, B2, C2m, D1, D2);
        else
            print("degenerate case: gx=gy=gz=0");
            next;
        end if;
        if D2 < 0 then
            print(critical*point*sols[i]*is*a*saddle*point);
        elif D1 > 0 and D2 > 0 then
            print(critical*point, sols[i], is*a*minimum*point);
        elif D1 < 0 and D2 > 0 then
            print(critical*point*sols[i]*is*a*maximum*point);
        else
            print(critical*point*sols[i], is*a*degenerate*point);
        end if;
    end do:
```

References

1. Adeleke, O.J.; Olukanni, D.O. Facility Location Problems: Models, Techniques, and Applications in Waste Management. *Recycling* **2020**, *5*, 10. [CrossRef]
2. Gao, X.; Park, C.; Chen, X.; Xie, E.; Huang, G.; Zhang, D. Globally Optimal Facility Locations for Continuous-Space Facility Location Problems. *Appl. Sci.* **2021**, *11*, 7321. [CrossRef]
3. Liu, L.; Lee, L.S.; Seow, H.-V.; Chen, C.Y. Logistics Center Location-Inventory-Routing Problem Optimization: A Systematic Review Using PRISMA Method. *Sustainability* **2022**, *14*, 15853. [CrossRef]
4. Wei, Y.; Xu, Z. Dynamic Facility Location and Allocation Optimization for Sustainable Product-Service Delivery Using Co-Evolutionary Adaptive Genetic Algorithms. *Sustainability* **2025**, *17*, 8000. [CrossRef]
5. Xi, R.; Lv, D.; Yu, Y.; Huang, X.; Wang, Z.; Gu, L.; Zhu, Z.; Zhang, Y. Optimization of Location-Routing for Multi-Vehicle Combinations with Capacity Constraints Based on Binary Equilibrium Optimizers. *Axioms* **2024**, *13*, 31. [CrossRef]
6. Calvete, H.I.; Galé, C.; Hernández, A.; Iranzo, J.A. Bilevel Approach to the Facility Location Problem with Customer Preferences Under a Mill Pricing Policy. *Mathematics* **2024**, *12*, 3459. [CrossRef]
7. Lax, P.D.; Terrell, M.S. *Multivariable Calculus with Applications*; Springer: Berlin/Heidelberg, Germany, 2018. [CrossRef]

8. Maberly, E.D.; Pierce, R.M. An Alternative Approach to Understanding Second-Order Conditions for Constrained Optimization Lagrange Multipliers. *Appl. Math. Lett.* **2004**, *17*, 1397–1401. [CrossRef]
9. Bertsekas, D.P. *Nonlinear Programming*, 3rd ed.; Athena Scientific: Belmont, MA, USA, 2016.
10. Nocedal, J.; Wright, S.J. *Numerical Optimization*, 2nd ed.; Springer: New York, NY, USA, 2006. [CrossRef]
11. Rabe, M.; Gonzalez-Feliu, J.; Chicaiza-Vaca, J.; Tordecilla, R.D. Simulation-Optimization Approach for Multi-Period Facility Location Problems with Forecasted and Random Demands in a Last-Mile Logistics Application. *Algorithms* **2021**, *14*, 41. [CrossRef]
12. Haeser, G.; Oliveira dos Santos, D. A Simple Proof of Existence of Lagrange Multipliers. *arXiv* **2024**, arXiv:2402.05335. [CrossRef]
13. Strang, G. *Introduction to Linear Algebra*, 6th ed.; Wellesley-Cambridge Press: Wellesley, MA, USA, 2023.
14. Rovnyak, S.M.; Chong, E.K.P.; Rovnyak, J. First-Order Conditions for Set-Constrained Optimization. *Mathematics* **2023**, *11*, 4274. [CrossRef]
15. Maplesoft. *Maple Mathematical Software, version 2022.2*; Maplesoft: Waterloo, ON, Canada, 2022; Available online: https://www.maplesoft.com/ (accessed on 21 July 2025).
16. Meurer, A.; Smith, C.P.; Paprocki, M.; Čertík, O.; Kirpichev, S.B.; Rocklin, M.; Kumar, A.; Ivanov, S.; Moore, J.K.; Singh, S.; et al. SymPy: Symbolic Computing in Python. *PeerJ Comput. Sci.* **2017**, *3*, e103. [CrossRef]
17. Zhang, Q.; Mao, H. An Integrated Method for Locating Logistic Centers in a Rural Area. *Sustainability* **2022**, *14*, 5563. [CrossRef]
18. Wang, Y.; Li, Y.; Lu, C. Evaluating the Effects of Logistics Center Location: An Analytical Framework for Sustainable Urban Logistics. *Sustainability* **2023**, *15*, 3091. [CrossRef]
19. Beck, A.; Sabach, S. Weiszfeld's method: Old and new results. *J. Optim. Theory Appl.* **2015**, *164*, 1–40. [CrossRef]
20. Torres, G.A. A Weiszfeld-like Algorithm for a Weber Location Problem Constrained to a Closed and Convex Set. *arXiv* **2013**, arXiv:1204.1087. [CrossRef]
21. Venceslau, H.M.; Venceslau, M.B.K.; Xavier, A.E.; Maculan, N. A geometric perspective of the Weiszfeld algorithm for solving the Fermat–Weber problem. *RAIRO Oper. Res.* **2016**, *50*, 157–173. [CrossRef]
22. Figueiredo, B.; Lopes, R.B.; de Sousa, A. Location–Routing Problems with Sustainability and Resilience Concerns: A Systematic Review. *Logistics* **2025**, *9*, 81. [CrossRef]

Disclaimer/Publisher's Note: The statements, opinions and data contained in all publications are solely those of the individual author(s) and contributor(s) and not of MDPI and/or the editor(s). MDPI and/or the editor(s) disclaim responsibility for any injury to people or property resulting from any ideas, methods, instructions or products referred to in the content.

MDPI AG
Grosspeteranlage 5
4052 Basel
Switzerland
Tel.: +41 61 683 77 34

Vehicles Editorial Office
E-mail: vehicles@mdpi.com
www.mdpi.com/journal/vehicles



Disclaimer/Publisher's Note: The title and front matter of this reprint are at the discretion of the Guest Editors. The publisher is not responsible for their content or any associated concerns. The statements, opinions and data contained in all individual articles are solely those of the individual Editors and contributors and not of MDPI. MDPI disclaims responsibility for any injury to people or property resulting from any ideas, methods, instructions or products referred to in the content.



Academic Open
Access Publishing

www.mdpi.com

ISBN 978-3-7258-8544-2